Electromagnetic Radiation and Its Impact on Cancer Treatment

Thesis submitted to Cardiff University for the degree of Doctor of Philosophy

PhD Candidate: Han Gao

Centre for High Frequency Engineering, School of Engineering, Cardiff University

Cardiff China Medical Research Collaborative, School of Medicine, Cardiff University

Supervisor Team: Prof Johannes Benedikt, Dr Tracey Martin

August 2024

Acknowledgment

First and foremost, I would like to express my deepest gratitude to my supervisors, Professor Johannes Benedikt and Dr Tracey Martin, for your unwavering support, guidance, and encouragement throughout my PhD journey. Your insightful feedback and dedication have been invaluable in shaping this research. I am also sincerely thankful to Professor Wen G. Jiang for providing me with the opportunity to undertake this PhD project. Without you, I would not have the chance to study at Cardiff and be part of the CCMRC.

I extend my heartfelt thanks to the entire CCMRC family. Special thanks to Dr. Lin Ye for organizing numerous workshops that were crucial for troubleshooting various research challenges. I am immensely grateful to Miss Fiona Ruge for your efforts in maintaining an organized lab environment and for your helping with IHCs.

I am deeply appreciative of all my peers at CCMRC—Amber, Jimmy, Esther, Yufei, Rhiannon, Yali, and Carolyn. It has been a truly enriching experience working alongside you. Your willingness to teach me experimental techniques, answer my questions, and provide support has been a source of great relief and motivation throughout this PhD journey. Thank you to Amber and Esther for formatting my thesis.

Finally, I owe my deepest gratitude to my family—my parents and my sister. Thank you for your unconditional love and supports. Your belief in me has been a constant source of strength.

Thank you all for being an integral part of this journey.

Publications and presentations

Publications

Han Gao; Fiona Ruge; Lin Ye; Jane Lane; Eleri Davies; Wen G. Jiang; Tracey A. Martin
A tight junctional scaffold protein MUPP1/MPDZ and its docking proteins, angiomotins in breast cancer. Cancer Res (2023) 83 (5_Supplement): P2-11-35. doi:10.1158/1538-7445.SABCS22-P2-11-35

Han Gao, Zhe Zhao, Johannes Benedikt, Wen G Jiang, Tracey A Martin
Brain-derived neurotrophic factor (BDNF) and epithelial to mesenchymal transition (EMT), clinical perspective in colorectal cancers. Gut 70(Suppl 4), pp. A159-A159. doi: 10.1136/gutjnl-2021-BSG.295

Han Gao, Chang Liu, Johannes Benedikt, Wen G Jiang, Tracey A Martin
AF6 (Afadin/MLLT4) and tight junctional regulating SIPA1, expression and clinical/prognostic value in colorectal cancer. Gut 70(Suppl 4), pp. A159-A159. doi: 10.1136/gutjnl-2021-BSG.296

H. Gao, J. Benedikt, W. Jiang, T. Martin
Claudin-16, its clinical and prognostic value in colorectal cancer. Annals of Oncology 33, p. S324. doi: 10.1016/j.annonc.2022.04.301

Conference Presentations

Division of Cancer and Genetics PGR Day, University Hospital of Wales (UHW), Cardiff, UK. In Oct. 2021.

European Society for Medical Oncology (ESMO) Congress 2022, Barcelona, Spain. In June. 2022.

Abbreviations

5-FU	5- Fluoropyrimidine
AC	Alternating current
AFDN	Afadin, adherens junction formation factor
AFP	Alpha-fetoprotein (Alpha-1-fetoprotein)
AHSG	Alpha-2-HS-glycoprotein
AJ	Adhesion junction
AKT1	RAC-alpha serine/threonine-protein kinase
AKT2	RAC-beta serine/threonine-protein kinase
AKT3	RAC-gamma serine/threonine-protein kinase
ALB	Albumin (BSA) (allergen Bos d 6)
AMBP	Alpha-1-microglobulin (EC 1.6.2.-)
ANK1	Ankyrin-1
ANK2	Ankyrin 2
ANK3	Ankyrin-3
ANXA1	Annexin A1
APMAP	Adipocyte plasma membrane-associated protein
ARHGAP1	Rho GTPase-activating protein 1
ARHGAP10	Rho GTPase-activating protein 10
ARHGAP11A	Rho GTPase-activating protein 11A
ARHGAP12	Rho GTPase-activating protein 12
ARHGAP15	Rho GTPase-activating protein 15
ARHGAP18	Rho GTPase-activating protein 18
ARHGAP21	Rho GTPase-activating protein 21
ARHGAP22	Rho GTPase-activating protein 22
ARHGAP23	Rho GTPase-activating protein 23
ARHGAP25	Rho GTPase-activating protein 25
ARHGAP27	Rho GTPase-activating protein 27
ARHGAP27	Rho GTPase-activating protein 27
ARHGAP28	Rho GTPase-activating protein 28

ARHGAP35	Rho GTPase-activating protein 35
ARHGAP4	Rho GTPase-activating protein 4
ARHGAP5	Rho GTPase-activating protein 5
ARHGAP6	Rho GTPase-activating protein 6
ARHGAP9	Rho GTPase-activating protein 9
AWG	Arbitrary waveform generator
BAD	Bcl2-associated agonist of cell death
BAK1	Bcl-2 homologous antagonist/killer (Apoptosis regulator BAK) (Bcl-2-like protein 7)
BAX	Apoptosis regulator BAX (Bcl-2-like protein 4)
BBB	Blood-brain barrier
BCL10	B-cell lymphoma/leukaemia 10
BCL2L1	Bcl-2-like protein 1
BCL7A	B-cell CLL/lymphoma 7 protein family member A
BCL7B	B-cell CLL/lymphoma 7 protein family member B
BCL7C	B-cell CLL/lymphoma 7 protein family member C
BCL9L	B-cell CLL/lymphoma 9-like protein
BCLAF1	Bcl-2-associated transcription factor 1
BE	Before experiment
BET1	BET1 homolog
BID	BH3-interacting domain death agonist
BIRC5	Baculoviral IAP repeat-containing protein 5 (Apoptosis inhibitor 4)
BLBC	Basel-like breast cancer
BNIP2	BCL2/adenovirus E1B 19 kDa protein-interacting protein 2
BRCA	Breast cancer
C3	Complement C3
CA	Complete ablation
CAAP1	Caspase activity and apoptosis inhibitor 1
CANISC	Cancer Network Information System Cymru
CAP	Capecitabine
CARD19	Caspase recruitment domain-containing protein 19

CASK	Peripheral plasma membrane protein
CASP1	Caspase-1
CASP2	Caspase-2
CASP3	Caspase-3
CASP6	Caspase-6
CASP7	Caspase-7
CASP8	Caspase-8
CAV1	Caveolin-1
CAV2	Caveolin-2
CCN1	CCN family member 1 (Cellular communication network factor 1)
CD226	CD226 molecule
CDC5L	Cell division cycle 5-like protein
CDH3	Cadherin-3
CDH6	Cadherin-6
cDNA	Complementary DNA
CEACAM8	Carcinoembryonic antigen-related cell adhesion molecule 8
CERS4	Ceramide synthase 4
CFAP100	Cilia- and flagella-associated protein 100
CFAP54	Cilia- and flagella-associated protein 54
CGN	Cingulin
CI	Confidence interval
CIR1	Corepressor interacting with RBPJ 1
CLDN11	Claudin-11
CLDN5	Claudin-5
CLDN6	Claudin-6
CLTC	Clathrin-0.22 heavy chain
COAD	Colon adenocarcinoma
CRADD	Death domain-containing protein CRADD
CRC	Colorectal cancer
CT	Computed tomography
CTC	Computed tomography colonography

CTNNA1	Catenin alpha-1
CTNND1	Catenin delta-1
CXCL1	Growth-regulated alpha protein (C-X-C motif chemokine 1)
DC	Dendritic cell
DC	Direct current
DCIS	In situ ductal carcinoma
DEPC	Diethylpyrocarbonate
DFS	Disease-free survival
DLC1	Rho GTPase-activating protein 7
DMEM	Dulbecco's Modified Eagle's Medium
DMSO	Dimethyl sulfoxide
DNMT1	DNA (cytosine-5)-methyltransferase (EC 2.1.1.37)
dNTPs	deoxynucleotide triphosphates
DSC2	Desmocollin-2
DSC3	Desmocollin-3 (Cadherin family member 3)
DSG2	Desmoglein-2 (Cadherin family member 5)
ECIS	Electric cell-substrate impedance sensing
EEG	electroencephalogram
EGFR	Epidermal growth factor receptor
EMF	Electromagnetic field
EML6	Echinoderm microtubule-associated protein-like 6
EMT	Epithelial to Mesenchymal
EPHA2	Ephrin type-A receptor 2
ER	Estrogen receptor
ERBIN	Erbb2-interacting protein
ERK	Mitogen-activated protein kinase
ERUS	Endorectal ultrasound
F11R	Junctional adhesion molecule A
FAM171A2	Protein FAM171A2
FAU	FAU ubiquitin-like and ribosomal protein S30
FCS	Foetal calf serum

FDR	False discovery rate
FITC	Fluorescein isothiocyanate
FMNL2	Formin-like protein 2
FMT	Focused microwave thermotherapy
FNBP1	Formin-binding protein 1
FRET	Fluorescence resonance energy transfer
GEO	Gene Expression Omnibus
GFP	Green fluorescent protein
GJ	Gap junction
GNA12	Guanine nucleotide-binding protein subunit alpha-12
GRK7	G protein-coupled receptor kinase 7
GSM	Global System for Mobile Communications
H1-3	Histone H1.3
HCC	Hepatocellular carcinoma
HEK	Human embryonic kidney
HER2	Human epidermal growth factor 2
HSP	Heat shock protein
HSP90B1	Heat shock protein 90 kDa beta member 1
HSPA12A	Heat shock 70 kDa protein 12A
HSPA13	Heat shock 70 kDa protein 13
HSPA1B	Heat shock 70 kDa protein 1B
HSPA2	Heat shock-related 70 kDa protein 2
HSPA5	Heat shock protein 70 family protein 5
HSPA8	Heat shock protein family A (Hsp70) member 8
HSPB1	Heat shock protein beta-1
HSPD1	Heat shock protein 60
HTSTs	High-throughput screening techniques
IDC	Invasive ductal carcinoma
IF	Intermediate frequency
IFC	Immunofluorescence
IGF1R	Insulin-like growth factor 1 receptor

IGL@	Immunoglobulin light chain, lambda gene cluster
IHC	Immunohistochemistry
ILC	Invasive lobular carcinoma
IRI	Irinotecan
ITCH	E3 ubiquitin-protein ligase Itchy homolog
ITGA6	Integrin subunit alpha 6
ITGAL	Integrin alpha-L
ITGAV	Integrin alpha-V (Vitronectin receptor)
ITGB1BP2	Integrin beta-1-binding protein 2 (Melusin)
ITGB3	Integrin beta-3
ITGB6	Integrin beta-6
JNK	c-Jun N-terminal kinase
KALRN	Kalirin RhoGEF kinase
LCIS	In situ lobular carcinoma
LHECs	Lens epithelial cells
LO	Local oscillator
LR	Local recurrence
LTP	Local tumour progression
LV	Leucovorin
MAGI1	Membrane-associated guanylate kinase, WW and PDZ domain containing 1
MAP2K2	Dual specificity mitogen-activated protein kinase 2 (MAP kinase kinase 2)
MAP2K6	Dual specificity mitogen-activated protein kinase 6 (MAP kinase kinase 6)
MAPK1	Mitogen-activated protein kinase 1 (MAP kinase 1)
MAPK10	Mitogen-activated protein kinase 10 (MAP kinase 10)
MAPK13	Mitogen-activated protein kinase 13 (MAP kinase 13)
MAPK14	Mitogen-activated protein kinase 14 (MAP kinase 14)
MAPK15	Mitogen-activated protein kinase 15 (MAP kinase 15)
MAPK3	Mitogen-activated protein kinase 3 (MAP kinase 3)

MAPK7	Mitogen-activated protein kinase 7 (MAP kinase 7)
MAPK8	Mitogen-activated protein kinase 8 (MAP kinase 8)
MARVELD1	MARVEL domain-containing protein 1
MarvelD3	Marvel domain containing 3
MBD1	Methyl-CpG-binding domain protein 1
MCL1	Induced myeloid leukaemia cell differentiation protein Mcl-1 (Bcl-2-like protein 3)
MDCK	Madin-Darby canine kidney
MI	Microwave imaging
MMP1	Matrix metalloproteinase-1
MMP8	Matrix metalloproteinase-8)
MMP9	Matrix metalloproteinase-9
MRI	Magnetic resonance imaging
MRPS33	28S ribosomal protein S33, mitochondrial
MS	Mass spectrometry
MTSS1	Metastasis suppressor protein 1
MTT	Thiazolyl Blue Tetrazolium Bromide
MW	Microwave
MWA	Microwave ablation
NCBI	National Center for Biotechnology Information
NDRG1	N-myc downstream-regulated gene 1 protein
NECTIN4	Nectin cell adhesion molecule 4
NMD3	60S ribosomal export protein NMD3
NOD1	Nucleotide-binding oligomerization domain-containing protein 1
NPI	Nottingham prognostic index
NS	No significance
NSCLC	Non-small cell lung cancer
NST	No special type
NT5E	5'-nucleotidase (5'-NT) (CD antigen CD73)
NUP50	Nuclear pore complex protein Nup50 (50 kDa nucleoporin)
OCLN	Occludin

ODAD3	Outer dynein arm-docking complex subunit 3
OPHN1	Oligophrenin-1
ORM1	Alpha-1-acid glycoprotein
OS	Oxidative stress
OS	Overall survival
OSCC	Oral squamous cell carcinoma
OX	Oxaliplatin
PAK2	Serine/threonine-protein kinase PAK 2 (EC 2.7.11.1)
PBS	Phosphate-buffered saline
PCDH17	Protocadherin-17
PCP	Paracellular permeability
PCR	Polymerase chain reaction
PEFE	Pulsed electromagnetic field exposure
PET	Positron emission tomography
PHF14	PHD finger protein 14
PIGQ	Phosphatidylinositol N-acetylglucosaminyltransferase subunit Q
PLIN2	Perilipin-2 (Adipophilin)
PPP1R3D	Protein phosphatase 1 regulatory subunit 3D
PR	Progesterone receptor
PRKCA	Protein kinase C alpha type
PRKCE	Protein kinase C epsilon type
PRKCQ	Protein kinase C theta type
PRKCZ	Protein kinase C zeta type
PRPF40A	Pre-mRNA-processing factor 40 homolog A
PSCA	Prostate stem cell antigen
PTEN	Phosphatidylinositol 3,4,5-trisphosphate 3-phosphatase and dual-specificity protein phosphatase
PTFE	Polytetrafluoroethylene
PTK2B	Protein-tyrosine kinase 2-beta (EC 2.7.10.2)
PTK7	Inactive tyrosine-protein kinase 7
PVDF	Polyvinylidene fluoride

PYCARD	Apoptosis-associated speck-like protein containing a CARD
qPCR	Quantitative PCR
RAB11B	RAB11B, member RAS oncogene family
RAB1B	Ras-related protein Rab-1B
RAB25	Ras-related protein Rab-25
RAB27A	Ras-related protein Rab-27A
RAB27B	Ras-related protein Rab-27B
RAB30	Ras-related protein Rab-30
RAB31	Ras-related protein Rab-31
RAB33A	Ras-related protein Rab-33A
RAB34	Ras-related protein Rab-34
RAB37	Ras-related protein Rab-37
RAB3B	Ras-related protein Rab-3B
RAB3C	Ras-related protein Rab-3C
RAB5B	Ras-related protein Rab-5B
RAB6B	Ras-related protein Rab-6B
RAB7A	RAB7A, member RAS oncogene family
RABL6	Rab-like protein 6
REV1	DNA repair protein REV1 (EC 2.7.7.-)
RF	Radiofrequency
RFFL	E3 ubiquitin-protein ligase rififylin
RGS3	Regulator of G-protein signalling 3
ROC	Receiver Operating Characteristic
ROS	Reactive oxygen species
RPL17	60S ribosomal protein L17
RPS6	40S ribosomal protein S6
RT	Reverse transcription
RYR3	Ryanodine receptor 3
SAFB	Scaffold attachment factor B1
SAGE	Serial analysis of gene expression
SAR	Specific absorption rate

SD	Standard deviation
SDS-PAGE	Sodium dodecyl sulfate-polyacrylamide gel electrophoresis
SEM	Scanning electron microscope
SERPINA1	Alpha-1-antiproteinase (Alpha-1-antitrypsin)
SERPINA3-4	Serpin A3-4
SFM	Serum-free medium
SH3BP5L	SH3 domain-binding protein 5-like
shRNA	Short hairpin RNA
SLC5A6	Sodium-dependent multivitamin transporter
SLC7A6OS	Probable RNA polymerase II nuclear localization protein SLC7A6OS
SMAD4	Mothers against decapentaplegic homolog 4
SNAP23	Synaptosomal-associated protein 23
SNAP29	Synaptosomal-associated protein 29
SRC	Proto-oncogene tyrosine-protein kinase Src
ST14	Suppressor of tumorigenicity 14 protein (EC 3.4.21.109) (Matriptase)
STAT3	Signal transducer and activator of transcription 3
STX11	Syntaxin-11
STX12	Syntaxin-12
STX16	Syntaxin 16
STX18	Syntaxin-18
STX3	Syntaxin-3
STX4	Syntaxin-4
STX7	Syntaxin-7
SYMPK	Symplekin
TAMP	TJ-associated marvel protein
TAPBPL	Tapasin-related protein (TAPASIN-R)
TBE	Tris-Boric-Acid
TBS	Tris-buffered saline
TCGA	The Cancer Genome Atlas
TER	Transepithelial electric resistance
TJ	Tight junction

TJAP1	Tight junction-associated protein 1
TMA	Tissue microarray
TMBIM1	Protein lifeguard 3 (Transmembrane BAX inhibitor motif-containing protein 1)
TMBIM6	Bax inhibitor 1
TMEM164	Transmembrane protein 164
TMT	Tandem Mass Tagging
TNM	Tumour, node and metastasis
TOP1MT	DNA topoisomerase I, mitochondrial (TOP1mt) (EC 5.6.2.1)
TPD52	Tumor protein D52
TRITC	Tetramethylrhodamine
UHF	Ultra high frequency
VI	Virtual instrument
VN1R5	Vomeronasal type-1 receptor 5 (G-protein coupled receptor GPCR26)
VOC	Voltage-controlled oscillator
VSA	Vector signal analyzer
VSIR	V-type immunoglobulin domain-containing suppressor of T-cell activation
VSWR	Voltage standing wave ratio
WB	Western blotting
XEL	Capecitabine
YS	Year survival
ZO-1	Zonula occludens-1

Summary

Microwave technology has emerged as a significant tool in medical applications, particularly in cancer treatment. Traditional microwave ablation generates high temperatures, leading to patient discomfort and potential unwanted tissue damage. Our research aims to apply microwave signals under normothermic conditions to minimize such effects. This thesis investigates the efficacy and underlying mechanisms of pulsed electromagnetic field exposure (PEFE) in treating breast and colorectal cancers, which are the most common and the fourth most common cancers in the UK, respectively.

A PCI eXtensions for Instrumentation (PXI)-based system was developed to improve efficiency, accuracy, and repeatability in PEFE applications. The new system integrates essential components, maintains a stable temperature, and automates processes, enhancing experimental consistency. The main purpose of this study is to reveal the potential mechanism of PEFE, applied at microwave range, in inducing cell deaths in vitro in both colorectal cancer (CRC) and breast cancer (BRCA). Further investigations revealed that PEFE treatment induces apoptosis in cancer cells, with tight junctions playing a crucial role in facilitating signal transduction. Therefore, we identified MarvelD3, a novel tight junction-associated protein, and explored its clinical and functional significance in colorectal cancer and breast cancer. MarvelD3 was found to be differentially expressed in breast and colorectal cancers. Its expression levels correlated with patient outcomes, suggesting its potential as a prognostic marker. By manipulating the expression of MarvelD3 in CRC and BRCA cell lines, we demonstrated that MarvelD3 regulates cellular adhesion, invasion, and migration negatively in both cancers. Interestingly, while MarvelD3 inhibits CRC cell growth, it promotes BRCA cell growth. MarvelD3 emerged as a biomarker for PEFE treatment; the knockdown of MarvelD3 led to decreased efficiency of PEFE in both CRC and BRCA cells. Proteomic analysis identified several dysregulated molecules post-PEFE treatment, particularly those involved in apoptosis, tight junction formation, and cell membrane integrity, confirmed by a series of Western blots.

In summary, this thesis demonstrates the potential of PEFE as an effective cancer treatment,

elucidates the role of tight junctions and MarvelD3 in mediating its effects, and highlights critical signalling pathways involved in cancer cell response to PEFE. These findings contribute to the development of more precise and less invasive cancer treatments.

Table of Contents

List of Figures

List of Tables

Chapter-1 Introduction

1.1 Microwave

Microwaves are a form of electromagnetic radiation with the wavelengths ranging from approximately one meter to one millimetre. The frequencies of microwaves are between 300MHz (1m) and 300 GHz (1mm), which are higher than that of general radio waves, and are therefore referred to as “ultra- high frequency electromagnetic waves”. Microwaves are important carriers for signal transmission as they consist of electric and magnetic fields which are perpendicular to each other. As shown in Figure 1.1, frequencies in the microwave range are often divided into several bandwidths which are referred to by their Institute of Electrical and Electronics Engineers (IEEE) radar band designations. The designations in the microwave range are listed in Table 1.1.

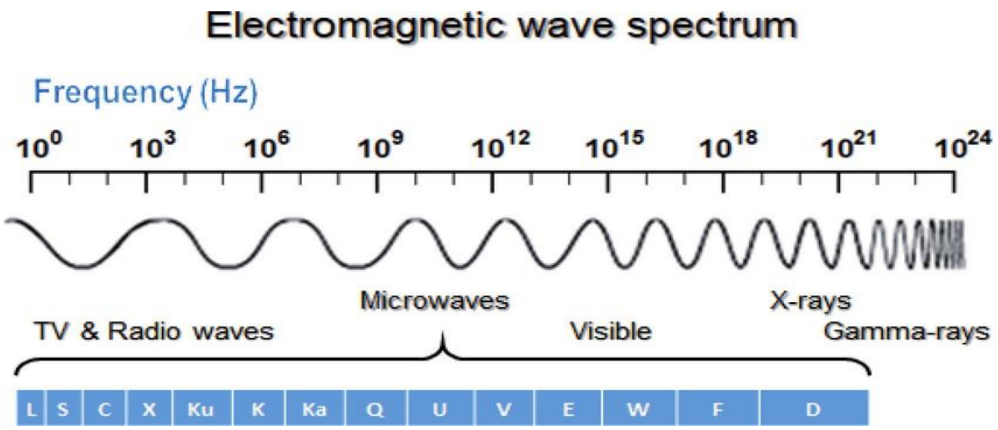

Figure 1.1 Spectrum of electromagnetic waves and microwaves (Adi et al. 2019)

Table 1.1 Band designation in microwave range. Available: http://www.radioing.com/eengineer/bands.html

Designation	Frequency	Wavelength
UHF	300—1000MHz	100cm—30cm
L Band	1—2GHz	30cm—15cm
S Band	2—4GHz	15cm—7.5cm
C Band	4—8GHz	7.5cm—3.75cm
X Band	8—12GHz	3.75cm—2.50cm
Ku Band	12—18GHz	2.50cm—1.67cm
K Band	18—27GHz	1.67cm—1.11cm
Ka Band	27—40GHz	1.11cm—0.75cm
V Band	40—75GHz	7.5mm—4.0mm
W Band	75—110GHz	4.0mm—2.7mm
mm Band	110—300GHz	2.7mm—1.0mm

Microwave energy is usually obtained by direct current or 50Hz alternating current through a specific device. Currently, two major types of devices have been identified to generate microwaves, including semiconductor devices and electric vacuum devices. The basic properties of microwaves usually present two characteristics, which are penetration and reflection. Water and food will absorb microwaves and become heated. For metal items, microwaves are reflected.

In recent decades, microwaves have been used in a wide range of applications in terms of communication, military, detection, measurement, heating, and navigation. Microwave applications have also been evolved for usage in the medical field for disease diagnoses, imaging and treatment.

1.2 Microwave application in medicine

Microwave application in the medical field is a novel field of a high interest throughout the world, with the rapid development since the early 80s (Vrba and Oppl 2008). Over the years, a large body of research looking at the effects on biological tissues by electromagnetic fields (EMF) has been published, making it possible to apply microwaves in the medical field (Gabriel et al. 1996). The many applications in medicine can be broadly divided into two categories, including diagnosis and treatment (Rosen et al. 2002). Some physical properties of biological tissues at the microwave range, such as dielectric properties, have been investigated and used in diagnosis and treatment for a long time (Edrich 1979).

In terms of diagnosis, microwave techniques, including imaging techniques and electromagnetic measurements, have been applied to biological tissue for further investigation for a long time, particularly the potential application of microwave imaging for the detection of early- stage human breast malignant tumours, which has made great progress in medicine (Töpfer and Oberhammer 2017). In addition to breast cancer, other clinical diagnoses include human bone (Kerketta and Ghosh 2020), torso scanners for thoracic fluid accumulation (Ahdi et al. 2017) and skin cancer (Mehta et al. 2006).

In regard to treatment, the development and investigation of microwave applications in

medicine can be traced back to the 1960s (Zhao 2020). These early studies used a wide variety of objects ranging from biomolecules to bacteria to tissue from higher organisms (Rojavin and Ziskin 1998), which led to the progress of mature microwave techniques used in cancer therapies for decades. Currently, microwave-based medical treatments are based on their thermal effect. In the last few years, an increase in thermal procedures to help patients who are suffering from back pain, liver cancer, and loose shoulder joints have been utilised (Rosen et al. 2002).

1.2.1 Microwave application in cancer diagnosis

Cancer is a major public health problem (Siegel et al. 2018), which is the leading cause of death worldwide. The incidence of and mortality from cancer are growing, with around 19.3 million newly diagnosed cases and 9.9 million cancer deaths in 2020 (GLOBOCAN 2020). The causes of cancer are complicated with both aging and population growth, together with socioeconomic development being confirmed as closely related to cancer (Omran 1971; Gersten and Wilmoth 2002). Among all cancer types, female breast cancer, lung cancer, colorectal cancer, prostate cancer, and stomach cancer are the top five in terms of incidence. With regards to mortality, lung cancer, colorectal cancer, liver cancer, stomach cancer, as well as female breast cancer make up the top five leading causes of cancer death, as shown in Figure 1.2.

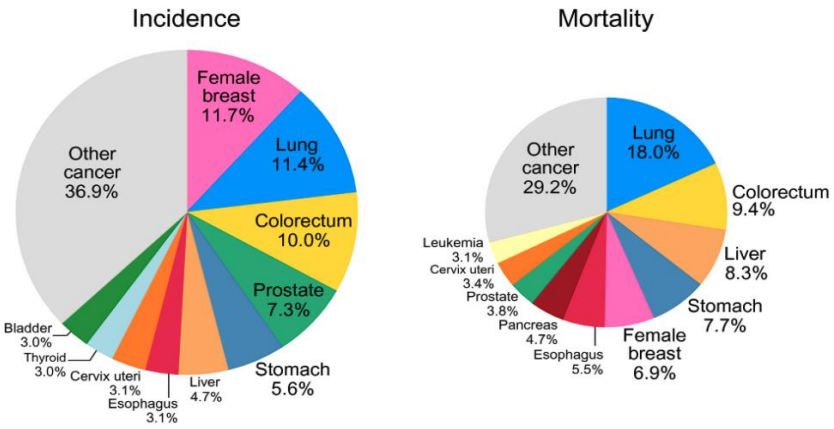

Figure 1.2 Distribution of incidence and mortality for the common cancers in 2018. Source: GLOBOCAN 2020.

Therefore, early cancer diagnosis is extremely important, not only because people with earlier

diagnosis are more likely to survive, but also patients have a better care experience, lower treatment morbidity and improved quality of life compared to those diagnosed late (Whitaker 2020). As a diagnostic technique, microwave imaging (MI) for breast cancer detection has been a topic of concern in the scientific community (Rosen et al. 2002). Several MI approaches have been developed and assessed in experimental settings. Recently, these techniques have been deemed as a safe and financially-friendly approach to mammography for breast cancer diagnosis (Wang 2017). There are two approaches of microwave technique for cancer diagnosis, namely passive and active diagnosis (Töpfer and Oberhammer 2017).

The characteristic of the passive microwave technique for cancer diagnosis is that there is no external radiation reacting to the tissue. Microwave radiometry is a passive microwave imaging method. As a newly developed technique, in recent years it has been broadly applied in the detection of breast cancer (Caferova et al. 2014). As shown in Figure 1.3, this technique relies on the different temperatures between healthy and cancer tissues, with the temperature of the tumour is often slightly higher than that of the surrounding normal tissue due to increased vascularization and metabolic activities (AlSawaftah et al. 2022). Radiometry involves receiving thermal radiation emitted spontaneously from the human body at a specific frequency or frequency range. The results can be reflected by the temperature distribution of the target area. Compared to normal tissue, local differences could be observed in the measured temperature distribution if the tumour tissue exists (Töpfer and Oberhammer 2017).

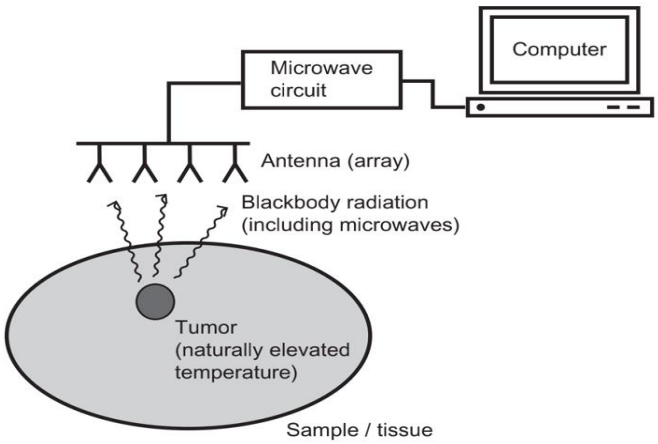

Figure 1.3 Schematic diagram of microwave radiometry for medical imaging (Töpfer and Oberhammer 2017).

Active microwave technique for cancer diagnosis has been of interest in medicine for some time. Probably more effort has been spent in breast cancer imaging (Meaney et al. 2012). In comparison to passive diagnosis, external microwave radiation is applied to deliver microwaves to the target organ or tissue, the penetrated and reflected signals are then measured, as illustrated in Figure 1.4(Töpfer and Oberhammer 2017). Due to elevated hydration and morphological alterations, the tumour tissues have higher water content than normal tissue (Schepps and Foster 1980). It has been reported that dielectric properties, including permittivity and conductivity, for cancerous breast tissue is three or more times higher than that of normal tissue (Bindu et al. 2006). Another example is that there is 5% more water in the cytoplasm of liver cancer cells than normal liver cells (Ross and Gordon 1982). When exposed to microwaves, a tumour tissue with high water content causes significant microwave scattering, which could contribute to the detection of cancer presence.

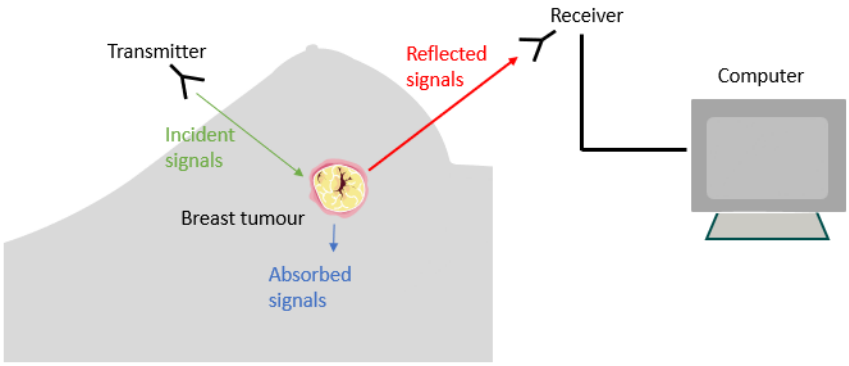

Figure 1.4 Schematic diagram of active microwave imaging for cancer diagnosis.

1.2.2 Microwave application in cancer treatments

The interaction of electromagnetic field and biological systems has been employed in the area of therapy for some times (Vrba et al. 2019). In the last few years, microwave therapies for cancer in humans have increased significantly. As a well-documented technique, microwave treatments are currently used in lots of cancer centers (Rosen et al. 2002). Nowadays, almost all microwave therapies used for treatment of patients are based on its thermal effect.

Microwave ablation (MWA) is a typical thermal therapy for tumour treatment, which was introduced to clinical use in the 1990s (Wu et al. 2016). At that time, due to the lack of shaft

cooling systems, it resulted in uncontrolled back-heating along the antenna. Since that time, massive technical advances have been made in order to improve this technique, resulting in the widespread use of the devices throughout the world (Dou et al. 2016). Recently, MWA has played an increasingly key role in cancer treatment for patients who are not eligible for traditional therapy including radiotherapy, surgery, and chemotherapy.

1.2.2.1 Principle of microwave ablation

The basic system of MWA consists of three components, including a generator, a power distribution system, and antennas. Because of the shaft heating caused by reflected power, a cooling system is a crucial component of almost all microwave antennas to avoid thermal damages (Lubner et al. 2010).

In MWA, the antenna is inserted into the target tissue. After insertion, the alternating electromagnetic field in the tissue vibrates water molecules based on the phenomenon of dielectric heating, which results in the frictional heating of the tissue, as shown in Figure 1.5. Therefore it can cause irreversible damages to the cells in the ablation area (Yang et al. 2007). Experiments have been conducted to confirm that tissue destruction occurs when tissues are heated to 52°C from an applied electromagnetic field, typically at 915 MHz or 2.4 GHz (Wang et al. 2015; Wu et al. 2016). During this minimal invasion treatment, the aim of MWA is to generate heat in the target tumour without damaging surrounding vascular and normal tissue (Keangin and Rattanadecho 2013).

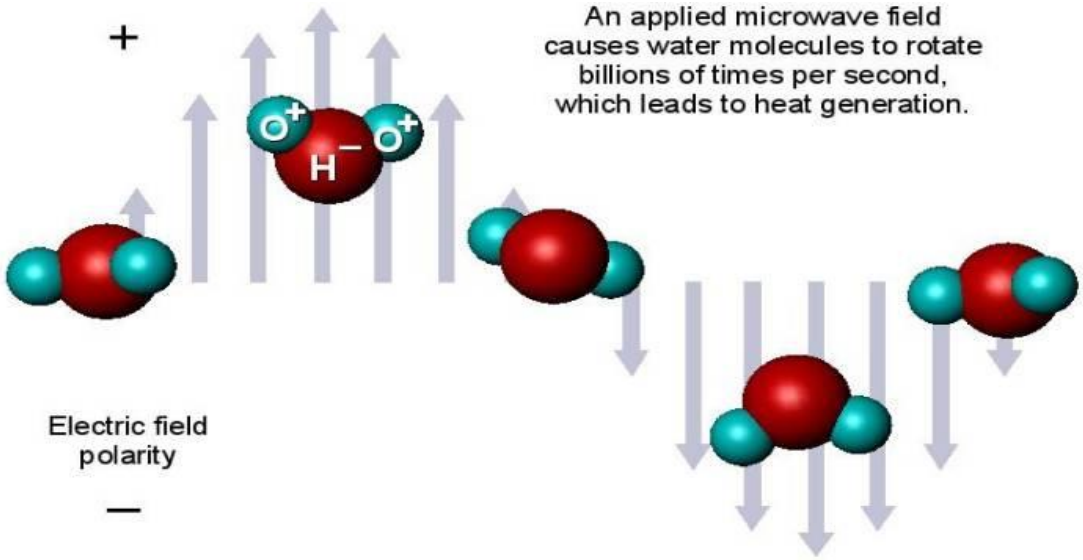

Figure 1.5 The principle of microwave ablation. MWA relies on the interaction of the alternating EMF with water molecules in the tissue (Brace 2009).

Some people believe that due to the application of microwaves, electric fields are the main factor leading to cell necrosis. However, the more fundamental problem is that the energy needs to be transmitted to the tissue to observe the effect. The delivered energy is a function of the the delivered power, which is best described by the following equation as the specific absorption rate (SAR) (Lin et al. 2000).

$$SAR = \frac{\sigma}{2\rho} E^2$$

Where E is the electric field amplitude (V/m), ρ is tissue mass density (kg/m^3), σ represents the conductivity of the tissue (S/m), and SAR is the specific absorption rate (W/kg). As the rate of power deposition in tissue, SAR can effectively reflect the damage inflicted to the tissue.

1.2.2.2 Microwave ablation techniques

In MWA, microwaves can be delivered through a dedicated applicator, then penetrated to the target tumour to generate heat. Nowadays, there are two major techniques for microwave delivery, namely focused microwave thermotherapy (FMT) and percutaneous microwave ablation (PMA).

FMT is a guaranteed approach for targeted treatment of breast cancer cells (Dooley et al.

2010). As a non-invasive microwave hyperthermia technique, the aim of FMT is to increase the local temperature, and simultaneously maintain a normal temperature in other areas (Simonov and Son 2019). As shown in Figure 1.6, when applying FMT, a pair of compression plates made of microwave waveguide are used as the applicators to deliver the focused microwave fields to the targeted breast tumours transcutaneous. Each compression plate has a well-designed rectangular aperture, in which a cooling system can be installed to reduce skin burns. Normally, the local temperature of the tumour under FMT process ranges from 43°C to 52°C. The microwave-focusing probe and the sensor catheter in the temperature sensor are inserted into the tumour site to monitor amplitude of the microwave field and temperature respectively. This sensor catheter is placed under the guidance of ultrasonic transducers which are installed in the rectangular aperture on each compression plate. The measured data can be given back to adjust the input microwave power to reach the required temperature of the tumour region (Gardner et al. 2002; Fenn 2007).

A

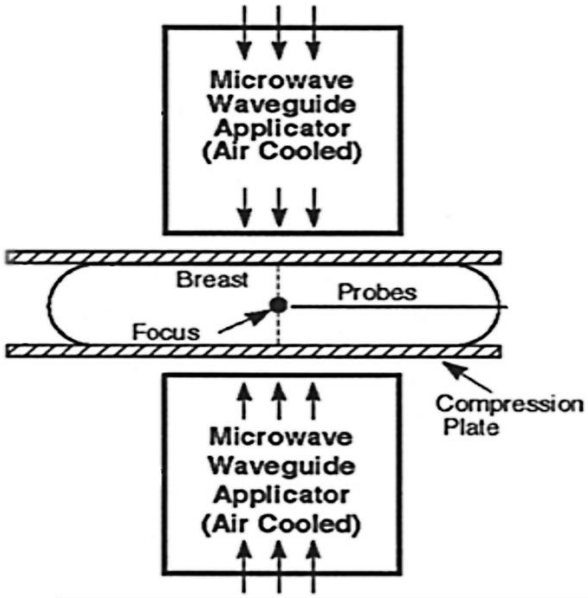

B

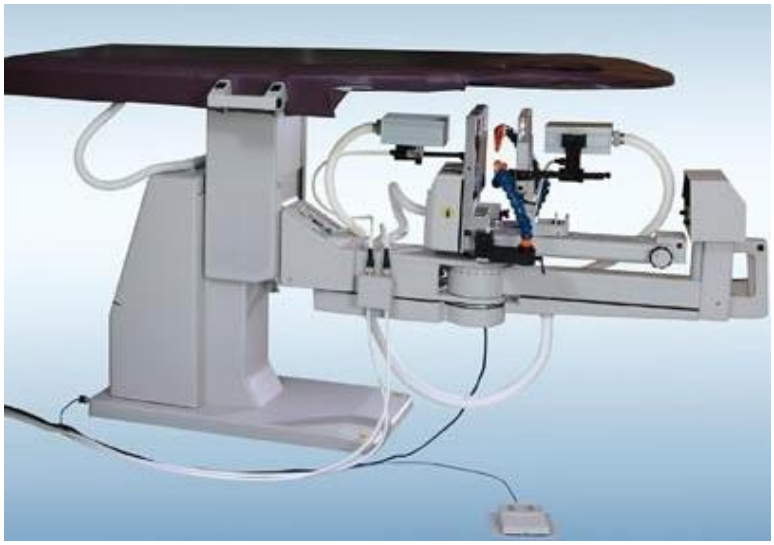

Figure 1.6 Focused microwave thermotherapy. (A) Schematic diagram of FMT for the breast cancer treatment. The breast-compression plates are employed to transmit microwave. Air cooling through rectangular waveguide applicators is used to alleviate the burn on the skin surface. The applicators generate a focused microwave field radiation which will contact a large volume of breast tissue. The characteristic of high-water content of such breast carcinomas enable FMT to heat more rapidly compared to surrounding normal breast tissue (Gardner et al. 2002). (B) An example of the current clinical FMT devices. Available: https://news.mit.edu/2007/cancer-radar-1128

PMA is another technique which requires a dedicated microwave applicator, together with the help of image guidance to localize the target tumour, inform the location of device, and facilitate confirmation of the treatment area after ablation. Ultrasound and computed tomography (CT) are the most commonly used imaging methods to guide ablation procedures

(Desgazer et al. 2016). As depicted in Figure 1.7, during the process of PMA, a needle-shaped applicator that delivers a quantitative microwave energy into the cancerous tissue. The microwave energy is emitted once the applicator is well-placed. Then such energy is absorbed by the tissue and generate heat by interacting with water molecules (McEwan et al. 2014). During recent years, PMA has been widely used in a variety of cancer treatments, including breast (Yu et al. 2017b), lung (Splatt and Steinke 2015), liver (Liang et al. 2009), and kidney (Yu et al. 2012).

A

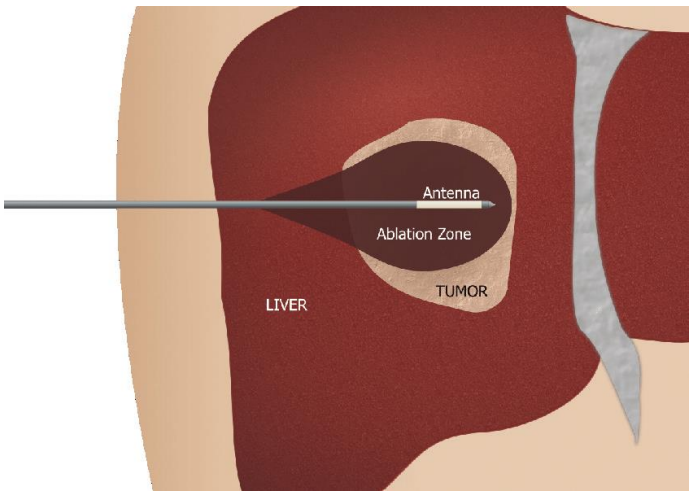

B

Figure 1.7 Percutaneous microwave ablation. (A) The schematic diagram of PMA. The applicator is places percutaneously into the tumour mass before microwave energy is applied to heat the tumour (Brace 2010). (B) Current clinical PMA device. Available: https://www.keymax.com.hk/products/helios-microwave-ablation-system-h-1

1.2.2.3 Clinical application of microwave ablation

Even though MWA has been wildly applied in cancer treatment, the disadvantages of it cannot be underestimated. To start with, currently, existing MWA techniques restrict the frequencies to the low-frequency spectrum such as 915MHz or 2.4 GHz, together with a high microwave input power of several tens of Watts (0-150W), as shown in Table 1.2 (Copty et al. 2004; Luigi et al. 2012; Saccomandi et al. 2015). Besides, with the heating generated by excessive microwave input power, the cooling system must be designed to alleviate it (Cheng et al. 2011; Sun et al. 2012). Therefore, greatly increasing size and cost of the equipment is required to fulfil these functions. Apart from these, it is impossible to kill every tumour cell without damaging the surrounding normal tissues by using only one antenna, as the shape and size of each tumour is different (Wang et al. 2015). Moreover, a high percentage of the energy from the source is reflected as the mismatched impedance between target tumour and the microwave applicator, making the ablation process increasing unpredictable (Jones et al. 2012).

Table 1.2 Main microwave ablation devices available on the market (Lubner et al. 2010; Baere and Deschamps 2014)

Company	Generator frequency	Generator power	Cooling type	Antenna size
MedWaves (USA)	915 MHz	45W	None	12 to 16-g
Covidien (USA)	915 MHz	45W	Water	14-g
BSD Medical (USA)	915 MHz	60W	Water	14-g
NeuWave (USA)	2450 MHz	140W	Gas (CO_2)	17-g
Hospital Service (Italy)	2450 MHz	100W	Water	11-g 14-g 16-g
Acculis (UK)	2450 MHz	100W	Water	15-g
Kang-you Medical (China)	915 MHz 2450 MHz	100W	Water	15-g

In recent years, some studies have been devoted to improving the technology with higher frequency and lower power levels to solve the limitation of traditional MWA techniques (Jeiwon et al. 2006). Yoon et al. conducted the in vivo experiments with xenografted mice tumours under the conditions of high frequency (0.9-30 GHz) and low power levels (1-3

Watts), suggesting that the frequency at 18 GHz was identified as the best for MWA (Yoon et al. 2011). Besides, by comparing the performance of MWA system at 10 GHz and the system at 1.9 GHz, Luyen et al. demonstrated the feasibility of applying high-frequency microwaves for tissue ablation (Luyen et al. 2014). Similarly, Jones et al. applied a novel high-frequency microwave (14.5GHz) to investigate how ablation influences cells, and to confirm non-viability (Jones et al. 2012). According to these results, the usage of higher frequencies and low power level compared with the traditional MWA contributes to the desired ablation size to be created in a relatively shorter period of time.

1.2.2.4 Microwave ablation for cancer treatment

MWA achieves the purpose of destroying tumours through direct and indirect thermal effects. The direct effect reflects a local temperature increase, which can cause immediate cell death by interrupting cell metabolism. There is also an indirect effect that leads to a growing area of necrosis after the thermal simulation is stopped. The evolving area of tumour marginal necrosis may be related to the balance of several interaction mechanisms, including HSP (Heat shock protein)-induced thermotolerance, altered apoptosis, localized cytokine stimulation, growth factor release, and triggering of the immune response (Nikfarjam et al. 2005).

As a thermal technology, taking anatomical location of the tumours, stage and patient's conditions into consideration, MWA as a treatment option has only been used as an alternative to certain cancer types, including breast and colorectal cancer.

In breast cancer treatment, even though radical mastectomy has been applied as an effective treatment for breast cancer worldwide, there are still lots of challenges for breast cancer patients that are at an advanced age due to the health conditions of the patients which often makes this group not eligible for surgery or chemotherapy. Currently, MWA is promising in small breast carcinomas and many studies have reported its correlation with clinical outcomes, as listed in Table 1.3.

Table 1.3 Clinical outcomes of microwave ablation in breast cancer treatment

Patients (lesions)	Size (cm)	CA[1]	Complications	Reference
10 (10)	1.0-8.0	--	flap necrosis, blister	2002 (Gardner et al. 2002)
25 (25)	0.7-2.8	68.0%	short-lived erythema, pain, burn, oedema	2004 (Vargas et al. 2004)
41 (41)	0.7-2.73	85.3%	skin burn, nipple retraction, seroma, abscess	2010 (Dooley et al. 2010)
15 (15)	2.0-7.8	--	skin burn	2010 (Dooley et al. 2010)
41 (41)	1.0-3.0	90.0%	skin injury, pectoralis muscle injuries	2012 (Zhou et al. 2012)
12 (12)	2.5-3.5	--	No major complications	2014 (Zhou et al. 2014)
39 (44)	--	97.5%	No major complications	2016 (Zhou et al. 2017)
122 (198)	0.7-4.9	99.5%	slight pain	2017 (Yu et al. 2017a)
56 (107)	0.3-2.4	100%	slight/moderate pain	2018 (Xu et al. 2018)
314 (725)	0.5-1.6	97.8%	pricking, skin scalding	2019 (Zhang et al. 2019)
21 (22)	0.3-5.0	--	No major complications	2020 (Yu et al. 2020)
440 (755)	1.0-3.0	100%	slight pain, fat liquefaction, skin scalding	2020 (Yang et al. 2020)

Note: 1 CA: Complete ablation

In colorectal cancer, surgery, chemotherapy, radiotherapy, immunotherapy, and targeted therapy are the most common treatment techniques currently. Despite surgery is the most ideal treatment for patients with colorectal cancer, most of the patients are not eligible for such therapy due to unresectable disease, cancer metastasis, or patients' comorbidities. MWA therefore obtains it popularity in colorectal cancer management (Takahashi and Berber 2020). A few clinical trials have been undertaken to investigate the impact of MWA in colorectal cancer, as listed in Table 1.4.

Table 1.4 Clinical outcomes of microwave ablation colorectal cancer treatment

Patients (lesions)	Size (cm)	Metastasis location	YS[1], LTP[2], LR[3]	Date
75 (257)	≤5	Liver	1-YS: 82.72%, 3-YS: 41.66%, LTP: 6.8%	2022 (Vogl et al. 2022)
31 (45)	≤3	Lung	1-YS: 93.5%, 2-YS: 80.6%, 3-YS: 61.3%, LR: 9.7%	2022 (Han et al. 2022)
50 (90)	0.3-3.2	Lung	1-YS: 94%, 2-YS: 84%, 3-YS: 60%, LTP: 10.0%	2018 (Kurilova et al. 2018)
33 (49)	0.5-5.5	liver	1-YS: 94%, 5-YS: 43%	2015 (Eng et al. 2015)
73 (129)	--	Hepatic	LTP: 6%	2014 (Correa-Gallego et al. 2014)
137 (411)	0.5-6.7	Liver	1-YS: 98.1%, 2-YS: 90.6%, 3-YS: 85.9%, LTP: 16.06%	2019 (Qin et al. 2019)
210 505)	0.7-3.7	Liver	1-YS: 98.6%, 2-YS: 73.3%, 3-YS: 53.3%	2021 (Shi et al. 2021)
199 (318)	≤3	Liver	Estimated 5-YS: 27.9%	2016 (Zhang et al. 2016a)
179 (602)	0.2-6.6	Liver	LR: 7.5%	2021 (Erten et al. 2021)

Note: 1 YS: year survival; 2 LTP: Local tumour progression; 3 LR: Local recurrence

1.2.2.5 Advantages and disadvantages of microwave ablation

Advantages

Compared with other ablation devices, MWA has many advantages. The advantages of MWA can be summarized as follows.

1. ***Rapid temperature progress***. MWA is characterized by rapid temperature rise, which accelerates tissue necrosis (Karampatzakis et al. 2013). The faster ablation characteristics of MWA increase the chance of obtaining a larger ablation volume, which is of particular concern (Zhou et al. 2013). This is because there is a strong connection between incomplete ablation of infected cells in the tissue and the high recurrence rate (Wei et al. 2018).

2. ***Wide range of applications.*** Microwave frequencies can spread in all types of biological

tissues, even those with low electrical and thermal conductivities (Tammam et al. 2020). Taking bone and lung as an example, these two types of tissues have relatively lower conductivity and permittivity. So MWA is more suitable and can achieve higher efficacy than other ablation techniques such as radiofrequency (RF) ablation (Karampatzakis et al. 2013; J. Louis et al. 2014). Besides, MWA is a suitable option for tumours which lies in close proximity to blood vessels (Carrafiello et al. 2008).

3***. Selectivity***. Due to the difference in electric properties between healthy and tumour breast tissue, microwaves can generate local heat in the tumour without damaging the normal healthy tissue and surrounding vascular (Sha et al. 2002; Vargas et al. 2004). Moreover, MWA has less procedural pain in comparison with other ablation techniques (Carrafiello et al. 2008).

Disadvantages

Even though MWA has superior performance compared to other cancer treatment technologies, is still has some challenges that need further exploration.

1. ***Unfriendly in space and price***. So far, as demonstrated before, the frequencies applied in the current MWA systems are limited to low frequency such as 915MHz or 2.5GHz. Due to the inherent low radiation efficiency, high microwave input powers of several tens of watts (0-150 W) are required at these frequencies (Copty et al. 2004). Apart from this, since too much microwave power can cause self-heating, an additional internal cooling system must be installed to control the temperature. Otherwise, the incidental damage would cause treatment failure (Sun et al. 2009; Cheng et al. 2011). All this results in greatly increasing the cost and size of the equipment.

2. ***Complexity***. The main requirement of the MWA applicator is to properly match the impedance to the biological tissue under ablation (Ibitoye et al. 2015). However, one of the drawbacks associated with the conventional MWA system is that as tissue impedance changes, most of the energy from the source is reflected. Consequently, the ablation process becomes more and more complicated (Jones et al. 2012).

3. ***Unpredicted side effects***. Ablation may cause undesirable tissue damage and cause side effects, including pain during the procedure, fever, mild pleural effusion, as well as complications of patients, as mentioned before. These side effects usually exist in thermal ablation (Lahat et al. 2014).

1.3 Non-thermal biological effects of microwave

Currently, numerous electronic devices have been invented and utilized in health, food, military, and communication industries (Zielinska et al. 2020). For example, with the use of mobile phones and other wireless technologies, humans are easily exposed to artificial electromagnetic radiation at microwave frequencies in their daily life (Kim et al. 2019). The effects of microwaves on biological samples have been broadly reported (Banik et al. 2003; Antonio and Deam 2007). When a biological sample is exposed to an electromagnetic field (EMF) at a microwave frequency range, the electric or magnetic field will directly interact with it, and the frequency is a key factor affecting the interaction. In the extremely low frequency range, the magnetic field is the main possible form of interaction with biological samples. On the contrary, the electric field mainly affects biological samples in the microwave frequency range (Kim et al. 2019). The mechanism of microwaves and its impact on biological samples are primarily based on both their thermal and non-thermal effects, while there are a few studies reported how microwaves interact with such samples based on their non-thermal effects (Asay et al. 2008).

1.3.1 Biological effects of non-thermal exposure on normal biological samples

Since the impact of microwave interaction with biological samples is controversial, there is insufficient data on the biological hazards that may be involved. Previous experiments have been conducted on different models *in vitro* and *in vivo*, presenting changes mainly in brain and nerve activities (Kleinlogel et al. 2008), male and female reproductive systems (Altun et al. 2018), hormone levels, genotoxicity (Phillips et al. 2009), gene and protein expression and oxidative stress (Jiang et al. 2016).

1.3.1.1 Non-thermal exposure on brain and nerve activities

Electromagnetic waves emitted by mobile phone are absorbed into the brain, thereby affecting the activity of neurons (Volkow et al. 2011). After acute exposure to mobile phone radiation, many people's brain electrical activity changes using electroencephalogram (EEG) recordings (Kesari et al. 2013). These changes occurred in event-related potentials (Bak et al. 2010), alpha-wave power of EEG (Croft et al. 2008), increased slow-wave activity in humans (Lustenberger et al. 2013) and spread of neural synchronization (Vecchio et al. 2007). Although these acute changes in EEG caused by microwaves do not show a direct relationship with causing disease and may not have an adverse effect on health, they do indicate that there may be changes related to brain function (Volkow et al. 2011).

Apart from these data, the exposure of EMF has also been indicated to induce electrophysiological changes in the brain, causing a series of behavioural effects. The influences on humans in studies include reduction in behavioural arousal (de Tommaso et al. 2009), sleep latency (Hung et al. 2007), cognitive functions (Regel et al. 2007), spatial working memory (Luria et al. 2009), well-being (Miller et al. 2019), thermal pain threshold (Vecsei et al. 2013) and motor activity (Lustenberger et al. 2013). The behavioural alterations shown in animal studies include learning and memory deficit (Hao et al. 2012), anxiety-related behaviour (Sokolovic et al. 2012), cognitive functions (Deshmukh et al. 2013) and passive avoidance deficit (Narayanan et al. 2010).

Some other studies also demonstrate that microwaves can change the permeability of the blood-brain barrier (BBB). Eberhardt et al conducted experiments and found that pulse-modulated exposure at 915 MHz in rats without hyperthermia for 2 hours caused increased albumin into the brain (Eberhardt et al. 2008). Similar experiment has been conducted by Nittby et al reporting that when rats are exposed to 900 MHz electromagnetic fields, the leakage of albumin was found via BBB (Nittby et al. 2009). This research indicates that pulsed microwave exposure may have a damaging effect through the BBB based on their non-thermal effects.

1.3.1.2 Non-thermal exposure on reproduction

It has been wildly studied that microwaves have severe impacts on reproductive function through their non-thermal effects for both fame and female (Blackwell 1979). Lots of factors that can influence spermatozoa quality, including decrease in sperm count, motility, viability, as well as normal morphology, have been confirmed to be related to the exposure of cell phones. Davoudi et al., conducted an in vitro experiment involving 13 men with normal semen analysis. It was found that using a GSM mobile (6 hours, 850MHz GSM) could reduce the motility of sperm in human spermatozoa *in vitro* (Davoudi et al. 2002). In a *In vivo* experiment, 30 adult male rabbits were selected to be exposed low power microwave from a mobile phone (900 MHz GSM, 8h/day for 12 weeks), presenting a significantly dropped sperm motility (Salama et al. 2009). Apart from these, it has been reported that microwave radiation from cell phones can result in morphological abnormality in spermatozoa (Otitoloju et al. 2010). According to Agarwal er al, 114 persons were exposed from mobile phones for more than 4 hours a day showed that only 18.4% had normal morphology (Agarwal et al. 2008). Besides, it has also been well-studied that the exposure of microwaves from cell phones was able to result in DNA damage in sperm. Aitken et al demonstrated that exposure of mice to mobile phone radiation at 900 MHz (12 hours a day, 7 days, SAR at 0.09 W/kg) resulted in DNA damages in sperm (Aitken et al. 2005). Another *in vitro* experiment was conducted with purified human spermatozoa when it was exposed to mobile phone energy at 1.8 GHz (SAR 0.4 W/kg-27.5 W/kg) for 16 hours, a significant increase in DNA fragmentation when specific absorption rates were at 2.8W/Kg ($p=0.05$) and 29% of the cells expressed significant DNA fragmentation at the highest SAR level (27.5 W/kg) (De Iuliis et al. 2009).

Apart from male fertility, non-thermal exposure of microwave can also affect pregnancy and female fertility. It has been reported that long-term exposure of microwave from many appliances may decrease female fertility (Al-Akhras et al. 2001). During pregnancy, changes have been verified by alterations in both offspring and pregnant women. An experiment conducted by Rezk et al with pregnant women (aged 18-33 years, n=90) and full-term healthy newborn infants (n=30) showed that exposing both pregnant mothers and the infants to EMF emitted by a cell phone (10 minutes, dialling mode) would result in a remarkable increase in foetal and neonatal heart rate and a significant decrease in stroke volume and cardiac output

(Rezk et al. 2008). Alchalabi et., al conducted an experiment involving pregnant rats with whole-body microwave irradiation (1.8 GHz, SAR 0.048 W/kg, 1 h/day for 2 weeks) and showed uterine congestion, haemorrhage, death and subsequent reabsorption of foetuses (Alchalabi et al. 2016). Furthermore, when the duration was changed to 2 hours a day, malformation, haematoma, and oedematous foetuses were observed by Alchalabi et al., Apart from these data, Odaci et al., report that consistent exposure of prenatal rats to electromagnetic fields (0.9GHz, power density 1mW/cm^2) affects the formation and differentiation of neural stem cells during embryonic development (Odaci et al. 2008).

1.3.1.3 The hormone melatonin

Melatonin has been identified as a regulator of normal sleep in most animals (Reiter 1993; Cajochen et al. 2003). Therefore, it has been debated whether microwaves can affect sleeping since a large amount of people prefer to keep their cell phone close to head when sleeping (Zhang et al. 2016b). Nowadays, lots of effort has been made to evaluate whether microwaves may have an impact on sleep by affecting the levels of melatonin (Hyland 2000; Krewski et al. 2001). Jarupat et al., found that there is remarkably decreased melatonin in saliva by approximately 36% when exposing the volunteers to continuous microwave emitted by a cell phone (1.96GHz, power density 2.5mW/cm^2, 30min/h, 17.00 p.m.-01.00a.m.) (Jarupat et al. 2003). Burch et al also did an experiment with 77 volunteers and found that the exposure to cell phones (>25 minutes/day, mean average 34 minutes/day, for 13 days) could significantly decrease the concentration of the hormone melatonin in urine by 34% (Burch et al. 2002).

1.3.1.4 Oxidative stress

Lots of studies have shown the oxidative stress (OS), a biomarker of the imbalance between oxidants and antioxidants, can cause many biochemical changes and therefore an important factor results in a variety of human chronic diseases, including cardiovascular diseases, neurodegenerative diseases and cancer (Luukkonen et al. 2009). Currently, several studies have investigated the OS and its association with microwave exposure both *in vivo* and *in vitro*, indicating that microwave exposure could increase reactive oxygen species (ROS) levels (Verschaeve 2009). The *in vitro* experiment has found an increase in ROS level in human sperm

(Agarwal et al. 2009; De Iuliis et al. 2009), human lens epithelial cells (LHECs) (Yao et al. 2008; Ni et al. 2013), and in different cell types from rats (Gajski and Garaj-Vrhovac 2009; Luukkonen et al. 2009; Campisi et al. 2010; Liu et al. 2012a). Apart from these, *in vivo* experiments have also been conducted and presented the increased reactive oxygen species (ROS) levels induced by microwave irradiation at different microwave frequencies (Guler et al. 2010; Kesari and Behari 2010; Güler et al. 2012). In summary, long-term exposure to microwaves may cause changes in reactive oxygen species (ROS). However, the nature and extent of the changes vary with experimental conditions and cell types.

1.3.1.5 Gene and protein expression

The biological effects of electromagnetic exposure at microwave frequencies might significantly result in changes in cell behaviour, particularly the changes in gene and protein expression (Jacques and Luc 2008). When applied in gene expression, various technologies have been used, including cDNA microarray, serial analysis of gene expression (SAGE) method, gene expression microarray, Gene Chip, high-throughput screening techniques (HTSTs), and Gene Array.

Several studies have reported that when exposing cells to long-term microwave fields, the expression of genes regulating cell apoptosis are altered. Trivino Pardo et al reported that after continuous microwave exposure at 900 MHz on human T-lymphoblastoid leukaemia (CCRF-CEM) cell line for short (2 hours) and prolonged (48 hours) times, certain apoptotic genes and cell cycle arrest genes were found to be overexpressed (Trivino Pardo et al. 2012). In an experiment conducted in primary cultured neurons and astrocytes, Zhao et al. observed that the expression of genes related to cell death pathways such as caspase-2, caspase-6 and Asc showed up-regulation after exposing to a working GSM mobile phone at 1900 MHz for 2 hours (Zhao et al. 2007b). In addition to these, it has been found that there is a down-regulation in the expression of the signal transducer and activator of transcription 3 (STAT3) gene, which plays an important role in the anti-apoptotic pathways, after exposing to RF waves (10.715 GHz, 6h in 3 days, SAR 0.725 W/kg) in cultured mice brain cells (Karaca et al. 2011).

Apart from apoptosis, some other genes which are associated with multiple cellular functions, such as the cytoskeleton, signal transduction pathway, metabolism (Zhao et al. 2007a) and structural maintenance (Chen et al. 2012), were found to be affected by microwave exposure under different conditions.

In terms of protein expression, many proteins have been found to be affected by long-term microwave exposure. It is widely studied that heat shock proteins (HSPs), which play an important role in maintaining cell survival under some conditions such as cold, heat, and other environmental stresses, are influenced by such microwave-radiation emissions (McNamee and Chauhan 2009). Czyz et al found a remarkable and stable up-regulation in transcript levels of HSP70 after exposing pluripotent embryonic stem cells to RF radiation (GSM, 1.71 GHz, SAR 1.5 W/kg for 48h) (Czyz et al. 2004). Nylund and Leszczynski et al. reported that exposing EA.hy 926 cells to RF-EMF (GSM, 900 MHz, SAR 2.0 W/kg, 1hour) presented an overexpression of a 27 kDa heat shock protein (HSP27), together with an increase in its hyper-phosphorylation status.

Apart from heat shock proteins, some other proteins have also been found to be affected by chronic microwave exposure. Sypniewska et al. reported that when exposing the rat cells to continuous microwave field (35 GHz, power density at 75mW/cm^2, 46 minutes), the alterations in the expression of 11 proteins related to cytoplasmic structures was found (Sypniewska et al. 2010). Fragopoulou et al., applied chronic mobile phone irradiation (SAR 0.17-0.37 W/kg, 3h/day, 8 months) to Balb/c mice and found that several proteins related to neural function and brain metabolism showed alteration in expression (Fragopoulou et al. 2012).

1.3.2 Biological effects of non-thermal exposure on cancer cells

Recent studies have presented that microwave radiation could result in a variety of chemical reactions at lower temperatures when compared with conventional heating methods such as applying an oil bath (Kappe 2004; Herrero et al. 2008). Compared to technologies based on hyperthermia, a newly-developed cancer treatment named “oncothermia” has been introduced. This therapy can kill cancer cells under normothermic radiofrequency irradiation,

which has the possibility to become a candidate for standard cancer treatment (Andocs et al. 2009; Szasz 2013). This technology implies that microwave irradiation can achieve its nonthermal effect to kill cancer cells. Based on these reports, it could be argued that microwave radiation can result in the death of cancer cells by itself, rather than the heat it has generated. If cancer cells can be killed by microwave irradiation without hyperthermia, this could be applied as a new treatment in the future (Asano et al. 2017a)

After the idea of microwave irradiation induced death of cancer cells under normothermic conditions, Asano et al successfully conducted an experiment where eight cultured cell lines from different cancer types, including MCF- 7 (breast cancer), T98G (glioblastoma), KATOIII (gastric cancer), HGC-27 (gastric cancer), HL-60 (leukaemia), MDA-MB-231 (breast cancer), Panc-2 (pancreatic cancer) and MCF-12A (immortalised normal mammary epithelial cells) were used. Asano et al exposed these cell lines to continuous microwave irradiation for 1 hour, utilising a dedicated irradiation system constituted with semiconductor microwave oscillator (2.45GHz) and thermos-regulatory applicator, which could emit microwave at varied output power to maintain the temperature of the subjects at 37℃. After microwave irradiation, seven out of eight types of cancer cells were successfully killed as confirmed by their decreased viability, excluding MCF-12A (Asano et al. 2017a). This is a very interesting finding, as it indicated that microwave irradiation might have different actions between cancer cells and normal cells in addition to induction of cell death of cancer cells. This experiment was followed by further research to investigate the mechanism of cell death after microwave irradiation under normothermic conditions. The results showed that most of the cells killed by microwave irradiation underwent a caspase-independent apoptosis pathway. It is worth noting that the microwave radiation also prevented the up-regulation of HSP70 expression, indicating that this treatment can potentially avoid heat resistance (Asano et al. 2017b).

1.4 A focus on breast cancer

1.4.1 Incidence of breast cancer

In UK, breast cancer is the most common cancer, accounting for 15% of all newly diagnosed cancer cases between 2016 to 2018, as shown in Figure 1.8. In females in the UK, breast

cancer is the most frequent malignancy, with around 55,500 new cases, accounting for 30% of all new female cancer cases. In males in the UK, breast cancer is not listed in the 20 most common cancers, with it begin less than 1% of all new male cancer cases. For women, the incidence rates of breast cancer in the UK increased by 24% during 1993-2017. It has been predicted that there could be approximately 69,900 newly diagnosed breast cancer cases every year in the UK by 2038-2040. Notably, there is a strong correlation between breast cancer incidence and age, as the highest incidence rates are in older people. According to UK Cancer Research, in the UK, an average of about a quarter (24%) of new cases of breast cancer per year were in people aged 75 and older in 2016-2018, as shown in Figure 1.9(Cancer Research UK).

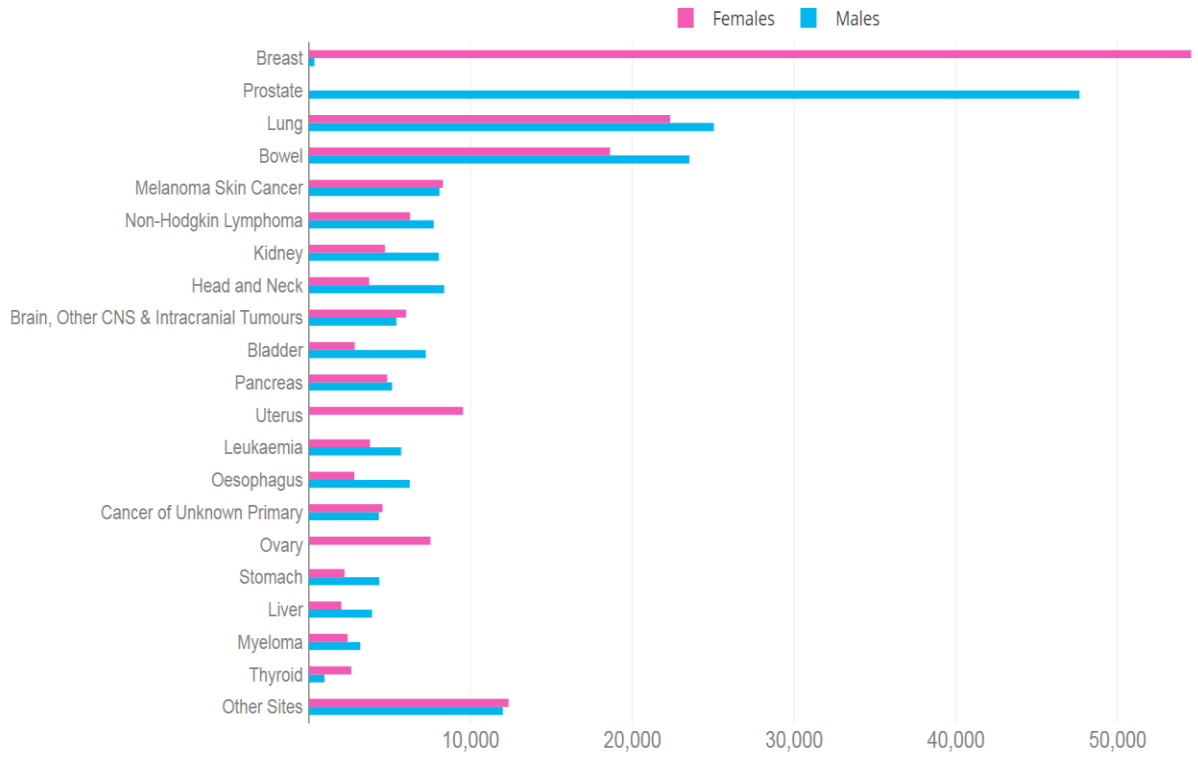

Figure 1.8 The incidence of common cancer in the UK (2016-2018). Breast cancer is the most common cancer in UK. Source: Cancer Research UK.

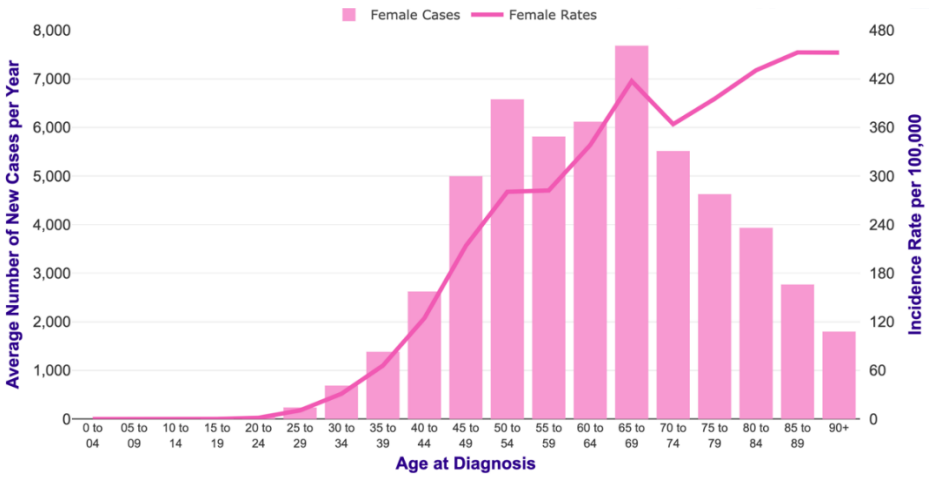

Figure 1.9 Average number of new cases of breast cancer each year at different ages. Incidence Rates per 100,000 Females, UK, 2016-2018. Source: https://www.cancerresearchuk.org/health-professional/cancer-statistics/statistics-by-cancer-type/breast-cancer/incidence-invasive#heading-One.

1.4.2 Mortality of breast cancer

In the UK, breast cancer is the fourth most common cause of cancer deaths, accounting for 7% of all cancer deaths in 2017-2019. There were approximately 11,400 breast cancer deaths each year from 2017 to 2019, as shown in Figure 1.10. Among British women, breast cancer is the second most common cause of cancer death, accounting for 15% of all cancer deaths. With current technology, the mortality rate of breast cancer has been improved remarkably due to the prevalence of breast-cancer-screening programs, which rise patients' self-awareness of breast symptoms and consequently result in early provision to breast clinics for further evaluation (Ahmed et al. 2015). For women, breast cancer mortality rate in the UK dropped by 37% between 1971-1973 and 2015-2019, as shown in Figure 1.11. Breast cancer mortality rates are anticipated to fall by 13% in the UK between 2023-2025 and 2038-2040 (Cancer Research UK).

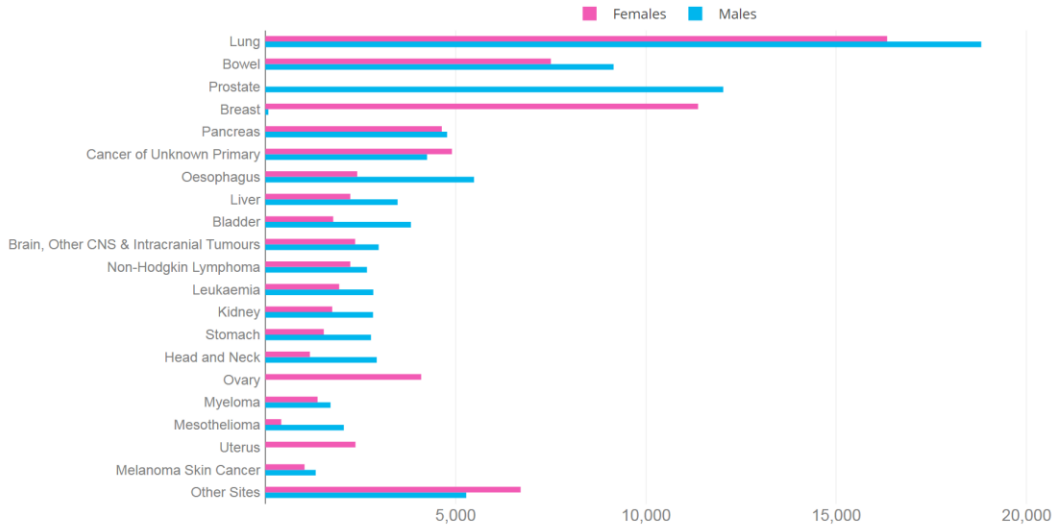

Figure 1.10 The mortality of common cancer in the UK, 2017-2019. Breast cancer is the fourth most common cause of cancer deaths. Source: Cancer Research UK.

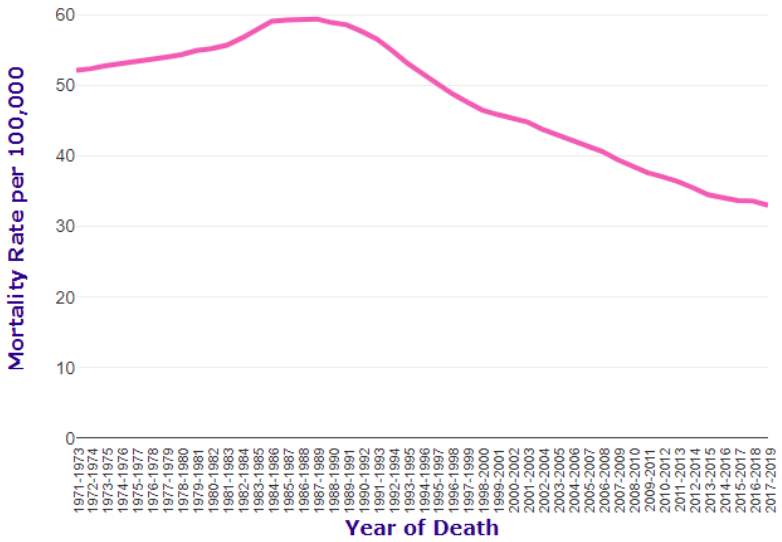

Figure 1.11 Breast Cancer Mortality Rates per 100,000 Population, UK, 1971-2019. Source: https://www.cancerresearchuk.org/health-professional/cancer-statistics/statistics-by-cancer-type/breast-cancer/mortality#heading-Two.

1.4.3 Survival of breast cancer

It has been reported that 95.8% of female breast cancer patients can survive for at least one year, while those who survive for 5 years or longer drop to 85.0%, and the predicted 10-year survival rate is 75.9% in the UK, as shown in Figure 1.12. with the well-established diagnosis and treatment techniques, breast cancer survival has doubled in the last 50 years in the UK (Cancer Research UK).

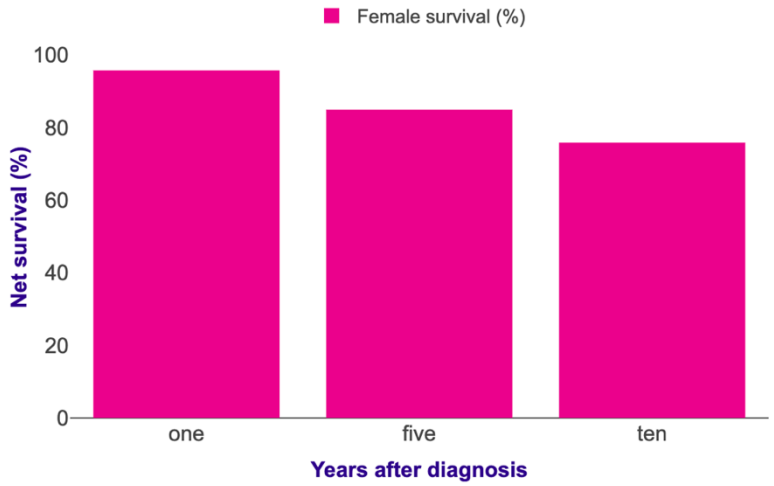

Figure 1.12 One-, Five- and Ten-year net survival rate of female breast cancer patients (aged 15-99) in the UK, 2013-2017. Source: Cancer Research UK.

1.4.4 Classification of breast cancer

1.4.4.1 Staging of breast cancer

The stage of cancer describes the size of the cancer and how far it has spread. Stage is very important as it is the best indicator for prognosis of breast cancer (Rosenberg et al. 2005). It can be useful for doctors to decide the method of treatment, and to monitor progress against the disease (Jemal et al. 2012). There are several different breast cancers staging systems in the UK, one of the most used is the TNM system. TNM stands for tumour, node and metastasis respectively, or in other words, the size of the tumour, whether the lymph nodes are affected, and if cancer has spread to other parts of the body have been taken consideration. Based on these, four stages have been designated as listed in Table 1.5.

Table 1.5 Staging and TNM classification of breast cancer.

Stage-IA	Tumour less than 2cm and has not spread to lymph nodes.
Stage-IB	No cancer cells in the breast but spread to a few lymph nodes in the armpit, or tumour less than 2cm and spread to a few lymph nodes in armpit.
Stage-IIA	No cancer cells in the breast and spread to 1-3 lymph nodes in the armpit, or tumour less than 2cm and spread to 1-3 lymph nodes in armpit, or tumour 2-5cm and has not spread to lymph nodes.
Stage-IIB	Tumour 2-5cm and spread to 1-3 lymph nodes in armpit, or tumour large than 5cm and has not spread to lymph nodes.
Stage-IIIA	Tumour less than 5cm but spread to 4-9 lymph nodes in armpit or near the breastbone, or tumour large than 5cm and spread to 1-9 lymph nodes in armpit or near the breastbone.
Stage-IIIB	Tumour can be any size and spread to the skin of the breast or chest wall, and spread up to 9 lymph nodes in armpit or near the breastbone.
Stage-IIIC	Tumour can be any size and spread to the skin of the breast or chest wall and spread to more than 10 lymph nodes in armpit or near the breastbone.
Stage-IV	Tumour can be any size, but the cancer has spread to other parts of the body, such as distant lymph nodes, lungs, bones, liver or brain (metastasis).

1.4.4.2 Breast cancer histological subtypes

Histological subtypes of breast cancer, referring to the growth pattern of the tumours, is associated with clinical presentations and outcomes (Weigelt et al. 2010). There are lots of different types of breast cancer defined by where the origin of it is. Currently, breast cancer is histologically classified as in situ carcinoma (non-invasive) and invasive carcinoma based on whether the tumours have spread into surrounding breast tissues from their origins, as demonstrated in Table 1.6 (Kim et al. 2023).

Breast carcinoma in situ, means it has not spread beyond the breast tissue from its original location, could further sub-classified as ether in situ ductal carcinoma (DCIS) or in situ lobular carcinoma (LCIS). DCIS is more common than its lobular counterpart (Malhotra et al. 2010). It is reported that In situ carcinoma has great potential to develop as invasive cancer, which is the reason it must be treated to prevent the patient from developing invasive cancer (Vaidya et al. 2015).

Invasive carcinoma means that the cancer cells have grown through their origin into the surrounding breast tissue. It can further sub-classified as special type and no special type (NST). Most invasive breast cancer has no special features so are classed as no special type (NST), including invasive ductal carcinoma (IDC) and invasive lobular carcinoma (ILC). IDC is the most common cancer type, accounting for approximately 70% for all breast cancer cases. Special types, also called rare cancer type, are defined by when the doctor sees the cancer cells under a microscope, the cells have particular features. These include tubular, medullary, mucinous, cribriform, papillary, and metaplastic carcinoma.

Inflammatory breast cancer is a very rare, and highly aggressive breast cancer that accounts 1% to 5% of all breast cancer cases and causes 8% to 10% of breast cancer-related death(Hester et al. 2021). Paget's disease of the breast is also an uncommon disease often associated with an underlying malignancy, accounting for 1%–4 % of all breast carcinomas (Sandoval-Leon et al. 2013).

Table 1.6 Breast cancer histological subtypes

Histological subtypes	**Frequency**
In situ carcinoma (non-invasive)	
In situ ductal carcinoma (DCIS)	Around 12%
In situ lobular carcinoma (LCIS)	Around 1%
Invasive carcinoma (No special type)	
Invasive ductal carcinoma (IDC)	Around 70%
Invasive lobular carcinoma (ILC)	15%
Invasive carcinoma (special types)	
Tubular carcinoma	2%
Medullary carcinoma	<5%
Mucinous carcinoma	1%-2%
Cribriform carcinoma	<1%
Papillary carcinoma	<1%
Metaplastic carcinoma	<5%
Other types of breast cancer	
Inflammatory breast cancer	1%-5%
Paget's disease of the breast	1%-4%

1.4.4.3 Breast cancer molecular subtypes

Contributed to the gene expression profiling techniques, some studies have recognized several breast cancer subtypes which are markedly differ in terms of patients' prognosis (Feng et al. 2018). Now several clusters of genes related to breast cancer have been identified to differentiate these subtypes, including estrogen receptor (ER) expression, human epidermal growth factor 2(HER2) expression, and progesterone receptor (PR) expression. Molecular subtypes of breast cancer are then divided into four groups based on the expression pattern of these genes, as listed in Table 1.7.

Table 1.7 Molecular subtypes of breast cancer

Molecular subtypes	Immunohistological characteristics
Luminal A breast cancer	ER+, and/or PR+, HER2-
Luminal B breast cancer	ER+, and/or PR+, HER2+
HER2-enriched breast cancer	ER-, PR-, HER2+
Basal-like breast cancer (BLBC)	ER-, PR- HER2-

1.4.5 Diagnosis of breast cancer

Currently, diagnosis of breast cancer is the best way to save lives and consequently, reduce breast cancer death rates remarkably in a long term (Migowski 2015). Several technologies in terms of the diagnosis of breast cancer have been well-developed for the purpose of providing patients with fewer invasive options and better diagnosis, including mammography, ultrasonography, Magnetic resonance imaging (MRI), positron emission tomography (PET), computed tomography (CT), and Breast biopsy (Narod et al. 2015).

1.4.5.1 Mammography

Mammography is the current standard breast screening technique, which is suitable for women over 40 years old (Hellquist et al. 2015). The process of mammography is to use low-energy X-rays to examine breasts for the purpose of diagnosis and screening. This technique applies a dose of ionizing radiation to create images and then to analyze abnormalities in these images (Wang 2017). In the UK, it is suggested that all women between the ages of 50

to 71 should receive a mammography every three years. Due to its wide application, the mortality rate of women aged 50-69 who were assigned for mammography screening decreased by 16% to 35% (Humphrey 2002), while women aged 40 to 49 had a relatively smaller but also significant reduction of 15% to 20% (Fletcher and Elmore 2003). However, it is reported that the false-positive and false-negative rates of mammography are relatively high, this is especially true for patients under 40 years old (Pisano et al. 2005; Nelson et al. 2009).

1.4.5.2 Ultrasonography

Breast ultrasonography has been used as an additional imaging tool for mammography (Ozmen et al. 2015). This technique is a cost-effective and widely applied screening tool, which detects tumours by rebounding acoustic waves from breast tissue. When compared with mammography, ultrasonography are more detective and sensitive as it can increase the tumour detection rates for subjects with high breast cancer risk (Wang 2017). Based on these advantages, breast ultrasonography has been suggested as an alternative to mammography for subjects who are pregnant women and who are not eligible for mammography (Hooley et al. 2013)

1.4.5.3 Magnetic resonance imaging (MRI)

Magnetic resonance imaging (MRI) can create images more flexible by applying strong magnetic field with radiofrequency signals. This technique has been suggested for patients with high breast cancer risk, but it is not recommended to the public. This is because its characteristics of high false-positive rate, high cost, and time consumption. Apart from these, MRI is less specific but more sensitive to detect small tumour in patients with high breast cancer risk in comparison with mammography and ultrasonography (Schneble et al. 2014).

1.4.5.4 Positron emission tomography/ computed tomography (PET/CT)

Positron emission tomography (PET) and computed tomography (CT) are newly-developed technologies, which has remarkably improved the management of cancer since the late 1990s

(Auguste et al. 2011). It is reported that the integrated PET/CT system is more accurate for tumour staging than the usage of PET or CT individually (Vansteenkiste et al. 1998; Kluetz et al. 2000). Compared with conventional imaging such as mammography and ultrasonography, PET/CT is an extremely accurate tool for identifying lymph nodal and distant metastasis.

1.4.5.5 Breast biopsy

Breast biopsies are regarded as the best technique for the diagnosis of breast cancer (Diego et al. 2016). Usually, the biopsy is performed after suspicious lesions are found in mammography or ultrasound to obtain tissue for further pathological diagnosis (Jain et al. 2017). For a patient, when a breast biopsy is conducted, many factors, including size, location, and appearance need to be taken into consideration to decide the most suitable approach (Wang et al. 2017). Normally, 5-10 biopsies of a suspicious breast lesion will diagnose a case of breast cancer (Longo et al. 2015).

1.4.6 Traditional breast cancer therapy

In terms of the breast cancer therapy, the aim is to preserve quality of life together with prolonged life expectancy (Akram et al. 2017). There are several therapy techniques depending on several factors, including the type and stage of the cancer, the patient's sensitivity to hormone, the age, health condition, and personal preferences. Surgery, chemotherapy, radiation therapy, targeted therapy, hormone therapy, and immunotherapy are the most common and traditional breast cancer therapy. Sometimes there are applied individually or in combination with other therapies to achieve better results.

1.4.6.1 Surgery

Surgery is the primary treatment strategy for patients whose breast cancer has not spread to the other parts of the body, and it is also an option for further worse stages of the disease (Ellis et al. 2017; Houssami et al. 2017). The types of breast cancer surgery can be different when considering the quantity of tissue which is excised with the cancer. This depends on the characteristics of cancer and whether it has spread to other sites of the body.

Lumpectomy, also known as breast-conserving surgery, is the process of removing the part of the breast which contains malignant tumour, as well as some normal tissues and surrounding lymph nodes, trying to keep most of the breast intact (Fisher et al. 1995). For patients who are in their initial phase of breast cancer, lumpectomy is the most common choice. While patients also require another kind of therapy such as radiation therapy or chemotherapy together with lumpectomy to achieve better results. It is reported that most patients prefer lumpectomy rather than the whole breast removal (mastectomy) (Dorval et al. 1998). However, the side effects of lumpectomy include temporary inflammation, tenderness, and changed appearance of breast, etc (Yarnold et al. 2005).

Mastectomy is regarded as the most effective technique to deal with an already locally spread breast cancer case, in which the breast is completely removed. Normally, when the breast tumour is more than 5cm is not eligible for lumpectomy, mastectomy is operated upon in order to decrease the risk of further development of breast cancer (Voogd et al. 2001). However, in most women, loss of the whole breast leads to loss of self-confidence and subsequent depression (Keskin and Gumus 2011). Breast renovation, namely reconstructive surgical treatment, is recommended for females who have finished their mastectomy to help them rebuild their confidence (Rowland et al. 2000).

1.4.6.2 Chemotherapy

Chemotherapy is known as killing cancer cells with certain medicines (Masood 2016). It can be applied both before and after surgery, depending on the condition of the patient. Chemotherapy is mainly applied in breast cancer cases of stage II- IV, and is particularly beneficial for ER- disease (Onitilo et al. 2009). The principle of most chemotherapy medicines is to destroy fast-growing and/or fast-dividing cancer cells by causing DNA damage or other mechanisms (Kitao et al. 2018). Although chemotherapy has side effects such as causing damage to the heart muscle, it can help control the progression of the disease for several years for patients with metastatic cancer (Harrington and Smith 2008).

1.4.6.3 Radiation therapy

Radiation therapy, also known as radiotherapy, is a kind of breast cancer therapy that uses ionizing radiation to control or kill treat target tumours. This therapy is most often given after surgery to the tumour bed area and local regional lymph nodes to destroy any remaining cancer cells (Yang and Ho 2013). Currently, a combination of a lumpectomy and radiotherapy is being increasingly applied in the patients at their early stage of breast cancer (Hall and Brenner 2008). Radiation therapy can be delivered both externally and internally. External radiation therapy uses a machine from outside the body to send radiation into the cancer. The principle of internal radiation therapy is to put a needle or catheter with radioactive material directly into or near the cancer.

1.4.6.4 Targeted therapy

Targeted therapy is one of the main methods of cancer medical treatment. As a form of molecular medicine, targeted therapy affects the specific genes and proteins related to cancer growth and survival. This kind of treatment blocks the growth and spread of cancer cells and minimizes damage to normal cells, rather than simply interfering with all rapidly dividing cells such as in traditional chemotherapy (Mohamed et al. 2013). Monoclonal antibodies, aromatase inhibitors, and mammalian target of rapamycin (mTOR) inhibitors are types of targeted therapies used to treat breast cancer (Masoud and Pagès 2017).

1.4.6.5 Hormone therapy

Certain types of breast cancer are affected by hormones, such as oestrogen and progesterone. Breast cancer cells have receptors (proteins) that attach to such hormones, which enable them to grow. The treatment that prevents these hormones from attaching to these receptors is called hormone therapy. Hormone therapy is usually applied as an adjuvant therapy to reduce the cancer coming back after surgery. The female hormone oestrogen is mainly produced by the ovaries and acts on the oestrogen receptor (ER) to promote the growth and spread of breast cancer cells (Gupta and Kuperwasser 2006). Hormone therapy can prevent the growth of cancer cells by preventing hormone secretion or blocking its function.

Compared with chemotherapy, hormone therapy has few side effects, such as eyesight changes, weight gain, memory and mood problems.

1.4.6.6 Immunotherapy

Immunotherapy, also called biologic therapy, uses the immune system of the body to boost the natural defences to fight against the target cancer cells. Over the last few decades, the development of immunotherapy has been intense (Hadden 1999). Immunotherapy plays an important role in the treatment of breast cancer in many different forms. One example is the development and use of vaccines. Part of the cancer cells can also be used to produce vaccines and then promote the human immune system to fight cancer. Syn et al reported that the efficacy of immunotherapy is increased by 20-30% when it is combined with traditional breast cancer therapy (Syn et al. 2017).

1.5 A focus on colorectal cancer (CRC)

1.5.1 Introduction of colorectal cancer

Colorectal cancer, also known as bowel cancer, starts in the colon and rectum. It can also be defined as colon cancer or rectal cancer, based on their origin. Due to the commonality of their characteristics, colon cancer and rectal cancer are often grouped together.

As the first part of the large bowel, colon has four sections, in which cancer can occur in any of them. The sections of the colon include ascending colon, transverse colon, descending colon, and sigmoid colon, as illustrated in Figure 1.13.

Rectal cancer develops in the last part of the large bowel. The function of this part is to store the stool until it is ready to be passed out of the body.

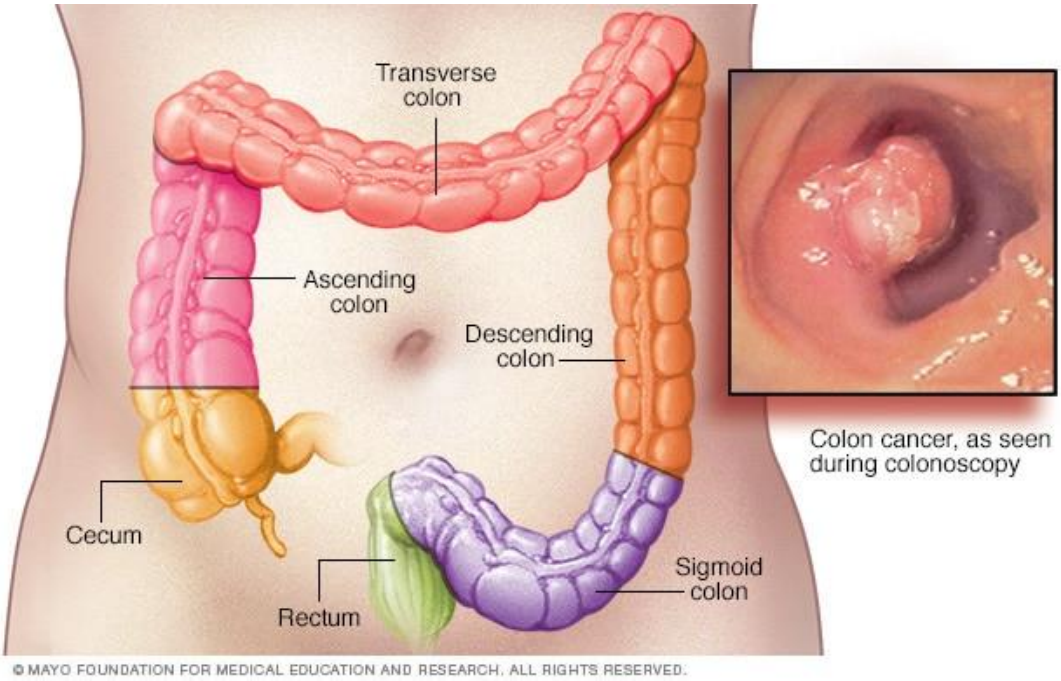

Figure 1.13 The composition of the colon and rectum. Source: https://www.mayoclinic.org/diseases-conditions/colon-cancer/symptoms-causes/syc-20353669

1.5.2 Incidence of colorectal cancer

Worldwide, colorectal cancer ranks third in terms of incidence. It is estimated that more than 1.9 million new cancer cases occur in 2020 (Sung et al. 2021). The highest incidence rate of colorectal cancer is in Eastern Asian (around 39%), followed by Northern America (Vekic et al. 2020). In the UK, colorectal cancer is the 4th most common cancer, accounting for 11% of all new cancer cases in 2017, with 44% of female cases and 56% of male cases (Cancer Research UK). The etiology of colorectal cancer is multifactorial. Apart from genetic diseases, environmental risk factors and lifestyle, including smoking, alcohol, obesity, diabetes and high-fat diet, have also been identified to have substantial impact on the development of colorectal cancer. It has been reported that colorectal cancer is closely related to age, with the highest incidence being in the elderly, as demonstrated in Figure 1.14. According to Cancer Research UK, more than 44% of newly diagnosed cases were in people aged 75 and over (Cancer Research UK).

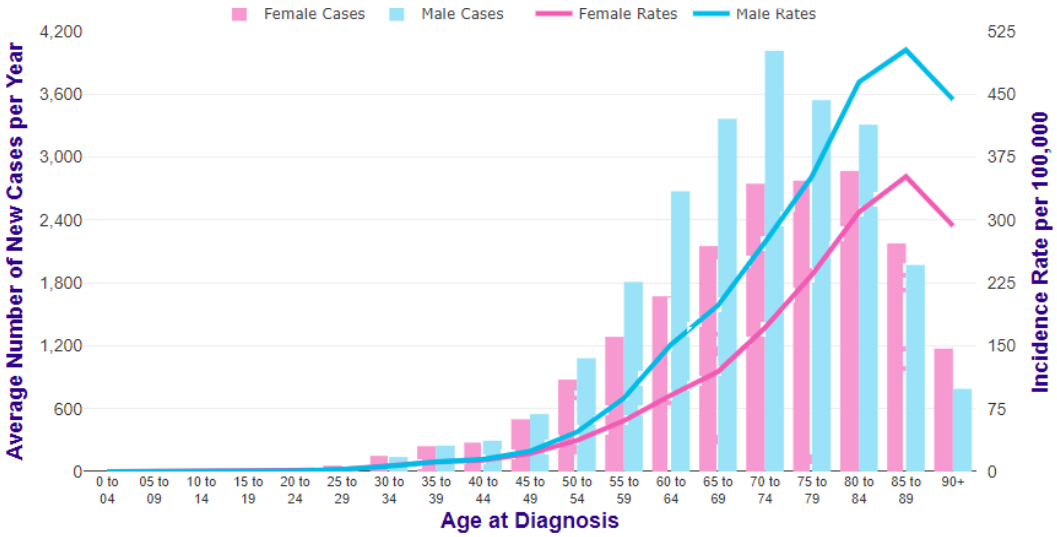

Figure 1.14 Average number of newly diagnosed CRC cases per year with age-specific Incidence rates per 100,000 population in UK (2016-2018). Source: https://www.cancerresearchuk.org/health-professional/cancer-statistics/statistics-by-cancer-type/bowel-cancer/incidence#heading-One.

1.5.3 Mortality of colorectal cancer

Globally, colorectal cancer is one of the major malignant tumours, which ranks second in annual mortality among all cancers in 2020. In accordance with the global trend, it is expected that the incidence and mortality of colorectal cancer will continue to increase, reaching more than 2.2 million new cases and 1.1 million cancer deaths by 2030 (Arnold et al. 2017). In the UK, colorectal cancer is the 2nd most cause of cancer death, with around 16,600 mortality cases, accounting for 10% of all cancer death in 2018. It has been also reported that there are approximately 58% of colorectal cancer death in the UK occurred in people aged 75 and above (Cancer research UK). Attributing to the early screening programs and well-established treatments, a remarkable decrease has been observed in the mortality rate. Over the last decade, colorectal cancer mortality rates have dropped by 12% in the UK, as illustrated in Figure 1.15 (Cancer research UK).

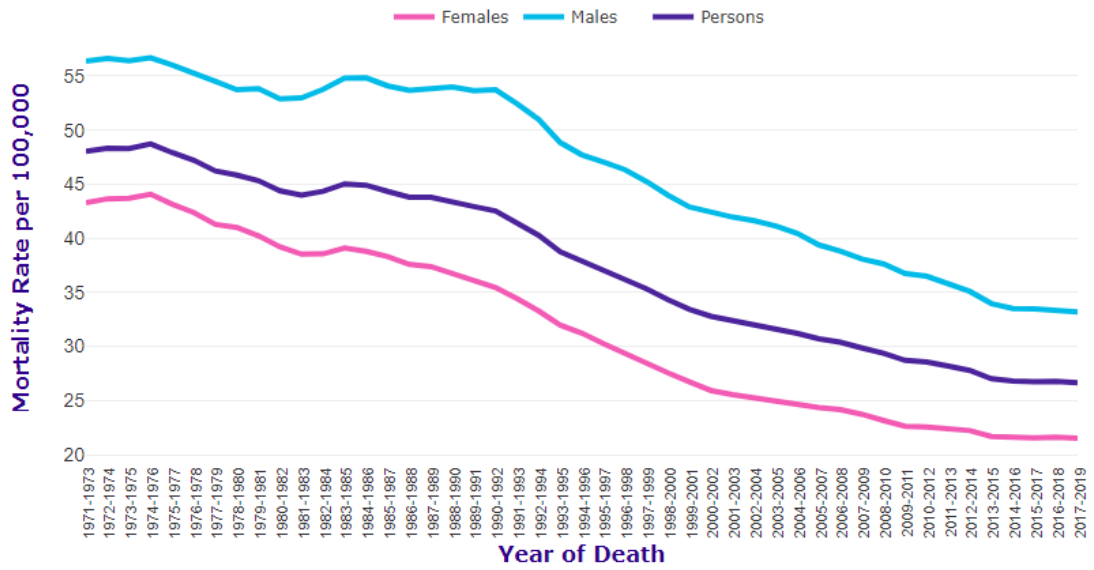

Figure 1.15 Colorectal cancer mortality rates in the UK from 1971 to 2018. Source: https://www.cancerresearchuk.org/health-professional/cancer-statistics/statistics-by-cancer-type/bowel-cancer/mortality#heading-Two

1.5.4 Survival of colorectal cancer

In the UK, 78.3%, 58.4% and 52.9% of patients with colorectal cancer survive their disease for more than one year, five years and ten years from 2013 to 2017, respectively. It is reported that colorectal cancer survival is improving and has more than doubled in the past 40 years.

Also, survival of colorectal cancer is strongly related to the stage of the disease at diagnostic phase. At the earliest stage of diagnosis, almost all (98%) patients with colorectal cancer can survive the disease for at least one year, compared with 44% for those diagnosed at the latest stage (Cancer research UK).

1.5.5 Staging of colorectal cancer

As mentioned in section 1.4.4, the stage of cancer is crucial for both patients and doctors. For patients, cancer staging suggests the most likely outcome and gives them an estimate of life expectancy. For doctors, cancer staging is an index that gives them an information of what treatment should be planed and recommended (Neal et al. 2007). The staging of colorectal cancer is listed in Table 1.8.

Table 1.8 Staging and TNM classification of colorectal cancer.

Stage-0	Cancer cells only exist in the mucosa or inner wall of the colon or rectum.
Stage-I	Cancer cells have grown through the mucosa and invaded the muscle layer of the colon or rectum. It has not spread to nearby tissues or lymph nodes.
Stage-IIA	The cancer has grown through the wall of the colon or rectum but has not spread to surrounding tissues or surrounding lymph nodes.
Stage-IIB	The cancer has grown through the muscle layer to the inner wall of the abdomen. It has not spread to nearby lymph nodes or elsewhere.
Stage-IIC	The tumour has spread to the wall of the colon or rectum and has grown into nearby structures. It has not spread to nearby lymph nodes or elsewhere.
Stage-IIIA	The cancer has grown through the inner wall or into the muscle layer of the intestine. It has spread to 1 to 3 lymph nodes or tumour cell nodules in the tissues around the colon or rectum, which do not appear to be lymph nodes but have not spread to other parts of the body
Stage-IIIB	The cancer has grown through the intestinal wall or surrounding organs and has spread to 1 to 3 lymph nodes or tumour nodules in the tissues around the colon or rectum that do not appear to be lymph nodes. It has not spread to other parts of the body.
Stage-IIIC	Tumour has spread to 4 or more lymph nodes but has not spread to other distant parts of the body.
Stage-IV	Tumour can be any size, but the cancer has spread to other parts of the body, such as lungs and liver (metastasis).

1.5.6 Diagnosis of colorectal cancer

Early diagnosis is extremely important to provide patients with a suitable treatment strategy, therefore a longer life expectancy with improved quality of life (De Rosa et al. 2015). In the last few decades, it was reported that more than 20% decrease of mortality rate was achieved attributing by the continuous development in diagnostic techniques and improvement of treatment methods (Kekelidze et al. 2013). Currently, clinically popular diagnostic techniques for colorectal cancer include colonoscopy, computed tomography colonography (CTC), Magnetic resonance imaging (MRI), positron emission tomography (PET), and endorectal ultrasound (ERUS).

1.5.6.1 Colonoscopy

Colonoscopy is the most effective and common screening technique against colorectal cancer contributing to its high diagnostic performance (Kekelidze et al. 2013). The principle of this endoscopic examination is that a long, flexible tube being attached with a dedicated camera, or a fiber optic is inserted through the anus into the rectum and the colon. As a result, the entire length of the colon and rectum can be detected, providing the opportunity for removing suspected polyps, thereby improving the prevention of colorectal cancer death (CHENG et al. 2012).

1.5.6.2 Virtual colonoscopy

Virtual colonoscopy, also known as computed tomography colonography (CTC), is also an imaging technique for colorectal cancer diagnosis (Heiken et al. 2005). In these years, CT colonoscopy became more popular because lots of studies reported its good clinical performance, safety and cost effectiveness (Kijima et al. 2014). The principle of CTC is that a small, dedicated tube is inserted into the rectum and air, or carbon dioxide is applied to inflate the colon after patient's intestines have been cleaned. Through supine and prone thin-section helical CT of the abdomen and pelvis, the colon wall could be inspected (Chaoui et al. 2000). During the CT colonoscopy process, low X-ray energy is sufficient to create image, meaning that there is a low radiation does applied to patients (Yee et al. 2013). As a relatively new diagnostic tool, CTC has a few advantages in comparison with the conventional colonoscopy. It is a non-invasive technique with no requirement of sedation, and it can be finished in a much short time. Apart from this, low X-ray energy is sufficient for CT colonoscopy.

1.5.6.3 Biopsy

A biopsy is the diagnostic technique by removing a small amount of tissue for the examination under a microscope. The combination of colonoscopy and biopsy is considered the gold standard to diagnose the colorectal lesions (Barret et al. 2013). Usually, the biopsy is applied during a colonoscopy if a suspected colorectal cancer is found by any diagnostic technique. However, the best test results are achieved for lesions more than 6mm. This is largely because

a complete colonoscopy cannot be detected in many patients due to poor bowel conditions, tolerability, obstruction, or other technical difficulties (Graser et al. 2009).

1.5.6.4 Magnetic resonance imaging (MRI)

The principle of clinical MRI is based on the magnetic property of hydrogen and its interaction with both a large magnetic field and radio waves to generate highly detailed images of the human body (Saklani et al. 2014). It is suggested that MRI is the most accurate imaging tool for detecting nodal disease with a sensitivity of 85% and specificity of 97%. Therefore, MRI is essential for accurately staging patients with rectal cancer in order to select indications for preoperative treatment or to determine the extent of radical surgery (De Rosa et al. 2015).

1.5.6.5 Endorectal ultrasound (ERUS)

Ultrasound uses sound waves to generate pictures of internal organs to determine if cancer has spread to other part of the body. Endorectal ultrasound, which is another mature way to assess the integrity of the rectal wall, is often utilised to find out the depth of growth of rectal cancer and can be used to help plan treatment (De Rosa et al. 2015). However, ERUS cannot accurately detect cancer that has spread to nearby lymph nodes or beyond the pelvis. As reported by *Swartling et al.*, the combination of MRI and ultrasound improves the accuracy of diagnosis (Swartling et al. 2013).

1.5.6.6 Positron emission tomography/ computed tomography (PET/CT)

PET, which is a nuclear medicine technology, utilised short-lived radionuclides attached to biomolecules to visualize metabolic processes in the body by generating distributed images (Tutt et al. 2004). A PET scan is usually combined with a CT scan and is called a PET-CT scan. PET and PET/CT have been identified to change the treatment of nearly one-third of patients with advanced primary rectal cancer (Heriot et al. 2004). Nowadays, PET/CT is only recommended for the evaluation of suspected colorectal cancer recurrence and preoperative staging before resection of metastases (Nagata et al. 2008).

1.5.7 Traditional colorectal cancer therapy

Contributing to the advanced diagnostic and treatment techniques, the survival time in patients with colorectal cancer has been improved significantly (Xie et al. 2020). Treatment of colorectal cancer depends on the stage of diagnosis, as listed in Table 1.8. Currently, surgery, chemotherapy, radiotherapy, immunotherapy and targeted therapy are the most common treatment techniques in colorectal cancer.

1.5.7.1 Surgery

Typically, surgery is the most ideal treatment for patients with non-metastasized colorectal cancer, in which the tumour can be removed completely (Kuipers et al. 2015). However, there are still approximately 25% of CRCs are diagnosed at late metastasis, which brings difficulties to surgery and follow-up treatment (Keum and Giovannucci 2019). The most common sites of metastasis are liver, lung, peritoneum and retroperitoneum (Goodwin and Asmis 2009). In addition to this, the outcome of the surgery is closely related to the quality of the surgery and treatment selection (van de Velde et al. 2014). In this situation, chemotherapy or radiotherapy may be applied as neoadjuvant or adjuvant therapy before or after surgery to minimize and stabilize the tumour (Labianca et al. 2013; Van Cutsem et al. 2014).

1.5.7.2 Chemotherapy

Whilst surgery remains the primary treatment for patients with colorectal cancer, it is recommended that chemotherapy can be applied as an adjuvant therapy after surgery for any medically-fitted patient with stage II colorectal cancer (Gill et al. 2003; Jonker et al. 2011). Current chemotherapy includes both single-agent therapy mainly based on fluoropyrimidine (5-FU) and multi-drug regimens containing one or several drugs, including oxaliplatin (OX), irinotecan (IRI) and capecitabine (CAP or XEL) (Xie et al. 2020). Apart from these, Leucovorin (LV) itself is not a chemotherapy drug, but it is used together with these chemotherapy drugs to enhance the anti-cancer effect. Nowadays, 5-FU has remained the most effective drug for colorectal cancer treatment (Köhne-Wömpner et al. 1992). It was reported that the disease-free survival at 3 years increased to 78.2% in adjuvant colon cancer when using 5-FU plus LV

and OX, compared with using 5-FU-based chemotherapy alone (72.9%) (Gramont et al. 2007).

1.5.7.3 Radiotherapy

Radiotherapy has been utilized as one of the main treatment methods together with surgery for patients with colorectal cancer, especially for rectal cancer, which could improve patients' prognosis (Häfner and Debus 2016). During these few decades, radiotherapy technique has made significant progress. Initially, only patients who were basically inoperable or had local recurrence received radiotherapy. And now, radiation is used more frequently in all possible treatment settings, ranging from radiation as a single modality to radiation before, during and after surgery (Aleman et al. 1995).

1.5.7.4 Targeted therapy

Targeted therapy can inhibit cell proliferation, differentiation and migration by selective targeting specific molecular pathways involved in tumourigenesis or tumour progression (Oh and Bang 2020). The tumour microenvironment, such as local blood vessels and immune cells, may also be altered by targeted drugs to prevent tumour (Ferguson and Gray 2018). Small molecules, such as monoclonal antibodies, are major players in targeted therapy (Xie et al. 2020). Compared with chemotherapy, target therapy more selective and it does not affect the pathways that are common to normal tissues and tumours to a large extent (Jr 2005).

1.5.7.5 Immunotherapy

In recent years, lots of understanding of the intricate relationship between the immune system and cancer has made some significant progress, which has led to major developments in tumour immunotherapy. One of the most popular techniques is cancer vaccination. Cancer vaccination has been utilized for several tumour types to trigger an anti-tumour immune response, thereby eliminating the tumour and providing continuous monitoring to prevent its re-growth. The types of vaccines used for colorectal cancer in the past decade include autologous, peptide, viral vector and dendritic cell (DC) (Kalyan et al. 2018)

1.6 Tight junctions (TJs)

Cells may have several different types of specialized cell-cell contacts known as cell junctions, which play an important role in maintaining the integrity of tissue structure and coordinating the function of the cells. Cell junctions runs from the apical to the basal membranes and are broadly divided into five categories according to their difference in structure and function, including Tight Junctions (TJ), Adherens Junctions (AJ), Gap Junctions (GJ), Desmosomes, and integrins (Martin et al. 2013), as shown in Figure 1.16. TJs play a vital role in maintaining the intercellular permeability of epithelial and endothelial cells (Martin et al. 2011).

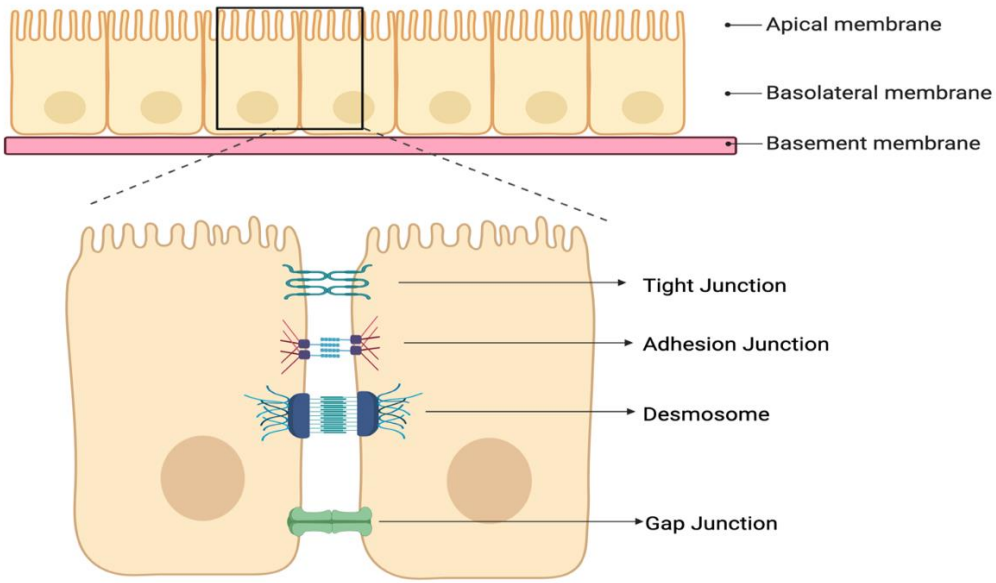

Figure 1.16 The main structure for cell-cell interaction in epithelial cells. The TJ is located at the most epical location.

1.6.1 The structure of tight junction

TJs are the most epical structure in epithelial and endothelial cells. TJs have a characteristic structure defined by electron microscopy, which can be seen as fusion sites between the outer plasma membrane of adjacent cells. TJs appear as continuous intramembrane particle strands on the surface of the protoplasm. These completely limit the apices of the cells as a network of intramembrane fibrils (Martin 2014).

1.6.2 The function of tight junction

There are four main functions contributed to epithelial/endothelial TJs (Martin et al. 2011):

1. TJ seals the intercellular space and separates the apical and basolateral fluid compartments of epithelial and endothelial cells due to the characteristic that it regulates the permeability of epithelium and endothelium, and it is an area where adjacent cell plasma membranes form a series of contacts that seem to completely close the extracellular space.

2. TJ plays a role in polarity, cell differentiation, cell growth and proliferation through the involvement of TJ molecules that act as intermediates and transducers of cell signalling. It is suggested that TJ is participated in the regulation of cell proliferation by controlling the microenvironment of epithelial cells (Tamura et al. 2008).

3. TJs act as cell-to-cell adhesion molecules.

4. The TJ functions as cell migration and motility barrier. Their function appears to be regulated by phosphorylation (Salvador et al. 2016).

1.6.3 The tight junction molecules

Generally, TJ proteins mainly consist of three components, including integral transmembrane proteins, peripheral or plaque anchoring proteins and TJ-associated or regulatory proteins, as listed in Table 1.9. Intact transmembrane proteins are the essential adhesion proteins responsible for the correct assembly of the TJ structure and the control of TJ function through homotypic and heterotypic interactions. The successful assembly and maintenance of TJ is achieved by anchoring transmembrane proteins with peripheral or plaque proteins (such as ZO-1), as shown in Figure 1.17 (Martin et al. 2011).

Table 1.9 Proteins involved in TJ structure, function, and regulation.

Integral transmembrane proteins	Peripheral or plaque anchoring proteins	TJ-associated or regulatory proteins
the TAMP proteins: Tricellulin (Marvel D2), Marvel D3, Occludin	ZO family: ZO1 ZO2 ZO3	Cingulin, 7H6, Symplekin, ZONAB, Rab-13, 19B1, ponsin, Rab 3B, PKC, l-afadin, c-src, Gαi-2, Gαi-12, α-catenin, Pals, PATJ, PKA, JEAP, Pilt, PTEN, ZAK, SCRIB, ITCH, Rho-GTPases, WNK4, vinculin
	MAGI-1 MAGI-2 MAGI-3	
	s-afadin/AF6	
Claudin family	Par3/ASIP	
JAMs (Junctional adhesion molecules)	Par6	
Nectins	MUPP-1	
CTX family: Coxsackie adenovirus receptor (CAR)	CAROM	
	CASK	

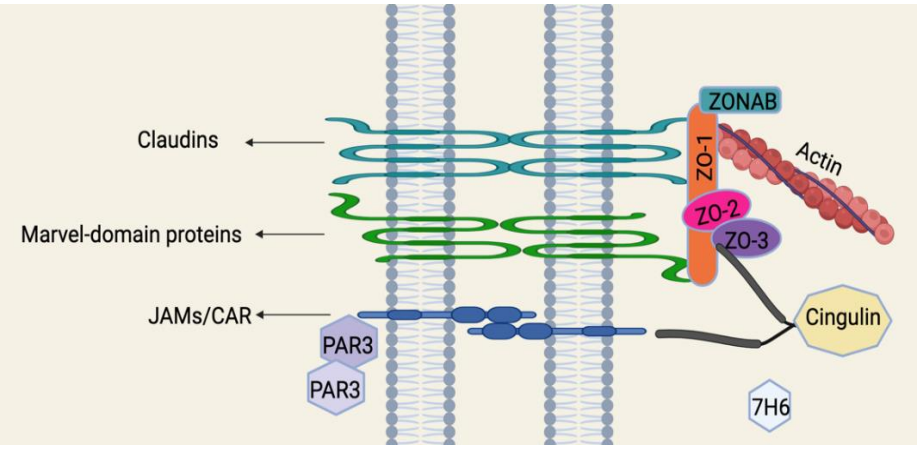

Figure 1.17 The structure features of TJ proteins. TJs main consist of three components, including integral transmembrane proteins, peripheral or plaque anchoring proteins and TJ-associated or regulatory proteins.

1.6.4 The role of tight junction in cancer metastasis

Cancer metastasis, which is the spread of tumour cells to a distant site, is the most life-threatening event in patients with diagnosed cancer (Martin et al. 2013). In order to metastasize successfully, several steps must be completed, including invasion, intravasation and extravasation, as illustrated in Figure 1.18 (Jiang et al. 1994). Invasion is characterized by the loss of cell-cell adhesion ability that enables cancer cells to dissociate form the primary tumour mass. The process of intravasation is the initialization of angiogenesis so that the blood vessels near the tumour can then provide a way for the detached cells to enter the circulatory system and transfer to distant sites. Once the tumour cell reaches the possible point of extravasation, it will interact with the endothelial cells to form stronger adhesion,

thereby penetrating the endothelium and basement membrane; the process of extravasation (Martin et al. 2013).

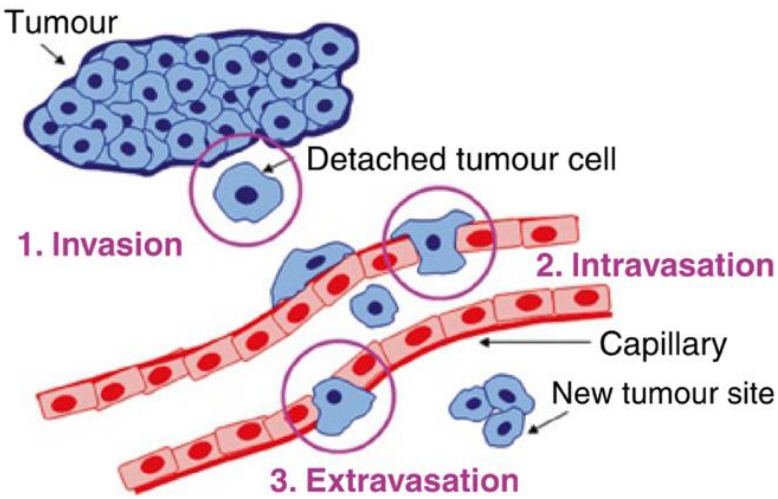

Figure 1.18 Main process of cancer metastasis, including invasion, intravasation and extravasation (Martin et al. 2013).

In epithelial cells, the TJ functions in an adhesive manner to prevent cell dissociation. Whilst in endothelial cells, TJ acts as a barrier through which molecules and inflammatory cells can pass (Martin and Jiang 2012). TJs are therefore the first barrier that cancer cells must overcome in order to metastasize (Martin and Jiang 2001). Currently, there have been a number of studies focused on the relationship between TJ and colorectal cancer (Gröne et al. 2007; Bornholdt et al. 2011), breast cancer (Martin et al. 2004; Martin et al. 2007) and pancreatic cancer (Kleeff et al. 2001; Kojima et al. 2011). Changes in tumours and endothelial cells are an indispensable process for the successful growth and spread of cancer cells. By upregulating or downregulating related TJ proteins, cancer cells lead to loss of intercellular association and cell contact inhibition, leading to uncontrolled growth, loss of adhesion to and degradation of the basement. These must be the simultaneous loss of cell-cell contact in the endothelium and the regulation of TJ proteins involved in promoting the passage of cancer cells through this barrier (Martin et al. 2013).

Epithelial to Mesenchymal Transition (EMT) is a process during which cells lose their epithelial properties, such as intercellular adhesion and cell polarity, and obtain mesenchymal characteristics to become mesenchymal stem cells (Vu and Datta 2017). In the past decade,

many studies have shown that EMT plays a vital role in cancer progression and metastasis in different types of malignancies including colorectal cancer (Cao et al. 2015). A group of key biomarkers are involved in the process of EMT, including Twist, Snail-1, Slug, E-cadherin and N-cadherin. EMT is characterized as the loss of E-cadherin and obtain of N-cadherin. As an epithelial cell-cell adhesion molecule, E-cadherin has been reported as a tumour suppressor. On the contrary, N-cadherin, a kind of transmembrane protein, helps cancer cells enhance their ability of migration and invasion (Yan et al. 2015). Apart from these, several EMT-activating transcription factors are required to promote transcriptional mechanism. Snail can bind to proximal E-box at the E-cadherin promoter for E-cadherin silencing to achieve the progression of tumours (Bolós et al. 2003). Basic helix-loop-helix protein Twist, known as an antiapoptotic factor, is also found to trigger EMT mechanisms by repressing E-cadherin and inducing the expression of N-cadherin (Yang et al. 2004).

Nowadays, lots of studies report the role of TJs in the EMT. For instance, in breast cancer, the expression of some 'Claudin-low' molecules are inhibited by EMT-inducing transcription factors such as ZEB1/2, Snail1/2 and Twist1/2 (Prat et al. 2010). Claudin-7 inhibits ERK/Src signalling and suppresses EMT in colorectal cancer cell (Bhat et al. 2015a). Whereas Claudin-1 can promote EMT by regulating the β-Catenin/Tcf/Lef signalling pathway in colorectal cancer (Miwa et al. 2001). All these findings indicated that TJs have distinct tissue-specific and cancer-specific regulatory mechanisms, enabling them to play different roles during EMT.

1.6.5 Changes of tight junction in colorectal cancer

TJ plays an important role in colon structure since it helps to maintain the integrity of the intestinal wall, which is critical for the absorption of nutrients and the prevention of harmful substances from entering the bloodstream. Lots of studies have revealed that there is a strong relationship between the abnormal expression of TJ proteins and colorectal cancer, and the permeability of TJ structure in colorectal cancer tumours is higher than those of normal colon (Soler et al. 1999).

It has been reported that the expression of claudin-1 and Smad4, a tumour suppressor protein, in colon cancer cell lines is inverse (Shiou et al. 2007). The loss of Claudin-7 in colorectal cancer

can cause the increase of EMT, which is a key process in cancer progression and metastasis (Bhat et al. 2015b). In addition to downregulation, TJ proteins can also be mislocalized in colorectal cancer. It has been found that the location of Claudin-1 is in the cytoplasm of cancer cells, instead of being localized in the cell membrane, leading to increased tumour invasion and metastasis (Dhawan et al. 2005). Resnick et al. investigated the expression of some TJ proteins, including Claudin-1, claudin-3, occluding and ZO-1 in a colon cancer cohort, and found that low expression of these proteins were directly related to higher tumour grade (Resnick et al. 2005).

1.6.6 Changes of tight junction in breast cancer

A wide range of studies indicated that breast cancer progression is strongly correlated with abnormal TJ proteins. For example, some key TJ components such as Claudin-1, occludin, and ZO-1 cannot be detected in breast cancer MDA-MB-435 cells, while they are normally expressed in most of the mammary gland-derived epithelial cells (Hoevel et al. 2002). Some studies indicated that Claudin-7 was down-regulated in breast cancer compared with normal breast epithelium, and the absence of Claudin-7 is reported to be related to histological grade in ductal carcinoma in situ and invasive ductal carcinoma of the breast (Usami et al. 2006; Constantinou et al. 2018). Apart from these, Claudin-16 was found to be reduced in breast cancer patients with metastasis, recurrence or mortality compared with the healthy patients (Martin and Jiang 2009). Some in vitro experiment purposed that the overexpression of JAM-A inhibited migration and invasion ability of breast cancer MDA-MB-231 cells (Naik et al. 2008). In vivo xenografted MCF-7 cell lines into mice experiment presented that knockdown of Claudin-4 could suppressed the growth of tumour (Ma et al. 2015).

1.7 Marvel domain containing 3 (MarvelD3)

1.7.1 The structure and expression of MarvelD3

MarvelD3 is transmembrane protein belongs to the TJ subfamily TJ-associated marvel protein (TAMP) family, together with Occludin (MarvelD1) and Tricellulin (MarvelD2). MarvelD3 was firstly identified by Raleigh *et al.* in 2010 (Raleigh et al. 2010a). Bioinformatic analysis

indicated that human MarvelD3 has two splicing variants, namely MarvelD3 v1 containing 410 amino acids with a molecular mess 46 kDa, and MarvelD3 v2 containing 401 amino acids with a molecular mess 45 kDa. Both variants are suggested to contain four transmembrane domains, with both N- and C- terminal domain orientating towards the cytoplasm, as illustrated in Figure 1.19A. It was found that MarvelD3 v1 and v2 have the same N-terminal cytoplasm domain of 198 amino acids, but show different sequence of their Marvel (transmembrane) domains and short C-terminal domains, as shown in Figure 1.19B (Raleigh et al. 2010a; Steed 2011). The RT-PCR was performed on adult mice confirmed that both MarvelD3 v1 and v2 are widely expresses in several organs, including lung, colon, small intestine, stomach, and kidney. However, different expression patterns of these two variants are also noticed in liver, with only MarvelD3 v1 expression is detectable there (Steed et al. 2009). In cancer, it has been reported that the expression of MarvelD3 is reduced in cells with a metastatic phenotype (Steed 2011).

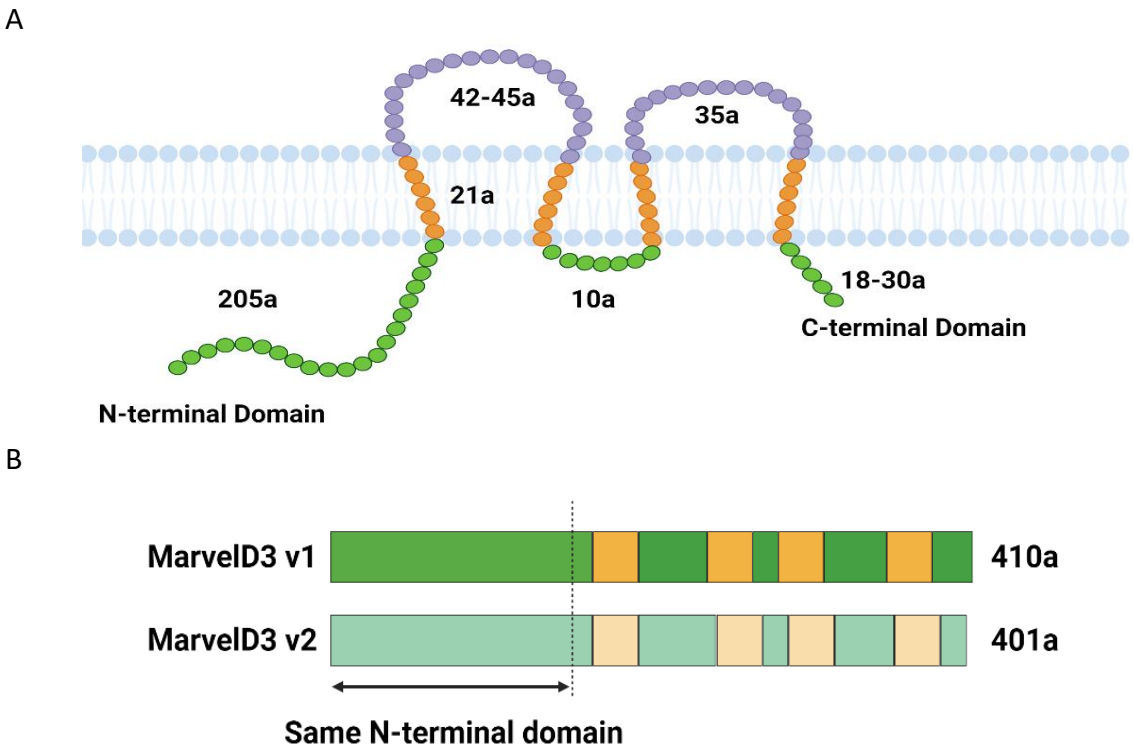

Figure 1.19 Schematic diagram of MarvelD3 structure : (A) the cytosolic domains colored in green, the transmembrane colored in orange, and the extracellular domains colored in purple. (B) two human variants of MarvelD3, MarelD3 v1 and MarelD3 v2, with transmembrane domains colored with orange and yellow respectively. Two variants share the same N-terminal domain of 198 amino acids but show different sequences of their Marvel (transmembrane) domains and short C-terminal domains.

1.7.2 The location of MarvelD3

Previous study found that Occludin primarily locates in the bicellular junction regions, and Tricellulin mainly localizes in the tricellular junction regions, while MarvelD3 is found in both junction regions (Shi et al. 2018). Antibody-stained assay was conducted in some epithelial cell lines proposing that MarvelD3 colocalised with Occludin (Steed 2011), and Tricellulin (Cording et al. 2013), suggesting that MarvelD3 is a component of the apical junctional complex. The whole TAMPs structure is demonstrated in Figure 1.20.

ZO-1 (Zonula occludens-1), the first recognised TJ proteins, plays a vital role in the organization of components in TJs (Fanning et al. 1998). Previous studies indicated that the localisation for both Occludin and Tricellulin by their C-terminal cytoplasmic domains is necessarily associate with ZO-1 (Fanning et al. 1998; Riazuddin et al. 2006). Therefore, it was expected that MarvelD3, the last identified member of TAMPs, might have the same or similar characteristic. Oppositely, some studies showed no interaction between MarvelD3 and ZO-1, suggesting that the localisation of MarvelD3 is not related to ZO-1 (Raleigh et al. 2010a; Steed 2011).

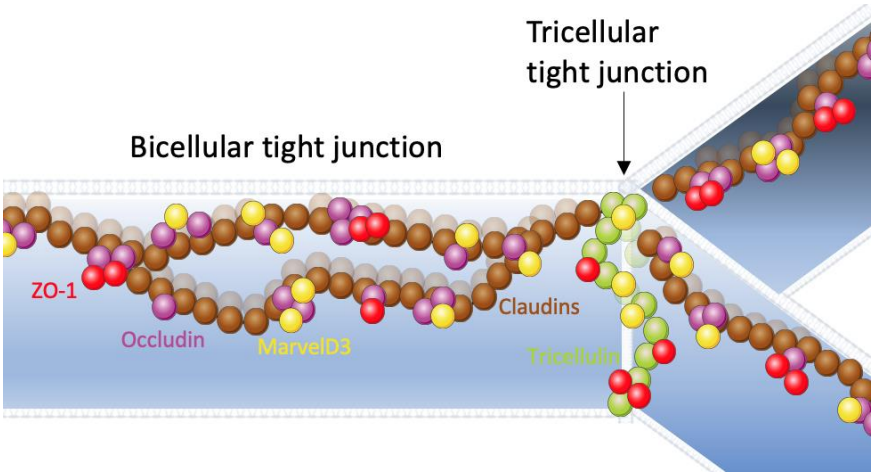

Figure 1.20 Schematic diagram of the TAMP location molecules. Occludin and Tricellulin mainly localizes in the bicellular and tricellular junction regions respectively, while MarvelD3 colocalizes in both junction regions with occludin and Tricellulin. ZO-1 is associated with the localisation of Occludin and Tricellulin, but not MarvelD3.

1.7.3 Function and functional interacting partners of MarvelD3

1.7.3.1 Function of MarvelD3 at TJs

The predominant role of TJ proteins is the regulation of permeability and therefore maintain the integrity of TJ (Vermette et al. 2018). Some members of Claudin family enhances barrier forming such as claudin-3, 4, 5, 8, 11, 14 and 19, while other Claudin members form ion pores like claudin-2, 10 (Günzel and Yu 2013). Some TJ proteins, such as ZO-1, 2, 3, act as receptors to regulate integral membrane proteins and other signalling proteins (Lee et al. 2018). Besides, numerous studies indicated the important role of Occludin and Tricellulin in the formation and maintenance of TJ structures and are required for the establishment of a permeability barrier for ions (Rao 2009; Mariano et al. 2011).

While the knockdown of MarvelD3 in CRC Caco-2 cell line suggested that MarvelD3 is not responsible for the formation of TJ, but it is a determinant of paracellular ion conductivity (Steed et al. 2009). Another research group conducted the TER and tracer flux measurement experiment with MarvelD3 knockdown in Madin-Darby canine kidney (MDCK) cells confirmed that MarvelD3 is not essential for the maintenance of TJ, also it is not involved in the establishment of tight permeability barrier (Saito et al. 2022). However, an in vitro experiment with MarvelD3 knockdown in pancreatic cancer cell HPAC resulted in the downregulation of barrier functions indicated by the resistance changes in TER experiment and the increase of permeability to fluorescent dextran tracers (Kojima et al. 2011). Taken together, the role of MarvelD3 is inconclusive, this might be caused by the limited studies, or maybe the role of MarvelD3 is cancer type/ cell line dependent.

1.7.3.2 MarvelD3 interacts with TJ proteins

Fluorescence resonance energy transfer (FRET) assays, as an indicator of heterophilic cis-interactions, revealed that MarvelD3 interacts with both Occludin and Tricellulin physically at cell-cell contacts in human embryonic kidney (HEK)-293 cells. In addition to the TAMPs, this research found that MarvelD3 interacts with some members of Claudin, including Claudin-1, 3, 4, 5 by the analysis of the colocalization of TAMPs with selected Claudins as well as their

cis-interaction. It would suggest that MarvelD3 might incorporate with some other TJs in the TJ network, although evidence remained less (Cording et al. 2013). The possible interaction partners of MarvelD3 are illustrated in Figure 1.21.

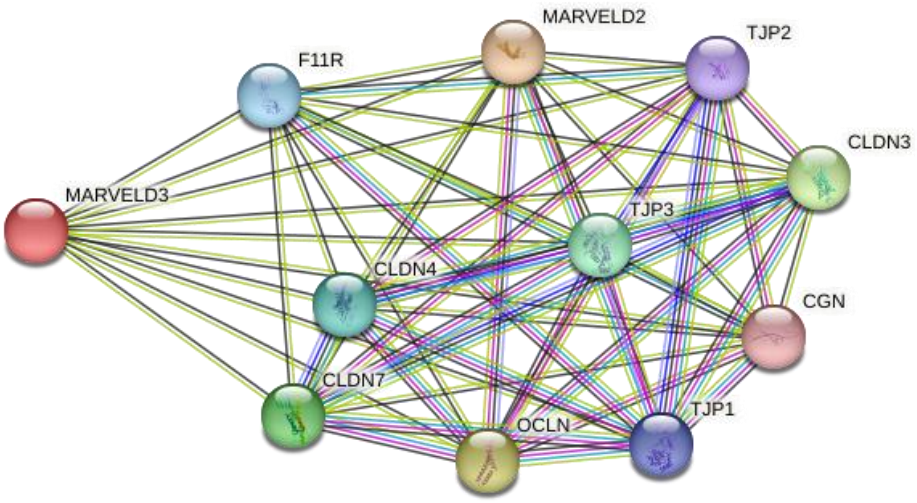

Figure 1.21 Network of interacting partners of MarvelD3. Picture was collected from the STRING, ELI'IR's Core Data Resources. Available: https://version-12-0.string-db.org/cgi/network?taskId=b0OEpD89j0qc&sessionId=bp7rWp4XCDSL

1.7.4 Multiple roles of MarvelD3 in cancer

1.7.4.1 Breast cancer

The role of MarvelD3 in cancer progression and metastasis has been studied in breast cancer in disease progression and clinical outcomes. The analysis of clinical cohort revealed that the transcript expression of MarvelD3 was significantly higher in breast cancer tissues in comparison with their paired normal tissues (JI et al. 2023). Another human survival analysis from online database suggested that the expression of MarvelD3 in primary breast tumours was correlated with recurrence-free survival in patients with basal, luminal A and luminal B subtype of breast cancer, but not in patients with Her2+ or normal-like subtype of breast cancer (Mamoor 2022). Taken together, it can be anticipated that MarvelD3 might play a role in maintenance and progression of breast cancer.

1.7.4.2 Oral squamous cell carcinoma (OSCC)

In a clinical cohort of patients with OSCC, it was found that MarvelD3 had significantly higher expression level in OCSS tissues than that of normal tissues. Also, the expression of MarvelD3 was correlated with poor overall survival in patients with OSCC, predicted that MarvelD3 could be identified as a novel prognostic factor for OSCC (Huang et al. 2022).

1.7.4.3 Pancreatic cancer

Western blotting and PCR was conducted to examine the expression of MarvelD3 in well and poorly differentiated human pancreatic cancer cell lines. It was found that MarvelD3 expression was strongly higher in well differentiated HPAC cells compared with poorly differentiated PANC-1 cells. Besides, in vitro experiment with the knockdown of MarvelD3 inhibits the barrier function in HPAC cells by the TER measurements. (Kojima et al. 2011). The research found that MarvelD3 showed to be downregulated during Snail-induced EMT subjected to hypoxia, TGF-β treatment and FOXA2 knockdown in HPAC (Kojima et al. 2011). This finding may support other studies that the expression of MarvelD3 is strongly reduced in cell lines with invasive phenotypes (Steed et al. 2009). Steed et al. indicated that overexpression of MarvelD3, could inhibit the migration and proliferation in MIA PaCa-2, a cell line that cannot detect the expression of MarveD3. Apart from this, in vivo xenografted Miacapa-2 cell lines into mice experiment presented that overexpression of MarvelD3 could suppressed the growth of tumour, indicating that MarvelD3 suppress proliferation of pancreatic tumour cells in vivo and in vitro. (Steed et al. 2014). Therefore, MarvelD3 might be possible as a new biomarker during pancreatic cancer progression.

1.7.4.4 Colorectal cancer

The role of MarvelD3 in colorectal cancer was investigated by Steed et al. Knockdown of MarvelD3 was established in Caco-2 cells and showed to promote the cell migration and proliferation. These changes are possibly because MarvelD3 interacts with MEKK1, thereby regulating cellular behaviours of colorectal cancer. Knockdown of MarvelD3 in Caco-2 cell line suppressed the interaction between MarvelD3 and MEKK1, resulting in the upregulation of

JNK phosphorylation. Consequently, the mechanism of MarvelD3 inhibits colorectal cancer migration and proliferation may occur by regulating MEKK1-JNK signalling pathway (Steed et al. 2014).

1.7.4.5 Hepatocellular carcinoma (HCC)

Western blotting and RT-PCR assays showed that the expression of MarvelD3 was significantly lower in HCC tissues that that of adjacent normal tissues from both protein and RNA levels. The immunohistochemistry staining indicated that lower expression of MarvelD3 was correlated with in poor tumour TNM stages. Apart from these, in vitro experiment revealed that the knockdown of MarvelD3 could promote migration and invasion in HCC Hep3B and Huh-7 cells. This is further verified by the overexpression of MarvelD3 suppressing the migration and invasion ability in these two cell lines. This study also detected the expression of MarvelD3 was decreased in Hep3B and Huh-7 cells with transforming growth factor β1-inducted EMT. The knockdown of MarvelD3 could downregulate E-cadherin and upregulate vimentin, two key biomarkers involved in EMT, suggesting that MarvelD3 plays a role on regulating the EMT. Furthermore, this research also found the activation of NF- κB, a vital regulator of EMT and cell metastasis, in MarvelD3 knockdown models. Thereby, based on this study, it can be suggested that MarvelD3 inhibits EMT, migration and invasion of HCC by inactivation the NF- κB signalling pathway (Li et al. 2021a).

1.7.4.6 Non–small cell lung cancer (NSCLC)

In a Western blotting assay, MarvelD3 expression in NSCLC tissues were significantly lower compared with para-carcinoma tissues, and the decreased expression of MarvelD3 was found to be correlated with tumour metastasis. Also, MarvelD3 expression was decreased in TGF-β1-induced EMT process in NSCLC PC9 and HCC827 cells. Besides, knockdown of MarvelD3 in PC9 and HCC827 showed decreased expression of E-Cadherin and increased expression of Vimentin. This might suggest that MarvelD3 involves in the regulation of EMT. Further in vitro experiment found the loss of MarvelD3 could promote cell migration and invasion in these two cell lines. Overexpression of MarvelD3 confirmed this finding, as cells overexpressed with MarvelD3 inhibits their invasion ability. In addition, the loss of MarvelD3 resulted in the

upregulation of c-Myc, cyclin D1, and nucleus β-catenin and downregulation of cytoplasmic β-catenin, which are some targeted genes involved in the Wnt/β-catenin pathway, a pathway known to promote EMT process. These results indicated that MarvelD3 can inhibit EMT and cellular behaviours by inactivating the Wnt/β-catenin signalling pathway, suggesting that MarvelD3 may have a role as a potential biomarker in the treatment of NSCLC (Li et al. 2023).

Taking together, although previous studies have implicated MarvelD3 in several cancer types, their regulatory roles in cancer progression, especially for breast and colorectal cancer, has not been fully established. The current study aims to explore the clinical and biological roles of MarvelD3 in breast and colorectal cancers.

1.8 Previous PEFE system

The previous pulsed electromagnetic field exposure (PEFE) system could induce cell death at the microwave range in breast cancer cell lines *in vitro*, independent of the thermal effect of microwaves. This technique also has significance in clinical application as confirmed using a nude mouse model xenografted with human breast cancer cells. PEFE used in this research was based on the pulse signal with repetitive microwave frequencies and adjustable duty cycle generated by a serial of microwave devises. PEFE could induce cell death through both necrosis and apoptosis. Necrosis was mainly caused by the breakdown of membrane structure and organelles, while apoptosis was triggered by the destruction of TJs (Zhao 2020).

1.8.1 Components of previous PEFE system

The previous PEFE system consists of a series of devices, including signal generator, amplifier, circulator, directional coupler, power sensors and temperature sensor, as shown in Figure 1.22.

The signal source was generated by a RF signal generator in this system. A dedicated power amplifier was used to boost signals from the signal generator to the desired value. Due to the equivalent impedance mismatch between the biological sample and coaxial cable (probe), both incident signals and reflected signals were generated. The reflected signal will transfer

from the end of the probe to the amplifier, which will disturb the output power and cause waveform distortion, resulting in inaccurate measurement outcome. Therefore, a circulator attaching with a 50 ohms termination was installed after the amplifier to solve this problem. Also, a directional coupler was utilized to separate these two signals and measure it through two power sensors.

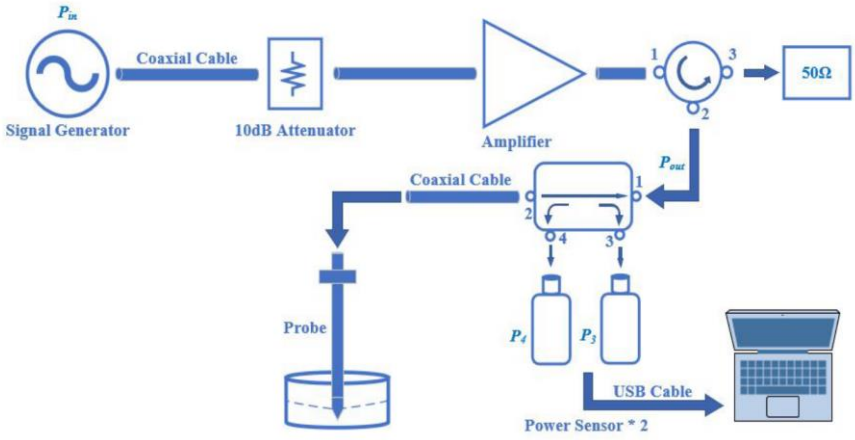

Figure 1.22 Previous PEFE system conducted by a series of microwave devices (Zhao 2020).

1.8.2 A brief conclusion of previous PEFE experiment

In the previous study, the PEFE system was applied to biological samples at different frequencies and power levels. Both *in vitro* and *in vivo* experiments were conducted to evaluate its effect on cell death and tumour growth. It showed that PEFE has potential significance as a clinical application.

1.8.2.1 *in vitro* experiment

As mentioned before, PEFE was developed to kill cancer cells in normothermic conditions. Zhao reported that after breast cancer cells were subjected to PEFE at 2.2 GHz and 30 watts for forty-eight hours, the death rate of treated cells was 43.28%, which was much higher than that of control group (13.19%) (Zhao 2020). Further experiments verified that cancer cells were killed via both necrosis and apoptosis, which was confirmed by visual inspection using scanning electron microscope (SEM) and apoptosis-related protein Kidins220. Also, protein kinase array showed that PEFE exposure caused remarkable signature changes in intracellular

signalling events resulting in apoptosis, including Mitogen-activated protein kinase (ERK) (Martin et al. 2021).

1.8.2.2 *in vivo* experiment

In the *in vivo* study with a nude mouse model xenografted with human breast cancer cells, tumours were grown to around 0.5 cm^3 before PEFE treatment. The experimental results showed that the tumour volume was significantly reduced after one week compared with the control group ($p<0.01$). Three weeks after PEFE treatment, it was found that most of the tumours disappeared, with no detectable scars and side effects (Zhao 2020).

1.8.3 Advantages and disadvantages of previous PEFE system

Advantages – current unmet clinical need

1. In comparison with existing ablation for cancer treatment such as laser, RF and MW, PEFE does not generate locally high temperature, and therefore there is no impact on surrounding vascular and normal tissue.

2. For patients who are not eligible for traditional surgery or receiving radiotherapies (elderly, pregnant/nursing, immunocompromised, unable to have anesthetic), this technique has potential in minimally invasive surgery for cancer treatment without associated physical consequences.

Disadvantages

Even though this system can complete all missions which were required in this study, there are still some drawbacks.

1. This system consists of several microwave instruments with large size, which occupies a large space and is difficult to transport.
2. PEFE system was developed to induce cell death at low temperature, therefore a

temperature sensor was used to monitor the temperature and strictly maintained it under 42℃ around the tip of the probe. When the temperature was close to 42℃, the signal generator needed to be switched off manually to prevent further temperature increase. When it returned back to about 37℃, generator was switched on again. Apart from this, this system does not support remote control. Consequently, this manually conducted work is extremely time-consuming, and also has a certain degree of damage to the equipment.

3. The power meters used in this system can only measure the power, but they do not provide information of where the power is at which frequency (i.e., phase).

1.9 Hypothesis and aims of this study.

Previous pulsed electric field exposure (PEFE) system successfully killed human breast cancer cells under normothermic conditions. The overall aims of this study were to further refine the PEFE system and investigate the possible mechanisms whereby PEFE technique mediates cell death.

The hypothesis of this study is that electromagnetic normothermic energy at specified frequencies can be used as a treatment in breast and colorectal cancer by further development and improvement of the PEFE device.

In order to improve both the functionality of the device and learn and implement new cell biology techniques to determine effectiveness and modality on human breast and colorectal cancer cells. The aims of this study were as follow:

1. To develop a new PXI-based PEFE system which can eliminate the drawbacks of the old system, attempting to kill breast and colorectal cancer cells *in vitro* and evaluate its significance in clinical application.

2. To examine MarvelD3 expression in clinical cohorts and TMA of breast and colorectal cancer and its association with patient clinicopathological information and prognosis.

3. To generate MarvelD3 knockdown cell lines and characterize the effects of their dysregulation on cellular traits associated with cancer development and metastasis.

4. Further determination of the link between PEFE and TJ and cell death.

Chapter-2 Materials and Methods

2.1 **Materials**

2.1.1 Cell lines

The human breast cancer cell lines involved in this study include MDA-MB-231, MCF-7, ZR-751, SKBR3, and BT-549 cells, human colorectal cancer, RKO, HT115, HRT18, and Caco-2 were also used. All cells were purchased from the American Type Culture Collection (ATCC, Rockville, MD, USA)/ (LGC Standard, ATCC UK agent). All cell stocks were verified as mycoplasma-free using a GENEFLOW kit (Geneflow Ltd., Litchfield, UK), and were stored in liquid nitrogen preservation at low passage. Details of these cell lines are listed in Table2.1 and Table 2.2.

Table 2.1 Details of Wild Type Breast Cancer Cell Lines used in this study

	MDA-MB-231	**MCF-7**	**ZR-75-1**	**SKBR3**	**BT-549**
Organism	Homo sapiens, human	Homo sapiens, human	Homo sapiens, human	Homo sapiens, human	Homo sapiens, human
Tissue	Mammary gland/breast	Mammary gland, breast	Breast; Duct; Mammary gland	Mammary gland, breast	Mammary gland, breast
Morphology	Epithelial	Epithelial	Epithelial	Epithelial	Epithelial
Culture Properties	Adherent	Adherent	Adherent	Adherent	Adherent
Age	51	69	63	43	72
Gender	Female	Female	Female	Female	Female
Disease	Adenocarcinoma	Adenocarcinoma	Ductal carcinoma	Adenocarcinoma	Ductal carcinoma

Table 2.2 Details of Wild Type Colorectal Cancer Cell Lines used in this study

	RKO	HT-115	HRT-18	Caco-2
Organism	Homo sapiens, human	Homo sapiens, human	Homo sapiens, human	Homo sapiens, human
Tissue	Colon	Colon	Colon	Colon
Morphology	Epithelial	Epithelial	Epithelial	Epithelial-like
Culture Properties	Adherent	Adherent	Adherent	Adherent
Age	?	?	67	72
Gender	?	Male	Male	Male
Disease	Carcinoma	Colorectal adenocarcinoma	Ileocecal colorectal adenocarcinoma	Colorectal adenocarcinoma

2.1.2 Cancer tissues collection

2.1.2.1 Colorectal cancer tissues collection and processing

Normal human colorectal tissues (n=80) and human colorectal cancer tissues (n=94) were collected at the University Hospital of Wales, Cardiff and Vale University Health Board, immediately after surgery from informed, consenting patients. Tissue was collected from the operating theatre during the procedure by a clinical research fellow, followed by evaluation by a consultant pathologist. Samples of colorectal carcinoma, normal matched colorectal tissue (>10cm away from tumour margin) were obtained. Tissue samples were placed in labelled sterile universal containers, frozen in liquid nitrogen, and stored in the research laboratory at -80°C until required. A subsequent pathological report was obtained for data stratification. Patients underwent routine clinical, colonoscopic and radiological follow up after the surgery and results were obtained using the hospital clinical portal system and Cancer Network Information System Cymru (CANISC) data. The median follow-up period was 65 months. Ethical approval for the use of tissue was obtained from the South East Wales Local Research Ethics Committee (reference number SJT/C617/08).

2.1.2.2 Breast cancer tissues collection and processing

This study also employed a human breast cancer cohort from University Hospital of Wales,

Cardiff and Vale University Health Board. Human breast cancer tissues (n=127) and background normal tissues (n=33) were obtained immediately after after surgical removal of breast cancer from the hospital and immediately stored in liquid nitrogen until use, as previously reported (Jiang et al. 2006). Written informed consent was required and obtained from patients, with the median follow-up period of 120 months (June 2004). The presence of tumour cells in collected tissues was confirmed by a consultant pathologist who examined H&E-stained frozen sections. Data from clinical records, including pathological, clinical, and follow-up information, were acquired and employed for subgroup analyses. The samples were collected under ethical approval (Bro Taf Health Authority; ethics approval numbers 01/4303 and 01/4046).

2.1.3 Instruments, software, and general cell culture plastic

The microwave instruments and software used in this study and their suppliers are given below in Table 2.3.

Table 2.3 Microwave instruments and software used in this study

Microwave Instruments	**Supplier**
NI PXIe-1095 18-Slot PXI Chassis	National Instruments Corporation Austin, TX, USA
NI PXIe-8133 3.06 GHz PXI Embedded Controller	National Instruments Corporation Austin, TX, USA
NI PXI-5441 16-Bit Arbitrary Waveform Generator	National Instruments Corporation Austin, TX, USA
NI PXIe-5654 250 kHz to 20 GHz RF Analog Signal Generator	National Instruments Corporation Austin, TX, USA
NI PXIe-5663E Vector Signal Analyzer ×2	National Instruments Corporation Austin, TX, USA
MILMEGA AS1860-50 Broadband Power Amplifier	MILMEGA Limited UK
Altan TecRF AS7122 Circulator	Atlantic Microwave Ltd
Directional Coupler 1.5-9.0GHz	
Times Microwave Unterminated to Unterminated RG 405 Coaxial Cable	RS Components Ltd. Corby, Northants, UK
Luxtron M922 Fiber Optic Temperature Sensor	Advanced Energy, LumaSense Technologies Inc., Frankfurt, Germany
U2021XA 50MHz-18GHz USB Peak and Average Power Sensor	Keysight Technologies UK Limited
Software	**Supplier**
LabVIEW 2018	National Instruments Corporation Austin, TX, USA

Software, biological instruments, and general plastic consumables used in this study are listed in Table 2.4.

Table 2.4 General biological materials and suppliers used in this study

General plastic consumables	**Supplier**
25cm^2 and 75cm^2 culture flasks	Greiner Bio-One Ltd, Gloucestershire, UK
Universal Tubes	Fisher Scientific UK, Leicestershire, UK
Microfuge Tubes	Greiner Bio-One Ltd., Gloucestershire, UK
6-well plates	Greiner Bio-One Ltd., Gloucestershire, UK
24-well plates	Greiner Bio-One Ltd., Gloucestershire, UK
96-well plates	Greiner Bio-One Ltd., Gloucestershire, UK
ECIS 96W1E	Applied Biophysics Ltd, Troy, New Jersey, USA
TC translucent inserts for the 24-well plate with 8.0µm pores	Greiner Bio-One Ltd., Gloucestershire, UK
TC translucent inserts for the 24-well plate with 0.4µm pores	Greiner Bio-One Ltd., Gloucestershire, UK
Countess™ cell counting chamber slides	Thermo Fisher Scientific, Waltham, MA, USA
TerraRack Pipette Tips	Mettler-Toledo Rainin, LLC, Oakland, CA, USA
Pipette	Mettler-Toledo Rainin, LLC, Oakland, CA, USA
Sterile Glass Pipette	Fisher Scientific UK, Leicestershire, UK
CRYO.STM tubes	Greiner Bio-One, Germany
MicroAmp Fast Optical 96-Well Reaction Plate with Barcode (0.1ml)	Thermo Fisher Scientific, Waltham, MA, USA
Optical seal	PrimerDesign, Southampton, UK
50ml Centrifuge tube	Greiner Bio-One Ltd, Gloucestershire, UK
Immobilon P PVDF membrane	Merck Millipore, Hertfordshire, UK
Biological instruments	**Supplier**
Neubauer Haemocytometer Counting Chamber	Fisher Scientific UK, Leicestershire, UK
Class II laminar flow cabinet	SafeF ST Classic, FASTER
Safety Bio Cabinet	Wolf Laboratories York, UK
Incubator	Wolf Laboratories York, UK
Countess™ II Automated Cell Counter	Thermo Fisher Scientific, Waltham, MA, USA
ECIS (Electric cell-substrate impedance sensing) Ztheta instrument	Applied Biophysics Ltd, Troy, New Jersey, USA
Implen nanophotometer	Geneflow Ltd, Litchfield, UK
Techne, Hybridiser HB-1D drying oven	Wolf Laboratories, York, UK
SimpliAmpTherm Cycler	Fisher Scientific UK, Leicestershire, UK
Leica DM IRB Microscope	Leica Microsystems (UK) Ltd., Milton Keynes, UK
AccuSpin Micro 17R	Fisher Scientific UK, Leicestershire, UK
Step One Plus Real Time PCR System	Thermo Fisher Scientific, Waltham, MA, USA
Syngene U: Genius 3 Fluorescence UV	Synoptics Ltd., Cambridge, UK

Transilluminator	
Consort EV243 electrophoresis power supply	Sigma-Aldrich, Pooled, Dorset, UK
Electrophoresis cassette	Scie-Plas Ltd., Cambridge, UK
G-BOX	Syngene, Cambridge, UK
Labinoco rotation wheel	Wolf Laboratories, York, UK
LEICA DFC3000 G microscope with Kubler CODIX system	Leica DMB, Milton Keynes, UK
UV light chamber	Germix, UK
Cryostat	Leica DMB, Milton Keynes, UK
Roller mixer	Stuart, Wolf-Laboratories, York, UK
LT4500 plate reader	Wolf Laboratories, York, UK
EVOS FL Auto 2 imaging system	Thermo Fisher Scientific, Waltham, MA, USA
EVOM² Epithelial Volt/Ohm Meter	World Precision Instruments, Hitchin, Hertfordshire, UK
GloMax® Multi Detection System	Promega, Southampton, UK
Software	**Supplier**
Prism 10	GraphPad Software, San Diego, USA
ECIS	Applied BioPhysics Inc., New Jersey, USA
Microsoft Excel	Microsoft In., Redmond, WA, USA
Step One software	Thermo Fisher Scientific, Waltham, MA, USA
Leica LAS EZ	Leica Microsystems (UK) Ltd, England, UK
Image J	Downloaded from https://imagej.nih.gov/ij
Minitab	Minitab Ltd. Coventry, UK

2.1.4 General compounds

The chemicals and reagents used in this study are listed inTable 2.5.

Table 2.5 General compounds used in this study

Material & Reagent	**Supplier**
10% Foetal calf serum (FCS)	Sigma-Aldrich Co, Poole, Dorset, UK
Antibiotic antimycotic solution (100x)	Sigma-Aldrich Co, Poole, Dorset, UK
Dimethylsulphoxide (DMSO)	Sigma-Aldrich Co, Poole, Dorset, UK
DMEM/Ham's F12 with L-Glutamine Medium	Sigma-Aldrich Co, Poole, Dorset, UK
RPMI-1640 Medium with L-glutamine and sodium bicarbonate	Sigma-Aldrich Co, Poole, Dorset, UK
Trypsin EDTA	Sigma-Aldrich Co, Poole, Dorset, UK
99.8% Ethanol	Fisher Scientific, Leicestershire, UK
Trypan Blue stain 0.4%	Thermo Fisher Scientific, Waltham, MA, USA
CellEvent™ Caspase-3/7 Detection Reagent (green)	Thermo Fisher Scientific, Waltham, MA, USA

10X PBS	Sigma-Aldrich Co, Poole, Dorset, UK
TRI Reagent	Sigma-Aldrich Co, Poole, Dorset, UK
1-bromo-3-chloropropane	Sigma-Aldrich Co, Poole, Dorset, UK
2-propanol	Fisher Scientific, Leicestershire, UK
DEPC (Diethylpyrocarbonate)	Sigma-Aldrich Co, Poole, Dorset, UK
GoScript™ Reverse Transcription Mix	Promega, Southampton, UK
PCR GoTaq Green master mix	Promega, Southampton, UK
GoScript™Reaction Buffer, Oligo (dT)	Promega, Southampton, UK
GoScript™ Enzyme Mix	Promega, Southampton, UK
Agarose	Melford Laboratories Ltd, Suffolk, UK
10x Tris-Boric-Acid (TBE) electrophoresis buffer	Sigma-Aldrich Co, Poole, Dorset, UK
Sybrsafe DNA stain	Fisher Scientific, Leicestershire, UK
PCR Ranger 100bp DNA Ladder	Norgen Biotek, Thorold, Canada
FAST 2x qPCR Master Mix	PrimerDesign, Southampton, UK
AmplifilourUniprimerTM Universal system	Biosearch Technologies, California, USA
Bovine serum albumin (BSA)	Sigma-Aldrich Co, Poole, Dorset, UK
Plasmid Transfection Reagent	Santa Cruz Biotechnology, Inc., Texas, USA
Plasmid Transfection Medium	Santa Cruz Biotechnology, Inc., Texas, USA
Puromycin	Fisher Scientific, Leicestershire, UK
Bio-RadDC Protein Assay Reagent	Bio-Rad Laboratories, Hercules, CA, USA
2x laemmli buffer	Sigma-Aldrich Co, Poole, Dorset, UK
Ammonium persulfate	Sigma-Aldrich Co, Poole, Dorset, UK
Protease Inhibitor Cocktail II (ab201116)	Abcam, Cambridge, UK
Protease Inhibitor Cocktail III (ab201117)	Abcam, Cambridge, UK
10X running buffer (tris – glycine-sds buffer)	Sigma-Aldrich Co, Poole, Dorset, UK
10X transfer buffer (Tris glycine buffer)	Sigma-Aldrich Co, Poole, Dorset, UK
30% Acrylamide/Bis-Acrylamide solution	Sigma-Aldrich Co, Poole, Dorset, UK
N,N,N',N;-Tetramethylethylenediamine (TEMED)	Sigma-Aldrich Co, Poole, Dorset, UK
Sodium dodecyl sulphate (SDS)	Melford Laboratories Ltd, Suffolk, UK
BLUeyePrestained Protein Ladder	Geneflow Ltd., Litchfield, UK
10x Tris buffered saline	Sigma-Aldrich Co, Poole, Dorset, UK
Tween-20	Sigma-Aldrich Co, Poole, Dorset, UK
EZ-ECL solution	Geneflow Ltd., Litchfield, UK
Tris (hydroxymethyl) aminomethane	Melford Laboratories Ltd, Suffolk, UK
Horse serum	Sigma-Aldrich, Pooled, Dorset, UK
Gill's Haematoxylin	Vector Laboratories Inc, Burlingame, CA, USA
VECTASTAIN® ABC Kit	Vector Laboratories Inc, Burlingame, CA, USA
3,3'-Diaminobenzidine (DAB)	Sigma-Aldrich Co, Poole, Dorset, UK
Xylene	Fisher Scientific, Leicestershire, UK
Thiazolyl Blue Tetrazolium Bromide	Melford Laboratories Ltd, Suffolk, UK

Matrigel	BD Biosciences, Oxford, UK
cytodex-2 beads	GE Healthcare, Cardiff, UK
Formalin	Sigma-Aldrich Co, Poole, Dorset, UK
Crystal violet solution	Sigma-Aldrich Co, Poole, Dorset, UK
DAPI (4',6-Diamidino-2-Phenylindole, Dihydrochloride)	Thermo Fisher Scientific, Waltham, MA, USA
Fluorescein isothiocyanate (FITC)	Sigma-Aldrich Co, Poole, Dorset, UK
Tetramethylrhodamine isothiocyante (TRITC)-dextran	Sigma-Aldrich Co, Poole, Dorset, UK
Fluorescein Phalloidin(F432)	Thermo Fisher Scientific, Waltham, MA, USA

2.1.5 Primers

Primers used in this study were designed by the Beacon Design Programme (Biosoft International, Palo Alto, California, USA) or Primer BLAST and synthesized by Sigma Genesis (Poole, Dorset, UK). The details of the primers used in conventional PCR and qPCR for this study are listed in Table 2.6.

Table 2.6 Details of the primers used in this study

Name	Sequence	Product size
MarvelD3 F8	ACGGAGTTTGGGAAAAAC	525 bp
MarvelD3 R8	CTCCACTACAGGCCATTG	
MarvelD3 F1	AGTCAGAGGCGGAAGGAC	101 bp
MarvelD3 zR1	ACTGAACCTGACCGTACAGATCAGCAAGTTCAGGAGAA	
GAPDH F8	GGCTGCTTTTAACTCTGGTA	421 bp
GAPDH R8	GACTGTGGTCATGAGTCCTT	
GAPDH F1	AAGGTCATCCATGACAACTT	1285 bp
GAPDH zR1	ACTGAACCTGACCGTACAGCCATCCACAGTCTTCTG	

Note: Z sequence 'ACTGAACCTGACCGTACA' is highlighted in red. Z-sequence presents on the specific primers containing a 5' hairpin structure labeled with a fluorophore (FAM).

2.1.6 Antibodies

Primary and secondary antibodies used for Western blotting and immunohistochemistry (IHC) are detailed below in Table 2.7.

Table 2.7 Primary and secondary antibodies used in this study

Antibody name	Host species	Molecular weight	Final concentration*	Supplier and catalogue number
MarvelD3	Rabbit	46kDa	1:2000	ORIGENE TA336071
Caspase3	Mouse	32kDa	1:1000	Santa Cruz Biotechnology sc-56053
Caspase8	Mouse	55kDa	1:1000	Santa Cruz Biotechnology sc-70501
Caspase9	Mouse	46kDa	1:1000	Santa Cruz Biotechnology sc-17784
HSP60	Mouse	60kDa	1:1000	Santa Cruz Biotechnology sc-59567
SMAD4	Mouse	60kDa	1:1000	Santa Cruz Biotechnology sc-7966
AF-6	Mouse	200kDa	1:1000	Santa Cruz Biotechnology sc-74433
Claudin-11	Rabbit	20kDa	1:1000	Santa Cruz Biotechnology sc-25711
NECTIN4	Mouse	66kDa	1:1000	Sigma-Aldrich MABT64
ZO-1	Mouse	200kDa	1:1000 (WB) 1:200 (IFC)	Invitrogen 33-9100
MMP9	Mouse	92kDa	1:1000	Santa Cruz Biotechnology sc-21733
Caveolin-1	Mouse	22kDa	1:1000	Santa Cruz Biotechnology sc-53364
GAPDH	Mouse	37kDa	1:1000	Santa Cruz Biotechnology sc-32233
Rabbit anti-mouse (whole molecule) IgG Peroxidise conjugate	Rabbit		1:1000	Sigma-Aldrich A5278
Anti-rabbit (whole molecule) IgG Peroxidise antibody	Goat		1:1000	Sigma-Aldrich A6154

2.2 Cell culture

2.2.1 Preparation of solutions for cell culture

2.2.1.1 Complete cell culture medium

In this study, breast cancer cell lines MDA-MB-231, MCF-7, BT-549, ZR-751 and colorectal

cancer cell lines RKO, HT115, Caco-2 were cultured in Complete Cell Culture Medium, which consisted of 500ml Dulbecco's Modified Eagle's Medium (DMEM) (cat:D8437) supplemented with 50ml 10% heat inactivated foetal calf serum (FCS) (cat: F9665) (Sigma-Aldrich, Poole, Dorset, UK) and 5ml of 100X antibiotic cocktail mixture including penicillin, streptomycin and amphotericin B (A5955, Sigma-Aldrich, Poole, Dorset, UK) to prevent bacterial and fungal contamination. Only breast cancer cells SKBR3 and colorectal cancer cells HRT-18 were cultured in RPMI-1640 Medium (R8758, Sigma-Aldrich, Poole, Dorset, UK), which was also supplemented with 50ml 10% heat inactivated foetal calf serum (FCS) and 5ml of 100X antibiotic cocktail mixture. Both mediums were stored in a freezer at 4℃ for no more than one month.

2.2.1.2 Phosphate-buffered saline (PBS)

10x stock PBS (P5493, Sigma-Aldrich, Poole, Dorset, UK) was dissolved in distilled water (dH_20). 500ml stock was added to 4500ml distilled water to give 1x stock at PH7.4. The final PBS buffer was then autoclaved and stored at room temperature.

2.2.1.3 Trypsin EDTA

10x stock Trypsin EDTA solution (T4174, Sigma-Aldrich Co, Poole, Dorset, UK) was diluted in sterile PBS to form a final 1x concentration, then aliquoted into universal tubes and stored at -20℃ until used.

2.2.2 Cell culture, maintenance, and storage

2.2.2.1 Cell culture

All cell lines in this study were cultured in complete cell culture medium. They were initially cultured in 25cm^2 flasks (Greiner Bio-One Ltd, Gloucestershire, UK), then subcultured to 75cm^2 flasks (Greiner Bio-One Ltd, Gloucestershire, UK) when confluency reaches 80%, or transferred to other plates, depending on the experimental purpose. All these wild type cell lines were kept in a dedicated incubator (Wolf Laboratories York, UK) at 37 ℃, 95%

humidification and 5% CO_2.

2.2.2.2 Cell Maintenance

The medium was changed every 2-3 days based on the condition of viability and confluency, which were checked by an inverted phase contrast microscope (Leica Microsystems (UK) Ltd., Milton Keynes, UK), to provide a healthy growth environment. Cells were washed with 5ml of PBS to remove dead cells after aspirating the medium with a dedicated sterile glass pipette (Fisher Scientific UK, Leicestershire, UK). This is followed by replenishing with the appropriate cell medium. Cell handling was conducted inside a Class II laminar flow cabinet (SafeF ST Classic, FASTER) to avoid any contamination.

2.2.2.3 Cell detachment and passaging

Cells were detached from the flasks by adding 1X trypsin/EDTA as mentioned in section 2.2.1.3. In order to remove the remaining cell culture medium containing serum which may inactivate the performance of trypsin, the cells were washed with PBS after the medium was aspirated. 5ml of trypsin/EDTA was added to the flasks, which were then placed back in the incubator for 5-10 minutes to allow the cells to detach from the bottom of the flasks. Once detached, 5ml medium was added and the flask was washed several times to form a cell suspension. This suspension was then transferred to a sterile universal tube (Fisher Scientific UK, Leicestershire, UK) and then centrifuged at 1,700 rpm for 5 minutes to form a pellet. After centrifugation, the supernatant was aspirated, and the cell pellet was resuspended with fresh cell culture medium. This resuspended cell was then used immediately for cell subculturing or for other experimental purposes.

2.2.2.4 Cell freezing

The medium was aspirated from a T75 flask, then PBS was added to wash cells several times and then aspirated. After that, the detachment of cells was undertaken after trypsin was added to make sure the surface of the flask was covered. The forming of the pellet was undertaken as described in section 2.2.2.3. The pellet was then resuspended in a final volume

of 5 ml cell culture medium containing 10% dimethyl sulfoxide (DMSO) (D8418, Sigma-Aldrich Co, Poole, Dorset, UK). After that, 1 ml of solution was transferred into 5 pre-labeled CRYO.STM tubes (Greiner Bio-One, Gloucestershire, UK) respectively, which were then frozen at -80℃. For long-term storage, tubes were kept at -196℃ in a liquid nitrogen tank.

2.2.2.5 Cell revival

The stored microfuge tube (Greiner Bio-One Ltd., Gloucestershire, UK) was taken out of the -80℃ freezer or liquid nitrogen tank and then defrosted in a 37°C water bath. The cell suspension was transferred to a universal tube (Greiner Bio-One Ltd, Gloucestershire, UK) containing 5 ml of fresh cell culture medium and left standing for 5 minutes before centrifuged. After centrifugation at 1,700 rpm for 5 minutes, the supernatant was aspirated, and the cell pellet was resuspended in 5 ml of fresh medium. The cell suspension was then transferred to a pre-labeled T25 flask and stored in an incubator.

2.2.3 Cell counting

Cell detachment and suspension were described in section 2.2.2.3. After centrifugation, the cell was resuspended in a suitable volume of culture medium depending on the size of the pellet. The cell counting was then performed using a 1mm x 1mm x 0.1mm Neubauer haemocytometer counting chamber (Fisher Scientific UK, Leicestershire, UK). After a cover slide was attached on the top of the chamber, 10µl of the cell suspension was added to the edge of the slide. Four corners and their left and upper edge of nine squared areas of the haemocytometer were counted under a microscope under the x10 objective lens. The number of cells was calculated using the following equation:

$$Num = (Sum/4) * 10^4$$

Where Num is the cell number per milliliter, Sum is the total number of cells in 4 counted corners.

2.2.4 Cell viability assessment

Cell detachment and resuspension were described above. Cell viability assessment was then

undertaken by adding 10µl mixture containing 10µl cell suspension and 10µl 0.4% Trypan Blue stain (T10282, Thermo Fisher Scientific, Waltham, MA, USA) into a dedicated Countess™ cell counting chamber slides (Thermo Fisher Scientific, Waltham, MA, USA). The slide was then inserted into the Countess™ II Automated Cell Counter machine (Thermo Fisher Scientific, Waltham, MA, USA) (Figure 2.1), and the cell viability was counting automated, as shown in Figure 2.2.

Figure 2.1 Cell counting chamber machine and slide. Source: Fisher Scientific UK Ltd. Available: https://www.fishersci.co.uk/shop/products/invitrogen-countess-cellcounting-chamber-slides-5/10399053

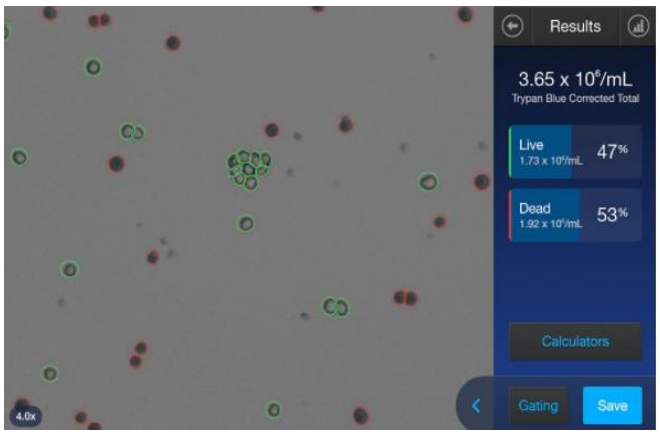

Figure 2.2 An example of cell viability assay using the countess machine . The total cell number, live cells, dead cells, and their ratio were counted automatically. Available: https://www.antteknik.com/en/products/?p=invitrogen-countess-3-automated-cell-counter

2.2.5 Cell apoptosis assessment

Cell apoptosis assessment was conducted to detect apoptotic cells, based on the activation of caspase-3/7 which is a crucial event during the process of apoptosis. CellEvent™

Caspase-3/7 Detection Reagent (green) (C10723, Thermo Fisher Scientific, Waltham, MA, USA) was used in this study. Caspase-3/7 Detection Reagent (2mM) was diluted 1:40 with complete cell-culture medium (DMEM) and stored as a stock solution (50μM) at -20℃ for future use. The solution was further diluted 10X before treating cells at a final concentration of 5μM. The cells were then incubated at 37℃ with 5% CO_2 for 90 minutes. Cell detachment and resuspension were described above. 10μl of cell suspension was added to the Countess™ cell counting chamber slides. The slide was then inserted into the Countess™ II Automated Cell Counter machine, and the apoptotic cells were detected automatically using the filter set FITC/GFP.

2.3 Cell transfection

2.3.1 Generation knockdown cell lines using shRNA-based transfection

The MarvelD3 knockdown in breast and colorectal cancer cell lines was conducted using shRNA (short hairpin RNA)-based transfection. MarvelD3 shRNA plasmid (sc-149278-SH), Plasmid Transfection Reagent (sc-108061) and Plasmid Transfection Medium (sc-108062) were purchased from Santa Cruz Biotechnology, Inc. (Dallas, Texas, USA), and cell transfection was followed the protocol from the manufacturer. In brief, cells were cultured in 6-well plate with antibiotic-free medium. Once the confluence of cells reached to 50-70%, solution A (containing 10μl of MarvelD3 shRNA plasmid and 90μl of transfection medium), and solution B (containing 3μl of plasmid transfection reagent and 97μl of plasmid transfection medium) were prepared. Solution A was then directly added to solution B and mixed gently before incubating in the dark at room temperature for 45 minutes. After incubation, cells were washed with 2ml of plasmid transfection medium twice and supplemented with 200μl of solution A plus solution B mixture and 800μl of plasmid transfection medium, before incubating at 37°C for 5-7 hour. After incubation, 1ml of cultured medium containing 20% FCS and 2X antibiotics was added into the 6 well plate and the plates were further incubated for 24 hours. Following this, cell selection with puromycin (Fisher Scientific, Leicestershire, UK) was conducted for up to 3 days to kill un-transfected cells, and the remaining transfected cells were maintained in normal growth medium containing puromycin until sufficient confluence was reached. Followed by this, qPCR and Western blotting was conducted to test the

knockdown efficacy in both RNA and protein levels.

2.3.2 Thiazolyl Blue Tetrazolium Bromide (MTT) based Killing curve

An MTT-based killing curve for cell lines which underwent transfection was performed to choose the best concentration for cell selection. Four 96-well plates were prepared for each cell line, which represented a reference plate, 24-, 48-, and 72h treatment plate. Cells were cultured and detached as described in previous sections, then seeded into the prepared 96-well plates, in which the cell density will be discussed in the later chapter.

MTT stock solution (5mg/ml) was made by adding 100mg Thiazolyl Blue Tetrazolium Bromide powder (MTT) (M92050, Melford Laboratories Ltd, Suffolk, UK) in 20ml PBS into a 30ml universal container covered by foil, and the tube was then placed on a roller mixer (Stuart, Wolf-Laboratories, York, UK) until the powder was dissolved thoroughly. The MTT stock was then stored at 4°C for further use.

For the reference plate, 200µl of cell suspension of each cell line were added in 6 repeats. After incubation at 37℃, 5% CO_2 for 24 hours, 22µl of 5mg/ml MTT solution was added into each well, followed by 4 hours incubation. After incubation, the medium was carefully aspirated and 100µl of DMSO was added to dissolve the crystal. The plate was then placed back in the incubator for further 10-minute incubation and placed into the LT4500 plate reader (Wolf Laboratories, York, UK) for detection at 540nm.

For the other 3 treatment plates, 5 sets of different concentrations of puromycin were designed for different cell lines (will be discussed in later chapter). 200µl cell suspension of each cell line were seeded, at the same time as the reference plate, in 6 repeats (5 different concentrations * 6 repeats = 30 wells for each treatment plate) respectively. Following 24 hours of incubation, the medium was aspirated and the fresh medium containing different concentrations of puromycin as designed was added to the plate. The incubation time is based on different time courses (24, 48, and 72 hours). After incubation, 22µl of 5mg/ml MTT solution was added into each well and incubated for 4 hours. Subsequently, the medium was removed and 100µl of DMSO was added and incubated for 10 minutes. The plate was then

read in the LT4500 plate reader (Wolf Laboratories, York, UK) for detection at 540nm. Data was collected, normalized, analyzed using Excel and presented as line chats using GraphPad.

2.4 RNA detection

2.4.1 Preparation of solutions for molecular biology experiments

2.4.1.1 Diethylpyrocarbonate (DEPC) water

Diethylpyrocarbonate (DEPC) water was used to help inhibit RNase action. The working solution was prepared by dissolving 500µl of DEPC (D5758, Sigma-Aldrich, Poole, Dorset, UK) in 9.5ml distilled water to make the stock of DEPC water. DEPC water was autoclaved before use.

2.4.1.2 75% Ethanol DEPC water

75% ethanol was used for RNA isolation. The solution was prepared by mixing 15ml of 99.8% ethanol (10437341, Fisher Scientific, Leicestershire, UK) and 5ml of DEPC water. The solution was prepared before being used in experiments.

2.4.1.3 GoScript™ Reverse Transcription Mix, Oligo (dT)

10µl of GoScript™ Reverse Transcription Mix was used for cDNA synthesis. This was prepared by mixing 4µl of Nuclease-Free Water, 4µl of GoScript™ Reaction Buffer, Oligo (dT) (Promega, Southampton, UK) and 2µl of GoScript™ Enzyme Mix (A2393, Promega, Southampton, UK), the solution was stored at -20℃ for further use.

2.4.1.4 Primers

Solutions of both forward and reverse primers were prepared at a stock solution of 10µM. For this study, primers were diluted 10 (for F and R primer) or 100 (for zR primer) times by adding 20µl of primer stock into 180µl or 4µl of primer into 396µl of PCR water respectively

(to give 10µM or 1µM stocks) before mixing and storing at 4℃ in the fridge for further experiments.

2.4.1.5 Tris-Boric-Acid (TBE) electrophoresis buffer

10x TBE buffer was purchased from Sigma Aldrich (T4415, Sigma-Aldrich Co, Poole, Dorset, UK), and was diluted with distilled water to form a final 1x stock and stored at room temperature for further use.

2.4.2 RNA extraction

2.4.2.1 RNA isolation

RNA extraction was conducted using the TRI Reagent Kit (T9424, Sigma-Aldrich, Poole, Dorset, UK) according to the manufacturer's instructions. In brief, after cells were cultured to a confluence of approximately 90%, medium was aspirated, and the cells were then washed with PBS. After that, 1ml TRI reagent was added to the cell monolayer to produce cell lysate. Subsequently, the cell lysate was transferred to a pre-labelled Microfuge tube (Greiner Bio-One Ltd, Gloucestershire, UK) and stood for 5 minutes at room temperature. Following this, 100µl of 1-bromo-3-chloropropane (B9673, Sigma-Aldrich Co, Poole, Dorset, UK) was added to the lysate and vigorously shaken for 15 seconds, before standing at room temperature for 2-15 minutes. This is followed by centrifuging the sample at 12,000 x g for 15 minutes at 4℃, resulting in the separation of the lysate into three phases: a colorless upper aqueous phase containing RNA, a thin interphase containing DNA, and a pink lower organic phase containing protein. For the further experiment, the upper phase, which contained RNA, was carefully collected and transferred to a new labeled Microfuge tube containing 500µl of 2-propanol (A461-500, Fisher Scientific UK Leicestershire, UK), the tube was then vortexed and stood for 5-10 minutes at room temperature. Subsequently, the sample was centrifuged at 12,000 x g for 10 minutes at 4℃, resulting in a pellet in the bottom of the tube. The supernatant was carefully removed, and the remaining pellet was washed with 1ml of 75% ethanol DEPC water, vortexed gently, and allowed to stand at room temperature for 5 minutes, before being centrifuged at 7,500 x g for 5 minutes at 4℃. The supernatant containing ethanol DEPC was

then carefully removed before drying briefly at 55℃ for a few minutes in the drying oven (Techne, Hybridiser HB-1D drying oven, Wolf laboratories, York, UK), to remove the remaining ethanol.

2.4.2.2 RNA quantification

The dried RNA pellet was dissolved in 50-100µl of DEPC water based on the size of the formed pellet. An Implen nanophotometer (Geneflow Ltd, Litchfield, UK) was used to quantify RNA against a DEPC water blank. After measurement, the concentration of RNA was calculated, allowing for standardization in reverse transcription or future experiments, and the RNA was stored at -80℃ for further experiments.

2.4.3 Reverse transcription of RNA

The reverse transcription, GoScript™ Reverse Transcription System Kit (Promega Corporation, Madison, WI, USA), was applied to obtain complementary DNA (cDNA) samples for further use such as conventional PCR or real time-quantitative PCR. 10µl of GoScriptTM Reverse Transcription Mix (RT Mix) was supplemented with 10µl of RNA solution, which was standardized with PCR water (500ng) and mixed to make up a 20µl solution.

The reverse transcription reaction was performed in a Simpliamp thermocycler (Fisher Scientific UK Leicestershire, UK). The reaction conditions were 25℃ for 5 minutes (1 cycle), 42℃ for 60 minutes (1 cycle), 70℃ for 15 minutes (1 cycle) and hold at 4℃. After the reaction was completed, 60µl of PCR water was added to dilute the cDNA sample for further experiments or storage at -20℃.

2.4.4 Polymerase chain reaction (PCR)

The conventional polymerase chain reaction (PCR) is a simple technique utilized to amplify the specific section of DNA. The process of PCR is illustrated in Figure 2.3. The targeted DNA contains the region to be copied, which can serve as the templates. A heat resistant DNA polymerase such as Taq polymerase was applied to synthesize DNA from nucleotides. The

sequence of two short regions of the nucleotides at either end of the region of the template is known to design two dedicated primers, which can be used to bind, or anneal to the template at their complementary sites and act as the starting point for DNA formation by the DNA polymerase, deoxynucleotide triphosphates (dNTPs) from which the polymerase can synthesize new DNA strands as new templates for further replication.

In this study, target genes were amplified using the GoTaq Green master mix (M7823, Promega, Southampton, UK). A total of 16µl reaction was prepared as described in Table 2.8 The Simpli-amp Thermocycler was used to provide repeated cycles of heating and cooling to the required temperatures for each step of the reaction, as listed in Table 2.9.

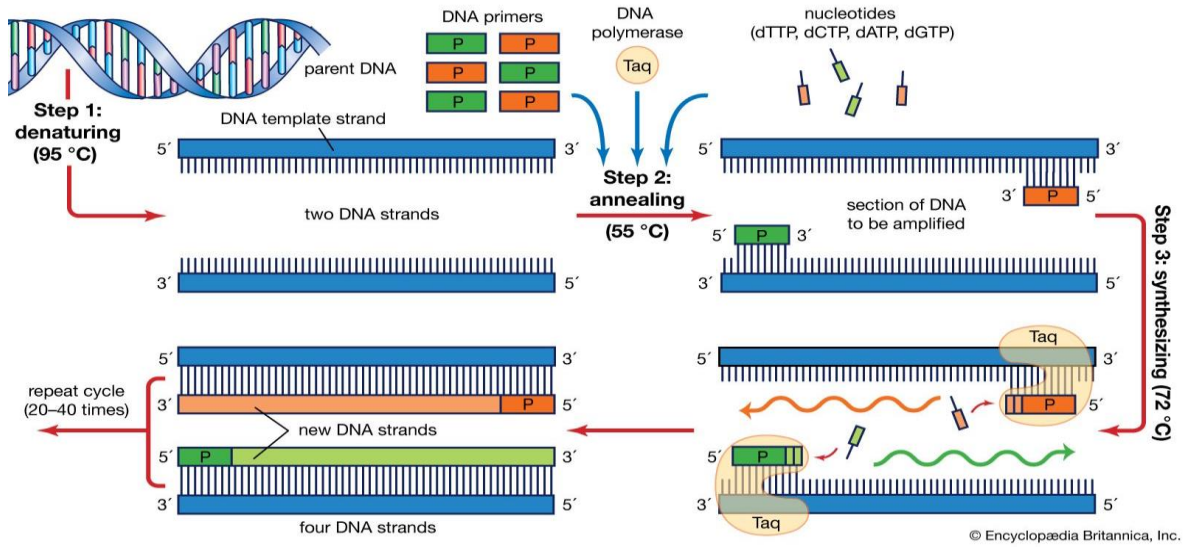

Figure 2.3 The Process of PCR. The first step is to separate two strands of the DNA molecule at 95℃. In the second step, the temperature was reduced to 55℃ so that the primers can anneal to the templates. In the third step, the temperature is raised to about 72 °C, and the DNA polymerase begins adding nucleotides onto the ends of the annealed primers. The DNA produced by PCR acts as a further template for replication resulting in the exponential amplification of DNA. Available: https://www.britannica.com/science/polymerase-chain-reaction

Table 2.8 The component of PCR reaction

Component	**Volume**
cDNA sample	1µl
Forward Primer	1µl
Reverse Primer	1µl
PCR water	5µl
2x GoTaq Green Master Mix	8µ
Total	16µl

Table 2.9 The reaction condition of PCR

Process	Temperature	Time	Cycles
Initialization	94℃	5 minutes	1
Denaturation	94℃	20 seconds	32
Annealing	55℃	20 seconds	
Extension	72℃	50 seconds	
Final extension	72℃	5 minutes	1
Final hold	4℃	∞	1

2.4.5 Agarose gel electrophoresis and DNA visualization

2.4.5.1 Agarose gel electrophoresis

Agarose gel electrophoresis was undertaken to separate and analyze DNA samples following PCR amplification. The principle of this technique is using electrical current to electrophoretically separate negatively charged DNA to a positive electrode through an agarose gel matrix and compared to a PCR ladder to allow determination of approximate band sizes.

Based on the size of the target DNA fragments, different agarose gels, containing different concentrations of agarose, were chosen. In this study, a 1% or 1.5% agarose gel, made from 1g or 1.5g of agarose powder (A20090, Melford Chemicals, Suffolk, UK), was used. The solution was heated after adding 100ml of 1x TBE buffer in a microwave oven for 3 minutes until the agarose was completely dissolved. After cooling down for 5 minutes, the solution was mixed with 8µl of SYBR Safe DNA Gel Stain (S33102, Fisher Scientific UK Leicestershire, UK). The solution then was poured to an electrophoresis cassette (Scie-Plas Ltd., Cambridge, UK), and combs were placed before letting it stand at room temperature for 30-40 minutes to set solidified. The firmed gel was then transferred to the reaction tank and topped up with 1x TBE buffer, to ensure it exceeded 5mm of the gel surface, before removing the combs. 5µl of the PCR Ranger 100 bp DNA Ladder (11300, Norgen Biotek, Thorold, Canada) and 8µl of the DNA samples were added into each well respectively. The gel was then run at 120V, 100mA, 50W for 30-50 minutes powered by an electrophoresis power supply (Gibco BRL, Life Technologies Inc.).

2.4.5.2 DNA visualization

When the visible dye line had moved the desired distance required for the product size, the electrodes were disconnected. The gel was then transferred to a Syngene U: Genius 3 Fluorescence UV Transilluminator (Synoptics Ltd., Cambridge, UK). Images of DNA fragments and ladders were visualized and captured under blue light. The images were saved on the systems and printed with a thermal printer.

2.4.6 Real-time quantitative PCR (qPCR)

Real-time quantitative PCR is an optimal technique by which the amount of gene expression can be quantified in real-time. In comparison with conventional PCR in which the amplification could only be detected at the end of the reaction, qPCR can measure the accumulation of PCR product amplification as the reaction processes. This technique involves a dedicated fluorescent reporter probe which can bind to the target DNA amplification. As a result, the fluorescent probe is increasing during the amplification. This process is continuously recorded by a sensitive camera attached to the system.

In this study, The Amplifilour^{TM} Uniprimer^{TM} Universal system (AMP-FD-15p, Biosearch Technologies, California, USA) was used. In order to bind the fluorescent probe with the target DNA, an 18-nucleotide sequence called the Z sequence extends from the 5' end of one target-specific PCR primer; the same sequence forms the 3' end of the uniprimer (ACTGAACCTGACCGTACA). The Uniprimer is a hairpin structure labelled with a fluorophore (FAM). The fluorophore is attached to an acceptor moiety inside the hairpin structure, in which the fluorescence emitted by the fluorophore can be quenched, so any fluorescent signal can be prevented from being detected.

The principle of qPCR process is illustrated in Figure 2.4. In the first round of the amplification, the ZR primer, which is one of the target-specific primers, anneals and extends to form a product. In the second round, the other primer of the pair (F primer) binds to the newly formed product from the first round and extends to form the second strand. This strand is then used as a template for the Uniprimer. Extension causes the Uniprimer to unfold,

therefore the fluorophore can be released from quenching.

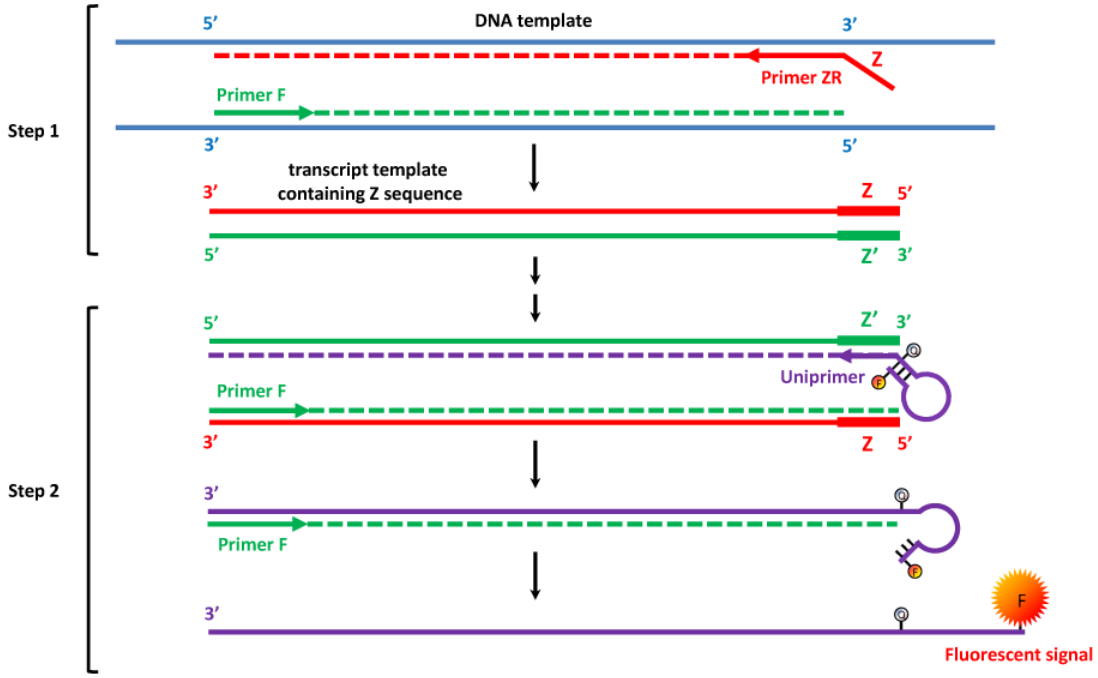

Figure 2.4 qPCR using the fluorescent marked Uniprimer. In first step, the zR primer anneals and is extended in the first amplification. In the second step, the Z sequence could be recognised by the Uniprimer. Further extension causes the Uniprimer to unfold, resulting in releasing the fluorescent signal for detection (Liu 2020)

qPCR was conducted using a MicroAmp Fast Optical 96-Well Reaction Plate with Barcode (0.1ml) (Fisher Scientific UK Leicestershire, UK), Optical seal (PrimerDesign, Southampton, UK) and a Step One Plus Real-Time PCR System (Fisher Scientific UK Leicestershire, UK) (Figure 2.5). Table 2.10 listed the unknown sample solution of each well to a total volume of 10 µl. In addition, podoplain (PDPL) was run alongside a standard of a known transcript number (ranging from 10^8 to 10), which allows calculating relatively copy numbers of the target gene. It can also act as a reference control gene for a standard curve to make sure any differences were not caused by technical errors and allowed the normalization of results. After adding the unknown sample mixture and PDPL standard, the 96-well plate can be placed in the Step One Plus Real-Time PCR System, the reaction was run as listed in Table 2.11.

The fluorescence signal was detected by the machine during the annealing phase, and its growth is directly related to the exponential growth of the product. The software can then determine the quantitative threshold for genes amplified in each reaction automatically.

When the fluorescence signal reached a threshold, the cycle number of the reaction is used to determine the copy number of the target transcript.

The transcript copy number of the target gene in each sample can be accurately calculated by comparing the amount of fluorescence emitted by each sample using the degree of fluorescence emitted by a series of standards with a known copy number of PDPL. Each sample of target gene was tested at least three times, and the transcript copy number of each sample was normalized based on GAPDH copy numbers.

Table 2.10 The component of sample solution for qPCR.

Component	**Volume**
precisionFAST2x qPCR Master Mix (PrimerDesign, Southampton, UK)	5µl
Forward primer	0.3µl
Reverse primer (containing the Z sequence)	0.3µl
Uniprimer	0.3µl
cDNA	1µl
PCR water	3.1µl
Total	10µl

Table 2.11 the reaction condition of qPCR

	Stage 1	Stage 2		
Cycle	1	100		
Temperature	95℃	95℃	55℃	72℃
Time	10 minutes	10 seconds	35 seconds	10 seconds

Figure 2.5 Step One Plus Real Time PCR System.

2.5 Protein detection

2.5.1 Protein extraction

Once cells reached sufficient confluence, the medium was aspirated, and the cell monolayer was washed with PBS twice. 5ml PBS was then added to the flask and the cells were collected using a sterile cell scraper and transferred to a universal tube, followed by centrifuging at 2,000rpm for 10 minutes. After centrifugation, cell pellet was formed at the bottom of the tube, and the supernatant was aspirated. 250µl -400µl of lysis buffer (consists of 25 mM Tris-HCl [PH 7.6], 150mM NaCl, 1% NP-40, 1% sodium deoxycholate and 0.1% SDS), depend on the size of the pellet, was added to resuspend the pellet. The suspension was then transferred to an Microfuge tube and placed on a Labinoco rotation wheel (Wolf Laboratories, York, UK) at 4°C for a least an hour. After rotation, the Microfuge tube was centrifuged at 13,000 rpm for 15 minutes at 4°C and a pellet was formed. The pellet was discarded and supernatant containing proteins was collected and transferred to a labelled microfuge tube, before quantifying for Western blot or storing at -20°C until further use.

2.5.2 Protein quantification

Protein quantification was conducted to standardize the concentration for further

experiments. The protein samples were quantified using BioRadDC Protein Assay (BioRad Laboratories, Hertfordshire, UK) according to the manufacturer's protocol. In brief, 50mg/ml BSA standard (Sigma-Aldrich, Poole, Dorset, UK) was serially diluted in lysis buffer to produce a concentration ranging from 0.78mg/ml to 50 mg/ml, which could create a standard curve for determining concentration of the protein samples. After this, either 5µl of each standard or protein sample was added to each well of the 96-well plate in triplicate. 25µl of Reagent A', prepared by mixing 20µl of reagent S with every 1ml of reagent A, was added to each well followed by 200µl of Reagent B. The plate was then incubated in the dark at room temperature for 15 minutes after mixing. The absorbance of each well was then measured at a wavelength of 620nm in an LT4500 spectrophotometer (Wolf Laboratories, York, UK). The standard curve was created based on the standards. Tested protein concentration was then calculated according to the standard curve. Appropriate amounts of lysis buffer were added to standardise the protein samples to a final concentration of 1-2mg/ml to make the consistent concentration. This protein sample was finally diluted 1:1 with 2x Laemmli SDS sample buffer concentrate (S3401, Sigma Aldrich, Dorset, UK), followed by boiling at 100°C for 5 minutes and stored at -20°C until further use.

2.5.3 Sodium dodecyl sulfate-polyacrylamide gel electrophoresis (SDS-PAGE)

SDS-PAGE was conducted to separate proteins by mass. Four glass plates were tightly assembled in two gel cassettes on a casting stand, and ethanol was added to fill the space between the glass plates, waiting for 10 minutes, to check any leakages. Two different types of gel, a 5% stacking gel and a 10% resolving gel (depends on the protein size) were prepared by adding all the constituents listed in Table 2.12 and Table 2.13 respectively. The resolving gel was gently added between two glass plates to the appropriate height, before overlaying with ethanol to ensure a smooth edge. After the resolving gel was set, the overlaid ethanol was removed, and the stacking gel was added on the top of the resolving gel. A comb was then inserted in the gel immediately after the addition of stacking gel and allowed to set at room temperature.

Once the gel was set, the cassette was transported into an electrophoresis tank and supplement with 1X running buffer (diluted 10X running buffer (T7777, Sigma-Aldrich Co,

Poole, Dorset, UK) 1:10 with distilled water) before the comb was gently removed from the gel. Then 20µl of protein samples and 5µl of BLUeye Prestained Protein Ladder (56-0024, Geneflow Ltd., Litchfield, UK) were added. The electrophoresis was run at 120V, 50W and 50mA for 1.5-2h until sufficient separation was visualized.

Table 2.12 Component of the 5% stacking gel (for one gel)

Component	Volume
Distilled water	4.1ml
30% Acrylamide/Bis-Acrylamide solution	1ml
1.5M Tris pH (6.8)	0.75ml
10% SDS	0.06ml
10% ammonium persulfate	0.06ml
TEMED	0.006ml
Total	6.00ml

Table 2.13 Component of the 10% resolving gel (for one gel)

Component	Volume
Distilled water	5.9ml
30% Acrylamide/Bis-Acrylamide solution	5.0ml
1.5M Tris pH (8.8)	3.8ml
10% SDS	0.15ml
10% ammonium persulfate	0.15ml
TEMED	0.006ml
Total	15.00ml

2.5.4 Transfer proteins from gel to polyvinylidene fluoride (PVDF) membrane

Following SDS-PAGE separation, the gel containing protein samples was transferred to the Immobilon P PVDF membrane (7.8cm x 7.8cm in size) (Merck Millipore, Hertfordshire, UK), which was pre-activated with 100% methanol for one minute and then incubated in transfer buffer. The membrane with the gel on top was then placed on three pieces of filter paper (8cm x 8cm) and covered by another three pieces of filter papers (8cm x 8cm) to form a sandwich structure (Figure 2.6). This complex was then placed on a semi-dry transfer apparatus and run at 15V, 500mA, 20W for 50 minutes.

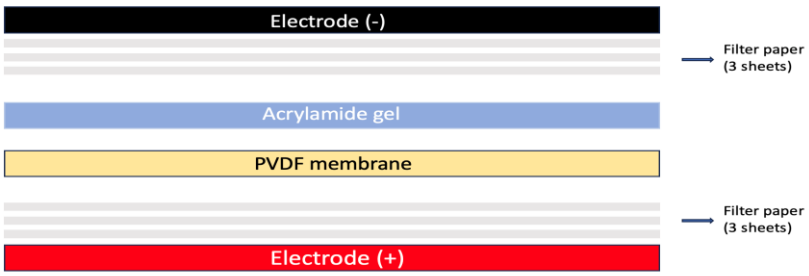

Figure 2.6 The sandwich structure of electrophoresis equipment transferring proteins from gel to membrane.

2.5.5 Immuno-Blotting

Once the transfer was completed, 10% milk solution (10% milk in tris-buffered saline [TBS] with 0.1% tween-20) was prepared to block the membrane at room temperature for 1 hour, followed by incubating in 3% milk solution supplemented with the desired antibody and concentration listed in Table 2.7, at 4℃ overnight. The membrane was washed with 3% milk solution for three times (15 minutes each round) to remove remaining unbound antibodies. The membrane was then incubated with 3% milk solution containing the secondary antibody at room temperature for an hour, followed by washing with TBS containing 0.1% tween-20 (TBS-T) three times, each time for 10 minutes, to remove the remaining secondary antibody. The membrane was then washed with TBS twice, 10 minutes each to remove the tween-20, before being incubated in EZ-ECL solution (equal parts of solution A mixed with solution B) (K1-0172, Geneflow Ltd., Litchfield, UK) for 3-5 minutes and placed in a G-BOX (Syngene, Cambridge, UK) to capture images of the membrane.

2.6 Immunohistochemical (IHC) staining and analysis

IHC staining was undertaken for MarvelD3, in paraffin embedded sections of colorectal tissues and breast tissues in the form of tissue microarrays. Briefly, the sections were dewaxed and rehydrated in the following solutions for 5 minutes sequentially: 100% xylene, 50% ethanol with 50% xylene, 100% ethanol, 90% ethanol, 70% ethanol, and 50% ethanol. was covered on the tissue sections were then immersed in Antigen retrieval buffer (1mM EDTA buffer) and heated the tissue section in the microwave for 20 minutes. The sections were then incubated

with a blocking solution (10% horse serum) (H1138, Sigma-Aldrich, Pooled, Dorset, UK) for 60 minutes at room temperature. This was followed by applying the MarvelD3 antibody (diluted to a concentration of 10µg/ml in blocking solution) for an hour, stringent washing, and then incubation with the relevant biotinylated secondary antibody (diluted 1:1000 in blocking solution) for 30 minutes at room temperature. After three washes with wash buffer, the staining was developed by incubation with 200µl avidin-biotin complex (ABC) reagent in VECTASTAIN® ABC Kit (PK-6200, Vector Laboratories, Inc., CA, USA) for 30 minutes. The ABC solution was removed by washing three times with wash buffer, before adding 3'3 diaminobenzidine (DAB) substrate (5mg/ml). The sections were subsequently counterstained with Gill's haematoxylin (H-3401, Vector Laboratories Inc, CA, USA), and dehydrated through a series of graded alcohols and cleared in xylene (Fisher Scientific, Leicestershire, UK) in sequence: 50% ethanol, 70% ethanol, 90% ethanol, 100% ethanol, 50% ethanol with 50% xylene, 100% xylene. After dehydration, slides were mounted with DPX mount and left to dry.

A colon cancer tissue microarray (TMA) (https://www.biomax.us/tissue-arrays/Colon/CO2161b), was purchased from US Biomax, Inc. (Derwood, MD, USA). The microarray includes pathology grade, TNM and clinical staging, containing 204 cases of adenocarcinoma, 4 signet-ring cell carcinoma, and 8 colon tissues (single core per case) (code: CO2161b), which can further expand our clinical study by conducting IHC assays. Detailed information regarding the TMA is listed in (Supplement-1).

A breast cancer tissue microarray (TMA) (https://www.biomax.us/tissue-arrays/Breast/BR1503f), was purchased from US Biomax, Inc. (Derwood, MD, USA). This microarray includes TNM and pathology grade, with IHC results of Her-2\ER\PR\Ki67, containing 3 each case of adjacent normal breast tissue and breast fibroadenoma, 2 breast cystosarcoma phyllodes, 7 breast intraductal carcinoma, plus 60 breast invasive ductal carcinoma, duplicate cores per case invasive ductal carcinoma and duplicate cores per case (code: BR1503f). Detailed information regarding the TMA is listed in (Supplement-2).

After the IHC was conducted, the TMA slides were imaged under a Leica MD IRB microscope (Leica GmbH, Bristol, UK). Staining intensity was determined independently by three researchers according to the standard: 0= Negative, 1= Weak staining, 2= Medium staining,

and 3= Intense staining.

2.7 Immunofluorescence (IFC) staining

Immunofluorescence staining was conducted to visualize the presence and localization of specific proteins. In brief, the 8-well glass chamber was pre-activated with normal cell culture medium and incubated at 37°C, 5% CO_2 overnight. Following this, enough number of cells (in 300µl mixture) was seeded to the chamber and allowed to reach 90% confluency in an overnight culture. After treatment was given, the medium was discarded, and the cells were fixed with 100% iced ethanol for at least half an hour. The cells were then washed with PBS three times, 10 minutes each time with the slide on a flat shaker. Following washing, the cells were treated with 0.1% Triton X100 (diluted with PBS) for 3 minutes. The solution was then gently aspirated, and the cells were washed with 8% horse serum (diluted with PBS) once. Following this, the cells were blocked with fresh horse serum for 2 hours at room temperature and placed on the flat shaker. After blocking, 200µl primary antibody, diluted with 8% horse serum to the desired concentration, was added to the chamber and incubated at room temperature for 2 hours. Following incubation, the cells were washed with PBS three times, each time for 10 minutes. 200µl secondary antibodies (1:3000 diluted with 3% horse serum) tagged with either FITC (fluorescein isothiocyanate) or TRITC (tetramethylrhodamine isothiocyanate), DAPI (1:1000 in 8% horse serum), and Phalloidin (1:400 in 8% horse serum) were added to the wells and incubated for another 1 hour. The slide should be avoided light from now on. The cells were washed with 8% horse serum three times, each time for 10 minutes, followed by PBS 4 x 10 minutes washing. After aspirating the supernatant, the camber was removed, and the slide was covered with Fluosave then a coverslip was carefully laid on top. The slide was then stored in the darkness and dried at 4°C. The slide could then be assessed under a fluorescent microscope and images photographs using a Hamamatsu Orca digital camera.

2.8 *In vitro* function assay

2.8.1 MTT-growth assay (proliferation)

MTT assay was conducted to investigate the proliferation ability of cells. Once enough confluence was obtained, cells were detached and subcultured as mentioned above, and 3,000 cells (200µl of cell suspension) of each targeted cell line were seeded into three 96-well plates (for recording day-1 (reference), day-3 and day-5 respectively) with 6 repeats. After incubating for 24 hours, 72 hours, and 120 hours, 22µl of 5mg/ml MTT solution was added into corresponding well and further incubated for 4 hours. After that, the medium was cautiously aspirated, and 100µl DMSO was added into the wells to dissolve the precipitates. The plate was then placed back to the incubator (37°C) for 10 minutes, and subsequently placed inside the LT4500 plate reader (Wolf Laboratories, York, UK) for detection at 540nm wavelength.

Data was collected, normalized, analyzed and presented as line chats using Excel (Microsoft In., Redmond, WA, USA) and GraphPad (GraphPad Software, San Diego, USA) with the following equation:
Increase (%) = [(day 3 or day 5 absorbance - day 1 absorbance)/ (day 1 absorbance-background absorbance)] x 100%

2.8.2 Matrigel adhesion assay

Matrigel adhesion assay was conducted to investigate adhesive abilities. Matrigel (356235, BD Biosciences, Oxford, UK) was diluted serum-free medium (SFM) to form a final concentration of 0.05mg/ml. Then 100µl final Matrigel solution was added to each well of the 96-well plate, the plate was then placed in the oven for drying at 55°C for 2-3 hours until the gel had completely dried. The Matrigel was rehydrated with 100µl sterile water for 30 minutes then carefully aspirated. After that, approximately 40,000 cells (200µl of cell suspension) of each cell line were seeded into each well of the 96-well plate with 6 repeats for 40-minute incubation (37℃ with 5% CO_2) (Figure 2.7). The medium was then carefully aspirated without damaging the monolayer, and the cells was washed with PBS to remove any non-attached

cells. The remaining adhesive cells were fixed with 4% formalin for 10-20 minutes. Subsequently, 100µl of DAPI (diluted 1:1000 with PBS) was added to cover the monolayer to stain attached cells for around 30 minutes. Cells were then observed in 4 random areas of each well under an EVOS® Onstage Incubator (Life technologies, CA, USA), and the photographs of the cells were captured using the EVOS® FL2 Auto Imaging System (Life technologies, CA, USA) (Figure 2.8). Cell counting was conducted using Image J software (https://imagej.nih.gov/ij) and data was analysed with GraphPad.

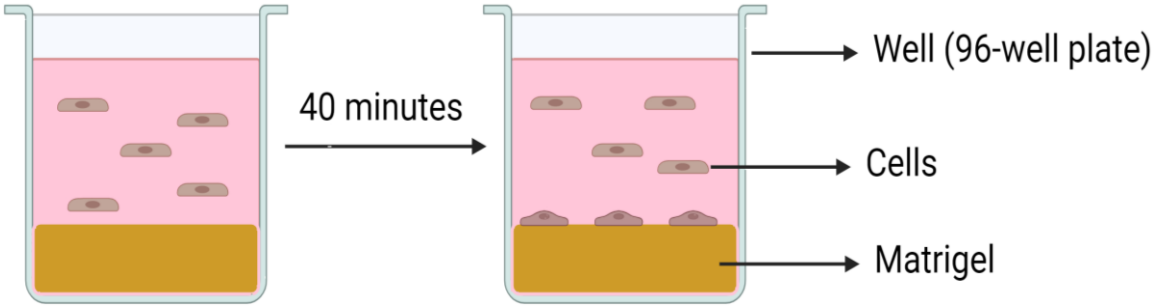

Figure 2.7 Schematic diagram of Matrigel adhesion assay. Cells are added to wells covered by Matrigel and the number of cells that had adhered to the Matrigel layer in 40 minutes was quantified. The figure was generated using BioRender (https://www.biorender.com/)

Figure 2.8 EVOS® FL2 Auto Imaging System with EVOS® Onstage Incubator, which provide the environment condition at 37°C, 5% CO_2 for cells, and capture the cells via the various zoom of microscope.

2.8.3 Matrigel invasion assay

Matrigel invasion assay was applied to investigate the invasive abilities of cells. Matrigel was

diluted to a final concentration of 0.5mg/ml. 8µm pore transwell inserts (Greiner Bio-One Ltd., Gloucestershire, UK) were placed into wells of a 24 well plate using sterile forceps in order to prevent contamination. Each insert (upper chamber) was coated with 50µg (100µl) of Matrigel (BD Biosciences, Oxford, UK). The 24-well plate containing the inserts was then dried at 55°C for 2-3 hours in the oven until completely solidified. The Matrigel was then rehydrated with 200µl sterile water at room temperature for 45 minutes. After the water was carefully discarded, 25,000 cells (200µl) of each cell type, were seeded into the upper chamber of the insert of duplicate inserts, then 600µl of culture medium was added to the bottom chamber of each well, to support cells that invaded through the insert, followed by incubating for 72 hours at 37°C with 5% CO_2, as illustrated in Figure 2.9.

After incubating, medium was carefully aspirated, the Matrigel layer and the non-invasive cells were then removed from the insert using a cotton bud. Invaded cells on the bottom side of the insert were then fixed in 4% formalin solution for 10 minutes, followed by staining with 0.5% crystal violet solution. After 10 minutes staining, the plate was washed with tap water to remove the redundant crystal violet, then allowed to dry overnight at room temperature. 100µl of 10% acetic acid was used to dissolve the crystal violet for 10 minutes and subsequently, the plate was placed inside the LT4500 plate reader for detection at 600nm wavelength to measure the optical density (OD). Data was analyzed with GraphPad.

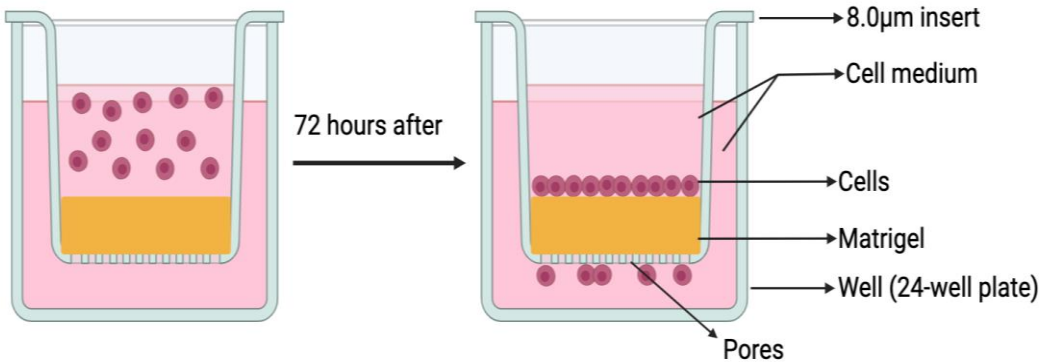

Figure 2.9 Schematic diagram of Matrigel invasion assay. Invasive cells through Matrigel and migrating to the bottom side of the insert. The figure was generated using BioRender (https://www.biorender.com/)

2.8.4 Beads-based migration assay

Some cell types like Caco-2 are clustered closely together when they were growing, therefore the conventional wound healing assay is not suitable for them. Beads-based migration assay was used as an alternative method to examine the migration ability of cells.

Briefly, $5x10^5$ of each cell type were seeded into a universal container containing 10ml of cell culture medium supplemented with 100µl of cytodex-2 beads (GE Healthcare, Cardiff, UK) and incubated for 3.5 hours to allow the cells to adhere to the beads. After incubation, the beads were carefully washed with 5 ml of PBS twice to remove any dead cells and non-adhered cells. After washing, the beads were resuspended with 1ml of cell culture medium before adding 200µl to each well of the 24-well plate containing 800ml of cell culture medium for 5 repeats. following overnight incubation, cells that had migrated from the cytodex-2 beads to the base of the well was fixed with 4% formalin for 10-20 minutes and then stained with 0.5% crystal violet solution for 10 minutes. 100µl of 10% acetic acid was then used to dissolve the crystal violet for 10 minutes and subsequently, the plate was placed inside the LT4500 plate reader for detection at 600nm wavelength to measure the optical density (OD). Data was analyzed with GraphPad.

2.8.5 Electric cell-substrate impedance sensing (ECIS) based cell adhesion and migration assay

Electric cell-substrate impedance sensing (ECIS) is a well-established method for monitoring a number of cellular behaviors, including adhesion, and migration (Giaever and Keese 1991). As a non-invasive, label-free, and real-time measurement system, ECIS has been utilized in different fields, such as cancer studies (Rahman et al. 2009; Hong et al. 2011), wound healing assay (Jiang et al. 2010; Sanders et al. 2011), toxicology (Lee et al. 2011; Tran et al. 2013), and blood brain barrier (Yamamoto et al. 2008).

As shown in Figure 2.10, ECIS is mainly composed of a pair of electrodes, a signal generator to apply AC signal, and a lock-in amplifier to record the impedance(Szulcek et al. 2014). The principle of ECIS is based on the insulating properties of cell membranes. To be specific, the

ECIS system offers a constant alternating current with a wide range of frequencies, typically ranging between 10 Hz and 100 kHz. Cells are seeded on the top of electrodes and allowed them to adhere. With the spreading and growth of cells on the electrodes, the current flow through the electrode is limited, resulting in an increase of impedance (Liu et al. 2012b).

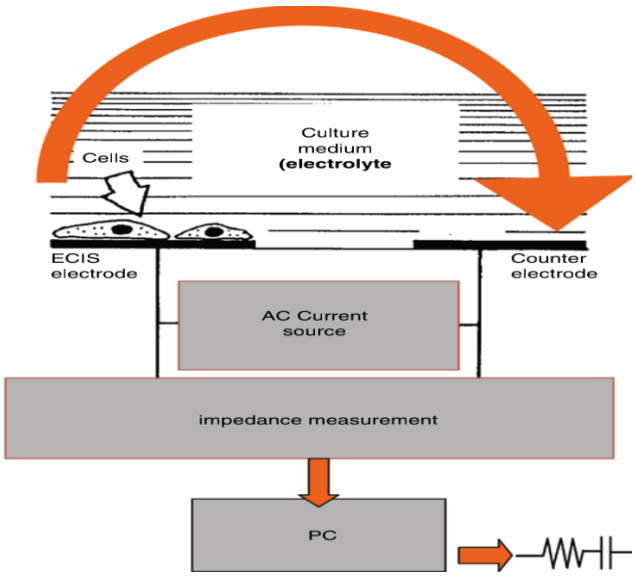

Figure 2.10 The basic composition of ECIS system. The cells are seeded on the top of electrodes and are cover with culture medium as the electrolyte (Giaever and Keese 2012).

Figure 2.11 shows the ECIS model. The current generated by ECIS could flow from the electrode interface and moving either in the narrow spaces beneath and between the cells (red arrows), or through the cell plasma membranes (green arrows). The measured impedance consists of two important parameters, resistance, and capacitance. Resistance, consisting of para- and trans-cellular current flow, is more likely to represent the quality and function of the cell barrier, whereas capacitance stands for the overall coverage of the electrodes. The relative amount of current through these two routes is dependent upon the AC frequency, as adherent cells have the ability to alter the flow of the current through the monolayer in a frequency-dependent manner. At low frequencies (100-10,000 Hz), the AC is hard to go through the cell membrane intracellularly due to the capacitive effect of the cell membrane largely resisting current flow ($X_c = \frac{1}{2\pi f C}$). Consequently, most of the current flows under the cells and through the spaces between the cells. Conversely, at high frequencies (>10,000 Hz), the current mainly flows through the insulating cell membranes with little current going through the paracellular path since the impedance of membrane is relatively

small (Robilliard et al. 2018).

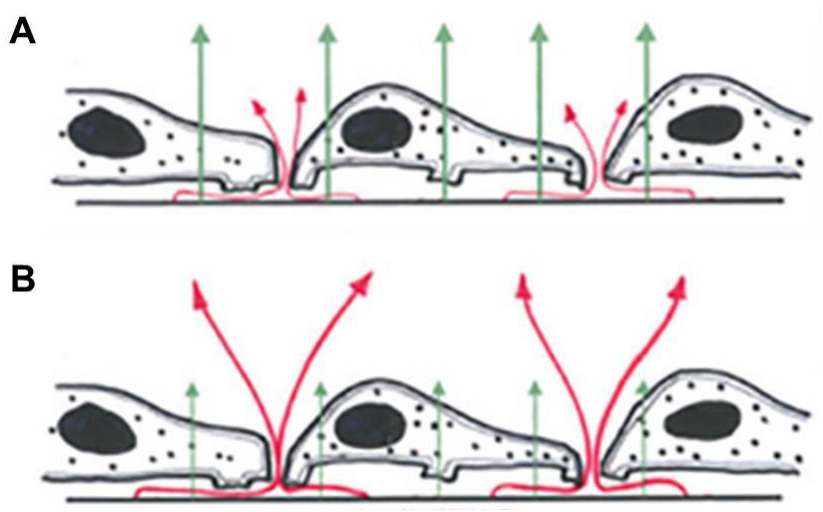

Figure 2.11 The ECIS model. A. At high AC frequency, the current mainly flows through the insulating cell membranes. B. At lower frequency, most of the current flows under the cells and through the spaces between the cells. Available: http://www.biophysics.com.

Before ECIS assays, 200µl serum-free medium was added to the 96-well ECIS W961E electrode arrays (Applied Biophysics Inc., NJ, USA), the plate was then placed on the array station inside the incubator, while the assay station was connected to the ECIS Ztheta instrument (Applied Biophysics Inc., NJ, USA) (Figure 2.12). The connection status of ECIS plate was then checked, and 30 minutes were required to stabilize the plate.

ECIS was then carried out by seeding 200µl cell solutions containing 20,000 cells, with the relevant culture medium for each cell model, into 96-well ECIS arrays in 5-6 repeats. The arrays were then placed on the ECIS instrument. After incubating for 5 hours to reach confluent monolayers, an electrical wound with 2000 mA for 20 seconds was applied in each well by the ECIS. This is followed by 10-24 hours incubation. Impedance of each well was recorded continuously over 1000 to 64,000Hz throughout the running of the instrument. Data was analysed using ECIS software (Applied Biophysics Inc., NJ, USA).

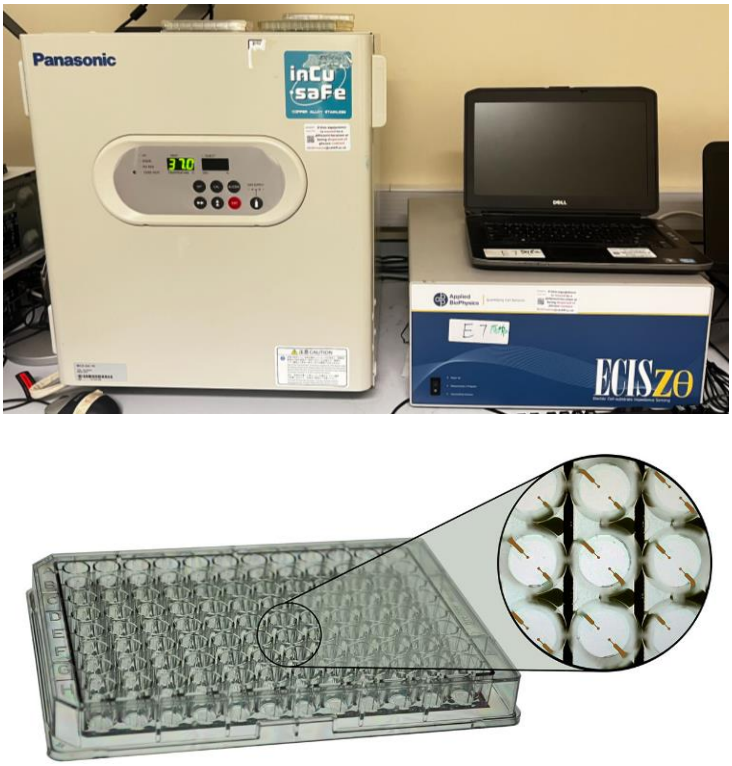

Figure 2.12 The ECIS instrument and ECIS microarray used in the present.

2.8.6 Transepithelial electric Resistance (TER)

TER is a well-established method to investigate the barrier function. Basically, cells were cultured inside the insert, which can separate and simulate the diffusion barrier between the apical and basolateral sides of cell monolayer. Once the cell monolayer was developed, a pair of dedicated electrodes were inserted in both the lower and upper compartments. The small AC current was then applied which can passed from one electrode to another. TER measured how much signal was blocked by the cell monolayer, thereby quantifying barrier integrity (Figure 2.13).

Transwell inserts with 0.4µm pores in 24-well plate (Greiner Bio-One Ltd., Gloucestershire, UK) were used in this study. $5x10^4$ cells in 500µl cell suspension were seeded into the inserts with 1.5mL medium in the wells of the 24-well plate. Cells were incubated at 37 °C, 5% CO_2 for 24-48 hours until reach fully confluent. Medium was then replaced and resistance across the membrane was then measured in triplicate immediately afterwards using the EVOM² Epithelial Volt/Ohm Meter (World Precision Instruments, Hitchin, Hertfordshire, UK) (Figure 2.14). With single measurements TER were analysed as fold change from controls.

Data was collected, normalised, analysed and presented as column chats using excel and GraphPad with following equation:

$$R_{Tissue}(\Omega) = R_{Total}(\Omega) - R_{Blank}(\Omega)$$

$$TER(\Omega * cm^2) = R_{Tissue}(\Omega) * S(cm^2)$$

In which R_{Tissue} is the measured resistance, R_{Blank} is the electrical resistance of a blank (cell insert in culture media without cells), S is the membrane area of the insert (0.336cm^2).

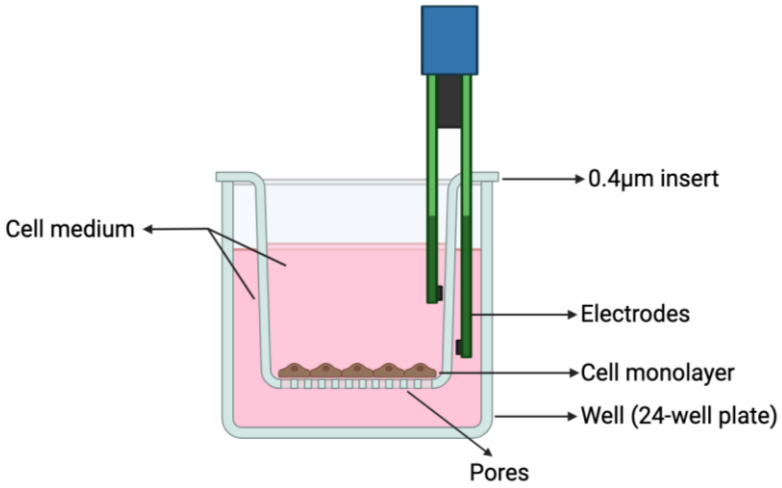

Figure 2.13 Schematic diagram of TER. A pair of electrodes was inserted in both the lower and upper compartments separated by an insert with the semi-permeable membrane. The small AC current was then applied which can passed from one electrode to another, and the resulting resistance can be measured. The figure was generated using BioRender (https://www.biorender.com/).

Figure 2.14 EVOM² Epithelial Volt/Ohm Meter with chopstick electrode for measuring the resistance between the two electrodes (World Precision Instruments, Hitchin, Hertfordshire, **UK).**

2.8.7 Paracellular permeability (PCP)

PCP was conducted to investigate the junction function of the cells. In this study, transwell inserts with 0.4µm pores in 24-well plates were used. $7x10^4$ cells (in 500µl cell suspension with medium) were seeded into the inserts with 1.5mL medium in the wells of the 24-well plate. Cells were incubated at 37 °C, 5% CO_2 until confluent. Cell medium was then replaced. 30µl of cell medium from outside of the inserts was transferred into a black 96 well cell culture microplate (Greiner Bio-One Ltd., Gloucestershire, UK) filled with 270µl PBS in each well, immediately after medium change. 0.2 mg/mL (1µl) of Fluorescein isothiocyanate (FITC)-dextran conjugate with an average molecular weight of 10 kDa (F5263, Sigma-Aldrich, Pooled, Dorset, UK) was then added to each insert (Figure 2.15). 30µl of the medium from outside of the insert was transferred to the 96 well plate filled with 270µl PBS with different time point, including 15, 30 minutes, 1, 2, and 4 hours, in duplicate after the FITC-dextran being added, and Fluorescence was then measured using the GloMax® Multi Detection System (Promega, Southampton, UK) at excitation 490 and emission 510-570. Measurements were then normalised to the 0-hour time point measurement via subtraction and data was analysed using GraphPad.

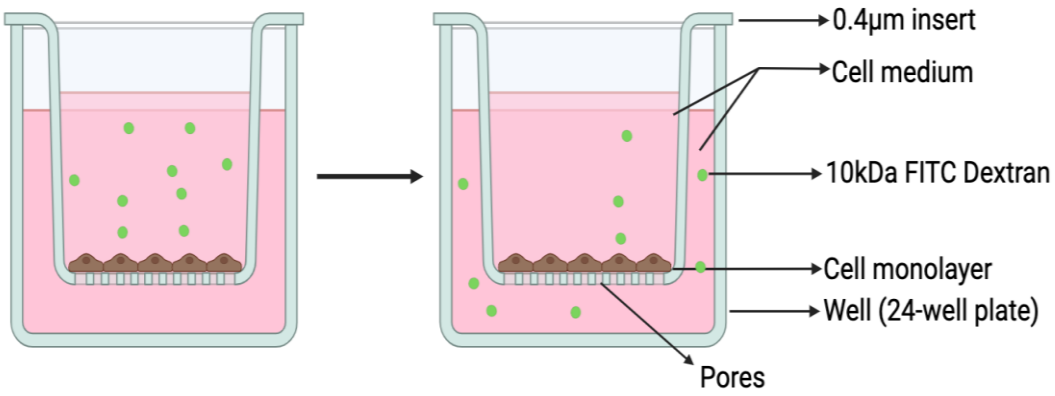

Figure 2.15 Schematic diagram of paracellular permeability assay. Insert with 0.4µm pore within a well of a 24 well plate was used. 40 kDa TRITC-Dextran and 10 kDa FITC-Dextran was added into the insert and the amount that moved to the outside of the insert was quantified every hour by measuring the amount of fluorescence produced from samples of cell medium. The figure was generated using BioRender (https://www.biorender.com/).

2.9 Proteomic analysis

2.9.1 Proteomic analysis using mass spectrometry Tandem Mass Tagging (TMT)

The alteration of molecules in response to PEFE treatment was explored via University of Bristol TMT-based mass spectrometry. After protein extraction and quantification, 100µl of the protein sample for each group (untreated and treated with PEFE) was packaged in dry ice and sent to University of Bristol for the proteomic analysis. Mass spectrometry was conducted using Tandem Mass Tagging.

Mass Spectrometry is a technique used to measure the strength of mass-to-charge ratio of ions, which can further identify a large scale of proteins based on their mass and charge. TMT is a labelling technique used in quantitative proteomics. It involves tagging peptides from different samples with isobaric chemical tags. These tags have the same mass, allowing them to co-migrate during the initial stages of mass spectrometry. However, upon fragmentation, they release distinct reporter ions, enabling the quantification of the original peptides.

2.9.2 Data analysis for proteomic analysis

Data analysis was performed to determine which proteins were affected when Caco2 was exposed under PEFE. Two separate analysis was performed: one to compare the total protein levels between the control group and the PEFE group and a second was to assess protein phosphorylation, in which a phospho-peptide enrichment method was utilized to identify the phosphorylation status of serine (S), threonine (T), and tyrosine (Y) residues across the same samples. The collected data were analyzed with Proteome Discoverer v2.4 software, which was carried out by a bioinformatician from University of Bristol, running a search against the Uniprot Human database and against a 'Common Contaminants' database, which was included in the searches.

The following are the key parameters collected and used for the data analyses:

Protein FDR Confidence - The confidence that the identified protein is truly in the sample.

Medium = Identified at <5% False Discovery Rate (FDR). High = Identified at <1% FDR. In this study, all the data was filtered using a 5% FDR cut-off.

Total - Log2 Normalized Abundance - The Total - Normalized Abundance of the master protein. These data are Log2 transformed to bring them closer to a normal distribution.

Phos - Adjusted Log2 Normalized Abundance - Generated by subtracting the Total - Log2 Normalized Abundance from the Phospho - Log2 Normalized Abundance. This facilitates the identification of genuine changes in phosphorylation rather than changes in the overall abundance of a protein whose phosphorylation level remains unchanged.

LogFC - The difference between the mean Total - Log2 Normalized Abundances for each condition. In this study, LogFC is calculated as: $LogFC=Log_2(PEFE) - Log_2(Control)$. Positive value of LogFC indicates that the gene expression was upregulated after PEFE treatment, while the negative value of LogFC corresponds to the downregulation.

2.10 Statistical analysis

Several statistical software was used for the data analysis in this study. Minitab (Minitab Ltd. Coventry, UK) was carried out to analyse transcript expression of target genes in clinical cohorts, which is not of a normal distribution, in comparison to clinical pathological information by using Mann Whitney U test (two data sets) and Kruskal-Wallis ANOVA on RANKS test (three or more data sets). SPSS (version 26) (IBM, Armonk, New York, USA) was used to do Kaplan-Meier survival analysis in clinical cohorts.

Prism 10 (GraphPad Software, San Diego, CA, USA) was used to analyse experimental data. Each experiment was conducted at least three times, unless otherwise stated, and data were presented as the mean of the repeats with the standard deviation (SD). Comparison between tested groups was applied with normally distributed data using two-tailed t test paired or unpaired. Detailed analysis methods for each dataset are also stated in the respective result chapters. P value of ≤ 0.05 was statistically significant.

Chapter-3 PEFE setup and calibration

3.1 PXI-based PEFE system

3.1.1 Introduction of PXI system

A PXI-based PEFE system has been developed to overcome the drawbacks of the previous system as mentioned in section 1.8.6. As a PC-based platform developed by National Instruments, PXI is mainly applied for measurement and automation. Due to its characteristics of high performance and low cost, the PXI system has been widely used for manufacturing tests, machine monitoring, automotive, and industrial tests. PXI systems mainly consist of three hardware components, including chassis, controller, and peripheral modules, driven by software such as LabVIEW. PXI chassis acts like a 'house' for holding controllers and PXI modules and connecting them with a backplane that provides timing and synchronization abilities. The embedded controller can replace the external PC which could make the whole system more portable and place-safely. All the required functions are then achieved by the PXI modules, which can obtain data and images, trigger and synchronize different devices, generate signals, and make a range of measurements.

3.1.2 Components in PXI-based PEFE system

The PXI-based PEFE system overview is shown in Figure 3.1, this system consists of a series of PXI components that cooperated with other dedicated devices, operating at microwave frequencies.

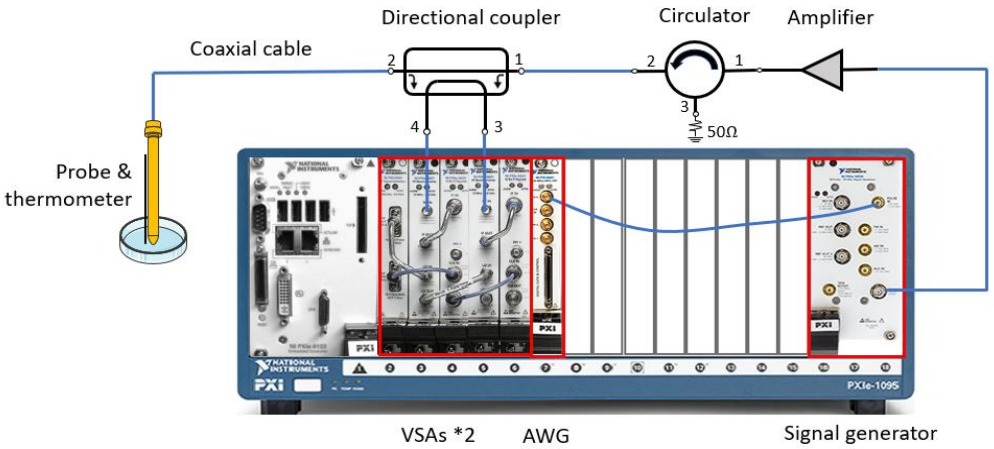

Figure 3.1 PEFE system consists of several PXI components and other microwave devices.

The PXI-based PXI system has the following components:

- An Arbitrary Waveform Generator (AWG) PIX-5441
- A RF Analog Signal Generator PXIe-5654
- Two Vector Signal Analyzers PXIe-5663E

The entire PXI instrument is hosted in PXIe-1095 chassis with a PXIe-8133 controller. In short, the pulsed signal was generated by the signal general. The generated signal was then boosted by the power amplifier to the desired power levels and transferred to biological samples through coaxial cable and a dedicated probe. Due to the impedance mismatch between the end of the probe and the biological samples, both incident and reflected signal were generated. Two VSAs (Vector Signal Analyzers) were used to monitor these two signals for further analysis of power dissipated into the biological samples. Also, a thermometer was required for this system to monitor the temperature of the targets and maintain it under 42 degrees.

The details of each PXI-based component will be discussed in the following sections.

3.1.2.1 Signal generator

The RF signal source used in this study was NI PXIe-5654 RF Analog Signal Generator (National Instruments Corporation Austin, TX, USA) with its on and off states controlled by NI PXI-5441 Arbitrary Waveform Generator (National Instruments Corporation Austin, TX, USA), as shown in Figure 3.2and Figure 3.3 respectively.

Figure 3.2 NI PXI-5441 16-Bit Arbitrary Waveform Generator. Source: https://www.ni.com/en-gb/shop/hardware/products/pxi-waveform-generator.html?modelId=123208

Figure 3.3 NI PXIe-5654 RF 250 kHz to 20 GHz RF Analog Signal Generator. Source: https://www.artisantg.com/TestMeasurement/82334-9/National-Instruments-PXIe-5654-20-GHz-RF-Analog-Signal-Generator

AWG used in this research aims to generate square wave to the PULSE IN port of signal generator, which can be seen as a trigger, as shown in Figure 3.4. In other words, the AWG tells the signal generator when to create a signal and when not. The pulsed RF signal is generated by uploading a repeatable square waveform to the AWG with the required timings. In addition, the use of the AWG can be readily used to stop the RF generator from producing any signal for any extended period by stopping the AWG from producing any output signal. The main parameters of the AWG in the specification are listed in Table 3.1.

The AWG on and off signalling is sent to the RF signal generator PXIe-5654 using the PULSE IN port on its front panel. It should be noted that accurate generation of the RF signals requires

a warm-up time after the AWG/ RF signal generator was loaded, normally at least 30 minutes, to ensure it at the stable operating temperature, as illustrated in Figure 3.5.

The important parameters of the specification of this signal generator are listed in Table 3.2. The maximum output of this RF signal generator is +13*dBm* (approximately 0.02 watts), which is much lower than the minimum power required in this study (30 watts). Therefore, a high-power amplifier is required to increase the input signals to the desired value.

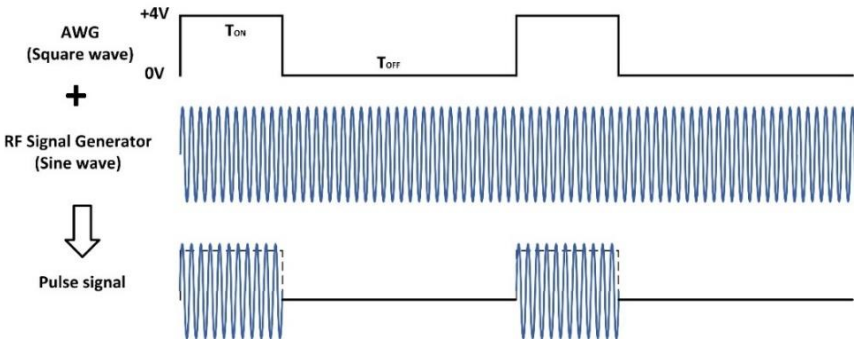

Figure 3.4 The Principle of the formation of a pulsed RF signal by the combination of AWG and RF Signal Generator.

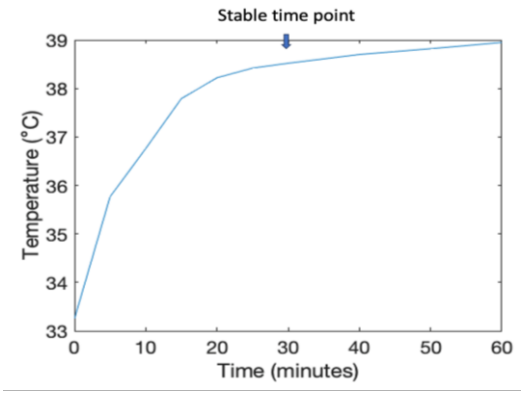

Figure 3.5 PXI war-up time. The temperature of the PXI system was recorded every five minutes. At least 30 minutes were required to achieve stable operating temperature.

Table 3.1 Main specification of NI PXI-5441 AWG

Specifications	
Suggested maximum frequencies (Square wave)	12.5MHz
Maximum output voltage (V_{pk-pk})	±12V
Amplitude resolution	<0.06% (0.004 dB)
Bandwidth	43MHz
Maximum sample rate	100MS/s
DAC resolution	16 bits
Ambient temperature range	0 to 55℃

Table 3.2 Main specification of NI PXIe-5654 RF Analog Signal Generator

Specifications	
Frequency range	250kHz-20GHz
Frequency resolution	0.001Hz
Output power range	+13*dBm* to -7*dBm*
Amplitude resolution	0.01dB
Ambient temperature range	0 to 55℃
Warm-up time	30 minutes
PULSE IN Port	
Repetition frequency	DC to 10 MHz
Input amplitude range	-0.5V to 5.5 V
Input impedance	>100 kΩ
Minimum pulse width	50 ns
Pulse overshoot	<10%

3.1.2.2 High power amplifier

An AS1860 solid state power amplifier (MILMEGA Limited UK) was utilized to increase the input signals to the desired values, as illustrated in Figure 3.6. Some advantages of this amplifier are listed as follow:

1. This amplifier covered a large frequency range of 1.8-6.0 GHz and generated high power up to 125W, which was more than sufficient for this study.

2. This amplifier was characterized by its linearity and low harmonics, which can operate precisely.

3. Fans were installed in this amplifier to control its temperature at acceptable levels. Otherwise, it may malfunction due to excessive temperature rise caused by low impedance mismatch.

Figure 3.6 MILMEGA AS1860 solid state power amplifier. Source: https://www.ametek-cts.com/products/brands/milmega/single-band-as1860-series-

The main specifications of this amplifier are listed in Table 3.3.

Table 3.3 Main specification of AS1860 power amplifier

Specifications	
Frequency range	1.8-6.0 GHz
Psat (min)	125 watts (50.969*dBm*)
P1*dB* (min)	100 watts (50*dBm*)
Gain (min)	46*dB*
Gain Variation (max)	+/- 3.0*dB*
Maximum input power	+15*dBm*
Input VSWR	2:1
Output VSWR	2:1
Operating Temperature range	0 to 40℃

The 1*dB* compression point (P1*dB*) is one of the most important specifications for power amplifiers. This point is the output power level when the gain is reduced by 1*dB* from its constant value. Once the amplifier reaches its P1*dB*, it will enter a compressed state and become a non-linear device, producing distortion and harmonics, as given in Figure 3.7.

When the amplifier was initially turned on, a drift in gain was observed as confirmed through power sensor measurements showing a decrease in output. The circuits inside the amplifier needed enough time to reach stable temperature to achieve accurate power transmission. Typically, 40 minutes to 1 hour, depending on the environmental temperature, were required to keep the performance stable.

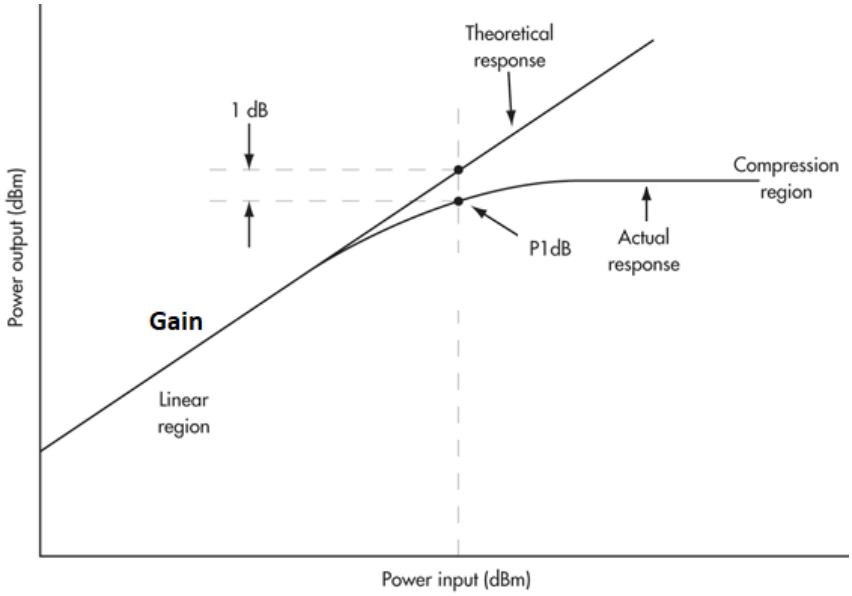

Figure 3.7 Illustration of gain compression. Source: https://www.everythingrf.com/community/what-is-p1*dB*#:~:text=The%201%20*dB*%20compression%20point,distortion%2C%20harmonics%20and%20intermodulation%20products

3.1.2.3 Circulator

When experimenting, an open-ended coaxial cable was used as a probe to deliver pulse signals to the biological samples. An impedance mismatch occurs when the input impedance of the biological samples does not match the output impedance of the signal sources, resulting in signal reflection. Such reflected signals will propagate from the tip of the probe to the amplifier, which will interfere with the output, resulting in inaccurate measurement outcomes. Therefore, a circulator was installed after the amplifier to address this problem.

The circulator consists of a three-port device formed by a Y-junction strip line coupled with a magnetically biased ferrite material, propagating electromagnetic waves in one direction only along the ring. In this research, the three-port circulator AltanTecRF AS7122 (Atlantic Microwave Ltd) was used, as given in Figure 3.8. Port 3 was terminated with a 50Ω load, so this circulator acts as an isolator for the incident signals and reflected signals. The propagation of microwave signals becomes unidirectional, which the signals insert into port 1 of the circulator and exit at port 2. The reflected signals enter at port 2 and are terminated by the 50Ω load at port 3. Consequently, no signal propagates from port 3 back to port 1, which

provides the amplifier with safe and precise operation conditions. This was also confirmed by the indicator of the amplifier, as illustrated in Figure 3.9.

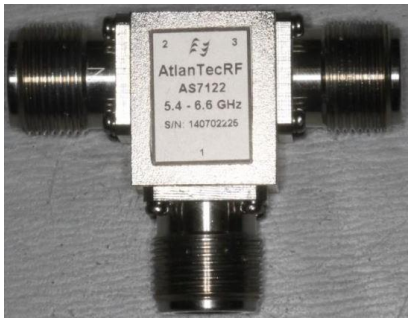

Figure 3.8 AltanTecRF AS7122 microwave circulator (Ehtaiba 2017)

Figure 3.9 The indicator of the higher power amplifier. Pi presents incident power, and Pr presents reflected power. After the circulator was involved, no light appeared in the Pr area, meaning that no reflected signal went back to the amplifier.

3.1.2.4 Directional coupler

As mentioned above, due to the impedance mismatch between the biological samples and the signal sources, both incident signals and reflected signals are generated during the measurement system. Both signals are critical and worth monitoring for further data analysis to calculate how much power, which is the difference between injected and reflected signal, is being injected into samples. Within the system set-up, a microwave directional coupler, which can separate incident signals and reflected signals, is used in this system.

The principle of this directional coupler is based on its structure, as given in Figure 3.10. It consists of two transmission lines, the main line, and the coupled line. A signal is injected through port 1 of the mainline and exits through port 2. Part of this signal appears in port 3. While a portion of the reflected signals travels from port 2 to port 1 and is coupled to port 4.

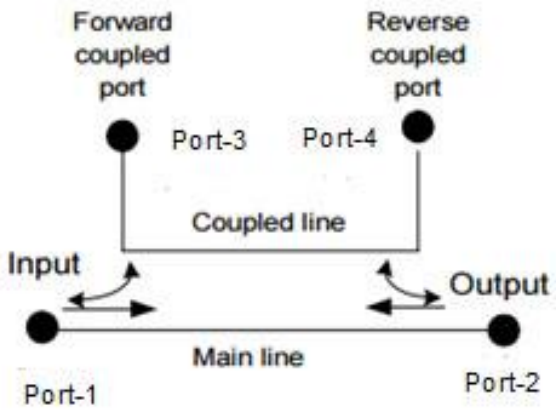

Figure 3.10 The principle of four-port directional coupler diagram (Matzner and Levy 2002)

The passive directional coupler utilized in this study is a four-port bidirectional coupler with a rated coupling factor of 30*dB* over a wide frequency range, as shown in Figure 3.11. Before the experiment, the system must be calibrated to determine the actual coupling factor and obtain a quantitative measurement of the actual signal injected into the sample, which will be discussed later.

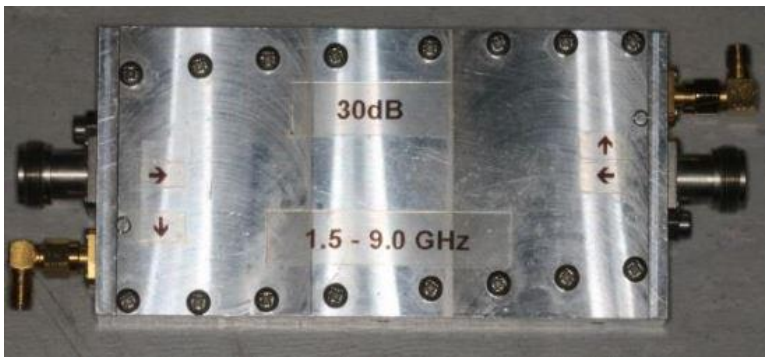

Figure 3.11 Microwave directional coupler used in this research (Ehtaiba 2017)

3.1.2.5 Vector signal analyzer (VSA)

As mentioned before, power meters used in previous systems can only measure the power

to describe the characteristics of the circuit. Furthermore, it measures only the total power of the signal and therefore does not allow distinguishing between the different frequency components. To avoid any such limitations, two vector signal analyzers (VSAs) are used to measure both amplitude and phase of incident signals and reflected signals, respectively.

VSA used in this study is PXIe-5663E (National Instruments Corporation Austin, TX, USA), which consists of three modules, including NI PXIe-5652 RF Signal Generator, NI PXIe- 5601 RF Downconverter, and NI PXIe-5622 IF Digitizer, as shown in Figure 3.12. This VSA provides a wide instantaneous bandwidth optimized for automated testing. Combined with a high-performance PXI controller and a high-speed PCI Express data bus, it can perform common automated measurements dramatically faster than traditional devices. The main specification of this VSA is listed in Table 3.4.

Figure 3.12 NI PXIe-5663E Vector Signal Analyzer. Source: https://www.ni.com/en-gb/shop/hardware/products/pxi-vector-signal-analyzer.html?modelId=123683

Table 3.4 Main specification of PXIe-5663E vector signal analyzer

Specifications	
Frequency range	10 MHz to 6.6 GHz
Tuning resolution	533 nHz
Equalized Bandwidth	50 MHz
Dynamic range	80dB
Operating Temperature range	0 to 55℃

The function of PXIe- 5601 RF Downconverter is to downconvert RF signals to intermediate frequency (IF) by an analog-to-digital (ADC) converter. To achieve this, PXIe-5652 serves as a

local oscillator (LO) source. It uses a voltage-controlled oscillator (VCO) architecture to allow for fast-frequency tuning speed. PXIe-5622, a 16-bit digital converter with a sampling rate of 150 MS/s, which can share timing and trigger signals between NI PXIe-5663E and other PXI modular instruments. Overall, the downconverter and digitizer work together as a frequency mixer to convert the RF signal into IF, then separate the complex signal into I and Q components and digitize the resulting signal. An important feature of the NI PXIe-5663E module is that it allows multiple instruments to share a common start trigger, a reference clock, and even an LO, as shown in Figure 3.13. This can then contribute to the synchronization between the VSAs and, therefore, ensure that both VSAs are measuring the signals at the same frequency and stable phases differences.

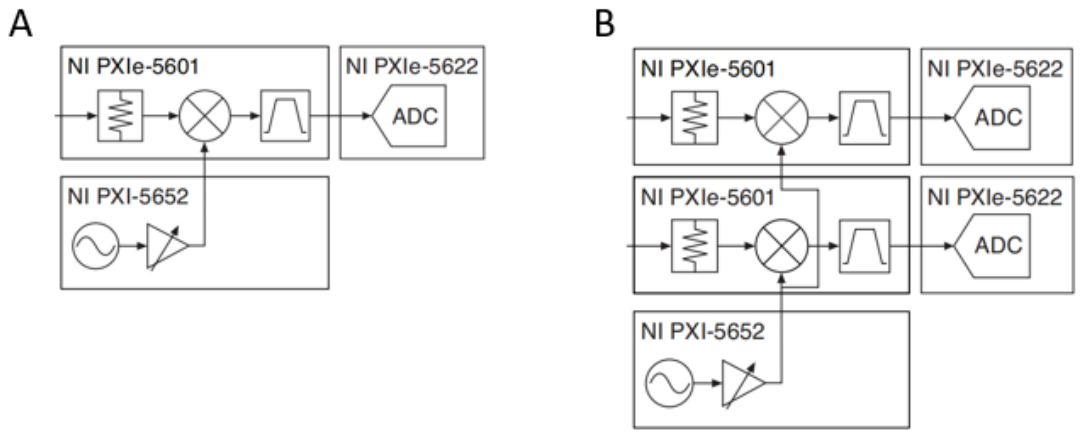

Figure 3.13 Block Diagram of NI PXIe-5663E. A. an signal NI PXIe-5663E; B. two Cascaded NI PXIe-5663E VSA (NiationalInstruments)

3.1.2.6 Open-ended microwave probe

The probe utilized in this study for both in vivo and in vitro treatment was made of RG-405 semi-rigid coaxial cable, which is showing in Figure 3.14. This microwave coaxial cable is characterized by its ability to effectively transmit electromagnetic signals at microwave frequencies. This cable is composed of an inner conductor, a dielectric layer, and an outer conductor, as shown in Figure 3.15. The inner and outer conductors are made of copper, and the dielectric layer is made of polytetrafluoroethylene (PTFE). One end of the coaxial cable was cut and polished into a pointed end, which is able to be easily inserted into a nude mouse when used in vivo. The other end of the probe was connected to the directional coupler

through a microwave coaxial cable.

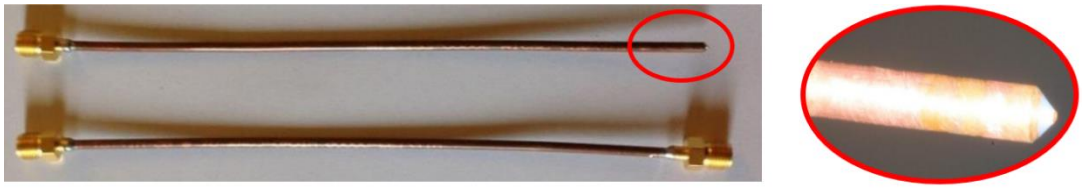

Figure 3.14 Open-ended coaxial cable probe used in this research and its pointed tip (Ehtaiba 2017)

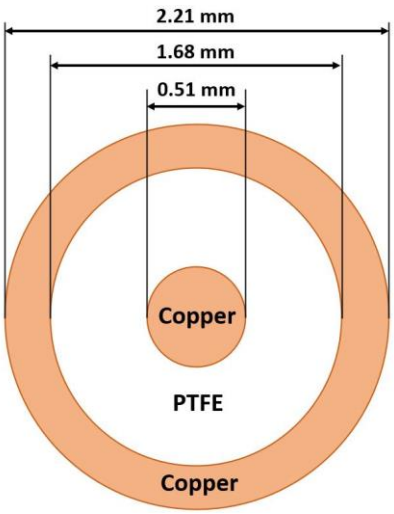

Figure 3.15 Cross section of the probe.

3.1.2.7 Temperature sensor

As mentioned before, PEFE was applied to biological samples at stable and low temperatures. Thus, a sensitive temperature sensor was necessary to monitor the temperature range between 20 and 42 degrees Celsius. In addition, due to the use of microwaves during the experiment, a sensor is required that is not impacted by the irradiation. For this reason, the temperature sensor used in this project was the Luxtron M922 Fiber Optic Temperature Sensor, with STB probe (Advanced Energy, LumaSense Technologies Inc., Frankfurt, Germany), as illustrated in Figure 3.16. This temperature sensor was connected to a USB port, making it portable. The specifications of this temperature sensor and probe are listed in Table 3.5. The temperature range of the probe is 0 to 120°C, which is enough for this project (under 42°C). Also, its small diameter (0.5mm) made it straightforward to place at its required position. Moreover, the smaller size helps to reduce the response time that it takes to react to changes in temperature.

Figure 3.16 Luxtron M922 Fiber Optic Temperature Sensor.

Table 3.5 Key parameters of Luxtron M922 Fiber Optic Temperature Sensor and STB probe

Specification	
Luxtron M922 Fiber Optic Temperature Sensor	
Measurement range	-100 to 330 °C, probe dependent
Accuracy (calibrated)	+/- 0.05 °C, probe dependent
Output Format	℃, °F, °K
Number of channels	2
Measurement resolution	0.01°C
Measurement rate	Up to 50Hz per channel
Operating Environment	°C to 60 °C
STB probe	
Temperature range	0 to 120 °C
Diameter	0.5mm
Response time	0.25s
Length	1 meter

3.1.3 LabVIEW program

In this study, all the PXI modules and temperature sensors were controlled and monitored by using LabVIEW 2018 (National Instruments Corporation Austin, TX, USA), which is National Instrument's software for graphical programming to control and measure instruments. LabVIEW, or Laboratory Virtual Instrument Engineering Workstation, is based on a virtual instrument (VI) to control data flow and perform data analysis. Each VI has a front panel and a block diagram. The block diagram is used for programming, and the front panel is used for

the user interface. Specific drivers were necessary and could be downloaded from NI for advanced configuration options for the PXI components, including NI-FIGN for the AWG, NI-RFSG for the RF signal generator, and NI-RFSA for the VSAs (National Instruments Corporation Austin, TX, USA). The driver NI-VISA (Virtual Instrument Software Architecture) (National Instruments Corporation Austin, TX, USA), a standard for configuring, programming, and troubleshooting instrumentation systems for USB interfaces, was required for the configuration of the temperature sensor. All the codes were written based on the programming examples given by the LabVIEW library; however, further programming and reconstruction of the code was made in order to achieve the purpose of the project. Figure 3.17 below describes the whole process for the PEFE instrumentation. Basically, it can be divided into five stages: initialization, configuration, initiation, data acquisition and analysis, and close.

In the initialization stage, all the components inside the PXI system, including the AWG, RF signal generator, and VSAs, and temperature sensor, were identified by the software. This is followed by the configuration stage. In this stage, each component needed to be pre-configurated before running. For AWG, this includes the configuration of sample rate, reference clock, and waveform. For the RF signal generator, this includes the configuration of reference clock, frequency, and power level. For the VSAs, this includes the configuration of acquisition type, reference level, I/Q rate, and reference clock. Notably, the reference clock for all PXI components were set to the same source to make sure they were synchronized. After that, it moved to initiation and data acquisition stage, all components started to run according to the previous configuration. In this stage, the temperature sensor started to monitor the temperature, the pulsed signal with specific frequency and power level was generated and the I/Q information of the incident and reflected signal was measured. The signal generator was controlled by the temperature value. If the temperature was higher than 42 degrees, the signal generator was switched off until the temperature cooled down to 37 degrees, then the signal generator was switched on to apply the microwave to the biological samples. This process was repeated until the code was stopped. All the IQ information and temperature were stored in the database for further data analysis.

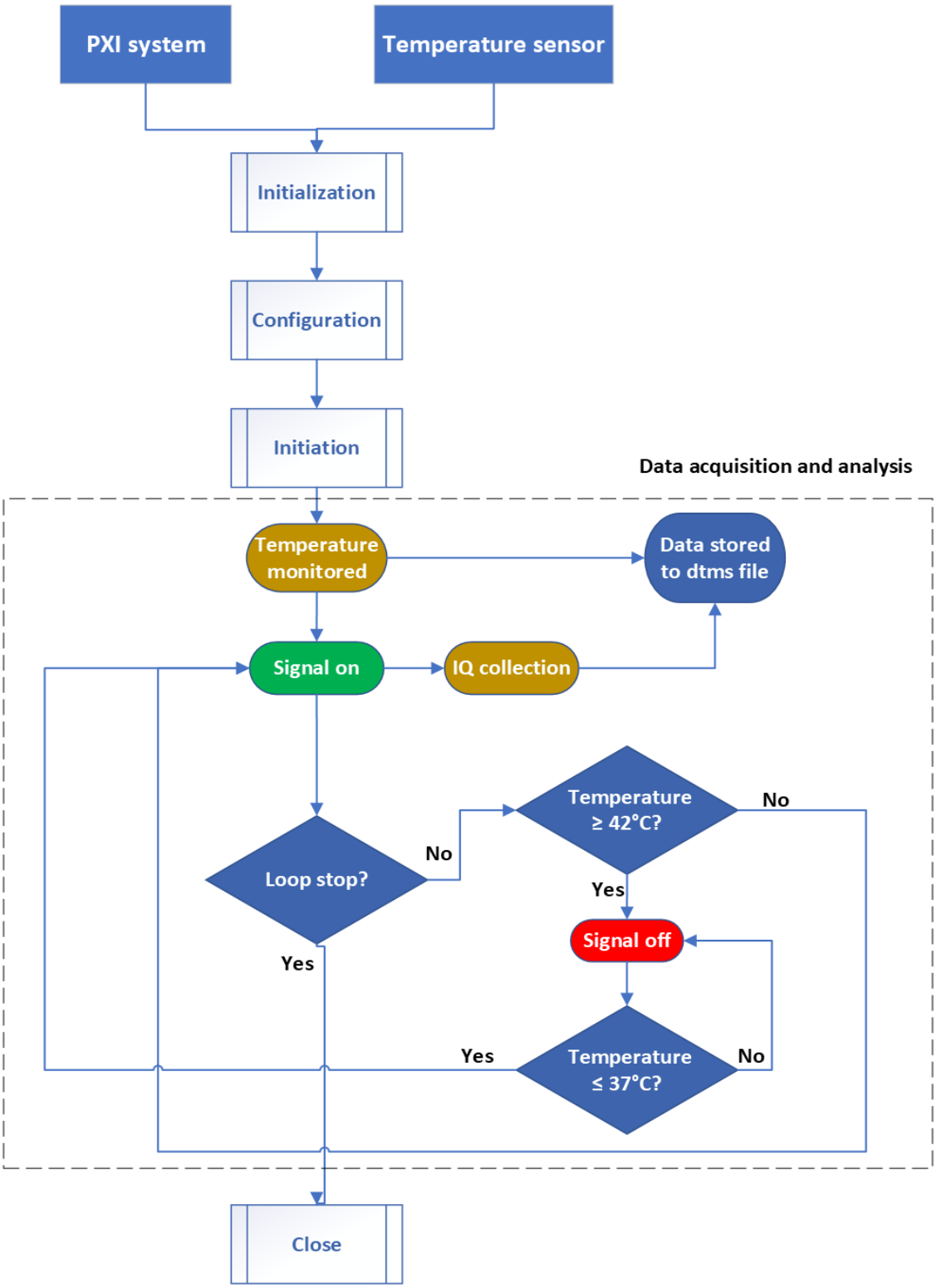

Figure 3.17 Flowchart of PEFE instrumentation programmed by LabVIEW. The entire instrumentation can be mainly grouped as five stages, including initialization, configuration, initiation, data acquisition and analysis, and close.

3.2 Calibration of the whole system

The PEFE instruments provide accurate readings at their input and output ports but do not account for the effects of the system components between these ports and the tip of the RF probe, where an impact on cells is created. To account for this, a calibration of the PXI system is essential to make sure known and accurate readings are made at the location where the experiment is taking place. This calibration allows for precise determination of the power injected into biological samples, making the experiments easier to reproduce. The components between the instrument ports and the probe tip are all but one passive and, therefore, linear, meaning their performance remains consistent regardless of increasing RF power that is flowing through these components. The only exception here is the power amplifier; however, as mentioned before, due to its large output power, it is used only within its linear region with maximum utilized power levels of about 50W. Therefore, the calibration mode was performed at low power levels using a continuous wave signal and then applied at the utilized higher RF powers.

In the calibration section, a U2021XA USB Wideband Power Sensor (50MHz - 18GHz) (Keysight Technologies UK Limited) was involved, as given in Figure 3.18. The key parameters of the specification are listed in Table 3.6. This power sensor draws power from a USB port and is driven by LabVIEW 2018 for data collection.

Figure 3.18 U2021XA USB Wideband Power Sensor. Source: https://www.keysight.com/us/en/product/U2021XA/usb-peak-and-average-power-sensor-50-mhz-18-ghz.html

Table 3.6 Main parameters of the power meter used for system calibration.

Specification	
Frequency range	50 MHz to 18 GHz
Dynamic range	-30dBm to +20dBm (peak/gated) -45dBm to +20dBm (average only)
Rise/fall time	≤13ns
Minimum pulse width	50ns
Minimum pulse repetition rate	10 MHz

Figure 3.19 below shows the block diagram of the power meter setup given in the LabVIEW library by Keysight. The operation of the power sensor consists of four stages, including initialization, configuration, data measurement, and closing. In the initialization stage, the power sensor is detected by the software. Then the configuration, including power units, working frequency, and measurement types were defined to the power meter. This is then followed by the measurement of average power and ended with close once the data was collected.

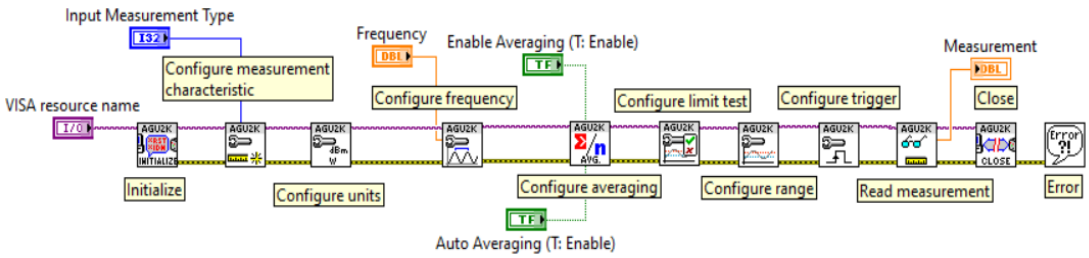

Figure 3.19 Block diagram of power meter's configurations in LabVIEW.

3.2.1 Calibration of two VSAs

The generator and VSAs calibration and verification were applied to inspect whether the generator and VSAs were working normally, verify the correct power levels at the desired frequency, and record the signal correctly. During the calibration, the frequency of 2.2GHz was selected. The calibration process focuses on the magnitude values of the signals only as it was not clear at this stage whether the phase represents any meaningful information for the purposes of carrying out experiments on cells.

In the first calibration step, the output of the RF signal generator was connected successively

with two VSAs to check the accuracy of the generator and VSAs, as illustrated in Figure 3.20.

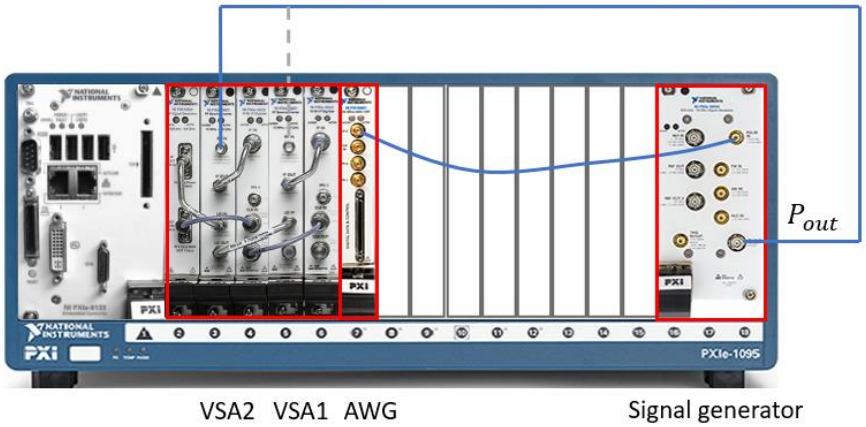

Figure 3.20 The calibration of VSAs. The output of the signal generator was connected with the two VSAs separately.

The IQ information was measured and stored in the database. The amplitude of the recorded IQ signal is the vector magnitude in volts, which is:

$$V_{VSA} = \sqrt{I^2 + Q^2}$$

Therefore, the power of IQ signal in watts is:

$$P_{VSA}(w) = V_{VSA}^2/2R$$

with R = 50 Ω as the input resistance of the VSA.

The power level was converted to dBm, which is:

$$P_{VSA}(dBm) = 10\log_{10} 1000P_{VSA}(w)$$

To verify these readings, a power meter was used as a reference to measure the output of the signal generator, as shown in Figure 3.21.

Therefore, the correction factor of the output power can be calculated as:

$$c1 = PM1 - P_{VSA1}(dBm)$$

$$c2 = PM1 - P_{VSA2}(dBm)$$

In which PM1 is the power level measured by the power meter in dBm, c1 and c2 are the correction factors (errors) of the power between two VSAs and power meter, respectively, in

dB. The calculated errors are listed in Table 3.7.

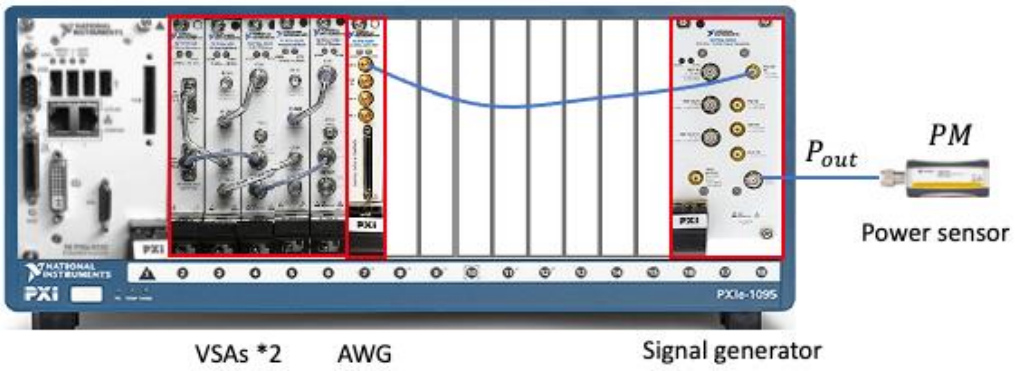

Figure 3.21 The Calibration of the signal generator. The power sensor was directly attached to the output of the signal generator.

As can be seen from the table, both correction factors are stable and independent of the power level. There is a difference of about 0.7 dB between the two correction factors, which is most probably due to the different output powers provided by the two generators for the same power setting. This is rather unsurprising as the two generators of the VSAs weren't calibrated at a National Instruments site for a few years.

Table 3.7 The calculated power errors between VSAs and power meter

power level (dBm)	$P_{VSA1}(dBm)$	$P_{VSA2}(dBm)$	PM (dBm)	c1 (dB)	c2 (dB)
12	10.73	9.98	11.35	0.62	1.37
10	8.74	8.01	9.34	0.6	1.33
8	6.73	6.02	7.35	0.62	1.33
6	4.75	3.99	5.34	0.59	1.35
4	2.73	1.97	3.33	0.6	1.36
2	0.74	-0.02	1.34	0.6	1.36
0	-1.27	-2	-0.66	0.61	1.34
-2	-3.27	-4	-2.65	0.62	1.35
-5	-6.27	-6.98	-5.63	0.64	1.35
-7	-8.26	-8.99	-7.64	0.62	1.35

At this stage, the two VSAs magnitude readouts were calibrated plus the end of the cable that was successively connected to both receivers was calibrated to provide known and accurate output powers.

3.2.2 Incident power calibration

When the signal was generated, it would be injected into port 1 of the directional coupler and output at port 2 with proportional coupled power appearing at port 3. In order to investigate the input signal and coupled signal, the calibration factor K1 was calculated.

When the signal was generated, the same cable from the previous calibration step was attached to port 1 of the directional coupler while its output at port 2 was terminated with 50Ω to prevent any reflections from going back into the coupler. Due to the function of the directional coupler, a part of the signal, which is proportional to the injected signal, appears at port 3. To determine the relationship between the input signal and coupled signal, the calibration factor K1 was calculated.

Figure 3.22 shows the used set-up for this calibration step. Here, port 4 was also connected to the second VSA2 as this linkage is required for the follow-on step.

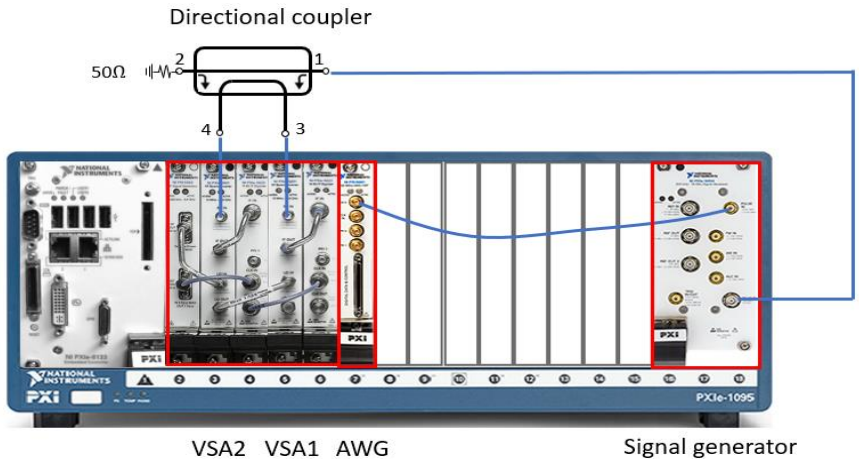

Figure 3.22 Coupler factor K1 calculation. The power was injected from port 1 of the coupler then measured by VSA1.

The frequency and power level of the signal generator were set to 2.2GHz and 12dBm, respectively. Then the incident coupled factor can be calculated as:

$$K1 = PM1 - (VSA1_{K1} + c1)$$

In which $VSA1_{K1}$ is the calculated power measured by VSA1, and PM1 is the relevant power meter readout from Table 3.7.

The calculated K1 from a few recent calibrations is listed in Table 3.8.

Table 3.8 The calculated K1 from a few recent calibrations

No.	PM1 (dBm)	$VSA1_{K1}$ (dBm)	c1 (dB)	K1 (dB)	Date of the calibration
1	11.32	-10.49	0.62	21.19	17/06/2024
2	11.35	-10.38	0.61	21.12	21/05/2024
3	11.31	-10.32	0.63	21	02/05/2024
4	11.35	-10.27	0.61	21.01	17/04/2024

3.2.3 Reflected power calibration

The reflected signals coming from the probe are injected at port 2 of the coupler and output at port 1 with the proportional coupled reflected signal appearing at port 4. The calibration factor K2 was calculated to determine the differences between the incident and reflected signals at port 2 and port 4.

The signal generator was connected to port 2 of the directional coupler, with port 1 linked to the power meter. Port 4 was connected to VSA2, and port 3 connected to VSA1 which as a 50Ω load, as illustrated in Figure 3.23.

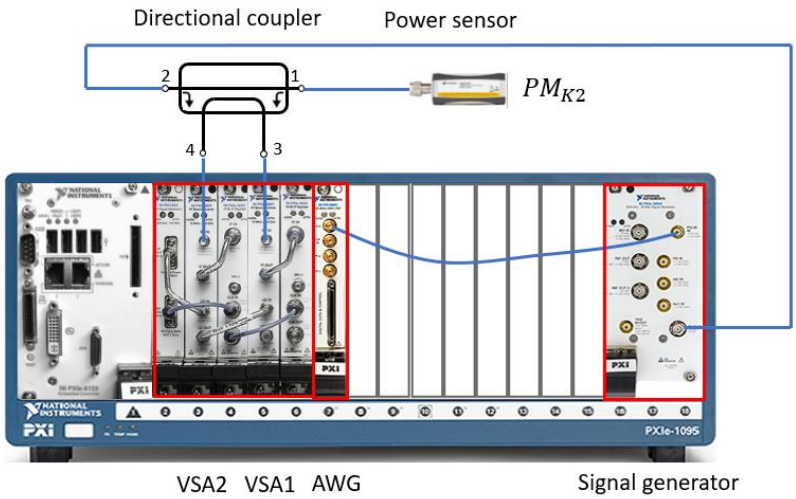

Figure 3.23 Coupler factor K2 calculation. Power was injected from port 2. The coupled power was measured by VSA2, and the output power was measured by the power meter.

The frequency and power level of the signal generator were set to 2.2GHz and 12dBm,

respectively. The reflected coupled factor can be calculated:

$$K2 = PM_{K2} - (VSA2_{K2} + c2)$$

In which VSA_{K2} is the calculated power measured and then calculated by VSA2, PM_{K2} presents the power measured by the power meter.

The PM_{K2} readout was utilized here to ensure that the proportional signal at port 4 is referenced to port 1, just like in the previous step when the signal at port 3 was referenced to the same port.

The calculated K2 from a few recent calibrations is listed in Table 3.9.

Table 3.9 The calculated K2 from a few recent calibrations

No.	PM_{K2} (dBm)	$VSA1_{K2}$ (dBm)	c2 (dB)	K2 (dB)	Date of the calibration
1	11.09	-11.78	1.37	21.5	17/06/2024
2	11.35	-11.7	1.35	21.7	21/05/2024
3	11.31	-11.55	1.33	21.53	02/05/2024
4	11.35	-11.64	1.35	21.64	17/04/2024

At this stage of the calibration, the PEFE set-up was able to accurately determine the injected and reflected signals flowing through port 1 of the coupler.

3.2.4 Loss calibration

In this process, the cabling and connector losses between port 1 of the coupler and the end of the probe tip were measured. The signal generator was connected with port 1 of the directional coupler, port 2 was connected with a double-ended probe, which is equivalent to the probe. Port 3 and port 4 were connected to VSA1 and VSA2, respectively. The other port of the double-ended probe was connected to the coaxial cable and linked to the power meter, as shown in Figure 3.24. The role of the connectorized double-ended coaxial cable is to represent the loss of the RF probe, which is made of the same cable and has the same length. The loss representation isn't ideal as it includes additional losses due to the second connector that is not present at the RF probe. However, this difference can be considered as relatively small.

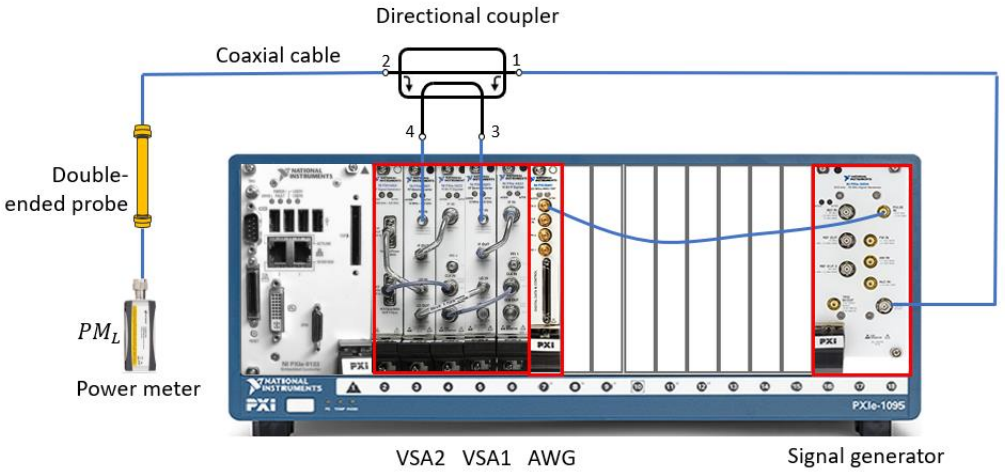

Figure 3.24 Loss calibration. The output power was measured by the power meter.

The frequency and power level of the signal generator were set to 2.2GHz and 12dBm individually. The loss of the cable can be calculated as follows:

$$L = PM1 - PM_L$$

In which PM_L is the power measured by the power meter, and PM1 is the relevant power meter readout from Table 3.7.

The calculated L from a few recent calibrations is listed in Table 3.10.

Table 3.10 The calculated L from a few recent calibrations

No.	PM1 (dBm)	PM_L (dBm)	L (dB)	Date of the calibration
1	11.32	9.92	1.37	17/06/2024
2	11.35	9.93	1.35	21/05/2024
3	11.31	9.83	1.33	02/05/2024
4	11.35	9.82	1.35	17/04/2024

3.2.5 Gain calibration

In this step, the gain of the amplifier was determined, so that the power set by the signal generator can be further determined to deliver the desired power to the cells at the end of the probe.

To achieve that, the power amplifier was connected after the signal generator to boost the power. A circulator was connected after the amplifier to minimize the reflected power from

the probe's end to go back to the amplifier. Also, a power meter was attached at the end by a double ended probe to verify the result, as shown in Figure 3.25.

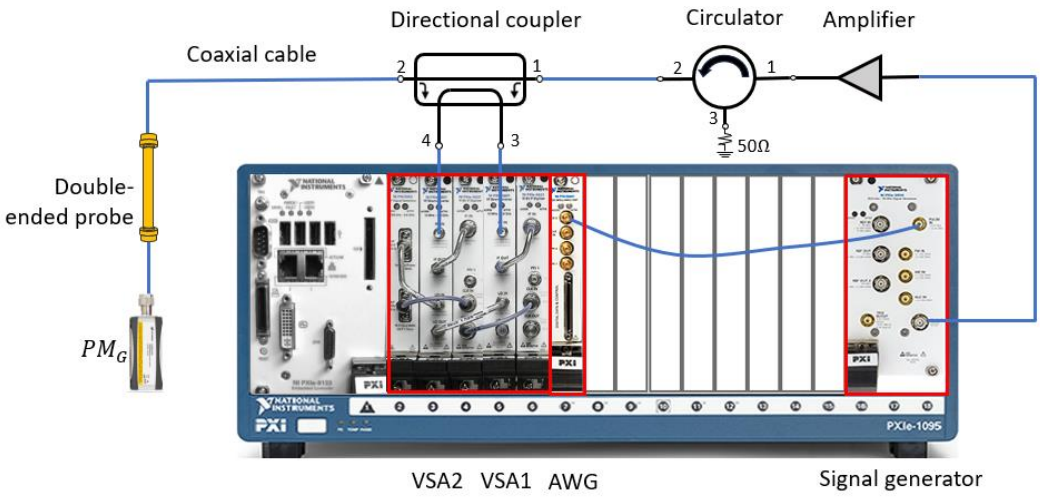

Figure 3.25 Gain calibration. The amplifier was combined in the system and the power meter was attached at the end.

For this calibration step, the frequency of the signal generator was 2.2GHz, while the power was set to -30dBm since the maximum input of the power meter is 20 dBm.

The total incident power can be calculated as:

$$VSA1_c = VSA1_{PA} + c1 + K1$$

In which $VSA1_c$ is the calculated total incident power, $VSA1_{PA}$ is the calculated power measured by VSA1.

The ideal power readout at the end of the probe should be calculated as:

$$P_R = VSA1_c - L$$

with L representing the losses between the coupler and the probe's end.

The error between the calculated power by power meter and power readout is calculated as:

$$error_{PA} = PM_G - P_R$$

The error is small enough, meaning that all the calibration procedures are working correctly.

Therefore, the estimated gain of the power amplifier can be calculated as:

$$Gain_E = P_R - PM1$$

In which PM1 is the power value measured by the power meter from the first calibration step. The calculated gain from a few recent calibrations is listed in Table 3.11.

Table 3.11 the calculated gain from a few recent calibrations

No.	$VSA1_{PA}$ (dBm)	P_R (dBm)	PM_G (dBm)	$error_{PA}$ (dB)	$Gain_E$ (dB)	Date of the calibration
1	-4.99	15.45	16.51	0.06	47.13	17/06/2024
2	-4.88	15.5	16.58	0.08	47.2	21/05/2024
3	-4.69	15.61	16.72	0.11	47.4	02/05/2024
4	-4.93	15.34	16.48	0.14	47.2	17/04/2024

Based on the formula $P_R = VSA1_{PA} + c1 + K1 - L$, and the desired powers for this project are 30W (44.77dBm), 40W (46.02dBm) and 50W (46.99dBm). The power set by the signal generator was assessed for several times until the P_r equals to the corresponding power value.

3.3 Experimental data analysis

The experimental data comprised incident power, reflected power, the power dissipated in the sample, and the reflection coefficient.

The incident power can be calculated as:

$$P_{inc} = P_{VSA1} + K1 + c1$$

In which P_{VSA1} is the calculated power measured by VSA1 in dBm.

The reflected power can be calculated as:

$$P_{ref} = P_{VSA2} + K2 + c2$$

In which P_{VSA2} is the calculated power measured by VSA2 in dBm.

Both values are then converted from dBm to watts:

$$P'_{inc} = \frac{10^{\frac{P_{inc}}{10}}}{1000}$$

$$P'_{ref} = \frac{10^{\frac{P_{ref}}{10}}}{1000}$$

Therefore, the total power dissipated inside the culture medium, in watts, can be calculated as:

$$P_D = P'_{inc} - P'_{ref}$$

The magnitude of the reflection coefficient can be calculated as:

$$|S_{11}| = \sqrt{\frac{P'_{ref}}{P'_{inc}}}$$

3.4 Experimental improvement

3.4.1 Sterilization of the experimental environment

After the PEFE system was built and calibrated, it was ready to be utilized to treat cancer cells. The initial experiment used MCF-7 breast cancer cells, which were seeded into the 96-well plate and cultured for two days until they reached full confluence. The plate was then placed on a movable platform capable of adjusting the location of the probe relative to the culture well, as illustrated in Figure 3.26. The microwave was injected at 2.2GHz with a power of 40 watts for a duration of 5 minutes, a protocol established from a previous study (Zhao, 2020). However, 24 hours post-treatment, contamination of the cancer cells was observed. This contamination was likely introduced by contaminants on the probe during the treatment process.

Figure 3.26 Microwave probe handling.

To address this issue, the microwave probe and thermometer probe were thoroughly sterilized to eliminate any attached bacteria or fungi. The sterilization process involved immersing the probes in a universal tube containing 70% ethanol for 10 minutes. Ethanol is a commonly used solution to disinfect medical laboratories. At 70% concentration, ethanol is highly effective because it penetrates the cell wall more completely, coagulating all proteins, thereby killing the cell. Following the ethanol disinfection, the probes were washed with sterilized PBS buffer three times to remove any residual ethanol that could potentially affect the cancer cells.

To ensure the effectiveness of the sterilization, the probes were evaluated by inserting them into the culture wells without generating any signals for 5 minutes, then the death rate of cells was detected at 0 hours, 24 hours, and 48 hours after the insertion. After 48 hours, no contamination was found inside the culture well, and the cells appeared to be normal. Additionally, there were no significant differences in the MCF-7 death rate between the control group (without probes insertion) and the group where the probes were inserted inside the well (Figure 3.27), indicating that the probe sterilization and the experimental environment is acceptable for the PEFE experiment.

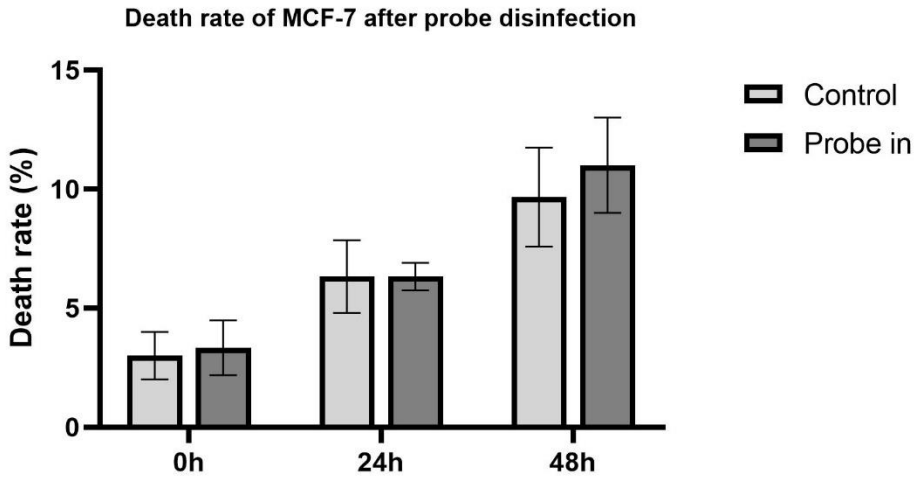

Figure 3.27 Death rate of MCF-7 breast cancer cells after probe disinfection. Data shown as mean ± SD, n=3. No statistical was found.

3.4.2 Temperature profile in response to the location between microwave probe and thermometer location

As mentioned before, the temperature during the PEFE treatment is maintained between 37-42℃ by the automatic switching of the signal generator. The temperature control is achieved through the utilisation of an RF pulse signal, as shown in Figure 3.4. However, the utilized RF pulsing (50μs on followed by 950μs off period) just reduced the rate of temperature increase during the experiment. The second taken measure was to switch on or off the RF pulse signal in response to the temperature detected by the thermometer. Once the temperature approached the maximum value of 42℃ the pulsed RF signal was switched off until the value dropped toward the lower range of about 37℃.

In the initial experiment, the tip of the microwave probe was aligned with the thermometer probe, positioned 1mm from the bottom of the well (cell monolayer) (Figure 3.28A). The temperature was monitored during the treatment, with the temperature profile demonstrated in Figure 3.28B, where the rising temperatures represent the time range when the pulsed RF signal was on, and the decreasing temperatures represent the time range when the pulsed RF signal was off. The microwave was applied to MCF-7 breast cancer cells, and the death rate was detected 15 minutes, 24 hours, and 48 hours after the experiment. Despite applying the microwave at 2.2 GHz, 40 watts for 5 minutes to MCF-7 breast cancer cells, cell

death rates measured at 15 minutes, 24 hours, and 48 hours post-treatment showed minimal increase compared to the control group (Figure 3.28C).

A

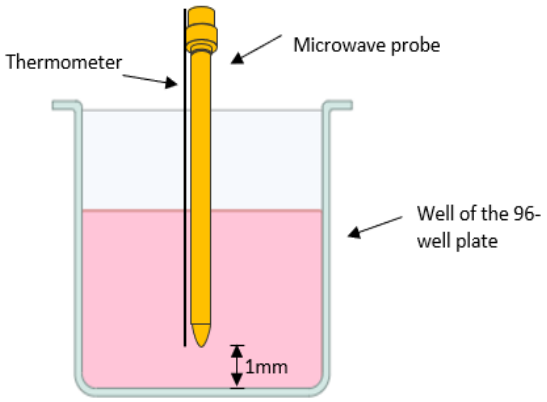

B

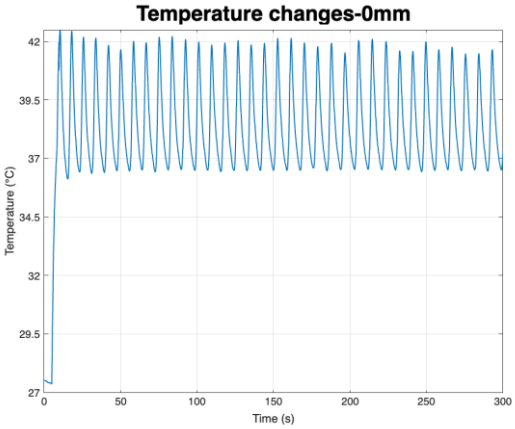

C

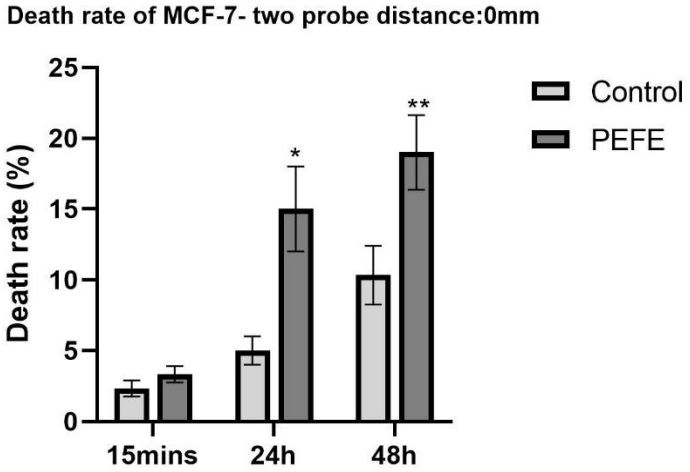

Figure 3.28 Experimental setup with the microwave probe tip aligned with the thermometer probe tip. (A) schematic diagram of the location of the probes. (B) Temperature profile during the treatment. (C) Death rate of MCF-7 cells after PEFE treatment. Data presented as mean ± SD (n=3), * represents $p<0.05$, ** represent $p<0.01$.

Since the temperature was controlled by the signal generator, in which temperature increase/decrease represents the signal generator on/off. The rapid fluctuations of the temperature indicated that the signal generator switched on and off frequently, with only around 2 seconds of power on for each period. Therefore, we hypothesized that the fast cycling likely led to a more unstable and non-sustained exposure to the cancer cells. The cells had less time to experience the effects of the continuous signal exposure, resulting in the non-effective killing effect.

Electric and magnetic fields would be generated when the pulsed signal was applied and delivered to the culture medium containing cancer cells. Both components can penetrate and exert influence when such a field interacts with a medium. It has been reported that the electric field tends to dominate at such a high frequency. To further understand the interaction between electromagnetic fields and biological samples, the COMSOL Multiphysics simulation was conducted to map the electric field distribution during the PEFE treatment.

The simulation, assuming axisymmetric conditions, used a 2D model based on the dimensions of a 96-well plate and an RG405 coaxial cable found in the manuals. Since the majority component of the cell culture medium is water, the medium's material was modelled as water with a relative permittivity (ε_r) of 78.54 and conductivity (σ) of $5.5\times10^{-6}\ \mathrm{S/m}$ (Ehtaiba, 2017). After the configuration of the materials, the 'Electromagnetic Waves, Frequency domain' was studied to simulate the experiment setup at 2.2GHz, 40 watts. Based on the simulation, it is clearly shown that the most intensive electric field is distributed around the tip of the microwave probe, decreasing with distance, as demonstrated in Figure 3.29. This suggests that the highest dielectric temperature increase occurs near the probe tip, while the temperature drops in areas farther away due to reduced electric field intensity and heat dispersion, by the power dissipated per unit volume (P) in the medium due to dielectric heating given as:

$$P = \frac{1}{2}\sigma|E|^2$$

where E is the electric field strength (V/m), σ is the electrical conductivity of the material (S/m).

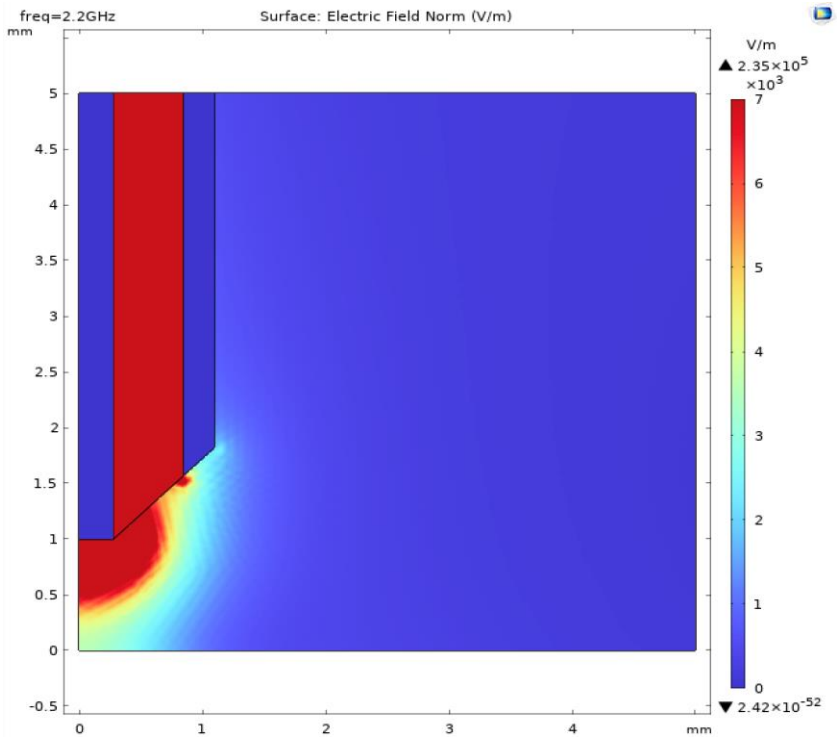

Figure 3.29 COMSOL simulation of electric field distribution during the PEFE treatment.

The initial probes' location measured the temperature around the tip of the microwave probes rather than the temperature of the cancer cells, which is the one we are concerned about. Then, we improved the experiment by repositioning the thermometer probe closer to the cell monolayer without touching it, keeping the microwave probe tip distance at 1mm from the well bottom. This adjustment aimed to measure temperatures more representative of the cells.

After the initial experiment, the obtained temperature profile provided information to determine the precise on-off cycling of the signal generator, including the duration of each on and off period. To investigate and accurately control the temperature experienced by the cell monolayer, a follow-up experiment was designed. In this experiment, we manually switched the signal generator on and off based on this temperature profile and measured the temperature at the cell monolayer. By combining the initial temperature readout, we compared the results and found that, when applying the same signal as in the initial experiment, the temperature recorded at the cell monolayer was significantly lower, with the maximum temperature recorded throughout the experiment being 36.32°C, as shown in Figure 3.30.

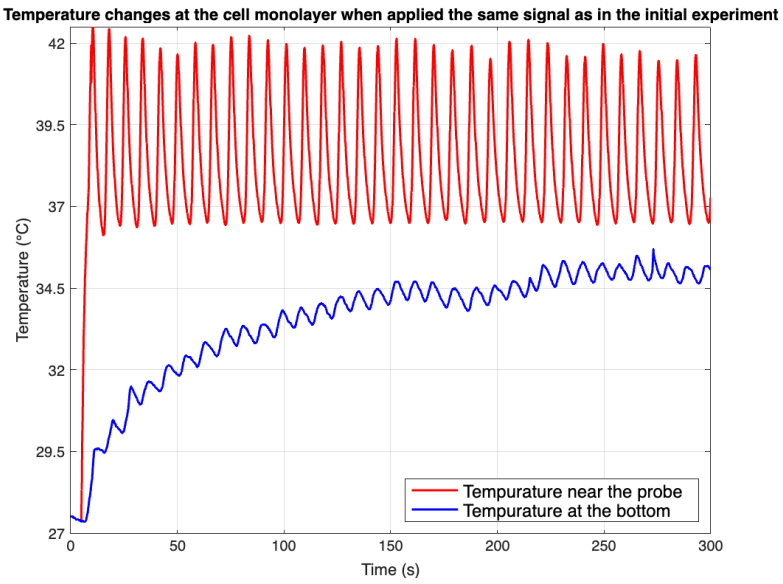

Figure 3.30 Temperature profile of when applied the same signal as in the initial experiment by manually controlling the signal generator.

Following the insights gained from the previous experiments, we used the repositioned probe location to treat the cells again (Figure 3.31A). This time, the temperature at the cell monolayer was maintained between 37 to 42℃ by automatically switching on/off the signal generator. The new setup showed a slower temperature increase, indicating longer continuous microwave exposure (Figure 3.31B). When looking at the death rate 15 minutes, 24 hours, and 48 hours after the treatment, it can be found that the death rate of MCF-7 breast cancer cells was significantly higher in the treated group than in the control group among all the tested time points, as illustrated in Figure3.31C.

Subsequently, the temperature around the probe was also measured by manually generating the signal based on the temperature profile obtained from the second experiment, employing longer on-off cycles. It can be found that the temperature around the probe was significantly higher than that near the bottom (Figure 3.32). However, it should be stressed that these high temperatures were not affecting the cell monolayer that was located 1mm further below.

A

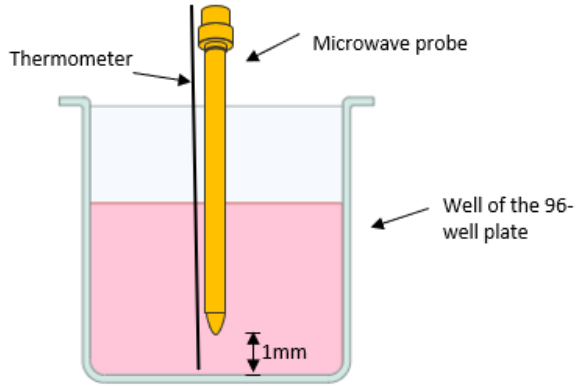

B

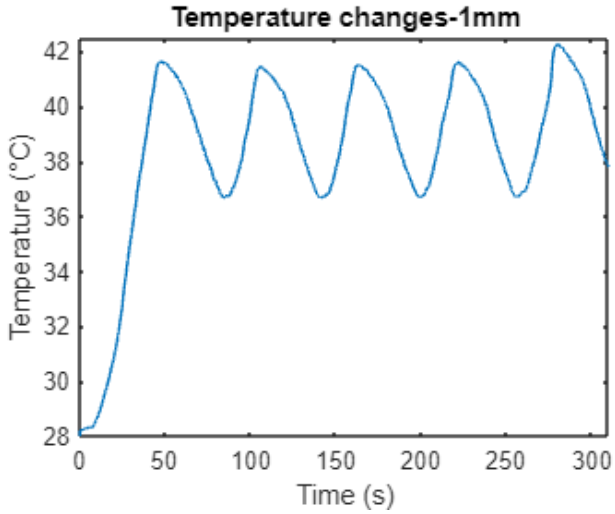

C

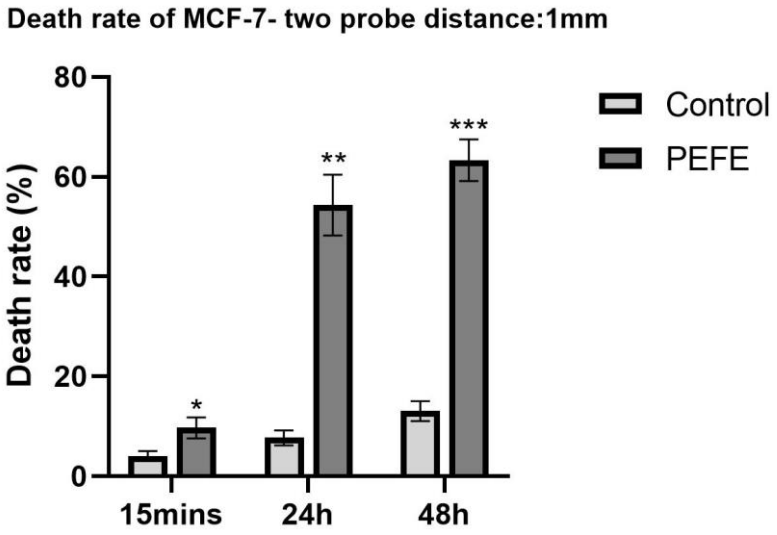

Figure 3.31 Experimental setup with the thermometer probe positioned close to the cell monolayer. (A) schematic diagram of the location of the probes. (B) Temperature profile during the treatment. (C) Death rate of MCF-7 cells after PEFE treatment. Data presented mean $\pm$ SD (n=3), * represents $p<0.05$, ** represents $p<0.01$, *** represents $p<0.001$.

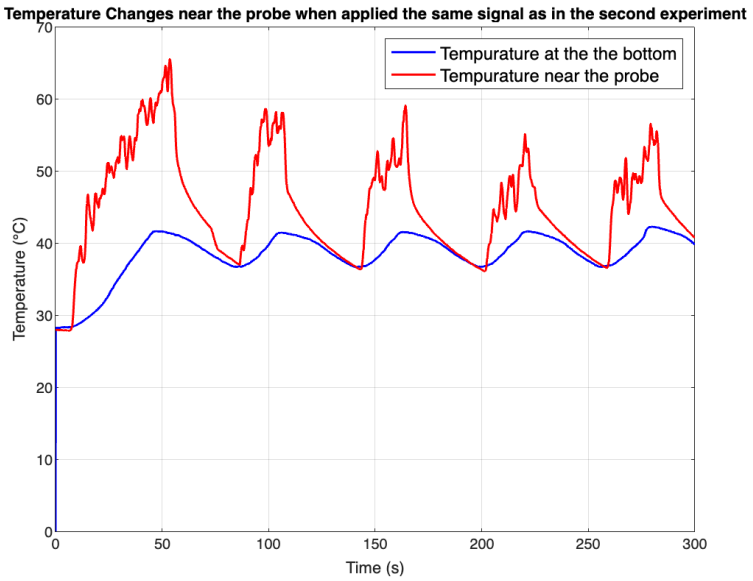

Figure 3.32 Temperature profile of when applied the same signal as in the second experiment by manually controlling the signal generator.

3.5 Discussion

The previous PEFE system consisted of several individual microwave instruments, complicating the overall setup. Additionally, once the microwave is injected into the medium, heat will be generated, causing an increase in temperature. We aimed to apply microwave signals into the culture medium under normothermic conditions. Therefore, the temperature sensor was combined into the system to monitor and maintain the temperature between 37-42℃ during the experiment. In the previous PEFE system, temperature control was achieved manually by switching the signal generator on and off, a process that was both time-consuming and inconsistent. To address these issues, we developed a PXI-based system with desired frequency and power levels, operated by LabVIEW. This system combines essential components, such as the signal generator and vector signal analyzers (VSAs), into a single unit, effectively saving space and improving portability. Moreover, with LabVIEW controlling the system, the temperature can be maintained within the normothermic range by automatically switching the signal generator on and off, enhancing efficiency, accuracy, and repeatability.

A thorough calibration was conducted to ensure all components function accurately and to understand and calculate the inherent characteristics of the microwave components. After

the calibration, the first experiment was conducted using MCF-7 breast cancer cells. However, contamination was visualized inside the medium, significantly affecting the experimental results. Consequently, the sterilization of the microwave probe and thermometer probe was applied to disinfect all the bacteria and fungi adhered to the probes. In a subsequent experiment, no contamination was detected 48 hours post-treatment. Furthermore, the death rate of the cells was detected using the Trypan blue staining, which is effective for cell viability assay. The principle behind Trypan blue staining is based on the integrity of the cell membrane. Specifically, live cells have intact cell membranes that exclude the dye, while dead cells have compromised membranes that allow the dye to penetrate. This results in the dead cells taking up the dye and appearing dark blue under a microscope, whereas live cells remain unstained. The Countess machine was used to identify and count the live and dead cells by inspecting their brightness automatically. The death rate between the control group (without probes injected) and the treatment group (with probes injected) was similar and kept low. This indicates that the improved experimental environment is safe for further PEFE treatment.

Afterwards, PEFE treatment was conducted again with the serialized probes. This time, microwave signals were generated at 2.2GHz and 40 watts for 5 minutes, in which the distance between the tip of the probes and the bottom of the 96-well plate was fixed at 1mm, based on settings from previous studies that showed optimal killing effects. The death rate of cancer cells was assessed at 15 minutes, 24 hours, and 48 hours post-treatment. Although some cells were killed in the treated group compared with the control counterpart, the results were not as effective as those in previous studies. To understand this discrepancy, the temperature profile was examined and revealed rapid fluctuations due to the frequent, short period switching of the signal generator. This indicated that the cells were not receiving continuous microwave exposure, weakening the PEFE's efficacy.

To further investigate the interaction between the microwave and the cells, a COMSOL simulation was performed to visualize the electric field distribution within the culture medium at the specified frequency and power level. The simulated result demonstrated that the most intensive electric field was concentrated around the tip of the probe, and the microwave was able to penetrate toward the cancer cells, though with a weaker distribution further away. This explained the rapid temperature changes observed during treatment, as the temperature

was measured near the probe's tip. To address this, we adjusted the positioning of the microwave and thermometer probes to better measure the temperature of the cancer cells rather than the medium around the probe tip. The thermometer probe was repositioned close to the cell monolayer without touching it, while the microwave probe remained 1mm above the bottom of the culture well. Subsequent PEFE treatments with this new positioning showed a slower temperature rise, indicating that the cells experienced longer continuous microwave exposure. Also, the death rate after the PEFE treatment showed a prominent killing effect. These results highlight that besides the intensity of the E-field, other factors such as continuity of the E-field exposure play a role in the cell death mechanism.

In this chapter, we tackled the complexities and inefficiencies of the previous PEFE system by developing a PXI-based system operated by LabVIEW. This new system streamlines the setup and automates temperature control, enhancing efficiency, accuracy, and repeatability. We conducted a thorough calibration to ensure all components functioned accurately. The experimental setup was improved to achieve better cancer cell-killing efficacy, addressing initial issues such as probe contamination and inconsistent temperature maintenance. Subsequent experiments demonstrated that our modifications led to significantly improved results. The next chapter will explore the impact of PEFE on various breast and colorectal cancer cells and investigate deeper into the underlying mechanisms of its effects.

Chapter-4 PEFE and its impact on cancer treatment

4.1 Introduction

Over the past few decades, microwave-based techniques have become extensively used in the medical field for the diagnosis and treatment of various human diseases, particularly cancer. One prominent application is MWA, which serves as an adjunctive treatment for patients unsuitable for traditional cancer therapies. Despite its effectiveness, MWA has faced numerous patient complaints, such as inflammation, swelling, and bleeding, primarily due to the high temperatures generated during the procedure. Considering these issues, we have identified that pulsed electromagnetic field exposure (PEFE), operating at high power levels ranging from 30 to 50 watts, presents a promising alternative. This technique has the potential to effectively kill cancer cells while maintaining temperatures below 42°C, thereby minimizing thermal damage to surrounding healthy tissues and improving patient comfort and safety.

Previous studies have primarily focused on breast cancer because breast cancer is quite an easy target. These studies demonstrated that PEFE can kill breast cancer cells both *in vitro* and *in vivo* effectively, with significant changes observed in the metabolic functions of the treated cells (Zhao 2020).

As discussed in Chapter 3, we have enhanced the PEFE system to be more portable, automated, and data organized. Also, we realized that there is no reason why this technique cannot be used for other cancer types. Given this, we propose targeting colorectal cancer, which is also relatively accessible and can benefit from existing imaging techniques. Patients undergoing colorectal cancer screening often have endoscopies. Integrating the PEFE probe with the endoscopic procedure would allow for the secure and precise treatment of tumours.

Moreover, we aimed to investigate further how the cancer cells were killed. According to morphological characteristics and the signal cascades activated, cell death is broadly divided into two categories: necrosis and apoptosis. Necrosis occurs due to some form of extreme stress, such as chemical and physical insults. As non-programmed cell death, necrosis involves changes in cell morphology, such as cell swelling and plasma membrane rupture. Apoptosis, also named as programmed cell death, is triggered by mitochondrial dysfunction or

stimulation of death receptors. Apoptosis occurs because of characteristic cellular changes, including cell shrinkage, nuclear fragmentation, chromatin condensation, and chromosomal DNA fragmentation. Due to its programmed process, apoptosis requires a longer time to complete (Fink and Cookson 2005).

Microwave irradiation can induce cell necrosis, contributing to its thermal effects. Besides, several studies have reported that microwave irradiation can induce cell death via apoptosis. In neuronal cells, it has been reported that the exposure of 900MHz with SAR 2W/kg MW-EMF for 24h might induce neuronal apoptosis via the caspase-independent pathway (Joubert et al. 2008). In cancer, Caraglia et al., found that MW-EMF exposure at 1.95GHz with a SAR of 3.6 ± 0.2 W/kg can induce time-dependent apoptosis in the human oropharyngeal epidermoid carcinoma KB cancer cell line (20% apoptotic cells after 1h exposure, 45% after 3h exposure) (Caraglia et al. 2005). Moreover, in pancreatic cancer, exposure to microwaves can cause cell apoptosis in JF305 cells, with the increased activity of caspase-9 and caspase-3 (Zhu et al. 2014). In breast cancer, microwave exposure at 2.2GHz, 2 watts for 7 hours could induce cell apoptosis for MCF-7, confirmed by DAPI staining with the changes in nuclear morphology being witnessed. Also, further confirmation of cell apoptosis by examining key proteins in apoptosis signalling pathways indicates that the expression of caspase-3 and -9 was increased at the protein level after exposure (Zhao 2020).

The current chapter aims to explore the effects of PEFE on cell death in breast cancer and colorectal cancer. Specifically, we aimed to determine whether the cancer cells undergo necrosis or apoptosis following PEFE treatment. Furthermore, the breast and gastrointestinal tract (including the colon) possess some of the body's most intact tight juntion structures in the body. However, when these junctions fail to function properly, various pathological conditions can arise, including cancer. Therefore, this study also aimed to explore the role of TJs in the PEFE treatment. Moreover, the changes in cellular components, including cell membrane, nucleus, and cytoskeleton, were assessed to understand further how cancer cells respond to PEFE treatment.

4.2 Methods

4.2.1 Cell lines used for PEFE treatment

The breast cancer cell lines MDA-MB-231, MC-7, BT549, ZR751, and SKBR3, colorectal cancer cell lines RKO, HRT18, HT115, and Caco-2 were used for PEFE treatment, to explore whether PEFE affects specific cell lines. All cells were cultured in T25 flask. Once enough confluence was reached, $7.5x10^4$ cells (in 200µl medium) per well were seeded in the 96-well plate. The cells were incubated at 37℃, 5% CO_2 and were allowed sufficient time to adhere to the culture well. The cells were then cultured until the monolayer was formed. Before the PEFE experiment, the growth medium was replaced with 200µl fresh cell culture medium. In these experiments, triplicate setups were conducted to ensure consistency.

4.2.2 PEFE treatment instrumentation

In this study, the frequency of the PEFE system was 2.2GHz. the input power level was set to 40 watts, which was the best condition obtained from the previous study (Zhao 2020). Before the PEFE treatment, the PXI system needed to be calibrated to make sure each component worked accurately, as demonstrated in Chapter 3. The microwave probe and thermometer probes were immersed in 70% ethanol for 5 minutes to be disinfected, then washed with autoclaved PBS buffer to remove the attached ethanol. Once the disinfection was complete, both probes were inserted into the treated well, with the tip of the thermometer probe close to the cell monolayer, while the distance between the microwave probe tip and the bottom of the well was fixed at 1mm. The PEFE experiment lasted for 5 minutes with three repeats for each group. The temperature was monitored throughout the entire PEFE experiment and strictly controlled between 37 to 42℃.

4.2.3 Cell viability assessment

Cell viability was inspected before PEFE treatments and after treatment with different time courses, using Countess machine with trypan blue staining. When the PEFE treatment was completed, the medium in the well was completely transferred to a fresh 1.5ml Eppendorf

tube. Then, the cells were washed with 30µl PBS, followed by adding 30µl EDTA-trypsin buffer to the well; then the well was placed inside the incubator at 37℃, 5% CO_2, for a few minutes. Once all cells were detached, 50µl cell culture medium was added into the wells to neutralize the trypsin by mixing gently. The cell suspension was then transferred to the Eppendorf tube containing the old medium and PBS. This can ensure all the cells, including the dead cells, which might float in the medium, and the cells attached to the well are collected and the tube was centrifuged at 1600 rpm for 5 minutes, and the cell pellet could then be formed. After that, the supernatant was carefully aspirated, and the cell pellet was re-suspended with 12µl normal cell culture medium. Subsequently, 10µl cell suspension was transferred to a 0.5ml tube containing 10µl trypan blue (Thermo Fisher Scientific, Waltham, MA, USA), followed by gentle mixing. 10µl of the mixture was then transferred to cell counting chamber slides (Thermo Fisher Scientific, Waltham, MA, USA), and the death rate of the treated cells was calculated automatically using a Countess™ II Automated Cell Counter (Thermo Fisher Scientific, Waltham, MA, USA).

4.2.4 Cell apoptosis assessment using Countess machine

A cell apoptosis assay was conducted before PEFE treatments and after treatment in different time courses. Cell detachment and centrifugation were described in Chapter 4.2.3 Stock CellEvent™ Caspase-3/7 Detection Reagent (green) (Thermo Fisher Scientific, Waltham, MA, USA) was 1:10 diluted with the normal cell culture medium before transferring 15µl to re-suspend the cell pellet. Then, the cell suspension was incubated at 37℃, 5% CO_2, for 1 hour to ensure the complete detection. 10µl of cell suspension was added to the Countess™ cell counting chamber slides (Thermo Fisher Scientific, Waltham, MA, USA). The slide was then inserted into the Countess™ II Automated Cell Counter machine (Thermo Fisher Scientific, Waltham, MA, USA), and the apoptotic cells were detected automatically using the filter set FITC/GFP.

4.2.5 The interaction between TJs and PEFE using cell scratching assay

$2x10^5$ MCF-7 breast cancer cells (in 500µl cell suspension) were seeded into the 48-well plate and incubated at 37℃, 5% CO_2, until the cells reached full confluence. At this point, a 10µl

pipette tip was used to scrape the cell monolayer, creating two vertical wounds, as depicted in Figure 4.1. This procedure divided the monolayer into three distinct sections. The cells were washed with PBS twice, and 500µl fresh medium was refilled. The PEFE treatment was then applied at 2.2GHz, 40 watts, for 10 minutes, with the microwave probe positioned in the middle of the well. After 24 hours of incubation, the cells were then visualized and imaged using an EVOS® FL2 Auto Imaging System (Thermo Fisher Scientific, Waltham, MA, USA) with 4X magnification.

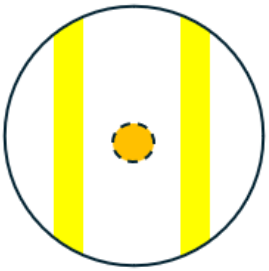

Figure 4.1 The schematic diagram of the cell scratching assay. Yellow areas represent the scratched wounds, one on each side. The orange area represents the position of the microwave probe which is at the centre of the well.

4.2.6 Protein extraction, SDS-PAGE, and Western blot analysis

The protein was extracted from the cells treated with PEFE during a time course: 15 minutes, 1 hour, and 4 hours post-treatment. Proteins were quantified using BioRadDC Protein Assay (BioRad Laboratories, Hertfordshire, UK). After SDS-PAGE separation, the protein was transferred onto PVDF membranes and probed with various primary antibodies and a corresponding peroxidized-conjugated secondary antibody. The information and concentration of the antibody used in this research were listed in chapter 2.1.6, and the full description of Western blotting please refers to chapter 2.5. Protein bands were processed and quantified using ImageJ, data were analyzed using Excel, and figures were generated using GraphPad.

4.2.7 DAPI staining

The cancer cells that underwent PEFE treatment were incubated at 37℃, 5% CO_2 for 8 hours,

and then the DAPI staining was conducted. The culture medium in the well was changed with 200µl DAPI (Thermo Fisher Scientific, Waltham, MA, USA) 1:1000 diluted with PBS buffer. This is followed by 1 hour incubation at 37℃. The stained cells were then visualized using an EVOS® FL2 Auto Imaging System (Thermo Fisher Scientific, Waltham, MA, USA) with 40X magnification.

4.2.8 Immunofluorescence (IFC) staining for ZO-1 and cytoskeleton

Colorectal cancer cells from the Caco2 cell line were seeded into Millicell® EZ slide (Merck KGaA, Darmstadt, Germany) and cultured until full confluence was reached. Then, cells were treated with PEFE for 10 minutes and incubated at 37℃, 5% CO_2 during a time course, including 15 minutes, 1 hour, and 4 hours. Post-treatment, the cells were fixed with 4% formalin and stained with ZO-1, cytoskeleton, and nucleus using IFC; please refer to Chapter 2.7.

4.3 Results

4.3.1 The impact of PEFE on breast and colorectal cancer cell death

To investigate whether PEFE can kill breast cancer and colorectal cancer cells selectively or not, a range of BRCA cells, including MDA-MB-231, MCF-7, BT549, ZR751, and SKBR3, CRC cells RKO, HRT18, HT115, and Caco2, were treated with PEFE. These cells are commonly used in biological and medical research. The death rate was inspected before the experiment, 15 minutes, 24 hours, and 48 hours after PEFE treatment. The results are shown in Figure 4.2 for breast cancer cell lines and Figure 4.3 for colorectal cancer cell lines, with the fold change between control and PEFE groups at different time points in these two cancer types illustrated in Figure 4.4 and Figure 4.5, respectively. Table 4.1 and Table 4.2 compare the fold change result with t-tests.

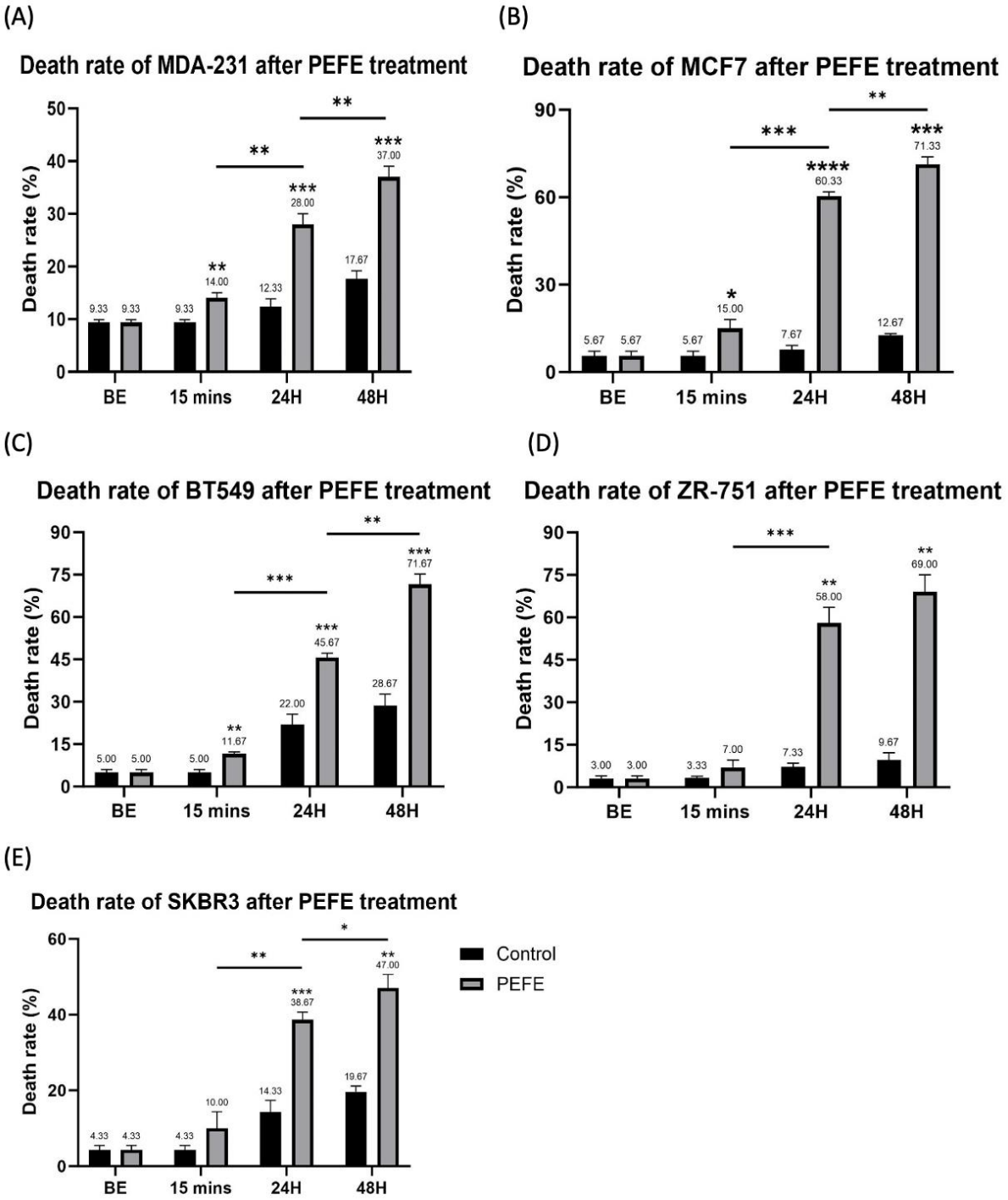

Figure 4.2 The death rate of different breast cancer cell lines that underwent PEFE treatment and their control groups at 2.2GHz and 40 watts for 5 minutes, including (A) MDA-MB-231, (B) MCF-7, (C)BT549, (D)ZR751, and (E) SKBR3. Cell viability was assessed before treatment (BE), immediately after treatments (15 mins), and 24 and 48 hours after treatments. Black bars represent the control group, and the grey bars represent the PEFE group. Data shows mean $\pm$ SD, n=3. T tests were carried out to show the significance between groups. * represents $p < 0.05$, ** represents $p<0.01$, *** represents $p < 0.001$, **** represents $p<0.0001$.

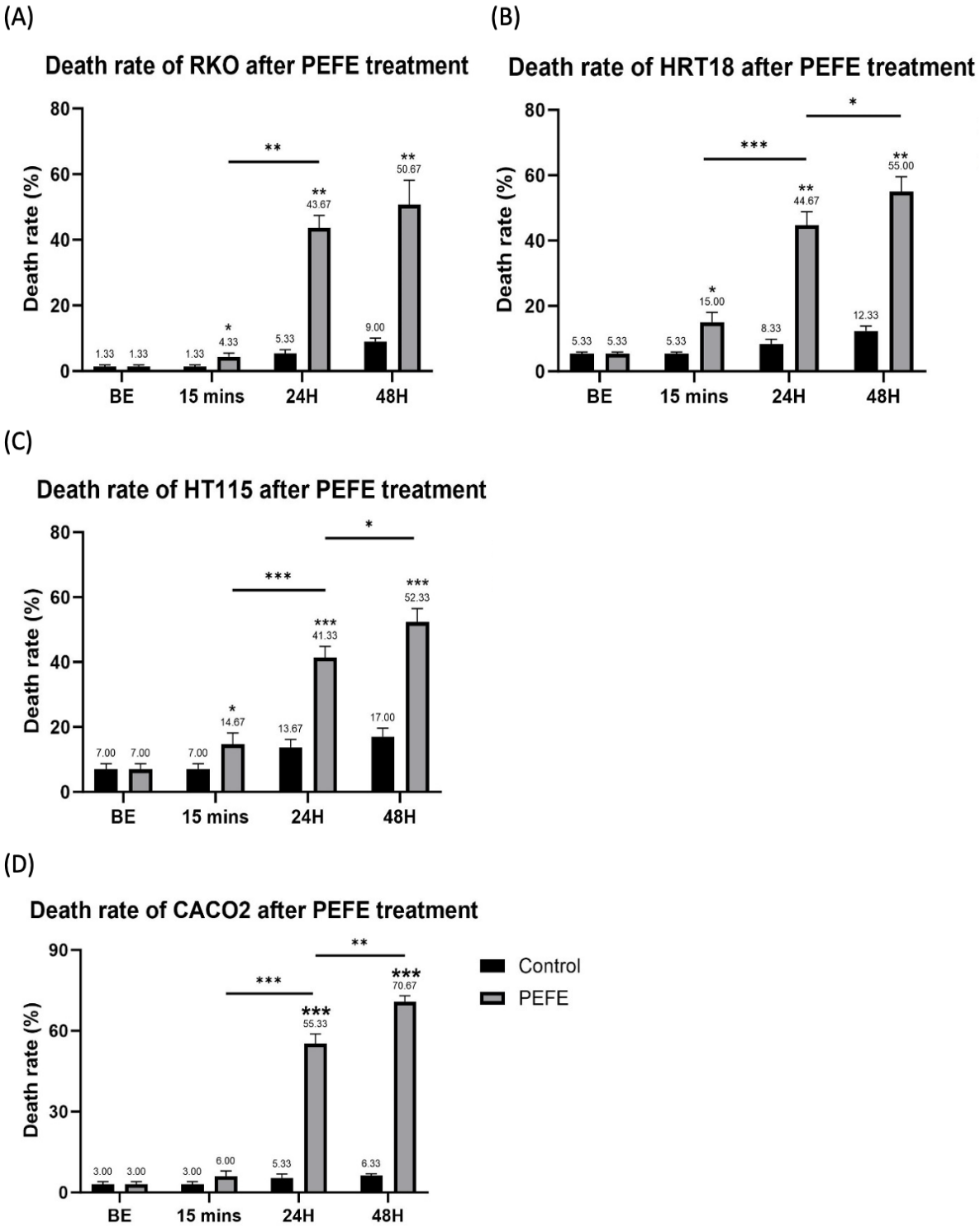

Figure 4.3 The death rate of different colorectal cancer cell lines that underwent PEFE treatment and their control groups at 2.2GHz and 40 watts for 5 minutes, including (A) RKO, (B) HRT18, (C)HT115, and (D) Caco2. Cell viability was assessed before treatment (BE), immediately after treatments (15 mins), and 24 and 48 hours after treatments. Black bars represent the control group, and the grey bars represent the PEFE group. Data shows mean $\pm$ SD, n=3. T-tests were carried out to show the significance between groups. * represents $p < 0.05$, ** represents $p<0.01$, *** represents $p < 0.001$.

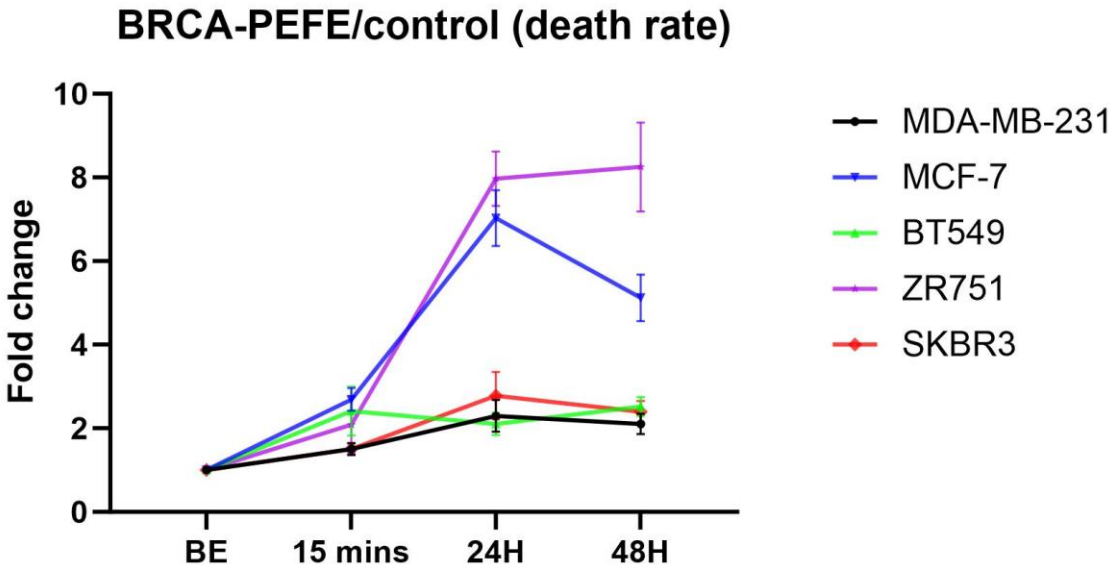

Figure 4.4 Fold change in death rate results at different time points among five breast cancer cell lines for PEFE treatment. Data shows mean +/- SD, n=3.

Table 4.1 Statistical significance of the t-test when comparing breast cancer cell lines results between different time points (*p<0.05, **p <0.01, ***p<0.001, NS-no significance).

	MDA-MB-231	MCF-7	BT549	ZR751	SKBR3
BE vs 15mins	**	***	*	*	NS
BE vs 24H	**	**	**	***	**
BE vs 48H	**	***	***	***	***
15mins vs 24H	*	**	NS	***	NS
15mins vs 48H	*	***	NS	**	NS
24H vs 48H	NS	**	NS	NS	NS

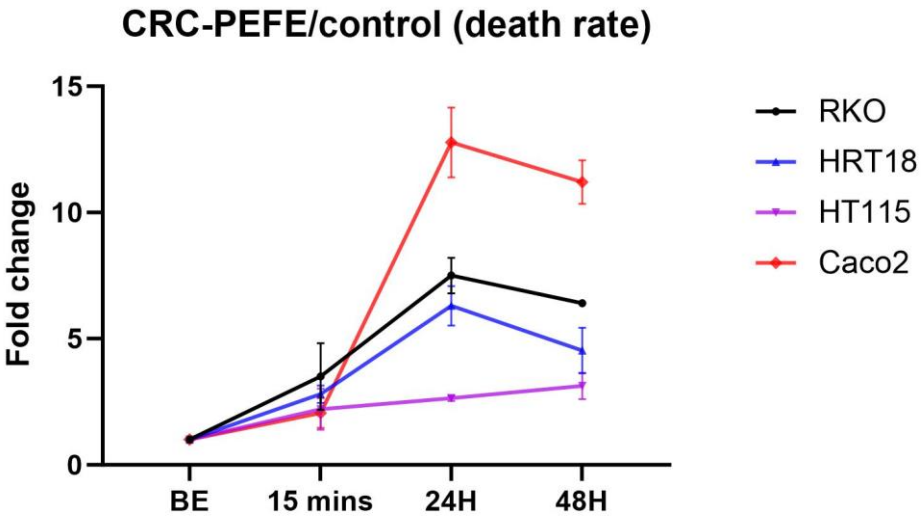

Figure 4.5 Fold change in death rate results at different time points among four colorectal cancer cell lines for PEFE treatment. Data shows mean +/- SD, n=3.

Table 4.2 Statistical significance of the t-test when comparing colorectal cancer cell lines results between different time points (*p<0.05, **p <0.01, ***p<0.001, NS-no significance).

	RKO	HRT18	HT115	Caco2
BE vs 15mins	*	***	NS	*
BE vs 24H	**	**	*	**
BE vs 48H	**	**	**	***
15mins vs 24H	*	*	NS	**
15mins vs 48H	NS	*	NS	***
24H vs 48H	NS	NS	NS	NS

The experimental results demonstrated that PEFE effectively induces significant cell death among all tested breast and colorectal cancer cell lines, regardless of their different morphology and molecular subtypes. This suggests that PEFE exhibits a non-specific and anti-cancer activity, highlighting its potential as a promising candidate for clinical treatment in both breast cancer and colorectal cancer.

Regarding the results immediately after PEFE treatment (15 minutes), not too much dead cells were found in the PEFE group compared with their control counterparts, the death rate was roughly doubled. This immediate response might be due to the cells being subjected to such high-power microwave, inducing cellular stress response, potentially resulting in some level of cell necrosis. However, after 24hours, the death rate increased dramatically. This delayed cell death suggested that cells that underwent PEFE treatment might be killed via apoptosis. Further experiments should be conducted to confirm the mode of cell death.

Additionally, it is interesting to note that among these different cell lines, breast cancer cell lines MCF-7 and ZR751, as well as colorectal cancer cell lines Caco2, exhibit relatively better killing effects in response to PEFE than the other cell lines. Despite these three cell lines showing different tissue origins or hormone receptors, they share the same characteristics: these cell lines exhibit growth patterns by forming clusters and maintaining TJs. Therefore, the role of TJs in response to PEFE treatment should be further investigated to understand their potential impact on PEFE treatment efficacy.

4.3.2 Cell death after PEFE treatment

4.3.2.1 Confirmation of cell death with more time intervals

The initial experiment only evaluated cell death at three specific time points-15 minutes, 24 hours, and 48 hours, following PEFE treatment. To better understand cell death dynamics induced by PEFE, CRC cell line Caco2 was subjected to PEFE, and multiple intervals were introduced to monitor cell viability. The results of cell death at these different time points are shown in Figure 4.6, and the statistical analysis using t-test results is summarized in Table 4.3. It was found that there was no significant increase in cell death until 4 hours post-treatment. At this point, a marked rise in cell death was detected, and this upward trend continued until 48 hours post-treatment, suggesting that PEFE induces cell death in a programmed manner.

Moreover, the cell morphology was visually examined under a microscope 24 hours after PEFE treatment, as depicted in Figure 4.7. In the untreated control group, the cells displayed normal morphology and good cell monolayer. In contrast, the cells in the treated group exhibited significant morphological changes 24 hours post-treatment, in which cells became rounded, and the cell monolayer was disrupted. The shrinkage of the cells is a sign of cell apoptosis.

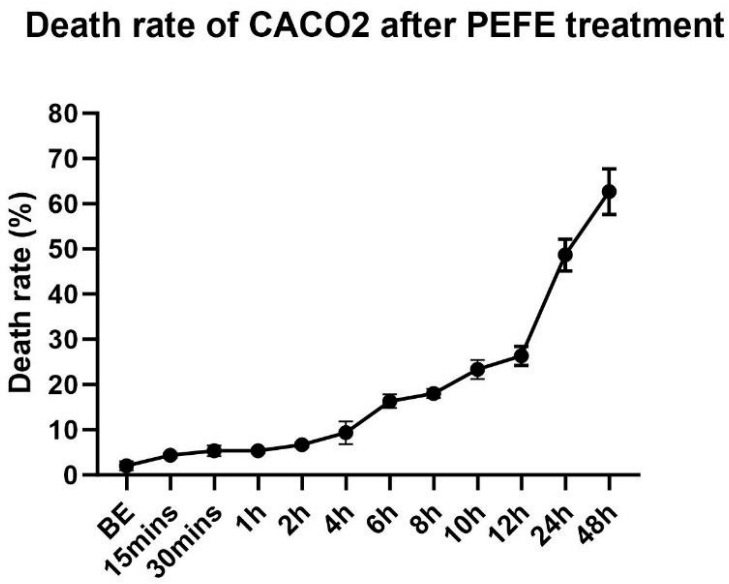

Figure 4.6 The death rate of CRC cell line Caco2 after PEFE treatment at 2.2GHz and 40 watts for 5 minutes. Data shows mean ± SD, n=3.

Table 4.3 Statistical significance of the t-test when comparing death rate results between different time points (*p<0.05, **p <0.01, ***p<0.001, ****p<0.0001 NS-no significance).

	BE	15mins	30mins	1h	2h	4h	6h	8h	10h	12h	24h	48h
BE	NS	NS	NS	NS	NS	*	***	***	***	***	***	***
15mins		NS	NS	NS	NS	NS	**	***	**	**	**	**
30mins			NS	NS	NS	NS	***	***	***	***	***	**
1h				NS	NS	NS	**	***	**	**	**	**
2h					NS	NS	***	****	***	****	****	****
4h						NS	*	**	**	***	****	****
6h							NS	NS	**	**	***	***
8h								NS	*	**	***	***
10h									NS	NS	***	***
12h										NS	***	***
24h											NS	*
48h												NS

(A)

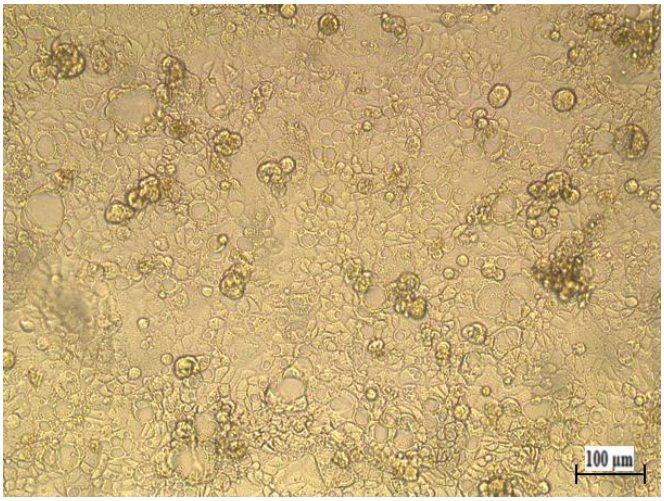

(B)

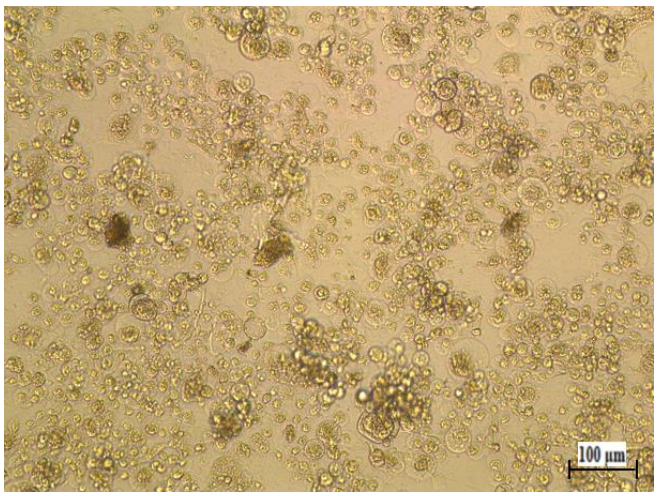

Figure 4.7 Inspection of cell morphology 24 hours post-treatment in CRC cell line Caco2. (A) control untreated cells exhibit healthy morphology and good monolayer. (B) treated cells exhibit altered morphology. Scale bar: 100µm. Magnification: 10x.

4.3.2.2 The detection of apoptotic cells

The Caspase-3/7 Detection Reagent, which detects and stains the apoptotic cells with green fluorescence, was used to confirm the manner of cell death further. In this experiment, BRCA cell line MCF-7 and CRC cell line Caco2 were used and subjected to PEFE, and the staining was conducted before the experiment, immediately after the experiment (15 minutes), 24 hours, and 48 hours after treatment. At the same time, the total dead cells were also detected and combined into the result to compare any differences between apoptotic and total death rates. The results are presented in Figure 4.8 and Figure 4.9.

The data clearly show that the apoptotic rate is relatively low but closely mirrors the death rate at these different time points in both MCF-7 and Caco2 cell lines. This strongly suggests that primary mode of cell death induced by PEFE treatment in cancer cells is apoptosis.

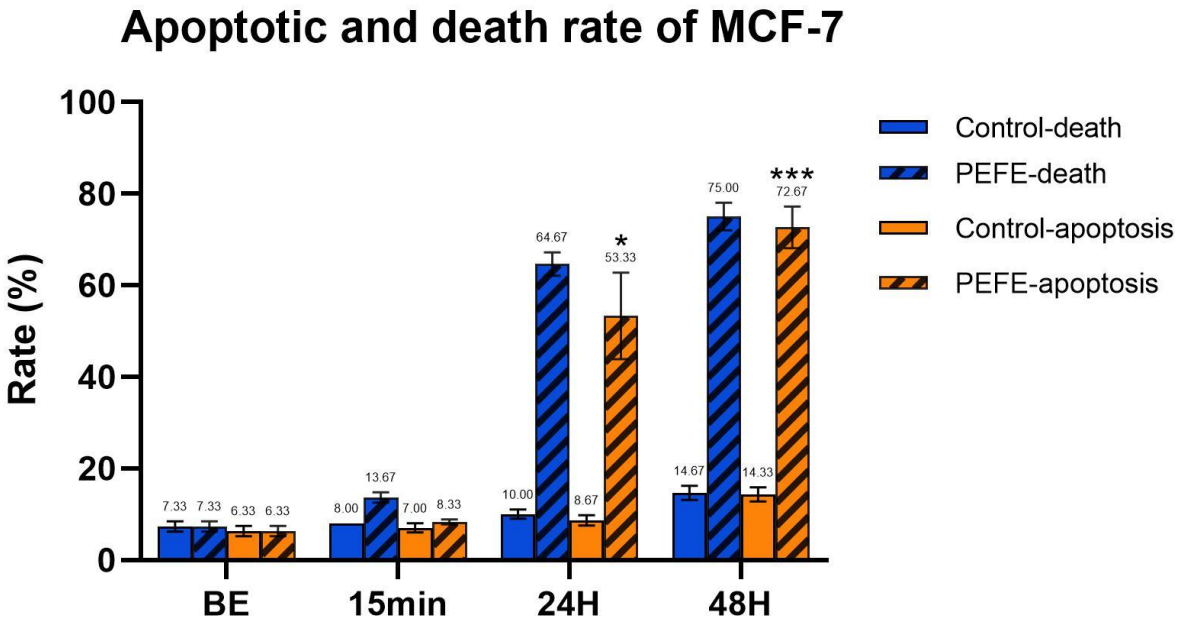

Figure 4.8 The detection of MCF-7 cell apoptosis and death rate following PEFE treatment at 2.2GHz and 40 watts for 5 minutes. The apoptotic rate, while slightly lower, is close to the total death rate, indicating that apoptosis is the predominant mechanism of cell death in response to PEFE treatment. Data shows mean ± SD, n=3. T-tests were carried out to show the significance in apoptosis rate at different time points. * represents $p < 0.05$, *** represents $p < 0.001$.

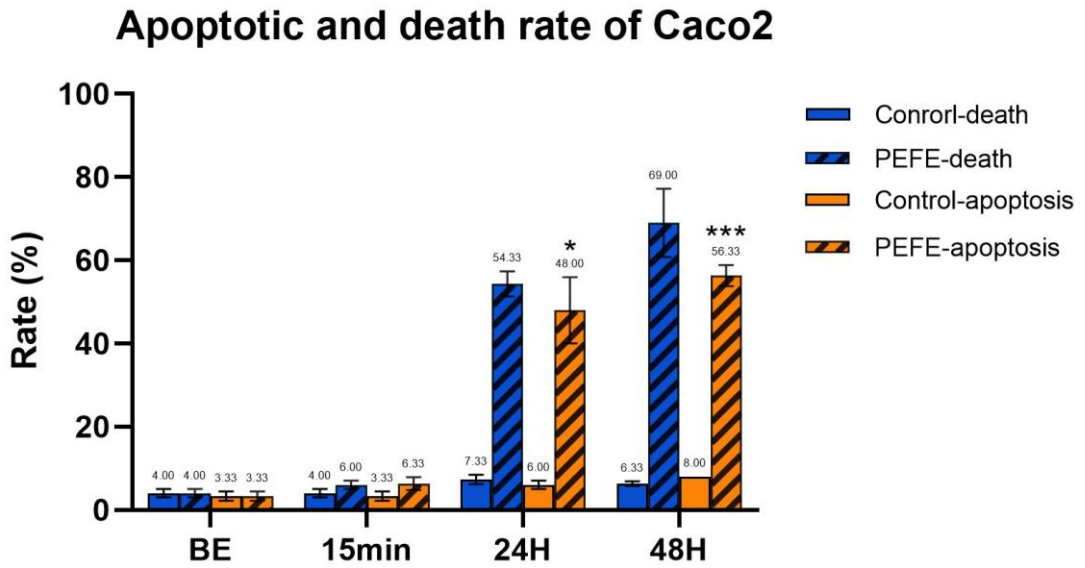

Figure 4.9 The detection of Caco2 cell apoptosis and death rate following PEFE treatment at 2.2GHz and 40 watts for 5 minutes. The apoptotic rate, while slightly lower, is close to the total death rate, indicating that apoptosis is the predominant mechanism of cell death in response to PEFE treatment. Data shows mean $\pm$ SD, n=3. T-tests were carried out to show the significance in apoptosis rate at different time points. * represents $p < 0.05$, *** represents $p < 0.001$.

4.3.2.3 Nuclear changes after PEFE treatment

The Caco2 cells were subjected to PEFE treatment and incubated for 24 hours incubation. After incubation, the cells were stained with DAPI to observe any nuclear changes in response to PEFE, as depicted in Figure 4.10. The results showed that the nuclei in the control group maintained normal shape. In contrast, the treated group exhibited several markers of apoptosis, including nuclear fragmentation, and the formation of apoptotic nuclei (red arrows). These observations highly indicate that cells are undergoing apoptosis due to the PEFE treatment.

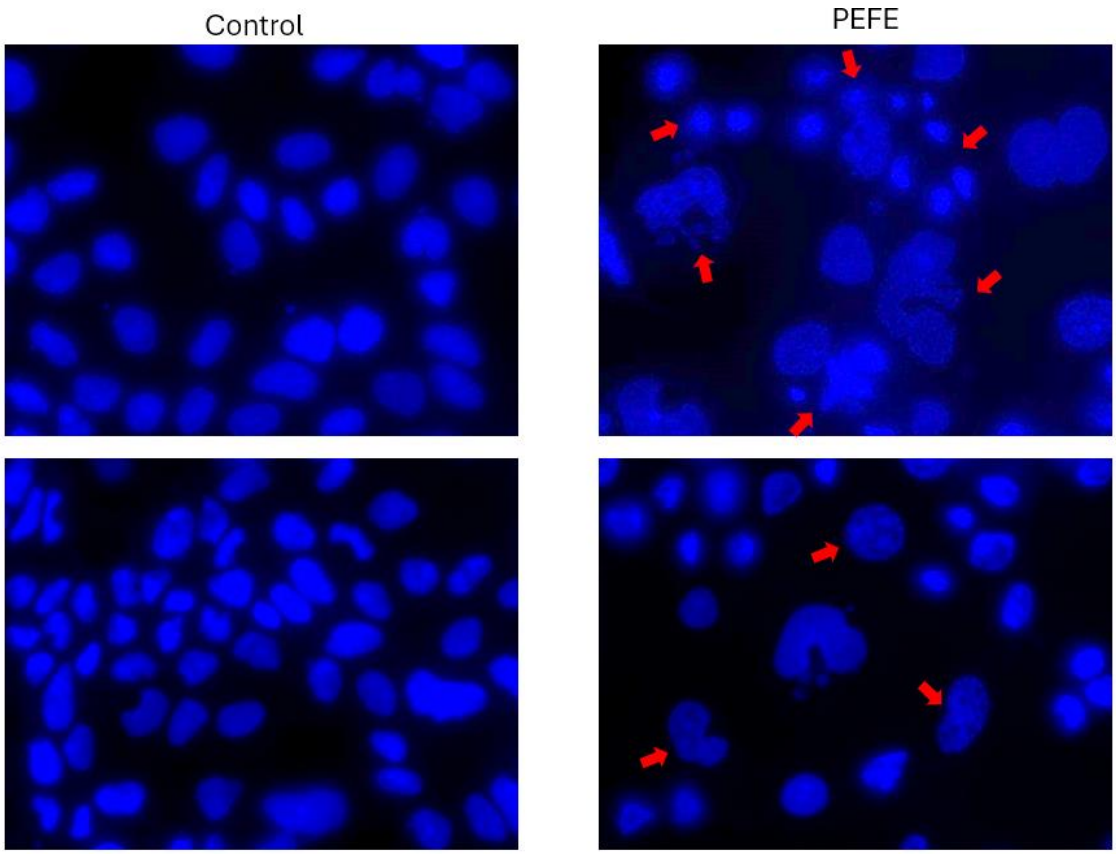

Figure 4.10 DAPI staining of cell nuclei on CRC cell line Caco2. Left: nuclear of Caco-2 control cells. Right: The nuclear of Caco-2 underwent PEFE treatment at 2.2GHz and 40 watts for 5 minutes. Red arrows indicate nuclear fragmentation and the formation of apoptotic nuclei. Magnification:40X.

4.3.2.4 Caspases dysregulation in response to PEFE

Based on previous experiments, more evidence suggested that cancer cells that underwent PEFE treatment were primarily killed via apoptosis. Here, Western blotting was employed to examine several key apoptosis-related molecules associated with cellular apoptosis, including Caspase-3, -8, and -9, at protein level in response to PEFE treatment.

Cells were treated with PEFE, and the protein was collected after 15 minutes, 1 hour, and 4 hours. Western blot was then conducted to assess the expression changes of caspases in response to PEFE. Western blot result was processed using ImageJ. Data was normalized against GAPDH and analyzed for fold change in Excel, with the figure created using GraphPad. As depicted in Figure 4.11, the expression level of Caspase-3 was increased after PEFE treatment. In particular, at 15 minutes and 1 hour post-treatment, the activity of Caspase-3

was slightly increased in comparison with their control groups, whereas its expression was significantly increased 4 hours post-treatment.

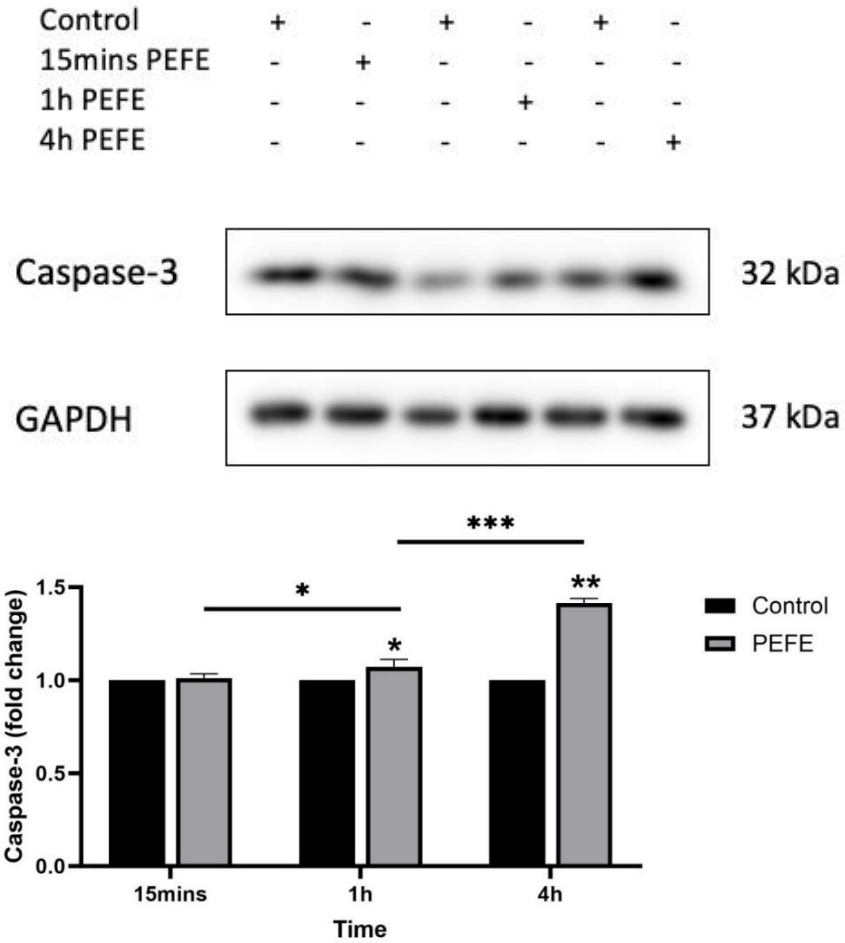

Figure 4.11 Western Blot analysis of Caspase-3 expression in response to PEFE. Image (top) obtained using G-BOX (Syngene), showing the Western blot result of Caspase-3 expression in control group and PEFE group (after 15 minutes, 1 hour, and 4 hours), indicated by '+'. Quantitative analysis of the bands was performed using Image J software. The expression was then normalized against GAPDH, to reveal any changes by fold change (down). Error bars show SD for three repeats. *p<0.05, **p <0.01, ***p<0.001.

Regarding Caspase-8, even though its expression was decreased when comparing PEFE treatment after 15 minutes and it control counterpart. However, after 1 hour and 4 hours, the expression level of Caspase-8 was significantly higher in the PEFE group compared with their control groups (Figure 4.12).

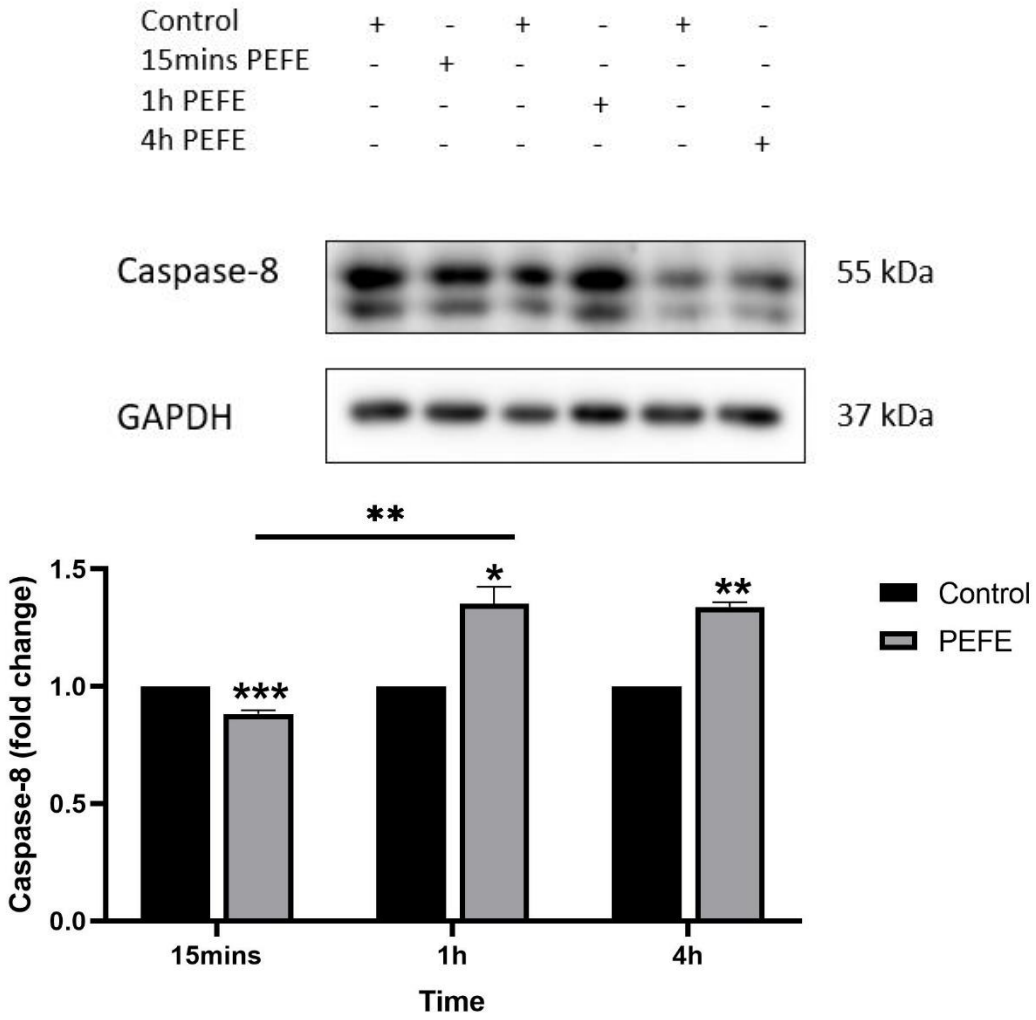

Figure 4.12 Western Blot analysis of Caspase-8 expression in response to PEFE. Image (top) obtained using G-BOX (Syngene), showing the Western blot result of Caspase-8 expression in control group and PEFE group (after 15 minutes, 1 hour, and 4 hours), indicated by '+'. Quantitative analysis of the bands was performed using Image J software. The expression was then normalized against GAPDH, to reveal any changes by fold change (down). Error bars show SD for three repeats. **p <0.01.

Similarly to Caspase-8, the expression of Caspase-9 was less changed following PEFE treatment after 15 minutes. However, a noteworthy increase was visualized at both 1 hour and 4 hours post-treatment, as shown in Figure 4.13.

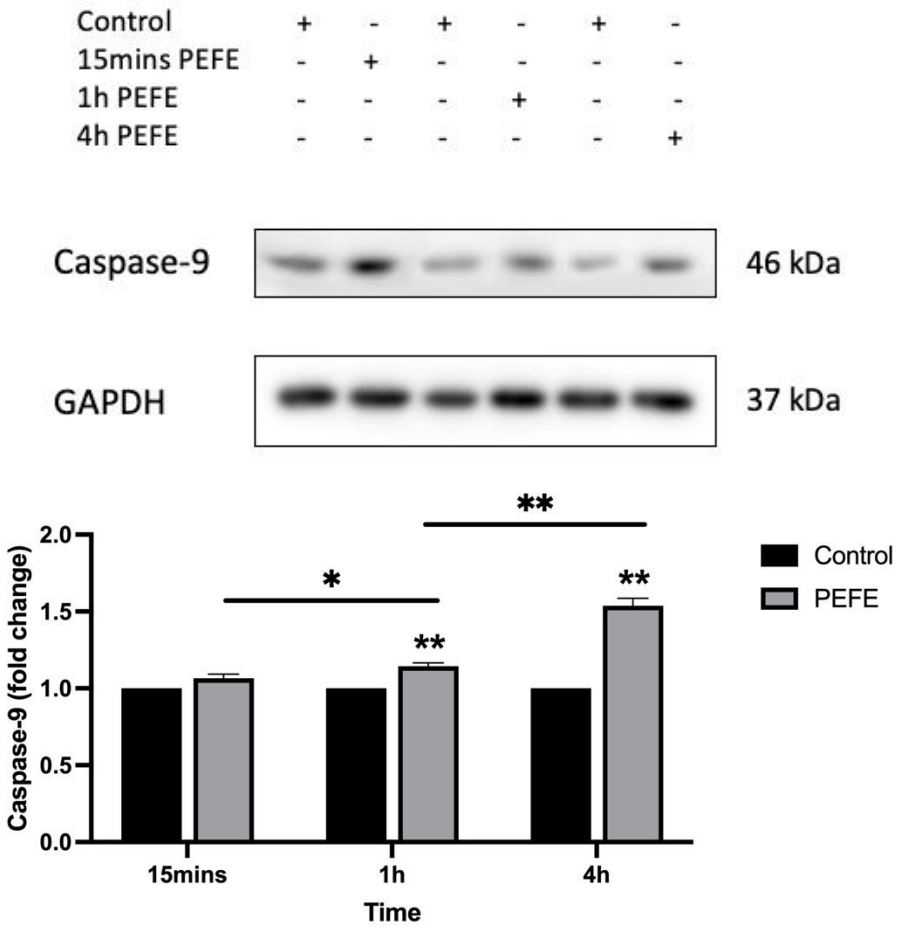

Figure 4.13 Western Blot analysis of Caspase-9 expression in response to PEFE. Image (top) obtained using G-BOX (Syngene), showing the Western blot result of Caspase-9 expression in control group and PEFE group (after 15 minutes, 1 hour, and 4 hours), indicated by '+'. Quantitative analysis of the bands was performed using Image J software. The expression was then normalized against GAPDH, to reveal any changes by fold change (down). Error bars show SD for three repeats. *p<0.05, **p <0.01.

4.3.3 The interaction between PEFE and tight junctions

As described in Chapter 4.3.1, cancer cells that exhibit good TJs are more sensitive in response to PEFE compared with those with weak TJs. Additionally, PEFE initially induced cell death only in a small amount immediately after the treatment, in which the area directly below the tip of the microwave probe, while the number of death cells increased over time. Therefore, it was hypothesized that TJs might play a role in signal transduction, in which the cascade of signalling of cell apoptosis was transmitted across the cell membrane, extending its influence on cells situated farther away from the probe tip. Therefore, the interaction between PEFE and TJs was further investigated.

4.3.3.1 The interaction between TJs and PEFE assessed using a cell scratching assay

In this experiment, a disrupted cell monolayer was intentionally created, resulting in the division of cells into three distinct sections: left, middle, and right. The microwave probe was positioned at the center of the well, directly above the middle section. The objective was to observe the effects of PEFE treatment on the cells in all three sections, with a particular focus on the left and right sections, to determine if they were impacted by the treatment. at the same time, the cells without any scratching were introduced and applied with PEFE as control.

The imaging results showed a clear pattern of cell viability following the PEFE treatment. As illustrated in Figure 4.14 A, most of the cells were killed after PEFE treatment. While in the scratching group, most of the cells in the middle section of the well, where the microwave probe was localized, were significantly affected and exhibited cell death. In contrast, the cells located in the left and right sections, separated by the created wounds, remained unaffected by PEFE treatment (Figure 4.14 B). The disruption created by the wounds appears to have 'blocked' the signal transduction, preventing the PEFE treatment from affecting the cells in the left and right sections.

(A)

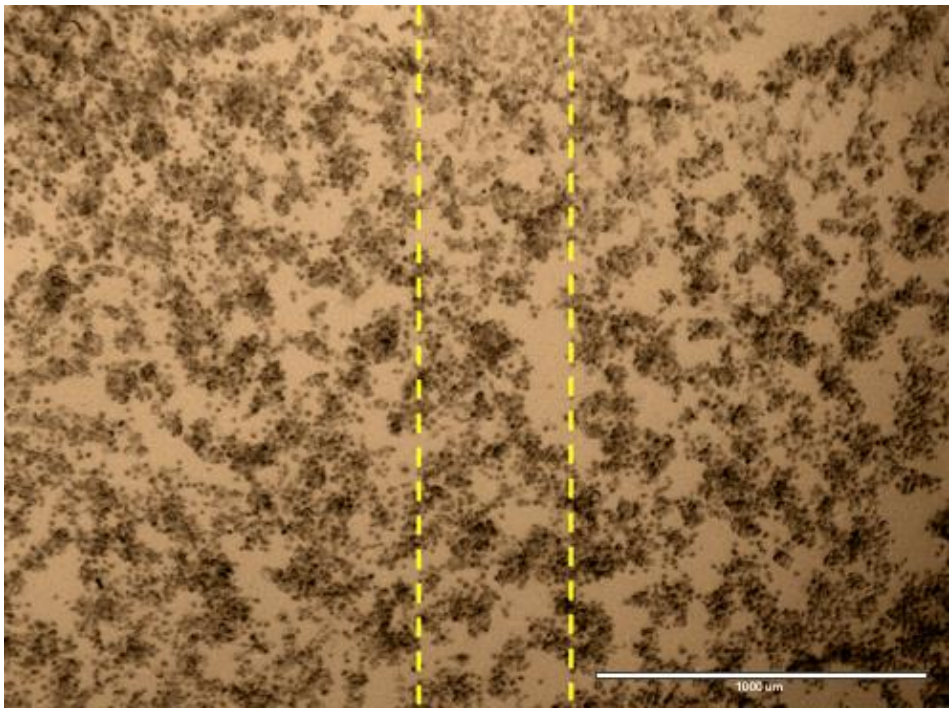

(B)

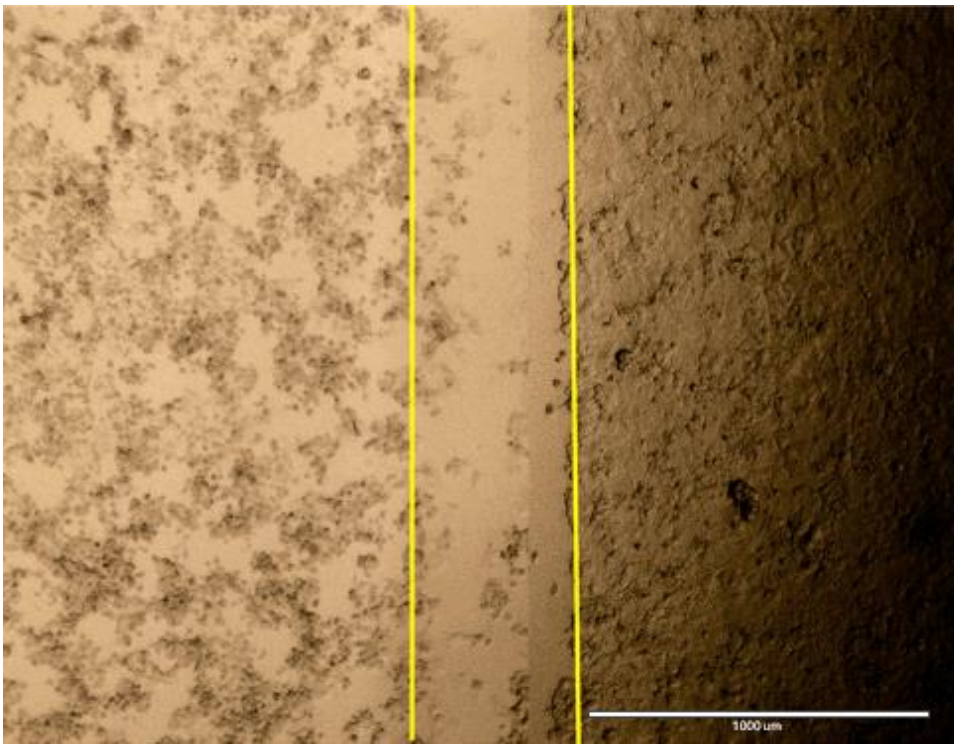

Figure 4.14 Inspection of cell morphology 24 hours post-treatment in MCF-7 breast cancer cells for: (A) control, (B) right scratching. Solid orange lines in the scratching group indicate the wound area; the orange dash lines in the control group correspond to the wound area created in the scratching group. Most of the cells were affected in the control group, while cells in the middle section were severely affected following PEFE treatment, while the cells in the left and right sections were not affected. Scale bar: 1000µm. Magnification: 4x.

4.3.3.2 ZO-1 dysregulation in response to PEFE by Western blot

Here, Western blotting was conducted to assess the expression of ZO-1 at the protein level in response to PEFE treatment. ZO-1 is widely used as a marker in research to identify and study TJs, contributing to its function as maintaining TJ integrity and signal transduction.

As illustrated in Figure 4.15, the levels of ZO-1 expression exhibited dynamic changes following PEFE treatment. At 15 minutes post-treatment, ZO-1 expression was decreased compared with the untreated control group. Interestingly, its expression experienced a substantial increase and was higher than its control counterpart after 1 hour. While the expression level of ZO-1 was significantly decreased after 4 hours. the result suggests that the most active initiation of apoptosis signal transduction might occur 1 hour after PEFE treatment.

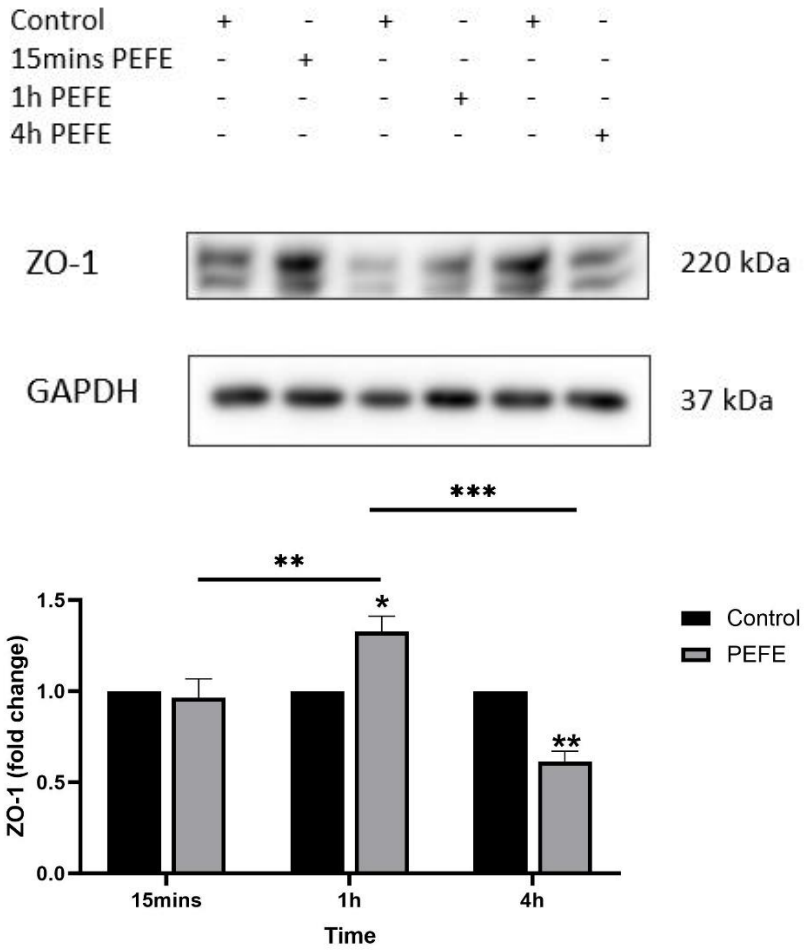

Figure 4.15 Western Blot analysis of ZO-1 expression in response to PEFE. Image (top) obtained using G-BOX (Syngene), showing the Western blot result of ZO-1 expression in the control group and PEFE group (after 15 minutes, 1 hour, and 4 hours), indicated by '+'. Quantitative analysis of the bands was performed using Image J software. The expression was then normalized against GAPDH, to reveal any changes by fold change (down). Error bars show SD for three repeats. *p<0.05, **p <0.01, ***p<0.001.

4.3.3.3 ZO-1 dysregulation in response to PEFE by IFC staining

Immunofluorescence analysis was conducted to assess the expression and localization of ZO-1 in response to PEFE treatment using Caco2 colorectal cancer cells, a cell line known for its well-formed and intact TJ structures. Cells were treated with PEFE and ZO-1 staining was performed at 15 minutes, 1 hour and 4 hours post treatment. Nuclear staining with DAPI was also performed to facilitate the identification of cell nuclei. As demonstrated in Figure 4.16, control group exhibits the normal localization of ZO-1 protein, with the protein continuously distributed along the cell borders where TJs are located (blue arrows). In contrast, after PEFE treatment, the integrity of the TJs was compromised, as evidenced by the disrupted and

fragmented distribution of ZO-1 (green arrows). 15 minutes after treatment, ZO-1 was less affected with the majority of them kept normal. However, by 1-hour post-treatment, significant discontinuity in ZO-1 expression was observed, alongside noticeable intracellular relocation of the protein (yellow arrows). At 4 hours post-treatment, ZO-1 expression was markedly weakened. These findings, based on immunofluorescence staining, clearly illustrate that PEFE treatment leads to the dismantling of TJs in Caco2 cells, as visualized by the altered distribution and weakened expression of ZO-1 over time. However, ZO-1 is an important scaffolding protein that connects TJ transmembrane proteins to the actin cytoskeleton, an important aspect that remains to be explored is whether the internalization of ZO-1 observed following PEFE treatment is associated with alterations in the cytoskeletal structure.

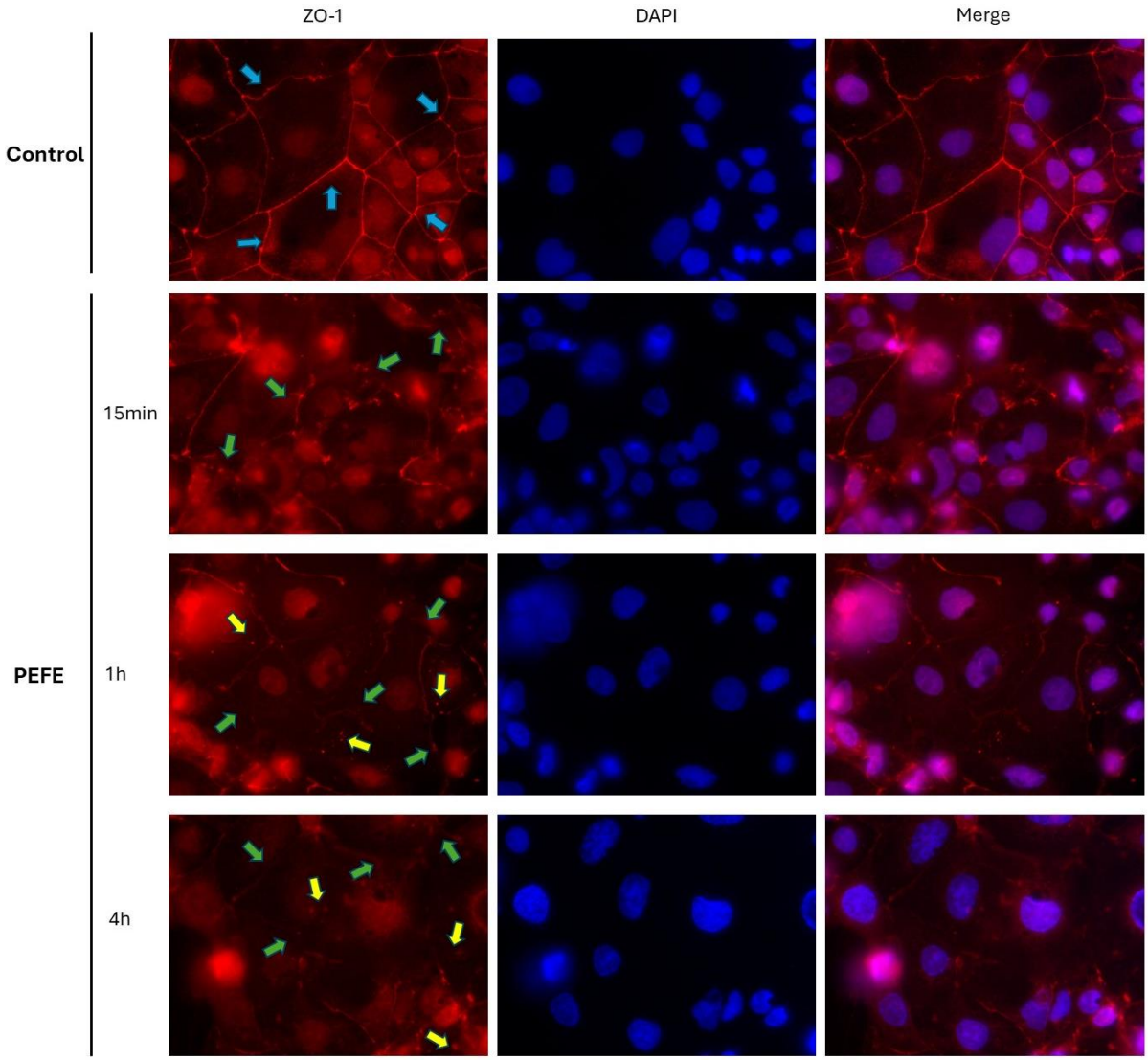

Figure 4.16 Immunofluorescence staining of ZO-1 in Caco2 colorectal cancer cells. ZO-1 was stained in the control untreated group, and cells underwent PEFE treatment at 2.2GHz, 40 watts for 5 minutes with TRITC secondary antibody. The images show the staining of ZO-1, nuclei and a merged image of both. Blue arrows points to the intact ZO-1 on cell membrane. Green arrows points to the disrupted ZO-1 expression following PEFE treatment. Magnification:40X.

4.3.3.4 Cytoskeleton alteration in response to PEFE treatment

Given the role of ZO-1 as a scaffolding protein that connects TJ proteins to the actin cytoskeleton, the study further explored whether the observed ZO-1 internalization post-PEFE treatment was associated with cytoskeletal alterations. To monitor any such changes, actin filaments were stained with Phalloidin (FITC). Caco2 cells were treated with PEFE and Phalloidin staining was applied at 15 minutes, 1 hour and 4 hours post treatment. Nuclear

staining with DAPI was also performed.

As depicted in Figure 4.17. In healthy control cells, the phalloidin staining demonstrated an evenly distributed, well-organized, parallel actin cytoskeleton with a clear structure, such as stress fibers, lamellipodia, and filopodia. While in the PEFE-treated group, the disrupted and fragmented actin cytoskeleton was visualized over time. Organized structures became disorganized or disappeared entirely, and actin filaments were more concentrated around the cell periphery or formed irregular aggregates. Given by these observations, it is suggested that the internalization of ZO-1 might be linked to cytoskeletal alterations. As ZO-1 relies on the actin cytoskeleton for its localization and stability at the cell membrane, the observed cytoskeletal disruptions likely contribute to the relocalization of ZO-1 into the cytoplasm. Or vice versa, It would be the breakdown of the TJs that cause changes in the cytoskeleton.

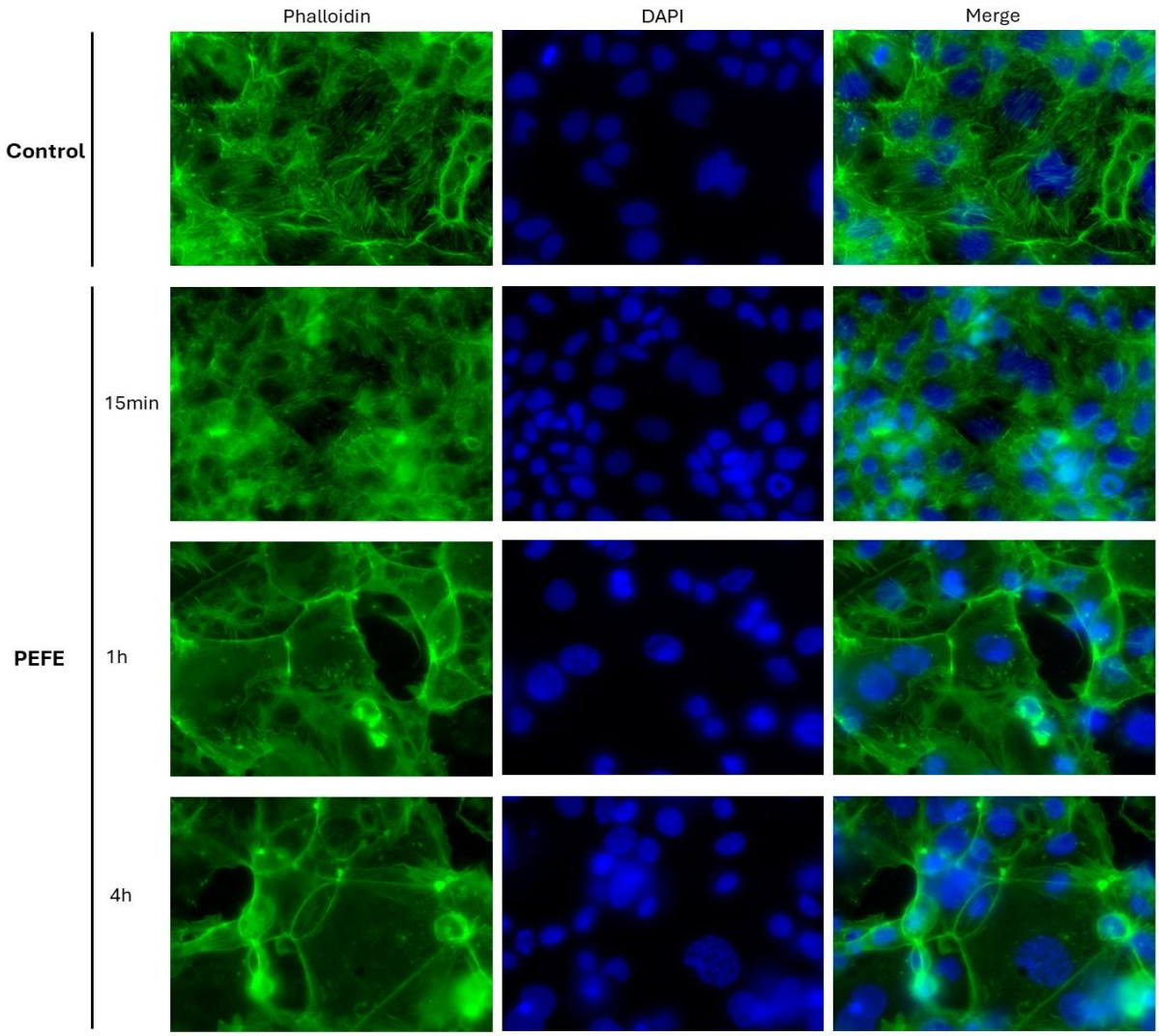

Figure 4.17 Immunofluorescence staining of actin filament detected by Phalloidin (FITC) in Caco2 colorectal cancer cells. Phalloidin was stained in the control untreated group, and cells underwent PEFE treatment at 2.2GHz, 40 watts for 5 minutes. The images show the staining of Phalloidin and nuclei and a merged image of both. Magnification:40X.

4.4 Discussion

Microwave-based techniques have become widely used in the medical field over the past few decades for diagnosing and treating various human diseases, particularly cancer. One prominent application is MWA, which serves as an alternative treatment for patients unsuitable for traditional cancer therapies. Given the high temperature generated during the procedure, numerous patient complaints have been reported due to pain, tissue breakdown, etc. Therefore, our study explores pulsed electromagnetic field exposure (PEFE) systems as a promising alternative, which subjected the cancer cells to high-power microwaves under

normothermic conditions, in which the temperature itself does not impact the cancer cells.

The present study explores the impact of PEFE on breast and colorectal cancer cells, providing significant insights into its potential as an alternative cancer treatment technique. Our findings demonstrate that PEFE induces significant cell death across various breast and colorectal cancer cell lines, regardless of their morphological and molecular differences, making it a promising candidate for broader clinical applications.

Our data revealed that PEFE treatment primarily induces cell death through apoptosis rather than necrosis. This is evidenced by the delayed increase in cell death observed 24 hours post-treatment, suggesting a programmed cell death mechanism. The use of Caspase-3/7 Detection Reagent confirmed apoptosis as the predominant mode of cell death, supported by the morphological changes observed via DAPI staining, such as chromatin condensation, and nuclear fragmentation. Further, the Western blot analysis revealed increased expression levels of key apoptosis-related proteins, including Caspase-3, -8, and -9, post-PEFE treatment. The sequential activation of these caspases underscores the involvement of both intrinsic and extrinsic apoptotic pathways.

An interesting aspect of our study is the differential sensitivity of cancer cell lines with different degrees of TJs to PEFE treatment. It was found that cells exhibit better TJs (e.g., MCF-7, ZR751, and Caco2), resulting in a better killing effect, suggesting a positive role of TJs involved in PEFE treatment. TJs, forming the most apical part of the junctional complex, play a crucial role in maintaining cell polarity and structural integrity, as well as regulating cellular communication and signal transduction (Anderson and Van Itallie 2009). Therefore, we suggested that a TJ might be involved in transmitting the PEFE signal. The cell scratching assay revealed that the disruption of cell monolayers appeared to 'block' the apoptotic signalling, indicating that intact TJs might facilitate signal transduction, leading to more efficient induction of apoptosis across the cell population. ZO-1 is a key scaffolding protein found within TJs. It links transmembrane TJ proteins, such as claudins and occludin, to the actin cytoskeleton. ZO-1 is not only crucial for the structural organization of TJs but also participates in various signalling pathways that regulate cellular processes and stress responses. By interacting with multiple proteins and signalling molecules, ZO-1 acts as a mediator of cellular

communication and signal transduction (González-Mariscal et al. 2003). Based on the Western blotting result presented here, the overall ZO-1 expression was decreased, while a substantial increase in ZO-1 expression was observed 1-hour post-treatment, exceeding the levels in the control group, suggesting that most dynamic signal transduction activity was observed one hour following PEFE treatment, in which it facilitated the apoptotic pathways, therefore spread the killing effect to the cells far away from the probe. The relationship between TJ, ZO-1, and apoptosis has been well-studied by numerous research. For example, ZO-1 can interact with Src kinase. This interaction is crucial for signalling transduction pathways regulating apoptosis (Fortner et al. 2022). Apart from Western blotting, the disruption of ZO-1 was further visualized by IFC, highlighting the potential interplay between TJs and apoptotic signalling pathways.

Since ZO-1 links TJ proteins to the actin cytoskeleton, it modulates cytoskeletal organization and cell shape. Our study demonstrated significant alterations in the actin cytoskeleton post-PEFE treatment, characterized by the disorganization of stress fibers and the formation of irregular actin aggregates. These cytoskeletal disruptions likely contribute to the observed internalization and relocalization of ZO-1, affecting TJ stability. The relationship between cytoskeletal integrity and apoptosis is well-documented, with actin filament disassembly being a hallmark of apoptotic cells (Desouza et al. 2012). The changes in cytoskeletal structure observed in our study support this notion and suggest that PEFE-induced cytoskeletal disruptions may facilitate or enhance the apoptotic process.

The details of the experiments done in this chapter and their results are summarized in the table below:

Experiments	Results
PEFE treatment among different breast and colorectal cancer cells	24-hour post treatment, the death rate of treated cells was significantly higher compared with their control counterparts. Moreover, cells exhibit good TJ seems to have better killing efficacy.
Confirmation of cell death with more time intervals	Significant cell death was found 4-hour post treatment.
The detection of apoptotic cells	Apoptotic rate of MCF-7 and Caco2 was close to their death rates, indicating that primary mode of cell death induced by PEFE treatment in cancer cells is apoptosis.
Nuclear changes after PEFE treatment	Nuclear fragmentation, and the formation of apoptotic nuclei, markers of apoptosis.
Caspases dysregulation in response to PEFE	Western blotting analysis revealed that the expression of Caspase-3, -8, and -9 was increased over time in response to PEFE treatment.
The interaction between TJs and PEFE assessed using a cell scratching assay	The cells in the middle section of the well were significantly affected, while the cells located in the left and right sections, separated by the created wounds, remained unaffected by PEFE treatment.
ZO-1 dysregulation in response to PEFE by Western blot	The expression of ZO-1 was increased 1-hour post treatment.
ZO-1 dysregulation in response to PEFE by IFC staining	After PEFE treatment, the integrity of the TJs was broken, alongside intracellular relocation of the ZO-1.
Cytoskeleton alteration in response to PEFE treatment	The disrupted and fragmented actin cytoskeleton was visualized over time.

In summary, this chapter revealed PEFE as an alternative cancer treatment, demonstrating its effectiveness in inducing apoptosis in both breast and colorectal cancer cells. We found that PEFE primarily induces cell death through apoptosis, with a significant role played by TJs in facilitating apoptotic signalling. In the next chapter, we will investigate the role of the TJ-related gene MarvelD3 in breast cancer and colorectal cancer, using a cohort study to understand its clinical function first and then explore its contribution to the effectiveness of PEFE treatment later.

Chapter-5 Expression of MarvelD3 in colorectal cancer and breast cancer and its clinical outcome

5.1 Introduction

Tight junctions are critical for maintaining cell polarity and barrier function in epithelial and endothelial tissues. In cancer, numerous studies reported that the dysregulation of TJ-associated proteins, either through upregulation or downregulation, resulted in the disruption of TJ structure, subsequently leading to increased permeability and loss of cell polarity, promoting tumour invasion and metastasis (Bhat et al. 2019).

MarvelD3, also known as Marvel domain containing 3, is a novel integral membrane component of TJs identified in 2009. It has two isoforms, variant 1 and variant 2. Both isoforms are expressed by different types of epithelial and endothelial cells. MarvelD3's involvement in cancer varies across various types of malignancies. In the context of oral squamous cell carcinoma (OSCC), high expression levels of MarvelD3 have been linked to poor prognosis, suggesting that MarvelD3 may contribute to the aggressiveness of OSCC (Huang et al. 2022). Conversely, research in hepatocellular carcinoma (HCC) showed that the expression of MarvelD3 was significantly lower in HCC tissues compared with their paired adjacent normal tissues, and its downregulation was correlated with the poor tumour stages, indicating that MarvelD3 may function as a tumour suppressor in HCC (Li et al. 2021b). Similarly, in non-small cell lung cancer (NSCLC), MarvelD3 expression was significantly reduced in the NSCLC tissues when compared with para-carcinoma tissues, and the downregulation was found to be related to tumour metastasis (Li et al. 2023).

Given this, MarvelD3 might be a possible prognostic biomarker for cancer progression. With the limited information regarding MarvelD3 in human colorectal cancer and breast cancer, together with the potential relationship between MarvelD3 and clinical outcomes, this chapter aims to explore the clinical significance of MarvelD3 in CRC and breast cancer using different resources, including clinical cohorts, online datasets and TMAs.

5.2 Methods

5.2.1 Cancer tissues collection

The colorectal cancer cohort contains 80 human colorectal cancer tissues and 94 human colorectal cancer tissues. The breast cancer cohort includes 127 normal human breast tissues and 33 background normal tissues. Methods for tissue collection and processing have been outlined in chapter 2.1.2.

5.2.2 RNA extraction, reverse transcription, and qPCR

RNA was extracted and converted to complementary DNA (cDNA) for subsequent quantification using real-time quantitative PCR (qPCR). Methods have been outlined in chapter 2.4.

5.2.3 Immunohistochemical (IHC) staining and analysis

IHC analysis was performed to assess MarvelD3 tissue expression in clinical samples, using tissue microarrays (TMA) for a colon cancer tissue array (code: CO2161b) and a breast cancer tissue array (BR1503f). Methods have been outlined in chapter 2.6.

5.2.4 Statistical analysis

In this chapter, Minitab (Minitab Ltd. Coventry, UK) was utilised to analyse transcript expression of MarvelD3 in clinical cohorts. Mann Whitney U test (two data sets) and Kruskal-Wallis ANOVA on RANKS test (three or more data sets) were performed to explore the statistical significance. Chi-square tests were performed to analyse the IHC score using Prism 10 (GraphPad Software, San Diego, CA, USA). SPSS (version 26) (IBM, Armonk, New York, USA) was used to do Kaplan-Meier survival analysis in clinical cohorts. $p<0.05$ is considered as statistical significance.

5.3 Results

5.3.1 Clinical significance of MarvelD3 in colorectal cancer

5.3.1.1 Expression profile of MarvelD3 in colorectal cancer online database

MarvelD3 expressions in CRC were first investigated through an online Gene Expression Omnibus (GEO) dataset, a database of gene expression curated profiles owned by NCBI.

Two individual GEO datasets, GDS4382 and GDS4396, were used to explore the expression of MarvelD3 in colorectal cancer. GDS4382 is the dataset for the analysis of paired CRC tumours and adjacent non-cancerous tissues with 34 samples in total (Reference Series: GSE32323) (Snipstad et al. 2010). GDS4396 is the dataset which focuses on the analysis of primary or metastatic lesions from patients with unresectable CRC with 29 samples in total (Reference Series: GSE28702) (Tsuji et al. 2012). Three individual probes are used, including 239148_at, 233634_at, and 239350_at, to detect the expression of MarvelD3. All analyses were conducted on the GPL570 platform (Affymetrix Human Genome U133 Plus 2.0 Array). Box plots were generated, and Mann Whitney test was used on each probe using GraphPad.

From the GDS4382 dataset, the expression of MarvelD3 in normal tissue (n=17) from two probes was significantly higher than the expression in tumour tissue (n=17) ($p=0.041$ for 239148_at, $p=0.0009$ for 233634_at). While there is no statistical significance observed for probe 239350_at, even though the median value of the normal group is higher than that of the tumour group, as shown in Figure 5.1.

From dataset GDS4396, the expression of MarvelD3 in the Primary lesion (n=23) was significantly higher than its expression in the metastatic lesion (n=6) in probe 239148_at ($p=0.0113$). The median values of the primary lesion were higher than those of the metastatic lesion, but there was no statistical significance observed in other probes 233634_at and 239350_at, as shown in Figure 5.2.

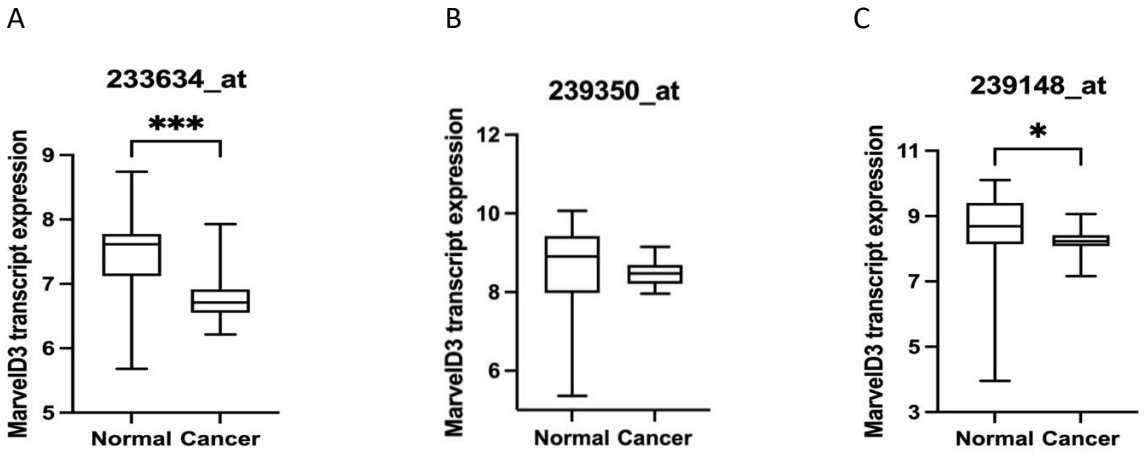

Figure 5.1 GEO dataset GDS4382 comparing MarvelD3 expression in colorectal cancer (n=17) and normal tissue (n=17) using 3 different probes (A) 233634_at, (B)239350_at, and (C) 239148_at. Box plot data presented in median (middle line in the box), Q1 and Q3 values, with 5th and 95th percentiles whiskers and outliers shown. *** represents $p < 0.001$, * represents $p<0.05$

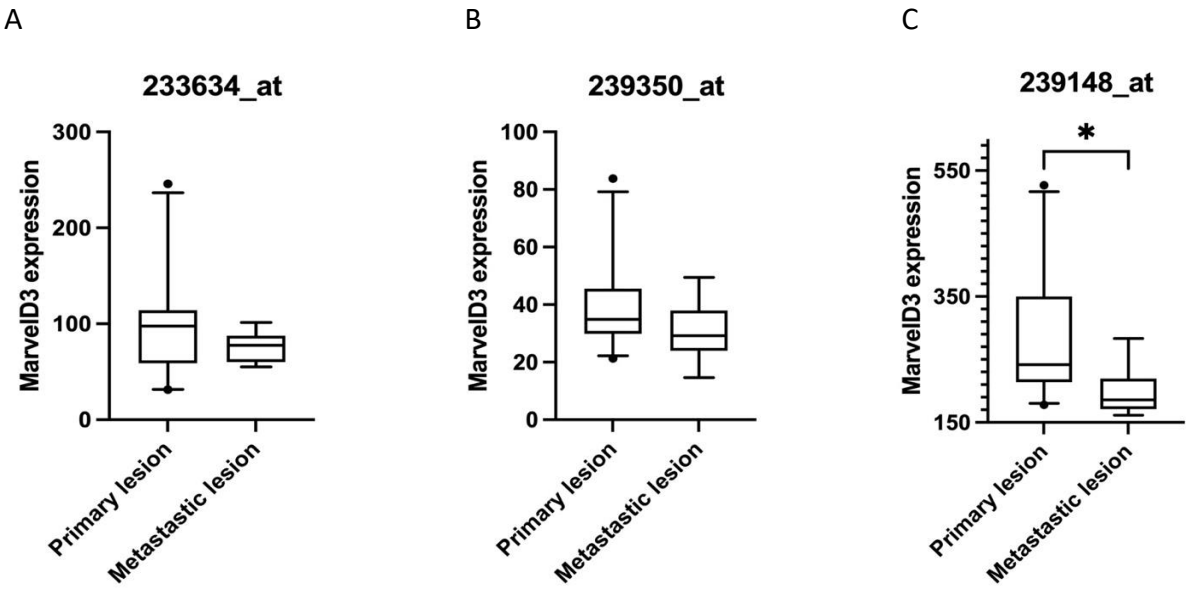

Figure 5.2 GEO dataset GDS4396 comparing MarvelD3 expression in CRC primary lesion(n=23) and metastatic lesion (n=6) using 3 different probes (A) 233634_at, (B)239350_at, and (C) 239148_at. Box plot data presented in median (middle line in the box), Q1 and Q3 values, with 5th and 95th percentiles whiskers and outliers shown. * represents $p<0.05$

5.3.1.2 Transcript level of MarvelD3 in colorectal cancer cohort

The expression of MarvelD3 in colorectal cancer was determined by exploring the transcript levels of MarvelD3 in the CRC cohort, which had 174 samples in total. Patients' clinical

outcomes for the levels of expression of MarvelD3 transcript are shown in Table 5.1. Statistical analysis used in the cohort study includes the Mann-Whitney U test for the comparison of two datasets and the Kruskal-Wallis ANOVA on the RANKS test for three or more data sets.

It was observed that the expression of MarvelD3 in the tumour group (n=94) was significantly higher than that of the normal group (n=80) by assessing the median of 77 vs 0.109 respectively ($p<0.0001$). The same upregulation was also observed when paired tissues were analyzed ($p<0.0001$) (Figure 5.3 and Figure 5.4, respectively). When considering the correlation with different CRC pathological characteristics, no significant differences were found in the analysis of differentiation, nodal involvement, TNM stage, T stage, and Dukes stage and no metastasis vs distant metastasis. Among them, regarding the metastasis status, the result from the clinical cohort exhibited that samples with distant metastasis (n=50) have lower transcript expression of MarvelD3 compared with samples without metastasis (n=19), with the median relative transcript copy numbers of 46.5 vs 75 respectively, in which the trend is in line with online GEO dataset. Besides, the analysis of different T stages showed a negative correlation between the T stage and the median transcript expression of MarvelD3, with the median transcript expression of MarvelD3 in T1 (n=2) being 290 while in T4 (n=18) being 39, again no significance was observed. This might be caused by the limited number of samples, and this finding should be confirmed by a larger cohort.

Table 5.1 The transcript expression profile of MarvelD3 compared to clinical pathological information of the Cardiff CRC cohort.

Characteristics	Sample numbers (n)	Median	Q1	Q3	p-value
Entire cohort					
Normal	80	0.109	0.019	0.646	
Tumour	94	77	10	250	<0.0001[a]
Paired Normal	68	0.155	0.023	0.646	
Paired Tumour	68	80	11	223	<0.0001[a]
Differentiation					0.583[b]
Low	2	152.3	*	*	
Moderate	54	56	8	204	
High	14	97.4	8.6	282.7	
Nodal involvement					
Node0	39	66	10	277	
Node1	16	44.7	0.000	133	
Node2	15	97	22	384	
TNM stage					0.424[b]
TNM1	9	189.7	58.4	374.9	
TNM2	30	46	10	229	
TNM3	26	76.3	0.7	230.3	
TNM4	6	25.7	0.6	153.3	
T stage					
T1	2	290	*	*	0.423[b]
T2	10	129.3	15.4	404.1	
T3	40	69	5	192	
T4	18	39	10	372	
Dukes stage					0.423[b]
Dukes A	7	139.6	20.50	208.2	
Dukes B	33	56	10	321	
Dukes C	32	73.5	1	194.4	
Metastasis					0.4559[a]
No metastasis	50	75	10	282	
Distant metastasis	19	46.5	1.9	149.6	

Note: [a] Mann Whitney; [b] Kruskal Wallis ANOVA on RANKS; $p<0.05$ represents statistical significance.

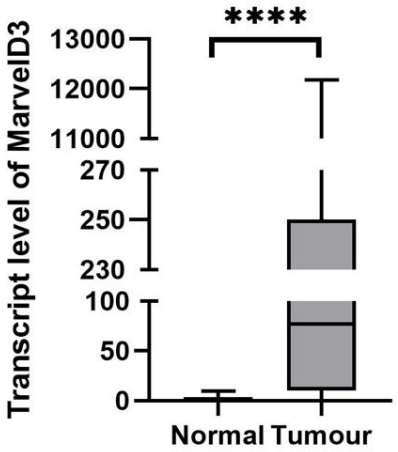

Characteristics	Sample numbers (n)	Median	Q1-Q3	Min-Max
Normal	80	0.109	0.019-0.646	0.000-9.576
Tumour	94	77	10-250	0-12180

Figure 5.3 The transcript level of MarvelD3 between normal tissues and colorectal cancer tissues. Box plot data presented in median (middle line in the box), Q1 and Q3 values, min and max whiskers. MarvelD3 transcript level was significantly higher in tumour tissues evaluated by a median. Statistical analysis was then performed using the Mann-Whitney test. **** represents p<0.0001

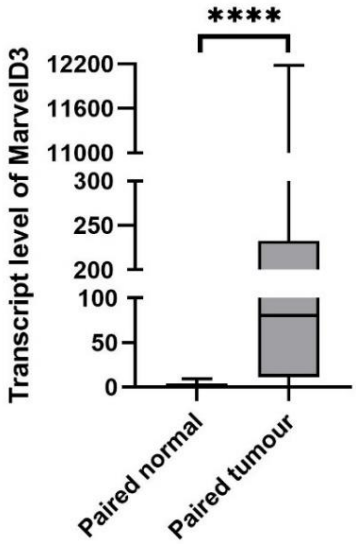

Characteristics	Sample numbers (n)	Median	Q1-Q3	Min-Max
Paired normal	68	0.155	0.023-0.646	0.000-9.576
Paired tumour	68	80	11-233	0-12180

Figure 5.4 The transcript level of MarvelD3 between paired normal tissues and colorectal cancer tissues. Box plot data presented in median (middle line in the box), Q1 and Q3 values, min and max whiskers. MarvelD3 transcript level was significantly higher in paired tumour tissues evaluated by a median. Statistical analysis was then performed using the Mann-Whitney test. **** represents p<0.0001

5.3.1.3 Further analysis of The Cancer Genome Atlas (TCGA) database

In addition to the GEO online datasets and clinical cohort, The Cancer Genome Atlas (TCGA) was also accessed to investigate further the expression of MarvelD3 in colorectal cancer on a large sample.

The analysis of MarvelD3 expression in colon adenocarcinoma (COAD) TCGA dataset based on individual cancer stages via the UALCAN platform was conducted, as shown in Figure 5.5. The expression of MarvelD3 in the T4 stage (n=39) was significantly lower than in other pathological stages ($p<0.05$ when comparing T1, T2, T3 to T4, individually), indicating that MarvelD3 expression decreased as colorectal cancer became more aggressive, which is consistent with the results observed in our clinical cohort.

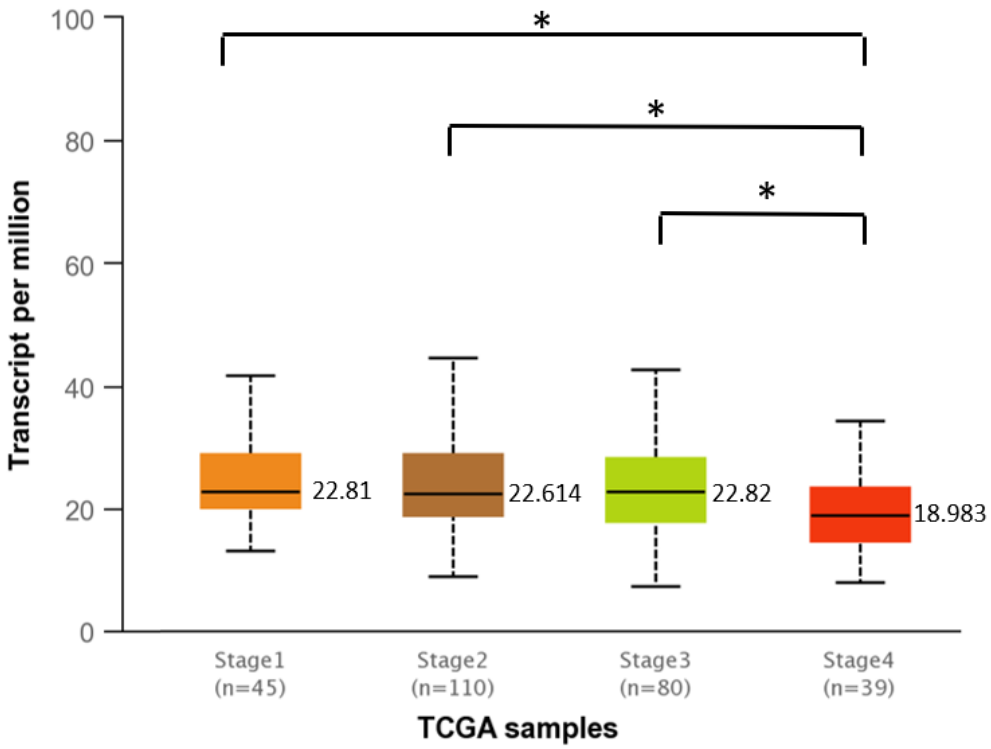

Figure 5.5 Expression of MarvelD3 in colon adenocarcinoma based on individual cancer stages. MarvelD3 expression is significantly lower in the T4 stage than that of other pathological stages (*represents $p<0.05$). Box plot data shown is median expression, Q1 and Q3 values from each dataset, whiskers represent 5th and 95th percentiles with outliers shown, obtained from UALCAN platform (https://ualcan.path.uab.edu/cgi-bin/TCGAExResultNew2.pl?genenam=MARVELD3&ctype=COAD).

5.3.1.4 MarvelD3 expression in colorectal cancer at the protein level, analysis by IHC

As described above, MarvelD3 exhibits higher expression in colorectal cancer tissues compared to the normal tissues at the transcript level in the clinical cohort. We subsequently investigated the presence and the pattern of MarvelD3 in a TMA of colon cancer and normal colon tissues, including pathology grade, TNM and clinical stage (n=216) (code: CO2161b). The intensity of MarvelD3 staining was scored and shown here as follows: 0 represents negative staining, 1 represents weak staining, 2 represents medium staining, and 3 represents intense staining. Table 5.2 summarizes the intensity of MarvelD3 staining and statistical analysis by way of Chi-square tests for colon cancer TMA.

Table 5.2 MarvelD3 staining of colorectal cancer TMA

	Total cases	Intensity				Statistical significance	
		0	1	2	3	Chi-square	P value
Entire cohort							
Carcinoma	142	44 (31%)	65 (46%)	27 (19%)	6 (4%)		
Normal	7	0	0	1 (14%)	7 (86%)		
Grade							
Grade1	6	1 (17%)	2 (33%)	3 (50%)	0 (0)		
Grade2	97	27 (28%)	48 (49%)	20 (21%)	2 (2%)		
Grade3	30	16 (53%)	10 (33%)	2 (7%)	2 (7%)	9.826	0.0201[a]
T stage							
T1	1	0 (0)	1 (100%)	0 (0)	0 (0)		
T2	15	4 (27%)	6 (40%)	5 (33%)	0 (0)		
T3	79	22 (28%)	36 (45%)	17 (22%)	4 (5%)		
T4	47	20 (42%)	22 (47%)	5 (11%)	0 (0)		
T1+T2	16	4 (25%)	7 (44%)	5 (31%)	0 (0)		
T3+T4	126	42 (33%)	58 (46%)	22 (18%)	4 (4%)		
TNM							
TNM1	14	3 (21%)	7 (50%)	4 (29%)	0 (0)		
TNM2	80	24 (30%)	38 (47%)	15 (19%)	3 (4%)		
TNM3	45	16 (36%)	19 (44%)	8 (18%)	2 (2%)	0.5032	0.9182[b]
TNM4	3	1 (33%)	1 (67%)	0 (0)	1 (0)		
TNM1+TNM2	94	27 (29%)	45 (48%)	19 (20%)	3 (3%)		
TNM3+TNM4	48	17(35%)	22 (46%)	8 (17%)	1 (2%)	0.8361	0.8408[c]

Note: [a] Compared with Grade2 group; [b] Compared with TNM2 group; [c] Compared with TNM1+TNM2 group.

Interestingly, among the 7 normal colon tissues, 6 of them exhibited intensive staining of

MarvelD3, one of them had medium staining, and all the tissues had both cytoplasmic and membrane staining. However, for the cancer tissues, only 4% of them were strongly stained with MarvelD3, and most of them exhibited negative (31%) or weak (46%) staining. Moreover, most of the staining was shifted from the cell membrane to the cytoplasm, as illustrated in Figure 5.6, with the clinicopathological details of the presented sections are summarized in Table 5.3.

Regarding the pathology staging of the colon cancer tissues, given the fact that some case numbers are too low to make any comparison, some groups were combined. In our study, we observed that less aggressive colorectal cancer (CRC) tissues exhibited higher MarvelD3 expression compared to more aggressive ones. Specifically, MarvelD3 expression was stronger in less aggressive tumour stages (T1 and T2) compared to more advanced stages (T3 and T4) (Figure 5.7). Additionally, a similar trend was found when comparing the CRC samples with clinical stages, in which MarvelD3 staining was stronger in TNM1 and TNM2 than those of TNM3 and TNM4 (Figure 5.8).

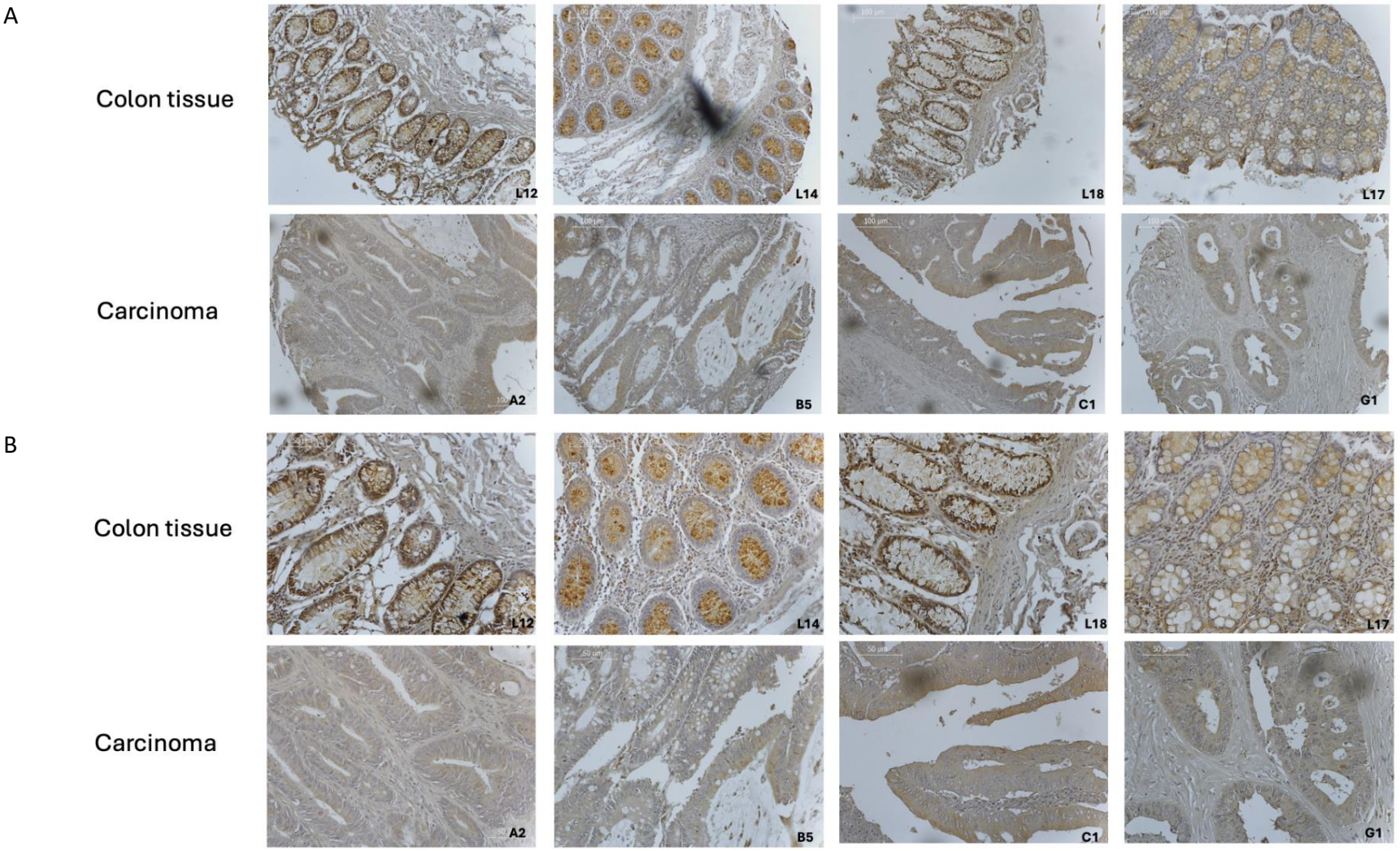

Figure 5.6 Representative images of MarvelD3 staining in colon cancer TMA (CO2161b) for normal colon tissues and cancer tissues. A. Magnification: 10x, scale bar: 100µm. B. Magnification: 20x, scale bar: 50µm.

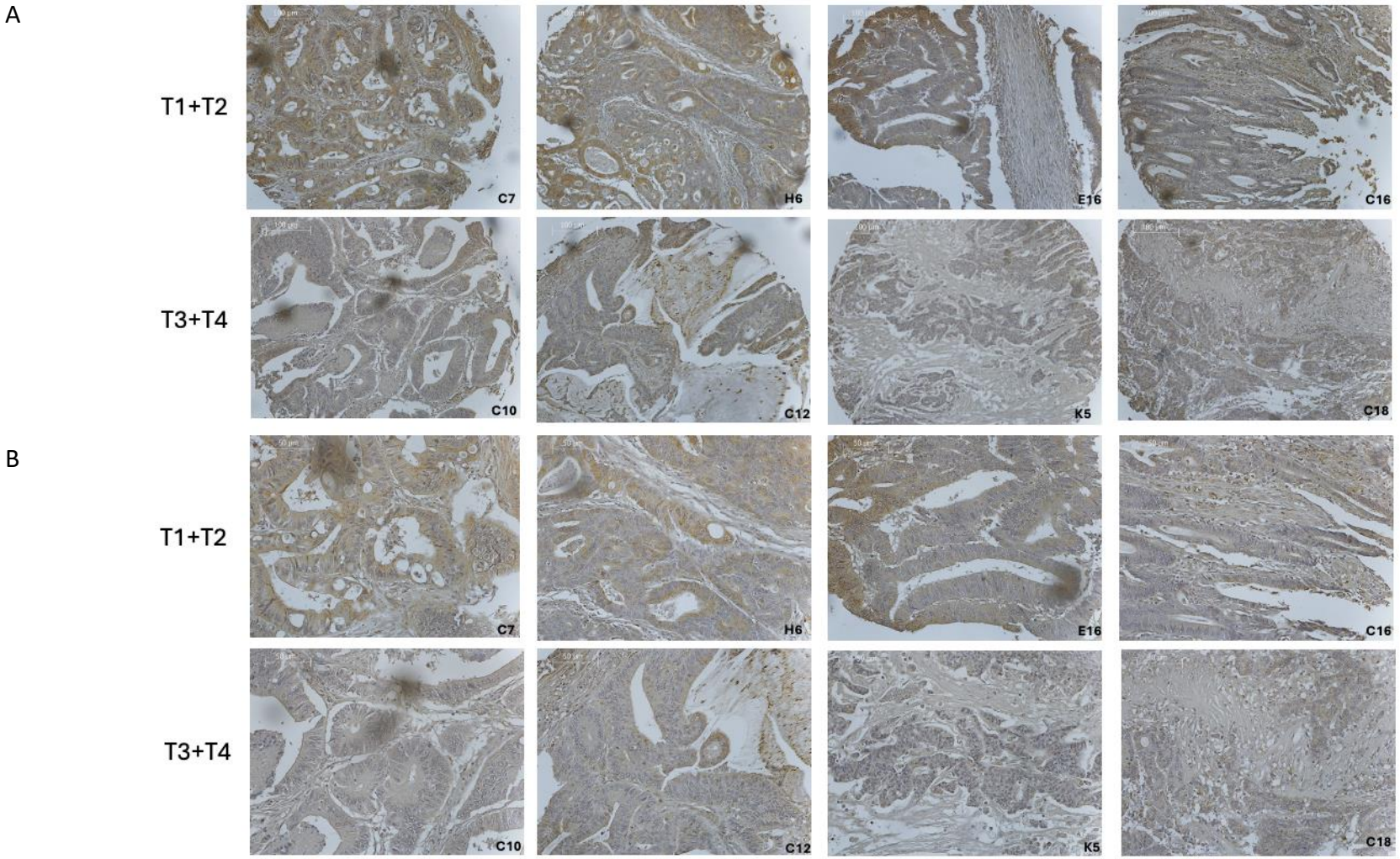

Figure 5.7 Representative images of MarvelD3 staining in colon cancer TMA (CO2161b) among different tumour stages. A. Magnification: 10x, scale bar: 100µm. B. Magnification: 20x, scale bar: 50µm.

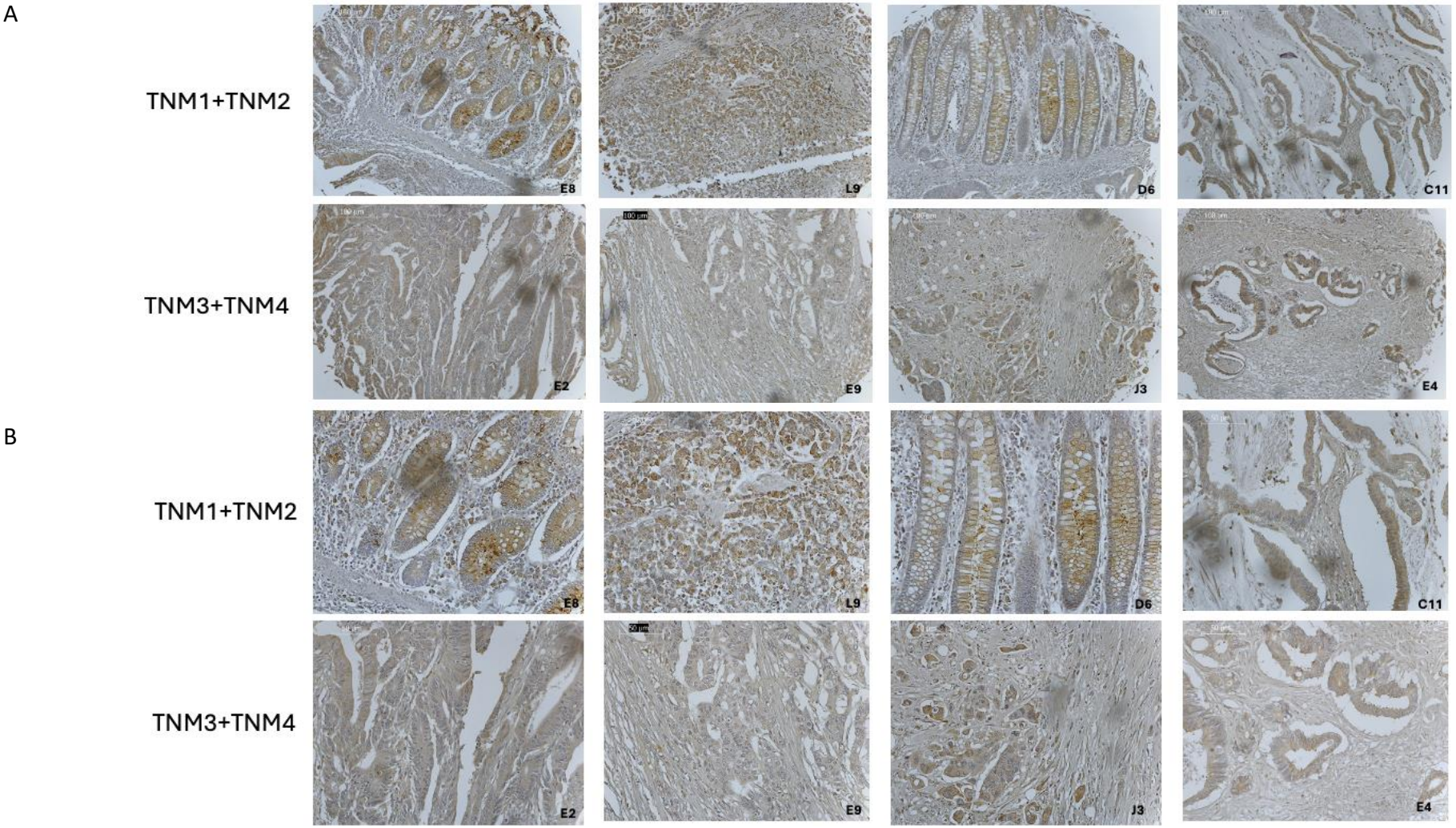

Figure 5.8 Representative images of MarvelD3 staining in colon cancer TMA (CO2161b) among different clinical stages. A. Magnification: 10x, scale bar: 100µm. B. Magnification: 20x, scale bar: 50µm.

Table 5.3 Information of representative samples of colon cancer TMA (CO2161b)

Position	Age	Sex	Organ/ Anatomic Site	Pathology diagnosis	TNM	Grade	Stage	Type
A2	46	M	Colon	Mucinous adenocarcinoma	T4N1M0	1	IIIB	Malignant
B5	24	F	Colon	Adenocarcinoma	T2N0M0	2	I	Malignant
C1	49	F	Colon	Adenocarcinoma	T3N1M0	2	IIIB	Malignant
C7	72	M	Colon	Adenocarcinoma	T2N0M0	2	I	Malignant
C10	43	M	Colon	Adenocarcinoma	T4N0M0	2	IIB	Malignant
C11	51	M	Colon	Adenocarcinoma	T2N0M0	2	I	Malignant
C12	50	M	Colon	Adenocarcinoma	T3N0M0	2	IIA	Malignant
C16	43	F	Colon	Adenocarcinoma	T1N0M0	2	I	Malignant
C18	40	M	Colon	Adenocarcinoma	T3N0M0	2	IIA	Malignant
D6	70	F	Colon	Adenocarcinoma	T3N0M0	2	IIA	Malignant
E2	38	F	Colon	Adenocarcinoma	T3N1M0	2	IIIB	Malignant
E4	64	F	Colon	Adenocarcinoma	T3N1M0	2	IIIB	Malignant
E8	63	F	Colon	Adenocarcinoma	T3N0M0	2	IIA	Malignant
E9	51	F	Colon	Adenocarcinoma	T4N0M1	2	IV	Malignant
E16	69	M	Colon	Adenocarcinoma	T2N0M0	2	I	Malignant
G1	70	M	Colon	Adenocarcinoma	T3N0M0	2	IIA	Malignant
H6	52	M	Colon	Adenocarcinoma	T2N0M0	2	I	Malignant
J3	48	F	Colon	Adenocarcinoma	T4N1M1	3	IV	Malignant
K5	50	M	Colon	Adenocarcinoma	T4N0M0	3	IIB	Malignant
L9	75	F	Colon	Signet ring cell carcinoma	T3N0M0	-	IIA	Malignant
L12	40	M	Colon	Colon tissue	-	-	-	Normal
L14	45	M	Colon	Colon tissue	-	-	-	Normal
L17	45	M	Colon	Colon tissue	-	-	-	Normal
L18	22	M	Colon	Colon tissue	-	-	-	Normal

5.3.1.5 Implications of MarvelD3 expression on clinical outcome of patients with CRC

The correlation between MarvelD3 expression and patients' survival was also explored in a Cardiff cohort. Patients were divided into two groups based on ROC (Receiver Operating Characteristic). Kaplan-Meier survival analysis was conducted in SPSS and the results are shown in Figure 5.9 and Figure 5.10. Patients with a high expression of MarvelD3 had significantly lower overall survival (OS) and disease-free survival (DFS) of 30.3 months (95%C.I. 0-62.7 months) and 29.3 months (95%C.I. 0-64.1 months) respectively, compared with those with low levels expression at 131.4 months (95%C.I. 114.2-148.6 months) and 128.8 months (95%C.I. 110.6-147.0 months) respectively (P=0.004 for OS and p<0.001 for DFS).

An online independent cohort database with larger samples was also analyzed to further verify MarvelD3 expression on patient survival. To achieve this, the Kaplan-Meier Plotter

(www.kmplot.com) was accessed, which also has data on the clinical outcome for patients with colorectal cancer. Patients were divided into high and low levels of MarvelD3 expression based on the best cut-off value according to KM. As shown in Figure 5.11, patients with high MarvelD3 expression showed significantly shorter overall survival, with the median survival months 106 and 145 for high and low MarvelD3 expression, respectively (p=0.013), which is the same as the Cardiff cohort. Regarding the correlation with disease-free survival, patients with high MarvelD3 expression exhibited longer DFS (p=0.0029), as illustrated in Figure 5.12.

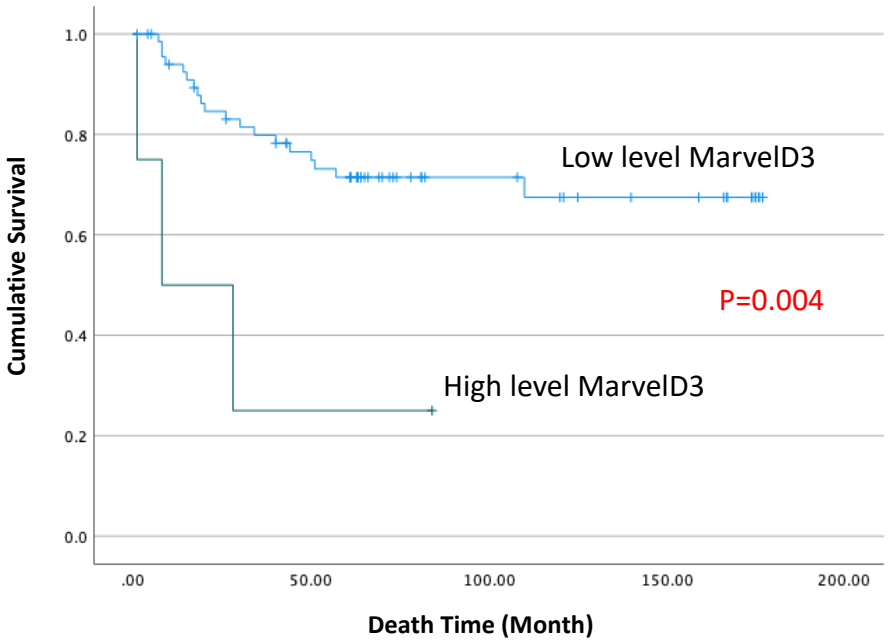

			Censored		Mean			
							95% confidence Interval	
	Total N	N of Events	N	Percent	Estimated	Std. Error	Lower Bound	Upper bound
Low level	69	19	50	72.5%	131.407	8.797	114.165	148.648
High level	4	3	1	25.0%	30.250	16.288	.000	62.174
Overall	73	22	51	69.9%	126.917	8.822	109.627	144.208

Figure 5.9 The Kaplan-Meier survival model of correlation between CRC patients' MarvelD3 transcript levels and overall survival. Using the ROC in the tumour group as the cut-off to divide patients into two groups with high and low MarvelD3 levels. Patients with high levels of MarvelD3 tend to have lower overall survival.

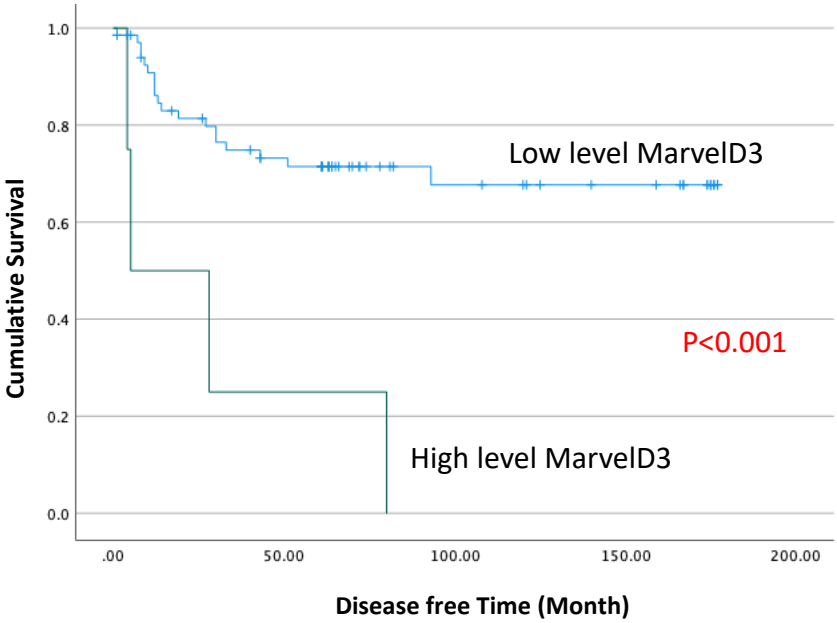

			Censored		Mean			
							95% confidence Interval	
	Total N	N of Events	N	Percent	Estimated	Std. Error	Lower Bound	Upper bound
Low level	69	19	50	72.5%	128.838	9.289	110.631	147.045
High level	4	4	0	0.0%	29.250	17.802	.000	64.141
Overall	73	23	50	68.5%	121.507	9.424	103.037	139.978

Figure 5.10 The Kaplan-Meier survival model of correlation between MarvelD3 transcript levels and disease-free survival. Using the ROC in the tumour group as the cut-off to divide patients into two groups with high and low MarvelD3 levels. Patients with high levels of MarvelD3 tend to have lower disease-free survival.

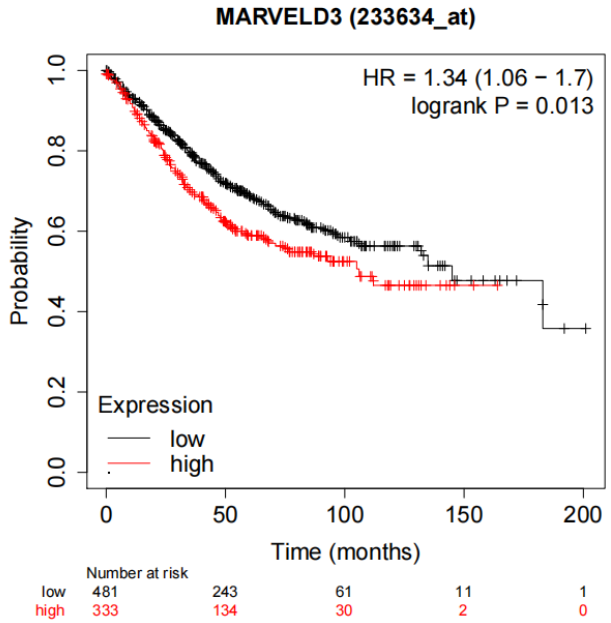

Figure 5.11 The correlation between the expression of MarvelD3 and CRC patients' overall survival outcome from an online database. Data was collected from Kaplan-Meier Plotter (www.kmplot.com), and the cut-off value was determined as the best cut-off value by the database. Patients with high levels of MarvelD3 might have shorter overall survival.

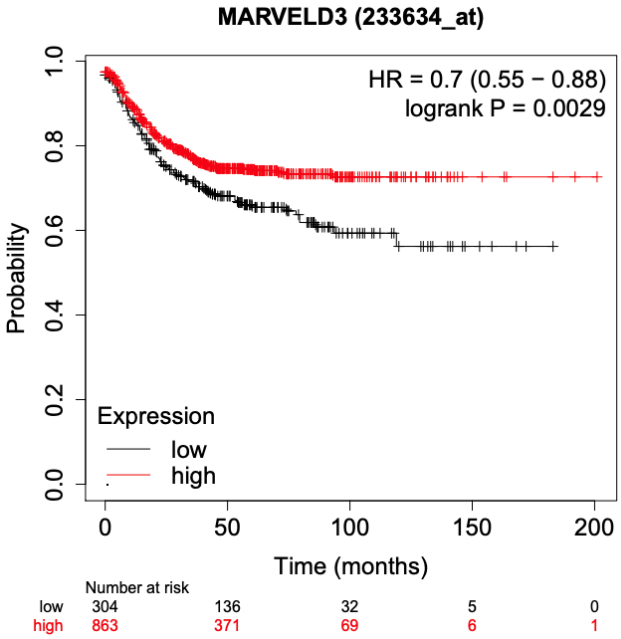

Figure 5.12 The correlation between the expression of MarvelD3 and CRC patients' disease-free survival outcome from an online database. Data was collected from Kaplan-Meier Plotter (www.kmplot.com), and the cut-off value was determined as the best cut-off value by the database. Patients with high levels of MarvelD3 might have longer disease-free survival.

5.3.2 Clinical significance of MarvelD3 in breast cancer

5.3.2.1 Expression profile of MarvelD3 in breast cancer online database

GEO datasets GSE42568 were used to detect the expression of MarvelD3 in breast cancer. GSE42568 is the dataset for analyzing breast cancer biopsies removed prior to any treatment from patients and normal tissues with 121 samples in total (Clarke et al. 2013). Three probes were used for this dataset, including 233634_at, 239148_at, and 239350_at. The analysis was conducted on platform GPL570 (Affymetrix Human Genome U133 Plus 2.0 Array). Box plots were generated, and Mann Whitney test was used on each probe using GraphPad.

From GSE42568 dataset, the expression of MarvelD3 in tumour group (n=104) was significantly higher than that of normal group (n=17) in both three probes 233634_at, 239148_at, and 239350_at ($p<0.0001$ for both), as shown in Figure 5.13.

In the same dataset, the cohort was then subgrouped according to the breast cancer grading, containing grade 1 (n=11), grade 2 (n=40) and grade 3 (n=53), and the relationship between MarvelD3 expression and breast cancer grading was explored in more detail. As illustrated in Figure 5.14, increased MarvelD3 expression is associated with higher breast cancer grades. This correlation was consistently observed across three different probes.

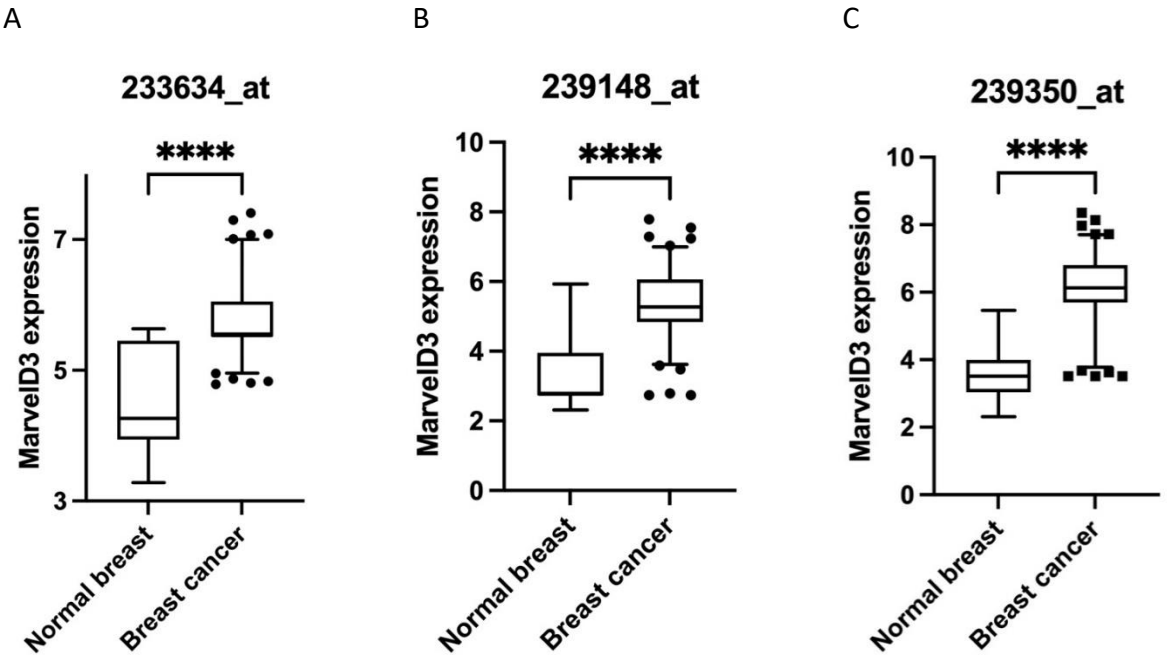

Figure 5.13 GEO dataset GSE42568 comparing MarvelD3 expression in breast cancer (n=104) and normal breast (n=17) using 3 different probes (A) 233634_at, (B)239148_at, and (C) 239350_at. Box plot data presented in median (middle line in the box), Q1 and Q3 values, with 5th and 95th percentiles whiskers and outliers shown. **** represents $p < 0.0001$.

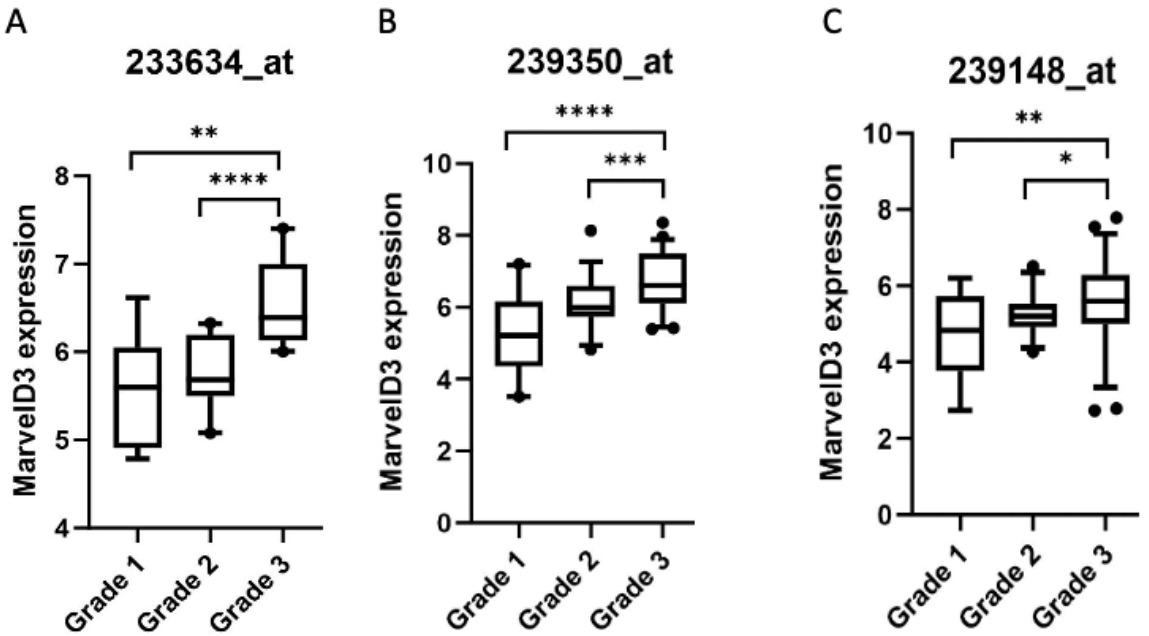

Figure 5.14 GEO dataset GSE42568 compares MarvelD3 expression in breast cancer with different grading using 3 different probes: (A) 233634_at, (B)239148_at, and (C) 239350_at. Box plot data presented in median (middle line in the box), Q1 and Q3 values, with 5th and 95th percentiles whiskers and outliers shown. * represents $p<0.05$, ** represents $p<0.01$, *** represents $p<0.001$, **** represents $p < 0.0001$.

5.3.2.2 Transcript expression of MarvelD3 in the clinical breast cancer cohort

Tissues were obtained following ethical approval from the University Hospital of Wales, together with pathological data analysis. 160 samples were analyzed in total, with 33 normal breast samples and 127 breast tumour samples. RNA extraction, quantification, standardization, and reverse transcription were performed to collect cDNA for qPCR to investigate the transcript expression. Mann-Whitney test was then performed to analyze the data.

Expression of MarvelD3 in breast cancer was determined by exploring the transcript levels of MarvelD3 in the Cardiff cohort. Patient's clinical and pathological features, as well as the levels of expression of the MarvelD3 transcript, are summarized in Table 5.4.

It can be observed that the expression of MarvelD3 in the breast cancer tumour group was significantly higher than that of the normal group by assessing the median 36 vs 0 respectively ($p=0.0114$). Also, the expression of MarvelD3 was significantly upregulated in the paired tumour group compared with normal breast tissues ($p=0.0121$) (Figure 5.15 and Figure 5.16).

The analysis of different Grade suggested that there is a positive correlation between MarvelD3 transcript level and breast cancer grade, in which the median relative transcript level of marvelD3 in Grade 1 ($n=24$) was 13 while in Grade 3 ($n=58$) was 58. Even though there is no significance being observed, potentially limited by the low sample numbers. However, there are no stable trends for other pathological types, including The Nottingham Prognostics Index (NPI) and TNM stage. Again, this is mainly due to the limited samples.

Interestingly, there was an observable trend indicating that MarvelD3 expression tended to be higher in samples without metastasis ($n=90$) compared to those with metastasis ($n=7$). This was evidenced by the median expression levels, which were 9 for the metastasis group and 35 for the non-metastasis group, even though no significance was observed.

Table 5.4 The transcript expression profile of MarvelD3 compared to clinical pathological information of the Cardiff breast cancer cohort.

Characteristics	Sample numbers (n)	Median	Q1	Q3	p-value
Entire cohort					
Normal	33	0	0	43	
Tumour	127	36	1	214	0.0114
Paired BG	27	0	0	42	
Paired tumour	27	13	1	134	0.0121
NPI					
NPI1	68	49	1	215	
NPI2	38	8.3	0.4	123.4	0.1964
NPI3	16	84	1	813	0.5985
Grade					
Grade1	24	13	1	109	
Grade2	43	35	0	134	0.9607
Grade3	58	45.8	1	344.1	0.2876
TNM stage					
TNM1	70	18	1	248	
TNM2	40	89	4	474	0.3475
TNM3	7	6.2	0.8	10	0.4405
TNM4	4	49.2	1	71	0.971
Early vs Late					
Early (TNM1)	70	18	1	248	
Late (TNM2/3/4)	51	52	1	242	
Clinical outcome					
Disease free	90	35	1	188	
With Metastasis	7	9	1	597	0.8455
With local recurrence	5	101	26	563	0.3838
Died of BrCa	16	99	5	583	0.2277
All BrCa Incidence	28	69	2	583	0.282

Note: In Mann Whitney, all categories were compared with the first group.

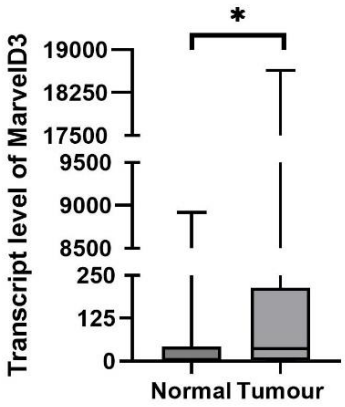

Characteristics	Sample numbers (n)	Median	Q1-Q3	Min-Max
Normal	33	0	0-43	0-8921
Tumour	127	36	1-214	0-18639

Figure 5.15 Transcript level of MarvelD3 between normal breast tissues and breast cancer tissues. Box plot data presented in median (middle line in the box), Q1 and Q3 values, min and max whiskers. MarvelD3 transcript level was significantly higher in tumour tissues evaluated by a median. Statistical analysis was then performed using the Mann-Whitney test. * represents $p<0.05$

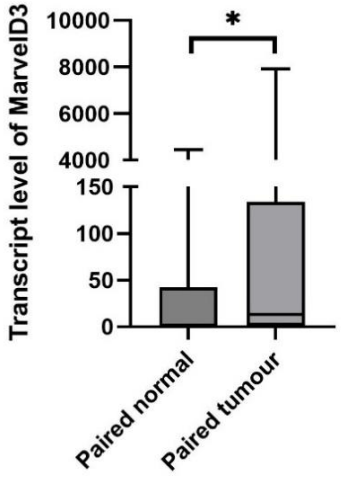

Characteristics	Sample numbers (n)	Median	Q1-Q3	Min-Max
Paired BG	27	0	0-42	0-4459
Paired tumour	27	13	1-134	0-7916

Figure 5.16 The transcript level of MarvelD3 between paired background tissues and breast cancer tissues. Box plot data presented in median (middle line in the box), Q1 and Q3 values, min and max whiskers. MarvelD3 transcript level was significantly higher in paired tumour tissues evaluated by a median. Statistical analysis was then performed using the Mann-Whitney test. * represents $p<0.05$

5.3.2.3 Further analysis of The Cancer Genome Atlas (TCGA) database

In addition to analyzing GEO online datasets and a clinical cohort, The Cancer Genome Atlas (TCGA) was utilized to further investigate MarvelD3 expression in a larger sample of breast cancer cases.

An analysis of MarvelD3 expression in the TCGA breast cancer dataset was performed, focusing on the metastasis status of the samples. As shown in Figure 5.17, the expression of MarvelD3 was significantly lower in samples with metastasis (n=7) compared to those without metastasis (n=1094) ($p<0.05$). This finding was in line with our clinical cohort result, suggesting a possible role of Marvel|D3 in breast cancer progression and metastasis.

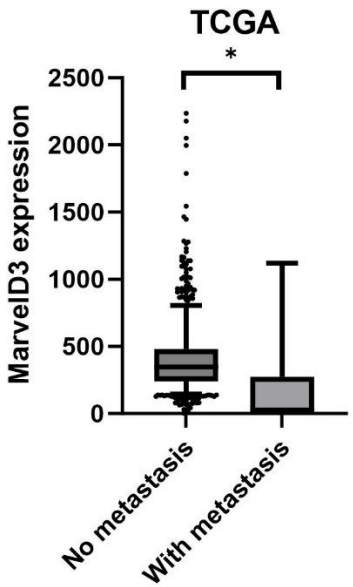

Figure 5.17 Expression of MarvelD3 in breast cancer based on metastasis status. MarvelD3 expression is significantly higher in the samples without metastasis (n=1094) than those with metastasis (n=7). Box plot data shown is median expression, Q1 and Q3 values from each dataset, whiskers represent 5th and 95th percentiles with outliers shown, data was obtained from TCGA BRCA cohort. * represents $p<0.05$.

5.3.2.4 MarvelD3 expression in breast cancer at the protein level, analysis by IHC

The presence and pattern of MarvelD3 protein in breast cancer TMA were also investigated by way of IHC. Table 5.5 summarises the MarvelD3 staining and statistical analysis of the

breast cancer tissue microarray. Representative TMA images are shown in Figure5.18, with associated clinicopathological information detailed in Table 5.6. The staining revealed that adjacent normal breast tissues (n=4) exhibited relatively weak MarvelD3 staining compared to invasive ductal carcinoma tissues (n=116). However, no clear trend was identified regarding tumour stages and differentiation, likely due to the limited sample size of the cohort.

Table 5.5 MarvelD3 staining of breast cancer TMA

	Total cases	Intensity				Statistical significance	
		0	1	2	3	Chi-square	P value
Entire cohort							
Adjacent normal breast tissue	4	0 (0)	4 (100%)	0 (0)	0 (0)		
Tumour	134	33 (25%)	61 (46%)	30 (22%)	10 (7%)		
Pathology type							
Adjacent normal breast tissue	4	0 (0)	4 (100%)	0 (0)	0 (0)		
Invasive ductal carcinoma	116	28 (24%)	49 (42%)	29 (25%)	10 (9%)		
Intraductal carcinoma	12	5 (42%)	7 (58%)	0 (0)	0 (0)		
Fibroadenoma	6	0 (0)	5 (83%)	1 (17%)	0 (0)		
Grade							
Grade1	4	2 (50%)	2 (50%)	0 (0)	0 (0)		
Grade2	75	11 (15%)	24 (32%)	34 (45%)	6 (8%)		
Grade3	29	9 (31%)	11 (38%)	6 (21%)	3 (10%)	6.567	0.0870[a]
T stage							
T1	6	2 (33%)	2 (33%)	0 (0)	2 (33%)		
T2	69	16 (23%)	27 (39%)	21 (30%)	5 (7%)		
T3	26	10 (38%)	10 (38%)	4 (15%)	2 (8%)	3.242	0.3558[b]
T4	15	0 (0)	10 (67%)	4 (27%)	1 (7%)		

Note: [a] Compared with Grade2 group; [b] Compared with T2 group.

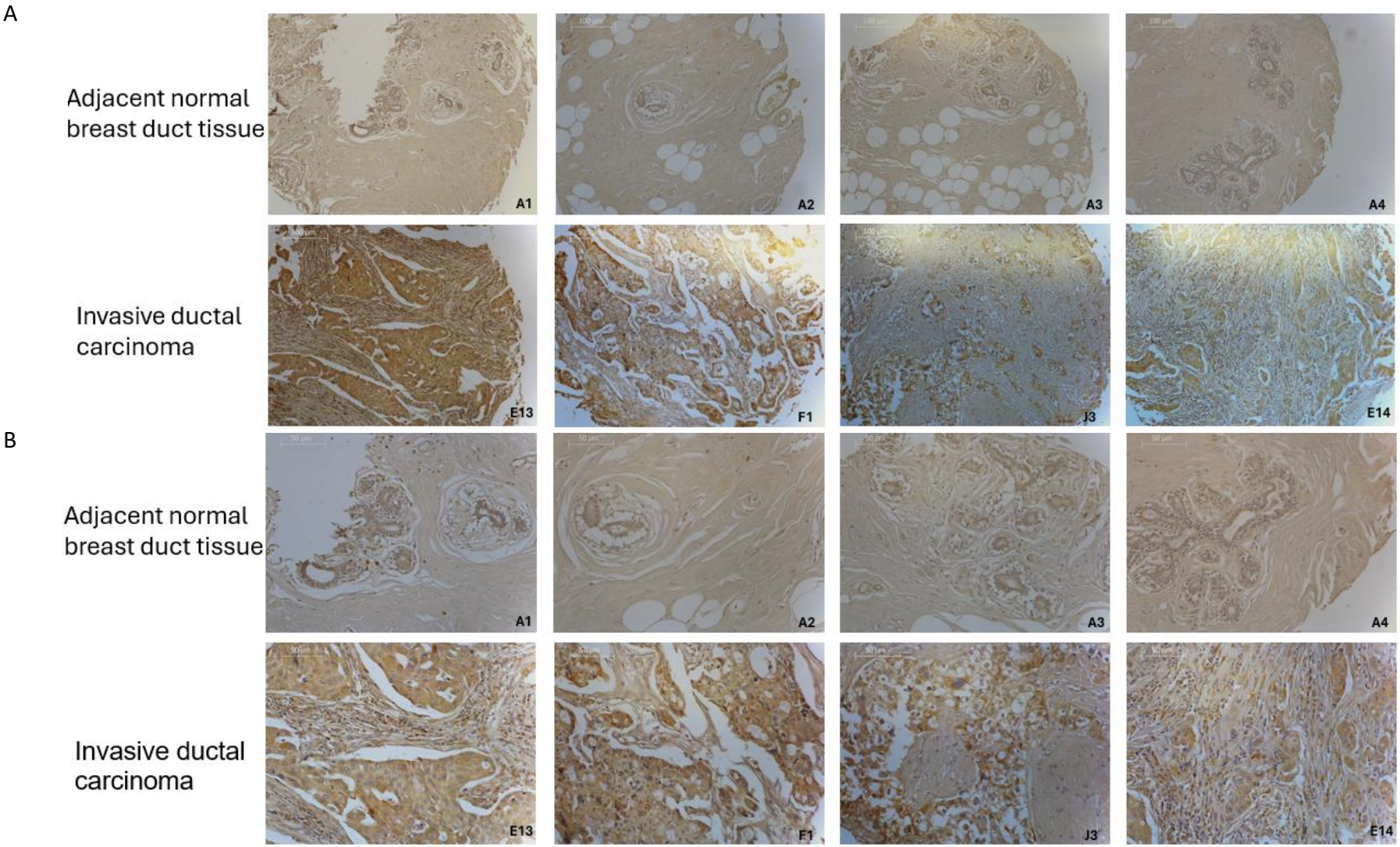

Figure 5.18 Representative images of MarvelD3 staining in breast cancer TMA (BR1503f) among adjacent normal breast duct tissues and invasive ductal carcinoma. A. Magnification: 10x, scale bar: 100µm. B. Magnification: 20x, scale bar: 50µm.

Table 5.6 Information of representative samples of breast cancer TMA (BR1503f)

Position	Age	Sex	Organ/ Anatomic Site	Pathology diagnosis	TNM	Gade	Type
A1	46	F	Breast	Adjacent normal breast duct tissue	-	-	NAT
A2	46	F	Breast	Adjacent normal breast duct tissue	-	-	NAT
A3	42	F	Breast	Adjacent normal breast duct tissue	-	-	NAT
A4	42	F	Breast	Adjacent normal breast duct tissue	-	-	NAT
E13	60	F	Breast	Invasive ductal carcinoma	T2N2M0	2	Malignant
E14	60	F	Breast	Invasive ductal carcinoma	T2N0M0	2	Malignant
F1	50	F	Breast	Invasive ductal carcinoma	T3N0M0	2	Malignant
J3	58	F	Breast	Invasive ductal carcinoma	T2N0M0	3	Malignant

5.3.2.5 Implications of MarvelD3 expression on clinical outcome of patients with breast cancer

MarvelD3 expression and its correlation with breast cancer patients' survival was explored in a Cardiff cohort. Based on the transcript expression levels of MarvelD3, patients were divided into two groups, high levels of MarvelD3 and low levels of MarvelD3, using the ROC as the cut-off value. Kaplan-Meier survival analysis was conducted in SPSS; the results are shown in Figure 5.19 and Figure 5.20. Patients with a high expression of MarvelD3 had significantly lower overall survival (OS) and disease-free survival (DFS) of 84.2 months (95%C.I. 54.4-113.9 months) and 77.1 months (95%C.I. 47.9-106.2 months) respectively, compared with those with low levels expression at 135.3 months (95%C.I. 123.8-146.8 months) and 128.4 months (95%C.I. 115.4-141.4 months) respectively (P=0.027 and p=0.03 for OS and DFS respectively).

In order to seek more evidence of MarvelD3 on breast cancer patients' survival, we also analyzed an independent cohort online. To conduct this, the data on breast cancer was found via the Kaplan-Meier Plotter (www.kmplot.com), and two probes, 239350_at and 239148_at, were used. As shown in Figure 5.21, patients with high levels (best cut-off value according to KMplot) also had shorter overall survival (P=0.0089 and P=0.043 respectively) (Figure 5.21 upper) and shorter disease-free survival (P=0.00033 and P=0.0051 respectively) (Figure 5.21 lower) in both probes. Overall, this independent data is in support of the findings from the Cardiff cohort.

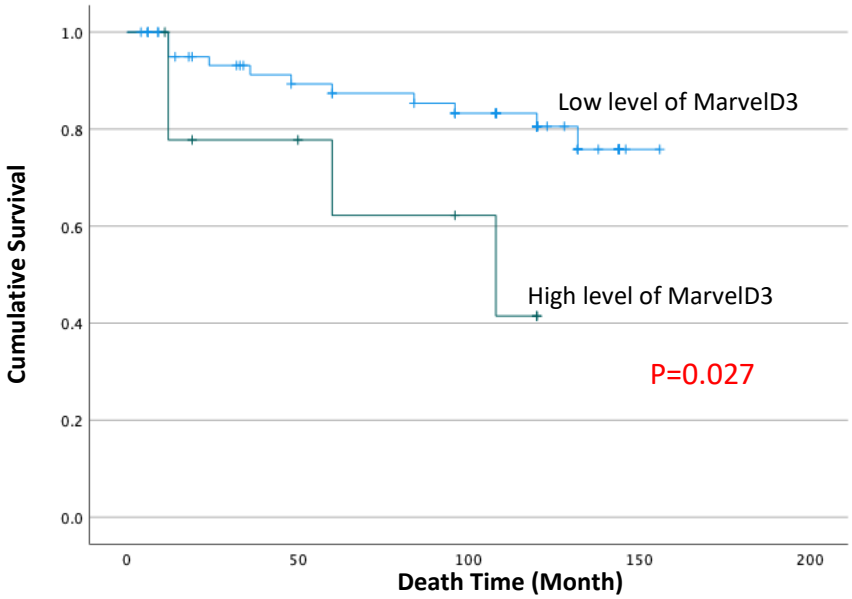

			Censored		Mean			
							95% confidence Interval	
	Total N	N of Events	N	Percent	Estimated	Std. Error	Lower Bound	Upper bound
Low level	66	11	55	83.3%	135.300	5.880	123.775	146.825
High level	10	4	6	60.0%	84.148	15.173	54.439	113.917
Overall	76	15	61	80.3%	130.940	5.943	119.292	142.588

Figure 5.19 The Kaplan-Meier survival model of correlation between MarvelD3 transcript levels and breast cancer patients' overall survival. Using the ROC in the tumour group as the cut-off to divide patients into two groups with high and low MarvelD3 level. Patients with high levels of MarvelD3 tend to have lower overall survival.

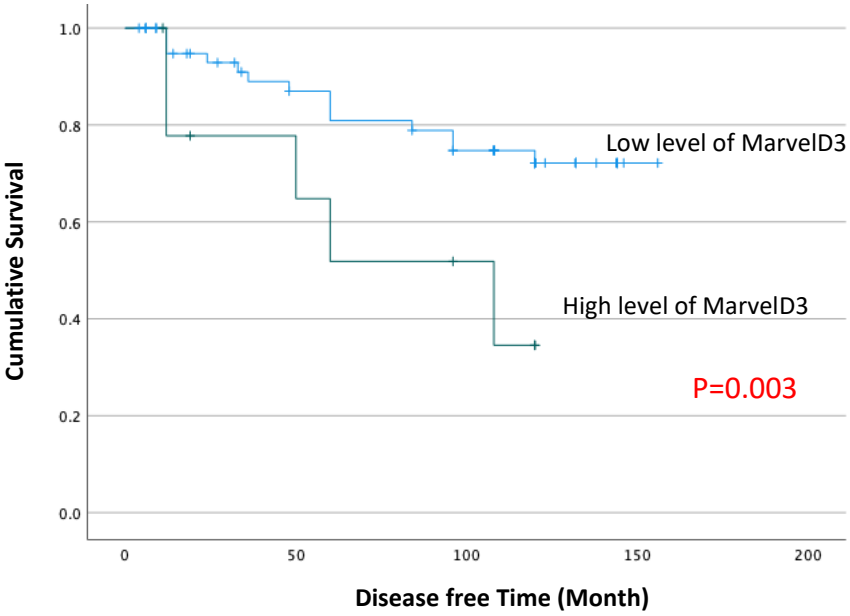

			Censored		Mean			
							95% confidence Interval	
	Total N	N of Events	N	Percent	Estimated	Std. Error	Lower Bound	Upper bound
Low level	64	14	50	78.1%	128.379	6.645	115.355	141.403
High level	10	5	5	50.0%	77.074	14.883	47.903	106.245
Overall	74	19	55	74.3%	123.259	6.572	110.379	136.140

Figure 5.20 The Kaplan-Meier survival model of correlation between MarvelD3 transcript levels and breast cancer patients' disease-free survival. Using the ROC in the tumour group as the cut-off to divide patients into two groups with high and low MarvelD3 level. Patients with high levels of MarvelD3 tend to have lower disease-free survival.

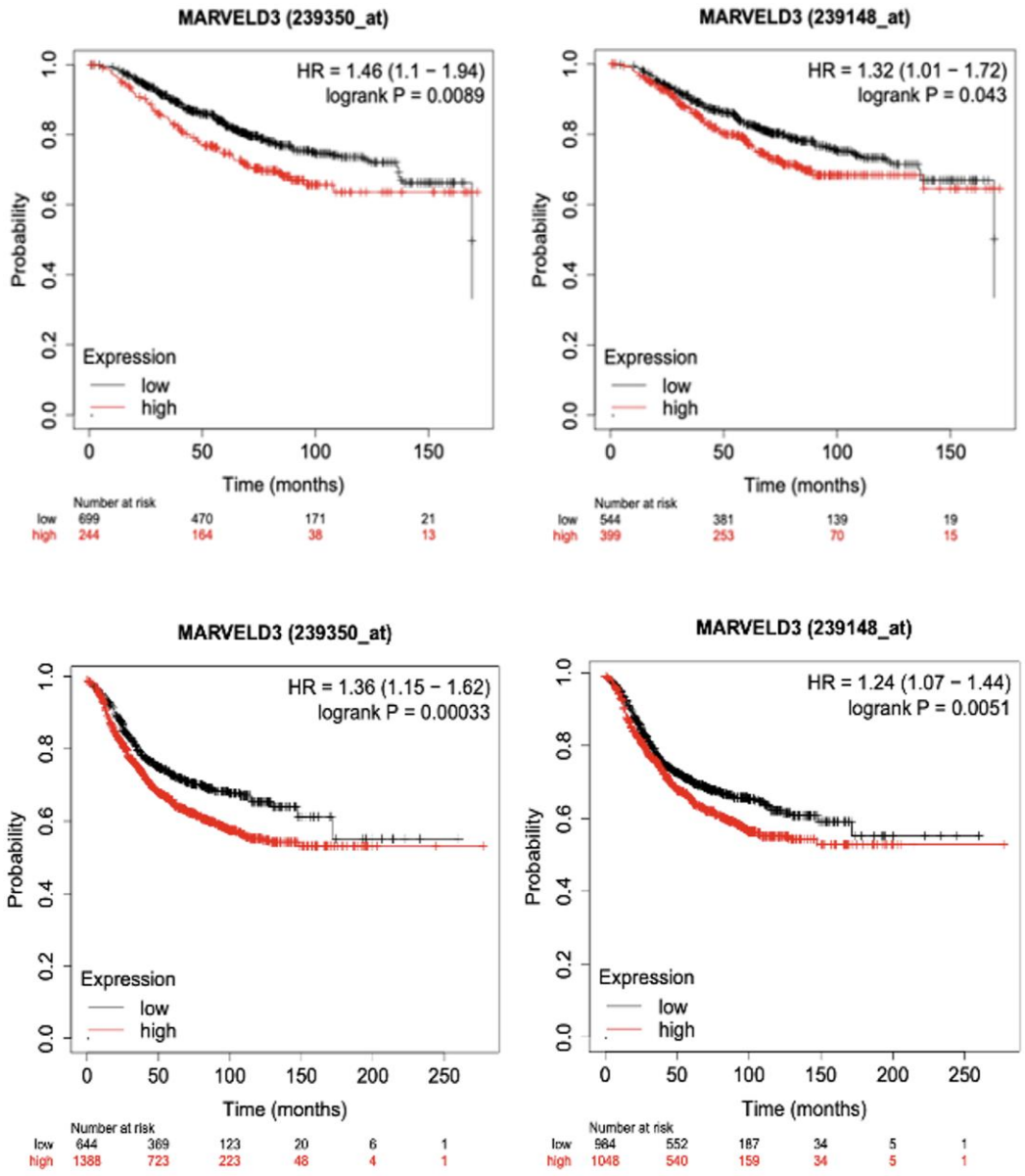

Figure 5.21 Survival Curve showing the impact of MarvelD3 expression on survival of breast cancer patients. Data was collected from Kaplan-Meier Plotter(www.kmplot.com). Patients with high levels of MarvelD3 tended to have a shorter overall (upper) and disease-free survival (lower) in both probes 239350_at and 239148_at.

5.4 Discussion

Within the limited literature investigating the expression level of MarvelD3 in human tumours, it was revealed that MarvelD3 might be involved in the progression of various cancers, exhibiting both tumour-promoting and tumour-suppressing roles depending on the context. In oral squamous cell carcinoma (OSCC), a cohort study based on the TCGA online database

suggested that MarvelD3 level was upregulated in human oral squamous cell carcinoma compared with normal tissue, and the elevated MarvelD3 expression contributed to the aggressiveness of OSCC, suggesting that MarvelD3 may promote tumour invasion and metastasis in this cancer type (Huang et al. 2022). Conversely, in hepatocellular carcinoma (HCC), MarvelD3 functions as a tumour suppressor. Li et al. reported significantly lower levels of MarvelD3 in HCC tissues than in adjacent normal tissues. The downregulation of MarvelD3 correlated with advanced tumour stages, indicating its potential role in inhibiting tumour progression in HCC levels (Li et al. 2021a). Similarly, in non-small cell lung cancer (NSCLC), MarvelD3 expression was significantly reduced in tumour tissues relative to para-carcinoma tissues. Also, the decreased MarvelD3 levels were associated with tumour metastasis, reinforcing the tumour-suppressive function of MarvelD3 in NSCLC (Li et al. 2023). Based on these studies, it is highlighted the dualistic nature of MarvelD3 in cancer progression. Also, studies examining the role of MarvelD3 in breast and colorectal cancer are very few, and the correlation between MarvelD3 and clinical outcomes in these two cancer types is still not clear. In this study, we evaluated MarvelD3 expression levels in the GEO datasets, the independent Cardiff breast cancer and colorectal cancer cohort, and TCGA.

The colorectal cancer cohort comprised 84 normal tissues and 94 colorectal cancer tissues, with 68 tumour tissues being paired. MarvelD3 transcript levels were higher in the tumour samples compared with the normal tissues ($p<0.0001$). This trend persisted when analyzing the paired tumour and normal tissues ($p<0.0001$). Consequently, the analysis of this CRC cohort suggests that at the mRNA level, Marveld3 is upregulated in CRC tumours compared with normal tissues, suggesting a potential role for MarvelD3 in the early stage of colorectal cancer tumour development. However, this finding is opposite to results gained from the online dataset GDS4382, in which the expression of MarvelD3 seems to be higher in the CRC normal tissues than that of the cancer tissues. One possible reason for this difference could be the cohort size. From the Cardiff cohort, there are 178 samples in total, while there are 34 samples for the GEO dataset. Another potential explanation for this discrepancy lies in the methodology used for collecting and extracting cancerous samples. For the cohort used in this study, part of the extracted samples are cancerous tissues; the samples also contain some non-cancerous tissues, including stromal cells (fibroblasts and endothelial cells), basal cells and immune cells, while the whole sample was homogenized to simplify the extraction

process. Consequently, the exact proportion of cancerous cells within the samples remains unclear, making the transcript levels of MarvelD3 potentially highly dependent on this variable.

In the Cardiff cohort, there was no significance found regarding pathological characteristics. Interestingly, transcript expression of MarvelD3 showed a negative correlation with the T stage (no statistical significance), which is opposite to the proposed tumour promotor role of MarvelD3. One of the possible reasons is the small number of samples. Only 2 samples were identified as T1 and 18 samples as T4 stage. When examining metastasis status, previous studies reported that MarvelD3 could inhibit the migration and proliferation abilities in the CRC Caco2 cell line, which are related to metastasis (Steed et al. 2014). The CRC cohort showed a trend that samples without metastasis exhibited higher MarvelD3 expression, although statistical significance was not reached. This trend aligns with observations from the GEO dataset GDS4396, with one of the probes reaching statistical significance ($p=0.0113$). Collectively, these findings suggest a potential role of MarvelD3 in CRC progression.

To gain a deeper understanding of MarvelD3's role in clinical CRC, we conducted immunohistochemistry (IHC) staining on colon cancer tissue microarrays (TMA). The results indicated that MarvelD3 protein levels were significantly higher in normal colon tissues compared to tumour tissues, which contrasts with the findings from our clinical cohort. Furthermore, MarvelD3 expression was generally lower in more advanced clinical stages than in less aggressive stages, consistent with the cohort results.

Several factors might explain these discrepancies in MarvelD3 expression in normal and tumour tissues between the clinical cohort and the TMA. Firstly, our clinical cohort is substantially larger and includes more normal tissues than the TMA cohort (80 vs. 7), enhancing its statistical power and reliability. Secondly, in our clinical cohort, the samples were fresh-frozen, which allowed us to perform a quantitative analysis of the MarvelD3 mRNA levels. This means we could measure the exact amount of MarvelD3 mRNA in the samples, providing precise data. In contrast, the TMA study used archival samples, which are preserved tissues stored for long periods. These samples are typically used for qualitative analysis, meaning that they provide information about whether MARVELD3 is present or absent, and

perhaps its general level (high or low) but not the exact quantity. This difference in sample nature affects the robustness of the results. Thirdly, potential discrepancies between gene transcription and protein translation for MarvelD3 cannot be excluded. Lastly, protein evaluation in this study was performed using IHC staining and scoring. Even though the intensity scores were determined independently by three researchers, it is still more subjective compared to the more specific laboratory techniques used for RNA extraction and analysis.

It is noteworthy that a distinct correlation between MarvelD3 transcript level and the clinical outcome of the patients with colorectal cancer was established with the present study and those from the independent cohort (Kaplan-Meier Plotter). Kaplan-Meier based survival analysis in the Cardiff clinical cohort indicated that patients with high expression of MarvelD3 had a significantly lower overall survival of 30.3 months compared to 131.4 months for patients with low MarvelD3 expression ($p=0.004$). Also, the same trend was found when considering disease-free survival, with 29.3 months for high-level MarvelD3 and 128.8 months for low-level ($p<0.001$). The data available from the Kaplan-Meier Plotter (www.kmplot.com), with a larger cohort, showed the same tendency between MarvelD3 expression and the overall survival, which reached statistical significance ($p=0.013$). However, the result for DFS from the Kaplan Meier Plotter is opposite from the Cardiff cohort, in which high expression of MarvelD3 contributes to significantly longer DFS. The difference in disease-free survival (DFS) results between our clinical cohort and the KMplot online tool might be due to several factors. Firstly, there is a difference in cohort composition, as our cohort may represent a specific demographic or have distinct clinical characteristics from the unique hospital (e.g., treatment protocols, stages of cancer, or genetic profiles), whereas KMplot aggregates data from multiple studies with a broader, more heterogeneous population. Secondly, data processing methods differ, with KMplot using preset algorithms to define high and low MarvelD3 expression based on best cut-off points, which might not match the ROC cut-off we used. Lastly, sample size and statistical power could also contribute to variability—the KMplot dataset contains 863 patients with high MarveelD3 expression while our cohort only has 4 patients categorized as high expression of MarvelD3. These factors can collectively lead to different survival outcome patterns between the two analyses.

Within the breast cancer cohort, containing 33 normal breast samples and 127 breast tumour samples (27 paired tumour samples), the transcript levels of MarvelD3 in the breast cancer tumour group were significantly higher than that of the normal group. (p=0.0114). Also, the expression of MarvelD3 was significantly upregulated in the paired tumour group compared with normal breast tissues (p=0.0121). This observation was further verified with an independent online GEO dataset, GSE42568, containing three individual probes. MarvelD3 expression was found to be significantly higher in the tumour group when compared with the normal group for all probes in the GEO dataset. In terms of the pathological characteristics, in the breast cancer cohort, the expression of MarvelD3 showed a positive correlation with tumour grade, even though no significance was observed. While in the same online GEO dataset, the same trend was observed. However, no obvious trend was found regarding NPI and TNM stages. Interestingly, an observable trend indicated higher MarvelD3 expression in metastatic breast cancer samples compared to non-metastatic ones, although this difference did not reach statistical significance. This trend was further validated with the TCGA online database containing larger sample sizes. Collectively, MarvelD3 is more highly expressed in tumours compared with normal breast tissues at the mRNA level, predicting a possible role of MarvelD3 in breast cancer progression.

IHC staining and scoring of the breast tumours and adjacent normal breast tissues indicated that the MarvlD3 protein levels were higher in invasive ductal carcinoma compared to the adjacent normal breast duct tissues, which is in line with our clinical cohort. However, no clear trend was observed for MarvelD3 expression concerning the differentiation and clinical stages of the tumour tissues. This lack of a discernible pattern may be attributed to the limited sample size, which restricts the ability to draw definitive conclusions regarding the relationship between MarvelD3 levels and tumour progression.

The Cardiff breast cancer cohort and the independent cohort (KMplot) can also establish a correlation between MarvelD3 expression and the clinical outcome of patients with breast cancer. In our cohort, highly expressed MarvelD3 had a shorter overall survival of 84.2 months compared to 135.3 months for patients with low expression of MarvelD3 (p=0.027). Also, patients with high levels of MarvelD3 had significantly shorter disease-free survival of 77.1 months compared with its counterpart of 128.4 months (p=0.03). The present finding is in line

with the result collected from Kaplan-Meier Plotter (www.kmplot.com), in which patients with high levels of MarvelD3 had shorter overall survival (P=0.0089 and P=0.043 respectively) and shorter disease-free survival (P=0.00033 and P=0.0051 respectively) in two probes, 239350_at and 239148_at. Collectively, these data indicate that MarvelD3 are linked to the clinical outcome of patients with breast cancer.

In summary, the details of the experiments and their results are summarized in the table listed below:

Cancer types	**Experiments**	**Results**
Colorectal cancer	Expression profile of MarvelD3 in GEO database	MarvelD3 transcript level was significantly higher in the normal tissues than that in tumour tissues. Moreover, primary lesion exhibits higher MarvelD3 expression compared with metastatic lesions.
	Transcript level of MarvelD3 in colorectal cancer cohort	MarvelD3 transcript level was significantly higher in the tumour tissues than that in the normal tissues.
	Further analysis of The Cancer Genome Atlas (TCGA) database	The expression of MarvelD3 in the T4 stage was significantly lower than in other pathological stages
	MarvelD3 expression in colorectal cancer at the protein level, analysis by IHC	MarvelD3 staining was weaker in most of the colon tumour tissues compared with normal colon tissues. Moreover, less aggressive CRC tissues exhibited higher MarvelD3 expression compared to more aggressive ones.
	Implications of MarvelD3 expression on clinical outcome of patients with CRC	Patients with a high expression of MarvelD3 had significantly lower overall survival and disease-free survival.
Breast cancer	Expression profile of MarvelD3 in breast cancer online database	MarvelD3 transcript level is significantly higher in the breast cancer samples compared with normal breast samples.
	Transcript expression of MarvelD3 in the clinical breast cancer cohort	MarvelD3 transcript level was significantly higher in the tumour tissues than that in the normal tissues.
	Further analysis of The Cancer Genome Atlas (TCGA) database	The transcript expression of MarvelD3 was significantly lower in samples with metastasis compared to those without metastasis.

	MarvelD3 expression in breast cancer at the protein level, analysis by IHC	Adjacent normal breast tissues exhibited relatively weak MarvelD3 staining compared to invasive ductal carcinoma tissues.
	Implications of MarvelD3 expression on clinical outcome of patients with breast cancer	Patients with a high expression of MarvelD3 had significantly lower overall survival and disease-free survival.

Overall, the expression patterns of MarvelD3 in both colorectal and breast cancer indicate its significant role in tumorigenesis and potential as a diagnostic and prognostic marker. The observed upregulation of MarvelD3 in tumour tissues and its association with poorer survival outcomes in both cancers support the important role of MarvelD3 in CRC and BRCA development and progression. Further work is warranted to investigate the role of MarvelD3 in cellular functions in CRC and BRCA.

Chapter-6 The functional significance of MarvelD3 in colorectal cancer and breast cancer

6.1 Introduction

MarvelD3 has been suggested to act as a tumour suppressor in certain cancer types, including hepatocellular carcinoma (HCC) (Li et al. 2021a). MarvelD3 can inhibit EMT and cell migration by suppressing the Wnt/β-catenin signalling pathway in non-small cell lung cancer (NSCLC) (Li et al. 2023). While some other studies have shown that MarvelD3 could act as a cancer promotor, including oral squamous cell carcinoma (Huang et al. 2022). However, it is unclear what role MarvelD3 plays in colorectal cancer (CRC). The analysis of the clinical cohort does not keep in line with the online dataset. This may be due to several factors, including the different nature of samples, the size of the datasets, or maybe different experimental techniques. It would suggest that MarvelD3 is involved in cancer progression and development in different cancer types. Therefore, it is important to understand the way that MarvelD3 impacts colorectal cancer biological functions.

Recently, MarvelD3 was found to be abnormally expressed in solid tumours, although the expression level differs in different tumour cell lines. In pancreatic cancer, MarvelD3 expression is highly expressed in HPAC cells compared with PANC-1 cells at both mRNA level and protein level (Kojima et al. 2011). In some other cancer types, it was shown that the expression of MarvelD3 was strongly correlated with invasive phenotypes. In breast cancer, MarvelD3 expression in MDA-MB-231, a cell line characteristic as more invasive, was significantly lower than that of MCF-7 at the protein level. Similarly, in prostate cancer, PC3 cells, which have relatively higher invasion potential, showed downregulated expression of MarvelD3 when compared with P3E6 and LnCap cells, which have a lower MarvelD3 level and are less invasive (Steed et al. 2014).

MarvelD3 knockdown and overexpression models in different cancer cell lines have been conducted with several methods. In previous studies, siRNA (interfering RNA) was used to knockdown MarvelD3 in colorectal cancer Caco2 cells (Raleigh et al. 2010b), non-small cell lung cancer HCC827 and PC9 cells (Li et al. 2023), hepatocellular carcinoma cells Hep3B and Huh-7 (Li et al. 2021a), and human pancreatic cancer HPAC cells (Kojima et al. 2011). shRNA was used to over-express MarvelD3 in hepatocellular carcinoma cells Hep3B and Huh-7 (Li et al. 2021a), and NSCLC HCC827 and PC9 cells (Li et al. 2023).

Several studies found that either knockdown or overexpression of MarvelD3 in different cancer cells lines lead to changes in their cellular biological function. *In vitro*, experiments showed that the absence of MarvelD3 could promote migration and invasion ability of NSCLC HCC827 and PC9 cells with no significant change in proliferation potential. On the contrary, overexpression of MarvelD3 reduced the ability of migration on HCC827 and PC9 cells, still the proliferation ability was not changed (Li et al. 2023). Similarly, another study showed that the silence of MarvelD3 could significantly upregulate cellular migration and invasion behaviors in HCC Hep3B and Huh-7 cells, while no significant proliferation changes were found (Li et al. 2021a). *In vitro* study found that loss of MarvelD3 resulted in increased cell migration and proliferation in colorectal cancer Caco2 cells. *In vivo,* the xenografted experiment showed that overexpression of MarvelD3 could strongly suppress the proliferation of tumour MIA PaCa-2 cells (Steed et al. 2014).

Current studies on the mechanisms of MarvelD3 in cancer are limited and, therefore, not sufficient to confirm its roles. In Chapter 5, it is clearly shown that MarvelD3 has an important clinical correlation with colorectal cancer and breast cancer. In this chapter, CRC and breast cancer cell models with different MarvelD3 expression profiles were built in order to investigate the effects of MarvelD3 on the cellular function of colorectal cancer and breast cancer.

6.2 Methods

6.2.1 Cell culture

In this chapter, breast cancer cell lines MDA-MB-231, MCF-7, BT-549, ZR-751, SKBR3 and colorectal cancer cell lines RKO, HT115, HRT18, Caco-2 were used. Details of cell culture are listed in Chapter 2.2.2.

6.2.2 RNA extraction, PCR, and qPCR

In this chapter, PCR and qPCR assessments were conducted to screen MarvelD3 expression in breast and colorectal cancer cell lines and to verify the knockdown efficacy at the mRNA level

following the transfection of cells. For PCR results, the expression in each cell line was quantified using Image J, semi-quantification band densitometry, and normalized against GAPDH. For qPCR results, data was normalized against GAPDH. Data was analyzed using Excel, and the figures were generated using GraphPad. Details are described in Chapter 2.4.

6.2.3 Protein extraction, SDS-PAGE, and Western blot analysis

The expression of MarvelD3 in breast cancer and colorectal cancer cell lines was screened at the protein level using Western blot. Moreover, the MarvelD3 knockdown of the cells was also verified at the protein level. Protein bands were analyzed using Image J, semi-quantification band densitometry, normalized against GAPDH. Details are described in Chapter 2.5.

6.2.4 Thiazolyl Blue Tetrazolium Bromide (MTT) based Killing curve

An MTT-based killing curve for colorectal cancer cell lines HRT-18, CaCo-2, and breast cancer cell lines MCF-7 and SKBR3 were performed to select the correct concentration of cell transfection and selection. Cells were seeded into the 96 well plates with different densities, and 5 sets of different concentrations of puromycin were designed, as listed in Table 6.1. Data was collected, normalized, analyzed using Excel, and presented as line chats using GraphPad. Details are described in Chapter 2.3.2.

Table 6.1 Seeding density and puromycin concentration used for the MTT killing curve experiment

Cell line	Seeding density	Puromycin concentration set
HRT-18	$2x10^4$ cells/ml	0μg/ml, 1μg/ml, 2μg/ml, 3μg/ml, 5μg/ml
CaCo-2	$2x10^4$ cells/ml	0μg/ml, 3μg/ml, 5μg/ml, 8μg/ml, 10μg/ml
MCF-7	$3x10^4$ cells/ml	0μg/ml, 0.5μg/ml, 1μg/ml, 2μg/ml, 3μg/ml
SKBR3	$3x10^4$ cells/ml	0μg/ml, 0.5μg/ml, 1μg/ml, 1.5μg/ml, 2μg/ml

6.2.5 Cell transfection

In this study, all knockdown cell line models were generated using shRNA-based transfection,

as discussed in Chapter 2.3.1. After cell transfection, puromycin with different concentrations, based on the killing curve, was used to select the cells and kill the cells without resistance genes. The selection was applied for up to 3 days, depending on the confluence of the remained cells. Post-selection, the cells were cultured in the cell growth medium supplemented with puromycin at half the concentration used during the selection phase.

6.2.6 *In vitro* MTT cell growth assay

MTT assay was conducted to explore the impact of MarvelD3 on cancer cell growth. Cells were seeded with different densities: 3,000 cells/ml were seeded for Caco2, and HRT18 CRC cell lines and 5,000 cells/ml were seeded for MCF-7 and SKBR3 breast cancer cell lines. Details are described in Chapter 2.8.1.

6.2.7 *In vitro* Matrigel cell adhesion assay

Please refer to Chapter 2.8.2.

6.2.8 *In vitro* Matrigel cell invasion assay

Matrigel invasion assay was conducted to explore the impact of MarvelD3 on cancer cell invasion. Cells were seeded with different densities: 20,000 cells/ml were seeded for Caco2 and HRT18 CRC cell lines, and 40,000 cells/ml were seeded for MCF-7 and SKBR3 breast cancer cell lines. Details are described in Chapter 2.8.3.

6.2.9 *In vitro* Beads-based migration assay

HRT18 and Caco2 CRC cell lines formed clusters when they were growing; it is hard to count and identify the single cells after staining with crystal violet. Therefore, 100µl of 10% acetic acid was used to dissolve the crystal violet for 10 minutes and subsequently placed inside the LT4500 plate reader for detection at 600nm wavelength to measure the optical density (OD). For details, please refer to Chapter 2.8.4.

6.2.10 ECIS-based cell adhesion and migration assay

Please refer to Chapter 2.8.5.

6.2.11 Transepithelial Resistance (TER) and Paracellular Permeability (PCP) assay

Please refer to Chapters 2.8.6 and 2.8.7.

6.2.12 PEFE treatment with MarvelD3 transfection cells

After the cells were knocked down with MarvelD3, the cells were treated with PEFE to investigate the role of MarvelD3 in response to PEFE. For cell lines, Caco2, HRT18, MCF-7, and SKBR3, both their control group and MarvelD3 shRNA group were seeded with 80,000 cells/ml into the 96-well plate and cultured until full confluence. The PEFE was then applied at 2.2GHz with 40 watts input power levels for 5 minutes. Cell viability was assessed before the experiment (BE), 15 minutes, 24 hours, and 48 hours after the treatment.

6.2.13 Statistical analysis

In this chapter, t-tests and Mann-Whitney test were applied for statistical analysis using the GraphPad 10 software. The analysis of PCR and Western blotting bands was carried out using Image J software. The results of the ECIS assay were analyzed using the ECIS software. Statistical significance was determined at a significance level of $p<0.05$.

6.3 Results

6.3.1 MarvelD3 expression screening in different cancer cell lines

All five breast cancer (BRCA) cell lines and four colorectal cancer (CRC) cell lines were cultured from a low passage within passage number 10. Once enough confluence was formed, RNA extractions and quantification were performed with different cell lines. After reverse transcription to produce cDNA samples, both PCR and qPCR were conducted to assess the

transcript expression of MarvelD3 in different breast cancer and colorectal cancer cell lines. In parallel, the protein of these cell lines was extracted, and after quantification, a Western blot was conducted to detect the MarvelD3 expression at the protein level. Three different sets of RNA and protein samples with different passages were collected in this study, and representative PCR, qPCR, and Western blot results for MarvelD3 screening were described in the following sections.

6.3.1.1 MarvelD3 expression screening in BRCA cell lines

Figure 6.1 A represents one of the PCR screenings of MarvelD3 in breast cancer cell lines, with the expression of MarvelD3 in each cell line quantified using Image J (National Institutes of Health, USA), semi-quantification band densitometry and normalized against GAPDH. The expression of MarvelD3 in MCF-7 was set to 100% and compared with other cell lines. Data was analyzed using Excel and the figures were generated using GraphPad, as shown in Figure 6.1 B. MarvelD3 was found to be highly expressed in MCF-7, followed by ZR751 and SKBR3 among these five cell lines, while weakly expressed in MDA-MB-231 and BT549. Quantitative PCR was then conducted to confirm the expression profile. A representative qPCR result was displayed (Figure 6.1 C). Data was normalized against GAPDH and analyzed in Excel, with the figure created using GraphPad. A similar expression trend was found in the qPCR result, with the highest expression of MarvelD3 shown in MCF-7, and the expression was weakened in MDA-MB-231 and BT549. Western blot was then conducted to explore MarvelD3 expression in breast cancer wild-type cell lines at the protein levels. As demonstrated in Figure 6.2, the expression of MavelD3 was shown to be highest in MCF-7 cells among the tested cell lines, followed by ZR-751 and SKBR3, with the lowest expression found in MDA-MB-231 and BT549 cells.

Interestingly, this finding is in line with other research in which MarvelD3 expression is negatively correlated with cell invasiveness.

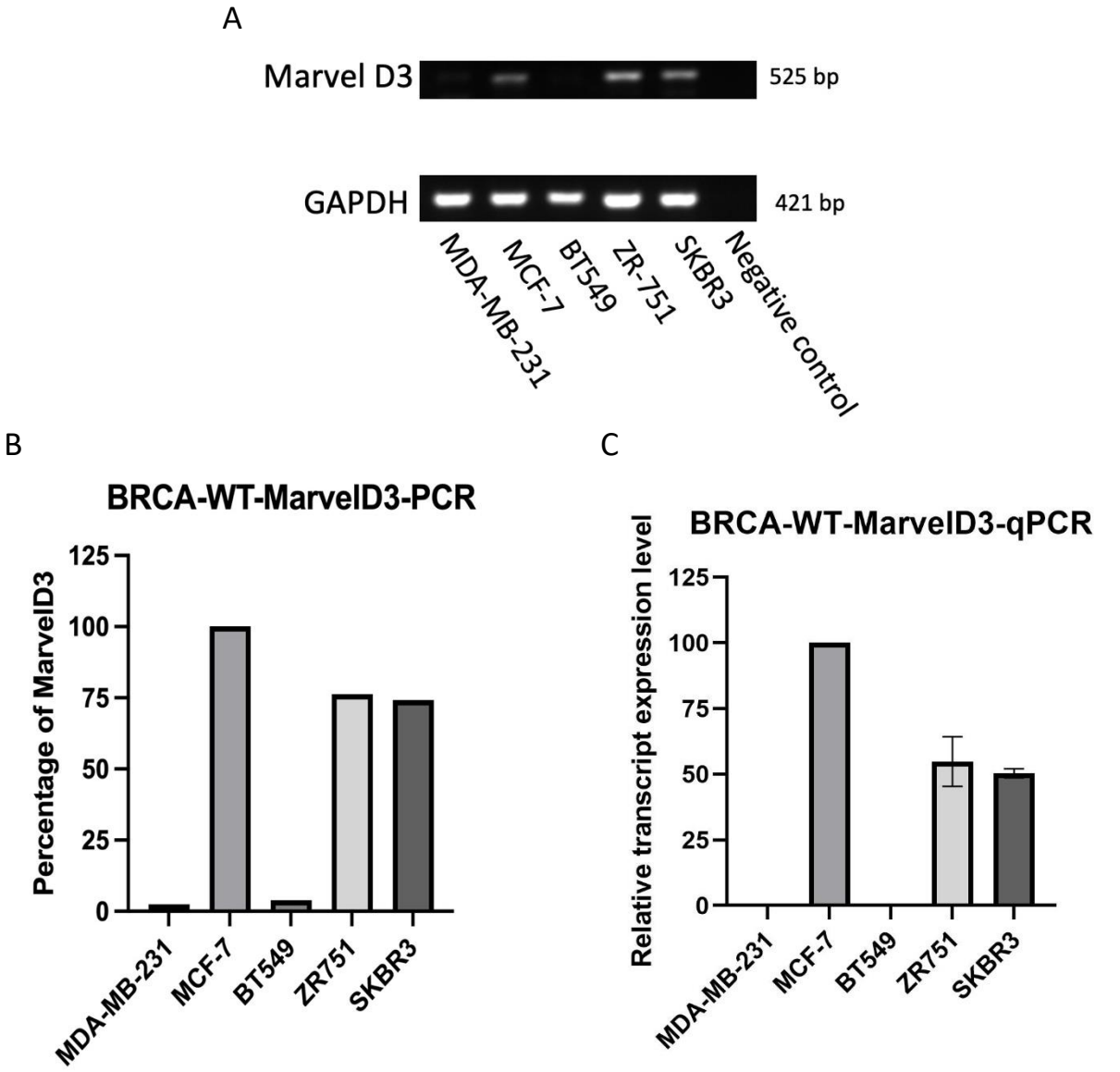

Figure 6.1 PCR and qPCR Screenings of MarvelD3 expression in breast cancer wild type cell lines. (A) Representative images of PCR screening for five breast cancer cell lines. Negative control was applied to determine whether there is any contamination of the experimental reagents. (B) Quantified PCR result using Image J normalized with GAPDH. The expression of MCF-7 was set to 100% (the highest expression among these five cell lines). (C) qPCR result for MarvelD3 screening in different breast cancer cell lines, normalized with GAPDH. Data represents mean ± SD, n=3. The expression of MCF-7 was referred to 100% for comparison.

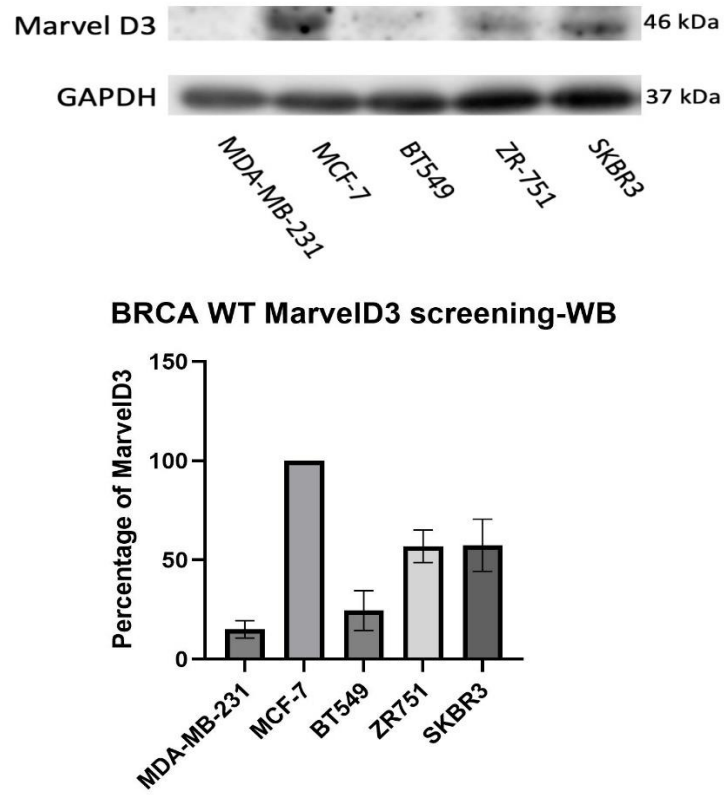

Figure 6.2 Western blot screening of MarvelD3 expression in breast cancer wild-type cell lines. Top: A representative image obtained using G box (Syngene). Down: Data from three different sets of samples were combined, and protein bands were quantified using Image J, and semi-quantification band densitometry, normalized against GAPDH. Expression of MCF-7 was set to 100% for comparison. Data shows mean ± SD, n=3.

6.3.1.2 MarvelD3 expression screening in CRC cell lines

The expression of MarvelD3 was also assessed across several common CRC cell lines. In Figure 6.3 A, a representative PCR screening of MarvelD3 in CRC cell lines is depicted. The expression of MarvelD3 in CaCo-2 was designed as 100%, serving as a reference for comparison with other cell lines, as shown in Figure 6.3 B. MarvelD3 demonstrated high expression levels in CaCo2 and HT115 among the screened cell lines, while its expression was notably weaker in RKO. To validate this expression profile, qPCR was then conducted, and a representative qPCR result was presented in Figure 6.3 C. The qPCR results mirrored the expression trend observed in PCR screening, with CaCo-2 exhibiting the highest MarvelD3 expression and the weakened expression was found in RKO.

A Western blot was then conducted to detect the MarvelD3 expression in CRC wild-type cell

lines at the protein level. Protein bands were analyzed using Image J, semi-quantification band densitometry, normalized against GAPDH, as illustrated in Figure 6.4.

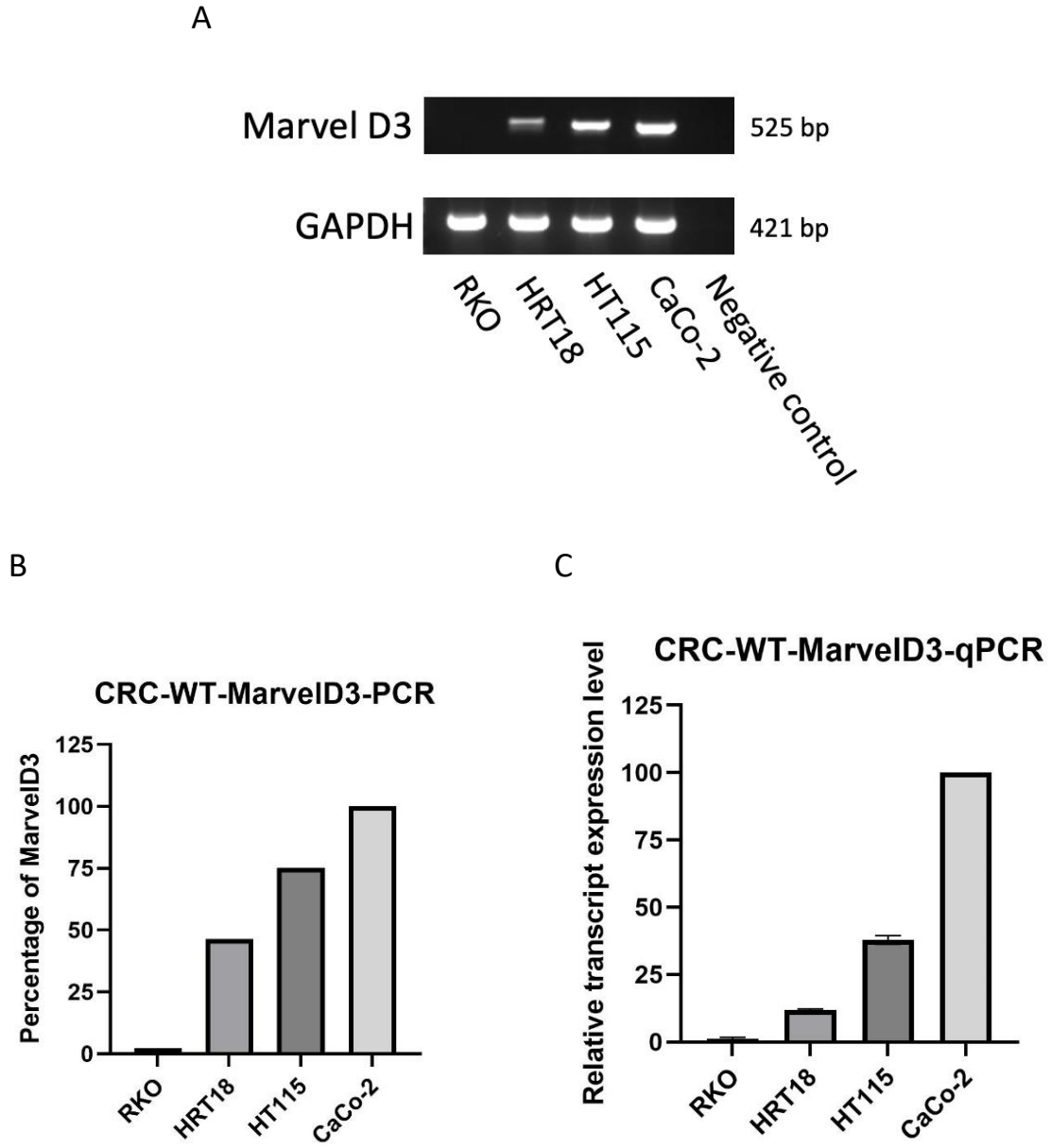

Figure 6.3 PCR and qPCR Screenings of MarvelD3 expression in colorectal cancer wild-type cell lines. (A) Representative images of PCR screening for four colorectal cancer cell lines. Negative control was introduced to check any contamination of the experimental reagents. (B) Quantified PCR result using Image J normalized with GAPDH. The expression of Caco-2 was set to 100%. (C) qPCR result for MarvelD3 screening in different colorectal cancer cell lines, normalized with GAPDH. Data represents mean ± SD, n=3. The expression of Caco-2 was referred to 100% for comparison.

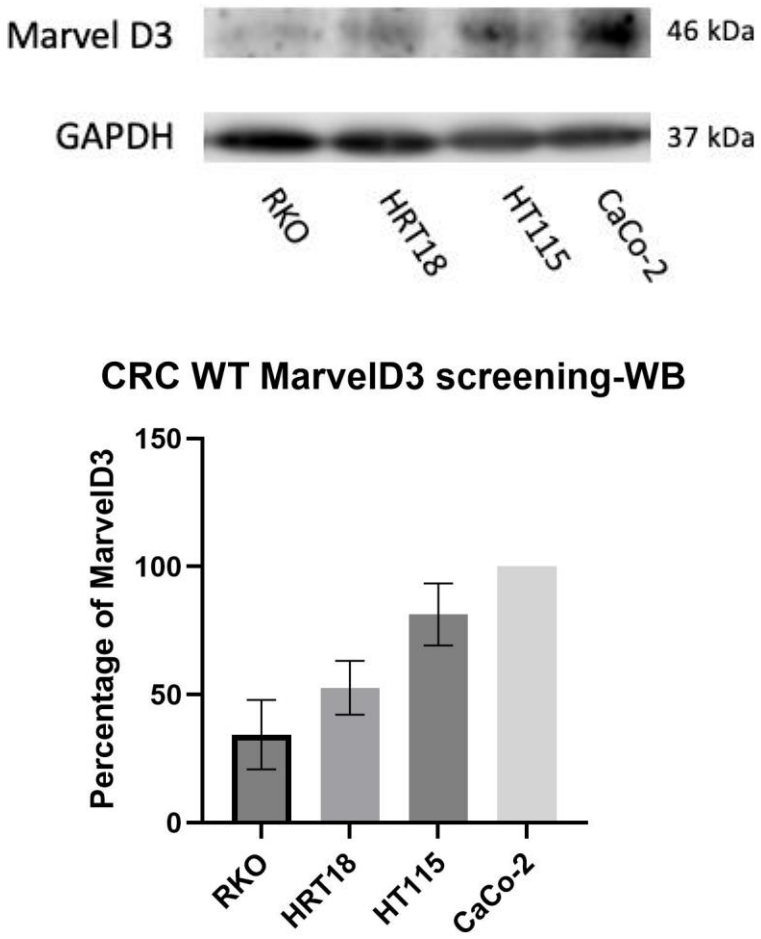

Figure 6.4 Western blot screening of MarvelD3 expression in colorectal cancer wild-type cell lines. Top: A representative image obtained using G box (Syngene). Down: Data from three different sets of samples were combined, and protein bands were quantified using Image J, and semi-quantification band densitometry, normalized against GAPDH. Expression of Caco2 was set to 100% for comparison. Data shows mean ± SD, n=3.

6.3.2 Transfection of BRCA and CRC cell lines

Based on the MarvelD3 expression profiles, MCF-7 and SKBR3 from breast cancer, and CaCo-2 and HRT18 from colorectal cancer were specifically selected to build the knockdown cell models since they exhibit relatively higher expression compared with other tested cell lines. Also, these cell lines exhibited better TJs compared with others.

6.3.2.1 Killing Curve and Transfection Process

To determine the most optimal antibiotic concentration for selecting transfected cells, an

MTT-based killing curve was conducted, assessing a range of concentrations of puromycin to establish suitable selection and maintenance conditions for the transfected cell lines. As shown in Figure 6.5 to Figure 6.8, the treatment duration lasted for 72 hours. In breast cancer cell lines, after 72 hours of puromycin treatment, 1µg/ml puromycin in MCF-7 cells exhibited an approximately 80% reduction in viable cells compared to the control (untreated) group, while a similar reduction rate was found at 2µg/ml puromycin in SKBR3. In colorectal cancer cell lines, the number of viable cells in 5µg/ml of puromycin in HRT18 was decreased by approximately 80% in response to puromycin treatment after 72 hours, while around 80% reduction was visualized in 10µg/ml for Caco-2.

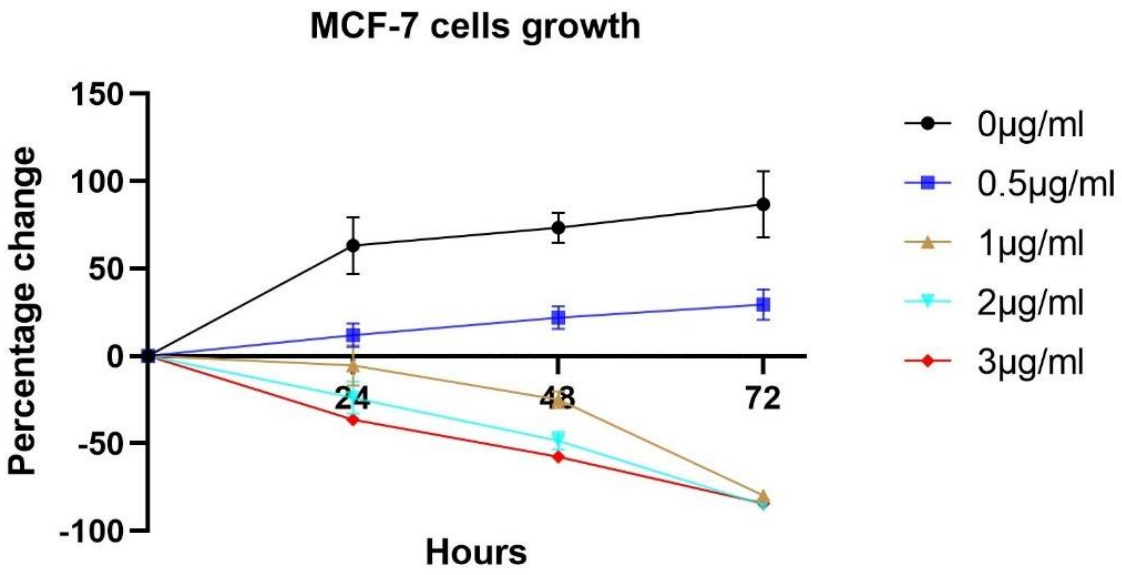

	0 Hour	24 Hours	48 Hours	72 Hours
0µg/ml	0	63.32955	73.40599	86.74791
0.5µg/ml	0	15.24332	21.98176	29.52297
1µg/ml	0	-5.25654	-24.8707	-79.647
2µg/ml	0	-23.755	-48.3678	-85.0736
3µg/ml	0	-36.4154	-57.7023	-84.168

Figure 6.5 Killing Curve of MCF-7 cell lines. Killing Curve was performed within 72 hours. Data was analysed by Excel, and the figure was generated using GraphPad, with mean +/- SD, 6 repeated for each concentration. The table below represents the percentage of MCF-7 cell growth based on the reference pattern (data shown as mean, n=6).

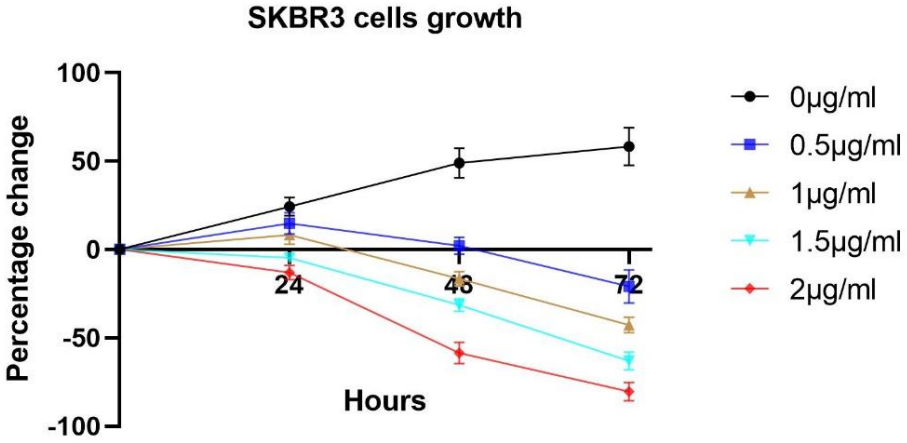

	0 Hour	24 Hours	48 Hours	72 Hours
0μg/ml	0	24.21123	48.99624	58.32475
0.5μg/ml	0	14.79794	2.129574	-20.9834
1μg/ml	0	8.2553	-16.5331	-42.7928
1.5μg/ml	0	-4.67085	-31.39	-63.0796
2μg/ml	0	-13.1058	-58.586	-80.405

Figure 6.6 Killing Curve of SKBR3 cell lines. Killing Curve was performed within 72 hours. Data was analysed by Excel, and the figure was generated using GraphPad, with mean +/- SD, 6 repeated for each concentration. The table below represents the percentage of SKBR3 cell growth based on the reference pattern (data shown as mean, n=6).

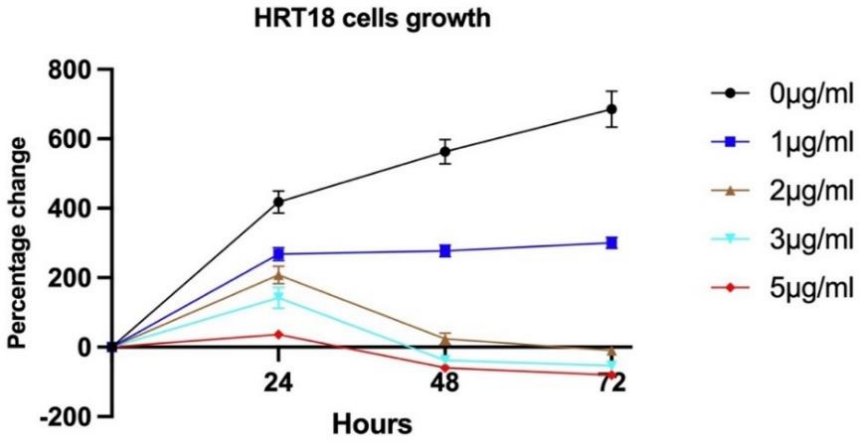

	0 Hour	24 Hours	48 Hours	72 Hours
0μg/ml	0	417.7578	562.7297	685.2143
1μg/ml	0	267.8415	276.7029	300.8124
2μg/ml	0	208.149	24.07199	-9.82377
3μg/ml	0	142.0197	-38.2202	-53.4433
5μg/ml	0	36.62042	-59.4801	-80.8149

Figure 6.7 Killing Curve of HRT-18 cell lines. Killing Curve was performed within 72 hours. Data was analysed by Excel, and the figure was generated using GraphPad, with mean +/- SD, 6 repeated for each concentration. The table below represents the percentage of HRT18 cell growth based on the reference pattern (data shown as mean, n=6).

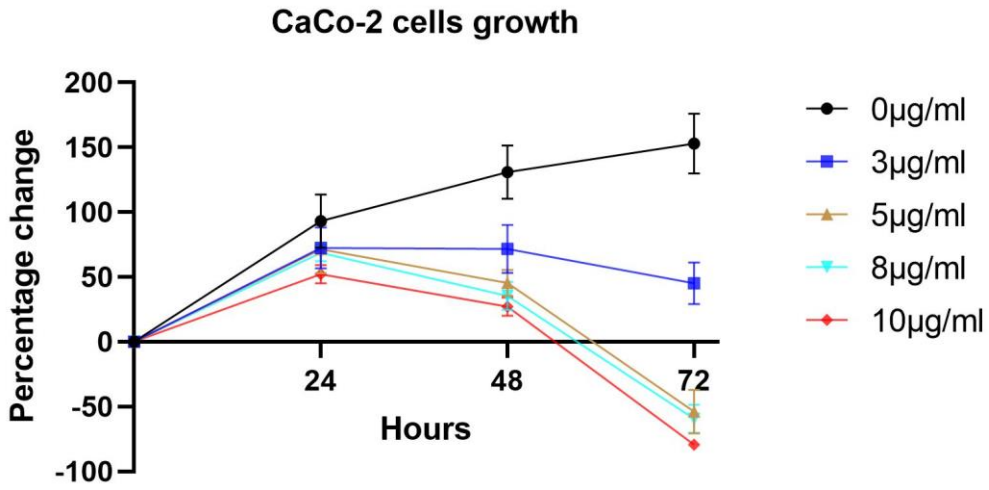

	0 Hour	24 Hours	48 Hours	72 Hours
0μg/ml	0	93.14634	130.8137	152.8343
3μg/ml	0	72.49298	71.72289	45.15124
5μg/ml	0	71.35163	45.34645	-53.9174
8μg/ml	0	68.67922	35.36874	-59.4533
10μg/ml	0	52.12018	27.24174	-79.3392

Figure 6.8 Killing Curve of CaCo-2 cell lines. Killing Curve was performed within 72 hours. Data was analysed by Excel, and the figure was generated using GraphPad, with mean +/- SD, 6 repeated for each concentration. The table below represents the percentage of Caco-2 cell growth based on the reference pattern (data shown as mean, n=6).

6.3.2.2 Knockdown of MarvelD3 in colorectal and breast cancer cell lines

6.3.2.2.1 Knockdown of MarvelD3 in colorectal cancer cell lines

shRNA-based technique was used to knockdown MarvelD3 in HRT18 and Caco-2 colorectal cancer cell lines. After transfection and puromycin selection, PCR, qPCR, and Western blot were conducted to verify the knockdown of MarvelD3 at both mRNA and protein levels.

As a representative PCR data set of three different sets of samples, the expression of MarvelD3 was significantly lower in the knockdown group compared with the control group (Figure 6.9). A similar trend was found in a representative qPCR data set, as illustrated in Figure 6.10, in which the MarvelD3 expression was decreased by around 94% for HRT18 ($p=0.008$) and 80% for Caco-2 ($p=0.004$), indicating that MarvelD3 was effectively knocked down at mRNA level in both cell lines.

A Western blot was also conducted to detect the expression of MarvelD3 in control and knockdown groups at the protein level in both cell lines. Three different sets of samples were run, and a representative result is shown in Figure 6.11. A similar trend was found as in the PCR and qPCR results. It could be found that the expression of MarvelD3 was significantly weakened in the gene knockdown group compared to the control group significantly for both HRT18 ($p<0.0001$) and Caco-2 ($p<0.0001$), indicating that MarvelD3 was successfully knocked down at the protein levels in both cell lines.

A

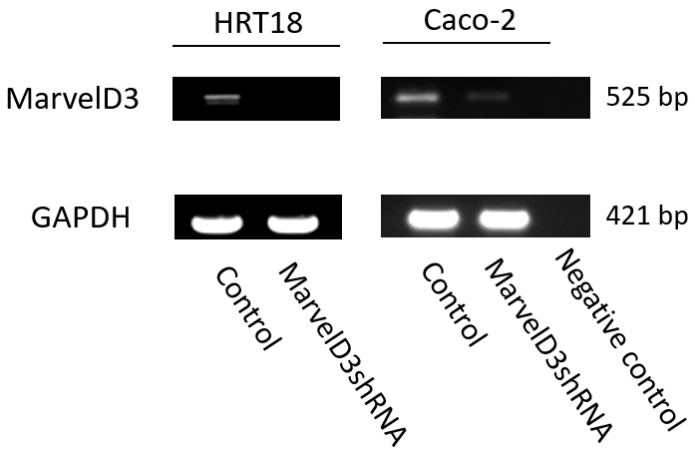

B

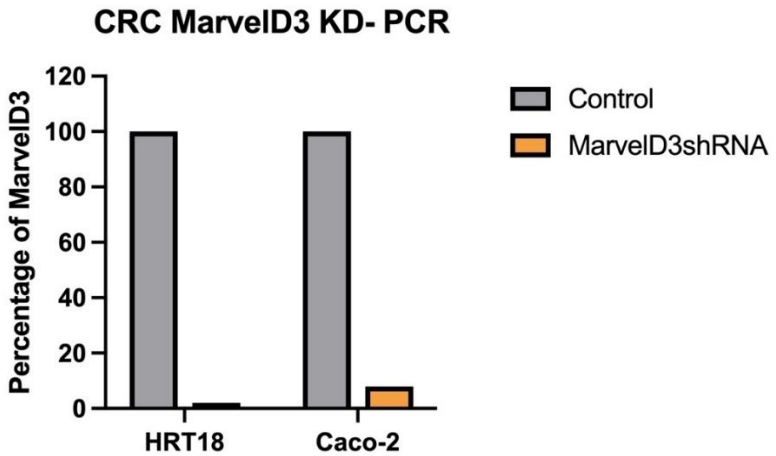

Figure 6.9 Verification of the knockdown of MarvelD3 in HRT18 and Caco-2 colorectal cancer cell lines in mRNA level using PCR. A. Representative imaging of screening MarvelD3 knockdown in HRT18 and Caco-2 CRC cell lines. B. Quantified PCR result using Image J normalized with GAPDH. The expression of Control was set to 100%.

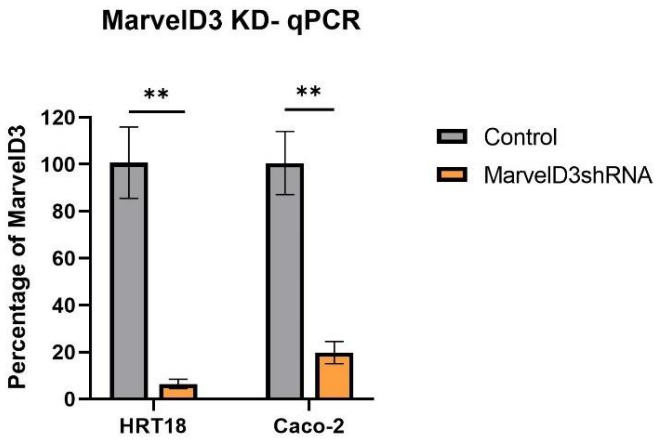

Figure 6.10 Verification of the knockdown of MarvelD3 in HRT18 and Caco-2 colorectal cancer cell lines at mRNA level using qPCR. The expressions of Control for each cell line were set to 100%, and the knockdown group compared to it. Data shows mean ± SD, n=3. ** represents $p < 0.01$.

A

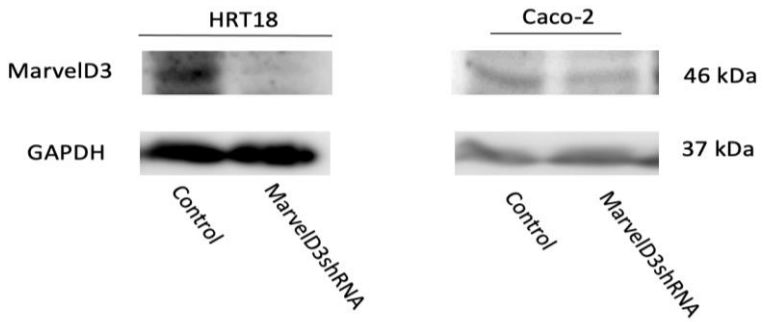

B

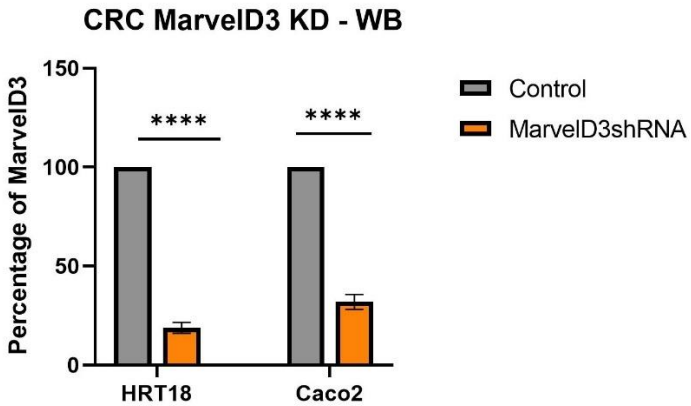

Figure 6.11 Verification of the knockdown of MarvelD3 in HRT18 and Caco-2 colorectal cancer cell lines at protein level using Western blot. A. Representative imaging of screening MarvelD3 knockdown in HRT18 and Caco-2 CRC cell lines. B. Data from three different sets of samples were combined, protein bands were quantified using Image J, and semi-quantification band densitometry was normalized against GAPDH. The expression of Control was set to 100%. Data shows mean ± SD, **** represents $p<0.0001$.

6.3.2.2.2 Knockdown of MarvelD3 in breast cancer cell lines

shRNA-based technique was used to knockdown MarvelD3 in MCF-7 and SKBR3 breast cancer cell lines. PCR, qPCR, and Western blot were conducted to verify the knockdown of MarvelD3 at both mRNA and protein levels.

A representative result of PCR is presented in Figure 6.12. The data clearly demonstrate a significant reduction in MarvelD3 expression in the knockdown group compared to the control group in both MCF-7 and SKBR3 breast cancer cell lines. This observation is corroborated by the qPCR data shown in Figure 6.13 , where MarvelD3 expression was decreased by approximately 85% for MCF-7 ($p=0.006$) and 67% for SKBR3 ($p=0.004$). These findings indicate a successful knockdown of MarvelD3 at the mRNA level in both cell lines. Western blot result further indicated that MarvelD3 was significantly knocked down in both MCF-7 ($p<0.0001$) and SKBR3 ($p<0.0001$) at the protein level (Figure 6.14).

A

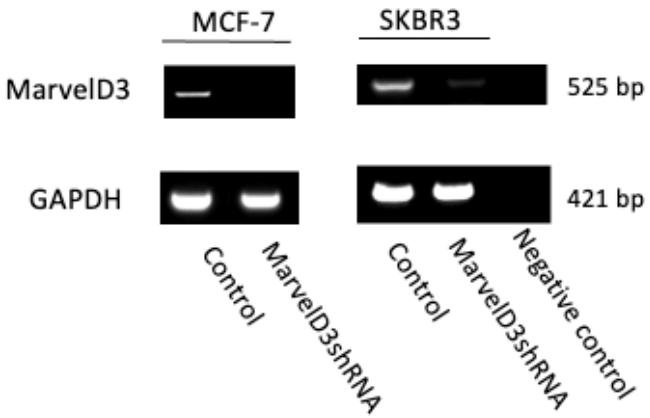

B

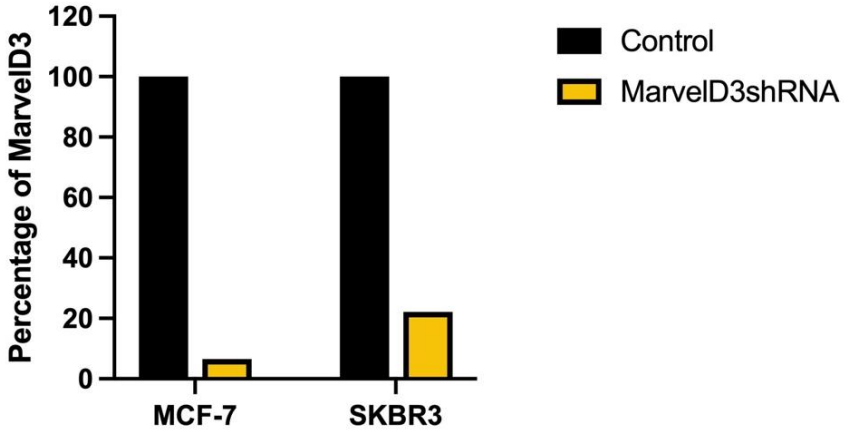

Figure 6.12 Verification of the knockdown of MarvelD3 in MCF-7 and SKBR3 breast cancer cell lines at mRNA level using PCR. A. Representative imaging of screening MarvelD3 knockdown in MCF-7 and SKBR3 BRCA cell lines. B. Quantified PCR result using Image J normalized with GAPDH. The expression of Control was set to 100%.

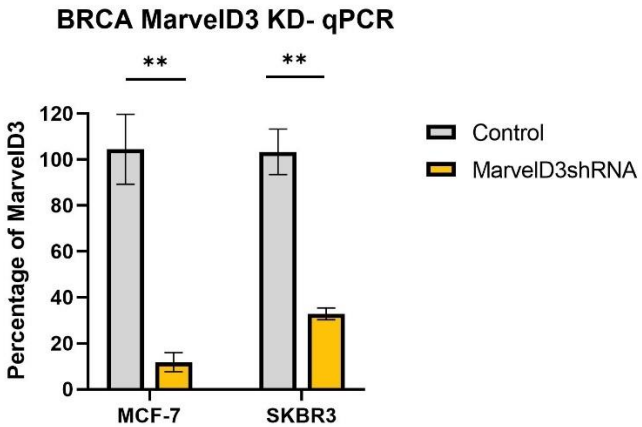

Figure 6.13 Verification of the knockdown of MarvelD3 in MCF-7 and SKBR3 breast cancer cell lines at mRNA level using qPCR. The expressions of Control for each cell line were set to 100%, and the knockdown group compared to it. Data shows mean ± SD, n=3. ** represents $p < 0.01$.

A

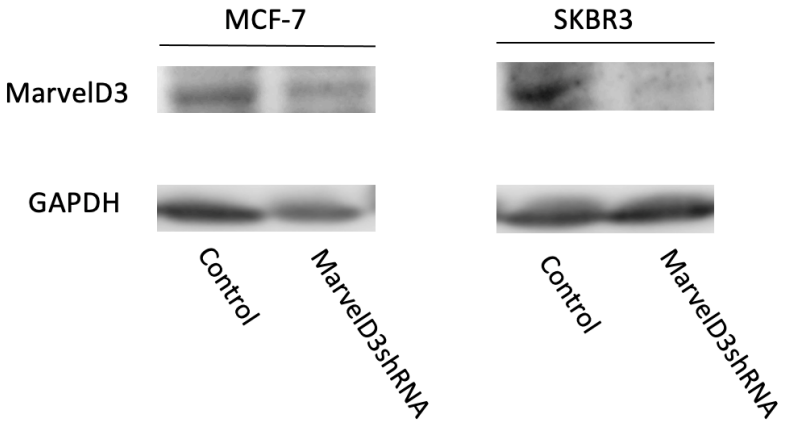

B

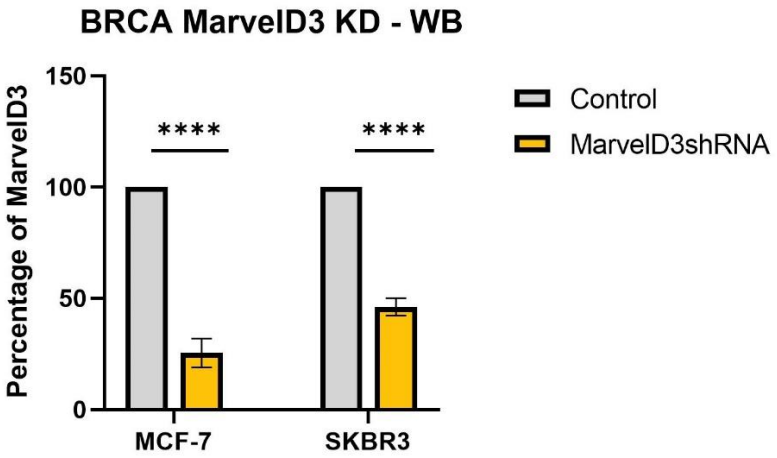

Figure 6.14 Verification of the knockdown of MarvelD3 in MCF-7 and SKBR3 breast cancer cell lines at protein level using Western blot. A. Representative imaging of screening MarvelD3 knockdown in MCF-7 and SKBR3 breast cancer cell lines. B. Data from three different sets of samples were combined and protein bands was quantified using Image J, and semi-quantification band densitometry, normalised against GAPDH. The expression of Control was set to 100%. Data shows mean ± SD, **** represents p<0.0001.

6.3.3 Impact of MarvelD3 on colorectal cancer cellular functions

6.3.3.1 Impact of MarvelD3 on colorectal cancer cells proliferation

To investigate how changes in MarvelD3 expression affect the growth of CRC cells, established MarvelD3 knockdown on HRT18 and Caco2 models was tested with an MTT-based cell growth assay over a period of five days. As shown in Figure 6.15, on Day3, HRT18 MarvelD3 knockdown (n=6, mean=452.06%) exhibited faster growth rate compared to HRT18 control (n=6, mean=348.48%) (p=0.0002). By Day 5, this difference became more pronounced. The

HRT18 MarvelD3 knockdown group (n=6, mean=1016.45%) showed significantly higher growth rate than that of HRT18 control group (n=6, mean=763.54%) (p=0.037). The same trend was found in Caco2 MarvelD3 knockdown models, in which both Day 3 and Day 5 indicated Caco2 MarvelD3 knockdown growth faster than the Caco2 control group (Figure 6.16). These results suggest that MarvelD3 plays a suppressive role in the growth of CRC cell lines.

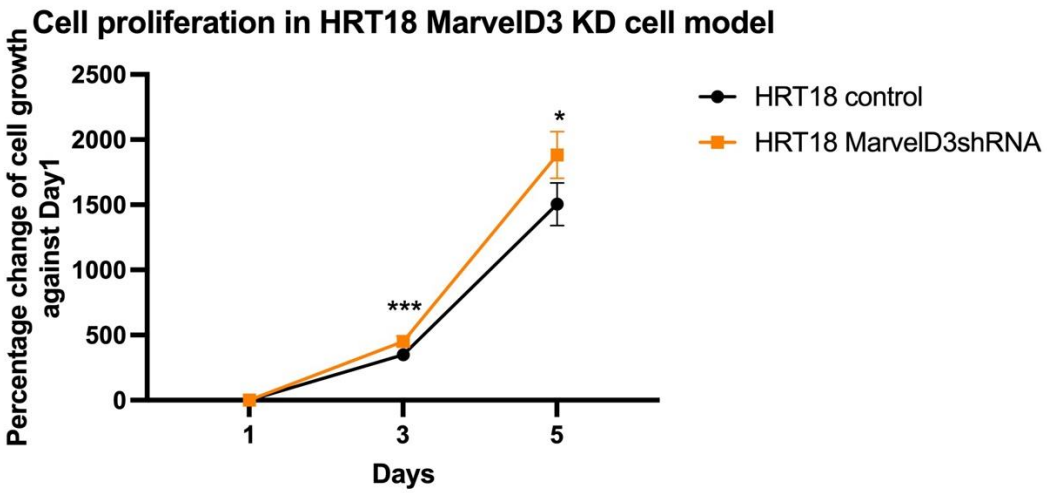

Figure 6.15 MTT growth assay on HRT18 cell models. Cell density on DAY1 was set as a reference for DAY3 and DAY5 groups. Marveld3 knockdown significantly increases the HRT18 cell growth. A representative set of data is presented (n=6), with the mean ± SD shown. * represents p<0.05, *** represents p<0.001.

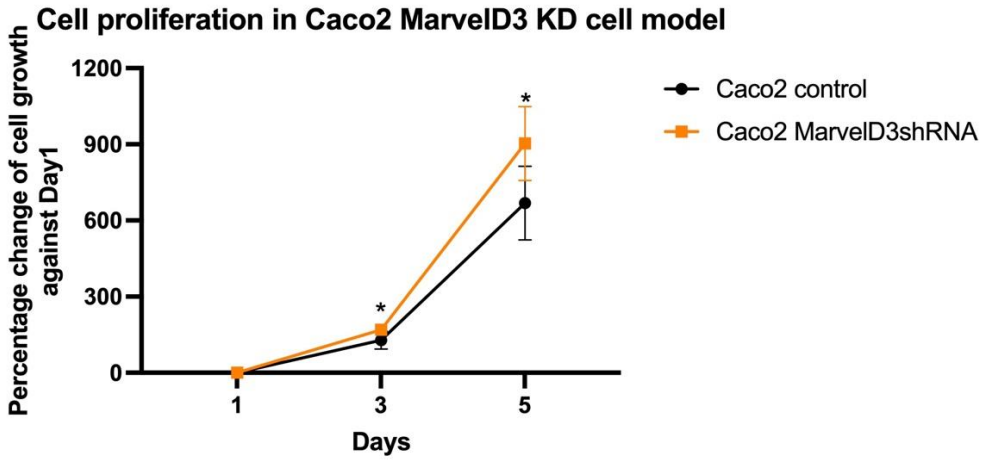

Figure 6.16 MTT growth assay on Caco2 cell models. Cell density on DAY1 was set as a reference for DAY3 and DAY5 groups. Marveld3 knockdown significantly increases the Caco2 cell growth. A representative set of data is presented (n=6), with the mean ± SD shown. * represents p<0.05.

6.3.3.2 Impact of MarvelD3 on colorectal cancer cells adhesion

The effect of MarvelD3 on the adhesive ability of colorectal cancer (CRC) cells was examined using Matrigel adhesion assays. A representative result is presented for both HRT18 and Caco2 cell models, as illustrated in Figure 6.17. According to Figure 6.17A, the HRT18 MarvelD3 KD group had significantly more cells adhered to the Matrigel than the control group ($p=0.002$). A similar trend but less prominent finding was observed in the Caco2 cell model ($p=0.021$) (Figure 6.17B), indicating that MarvelD3 plays a suppressive role in CRC cell adhesion.

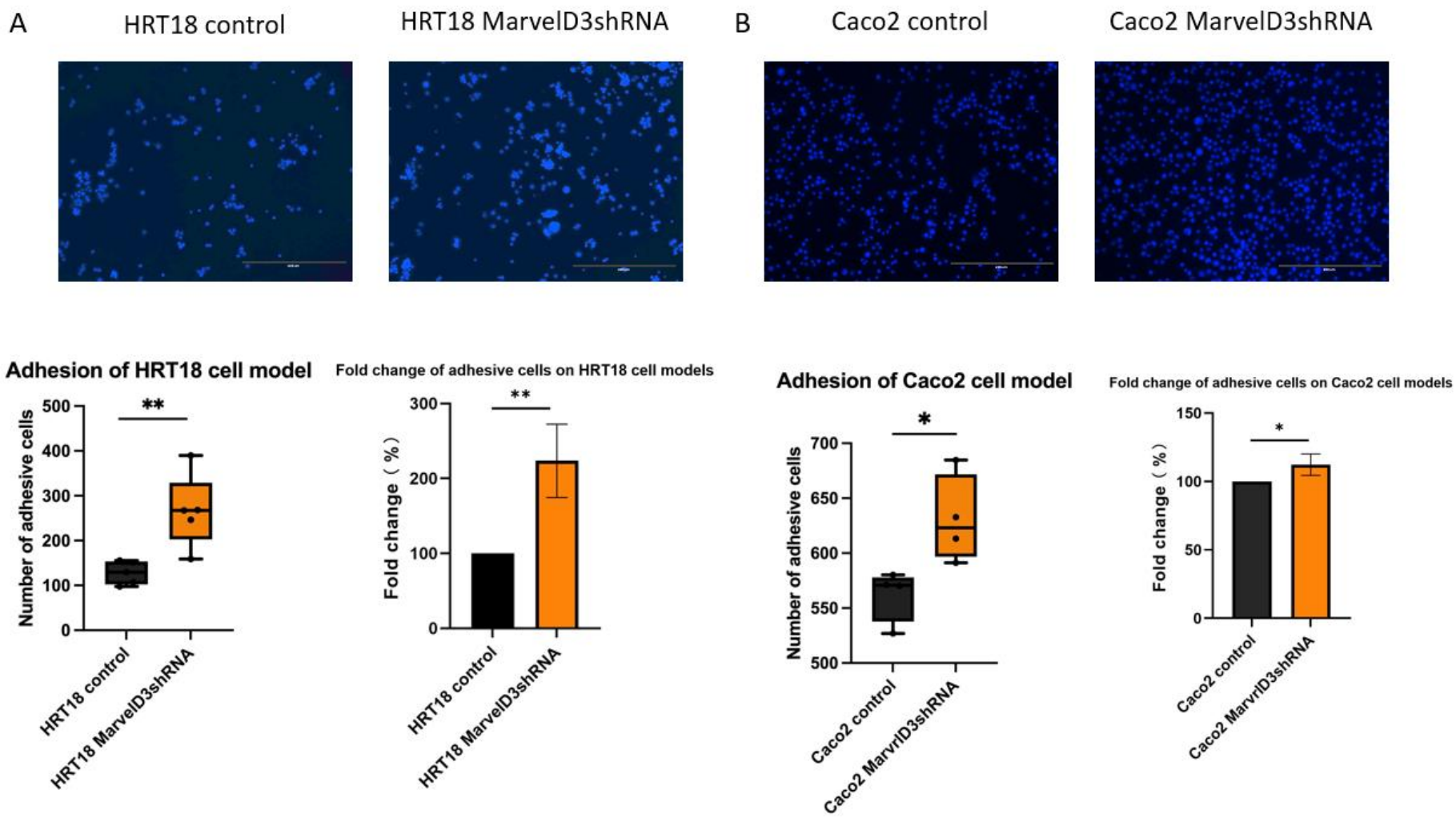

Figure 6.17 Knockdown of MarvelD3 increased the adhesion of the HRT18 and Caco2 cells significantly. Representative images of (A) HRT18 and (B) Caco2 adhesion cells after staining with DAPI (upper) and the adhesive cells were counted, with the box plot (down left) and fold change graph (down right) generated. Data is presented with mean ± SD, n=6. * represents $p<0.05$, ** represents $p<0.01$. Scale bar: 200μm. Magnification: 20x

6.3.3.3 Impact of MarvelD3 on colorectal cancer cells migration

The impact of MarvelD3 on the migration ability of colorectal cancer cells was then examined using a beads-based migration assay since both HRT18 and Caco-2 formed clusters when they were growing, which is unsuitable for the conventional wound healing assay. As depicted in Figure 6.18 and Figure 6.19, after MarvelD3 had been knocked down, both HRT18 and Caco2 exhibited a significantly increased cellular migration ability compared with their control counterparts by assessing the OD value (p=0.0003 for HRT18 and p=0.005 for Caco2).

A

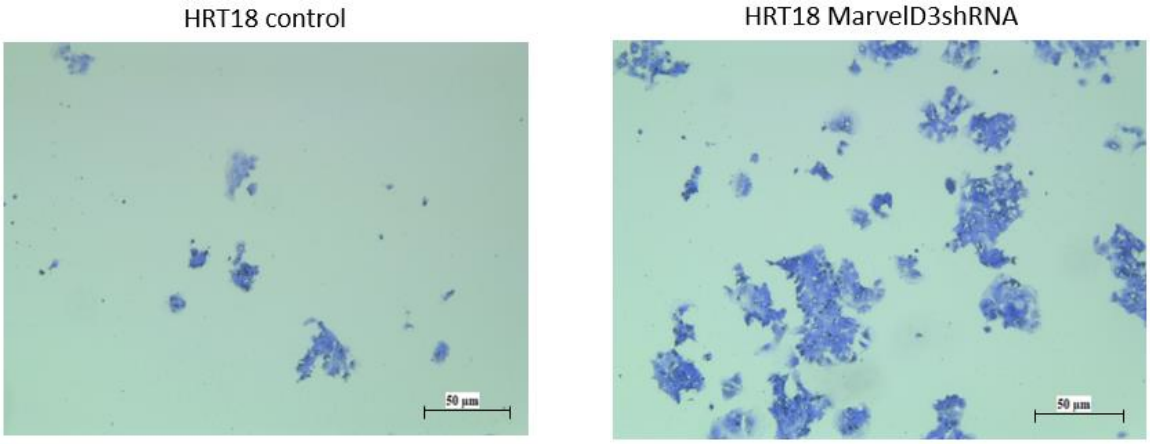

B

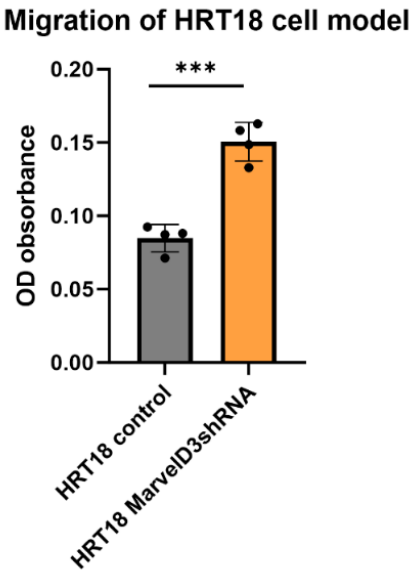

Figure 6.18 Knockdown of MarvelD3 increased the migration ability of the HRT18 cells significantly. Representative images of (A) HRT18 migrated cells after staining with crystal violet. Scale bar: 50µm. Magnification: 20x. (B) Optical density (OD) of the migrated cells. Data is presented with mean ± SD, n=5. * represents p<0.05, ** represents p<0.01.

A

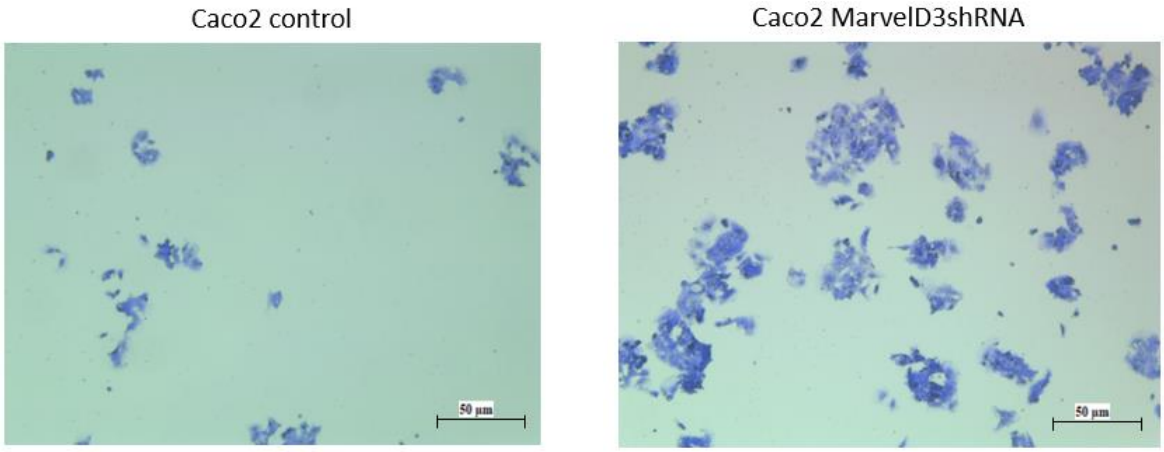

B

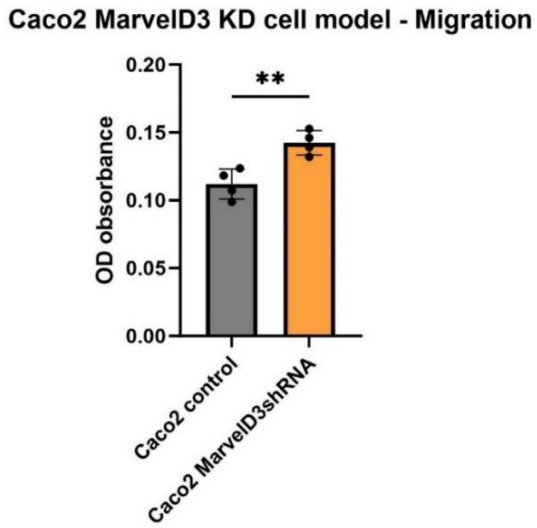

Figure 6.19 Knockdown of MarvelD3 increased the migration ability of the Caco2 cells significantly. Representative images of (A) Caco2 migrated cells after staining with crystal violet. Scale bar: 50µm. Magnification: 20x. (B) Optical density (OD) of the migrated cells. Data is presented with mean ± SD, n=5. * represents $p<0.05$, ** represents $p<0.01$.

6.3.3.4 Impact of MarvelD3 on colorectal cancer cells invasion

The established MarvelD3 knockdown cell models were used to explore MarvelD3's impact on the invasion of CRC cells. A representative set of data is presented here for the invasion assay of HRT18 and Caco2. As illustrated in Figure 6.20 and Figure 6.21, it was clearly shown that the invasive ability was significantly increased after MarvelD3 knockdown, with around 100% more cells for HRT18 invaded ($p=0.0001$) and 25% more cells for Caco2 ($p=0.03$) through the Matrigel.

A

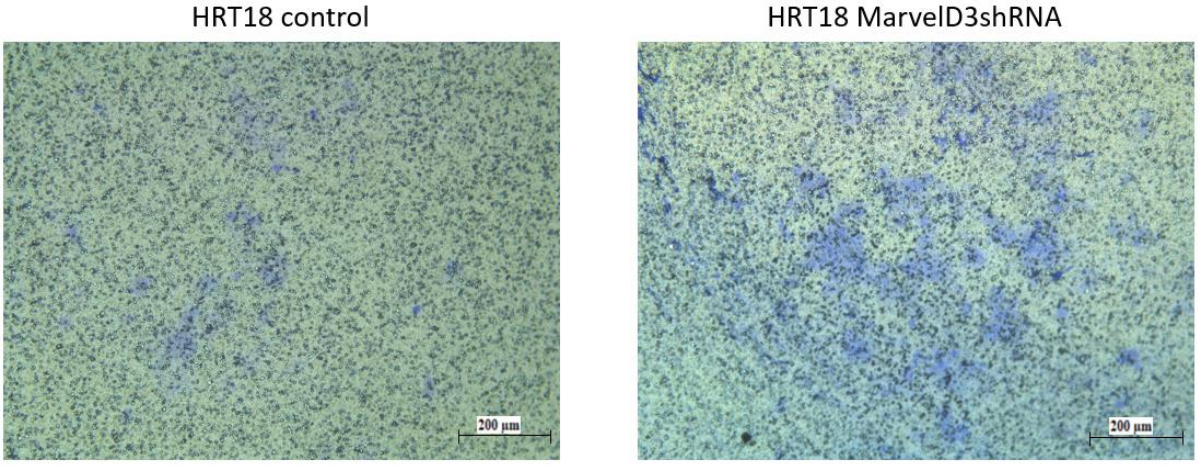

B

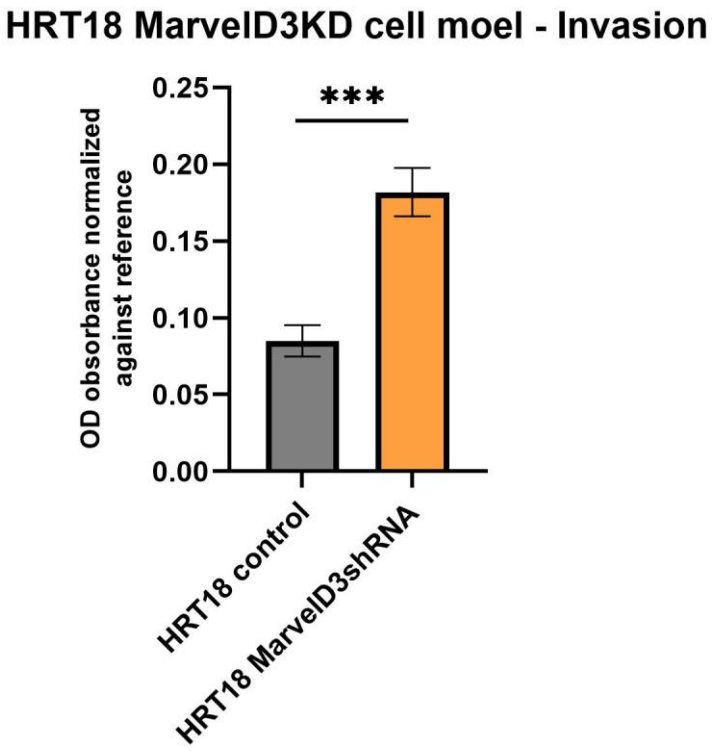

Figure 6.20 Knockdown of MarvelD3 increased the invasive ability of the HRT18 cells significantly. Representative images of (A) HRT18 invaded cells for the Control group (left) and the MarvelD3shRNA (right) through Matrigel after staining with crystal violet. Scale bar: 200µm. Magnification: 5x. (B) Optical density (OD) normalized against the reference of the invasive cells. Data is presented with mean ± SD, n=4, *** represents p<0.001.

A

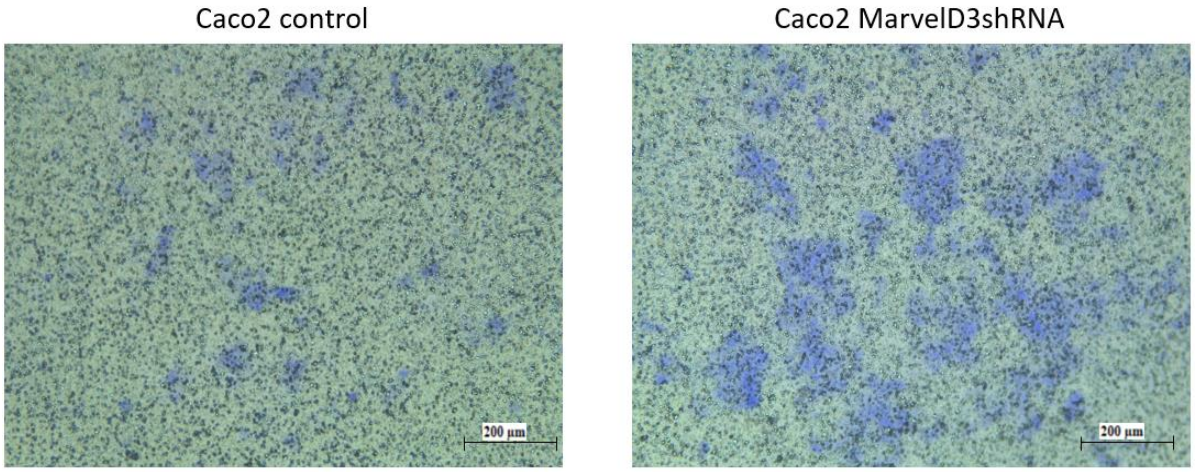

B

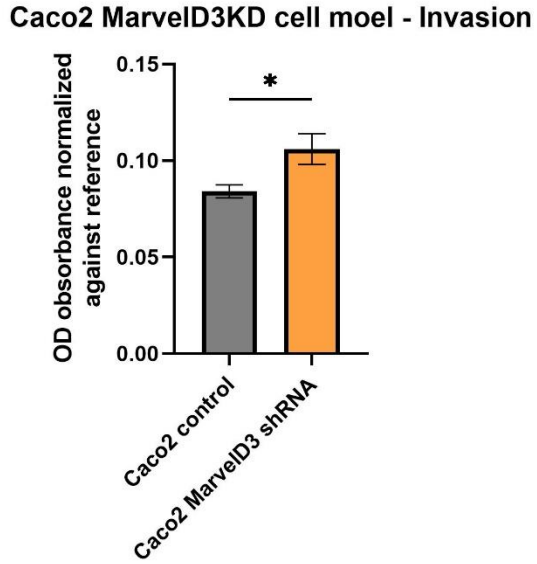

Figure 6.21 Knockdown of MarvelD3 increased the invasive ability of the Caco2 cells significantly. Representative images of (A) Caco2 invaded cells for the Control group (left) and the MarvelD3shRNA (right) through Matrigel after staining with crystal violet. Scale bar: 200µm. Magnification: 5x. (B) Optical density (OD) normalized against the reference of the invasive cells. Data is presented with mean ± SD, n=4, * represents $p<0.05$.

6.3.3.5 Further investigate the impact of MarvelD3 on colorectal cancer cell adhesion and migration using ECIS

Electric cell-substrate impedance sensing (ECIS), based on the insulation property of the cell membrane, was conducted to further understand the impact of MarvelD3 on CRC cell adhesion and migration. As shown in Figure 6.22 A, the resistance of HRT18 MarvelD3shRNA was always higher than the control group, indicating that more cells adhered to the well in the knockdown group. Also, HRT18 MarvelD3shRNA cells migrated at a faster pace than the

control group. A similar trend was observed for Caco2 (Figure 6.23), further supporting that the knockdown of MarvelD3 could increase the adhesion and migration abilities for both HRT18 and Caco2 CRC cell lines.

A

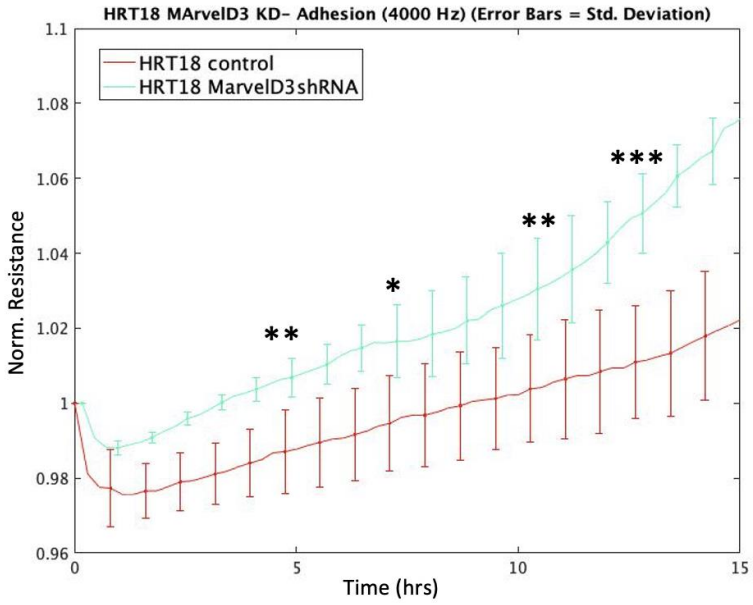

B

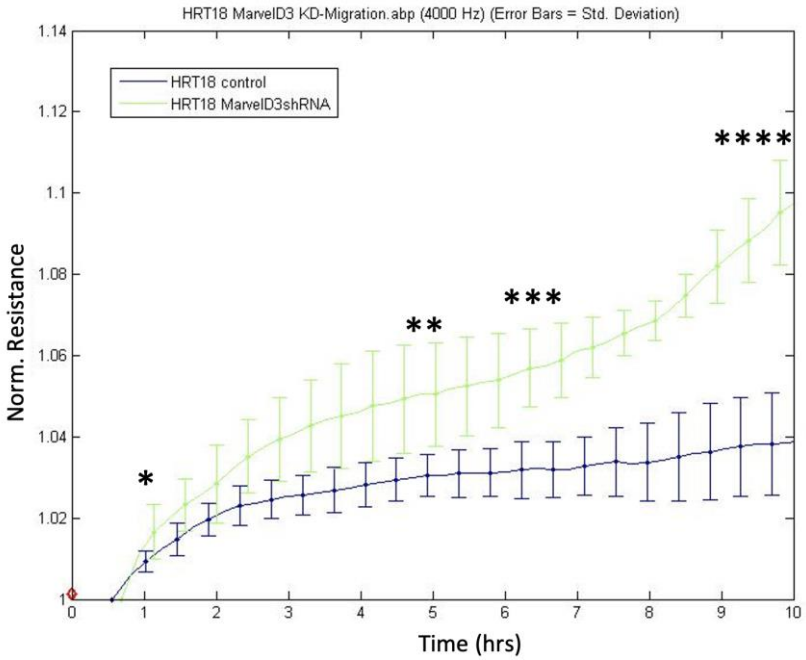

Figure 6.22 ECIS-based adhesion and migration assay on HRT18 cell models. (A) The adhesion ability of HRT18 cells was upregulated after MarvelD3 knockdown. (B) After wounding electrically, MarvelD3shRNA cells migrated faster than the control group. resistance data was recorded for 15 hours at a range of frequencies. Data was normalized based on the starting points by the ECIS system and shown at 4000Hz (n=6, mean ± SD). * represents $p<0.05$, ** represents $p<0.01$, *** represent $p<0.001$, **** represents $p<0.0001$.

A

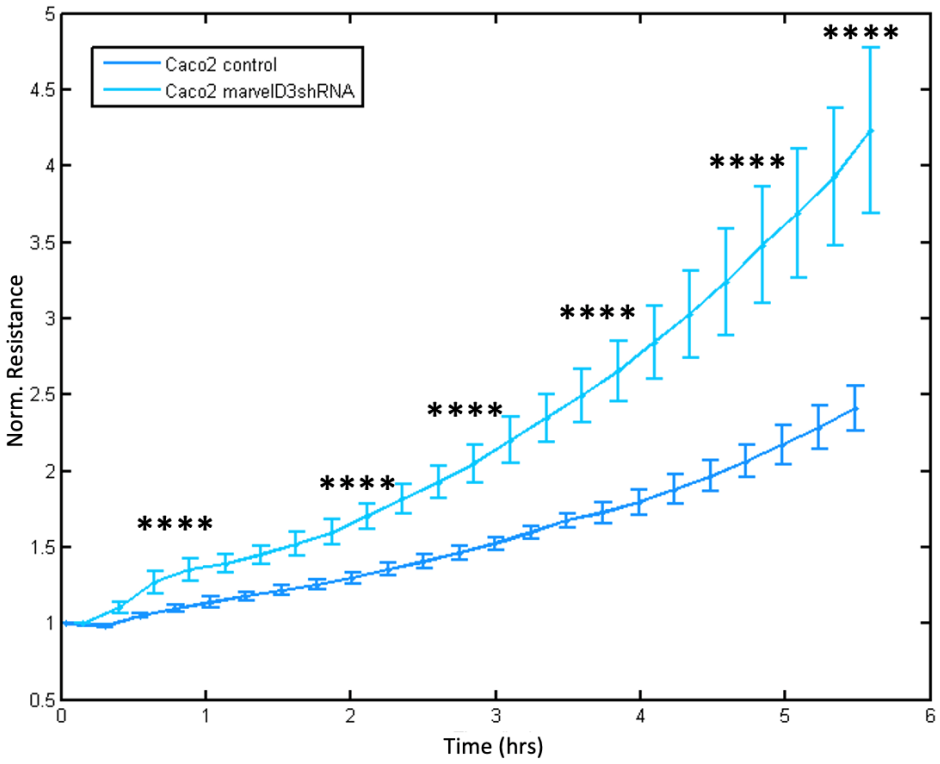

B

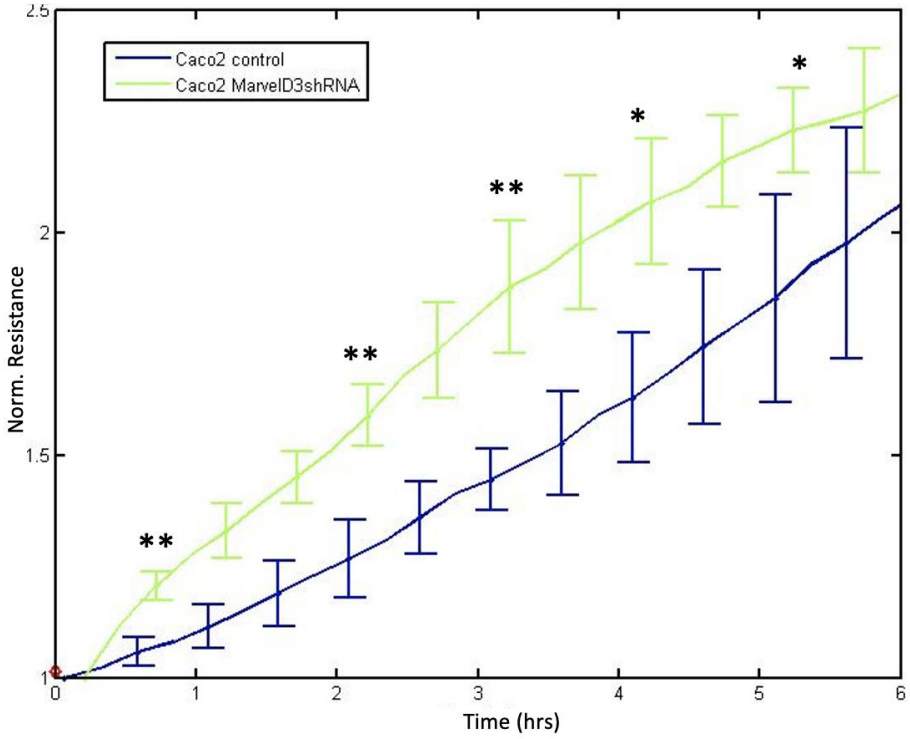

Figure 6.23 ECIS-based adhesion and migration assay on Caco2 cell models. (A) The adhesion ability of Caco2 cells was upregulated after MarvelD3 knockdown. (B) After wounding electrically, MarvelD3shRNA cells migrated faster than the control group. resistance data was recorded for 6 hours at a range of frequencies. Data was normalized based on the starting points by the ECIS system and shown at 4000Hz (n=6, mean ± SD). * represents $p<0.05$, ** represents $p<0.01$, **** represents $p<0.0001$.

6.3.3.6 Impact of MarvelD3 on tight junctions' function of colorectal cancer cells

As a member of the TJ family, the barrier and TJ function of MarvelD3 on colorectal cancer has not been studied yet. Therefore, to further explore it, transepithelial electric resistance (TER) and paracellular permeability (PCP) were conducted. TER is a well-known technique to measure the electrical resistance across a cell layer, reflecting the integrity of TJs. PCP is a technique that measures the rate at which the tracer molecules pass through the spaces between cells and directly reflect on TJ permeability.

It was clearly shown that after the MarvelD3 was knocked down in HRT18, the TER value was significantly decreased compared to the control group ($p<0.0001$), indicating that the TJ integrity was weakened after the MarvelD3 knockdown, as illustrated in Figure 6.24.

The permeability of the TJs was assessed by measuring the permeability to a fluorescent tracer over a period of 4 hours, as illustrated in Figure 6.25. Knockdown of MarvelD3 in HRT18 cells significantly increased paracellular permeability, as evidenced by higher fluorescence intensity values compared to the control group over a 4-hour period ($p<0.01$), suggesting that the cells were 'leakier' after MarvelD3 knockdown, therefore indicating that MarvelD3 plays a key role in regulating the permeability of TJs.

A similar trend was observed for both TER and PCP results in Caco2 cell lines, in which the knockdown of MarvelD3 significantly weakened the barrier function and enhanced the permeability in Caco2 (Figure 6.26 and Figure 6.27 respectively).

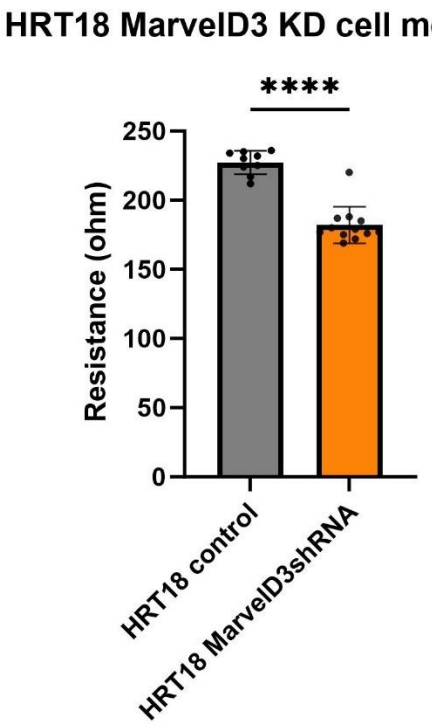

Figure 6.24 The Effect of MarvelD3 Knockdown on HRT18 cell barrier function detected using Transepithelial Electric Resistance (TER). Knockdown of MarvelD3 weakens TJ integrity significantly. Data is presented with mean ± SD, n=10, **** represents p<0.0001

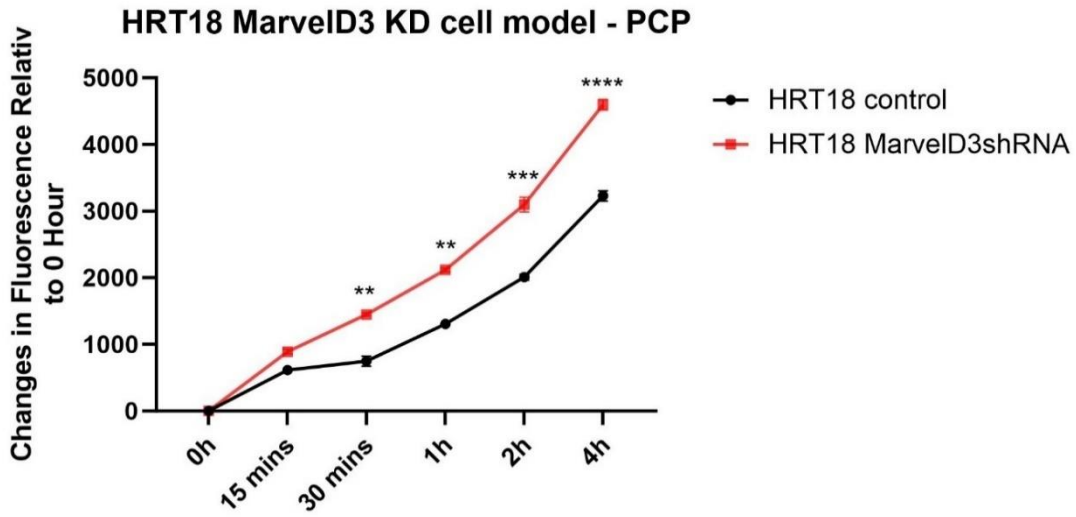

Figure 6.25 The Effect of MarvelD3 on HRT18 CRC cell paracellular permeability. FITC-dextran (10 kDa) was added to each insert, and the samples were taken from the outside of the insert fluorescence immediately after and for 4 hours. Data is presented with mean ± SD, n=3, ** represents p<0.01, *** represents p<0.001, **** represents p<0.0001.

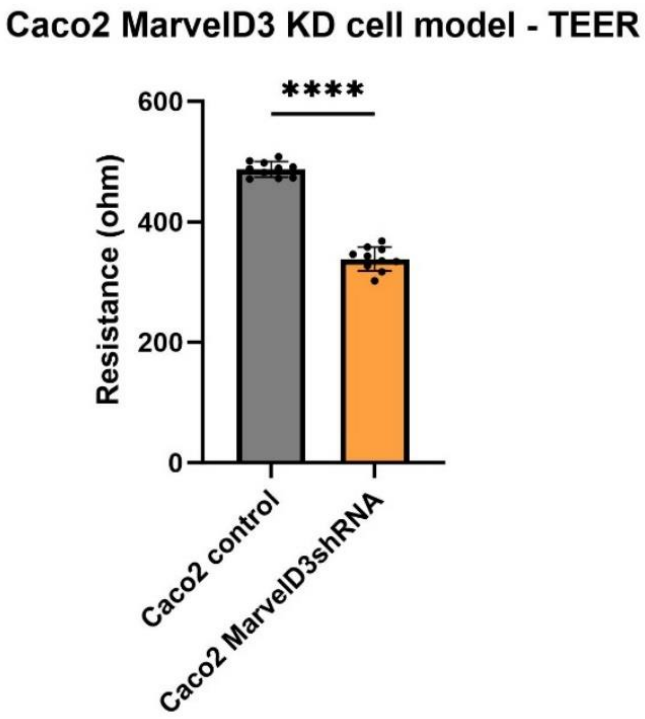

Figure 6.26 The Effect of MarvelD3 Knockdown on Caco2 cell barrier function detected using Transepithelial Electric Resistance (TER). Knockdown of MarvelD3 weakens TJ integrity significantly. Data is presented with mean ± SD, n=10, **** represents p<0.0001.

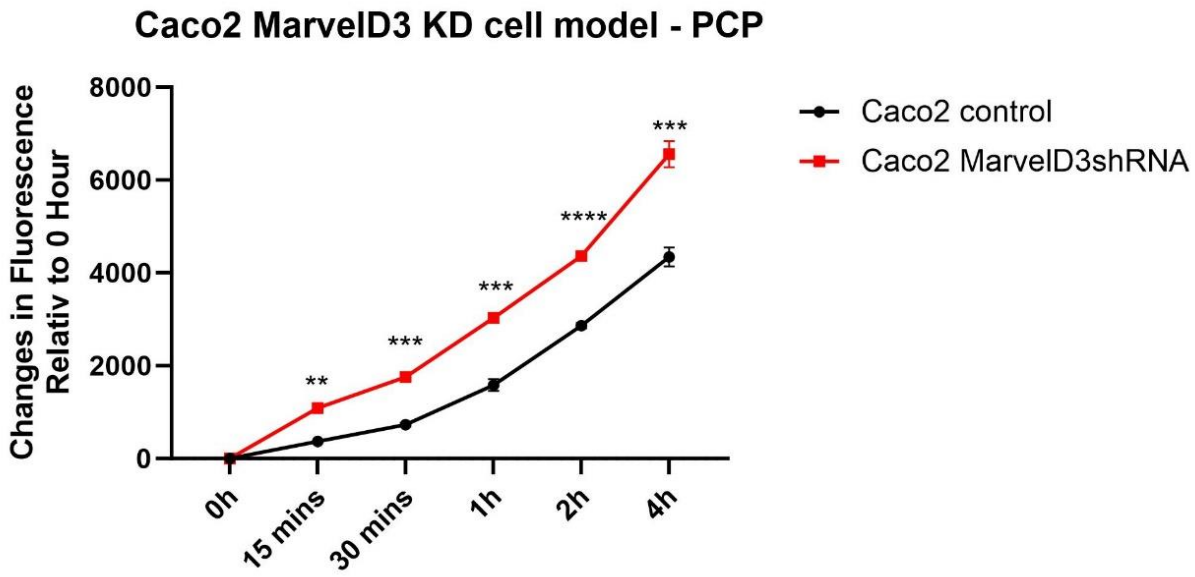

Figure 6.27 The Effect of MarvelD3 on Caco2 CRC cell paracellular permeability. FITC-dextran (10 kDa) was added to each insert, and the samples were taken from the outside of the insert fluorescence immediately after and for 4 hours. Data is presented with mean ± SD, n=3, ** represents p<0.01, *** represents p<0.001, **** represents p<0.0001.

6.3.4 Impact of MarvelD3 on breast cancer cellular functions

6.3.4.1 Impact of MarvelD3 on breast cancer cells proliferation

To investigate the impact of MarvelD3 on breast cancer cell growth, we performed an MTT-based cell growth assay over five days using established MarvelD3 knockdown models in MCF7 and SKBR3 cells. As shown in Figure 6.28, on Day3, the MFC-7 MarvelD3 knockdown (n=6, mean=306.32%) exhibited slower growth rate compared to MCF-7 control group (n=6, mean=330.79%). By Day 5, this difference became more pronounced, with the MCF-7 MarvelD3 knockdown group (n=6, mean=1158.88%) showing a significantly lower growth rate than the MCF-7 control group (n=6, mean=1307.02%) (p=0.011). A similar, but not significant trend was observed in the SKBR3 MarvelD3 knockdown models, where both Day 3 and Day 5 data indicated slower growth in the SKBR3 MarvelD3 knockdown group compared to its control group, even though no statistical significance was found (Figure 6.29). These results suggest that MarvelD3 plays a promotive role in the growth of breast cancer cell lines.

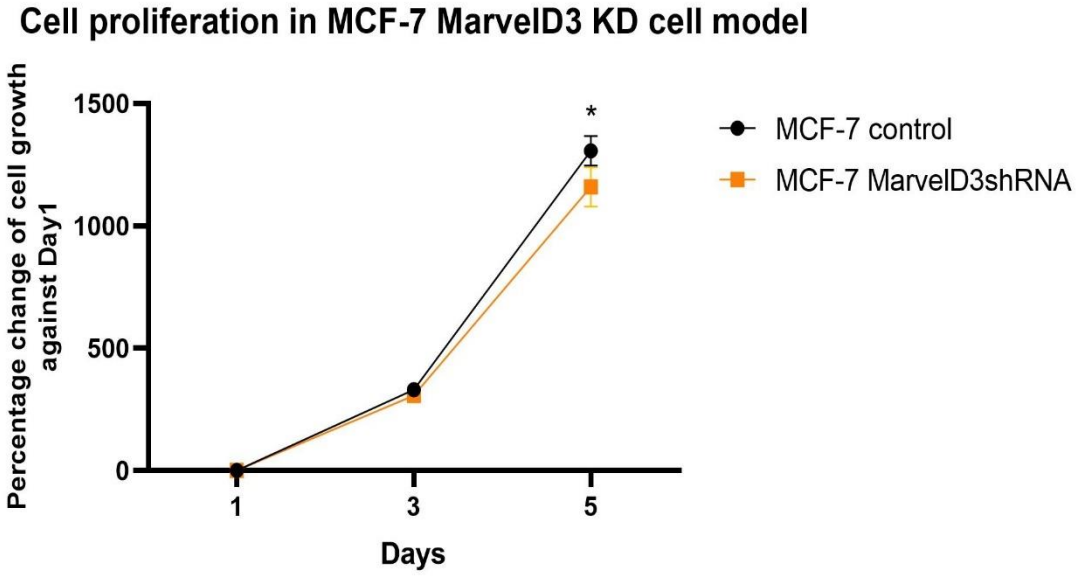

Figure 6.28 MTT growth assay on MCF-7 cell models. Cell density on DAY1 was set as a reference for DAY3 and DAY5 groups. Marveld3 knockdown significantly inhibited the MCF-7 cell growth. A representative set of data is presented (n=6), with the mean ± SD shown. * represents $p<0.05$.

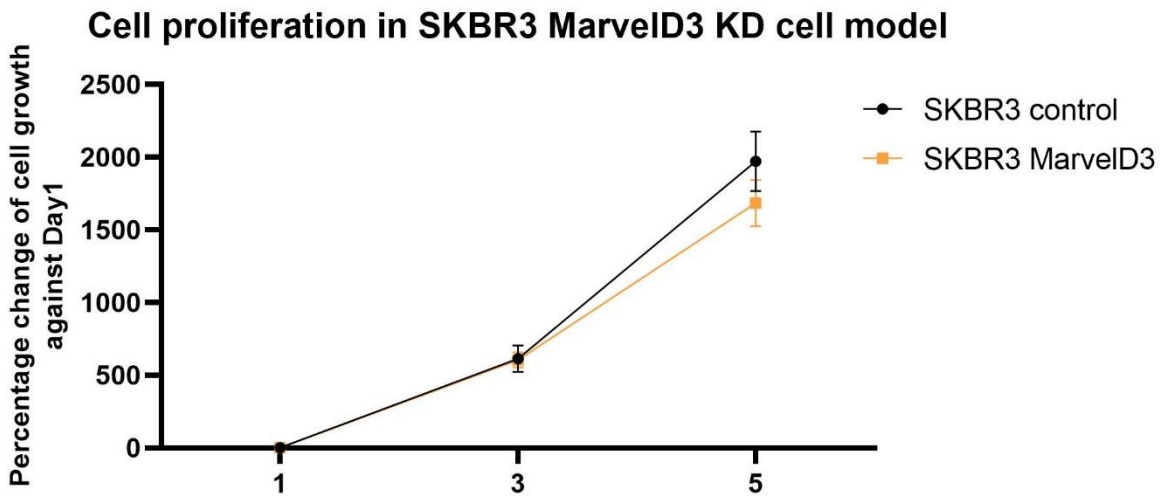

Figure 6.29 MTT growth assay on SKBR3 cell models. Cell density on DAY1 was set as a reference for DAY3 and DAY5 groups. Marveld3 knockdown inhibited the MCF-7 cell growth. A representative set of data is presented (n=6), with the mean ± SD shown.

6.3.4.2 Impact of MarvelD3 on breast cancer cells adhesion

The impact of MarvelD3 on the adhesive ability of breast cancer cells was evaluated using Matrigel adhesion assays. A representative result is presented for the MCF-7 cell model, as illustrated in Figure 6.30. The MCF-7 MarvelD3 knockdown group exhibited a significantly higher number of cells adhering to the Matrigel™ compared to the control group ($p=0.046$). This suggests that the knockdown of MarvelD3 enhances the adhesive capability of MCF-7 breast cancer cells, indicating a potential role of MarvelD3 in modulating cell adhesion dynamics in breast cancer.

A

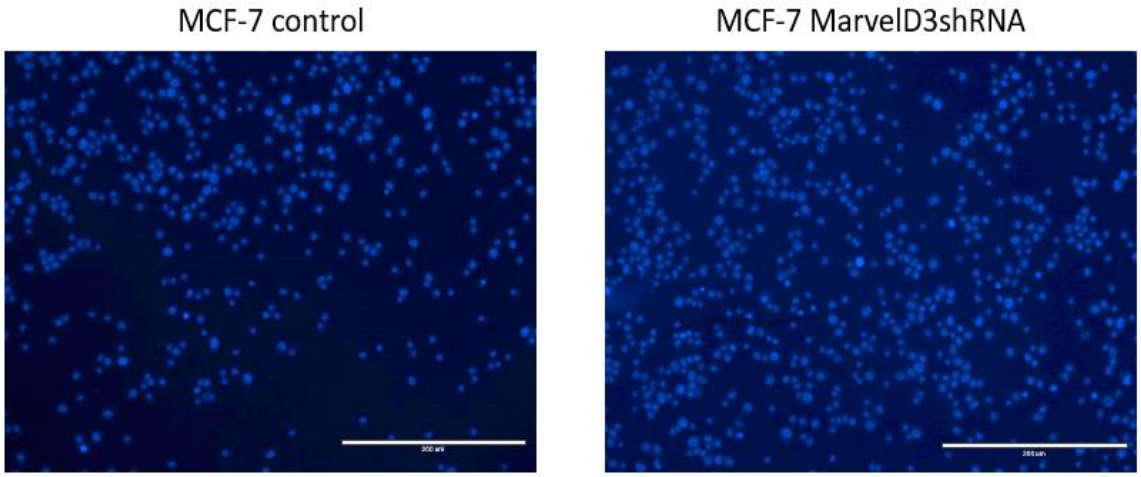

B

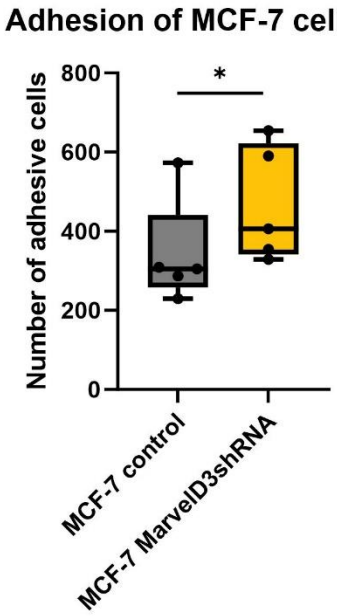

Figure 6.30 Knockdown of MarvelD3 increased the adhesion ability of the MCF-7 cells significantly. (A) Representative images of MCF-7 adhesion cells after staining with DAPI. (B) The number of adhesive cells was counted, and the data was presented as a box plot, * represents $p<0.05$. Scale bar: 200µm. Magnification: 20x.

6.3.4.3 Impact of MarelD3 on breast cancer cells adhesion and migration using ECIS

To further investigate the role of MarvelD3 in the adhesion and migration of breast cancer cells, we performed ECIS assays on MCF-7 and SKBR3 cell lines with MarvelD3 knockdown (MarvelD3shRNA) and compared them to control groups. As illustrated in Figure 6.22 A, the

resistance values recorded for MCF-7 MarelD3shRNA were consistently higher than those of the control group over the recorded period, indicating that a larger number of cells adhering to the substrate compared to the control group, as adhered cells increased the resistance to current flow across the electrodes.

During the migration assay, a wound was generated in the electrode area by applying a high electric field, temporarily disrupting the cell monolayer. As cells migrated to close the wound, resistance values increased. The faster increase in impedance values in the MCF-7 MarvelD3shRNA group indicates that MarvelD3 knockdown promotes cell migration, allowing cells to migrate more rapidly across the substrate compared to the control group.

A similar trend was observed for SKBR3 in both adhesion and migration assay (Figure 6.32), further supporting that the knockdown of MarvelD3 could increase the adhesion and migration abilities of breast cancer cells.

A

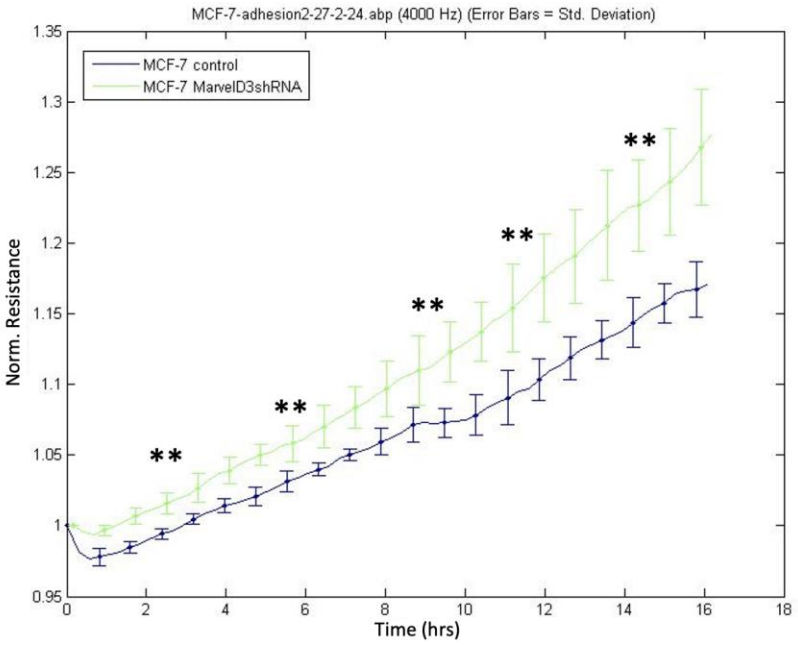

B

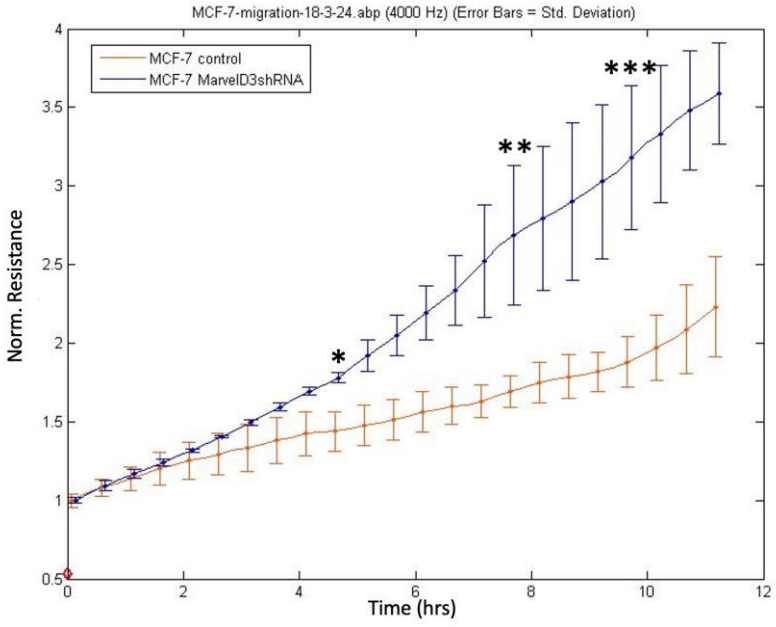

Figure 6.31 ECIS-based adhesion and migration assay on MCF-7 cell models. (A) The adhesion ability of MCF-7 cells was upregulated after MarvelD3 knockdown. (B) After wounding electrically, MarvelD3shRNA cells migrated faster than the control group. resistance data was recorded for 20 hours at a range of frequencies. Data was normalized based on the starting points by the ECIS system and shown at 4000Hz (n=6, mean ± SD). * represents $p<0.05$, ** represents $p<0.01$, *** represents $p<0.001$.

A

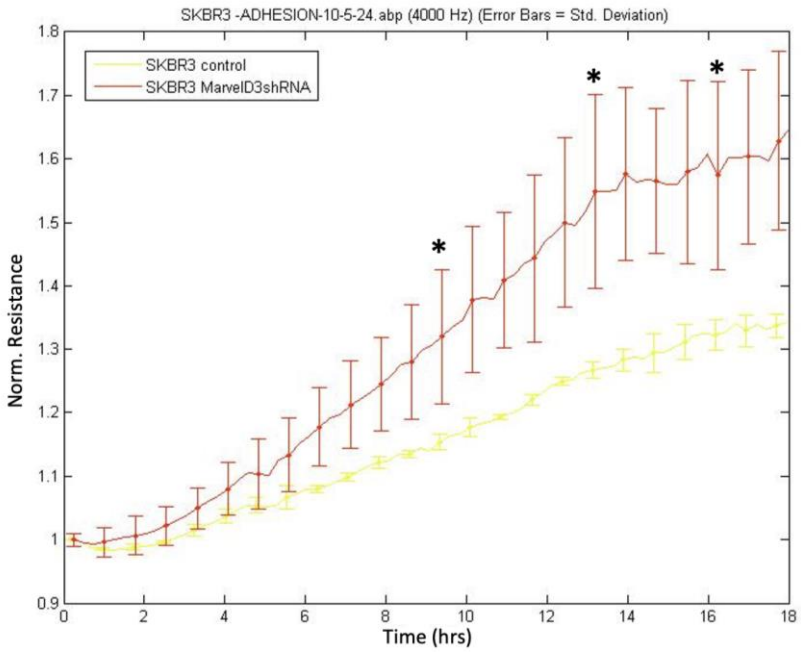

B

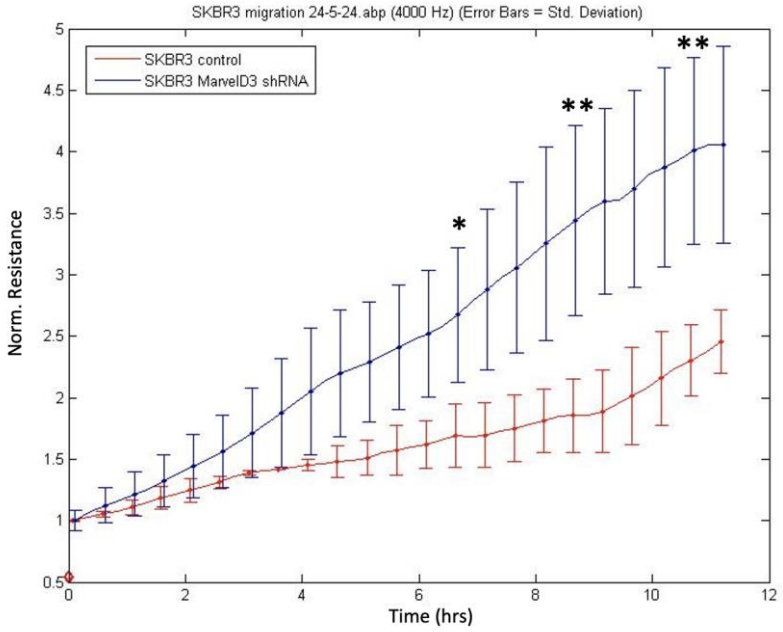

Figure 6.32 ECIS-based adhesion and migration assay on SKBR3 cell models. (A) The adhesion ability of SKBR3 cells was upregulated after MarvelD3 knockdown. (B) After wounding electrically, MarvelD3shRNA cells migrated faster than the control group. resistance data was recorded for 20 hours at a range of frequencies. Data was normalized based on the starting points by the ECIS system and shown at 4000Hz (n=6, mean ± SD). Two-way ANOVA analysis was conducted to make a comparison between groups. * represents $p<0.05$, ** represents $p<0.01$.

6.3.4.4 Impact of MarvelD3 on breast cancer cells invasion

The impact of MarvelD3 on the invasion function of breast cancer cells was performed using an in vitro transwell invasion assay. A representative result is demonstrated in Figure 6.33. The invasion ability was markedly enhanced after the knockdown of MarvelD3 in MCF-7 breast cancer cells compared to the control group (p=0.028).

A

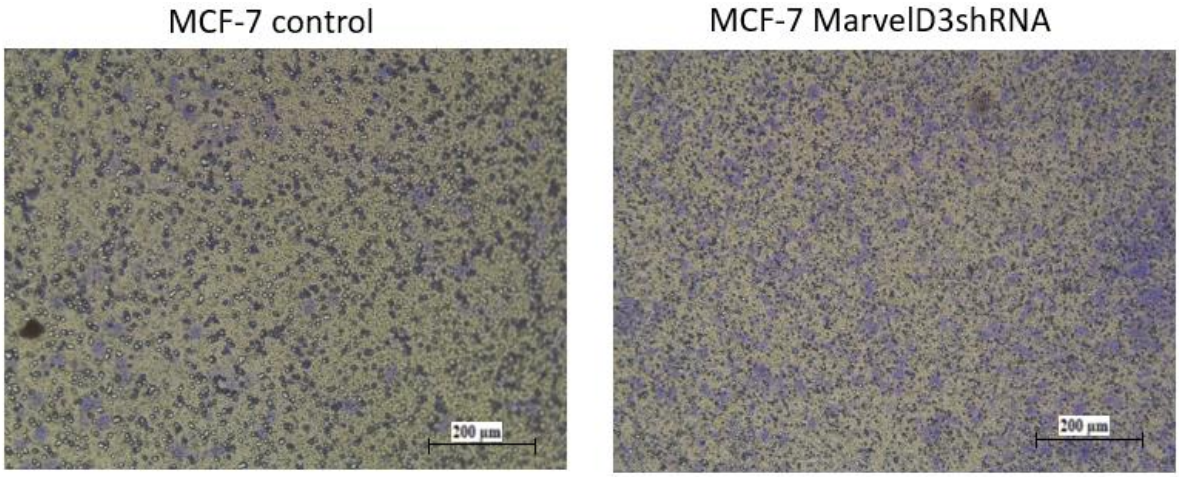

B

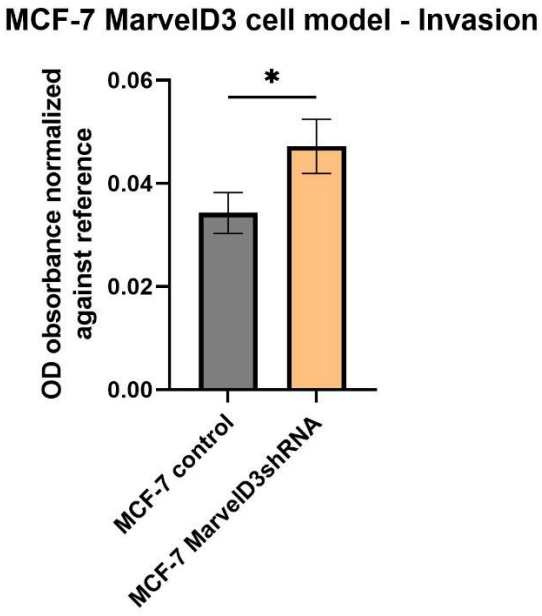

Figure 6.33 Knockdown of MarvelD3 increased the invasive ability of the MCF-7 cells significantly. Representative images of (A) MCF-7 invaded cells for the Control group (left) and the MarvelD3shRNA (right) through Matrigel after staining with crystal violet. Scale bar: 200µm. Magnification: 5x. (B) Optical density (OD) normalized against the reference of the invasive cells. Data is presented with mean ± SD, n=4, * represents $p<0.05$.

6.3.4.5 Impact of MarvelD3 on tight junctions' function of breast cancer cells

The junctional function of MarvelD3 in breast cancer was also explored by performing TER and PCP assays in the MCF-7 and SKBR3 MarvelD3 knockdown cell models. As demonstrated in Figure 6.34, in MCF-7 cells with MarvelD3 knockdown, a significant decrease in TER values was observed compared to the control group ($p<0.0001$). This decrease in resistance indicates a weakening of the TJs. The PCP assay evaluates the permeability of the cell monolayer by measuring the passage of fluorescent tracers through the paracellular space. The results showed a significant increase in permeability in the MarvelD3shRNA group compared to the control group over time (Figure 6.35). This heightened permeability further supports the conclusion that the knockdown of MarvelD3 disrupts TJ integrity, allowing more substances to pass through the paracellular route. Consistent with the findings in MCF-7 cells, SKBR3 cells also exhibited decreased TER values (Figure 6.36) and increased permeability (Figure 6.37) following MarvelD3 knockdown. Taken together, these results suggest that MarvelD3 is critical for maintaining the structural integrity of TJs

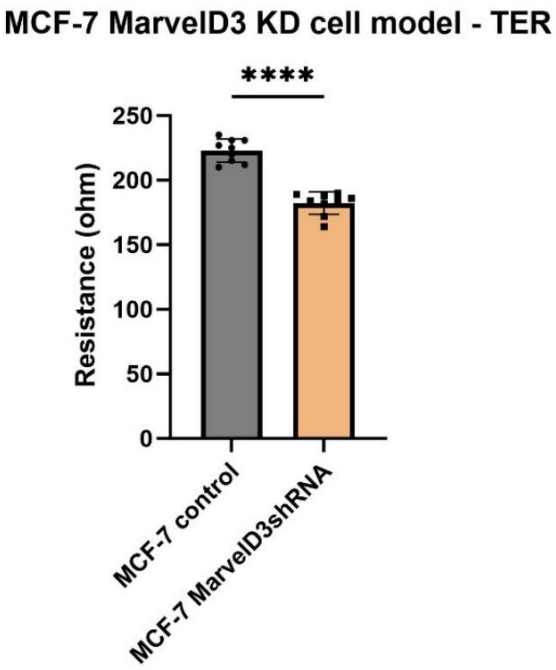

Figure 6.34 The Effect of MarvelD3 Knockdown on MCF-7 cell barrier function detected using Transepithelial Electric Resistance (TER). Knockdown of MarvelD3 weakens TJ integrity significantly. Data is presented with mean ± SD, n=10, **** represents $p<0.0001$.

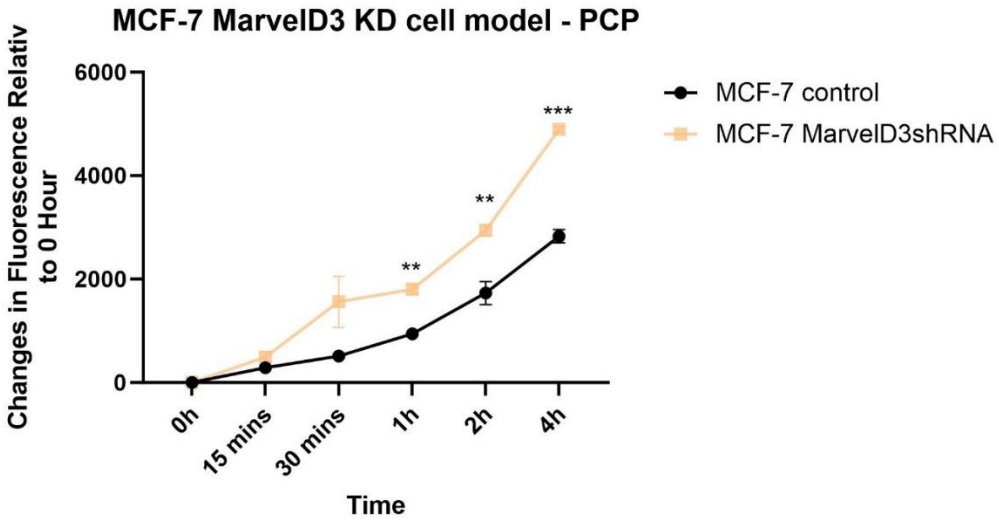

Figure 6.35 The Effect of MarvelD3 on MCF-7 breast cancer cell paracellular permeability. FITC-dextran (10 kDa) was added to each insert, and the samples were taken from the outside of the insert fluorescence immediately after and for 4 hours. Data is presented with mean ± SD, n=3, ** represents p<0.01, *** represents p<0.001.

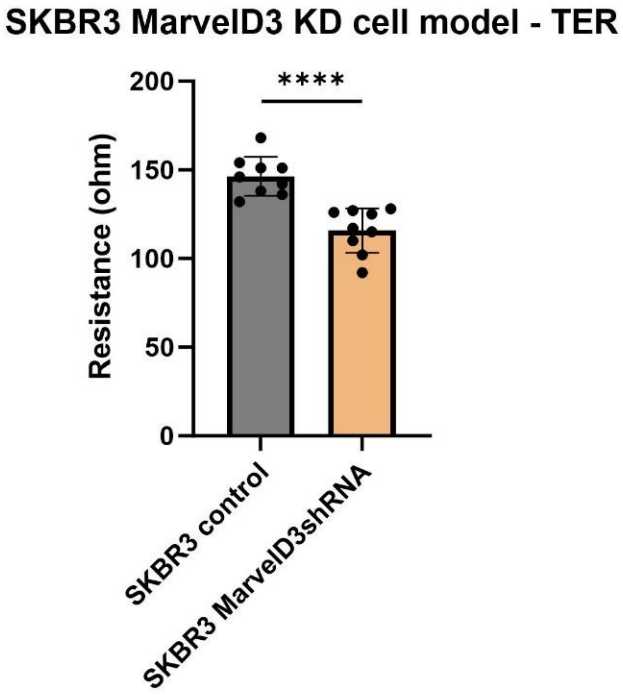

Figure 6.36 The Effect of MarvelD3 Knockdown on SKBR3 cell barrier function detected using Transepithelial Electric Resistance (TER). Knockdown of MarvelD3 weakens TJ integrity significantly. Data is presented with mean ± SD, n=10, **** represents p<0.0001.

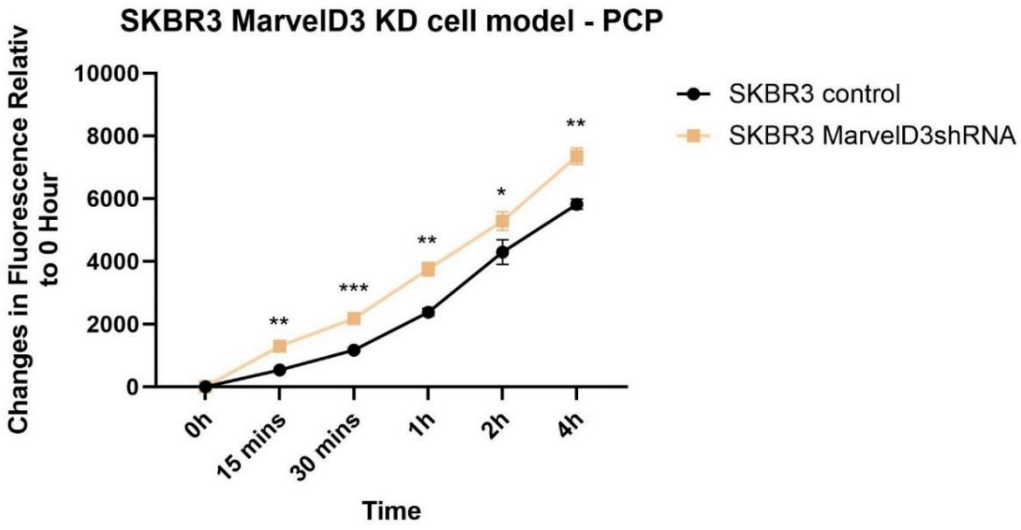

Figure 6.37 The Effect of MarvelD3 on SKBR3 breast cancer cell paracellular permeability. FITC-dextran (10 kDa) was added to each insert, and the samples were taken from the outside of the insert fluorescence immediately after and for 4 hours. Data is presented with mean ± SD, n=3, ** represents p<0.01, *** represents p<0.001, **** represents p<0.0001.

6.3.5 Predictive value of MarvelD3 as a biomarker for the efficacy of PEFE treatment

To investigate the role of MarvelD3 in modulating the efficacy of PEFE treatment, PEFE treatment was conducted on all the established MarvelD3 knockdown cell models. PEFE treatments were conducted at 2.2GHz with an input power level of 40 watts. The distance between the probe tip and the bottom of the well was fixed at 1mm. The viability of cells was then assessed before the experiment, 15 minutes, 24 hours, and 48 hours post-treatment.

As demonstrated in Figure 6.38 to Figure 6.41, the result exhibited a significant reduction in cell death after MarvelD3 was knocked down 48 hours post-treatment than those of control groups in Caco2 (p=0.001), HRT18 (p=0.016), MCF-7 (p=0.036), and SKBR3 (p=0.005). These findings suggest that MarvelD3 plays a critical role in enhancing PEFE treatment efficacy.

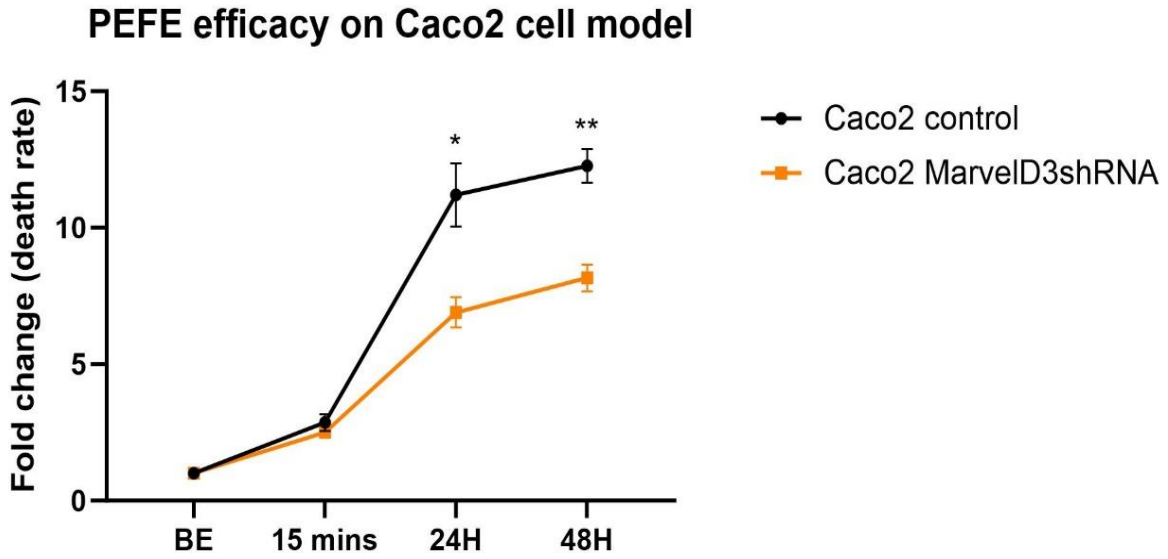

Figure 6.38 PEFE treatments using Caco2 colorectal cancer cell models with MarvelD3 knockdown and control. The cell death rate was assessed before the experiment (BE), 15 minutes, 24 hours, and 48 hours post-treatment. The result was presented by fold change. Data is presented with mean ± SD, n=3, * represents p<0.05, ** represents p<0.01.

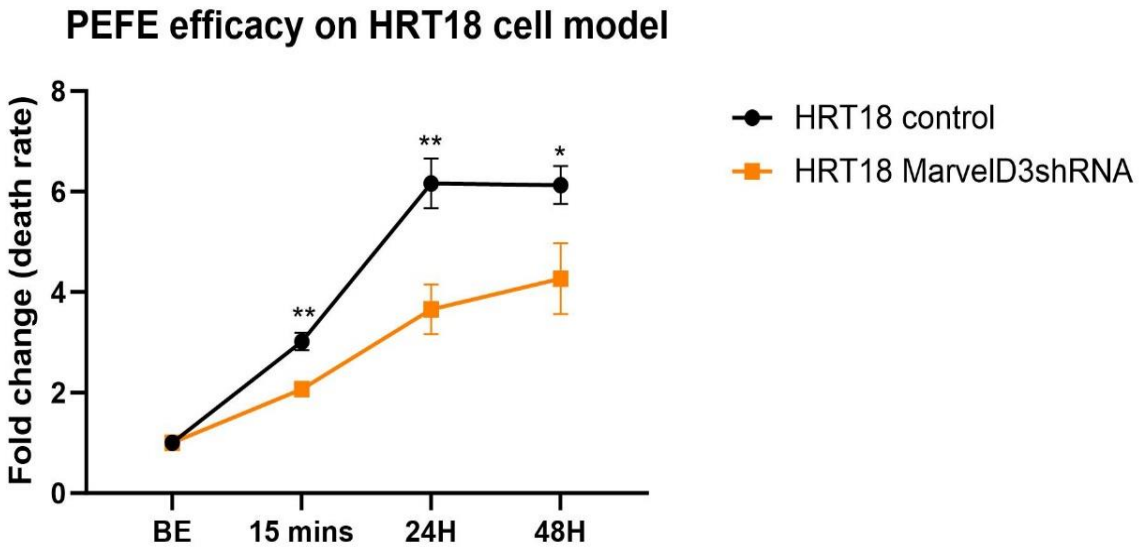

Figure 6.39 PEFE treatments using HRT18 colorectal cancer cell models with MarvelD3 knockdown and control. The cell death rate was assessed before the experiment (BE), 15 minutes, 24 hours, and 48 hours post-treatment. The result was presented by fold change. Data is presented with mean ± SD, n=3, * represents p<0.05, ** represents p<0.01.

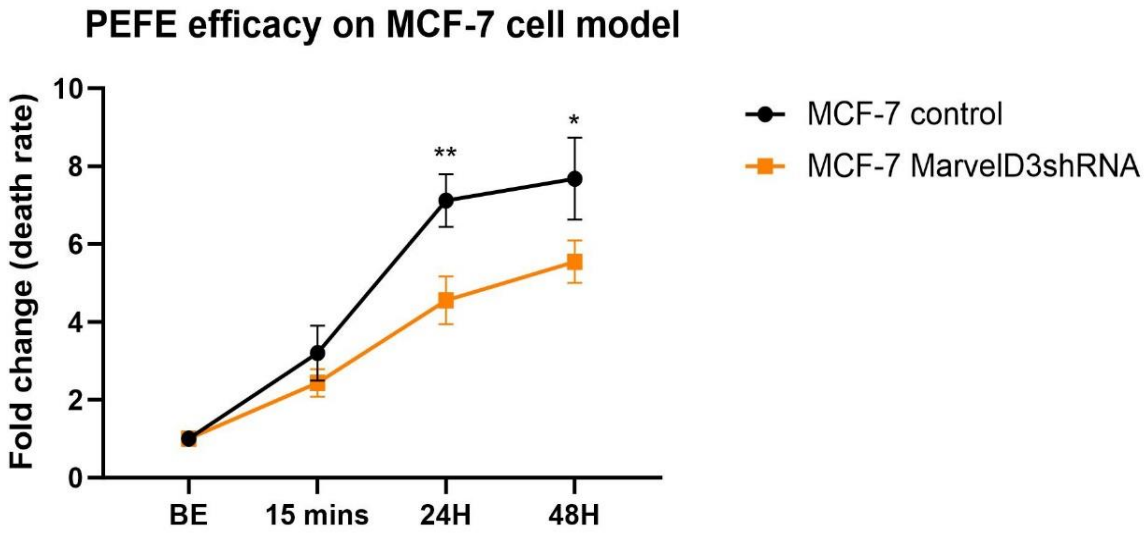

Figure 6.40 PEFE treatments using MCF-7 breast cancer cell models with MarvelD3 knockdown and control. The cell death rate was assessed before the experiment (BE), 15 minutes, 24 hours, and 48 hours post-treatment. The result was presented by fold change. Data is presented with mean ± SD, n=3, * represents p<0.05, ** represents p<0.01.

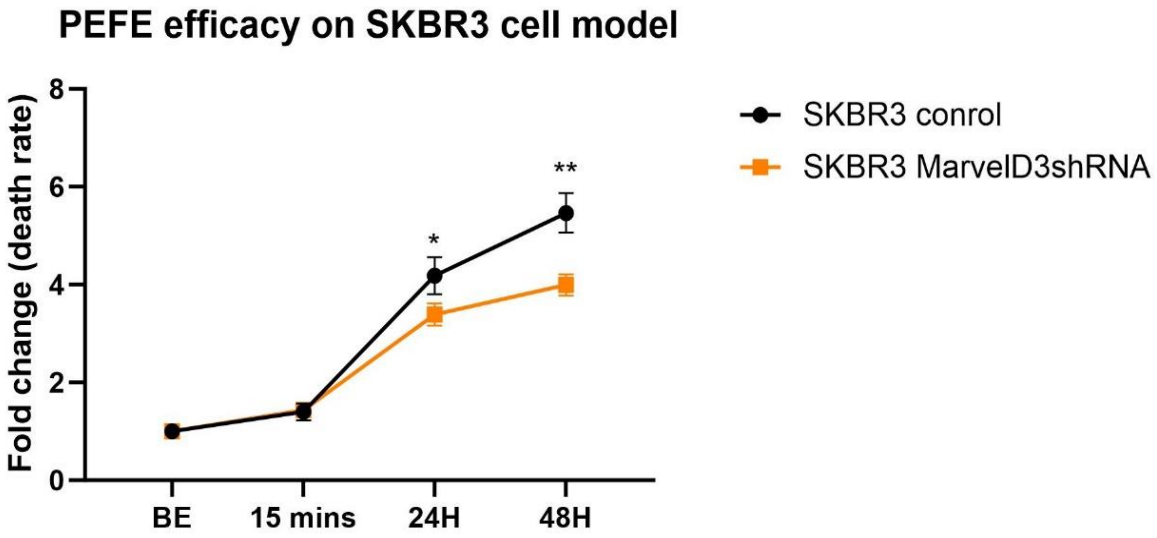

Figure 6.41 PEFE treatments using SKBR3 breast cancer cell models with MarvelD3 knockdown and control. The cell death rate was assessed before the experiment (BE), 15 minutes, 24 hours, and 48 hours post-treatment. The result was presented by fold change. Data is presented with mean ± SD, n=3, * represents p<0.05, ** represents p<0.01.

6.4 Discussion

Several studies have explored the impact of MarvelD3 on cellular function in various cancers, including non-small cell lung cancer (NSCLC) (Li et al. 2023), pancreatic cancer (Steed et al.

2014) and hepatocellular carcinoma (HCC) (Li et al. 2021a). However, the effects of MarvelD3 on colorectal cancer and breast cancer have not been fully investigated. As mentioned in Chapter 5, the expression of MarvelD3 was found to be higher in both colorectal and breast cancer tumour samples. Additionally, samples with metastasis exhibited relatively lower expression levels of MarvelD3 compared to those without metastasis, suggesting that MarvelD3 may influence cellular functions. Consequently, we explored the impact of MarvelD3 on the cellular and junctional function of both colorectal and breast cancer cells, focusing on its role as a member of the TJ family. We also examined the response of MarvelD3 knockdown models to PEFE treatment, given the significance of TJs in PEFE treatment discussed in Chapter 4.

Our findings revealed that MarvelD3 is differentially expressed in various breast and colorectal cancer cell lines. Higher expression levels of MarvelD3 were observed in cell lines with poor invasion ability, such as MCF-7 and SKBR3 breast cancer cells and CaCo-2 and HRT18 colorectal cancer cells, making these cell lines suitable models for knockdown studies. Successful knockdown of MarvelD3 was confirmed at both the mRNA and protein levels, validating the effectiveness of the shRNA-based transfection technique.

The knockdown of MarvelD3 significantly affected the proliferation of both colorectal and breast cancer cells, albeit in opposing directions. In colorectal cancer cells (HRT18 and Caco-2), MarvelD3 knockdown led to a significant increase in cell proliferation, suggesting a tumour-suppressive role of MarvelD3 in CRC. This aligns with the cohort study, in which low expression of MarvelD3 was correlated with worse T stage in colorectal cancer. Conversely, in breast cancer cells (MCF-7 and SKBR3), MarvelD3 knockdown resulted in decreased proliferation ability, suggesting that MarvelD3 might play a role in promoting cell proliferation in the context of higher expression, which is consistent with the cohort findings of higher MarvelD3 expression being correlated with worse clinical outcomes.

Cell invasion is a critical aspect of cancer progression, enabling cancer cells to breach the basement membrane and invade surrounding tissues, ultimately leading to metastasis (Chang and Chaudhuri 2019). The ability of cancer cells to metastasize is facilitated by various cellular functions, including altered cell invasion, migration, and adhesion properties (Lambert et al.

2017). Similarly to the knockdown in NSCLC (Li et al. 2023), The knockdown of MarvelD3 enhanced the adhesion, migration, and invasion capabilities of both breast and colorectal cancer cells. This observation was consistently supported by various assays, including Matrigel adhesion, beads-based migration, and transwell invasion assays. The increased adhesion and migration observed in ECIS assays further corroborate these findings.

TJs play a critical role in cancer metastasis by maintaining cell polarity and barrier function, and their disruption facilitates tumour cell detachment, invasion, and migration through altered signalling pathways and epithelial-mesenchymal transition (EMT), allowing them to invade surrounding tissues (Martin et al. 2011). Several studies have highlighted the role of other Marvel domain-containing proteins in cancer. MarvelD1 (occludin) and MarvelD2 (tricellulin), both part of this family, are implicated in maintaining TJ integrity and have been shown to play significant roles in cancer progression (Ikenouchi et al. 2005; Martin et al. 2010). Therefore, MarvelD3 was expected to influence TJ integrity and function. The TER and PCP assays demonstrated that MarvelD3 knockdown significantly weakened TJ integrity and increased paracellular permeability in both colorectal and breast cancer cells. TJs are the first barrier for cancer cells to overcome to metastasize to the other sides with the process of dissociation from the primary tumour, intravasation, and extravasation at a secondary tumour site in sequence. These findings indicate that MarvelD3 is essential for maintaining TJ structure and function, preventing the dissociation and migration of cancer cells.

One of the novel aspects of this study was evaluating MarvelD3's role in modulating the efficacy of PEFE treatment. The results showed that MarvelD3 knockdown significantly reduced cell death rates following PEFE treatment in both colorectal and breast cancer cell models. This suggests that higher MarvelD3 expression may enhance the sensitivity of cancer cells to PEFE treatment, positioning MarvelD3 as a potential predictive biomarker for PEFE therapy efficacy.

In summary, the details of the experiments and their results are summarized in the table listed below:

Cancer types	Experiments	Results
Colorectal cancer	MarvelD3 expression screening in CRC cell lines using PCR, qPCR and WB	MarvelD3 exhibits higher expression in Caco-2 and weaker expression in RKO cells
	Choosing the concentration of puromycin selection using MTT-based killing curve	10μg/ml puromycin for Caco2 cells; 5μg/ml puromycin for HRT18 cells.
	Verifying the knockdown of MarvelD3 in colorectal cancer cell lines using PCR, qPCR and WB	MarvelD3 was effectively knocked down at both mRNA and protein levels in Caco2 and HRT18 cells.
	Impact of MarvelD3 on colorectal cancer cells proliferation (MTT)	Proliferation ability was increased after MarvelD3 knockdown.
	Impact of MarvelD3 on colorectal cancer cells adhesion (Matrigel)	Adhesion ability was increased after MarvelD3 knockdown.
	Impact of MarvelD3 on colorectal cancer cells migration (beads)	Migration ability was increased after MarvelD3 knockdown.
	Impact of MarvelD3 on colorectal cancer cells invasion (Matrigel)	Invasion ability was increased after MarvelD3 knockdown.
	Further investigate the impact of MarvelD3 on colorectal cancer cell adhesion and migration using ECIS	Adhesion and migration abilities were increased after MarvelD3 knockdown.
	Impact of MarvelD3 on TJs' function of colorectal cancer cells (TER & PCP)	TJ structure was weakened, and the permeability was increased after MarvwlD3 knockdown.
	Predictive value of MarvelD3 as a biomarker for the efficacy of PEFE treatment on colorectal cancer	PEFE efficacy was decreased after MarvelD3 knockdown.
Breast cancer	MarvelD3 expression screening in BRCA cell lines using PCR, qPCR and WB	MarvelD3 exhibits higher expression in MCF-7 and weaker expression in MDA-MB-231 and BT549 cells.
	Choosing the concentration of puromycin selection using MTT-based killing curve	1μg/ml puromycin for MCF-7 cells; 2μg/ml puromycin for SKBR3 cells.
	Verifying the knockdown of MarvelD3 in breast cancer cell lines using PCR, qPCR and WB	MarvelD3 was effectively knocked down at both mRNA and protein levels in MCF-7 and SKBR3 cells.
	Impact of MarvelD3 on breast cancer cells proliferation (MTT)	Proliferation ability was decreased after MarvelD3 knockdown.
	Impact of MarvelD3 on breast cancer cells adhesion (Matrigel)	Adhesion ability was increased after MarvelD3 knockdown.
	Impact of MarvelD3 on breast cancer cells invasion (Matrigel)	Invasion ability was increased after MarvelD3 knockdown.

	Further investigate the impact of MarvelD3 on breast cancer cell adhesion and migration using ECIS	Adhesion and migration abilities were increased after MarvelD3 knockdown.
	Impact of MarvelD3 on TJs' function of breast cancer cells (TER & PCP)	TJ structure was weakened, and the permeability was increased after MarvwlD3 knockdown.
	Predictive value of MarvelD3 as a biomarker for the efficacy of PEFE treatment on breast cancer	PEFE efficacy was decreased after MarvelD3 knockdown.

Overall, this study highlights the complex and context-dependent role of MarvelD3 in cancer biology. Furthermore, the impact of MarvelD3 on the efficacy of PEFE treatment opens new avenues for therapeutic strategies. However, more extensive research is required to validate MarvelD3 as a suitable biomarker. The next chapter will focus on identifying the broader cellular network response to PEFE treatment and exploring the underlying signalling pathways.

Chapter-7 Possible signalling pathway involved in PEFE treatment

7.1 Introduction

Currently, lots of studies investigate the impact of electromagnetic field exposure on biological samples, in which microwave could bring about various changes at the cellular and molecular levels of biological samples, increasing the permeability of blood-brain barriers (Merritt et al. 1978), the induction of cell death (Asano et al. 2017b), the inhibition of cell proliferation (Zhu et al. 2013), the breaks of DNA single- and double-strand (Sagripanti et al. 1987), the alteration of gene expression in a wide range of cell types, the induction of oxidative stress (Megha et al. 2015), the alteration of the cell membrane structure (Rougier et al. 2014), and the changes of cellular metabolic functions (Zhao 2020). Nonetheless, since the impact of EMF on biological effects is complex, which poses challenges and controversies, there remains a need to further investigate the mechanism involved in this process (Zhao et al. 2021).

Based on the outcome of these previous experiments, it was found that PEFE induced apoptosis in cancer cells. Additionally, shrinkage of the cell membrane was visualized, resulting in the disruption of tight junctions following PEFE treatment. Considering the significant impact of PEFE on cancer treatment, this chapter is dedicated to a thorough and detailed investigation of the underlying mechanisms. Firstly, PEFE impact was assessed by using TMT (Tandem Mass Tagging)-based proteomic analysis. To commence this investigation, we hoped to uncover the changes in gene expression after PEFE treatment, particularly focusing on the genes associated with apoptosis, TJ, and the cell membrane. Subsequently, Western blotting was conducted to validate the key findings and explore the underlying mechanism.

7.2 Methods

7.2.1 Cell culture

Colorectal cancer cell line Caco2 was used for the protein assay. Caco2 cells were firstly cultured in a T25 flask and subcultured to 6 well plate. The method for cell culture was described in section 2.2.2.1.

7.2.2 PEFE treatment

Once 100% confluence was reached, the cells were washed with PBS twice, then changed with 3mL fresh cell culture medium. Before the experiments, the microwave probe and temperature probe were sterilized with 70% ethanol for five minutes, following washing with PBS buffer to remove the attached ethanol. The probes were then immersed inside the well, and the cells were treated with PEFE at 2.2 GHz, 40W for 1 hour, with the temperature controlled between 37-42℃. Once the PEFE treatment was finished, the samples were incubated at 37℃, 5% CO_2, with different time course settings, including 15 minutes, 1 hour, and 4 hours, before protein extraction.

7.2.3 Protein extraction

After treatment, the cells were washed with PBS twice, then 1mL PBS was added to each well. The cells were collected using scrapers, followed by transferring to a universal tube. The protein extraction was carried out by centrifuging the cell suspension at 2,000rpm for 10 minutes, and then resuspended with RIPA buffer (with no SDS) containing a cocktail of inhibitors for proteases (Cat No. ab201116) and phosphatases (Cat No. ab201117) (Abcam, Cambridge, UK), for both control group (untreated cells) and PEFE group. The suspension was transferred to a microfuge tube followed by incubation at 4℃ for 2 hours. After incubation, the microfuge tube was centrifuged at 13,000 rpm for 15 minutes at 4°C and a pellet was formed. The pellet was discarded and the supernatant containing proteins was collected and transferred to a labeled. The protein samples were then quantified using the Bio Rad DC Protein Assay kit (BioRad Laboratories, Hertfordshire, UK) to form a final concentration of 2mg/ml as described in section 2.5.2.

7.2.4 Proteomic analysis using mass spectrometry Tandem Mass Tagging (TMT)

After protein extraction and quantification, 100µl of the protein sample for each group was packaged in dry ice and sent to the University of Bristol for proteomic analysis. Mass spectrometry was conducted using Tandem Mass Tagging. The remaining samples were stored at -20℃.

7.2.5 Data analysis for proteomic analysis

Data analysis was performed to determine which proteins were affected when Caco2 was exposed under PEFE. Two separate analyses were performed: one to compare the total protein levels between the control group and the PEFE group, and a second was to assess protein phosphorylation, in which a phospho-peptide enrichment method was utilized to identify the phosphorylation status of serine (S), threonine (T), and tyrosine (Y) residues across the same samples. The collected data were analyzed with Proteome Discoverer v2.4 software, which was carried out by a bioinformatician from the University of Bristol, running a search against the Uniprot Human database and against a 'Common Contaminants' database, which was included in the searches. All data underwent filtration using a 5% False Discovery Rate (FDR) cutoff.

There are several key parameters involved in data analysis, the most important factor should be LogFC, also named Log fold change, which is the log-ratio of a gene's expression values in two different conditions. In this study, LogFC is calculated as: $LogFC=Log_2(PEFE) - Log_2(Control)$, in which all data were log-transformed by the University of Bristol. A positive value of LogFC indicates that the gene expression was upregulated after PEFE treatment, while a negative value of LogFC corresponds to the downregulation.

7.2.6 Western Blotting verification of proteomic analysis

Western blotting was performed to verify the proteomic analysis results. Selected molecules based on proteomic analysis were screened and expression levels were determined in cells after PEFE treatment for 15 minutes, 1 hour, 4 hours, and their control counterparts respectively. The information and concentration of the antibody used for the Western blot were listed in chapter 2.1.6, and the full description of Western blotting please refers to chapter 2.5. Protein bands were processed and quantified using ImageJ, data were analyzed using Excel, and figures were generated using GraphPad.

7.3 Results

7.3.1 Potential interacting proteins with most up/downregulation after PEFE treatment

To evaluate potential mechanisms and signalling pathways involved in PEFE treatment, Caco2 untreated cells (also named as a control in this chapter) and cells that underwent PEFE treatment (named as PEFE in this chapter) were sent to the University of Bristol for a TMT-based proteomic analysis. The proteomic analysis can identify and quantify thousands of proteins, therefore assessing the changes in expression of these molecules between the control and PEFE groups from both total protein level and phospho-protein level. Table 7.1 to Table 7.4 summarise the most significant changes of molecules from the microarray. Table 7.1 summarizes the top 30 molecules, detected by total protein levels, which were significantly upregulated in Caco2 cells when PEFE treatment was conducted. Table 7.2 displays the top 30 phospho-protein molecules that were significantly upregulated in Caco2 cells after PEFE treatment. Table 7.3 shows the top 30 molecules, detected by total protein levels, which were significantly downregulated in Caco2 cells after PEFE treatment. Table 7.4 shows the top 30 phospho-protein molecules that are significantly downregulated in Caco2 cells underwent PEFE treatment. Figure 7.1 to Figure 7.4 are graphical representations of molecules that were significantly up/downregulated in response to PEFE treatment in Caco2 cells. These figures were generated using GraphPad.

Among these molecules which exhibited significant dysregulation following PEFE treatment, some of them, displayed a noteworthy correlation with apoptosis, either directly or indirectly. Specially, FAU (FAU ubiquitin-like and ribosomal protein S30) had been identified as a pro-apoptotic regulator (Pickard et al. 2011). Additionally, PLIN2 (Perilipin-2) was proposed as an apoptotic inhibitor of gastric cancer cells (Sun et al. 2020). Furthermore, scientific report indicated that downregulation of CXCL1 (Growth-regulated alpha protein) has the potential to induce apoptosis (Han et al. 2015). Moreover, the suppression of MBD1 (Methyl-CpG-binding domain protein 1) has been linked to the apoptosis of pancreatic cancer cells (Wensheng et al. 2019). These molecules highlight the potential impact of apoptosis-related processes under PEFE treatment.

When examining the molecules associated with TJs based on the outcomes of the microarray with most dysregulation, among them, Claudin-5, occludin, and CTNND1 (Catenin delta-1) has been identified as direct participants within the TJ family. These specific molecules are directly implicated in the structural composition and regulation of TJs (Murakami et al. 2009; Yang et al. 2016; Ma et al. 2017). However, some of the molecules, while not belonging directly to the TJ family, have been reported to exert an indirect influence on TJ regulation. For instance, Sun et al., reported that the increase of CFAP100 (Cilia- and flagella-associated protein 100) could disrupt the TJ in the intestinal epithelium, thereby suggesting a regulatory role in the intestinal barrier integrity (Sun et al. 2023). Besides, it has been studied that the loss of DSC2 (Desmocollin-2) contributing to the increase of intestinal permeability *in vivo*, suggesting the role of DSC2 in the regulation of intestinal epithelial barrier function (Raya-Sandino et al. 2021). These dysregulations suggest the complexity molecular network involved in TJ regulation after PEFE treatment.

Concerning the results of these molecules with significant dysregulation, some of them have been reported to be linked to the cell membranes and the lipid bilayer. For example, LPIN2 is a major lipid droplet protein and plays a role in lipid metabolism (Itabe et al. 2017). While changes in lipid metabolism can influence the composition and properties of the cell membrane (Le Borgne et al. 2012), indicating that LPIN2 might be involved in the regulation of cell membrane indirectly. PIGQ (Phosphatidylinositol N-acetylglucosaminyltransferase subunit Q) act as membrane anchors which attach proteins to the cell membrane (Kinoshita and Fujita 2016).

Collectively, the changes observed in these molecules emphasize their participation and possible role in their regulation of apoptosis, TJs and cell membrane architecture in response to PEFE treatment. However, an in-depth investigation is required to identify the specific molecules involved in this process to underpin the effects of PEFE treatment on apoptosis, TJs, and cell membrane dynamics.

Table 7.1 Summary of top 30 molecules, sorted by total protein, upregulated in response to PEFE treatment in Caco2 cells

Protein name	Full protein name	Total Log2 Normalised Abundances-PEFE	Total Log2 Normalised Abundances-control	LogFC (PEFE vs control)
FAU	FAU ubiquitin-like and ribosomal protein S30	9.55	5.53	4.03
CFAP54	Cilia- and flagella-associated protein 54	8.02	5.84	2.18
AMBP	Alpha-1-microglobulin (EC 1.6.2.-)	8.76	6.61	2.15
SERPINA1	Alpha-1-antiproteinase (Alpha-1-antitrypsin)	12.27	10.15	2.11
CFAP100	Cilia- and flagella-associated protein 100	9.47	7.37	2.11
ORM1	Alpha-1-acid glycoprotein	10.50	8.39	2.11
AHSG	Alpha-2-HS-glycoprotein	12.14	10.09	2.05
SERPINA3-4	Serpin A3-4	9.24	7.23	2.01
ODAD3	Outer dynein arm-docking complex subunit 3	6.49	4.52	1.98
FAM171A2	Protein FAM171A2	5.17	3.25	1.92
ALB	Albumin	14.41	12.50	1.91
AFP	Alpha-fetoprotein (Alpha-1-fetoprotein)	11.41	9.50	1.91
GRK7	G protein-coupled receptor kinase 7	6.72	4.88	1.84
IGL@	Immunoglobulin light chain, lambda gene cluster	7.26	5.44	1.82
C3	Complement C3	11.08	9.26	1.81
SERPINA3-1	Serpin A3-1 (Endopin-1A) (Muscle endopin-1A) (mEndopin-1A)	7.88	6.07	1.80
LRG1	Leucine-rich alpha-2-glycoprotein 1	6.03	4.28	1.76
FETUB	Fetuin-B	10.32	8.56	1.75
GC	Vitamin D-binding protein (DBP) (VDB) (Gc-globulin) (Group-specific component)	10.85	9.11	1.74
IGK	IGK protein	5.40	3.67	1.74
APOA2	Apolipoprotein A-II	6.83	5.15	1.68
SERPIND1	SERPIND1 protein	8.21	6.54	1.67

TF	Serotransferrin (Transferrin)	12.40	10.75	1.65
SERPINC1	Antithrombin-III	9.88	8.25	1.63
C8A	Complement component C8 alpha chain	4.15	2.54	1.62
APOA1	Apolipoprotein A-I	10.92	9.33	1.59
ITIH2	Inter-alpha-trypsin inhibitor heavy chain H2	7.74	6.16	1.59
A1BG	Alpha-1B-glycoprotein	8.75	7.19	1.56
ITIH4	Inter-alpha-trypsin inhibitor heavy chain H4	9.87	8.34	1.53
ITIH3	Inter-alpha-trypsin inhibitor heavy chain H3	7.57	6.05	1.53

Table 7.2 Summary of top 30 molecules, sorted by phosphoprotein, upregulated in response to PEFE treatment in Caco2 cells

Protein name	Full protein name	Phospho Site (Human)	Phospho Adjusted Log2 Normalised Abundance-PEFE	Phospho Adjusted Log2 Normalised Abundance -control	LogFC (PEFE vs control)
RPS6	40S ribosomal protein S6	S247	-0.99	-5.24	4.25
H1-3	Histone H1.3	S189	0.23	-2.38	2.61
SLC7A6OS	Solute carrier family 7 member 6 opposite strand transcript	S308/S302	-2.03	-4.30	2.27
MRPS33	28S ribosomal protein S33	S15/Y7	-4.13	-6.32	2.19
NMD3	60S ribosomal export protein	T470	-2.84	-4.95	2.11
RPL17	60S ribosomal protein L17	S141	-4.43	-6.49	2.06
FMNL2	Formin-like protein 2	S171	-4.81	-6.77	1.96
CIR1	Corepressor interacting with RBPJ 1	S202	1.51	-0.20	1.72
RYR3	Ryanodine receptor 3	T3229	0.99	-0.72	1.71
CTNND1	Catenin delta-1	S349	-5.25	-6.92	1.67
CDC5L	Cell division cycle 5-like protein	S303	-3.55	-5.13	1.58
OCLN	Occludin	S408	-4.55	-6.09	1.55
DNMT1	DNA (cytosine-5)-methyltransferase	Ambiguous	-2.88	-4.42	1.53
PPP1R3D	Protein phosphatase 1 regulatory subunit 3D	S74/S77	-1.32	-2.82	1.50
NUP50	Nuclear pore complex protein Nup50	S221	-4.07	-5.42	1.36
KPNA4	Importin subunit alpha-3	S60	-3.82	-5.17	1.35
KDM3B	Lysine-specific demethylase 3B	S278	-2.34	-3.69	1.34
NUP133	Nuclear pore complex protein Nup133	S60	-5.69	-6.97	1.28
MBD1	Methyl-CpG-binding domain protein 1	S297	0.16	-1.10	1.26
BPTF	Bromodomain and PHD finger-containing transcription factor	S1310	-2.15	-3.39	1.23
SSR3	Translocon-associated protein subunit gamma	S105	-1.57	-2.78	1.21

CDK12	Cyclin-dependent kinase 12	Ambiguous	-0.42	-1.54	1.12
SERBP1	Plasminogen activator inhibitor 1 RNA-binding protein	S74	-6.43	-7.54	1.12
H1-2	Histone H1.2	S36	-0.85	-1.91	1.06
RBL1	Retinoblastoma-like protein 1	S975	2.35	1.34	1.01
SRC	Proto-oncogene tyrosine-protein kinase Src	Y419	-2.16	-3.17	1.00
USP13	Ubiquitin carboxyl-terminal hydrolase 13	T122	1.08	0.08	1.00
GPRC5A	Retinoic acid-induced protein 3	S345	-0.75	-1.75	1.00
BAD	Bcl2-associated agonist of cell death	S118	1.68	0.73	0.96
CLDN11	Claudin-11	S198	2.32	1.38	0.94

Table 7.3 Summary of top 30 molecules, sorted by total protein, downregulate in response to PEFE treatment in Caco2 cells

Protein name	Full protein name	Total Log2 Normalised Abundances-PEFE	Total Log2 Normalised Abundances-control	LogFC (PEFE vs control)
RYR3	Ryanodine receptor 3	6.86	8.81	-1.95
TOP1MT	DNA topoisomerase I, mitochondrial	2.17	3.82	-1.65
RGS3	Regulator of G-protein signalling 3	1.14	2.70	-1.56
CLDN5	Claudin-5	2.32	3.85	-1.53
EML6	Echinoderm microtubule-associated protein-like 6	1.93	3.23	-1.31
TMEM164	Transmembrane protein 164	1.58	2.89	-1.30
PLIN2	Perilipin-2 (Adipophilin)	6.59	7.87	-1.28
TAPBPL	Tapasin-related protein (TAPASIN-R)	1.68	2.91	-1.23
CXCL1	Growth-regulated alpha protein (C-X-C motif chemokine 1)	1.32	2.54	-1.21
PCDH17	Protocadherin-17	6.51	7.70	-1.19
CD226	CD226 molecule	1.85	3.04	-1.19
CCN1	CCN family member 1 (Cellular communication network factor 1)	8.11	9.30	-1.19
MBD1	Methyl-CpG-binding domain protein 1	6.02	7.19	-1.18
PIGQ	Phosphatidylinositol N-acetylglucosaminyltransferase subunit Q	2.93	4.10	-1.17
DSC2	Desmocollin-2	1.32	2.49	-1.16
MPC1	Mitochondrial pyruvate carrier 1	8.19	9.33	-1.14
DDX21	Nucleolar RNA helicase 2	11.88	13.02	-1.14
TTC21B	Tetratricopeptide repeat protein 21B	7.39	8.50	-1.11
METAP2	Methionine aminopeptidase 2	2.66	3.74	-1.09
RPL3	Ribosomal protein L3	2.51	3.56	-1.05
PPBP	Platelet basic protein (PBP)	1.68	2.72	-1.04

NSA2	Ribosome biogenesis protein NSA2 homolog	8.86	9.88	-1.02
PTPRQ	Phosphatidylinositol phosphatase	3.32	4.34	-1.02
UTP23	rRNA-processing protein UTP23 homolog	6.30	7.29	-0.99
H1-0	Histone H1.0	8.66	9.63	-0.97
TTF1	Transcription termination factor 1	6.16	7.13	-0.97
IFNGR1	Interferon gamma receptor 1	2.00	2.96	-0.96
ITGB1BP2	Integrin beta-1-binding protein 2	2.49	3.45	-0.96
PRKCE	Protein kinase C epsilon type	8.21	9.17	-0.96
SLC44A2	Solute carrier family 44 member 2	2.93	3.86	-0.93

Table 7.4 Summary of top 30 molecules, sorted by phosphoprotein, downregulated in response to PEFE treatment in Caco2 cells

Protein name	Full protein name	Phospho Site (Human)	Phospho Adjusted Log2 Normalised Abundance-PEFE	Phospho Adjusted Log2 Normalised Abundance -control	LogFC (PEFE vs control)
PHF14	PHD finger protein 14	S290/T278	1.06	2.98	-1.93
SAFB	Scaffold attachment factor B1	S604	-5.27	-3.51	-1.76
PAK2	Serine/threonine-protein kinase PAK 2 (EC 2.7.11.1)	S141	-6.29	-4.58	-1.72
FNBP1	Formin-binding protein 1	S296/S299	-3.99	-2.33	-1.65
RABL6	Rab-like protein 6	S641	-1.82	-0.29	-1.53
VSIR	V-type immunoglobulin domain-containing suppressor of T-cell activation	S248	-3.66	-2.28	-1.38
TPD52	Tumour protein D52	S176	-2.62	-1.29	-1.34
CERS4	Ceramide synthase 4	S350	-0.10	1.19	-1.29
KALRN	Kalirin RhoGEF kinase	S526	-5.18	-3.91	-1.26
BET1	BET1 homolog	S50	-2.60	-1.35	-1.25
PTK2B	Protein-tyrosine kinase 2-beta (EC 2.7.10.2)	T842	-4.16	-2.92	-1.24
OPHN1	Oligophrenin-1	S652	-0.03	1.16	-1.19
PRPF40A	Pre-mRNA-processing factor 40 homolog A	S883/S885	-2.97	-1.78	-1.18
SH3BP5L	SH3 domain-binding protein 5-like	S343	-1.24	-0.11	-1.13
REV1	DNA repair protein REV1 (EC 2.7.7.-)	S1051/S1053/S1055	1.19	2.31	-1.12
PDLIM2	PDZ and LIM domain protein 2	S129/ Ambiguous	-3.71	-2.65	-1.06
REEP4	Receptor expression-enhancing protein 4	S257	-0.07	0.94	-1.01
PDLIM4	PDZ and LIM domain protein 4	S112	-1.60	-0.60	-1.00
PAK1	Serine/threonine-protein kinase PAK 1	S144	-0.43	0.56	-0.99
ICE2	Little elongation complex subunit 2	S570/ S571/ T573	-3.06	-2.09	-0.97
LAT	Linker for activation of T-cells family member 1	S224	2.05	3.01	-0.96
AHSG	Alpha-2-HS-glycoprotein	S138	-1.96	-1.00	-0.96
CNN1	Calponin-1	S2/ S3	5.15	6.11	-0.96

TRPC6	Short transient receptor potential channel 6	S815	-4.25	-3.32	-0.93
PPP1R3E	Protein phosphatase 1 regulatory subunit 3E	S79/ S81	2.36	3.28	-0.93
SYMPK	Symplekin	S1259	-4.82	-3.89	-0.93
RPTOR	Regulatory associated protein of MTOR complex 1	S881	1.87	2.79	-0.92
UCHL3	Ubiquitin carboxyl-terminal hydrolase isozyme L3	S130	-5.67	-4.79	-0.88
TUBA4A	Tubulin alpha-4A chain	Ambiguous	-7.44	-6.56	-0.87
MPL	Thrombopoietin receptor	S531	-2.51	-1.64	-0.87

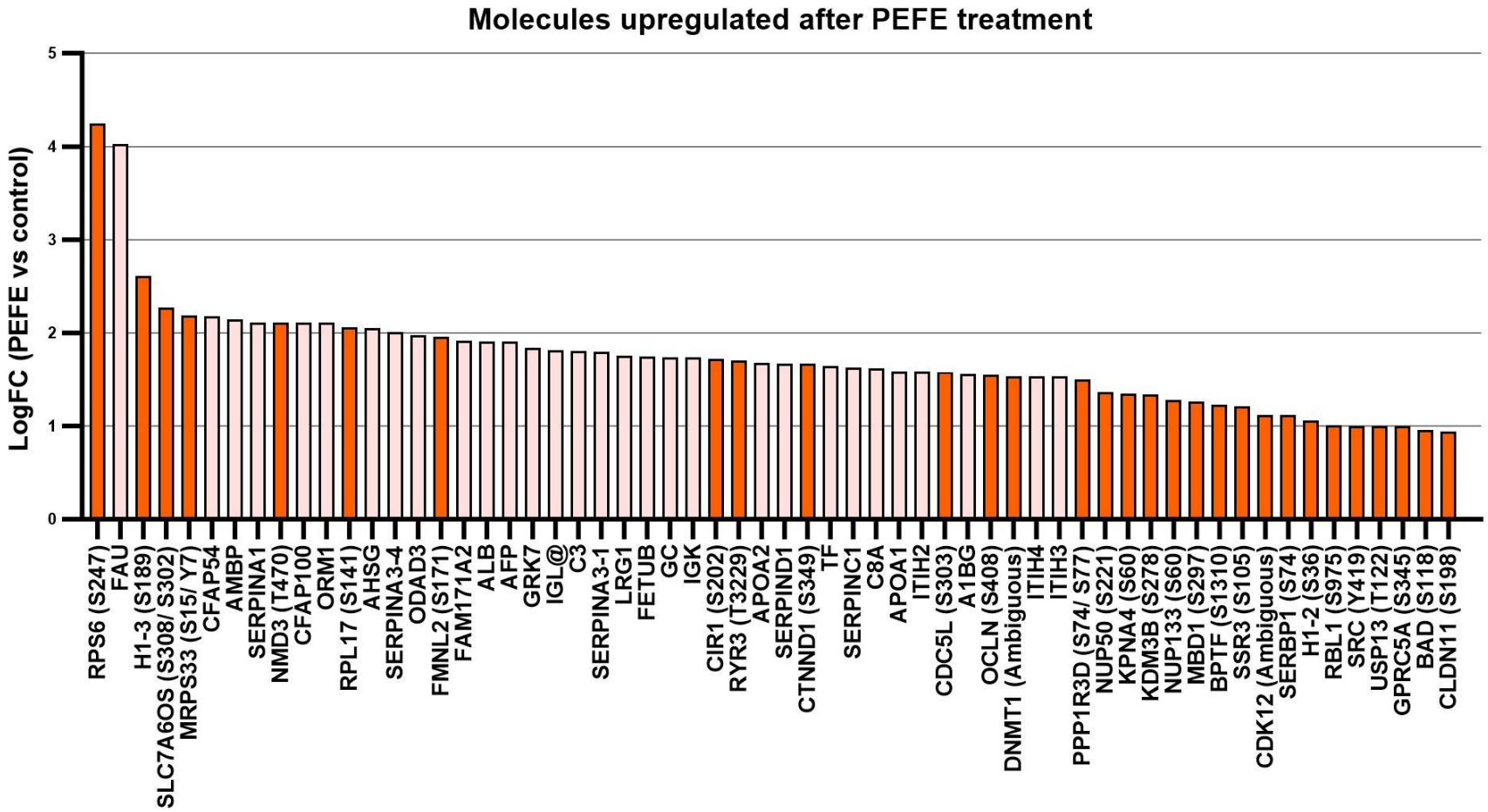

Figure 7.1 Protein microarray summary: top molecules for both total (pink bar) and phospho (orange bar) upregulated in response to PEFE treatment in Caco2 cells. The X-axis represents the name of the gene, and the y-axis represents the log fold change between the PEFE-treated group and the control group.

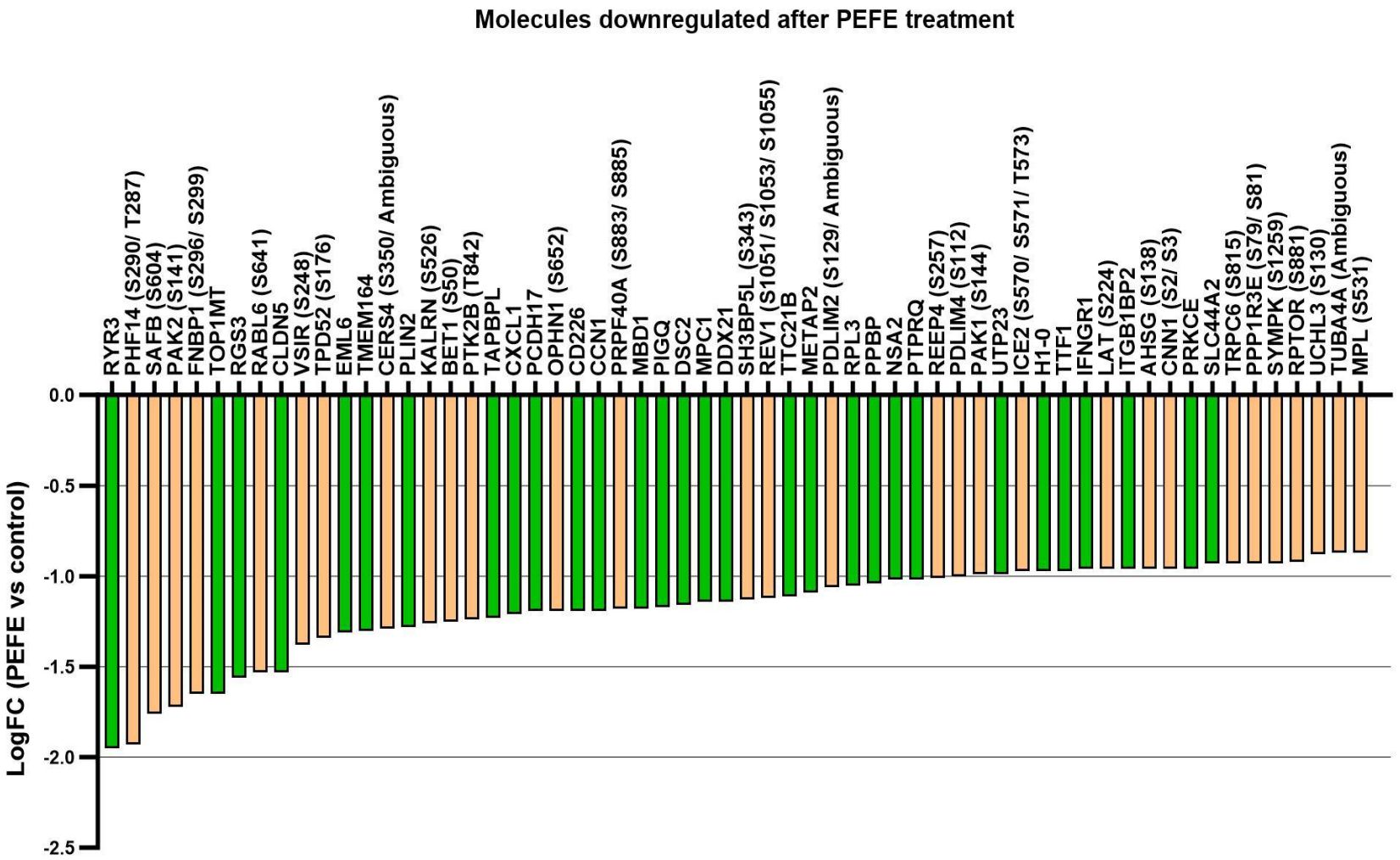

Figure 7.2 Protein microarray summary: top molecules for both total (green bar) and phospho (yellow bar) downregulated in response to PEFE treatment in Caco2 cells. The X-axis represents the name of the gene, and the y-axis represents the log fold change between the PEFE-treated group and the control group.

(A)

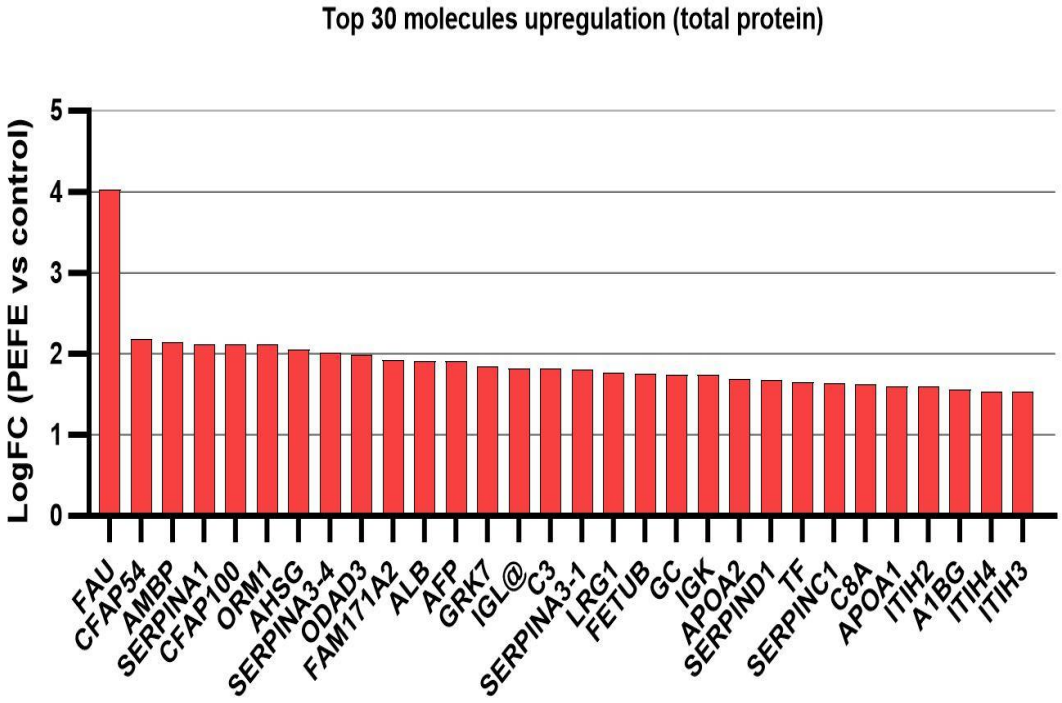

(B)

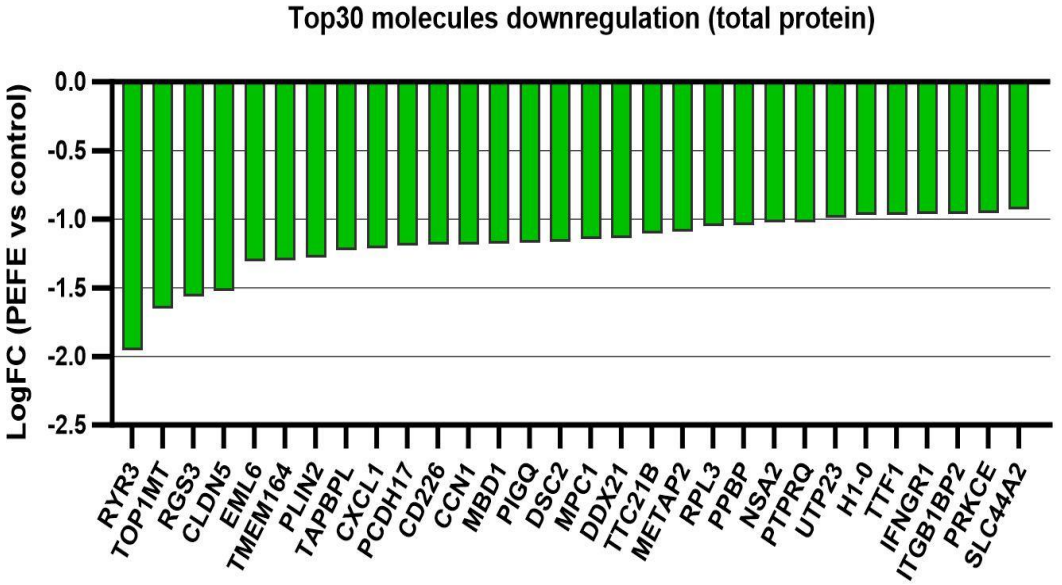

Figure 7.3 Top 30 total molecules up/downregulated in response to PEFE treatment in Caco2 cells. (A) Molecules with highest upregulated in response to PEFE treatment. (B) Molecules with highest downregulated in response to PEFE treatment. The X-axis represents the name of the gene, and the y-axis represents the log fold change between the PEFE-treated group and the control group.

(A)

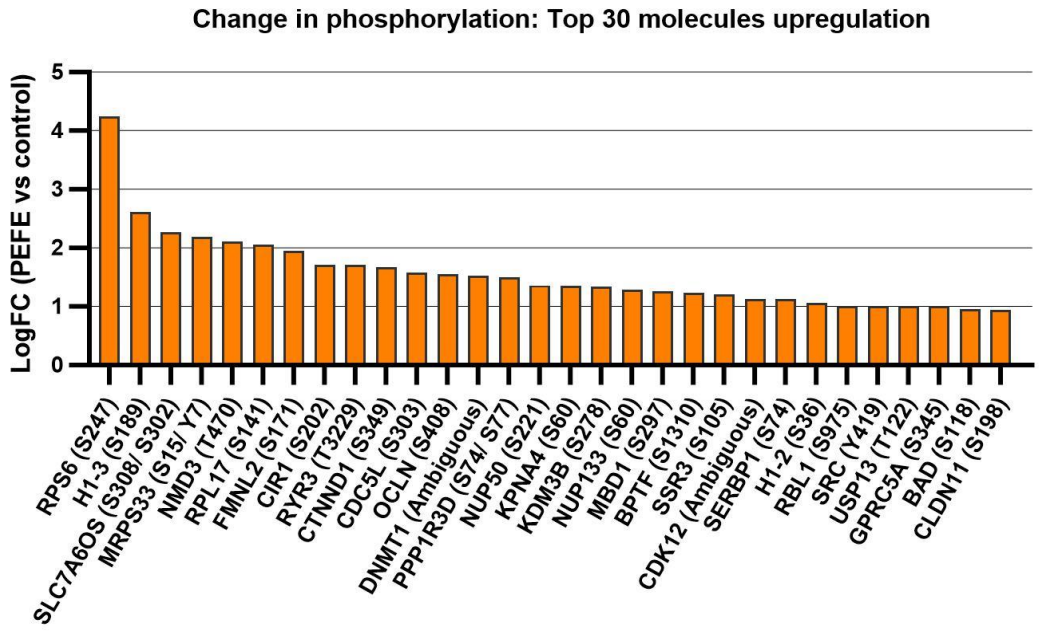

(B)

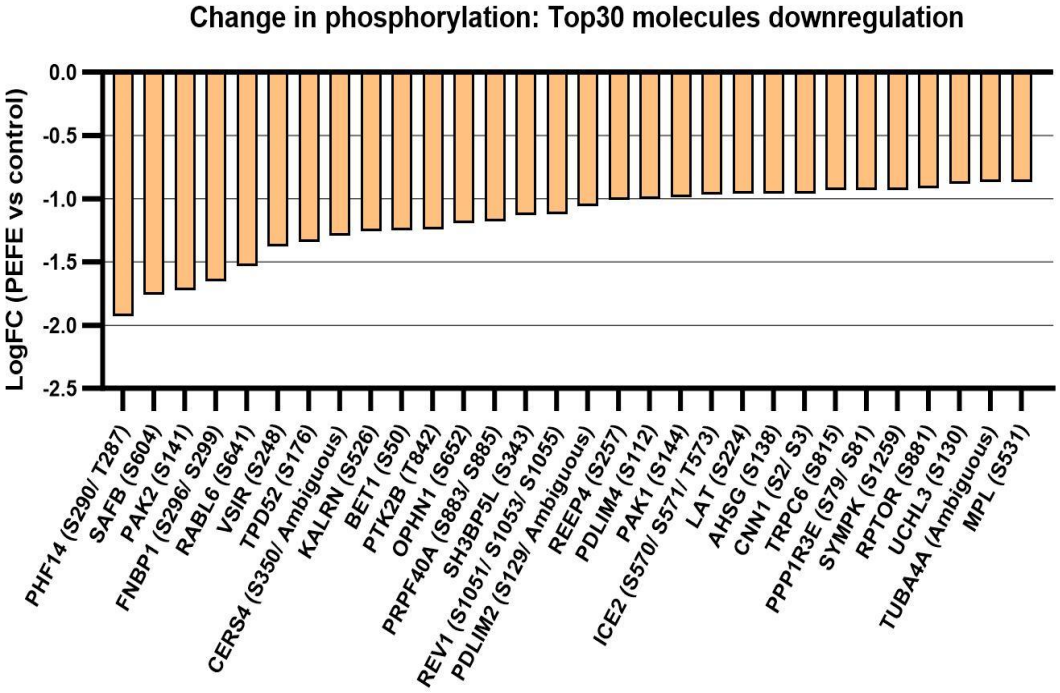

Figure 7.4 Change in phosphorylation (either up- or down-regulated) in response to PEFE treatment in Caco2 cells. (A) Phosphorylated molecules with highest upregulated in response to PEFE treatment. (B) Phosphorylated molecules with highest downregulated in response to PEFE treatment. The X-axis represents the name of the gene, and the y-axis represents the log fold change between the PEFE-treated group and the control group.

Based on proteomic analysis from the top list, we further conducted a Reactome analysis (www.reactome.org), which is an online pathway analyzing tool (Fabregat et al. 2016; Fabregat et al. 2017). Reactome allows us to enter a list of proteins and visualize the affected pathways, providing an overall view of potential key pathways that are involved in PEFE treatment. The genome-wide overview schematic diagram of the signalling pathways was initially generated to provide basic information on which cellular processes PEFE affected. As demonstrated in Figure 7.5, PEFE participates in pathways that are related to immune system, signal transduction, metabolism, programmed cell death, cell-cell communication, etc.

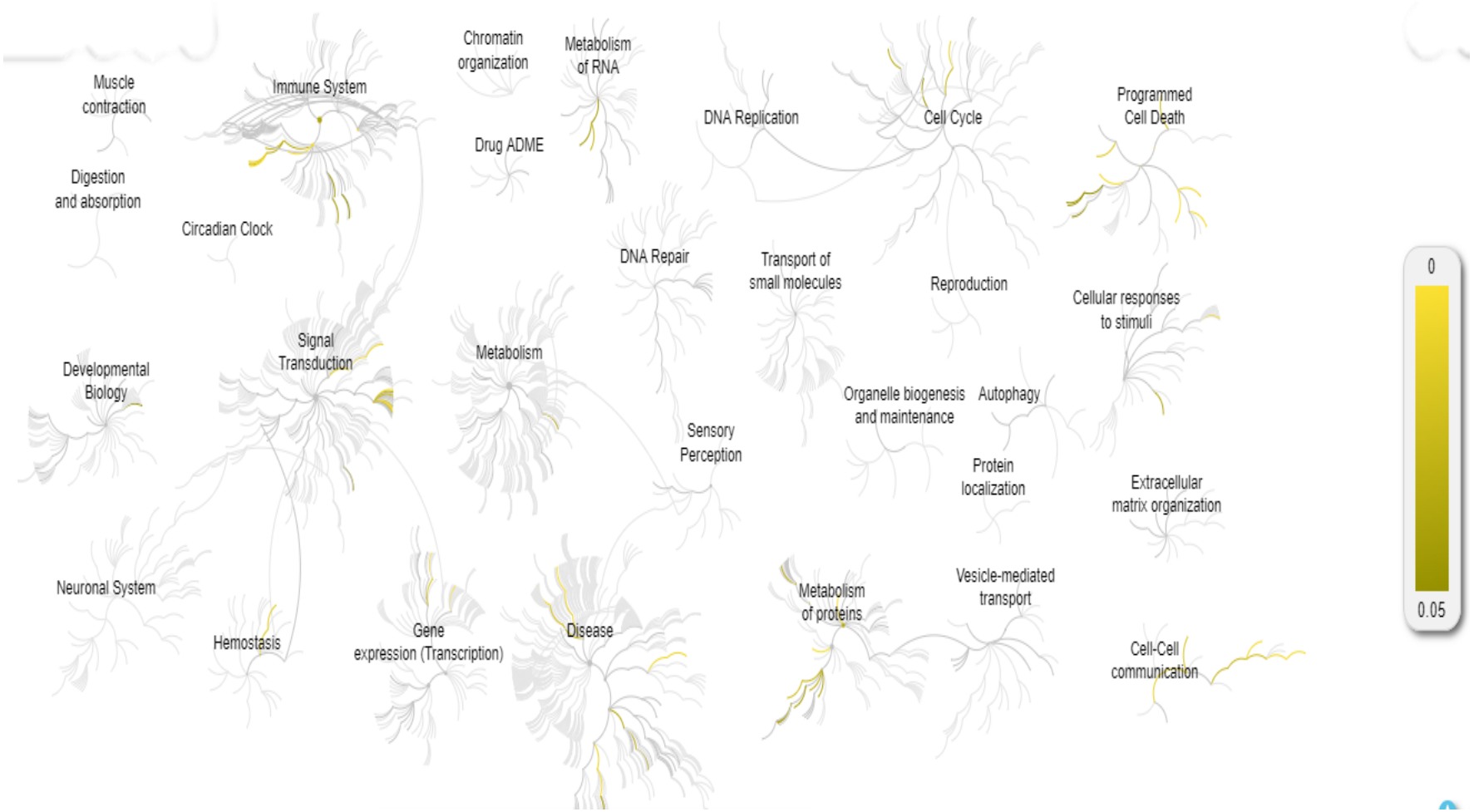

Figure 7.5 Genome-wide overview of the signalling pathway which was affected in response to PEFE. Reactome pathways are arranged in a hierarchy. The center of each of the circular "bursts" is the root of one toplevel pathway. Each step away from the center represents the next level lower in the pathway hierarchy. P-value, which is marked by the colour code, denotes over-representation of that pathway. Light grey signifies pathways that are not significantly over-represented. Generated from: www.reactome.org (20th July, 2024).

7.3.2 Potential TJ-related proteins involved in PEFE treatment

TJ plays a crucial role in the maintenance of the integrity and barrier function of the cells. Upon exposure to PEFE, numerous molecules associated with TJ exhibited altered expression, including integral transmembrane proteins like Claudins, MarvelD1 (Occludin), Nectin4, the peripheral or plaque anchoring proteins like MAGI1, CASK, AF6, and also TJ-associated or regulatory proteins like Cingulin, Symplekin, Rho GTPase-activating proteins, protein kinase C family, as detailed in Table 7.5 to Table 7.7. Table 7.5 and Table 7.6 presented an overview of the total TJ-linked proteins which were up- and down-regulated following PEFE treatment, respectively. Table 7.7 provides an overview of the dysregulation of phosphorylated TJ-linked proteins in response to PEFE treatment. Graphical representations in Figure 7.6 and Figure 7.7 illustrated the up/downregulation of these TJ-related molecules.

Among these molecules belong to the integral transmembrane proteins, when assessing the Claudin family, it is interesting to note that the total amount of Claudin-6 exhibited an increase, in contrast to Claudin-5 and Claudin-11, which experienced a decrease in levels following PEFE treatment. While the phosphorylated Claudin-11 (at S198) exhibited a decrease in response to PEFE. There was a slight increase in MarvelD1's total expression after exposure to PEFE, while the phosphorylation at S408 showed a significant increase. Regarding the peripheral or plaque anchoring proteins, MAGI1 and CASK demonstrated a relatively less increase and AF6 exhibited less decrease regarding the total protein in response to PEFE. When examining TJ-associated or regulatory proteins, Rho GTPase-activating protein (ARHGAP), a large family, displayed considerable dysregulation among these molecules. Specially, the total ARHGAP-1, -9, -12, -18, -27, -28 was somewhat upregulated following PEFE treatment, while total ARHGAP-5, -6, -10, -11A, -15, -22, -23 was downregulated in response to PEFE treatment. When comparing the phosphorylation status, various members such as the phosphorylated ARHGAP5 (unclear phosphorylated residue), ARHGAP35 (S1179), ARHGAP6 (T821), ARHGAP1 (S51), ARHGAP4 (S418) and ARHGAP25 (S487) exhibited varying degrees of upregulation. Conversely, phosphorylated ARHGAP27 (S466) and ARHGAP12 (unclear phosphorylated residue) was downregulated in response to PEFE. As for protein kinase C family, the total expression of PRKC-Z, -A, -Q was increased, while the total expression of PRKC-E was decreased.

Table 7.5 Summary of TJ-related molecules, sorted by total protein, upregulated in response to PEFE treatment in Caco2 cells

Protein name	Full protein name	Total Log2 Normalised Abundances-PEFE	Total Log2 Normalised Abundances-control	LogFC (PEFE vs control)
RAB11B	RAB11B, member RAS oncogene family	5.67	4.96	0.71
CLDN6	Claudin-6	4.65	4.20	0.45
ARHGAP27	Rho GTPase-activating protein 27	4.10	3.67	0.44
ARHGAP18	Rho GTPase-activating protein 18	7.99	7.64	0.35
PRKCZ	Protein kinase C zeta type	5.64	5.35	0.29
ARHGAP1	Rho GTPase-activating protein 1	9.68	9.44	0.24
TJAP1	TJ-associated protein 1	7.39	7.21	0.17
GNA12	Guanine nucleotide-binding protein subunit alpha-12	4.45	4.29	0.17
CASK	Peripheral plasma membrane protein	7.75	7.58	0.16
ARHGAP9	Rho GTPase-activating protein 9	2.49	2.32	0.16
ITCH	E3 ubiquitin-protein ligase Itchy homolog	9.16	9.00	0.16
PRKCA	Protein kinase C α type	6.50	6.34	0.16
ARHGAP12	Rho GTPase-activating protein 12	8.92	8.77	0.14
ARHGAP28	Rho GTPase-activating protein 28	5.42	5.28	0.13
PRKCQ	Protein kinase C θ type	7.83	7.70	0.13
MARVELD1	MARVEL domain-containing protein 1	4.97	4.85	0.12
MAGI1	Membrane-associated guanylate kinase, WW and PDZ domain containing 1	3.32	3.22	0.10
CTNNA1	Catenin α-1	10.56	10.46	0.10

Table 7.6 Summary of TJ-related molecules, sorted by total protein, downregulated in response to PEFE treatment in Caco2 cells

Protein name	Full protein name	Total Log2 Normalised Abundances-PEFE	Total Log2 Normalised Abundances-control	LogFC (PEFE vs control)
CLDN5	Claudin-5	2.32	3.85	-1.53
PRKCE	Protein kinase C ε type	8.21	9.17	-0.96
CLDN11	Claudin-11	2.26	3.05	-0.79
ARHGAP23	Rho GTPase-activating protein 23	2.85	3.38	-0.53
ARHGAP5	Rho GTPase-activating protein 5	7.45	7.82	-0.37
AFDN	Afadin, adherens junction formation factor	5.61	5.91	-0.29
PTEN	Phosphatidylinositol 3,4,5-trisphosphate 3-phosphatase and dual-specificity protein phosphatase	5.30	5.56	-0.26
SYMPK	Symplekin	10.48	10.74	-0.26
ARHGAP6	Rho GTPase-activating protein 6	6.73	6.97	-0.25
NECTIN4	Nectin cell adhesion molecule 4	2.85	3.04	-0.19
ARHGAP11A	Rho GTPase-activating protein 11A	7.07	7.24	-0.17
ARHGAP15	Rho GTPase-activating protein 15	3.94	4.09	-0.14
ARHGAP22	Rho GTPase-activating protein 22	5.27	5.38	-0.11
ARHGAP10	Rho GTPase-activating protein 10	8.11	8.22	-0.11
MTSS1	Metastasis suppressor protein 1	6.75	6.85	-0.10

Table 7.7 Summary of TJ-related molecules, sorted by phosphoprotein, dysregulated in response to PEFE treatment in Caco2 cells

Protein name	Phospho Site (Human)	Full protein name	Phospho Adjusted Log2 Normalised Abundance-PEFE	Phospho Adjusted Log2 Normalised Abundance -control	LogFC (PEFE vs control)
OCLN	S408	Occludin	-4.55	-6.09	1.55
CLDN11	S198	Claudin-11	2.32	1.38	0.94
ARHGAP5	Ambiguous	Rho GTPase-activating protein 5	0.54	-0.15	0.69
ARHGAP35	S1179	Rho GTPase-activating protein 35	-3.04	-3.65	0.61
ARHGAP6	T821	Rho GTPase-activating protein 6	-1.55	-2.14	0.58
CGN	S338	Cingulin	-0.62	-1.17	0.54
DLC1	S566	Rho GTPase-activating protein 7	2.39	1.87	0.52
ARHGAP1	S51	Rho GTPase-activating protein 1	-2.89	-3.25	0.36
F11R	S287	Junctional adhesion molecule A	-2.89	-3.22	0.33
ARHGAP4	S418	Rho GTPase-activating protein 4	-1.21	-1.48	0.26
ARHGAP25	S487	Rho GTPase-activating protein 25	-2.08	-2.34	0.25
ARHGAP21	Ambiguous	Rho GTPase-activating protein 21	1.76	1.58	0.18
CTNNA1	S641	Catenin α-1	-5.02	-4.72	-0.29
RAB1B	S123/T126/T127	Ras-related protein Rab-1B	-1.81	-1.50	-0.31
ITCH	S10/T15	E3 ubiquitin-protein ligase Itchy homolog	-6.79	-6.39	-0.40
ARHGAP27	S466	Rho GTPase-activating protein 27	2.18	2.70	-0.53
ARHGAP12	Ambiguous	Rho GTPase-activating protein 12	-1.57	-0.89	-0.68
SYMPK	S1259	Symplekin	-4.82	-3.89	-0.93

(A)

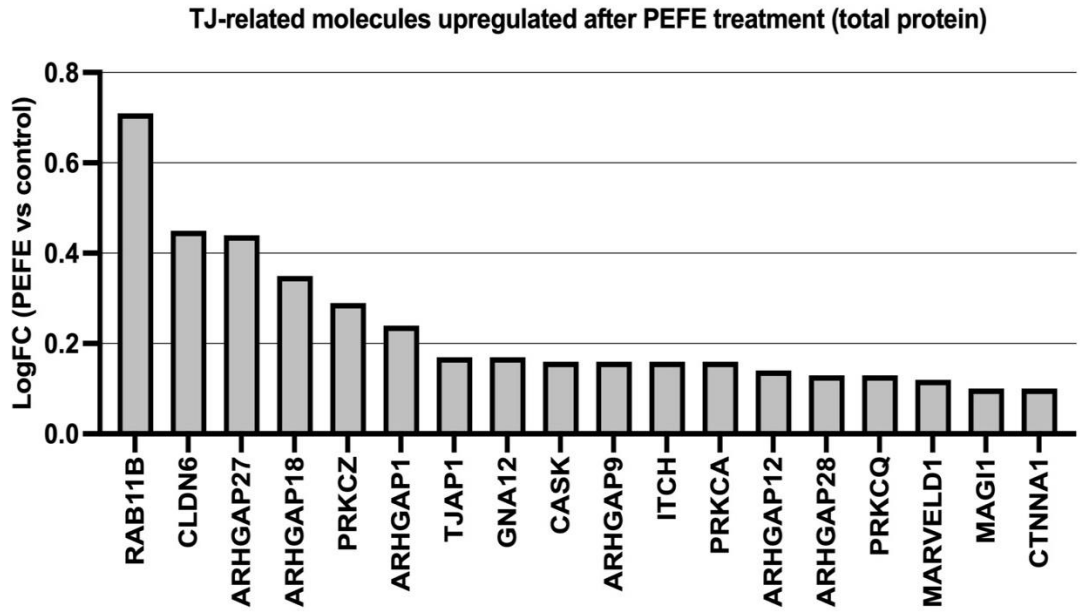

(B)

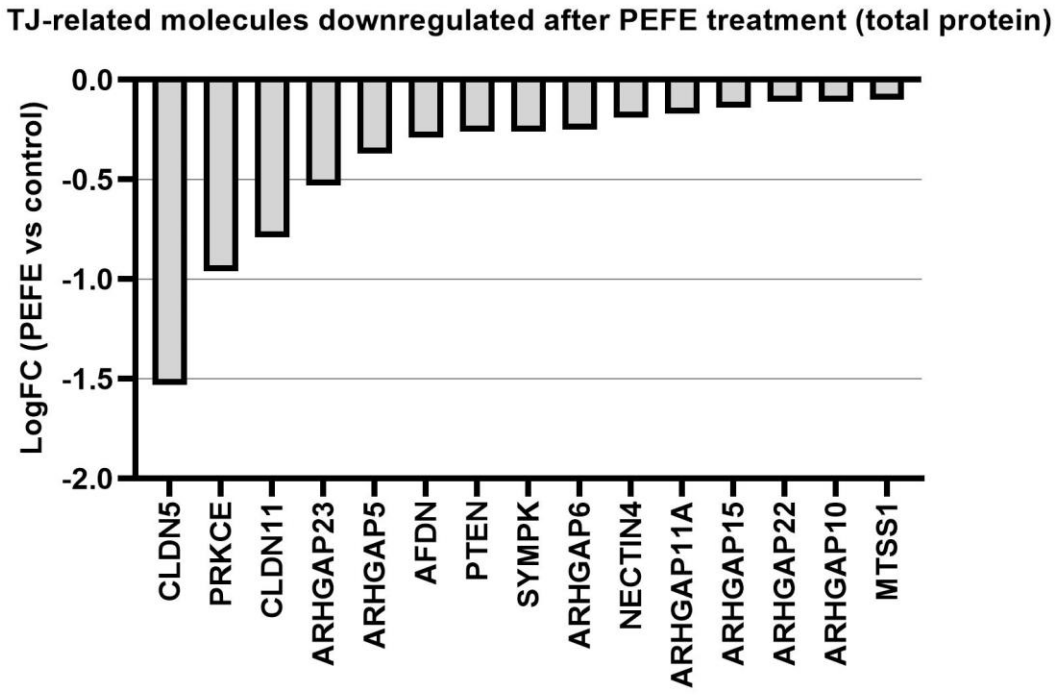

Figure 7.6 TJ-related molecules up/downregulated in response to PEFE treatment in Caco2 cells, sorted by total protein. (A) Molecules with upregulation in response to PEFE treatment. (B) Molecules with downregulation in response to PEFE treatment. The X-axis represents the name of the gene, and the y-axis represents the log fold change between the PEFE-treated group and the control group.

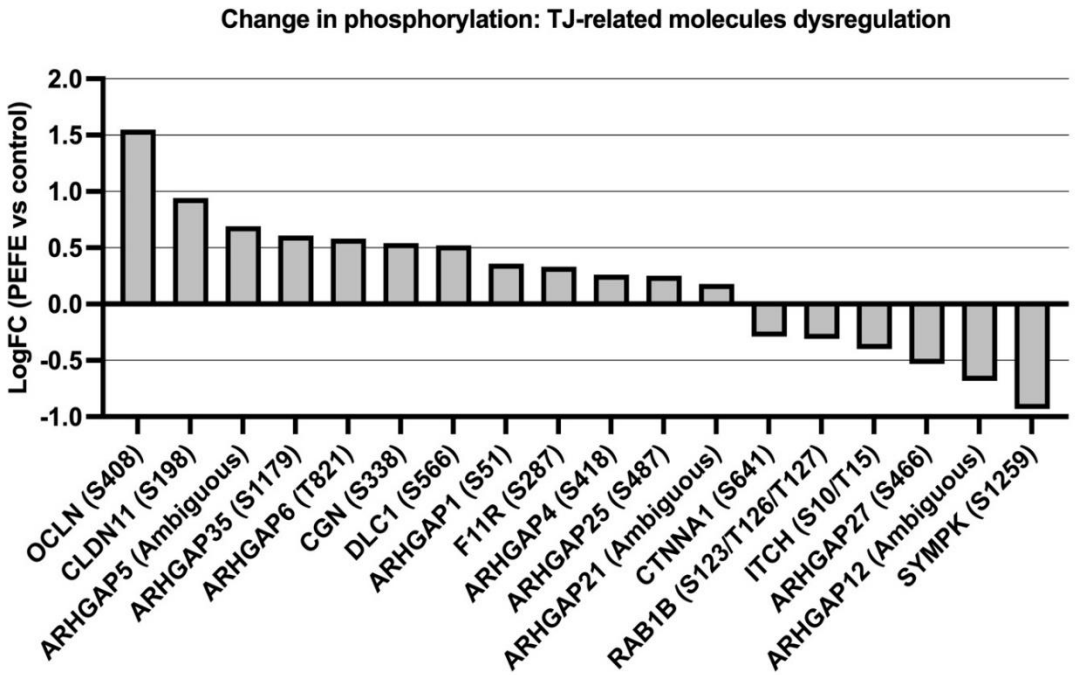

Figure 7.7 Phosphorylation changes of TJ-related molecules (ether up- or down-regulation) in response to PEFE treatment in Caco2 cells. The X-axis represents the name of the gene, and the y-axis represents the log fold change between the PEFE-treated group and the control group.

7.3.3 Potential apoptosis-related proteins involved in PEFE treatment

A variety of proteins linked to apoptosis, including Caspases, Bcl-2 family (B-cell lymphoma/leukaemia-2 genes), heat shock proteins, AKT (serine/threonine-specific protein kinase), MAPKs (mitogen-activated protein kinase), which exhibited altered expression patterns upon exposure to PEFE, as demonstrated in Table 7.8 to Table 7.10. Table 7.8 and Table 7.9 summarize the total apoptosis-associated proteins that were up- and down-regulated in response to PEFE, respectively. Table 7.10 summarizes the dysregulation of phosphorylated apoptosis-associated proteins resulting from exposure to PEFE. Figure 7.8 and Figure 7.9 are graphical representations that visually depict the up/downregulation of these apoptosis-related molecules.

Among these molecules, it is noteworthy that the total amount of all caspases, including caspase-1, -3, -6, -7, and -8 was increased following exposure to PEFE, whilst the phosphorylated caspase-2 (at S340) and Caspase-8 (at S60) exhibited a decrease in response to PEFE. When examining the MAPKs family, most of the members, regarding with total

protein, demonstrated an upregulation in response to PEFE, such as MAPK-1 (ERK2), -3 (ERK1), -7, -8, -10, -13, -14, -15, also MAP2K6 (MEK6) and MAP2K2 (MEK2). When comparing the phosphorylation status, the phosphorylated MAPK-1 (T185) and -3 (T202) was increased, while MAP2K2 (T394) and MAPK14 (Y182) was decreased in response to PEFE. As for AKT, PEFE had a relatively minor impact on both total and phosphorylated levels. Additionally, PEFE led to alterations in numerous members of members of the Bcl-2 family. Notably, BAX, BID, BCL10, BNIP2, and BCL9L was upregulated, whereas TMBIM6, TMBIM1, BCL7C, BCLAF1, BCL7B, and BCL2L1 was somewhat downregulated in response to PEFE. PEFE strongly influenced the phosphorylation of BAD (S118), leading to nearly a twofold increase in expression. Furthermore, the phosphorylation of TMBIM1, BCL10, BCL7C, BCL9L, BNIP2, BCLAF showed varying degrees of up/downregulation in response to PEFE. Concerning the heat chock protein family, some members also exhibited the dysregulation after PEFE exposure at both total and phosphorylated protein levels.

Table 7.8 Summary of apoptosis-related molecules, sorted by total protein, upregulated in response to PEFE treatment in Caco2 cells

Protein name	Full protein name	Total Log2 Normalised Abundances-PEFE	Total Log2 Normalised Abundances-control	LogFC (PEFE vs control)
MAP2K6	Dual specificity mitogen-activated protein kinase 6 (MAP kinase kinase 6)	3.29	2.35	0.94
CARD19	Caspase recruitment domain-containing protein 19	4.30	3.78	0.52
BAX	Apoptosis regulator BAX (Bcl-2-like protein 4)	9.42	8.92	0.50
MAPK10	Mitogen-activated protein kinase 10 (MAP kinase 10)	6.55	6.08	0.48
CASP6	Caspase-6	10.05	9.65	0.40
MAP2K2	Dual specificity mitogen-activated protein kinase 2 (MAP kinase kinase 2)	8.89	8.52	0.36
BID	BH3-interacting domain death agonist	6.99	6.66	0.33
HSPA2	Heat shock-related 70 kDa protein 2	5.83	5.50	0.32
CASP1	Caspase-1	5.60	5.27	0.32
CASP3	Caspase-3	8.59	8.27	0.32
MAPK3	Mitogen-activated protein kinase 3 (MAP kinase 3)	9.65	9.33	0.32
CASP8	Caspase-8	9.41	9.11	0.30
HSPA12A	Heat shock 70 kDa protein 12A	5.13	4.84	0.29
SMAD4	Mothers against decapentaplegic homolog 4	7.43	7.15	0.28
MAPK13	Mitogen-activated protein kinase 13 (MAP kinase 13)	7.50	7.22	0.28
BCL10	B-cell lymphoma/leukaemia 10	8.83	8.56	0.28
MAPK15	Mitogen-activated protein kinase 15 (MAP kinase 15)	6.68	6.42	0.26
HSPB1	Heat shock protein beta-1 (HspB1) (28 kDa heat	11.96	11.72	0.25

	shock protein)			
BAK1	Bcl-2 homologous antagonist/killer (Apoptosis regulator BAK) (Bcl-2-like protein 7)	7.55	7.31	0.24
MAPK1	Mitogen-activated protein kinase 1 (MAP kinase 1)	10.62	10.39	0.23
MAPK14	Mitogen-activated protein kinase 14 (MAP kinase 14)	10.23	10.01	0.22
AKT2	RAC-beta serine/threonine-protein kinase	9.63	9.42	0.21
AKT1	RAC-alpha serine/threonine-protein kinase	8.91	8.72	0.19
MAPK8	Mitogen-activated protein kinase 8 (MAP kinase 8)	9.82	9.64	0.18
RFFL	E3 ubiquitin-protein ligase rififylin	4.01	3.84	0.17
BNIP2	BCL2 Interacting Protein 2	7.21	7.04	0.17
MAPK7	Mitogen-activated protein kinase 7 (MAP kinase 7)	4.78	4.63	0.15
BCL9L	B-cell CLL/lymphoma 9-like protein	6.11	5.97	0.14
CASP7	Caspase-7	4.78	4.64	0.14
SRC	Proto-oncogene tyrosine-protein kinase Src	8.50	8.42	0.08

Table 7.9 Summary of apoptosis-related molecules, sorted by total protein, downregulated in response to PEFE treatment in Caco2 cells

Protein name	Full protein name	Total Log2 Normalised Abundances-PEFE	Total Log2 Normalised Abundances-control	LogFC (PEFE vs control)
TMBIM6	Bax inhibitor 1	6.31	7.00	-0.69
NOD1	Nucleotide-binding oligomerization domain-containing protein 1	1.72	2.41	-0.68
TMBIM1	Protein lifeguard 3 (Transmembrane BAX inhibitor motif-containing protein 1)	3.66	4.23	-0.58
CRADD	Death domain-containing protein CRADD	4.96	5.41	-0.44
BCL7C	B-cell CLL/lymphoma 7 protein family member C	6.46	6.90	-0.44
BCLAF1	Bcl-2-associated transcription factor 1	10.93	11.36	-0.43
HSPA8	Heat shock protein family A (Hsp70) member 8	5.56	5.91	-0.35
BIRC5	Baculoviral IAP repeat-containing protein 5 (Apoptosis inhibitor 4)	7.80	8.15	-0.35
CAAP1	Caspase activity and apoptosis inhibitor 1	8.64	8.97	-0.33
HSPA13	Heat shock 70 kDa protein 13	8.31	8.62	-0.31
AKT3	RAC-gamma serine/threonine-protein kinase	5.49	5.74	-0.25
HSPA5	Heat shock protein 70 family protein 5	13.18	13.37	-0.18
BCL7A	B-cell CLL/lymphoma 7 protein family member A	5.32	5.49	-0.17
HSP90B1	Heat shock protein 90 kDa beta member 1	12.40	12.54	-0.14
MCL1	Bcl-2-like protein 3	6.96	7.09	-0.13
BCL7B	B-cell CLL/lymphoma 7 protein family member B	7.48	7.61	-0.13
PYCARD	Apoptosis-associated speck-like protein containing a CARD	4.35	4.48	-0.13
BCL2L1	Bcl-2-like protein 1	6.63	6.75	-0.13
HSPD1	Heat shock protein 60	13.90	14.02	-0.12
HSPA1B	Heat shock 70 kDa protein 1B	12.66	12.76	-0.10

Table 7.10 Summary of apoptosis-related molecules, sorted by phosphoprotein, dysregulated in response to PEFE treatment in Caco2 cells

Protein name	Phospho Site (Human)	Full protein name	Phospho Adjusted Log2 Normalised Abundance-PEFE	Phospho Adjusted Log2 Normalised Abundance -control	LogFC (PEFE vs control)
SRC	Y419	Proto-oncogene tyrosine-protein kinase	-2.16	-3.17	1.00
BAD	S118	Bcl2-associated agonist of cell death	1.68	0.73	0.96
TMBIM1	S81	Transmembrane BAX inhibitor motif-containing protein 1	1.33	0.45	0.88
MAPK3	T202	Mitogen-activated protein kinase 3 (MAP kinase 3)	-1.99	-2.75	0.77
MAPK1	T185	Mitogen-activated protein kinase 1 (MAP kinase 1)	-4.70	-5.34	0.63
BCL10	S138	B-cell lymphoma/leukaemia 10	0.65	0.09	0.56
HSPB1	Ambiguous	Heat shock protein beta-1	-4.41	-4.90	0.49
BCL7C	S126	B-cell CLL/lymphoma 7 protein family member C	-0.22	-0.55	0.33
AKT2	T451	RAC-beta serine/threonine-protein kinase	-3.28	-3.54	0.25
BCL9L	S987	B-cell CLL/lymphoma 9-like protein	-0.59	-0.84	0.25
HSP90B1	S306	Heat shock protein 90 kDa beta member 1	-5.11	-5.35	0.24
HSPA1B	S631	Heat shock 70 kDa protein 1B	-5.55	-5.77	0.22
HSPD1	S70	Heat shock protein 60	-8.87	-9.08	0.21
BNIP2	Ambiguous	BCL2/adenovirus E1B 19 kDa protein-interacting protein 2	-0.13	-0.32	0.19
CASP2	S340	Caspase-2	2.65	2.79	-0.13
BCLAF1	S177	Bcl-2-associated transcription factor 1	-1.29	-1.13	-0.16
MAP2K2	T394	Dual specificity mitogen-activated protein kinase 2 (MAP kinase 2)	-1.92	-1.68	-0.23
HSPA5	T518	Heat shock protein 70 family protein 5	-5.68	-5.43	-0.25
MAPK14	Y182	Mitogen-activated protein kinase 14 (MAP	-2.75	-2.38	-0.36

		kinase 14)			
CASP8	S60	Caspase-8	-4.47	-4.03	-0.44
RFFL	Ambiguous	E3 ubiquitin-protein ligase rififylin	1.17	1.70	-0.53

(A)

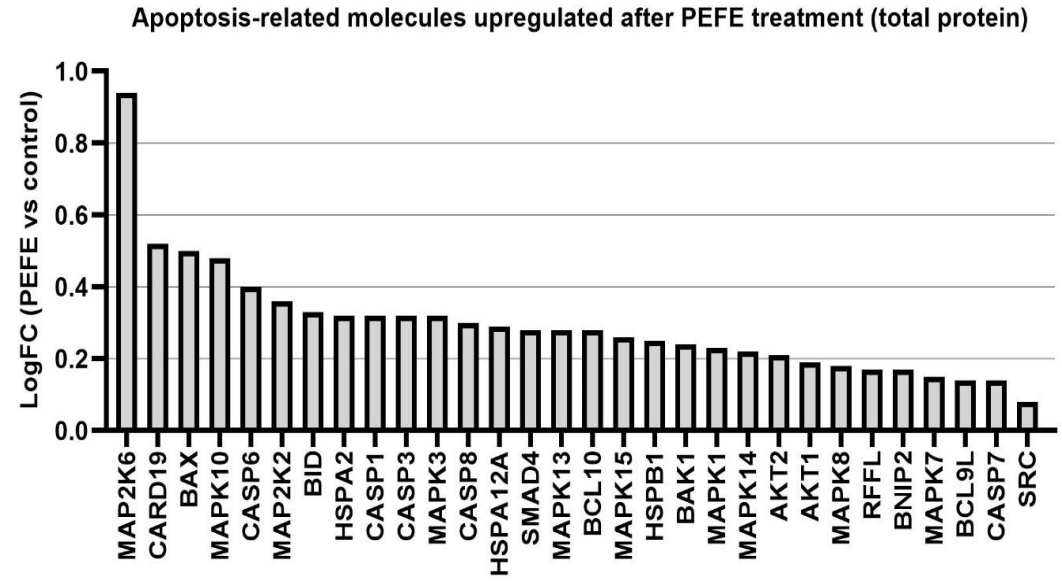

(B)

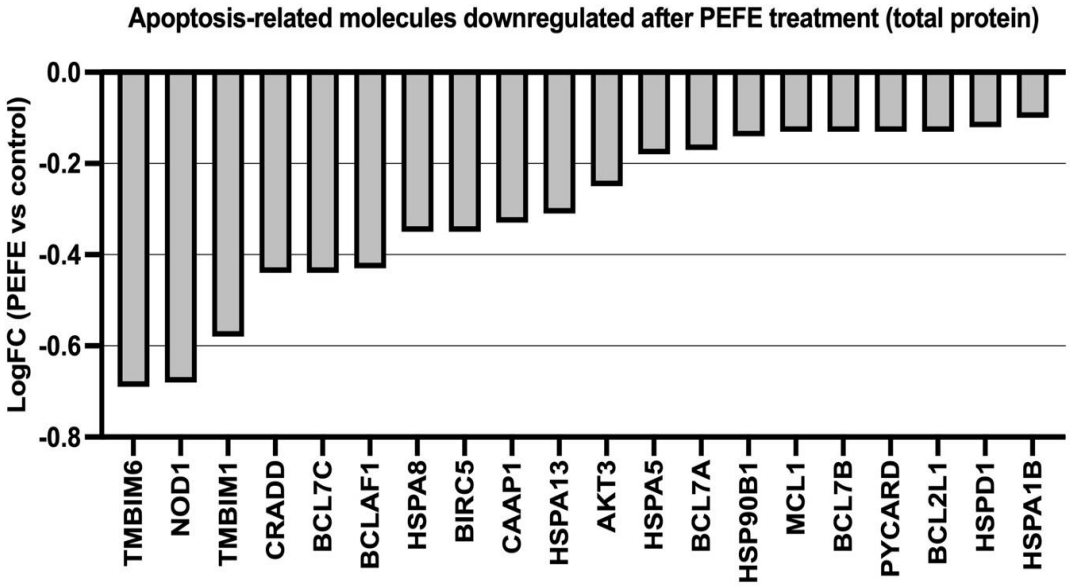

Figure 7.8 Apoptosis-related molecules up/downregulated in response to PEFE treatment in Caco2 cells, sorted by total protein. (A) Molecules with upregulation in response to PEFE treatment. (B) Molecules with downregulation in response to PEFE treatment. The X-axis represents the name of the gene, and the y-axis represents the log fold change between the PEFE-treated group and the control group.

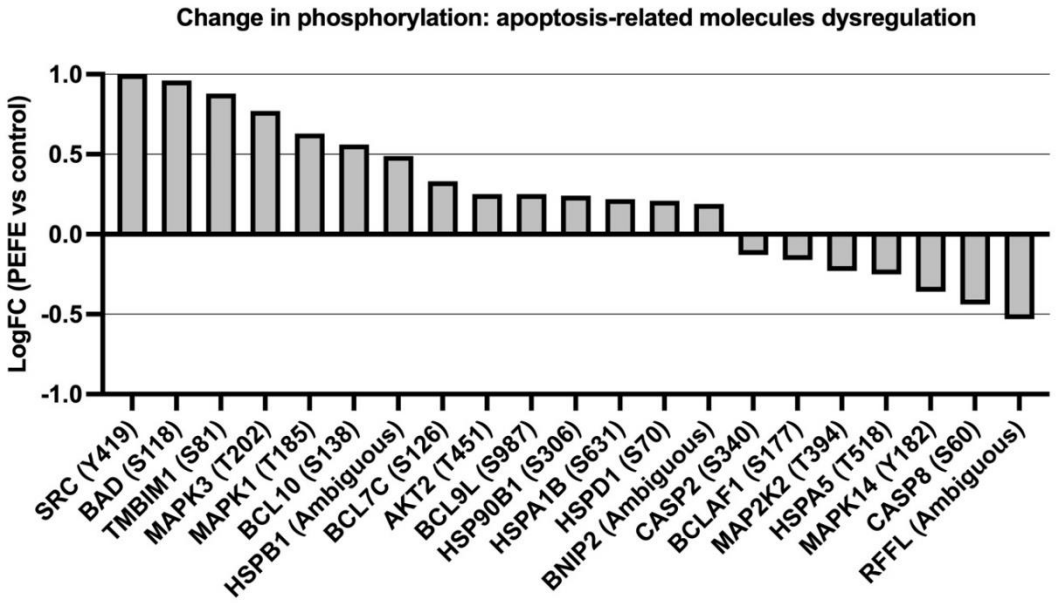

Figure 7.9 Phosphorylation changes of apoptosis-related molecules (either up- or down-regulation) in response to PEFE treatment in Caco2 cells. The X-axis represents the name of the gene, and the y-axis represents the log fold change between the PEFE-treated group and the control group.

7.3.4 Potential membrane/lipid-related proteins involved in PEFE treatment

After PEFE treatment, the cell membrane was shrunk, leading to the altered expression of various of cell membrane and lipid-related molecules. These affected molecules include RAS Oncogene Family, MMP family (matrix metalloproteinases), Syntaxin family, Integrins, and Cadherin Family, as summarized in Table7.11 to Table 7.13.Table 7.11 presented an overview of cell membrane-associated proteins, from total level, which were upregulated following PEFE treatment, Table 7.12 outlined the membrane associated molecules (total level) with downregulation. Table 7.13 provides an overview of the dysregulation of phosphorylated membrane-associated proteins in response to PEFE treatment. Graphical representations in Figure 7.10 and Figure 7.11 illustrated the up/downregulation of these membrane-associated molecules.

Remarkably, a considerable number of members in RAB family exhibited changes in their expression levels. At the total protein level, RAB-3C, -11B, -34, -5B, -37, 3B, 27A, L6 was increased, wile RAB-7A, -27B, -25, -33A, and -30 was decreased in response to PEFE treatment. When considering the phosphorylation status, phosphorylated RAB31 at T37 and RABL6 (S641)

decreased following PEFE treatment. Examining the Syntaxin family post-PEFE exposure, STX-3, -7, and -11 exhibited slight upregulation at total protein levels, while STX18 and STX12 were downregulated (total levels) in response to PEFE. The phosphorylated forms of STX-12, -4, and -18, on the other hand, were upregulated to varying degrees. In the case of Integrins, the total levels of ITGV6 and ITGVA were increased in response to PEFE. Conversely, total levels of ITGB1BP2, ITGAL, and ITGB6 were decreased following PEFE exposure. For the phosphorylation status, ITGAL (S1165), ITGB3 (unclear phosphorylated residue), and ITGA6 (S1049) exhibited dysregulation following PEFE treatment. As for matrix metalloproteinases, the total MMP9 was increased, while the total MMP1 and MMP8 were decreased in response to PEFE. Within the Cadherin family, after PEFE exposure, the total amount of CDH6 was slightly increased, whereas the total CDH3, DSG2 and DSC3 was decreased.

Table 7.11 Summary of cell membrane-related molecules, sorted by total protein, upregulated in response to PEFE treatment in Caco2 cells

Protein name	Full protein name	Total Log2 Normalised Abundances-PEFE	Total Log2 Normalised Abundances-control	LogFC (PEFE vs control)
RAB3C	Ras-related protein Rab-3C	2.68	1.96	0.71
RAB11B	RAB11B, member RAS oncogene family	5.67	4.96	0.71
RAB34	Ras-related protein Rab-34	2.32	1.81	0.51
RAB31	Ras-related protein Rab-31	3.72	3.23	0.49
CEACAM8	Carcinoembryonic antigen-related cell adhesion molecule 8	3.50	3.05	0.45
RAB5B	Ras-related protein Rab-5B	6.73	6.39	0.35
MMP9	Matrix metalloproteinase-9	6.99	6.66	0.32
RAB37	Ras-related protein Rab-37	6.09	5.76	0.32
ST14	Suppressor of tumorigenicity 14 protein (EC 3.4.21.109) (Matriptase)	6.33	6.03	0.30
STX16	Syntaxin 16	3.51	3.22	0.29
ITGA6	Integrin subunit alpha 6	8.19	7.92	0.27
IGF1R	Insulin-like growth factor 1 receptor	6.43	6.17	0.26
RAB3B	Ras-related protein Rab-3B	8.44	8.20	0.24
ANXA1	Annexin A1	9.18	8.95	0.23
RAB27A	Ras-related protein Rab-27A	7.13	6.90	0.23
RAB6B	Ras-related protein Rab-6B	5.51	5.29	0.22
ITGAV	Integrin alpha-V (Vitronectin receptor)	9.12	8.92	0.19
STX3	Syntaxin-3	9.15	8.95	0.19
CDH6	Cadherin-6	3.10	2.93	0.18
SNAP29	Synaptosomal-associated protein 29	8.31	8.14	0.17
STX7	Syntaxin-7	8.33	8.20	0.14
NDRG1	N-myc downstream-regulated gene 1 protein	8.27	8.13	0.14

NT5E	5'-nucleotidase (5'-NT) (CD antigen CD73)	6.62	6.48	0.13
RABL6	Rab-like protein 6	9.98	9.85	0.12
STX11	Syntaxin-11	6.98	6.88	0.11

Table 7.12 Summary of cell membrane-related molecules, sorted by total protein, downregulated in response to PEFE treatment in Caco2 cells

Protein name	Full protein name	Total Log2 Normalised Abundances-PEFE	Total Log2 Normalised Abundances-control	LogFC (PEFE vs control)
ITGB1BP2	Integrin beta-1-binding protein 2 (Melusin)	2.49	3.45	-0.96
RAB7A	RAB7A, member RAS oncogene family	2.32	2.93	-0.60
MMP1	Matrix metalloproteinase-1	4.31	4.83	-0.51
CDH3	Cadherin-3	5.11	5.44	-0.33
RAB27B	Ras-related protein Rab-27B	6.30	6.61	-0.32
CAV2	Caveolin-2	3.92	4.23	-0.32
RAB25	Ras-related protein Rab-25	3.66	3.96	-0.31
RAB33A	Ras-related protein Rab-33A	4.09	4.40	-0.31
CLTC	Clathrin-0.22 heavy chain	1.77	2.07	-0.30
ITGAL	Integrin alpha-L	5.50	5.81	-0.30
SLC5A6	Sodium-dependent multivitamin transporter	7.70	7.95	-0.24
SNAP23	Synaptosomal-associated protein 23	9.39	9.62	-0.23
ITGB6	Integrin beta-6	6.25	6.48	-0.23
ANK2	Ankyrin 2	6.22	6.45	-0.22
PSCA	Prostate stem cell antigen	3.95	4.17	-0.22
DSG2	Desmoglein-2 (Cadherin family member 5)	9.70	9.90	-0.20
ANK3	Ankyrin-3	5.71	5.89	-0.19
CAV1	Caveolin-1	6.60	6.78	-0.18
DSC3	Desmocollin-3 (Cadherin family member 3)	6.34	6.52	-0.18
STX18	Syntaxin-18	8.08	8.24	-0.17
APMAP	Adipocyte plasma membrane-associated protein	10.08	10.24	-0.16
STX12	Syntaxin-12	7.93	8.08	-0.15
RAB30	Ras-related protein Rab-30	5.99	6.14	-0.15
VN1R5	Vomeronasal type-1 receptor 5 (G-protein coupled receptor GPCR26)	2.83	2.96	-0.14
MMP8	Matrix metalloproteinase-8)	5.67	5.81	-0.14

Table 7.13 Summary of cell membrane-related molecules, sorted by phosphoprotein, dysregulated in response to PEFE treatment in Caco2 cells

Protein name	Phospho Site (Human)	Full protein name	Phospho Adjusted Log2 Normalised Abundance- PEFE	Phospho Adjusted Log2 Normalised Abundance - control	LogFC (PEFE vs control)
SRC	Y419	Proto-oncogene tyrosine-protein kinase Src	-2.16	-3.17	1.00
PTK7	S784	Inactive tyrosine-protein kinase 7	-2.22	-2.71	0.49
CAV2	S36	Caveolin-2	2.25	1.77	0.47
ITGAL	S1165	Integrin alpha-L	0.32	-0.11	0.43
STX12	S139	Syntaxin-12	0.59	0.28	0.31
DSG2	Ambiguous	Desmoglein-2	-2.86	-3.13	0.27
CAV1	S37	Caveolin-1	-0.15	-0.38	0.23
STX4	Ambiguous	Syntaxin-4	-1.44	-1.65	0.21
RAB31	T37	Ras-related protein Rab-31	0.75	0.95	-0.20
EGFR	T693	Epidermal growth factor receptor	-4.56	-4.29	-0.26
ERBIN	S857	Erbb2-interacting protein	-2.49	-2.22	-0.27
ITGB3	Ambiguous	Integrin beta-3	-4.79	-4.49	-0.30
EPHA2	Ambiguous	Ephrin type-A receptor 2	-3.76	-3.45	-0.31
ITGA6	S1049	Integrin subunit alpha 6	-2.31	-1.86	-0.44
ANK1	S834	Ankyrin-1	-6.30	-5.58	-0.72
RABL6	S641	Rab-like protein 6	-1.82	-0.29	-1.53

(A)

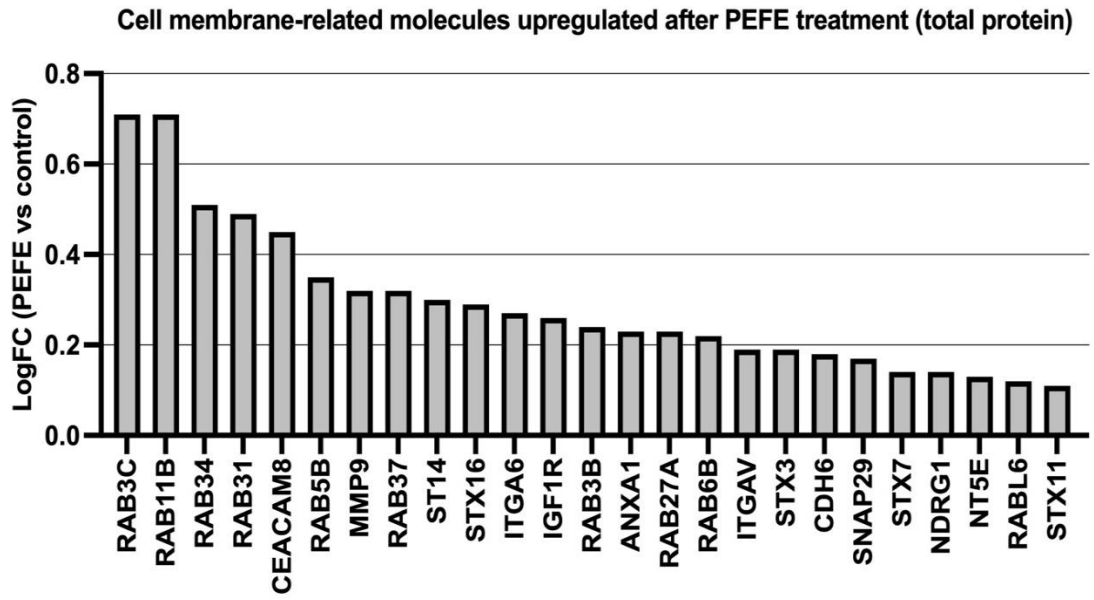

(B)

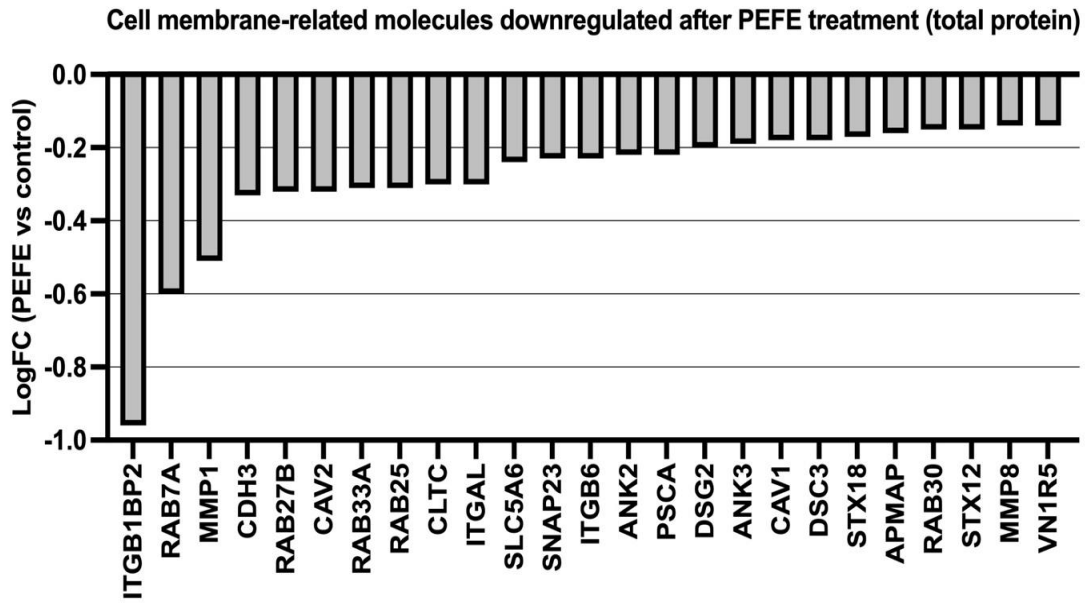

Figure 7.10 Cell membrane-related molecules up/downregulated in response to PEFE treatment in Caco2 cells, sorted by total protein. (A) Molecules with upregulation in response to PEFE treatment. (B) Molecules with downregulation in response to PEFE treatment. The X-axis represents the name of the gene, and the y-axis represents the log fold change between the PEFE-treated group and the control group.

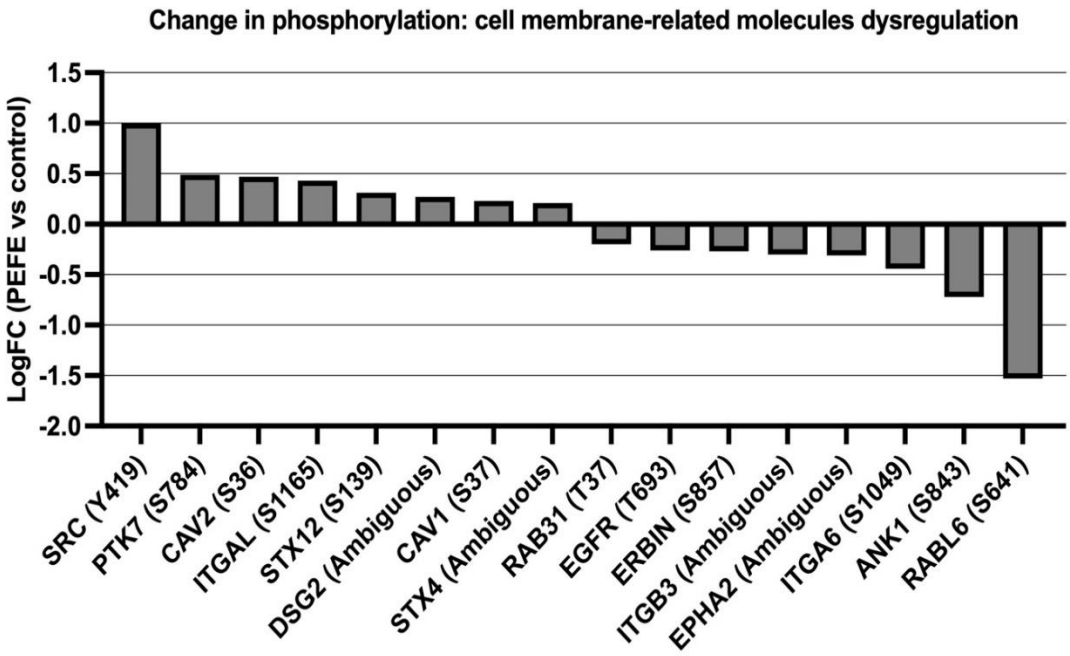

Figure 7.11 Phosphorylation changes of cell membrane-related molecules (either up- or down-regulation) in response to PEFE treatment in Caco2 cells. The X-axis represents the name of the gene, and the y-axis represents the log fold change between the PEFE-treated group and the control group.

7.3.5 Confirmation of the possible signalling pathways involved in PEFE treatment

Cells were treated with PEFE, and the protein was collected after 15 minutes, 1 hour, and 4 hours. Western blot was then conducted to verify the proteomic analysis result, also aiming to find the possible signalling pathway underly the PEFE treatment. Western blot result was processed using ImageJ. Data was normalized against GAPDH and analyzed with fold change in Excel, with the figure created using GraphPad.

7.3.5.1 Confirmation of heat shock of PEFE treatment by examining the expression of HSP60

To confirm the cancer cells were killed by PEFE itself, rather than the temperature, during the treatment, the expression of HSP60 (heat shock protein 60), a protein that plays a crucial role in cellular protection, especially in response to heat shock, was examined by Western blot first. As shown in Figure 7.12, 15 minutes after PEFE treatment, the expression of Hsp60 was slightly decreased compared to its control counterpart. This reduction of Hsp60 expression continued after 1 hour, in which the expression of Hsp60 was much lower in the PEFE group. However, after 4 hours, there was a partial recovery in the levels of HSP60, although they

remained lower than those in the untreated control cells.

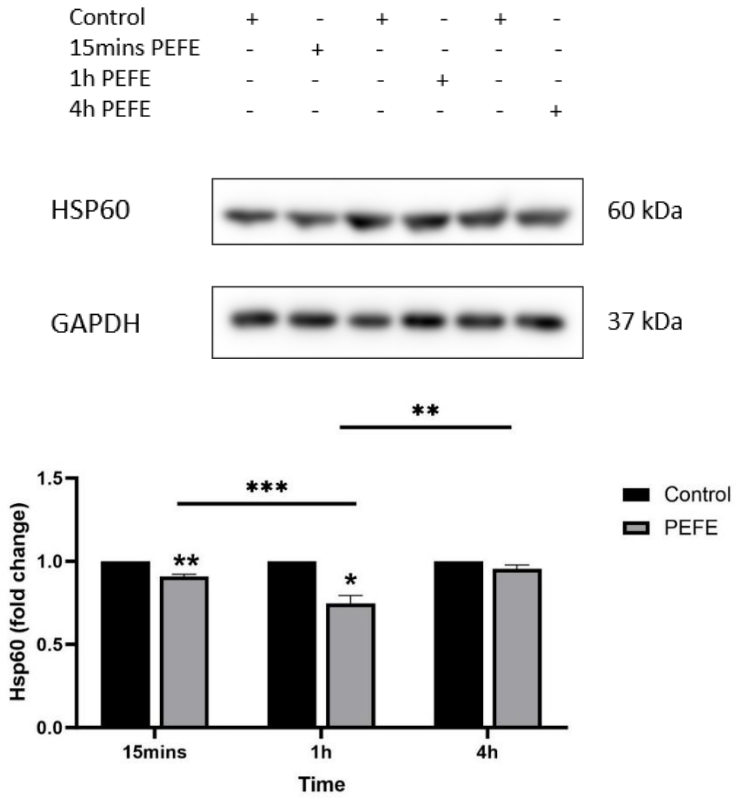

Figure 7.12 Western Blot analysis of HSP60 expression in response to PEFE. Image (top) obtained using G-BOX (Syngene), showing the Western blot result of HSP60 expression in control group and PEFE group (after 15 minutes, 1 hour, and 4 hours), indicated by '+'. Quantitative analysis of the bands was performed using Image J software. The expression was then normalized against GAPDH, to reveal any changes by fold change (down). Error bars show SD for three repeats. *p<0.05, **p <0.01, ***p<0.001.

7.3.5.2 Confirmation of cell apoptosis in response to PEFE treatment

Previous experiments already confirmed the increased expression of Caspase-3, -8, and -9 over time after PEFE treatment, indicating the cells were killed via apoptosis following PEFE treatment. In addition to the Caspase family, SMAD4, a member of the SMAD family, was also chosen for Western blot verification. Since SMAD4 plays different roles in different cellular contexts, making it an important target for investigation. As demonstrated in Figure 7.13, the expression levels of SMAD4 kept increasing 15 minutes, 1 hour, and 4 hours post-PEFE treatment. This sustained elevation in SMAD 4 expression suggests its involvement in the cellular response to PEFE treatment over time.

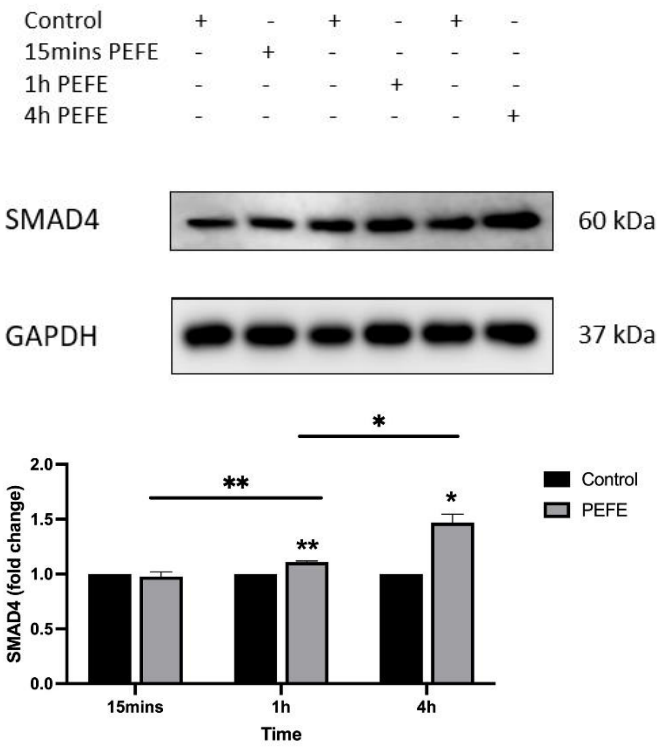

Figure 7.13 Western Blot analysis of SMAD4 expression in response to PEFE. Image (top) obtained using G-BOX (Syngene), showing the Western blot result of SMAD4 expression in the control group and PEFE group (after 15 minutes, 1 hour, and 4 hours), indicated by '+'. Quantitative analysis of the bands was performed using Image J software. The expression was then normalized against GAPDH, to reveal any changes by fold change (down). Error bars show SD for three repeats. *p<0.05, **p <0.01.

7.3.5.3 Further investigation on the interaction between PEFE and TJ

As described in the previous chapter, PEFE initially induced cell death only in a small amount in the area directly below the tip of the microwave probe, while the number of death cells increased over time. Also, cancer cells that exhibit good TJs are more sensitive in response to PEFE compared with those with weak TJs. Therefore, it was hypothesized that TJs might play a role in signal transduction, in which the cascade of signalling of cell apoptosis was transmitted across the cell membrane, extending its influence on cells situated farther away from the probe tip. Western blot was conducted for ZO-1 expression in response to PEFE treatment, as demonstrated in Chapter 4, in which the ZO-1 expression was decreased 15 minutes and 4 hours after PEFE treatment compared with the control group, while its expression was increased 1 hour post treatment.

To further investigate the interaction between PEFE and TJ, the expression of TJ-related molecules, AF6, was examined. AF6 also plays a pivotal role in TJ signal transduction. As illustrated in Figure 7.14, it shows similar expression changes as ZO-1. After 15 minutes, AF6 expression was decreased compared with the control group. While its expression increased dramatically at 1-hour post-treatment. However, a significant decrease in AF6 expression was visualized at 4 hours post-treatment. Both results of ZO-1 and AF6 suggest that the strongest initiation of apoptosis signal transduction might occur 1 hour after PEFE treatment.

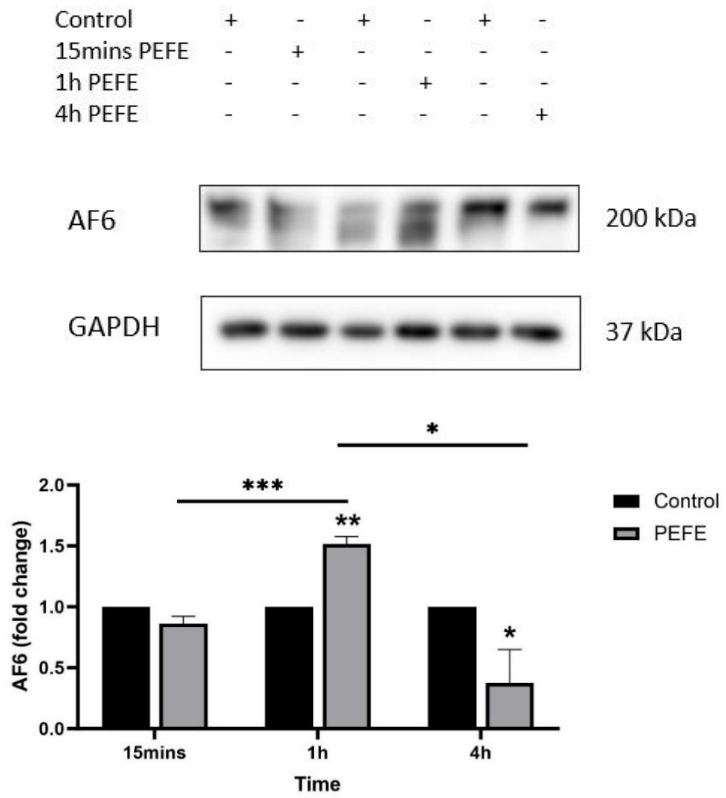

Figure 7.14 Western Blot analysis of AF6 expression in response to PEFE. Image (top) obtained using G-BOX (Syngene), showing the Western blot result of AF6 expression in the control group and PEFE group (after 15 minutes, 1 hour, and 4 hours), indicated by '+'. Quantitative analysis of the bands was performed using Image J software. The expression was then normalized against GAPDH, to reveal any changes by fold change (down). Error bars show SD for three repeats. *p<0.05, **p <0.01, ***p<0.001.

Furthermore, the expression level of Claudin-11, a member of the Claudin family, was examined by Western blotting. Unlike ZO-1 or AF-6, Claudin-11 is not involved in signal transduction; it plays a crucial role in the formation of TJs. As demonstrated in Figure 7.15, the expression of Claudin-11 was increased in the PEFE group in comparison with the control

group at 15 minutes post-treatment, while it decreased significantly 1 hour and 4 hours after PEFE treatment, which might be due to the broken TJ structure over time in response to PEFE.

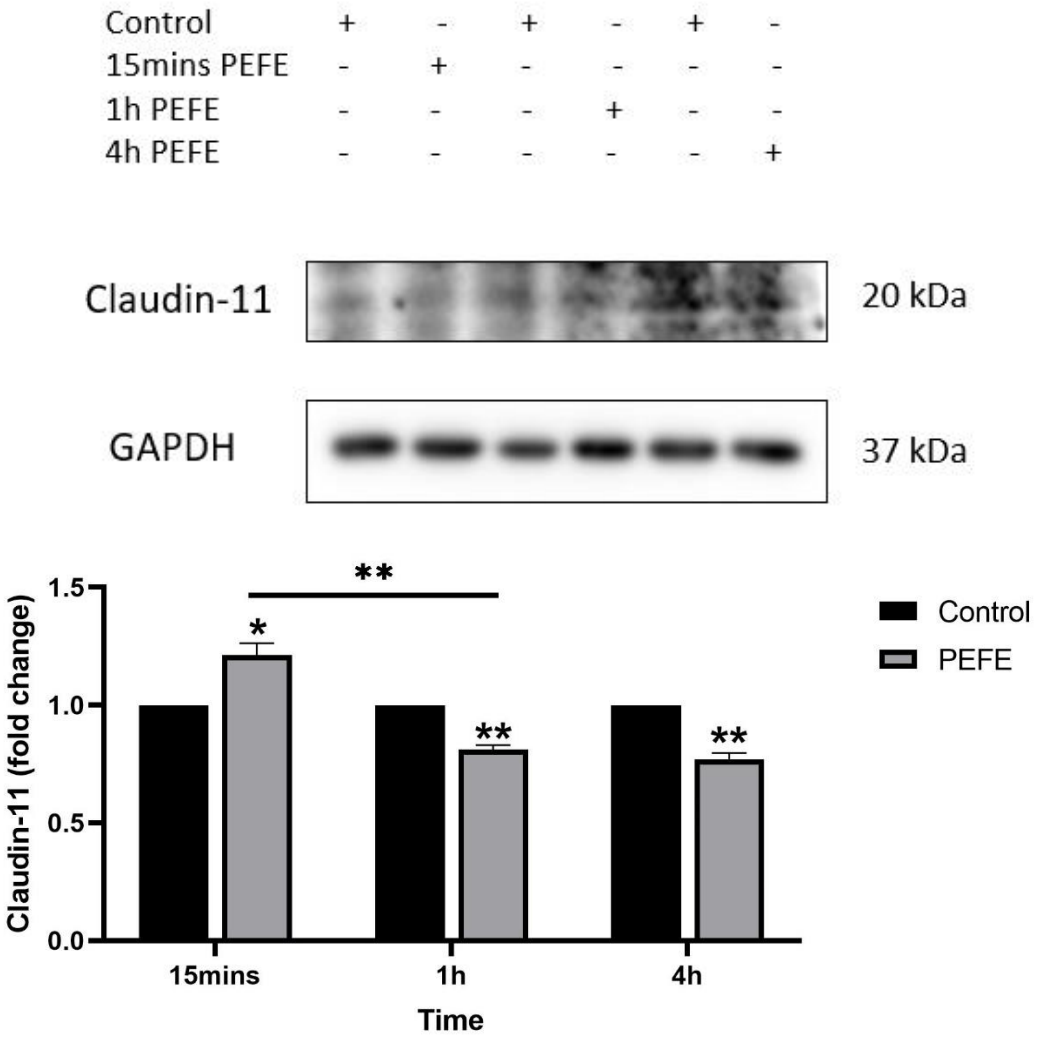

Figure 7.15 Western Blot analysis of Claudin-11 expression in response to PEFE. Image (top) obtained using G-BOX (Syngene), showing the Western blot result of Claudin-11 expression in the control group and PEFE group (after 15 minutes, 1 hour, and 4 hours), indicated by '+'. Quantitative analysis of the bands was performed using Image J software. The expression was then normalized against GAPDH, to reveal any changes by fold change (down). Error bars show SD for three repeats. *p<0.05, **p <0.01.

Apart from these, Nectin4 was also chosen for investigating it expression changes in response to PEFE treatment at protein level. Nectin4 participates in the formation of adherens junctions, which are interlinked with TJs and contribute to their stability and function. As illustrated in Figure 7.16, the expression of Nectin4 was stabled at 15 minutes post-treatment compare with the control group. However, its expression kept decreasing dramatically at 1

hour and 4 hour post-treatment.

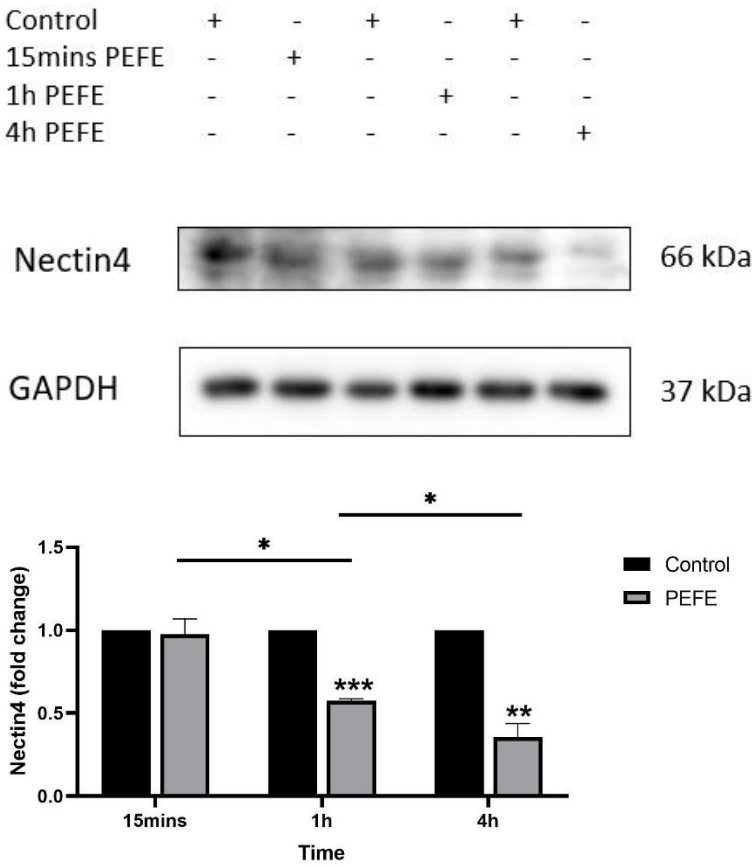

Figure 7.16 Western Blot analysis of Nectin4 expression in response to PEFE. Image (top) obtained using G-BOX (Syngene), showing the Western blot result of Nectin4 expression in the control group and PEFE group (after 15 minutes, 1 hour, and 4 hours), indicated by '+'. Quantitative analysis of the bands was performed using Image J software. The expression was then normalized against GAPDH, to reveal any changes by fold change (down). Error bars show SD for three repeats. **p <0.01, ***<0.001.

7.3.5.4 Further investigation on how PEFE affects cell membrane

After PEFE treatment, the cancer cells were killed via apoptosis, leading to the witness of distinct morphological alterations such as cell shrinkage. Therefore, the expression of some cell membrane-related molecules was examined by Western blotting.

The expression of Caveolin-1 was firstly assessed, considering its important role in maintaining cell membrane structure. As shown in Figure 7.17, it was observed that the expression of Caveolin-1 gradually decreased over time in response to PEFE treatment.

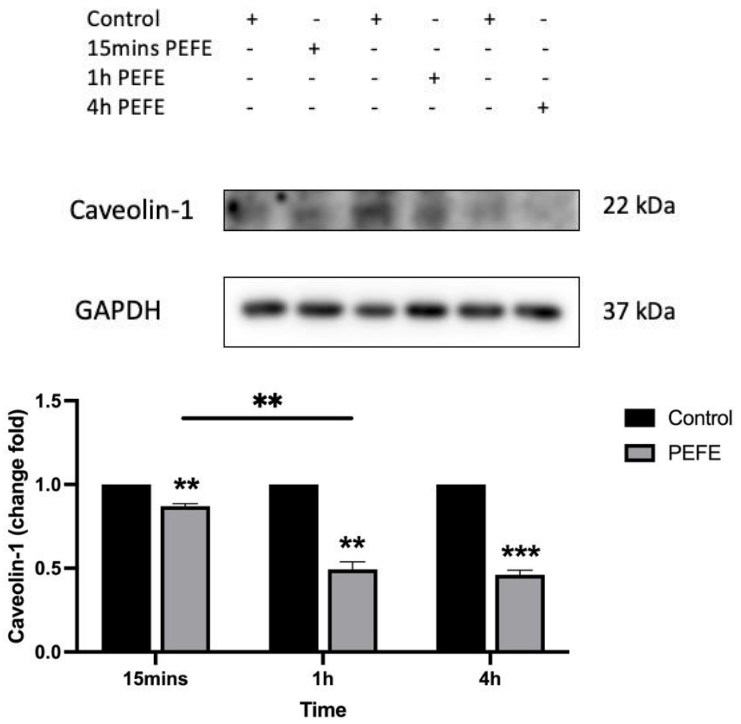

Figure 7.17 Western Blot analysis of Caveolin-1 expression in response to PEFE. Image (top) obtained using G-BOX (Syngene), showing the Western blot result of Caveolin-1 expression in the control group and PEFE group (after 15 minutes, 1 hour, and 4 hours), indicated by '+'. Quantitative analysis of the bands was performed using Image J software. The expression was then normalized against GAPDH, to reveal any changes by fold change (down). Error bars show SD for three repeats. **p <0.01, ***<0.001.

Furthermore, the expression of MMP9 at protein level was assessed, as illustrated in Figure 7.18. The expression of MMP9 at 15 minutes after treatment was increased compared with untreated control group. However, its expression went down significantly after 1 hour and 4 hours.

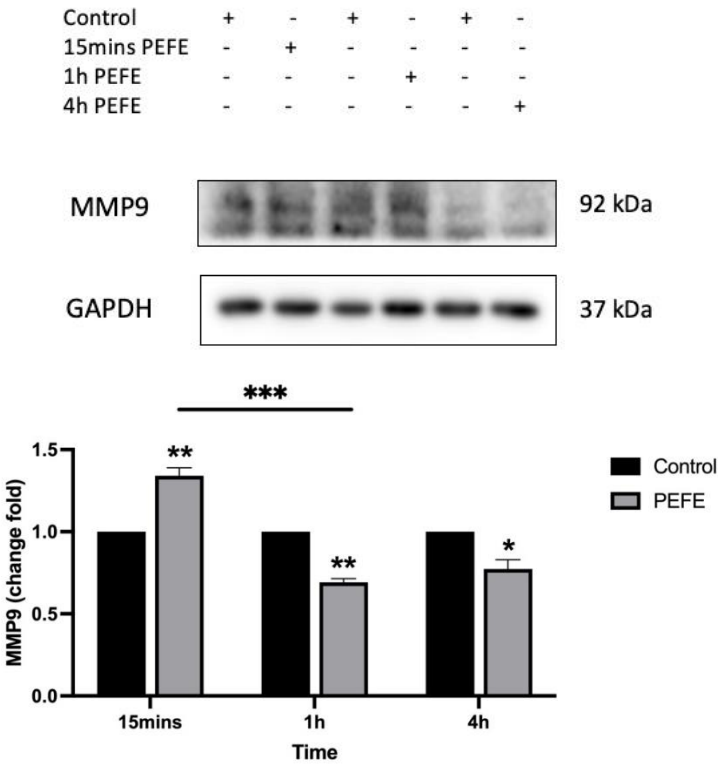

Figure 7.18 Western Blot analysis of MMP9 expression in response to PEFE. Image (top) obtained using G-BOX (Syngene), showing the Western blot result of MMP9 expression in the control group and PEFE group (after 15 minutes, 1 hour, and 4 hours), indicated by '+'. Quantitative analysis of the bands was performed using Image J software. The expression was then normalized against GAPDH, to reveal any changes by fold change (down). Error bars show SD for three repeats. *<0.05, **p <0.01, ***<0.001.

7.4 Discussion

This chapter aimed to explore the possible signalling pathways and mechanisms involved in cancer cells in response to PEFE treatment. Through proteomic analysis results, it was found that thousands of molecules were dysregulated after PEFE treatment. Among them, it is worth noting that many molecules participated in cellular apoptosis, TJ formation, and cell membrane integrity directly or indirectly from the top list of the most dysregulations, promoting a deeper investigation into these pathways. Subsequently, molecules associated with apoptosis, TJs, and cell membrane functions were picked from the proteomic result, and Western blotting was then conducted to validate these findings and also to gain a deeper understanding of how PEFE affects these fundamental cellular processes.

Given that the PEFE system controls temperatures below 42℃, it effectively circumvents any

direct impact of temperature on cancer cell treatment. Any temperature exceeding 42℃ would impose heat shock stress on cells, triggering the upregulation of HSPs (heat shock proteins) to fulfil their protective functions. Consequently, we first evaluated the expression level of HSP60, a key member of the HSP family. and its downregulation was observed in the PEFE group compared to the control untreated group, indicating that the temperature maintained during the PEFE treatment is safe for the cancer cells.

Previous experiments suggest that cancer cells were killed via apoptosis following PEFE treatment. To further validate this finding, the expression levels of specific members of Caspase family, including Caspase-3, -8 and -9 was examined in Chapter 4, in which the expression of these caspase members increased over time following PEFE treatment, providing additional evidence that cancer cell death occurred via apoptosis. Subsequently, attention turned to SMAD4, a molecule known to play diverse roles in apoptosis regulation, which was chosen for validation. It has been reported that the TGF-β/SMAD4 signalling pathway could either promote apoptosis by activating pro-apoptotic genes or promote cell survival and inhibit apoptosis (Zhao et al. 2018). After PEFE treatment, an upregulation of SMAD4 over time was visualized, suggesting its potential involvement in apoptotic signalling pathways, possibly through the activation of Caspases.

Regarding the Western blotting results for TJ proteins, both ZO-1 and AF6, the function of the protein in signal transduction, exhibited increased expression and higher than that of the control group 1 hour post-treatment, while decreased at the other two time points. This can provide information that the signalling activity peaked at the one-hour mark. When considering some other TJ proteins that play a role in the formation of TJs, like Claudin-11 and Nectin-4, they showed fluctuated expression in response to PEFE at different time points while still showing decreased overall expression compared with the control group. This decline aligns with the breakdown of TJ structures observed during apoptosis, consequently leading to the downregulation of these molecules. The fluctuation is attributed to the cells experiencing biphasic expression in response to microwave exposure during PEFE treatment.

Considering the morphological change of cell membrane after PEFE treatment, Western blotting results showed a notable decline in Caveolin-1 expression over time. Caveolin-1 plays

an important role in the formation of cell membranes. Intriguingly, MMP9, known for its role in affecting cell membrane integrity, demonstrated an upregulation in expression at 15 minutes post-treatment. This rapid response underscores the potential impact of PEFE treatment on the structural integrity of the cell membrane.

Overall, this chapter investigates the potential signalling pathways and mechanisms involved in cancer cells in response to PEFE treatment, utilizing proteomic analysis to identify significant dysregulation of molecules, especially those linked to apoptosis, TJ formation, and cell membrane integrity. PEFE induces apoptosis primarily via Caspase-3, -8, and -9 pathways without causing heat shock stress, as evidenced by downregulated HSP60. Upregulation of SMAD4 suggests involvement in the TGF-β/SMAD4 apoptotic pathway, which can enhance the expression of pro-apoptotic genes such as Caspases, amplifying the apoptotic signal. TJ proteins ZO-1 and AF6 showed peak expression one-hour post-treatment, highlighting their role in signal transduction during apoptosis. Other TJ proteins, such as Claudin-11 and Nectin-4, exhibited fluctuating expression, aligning with the breakdown of TJs during apoptosis. Additionally, cell membrane integrity was affected, as indicated by the decline in Caveolin-1 and the initial upregulation of MMP9, suggesting structural changes post-PEFE treatment.

Chapter-8 General discussion

8.1 The aim of this thesis

Breast and colorectal cancers are among the most prevalent and deadly cancers worldwide. Breast cancer is the most common cancer in the UK, while colorectal cancer ranks fourth, both significantly impacting morbidity and mortality rates. Microwave technology has been increasingly applied in the medical field for both diagnostic and therapeutic purposes. One prominent application is microwave ablation, which uses high-frequency microwave energy to generate heat and destroy cancerous tissues. However, this technique often results in high temperatures that can cause patient complications and unintended tissue damage. To address these issues, pulsed electromagnetic field exposure (PEFE) systems have been explored as a promising alternative. PEFE applies microwave signals under normothermic conditions, ensuring that the temperature remains controlled and does not contribute to cell damage. Despite its potential, previous PEFE systems had several drawbacks, including complex setups, manual temperature control, and inconsistent results due to equipment inefficiencies. This thesis aims to overcome these limitations by developing an advanced PEFE system. Moreover, we further evaluated the effects of PEFE treatment on breast and colorectal cancer cells, focusing on its ability to induce apoptosis under normothermic conditions and the role of TJs in response to the PEFE system. Also, we investigate the clinical and functional roles of MarvelD3 in BRCA and CRC, and its role in mediating the cellular response to PEFE treatment. we also conducted proteomic analysis to identify and validate key signalling pathways and molecular mechanisms involved in the cancer cell response to PEFE treatment (Figure 8.1).

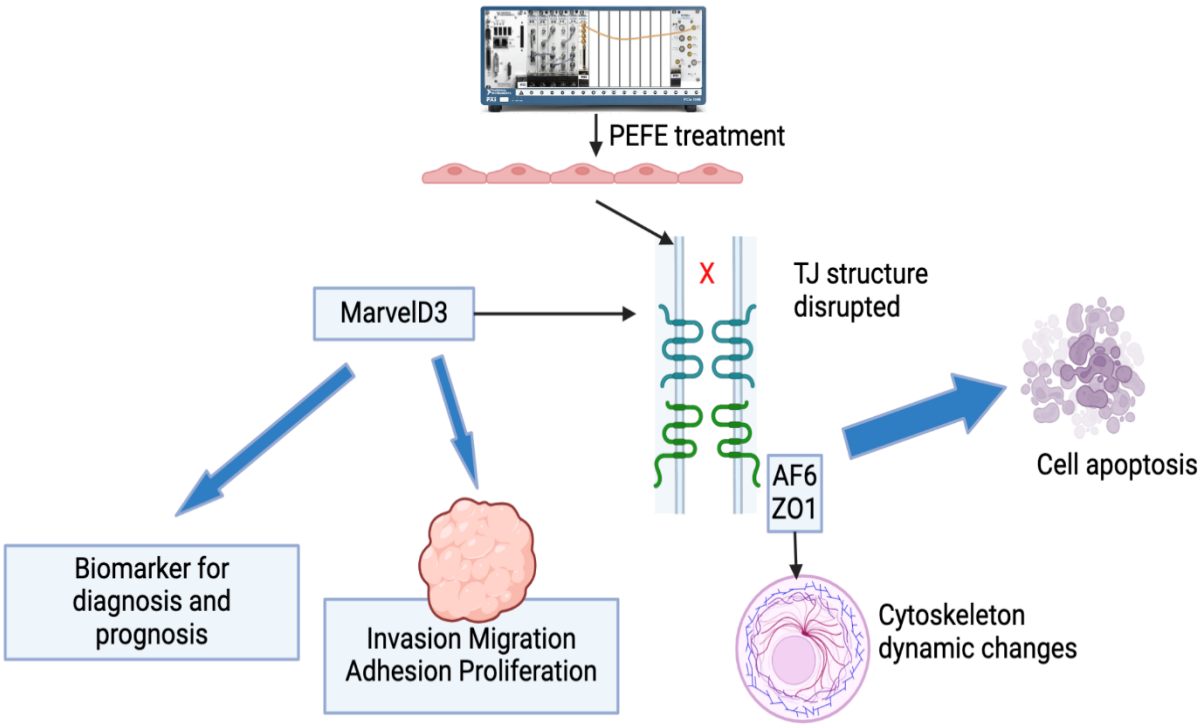

Figure 8.1 Diagram of the overview of the thesis outline. Schematic illustrates that disrupting tight junctions and cytoskeleton after PEFE treatment leads to cell apoptosis. Additionally, MarvelD3 plays a pivotal role in regulating the clinical and functional significance in colorectal CRC and BRCA, and also serves as a biomarker for PEFE treatment.

8.2 Development of a PXI-based PEFE system

The newly developed PXI-based system successfully addressed the complexities and inefficiencies of previous setups. The system automated temperature control, ensuring consistent and optimal conditions for PEFE treatment. This advancement not only improved the overall efficiency but also ensured accuracy and repeatability in the experimental procedures. Thorough calibration of the system was critical, ensuring all components functioned correctly and understanding the inherent characteristics of the microwave components. After the improvement of the experimental setup, by sterilizing the microwave probe and thermometer probe, and repositioning these two probes, subsequent experiments demonstrated the system's capability to maintain desired temperature ranges and induce effective cancer cell death rates, confirming the improved PXI system is suitable for further PEFE treatment.

8.3 Cancer cells in response to PEFE treatment

Microwave irradiation can induce either cell necrosis or apoptosis, with studies showing its ability to cause cell death via different pathways. Specifically, microwave exposure has been reported to induce apoptosis in neuronal cells (Joubert et al. 2008) and various cancer cell lines, including oropharyngeal carcinoma (Caraglia et al. 2005), pancreatic cancer (Zhu et al. 2014), breast cancer (Zhao 2020), and lung carcinoma (Song et al. 2011), often involving increased activity of Caspases.

Our study revealed that PEFE treatment primarily induces cell death through apoptosis rather than necrosis in both breast and colorectal cancer cells. This is evidenced by the delayed increase in cell death observed 24 hours post treatment, suggesting a programmed cell death mechanism. This finding was further supported using Caspase-3/7 analysis, morphological changes observed via DAPI staining, and Western blot analysis, which revealed increased expression levels of key apoptosis-related proteins, including Caspase-3, -8, and -9, post-PEFE treatment, confirmed apoptosis as the primary mode of cell death. These results underscored the involvement of both intrinsic and extrinsic apoptotic pathways.

Moreover, the differential sensitivity of cancer cell lines with varying degrees of TJs highlighted the importance of TJs in PEFE treatment. The disruption of cell monolayers in the cell scratching assay revealed that intact TJs might facilitate signal transduction, leading to more efficient induction of apoptosis across the cell population. This finding suggests that TJs are crucial in transmitting the PEFE signal, contributing to the overall effectiveness of the treatment. Western blot analysis and immunofluorescence staining (IFC) for ZO-1, a key TJ-associated protein, revealed significant changes post-PEFE treatment. The Western blot results showed a substantial increase in ZO-1 expression one hour post-treatment, which then decreased at later time points, indicating that ZO-1 might play its signal transduction role one hour post treatment. IFC staining demonstrated the disruption, followed by internalization and relocalization of ZO-1. Additionally, cytoskeletal staining highlighted the structural changes induced by PEFE treatment. Actin filament staining demonstrated disorganization and formation of irregular aggregates post-treatment. These cytoskeletal disruptions likely contributed to the observed internalization and relocalization of ZO-1, affecting TJ stability

and facilitating apoptotic signalling.

8.4 Clinical implication of MarvelD3 in colorectal and breast cancer

In order to further explore the role of TJ in PEFE treatment, we picked up a newly identified gene, MarvelD3, for further investigation. MarvelD3, a TJ-associated protein, plays a crucial role in maintaining cellular integrity and regulating various signalling pathways. Its role in cancer progression has been found to be context-dependent, exhibiting both tumour-suppressive and tumour-promoting functions depending on the cancer type. The clinical significance of MarvelD3 was studied in OSCC (Huang et al. 2022), HCC (Li et al. 2021a), and NSCLC (Li et al. 2023). While less studies focus on the role of MarvelD3 in colorectal cancer and breast cancer. Therefore, we firstly inspected the clinical role of MarvelD3 in BRCA and CRC. By doing the cohort study, MarvelD3 was found to be differentially expressed in breast and colorectal cancers, suggesting its dualistic nature in cancer progression. The analysis of the Cardiff cohort revealed that MarvelD3 transcript levels were higher in tumour tissues compared with normal tissues. Also, high expression of MarvelD3 had significantly lower overall survival and disease-free survival rates. These findings suggest that MarvelD3 may serve as a prognostic marker for breast and colorectal cancers.

8.5 The impact of MarvelD3 on BRCA and CRC cellular function

MarvelD3's functional impact have been studied across various cancer types, including non-small cell lung cancer (NSCLC), pancreatic cancer, and hepatocellular carcinoma (HCC), and colorectal cancer. MarvelD3 acts as a negative regulator for cellular growth in colorectal cancer (Steed et al. 2014), and cellular migration in NSCLC (Li et al. 2023), HCC (Li et al. 2021a), and CRC (Steed et al. 2014), and cellular invasion in NSCLC (Li et al. 2023) and HCC (Li et al. 2021a). In this study, similar cellular function was found in colorectal cancer, in which its downregulation leading to increased cell proliferation, migration, and invasion and adhesion. However, in breast cancer, MarvelD3 appears to have a context-dependent role, where its knockdown results in decreased cell proliferation but enhanced migration and invasion. These findings indicate that MarvelD3 plays a critical role in regulating cellular functions in breast and colorectal cancers, implicating its involvement in cancer development and progression.

In this study, the TJ function of MarvelD3 in CRC and BRCA was assessed using TER and PCP. MarvelD3 knockdown significantly weakened TJ integrity and increased paracellular permeability in both colorectal and breast cancer cells. This disruption of TJs likely facilitated the dissociation and migration of cancer cells, contributing to their invasive potential.

8.6 Marveld3 as a biomarker for PEFE treatment

The potential of MarvelD3 as a biomarker for PEFE treatment is significant, given its critical role in cellular functions and cancer progression. The expression levels of MarvelD3 have been shown to influence the sensitivity of cancer cells to PEFE treatment, making it a valuable indicator for predicting treatment efficacy. Our studies have demonstrated that knockdown of MarvelD3 in both breast and colorectal cancer cell models leads to a significant reduction in cell death rates following PEFE treatment. This suggests that higher expression levels of MarvelD3 enhance the susceptibility of cancer cells to PEFE-induced apoptosis. The regulation of TJ integrity by MarvelD3 is likely a key factor in this process. Intact TJs, maintained by MarvelD3, facilitate efficient signal transduction during PEFE treatment, leading to a more pronounced apoptotic response. Given the differential expression of MarvelD3 in cancer tissues and its correlation with clinical outcomes, MarvelD3 could serve as a predictive biomarker for PEFE therapy. Patients with higher MarvelD3 expression may experience better therapeutic responses to PEFE, characterized by increased apoptosis. Conversely, lower levels of MarvelD3 might indicate a reduced sensitivity to PEFE.

8.7 Possible signalling pathway involved in PEFE treatment

Proteomic analysis identified significant dysregulation of molecules involved in apoptosis, TJ formation, and cell membrane integrity post-PEFE treatment. Western blotting confirmed the involvement of key proteins in these processes, validating the proteomic analysis. PEFE treatment initiates cellular responses by affecting signalling pathways related to TJs, apoptosis, and cytoskeleton dynamics. The pathway begins with the induction of TJ integrity, involving key proteins such as ZO-1, MarvelD3, CLDN6, and AFDN. ZO-1 initially localizes at the cell membrane to maintain TJ integrity but relocates to inner cell regions upon PEFE treatment, disrupting TJs and facilitating apoptotic signalling (Anderson and Van Itallie 2009).

MarvelD3 interacts with TJ proteins, maintaining their integrity and facilitating signalling pathways. This interaction helps sustain the cellular structure until PEFE treatment causes MarvelD3 to play a role in apoptosis. Claudins, such as Claudin-6, contribute to the maintenance of TJs, and their presence is crucial for cellular barrier functions, which are disrupted during PEFE treatment (Krause et al. 2008). AFDN binds to actin filaments and connects TJs to the actin cytoskeleton, thus maintaining cell junction stability until it is affected by PEFE (Mandai et al. 1997).

Upon disruption of TJs, apoptotic signalling pathways are activated. The intrinsic apoptotic pathway is mediated by BAX/BAK1, which promotes mitochondrial outer membrane permeabilization (MOMP) and leads to the release of cytochrome c, a critical step for apoptosis. The release of cytochrome c activates Caspase-9, which then initiates the caspase cascade, leading to the execution phase of apoptosis (Li et al., 1997). In parallel, the extrinsic apoptotic pathway is activated by Caspase-8, which responds to external death signals and activates the downstream caspases, further amplifying the apoptotic response. Caspase-3, -6, and -7 act as executioner caspases, cleaving various cellular substrates and leading to the morphological and biochemical changes associated with apoptosis (Singh et al. 2019). Additionally, SMAD4, upregulated post-PEFE treatment, plays a role in the TGF-β signalling pathway, enhancing the apoptotic response through the regulation of pro-apoptotic genes (Zhao et al. 2018). The MAPK pathway, involving MAPK1, MAPK3, MAPK8, and MAPK14, is also activated and regulates apoptosis-related genes and proteins, further promoting cell death (Yue and López 2020). Moreover, the reduction of HSP60 causes mitochondrial Survivin to become unstable and degrade, leading to the deterioration of mitochondrial membrane integrity. This process triggers the proteolysis of effector Caspases and induces apoptosis (Tang et al. 2022).

Cytoskeleton and cell membrane dynamics are crucial in this signalling pathway. PEFE treatment induces actin filament disorganization, which disrupts the structural integrity of the cell and facilitates the relocation of ZO-1 and other TJ proteins, thereby promoting apoptotic signalling. RAB family proteins, such as RAB11B and RAB3C, regulate vesicle trafficking and membrane dynamics, which are crucial for maintaining cellular homeostasis and facilitating apoptosis when disrupted (Stenmark 2009). MMP9 is involved in degrading

extracellular matrix components, promoting cell detachment and migration during the apoptotic process (Cabral-Pacheco et al. 2020). Integrins, including ITGA6 and ITGAV, mediate cell adhesion and signalling, and their disruption during PEFE treatment contributes to changes in cell morphology and promotes apoptosis (Hynes 2002).

In conclusion, the coordinated disruption of TJ integrity, activation of apoptotic pathways, and alterations in the cytoskeleton and membrane dynamics by PEFE treatment effectively led to apoptosis in cancer cells. Considering all the datasets and the literature reports, we propose the mechanism of action during PEFE-induced cancer cell apoptosis, as illustrated in Figure 8.2.

The development and optimization of the PEFE treatment system hold significant relevance and benefits for patients, particularly those suffering from breast and colorectal cancers. This system aims to provide a more targeted and effective treatment option that minimizes damage to surrounding healthy tissues. The ability to precisely control the temperature that cancer cells are specifically targeted, reducing the likelihood of adverse side effects commonly associated with conventional therapies. Ultimately, the PEFE system will facilitate its adoption in clinical settings, offering patients a novel and promising therapeutic option that can be integrated into existing treatment protocols.

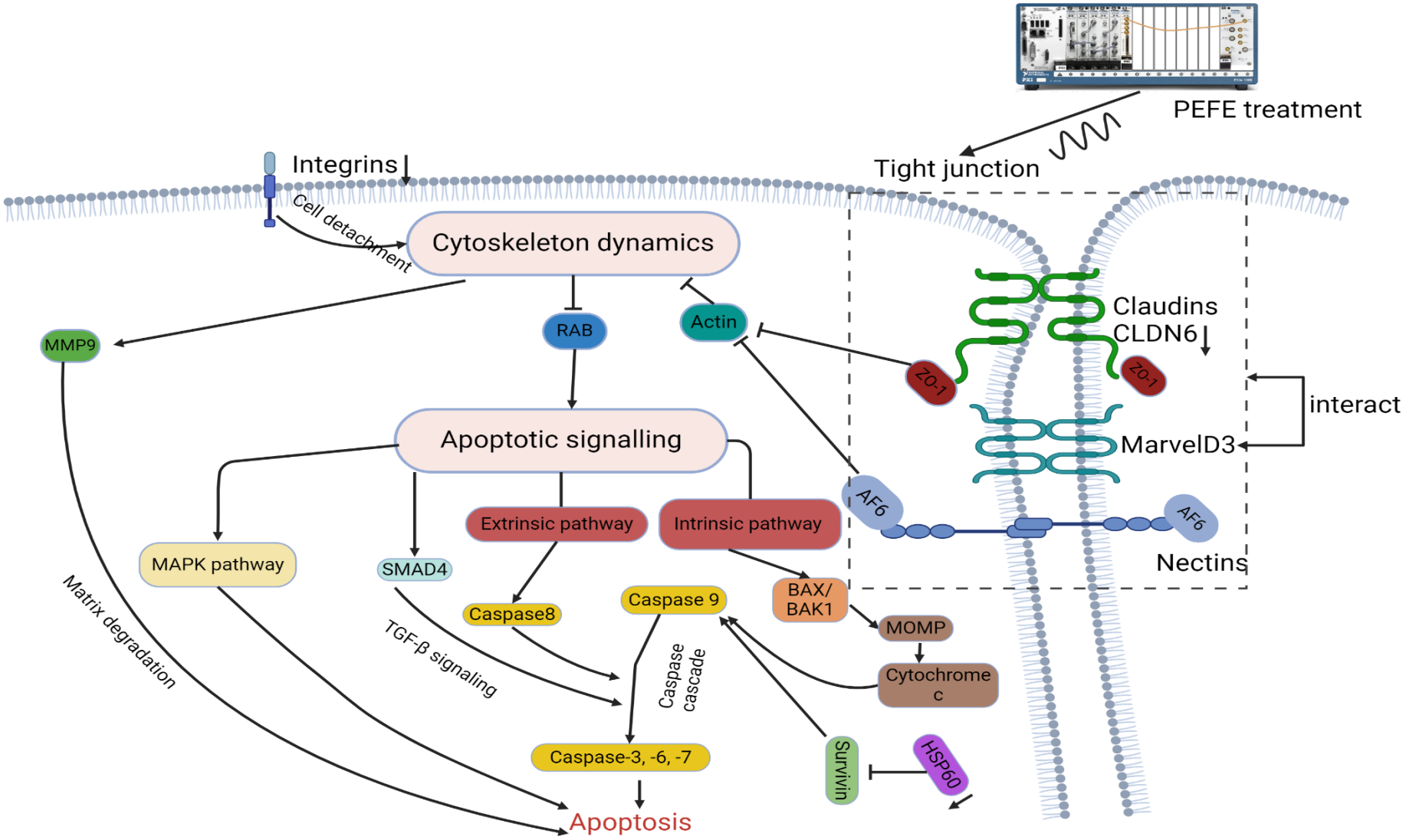
PEFE treatment
Integrins
Tight junction
Cell detachment
Cytoskeleton dynamics
MMP9
RAB
Actin
Claudins
CLDN6
ZO-1
ZO-1
interact
MarvelD3
Apoptotic signalling
AF6
AF6
Nectins
Extrinsic pathway
Intrinsic pathway
MAPK pathway
SMAD4
BAX/
BAK1
Caspase 9
Caspase8
MOMP
Matrix degradation
TGF-β signaling
Caspase
cascade
Cytochrome
c
Caspase-3, -6, -7
Survivin
HSP60
Apoptosis

Figure 8.2 Hypothetical signalling pathway of PEFE-induced cell apoptosis. The pathway starts with the application of PEFE treatment, which impacts TJ integrity and triggers downstream signalling events. Before the PEFE treatment, TJ integrity is maintained by TJ proteins such as ZO-1, MarvelD3, Claudins, and AF6. ZO-1 is located at the cell membrane to preserve TJ integrity but relocates to inner cell regions upon PEFE treatment, disrupting TJs. Moreover, AF6 binds to actin filaments, linking TJs to the actin cytoskeleton and preserving cytoskeleton stability until disrupted by PEFE, therefore facilitating the changes of cytoskeleton dynamics. Once actin filament was disorganized, the cancer cell structure was then disrupted. Subsequently, MMP9, a protein involved in degrading extracellular matrix components, was then activated. Also, Integrins, a family mediates cell adhesion and signalling, was disrupted. Both contributes to changes in cell morphology and therefore, activating the apoptosis signalling pathway ((Cabral-Pacheco et al. 2020; Hynes 2002). The intrinsic pathway, mediated by BAX/BAK1, promotes mitochondrial outer membrane permeabilization (MOMP) and cytochrome c release, a critical step for apoptosis. Cytochrome c activates Caspase-9, initiating the caspase cascade and leading to apoptosis (Li et al., 1997). Concurrently, the extrinsic pathway is triggered by Caspase-8, which responds to external death signals and activates downstream caspases, amplifying apoptosis. Caspases-3, -6, and -7 serve as executioner caspases, cleaving cellular substrates and inducing morphological and biochemical changes associated with apoptosis (Singh et al., 2019). Additionally, SMAD4, upregulated post-PEFE treatment, enhances the apoptotic response through TGF-β signalling, regulating pro-apoptotic genes (Zhao et al., 2018). The MAPK pathway, involving MAPK1, MAPK3, MAPK8, and MAPK14, is activated, regulating apoptosis-related genes and proteins and further promoting cell death (Yue and López, 2020). Furthermore, the reduction of HSP60 destabilizes mitochondrial Survivin, leading to mitochondrial membrane integrity deterioration, triggering effector caspase proteolysis and apoptosis (Tang et al., 2022). The diagram uses black arrows to indicate activation and promotion within signalling pathways, while black 'T'-shaped lines represent inhibition.

8.8 Further work

- ***In vivo* experiment**

Future work should prioritize these *in vivo* studies to validate the efficacy and safety of the PEFE treatment system in a biological context. Conducting *in vivo* experiments will allow us to observe the effects of the treatment in a living organism, providing critical insights into its therapeutic potential, and possible side effects. This step is essential for translating our findings from *in vitro* studies to clinical applications.

- **Simplification and user-friendliness of the system**

One primary goal for future work is to enhance the user-friendliness of the entire PEFE system. Currently, while some components have been integrated into the PXI system, several components still remain outside this unified system. Also, the calibration process remains

intricate and cumbersome by connecting and disconnecting various components. As we aim to eventually introduce this system into clinical trials and apply it to patient treatment, it is essential to streamline the setup and calibration process. To address this, we propose further integration to combine all microwave instruments into a single, unified control unit, which could be referred to as a "box”." Moreover, we propose to simplify the calibration process while ensuring that each component functions correctly. This will involve the development of automated or semi-automated calibration protocols, reducing the need for manual intervention and minimizing the risk of errors. By making the system full integration, we can facilitate its adoption in clinical settings, ultimately improving the efficiency and effectiveness of patient care.

- **Further development of dedicated combination probe**

Currently, our system utilizes a microwave probe (coaxial cable) and a thermometer attached to each other for treatment and temperature measurement respectively. Future work should focus on developing a dedicated combination probe that integrates both functions into a single probe. This integration will streamline the treatment process, enhance accuracy, and improve ease of use.

- **Further development of a multifunctional probe handling**

Additionally, we plan to develop a multifunctional probe handle to facilitate easier handling during the operation. This handle will allow for single button, quick and secure connection and disconnection of the probes. The multifunction handle will also feature several enhancements:

Integrated controls: The handle will have buttons for switching the microwave signal on and off, allowing to control the treatment directly from the handle.

Temperature display: A built-in screen on the handle will display real-time temperature readings, enabling to monitor the treatment conditions continuously.

Ergonomic design: The handle will be ergonomically designed to ensure comfort and ease of use during prolonged procedures.

- **Continuing MarvelD3 as a predictive and prognostic marker**

It will be crucial to further understand the underlying mechanisms by which MarvelD3 influences treatment outcomes. This can be achieved through in-depth molecular studies and functional assays that explore how MarvelD3 modulates cellular responses to PEFE. By elucidating these mechanisms, we can enhance our ability to predict which patients are most likely to benefit from PEFE treatment and tailor therapies accordingly. Integrating MarvelD3 assessment into clinical protocols could significantly improve the personalization and effectiveness of cancer treatment strategies.

References

Adi, W. A., Yunasfi, Y., Mashadi, M., Winatapura, D. S., Mulyawan, A., Sarwanto, Y. and Taryana, Y. 2019. Metamaterial: Smart Magnetic:Material for Microwave Absorbing Material. In: Kim Ho, Y. and Kazuhiro, H. eds. *Electromagnetic Fields and Waves*. Rijeka: IntechOpen, p. Ch. 8. doi: 10.5772/intechopen.84471

Agarwal, A., Deepinder, F., Sharma, R. K., Ranga, G. and Li, J. 2008. Effect of cell phone usage on semen analysis in men attending infertility clinic: an observational study. *Fertil Steril* 89(1), pp. 124-128. doi: 10.1016/j.fertnstert.2007.01.166

Agarwal, A., Desai, N. R., Makker, K., Varghese, A., Mouradi, R., Sabanegh, E. and Sharma, R. 2009. Effects of radiofrequency electromagnetic waves (RF-EMW) from cellular phones on human ejaculated semen: an in vitro pilot study. *Fertility and sterility* 92(4), pp. 1318-1325. doi: 10.1016/j.fertnstert.2008.08.022

Ahdi, R. S., Zamani, A., Blakowski, K. S. and Abosh, A. M. 2017. Novel Microwave Torso Scanner for Thoracic Fluid Accumulation Diagnosis and Monitoring. *Sci Rep* 7, p. 304. doi: https://doi.org/10.1038/s41598-017-00436-w

Ahmed, M., Rubio, I. T., Klaase, J. M. and Douek, M. 2015. Surgical treatment of nonpalpable primary invasive and in situ breast cancer. *Nature reviews. Clinical oncology* 12(11), pp. 645-663. doi: 10.1038/nrclinonc.2015.161

Aitken, R. J., Bennetts, L. E., Sawyer, D., Wiklendt, A. M. and King, B. V. 2005. Impact of radio frequency electromagnetic radiation on DNA integrity in the male germline. *Int J Androl* 28(3), pp. 171-179. doi: 10.1111/j.1365-2605.2005.00531.x

Akram, M., Iqbal, M., Daniyal, M. and Khan, A. U. 2017. Awareness and current knowledge of breast cancer. *Biol Res* 50(1), pp. 33-56. doi: 10.1186/s40659-017-0140-9

Al-Akhras, M., Elbetieha, A., Hasan, M., Al-Omari, I., Darmani, H. and Albiss, B. 2001. Effects of extremely low frequency magnetic field on fertility of adult male and female rats. *Bioelectromagnetics* 22(5), pp. 340-344. doi: https://doi.org/10.1002/bem.59

Alchalabi, A. S. H., Aklilu, E., Aziz, A. R., Malek, F., Ronald, S. H. and Khan, M. A. 2016. Different periods of intrauterine exposure to electromagnetic field: Influence on female rats' fertility, prenatal and postnatal development. *Asian Pacific Journal of Reproduction* 5(1), pp. 14-23. doi: https://doi.org/10.1016/j.apjr.2015.12.003

Aleman, B. M. P., Bartelink, H. and Gunderson, L. L. 1995. The current role of radiotherapy in colorectal cancer. *European Journal of Cancer* 31(7), pp. 1333-1339. doi: https://doi.org/10.1016/0959-8049(95)00280-V

AlSawaftah, N., El-Abed, S., Dhou, S. and Zakaria, A. 2022. Microwave Imaging for Early Breast Cancer Detection: Current State, Challenges, and Future Directions. *J Imaging* 8(5), doi: 10.3390/jimaging8050123

Altun, G., Deniz Ö, G., Yurt, K. K., Davis, D. and Kaplan, S. 2018. Effects of mobile phone

exposure on metabolomics in the male and female reproductive systems. *Environ Res* 167, pp. 700-707. doi: https://doi.org/10.1016/j.envres.2018.02.031

Anderson, J. M. and Van Itallie, C. M. 2009. Physiology and function of the tight junction. *Cold Spring Harb Perspect Biol* 1(2), p. a002584. doi: 10.1101/cshperspect.a002584

Andocs, G., Szasz, O. and Szasz, A. 2009. Oncothermia treatment of cancer: from the laboratory to clinic. *Electromagn Biol Med* 28(2), pp. 148-165. doi: 10.1080/15368370902724633

Antonio, C. and Deam, R. 2007. Can "microwave effects" be explained by enhanced diffusion? *Physical chemistry chemical physics : PCCP* 9, pp. 2976-2982. doi: https://doi.org/10.1039/B617358F

Arnold, M., Sierra, M. S., Laversanne, M., Soerjomataram, I., Jemal, A. and Bray, F. 2017. Global patterns and trends in colorectal cancer incidence and mortality. *Gut* 66(4), pp. 683-691. doi: 10.1136/gutjnl-2015-310912

Asano, M. et al. 2017a. Effects of Normothermic Conditioned Microwave Irradiation on Cultured Cells Using an Irradiation System with Semiconductor Oscillator and Thermo-regulatory Applicator. *Scientific Reports* 7(1), doi: 10.1038/srep41244

Asano, M., Tanaka, S., Sakaguchi, M., Matsumura, H., Yamaguchi, T., Fujita, Y. and Tabuse, K. 2017b. Normothermic Microwave Irradiation Induces Death of HL-60 Cells through Heat-Independent Apoptosis. *Scientific Reports* 7(1), doi: https://doi.org/10.1038/s41598-017-11784-y

Asay, B., Zinaida, T., Anastasia, V. and Maggie, W. 2008. Membrane composition as a factor in susceptibility of Escherichia coli C29 to thermal and non-thermal microwave radiation. *J. Exp. Microbiol. Immunol* 12, pp. 7-13.

Auguste, P., Barton, P., Hyde, C. and Roberts, T. E. 2011. An economic evaluation of positron emission tomography (PET) and positron emission tomography/computed tomography (PET/CT) for the diagnosis of breast cancer recurrence. *Health Technol Assess* 15(18), pp. 1-54. doi: 10.3310/hta15180

Baere, T. D. and Deschamps, F. 2014. New tumor ablation techniques for cancer treatment (microwave, electroporation). *Diagnostic and interventional imaging* 95(7), pp. 677-682. doi: 10.1016/j.diii.2014.04.001

Bak, M., Dudarewicz, A., Zmyslony, M. and Sliwinska-Kowalska, M. 2010. Effects of GSM signals during exposure to event related potentials (ERPs). *International journal of occupational medicine and environmental health* 23, pp. 191-199. doi: 10.2478/v10001-010-0021-8

Banik, S., Bandyopadhyay, S. and Ganguly, S. 2003. Bioeffects of microwave--a brief review. *Bioresour Technol* 87(2), pp. 155-159. doi: https://doi.org/10.1016/S0960-8524(02)00169-4

Barret, M. et al. 2013. Factors Associated with Adenoma Detection Rate and Diagnosis of Polyps and Colorectal Cancer during Colonoscopy in France: Results of a Prospective,

Nationwide Survey. *PLoS One* 8(7), p. e68947. doi: 10.1371/journal.pone.0068947

Bhat, A. et al. 2015a. Claudin-7 expression induces mesenchymal to epithelial transformation (MET) to inhibit colon tumorigenesis. *Oncogene* 34(35), pp. 4570-4580. doi: 10.1038/onc.2014.385

Bhat, A. A. et al. 2015b. Claudin-7 expression induces mesenchymal to epithelial transformation (MET) to inhibit colon tumorigenesis. *Oncogene* 34(35), pp. 4570-4580. doi: 10.1038/onc.2014.385

Bhat, A. A. et al. 2019. Tight Junction Proteins and Signaling Pathways in Cancer and Inflammation: A Functional Crosstalk. *Frontiers in Physiology* 9, doi: 10.3389/fphys.2018.01942

Bindu, G., Lonappan, A., Thomas, V., Aanandan, C. K., Mathew, K. T. and Abraham, S. J. 2006. Active microwave imaging for breast cancer detection. *Progress In Electromagnetics Research* 58, pp. 149-169. doi: 10.2528/PIER05081802

Blackwell, R. P. 1979. Standards for microwave radiation. *Nature* 282(5737), pp. 360-360. doi: 10.1038/282360a0
Full text linksCite

Bolós, V., Peinado, H., Pérez-Moreno, M. A., Fraga, M. F., Esteller, M. and Cano, A. 2003. The transcription factor Slug represses E-cadherin expression and induces epithelial to mesenchymal transitions: a comparison with Snail and E47 repressors. *J Cell Sci* 116(Pt 3), pp. 499-511. doi: 10.1242/jcs.00224

Bornholdt, J. et al. 2011. The level of claudin-7 is reduced as an early event in colorectal carcinogenesis. *BMC Cancer* 11(1), p. 65. doi: 10.1186/1471-2407-11-65

Brace, C. L. 2009. Microwave ablation technology: what every user should know. *Current problems in diagnostic radiology* 38(2), pp. 61-67. doi: 10.1067/j.cpradiol.2007.08.011

Brace, C. L. 2010. Microwave tissue ablation: biophysics, technology, and applications. *Critical reviews in biomedical engineering* 38(1), pp. 65-78. doi: 10.1615/critrevbiomedeng.v38.i1.60

Burch, J. B., Reif, J. S., Noonan, C. W., Ichinose, T., Bachand, A. M., Koleber, T. L. and Yost, M. G. 2002. Melatonin metabolite excretion among cellular telephone users. *International Journal of Radiation Biology* 78(11), pp. 1029-1036. doi: 10.1080/09553000210166561

Cabral-Pacheco, G. A. et al. 2020. The Roles of Matrix Metalloproteinases and Their Inhibitors in Human Diseases. *Int J Mol Sci* 21(24), doi: 10.3390/ijms21249739

Caferova, S., Uysal, F., Balcı, P., Saydam, S. and Canda, T. 2014. Efficacy and safety of breast radiothermometry in the differential diagnosis of breast lesions. *Contemporary oncology (Poznan, Poland)* 18(3), pp. 197-203. doi: 10.5114/wo.2014.42721

Cajochen, C., Kräuchi, K. and Wirz-Justice, A. 2003. Role of Melatonin in the Regulation of Human Circadian Rhythms and Sleep. *Journal of Neuroendocrinology* 15(4), pp. 432-437. doi:

10.1046/j.1365-2826.2003.00989.x

Campisi, A. et al. 2010. Reactive oxygen species levels and DNA fragmentation on astrocytes in primary culture after acute exposure to low intensity microwave electromagnetic field. *Neurosci Lett* 473(1), pp. 52-55. doi: 10.1016/j.neulet.2010.02.018

Cao, H., Xu, E., Liu, H., Wan, L. and Lai, M. 2015. Epithelial-mesenchymal transition in colorectal cancer metastasis: A system review. *Pathol Res Pract* 211(8), pp. 557-569. doi: 10.1016/j.prp.2015.05.010

Caraglia, M. et al. 2005. Electromagnetic fields at mobile phone frequency induce apoptosis and inactivation of the multi-chaperone complex in human epidermoid cancer cells. *Journal of Cellular Physiology* 204(2), pp. 539-548. doi: https://doi.org/10.1002/jcp.20327

Carrafiello, G. et al. 2008. Microwave tumors ablation: principles, clinical applications and review of preliminary experiences. *Int J Surg* 6 Suppl 1, pp. 65-69. doi: https://doi.org/10.1016/j.ijsu.2008.12.028

Chang, J. and Chaudhuri, O. 2019. Beyond proteases: Basement membrane mechanics and cancer invasion. *J Cell Biol* 218(8), pp. 2456-2469. doi: 10.1083/jcb.201903066

Chaoui, A. S., Blake, M. A., Barish, M. A. and Fenlon, H. M. 2000. Virtual colonoscopy and colorectal cancer screening. *Abdominal Imaging* 25(4), pp. 361-367. doi: 10.1107/s002610000012

Chen, G., Lu, D., Chiang, H., Leszczynski, D. and Xu, Z. 2012. Using model organism Saccharomyces cerevisiae to evaluate the effects of ELF-MF and RF-EMF exposure on global gene expression. *Bioelectromagnetics* 33(7), pp. 550-560. doi: 10.1002/bem.21724

CHENG, W. B., MOSER, M. A., KANAGARATNAM, S. and ZHANG, W. J. 2012. OVERVIEW OF UPCOMING ADVANCES IN COLONOSCOPY. *Digestive Endoscopy* 24(1), pp. 1-6. doi: https://doi.org/10.1111/j.1443-1661.2011.01181.x

Cheng, Z., Xiao, Q., Wang, Y., Sun, Y., Lu, T. and Liang, P. 2011. 915MHz microwave ablation with implanted internal cooled-shaft antenna: Initial experimental study in in vivo porcine livers. *European Journal of Radiology* 79(1), pp. 131-135. doi: https://doi.org/10.1016/j.ejrad.2009.12.013

Clarke, C. et al. 2013. Correlating transcriptional networks to breast cancer survival: a large-scale coexpression analysis. *Carcinogenesis* 34(10), pp. 2300-2308. doi: 10.1093/carcin/bgt208

Constantinou, C., Papadopoulos, S., Karyda, E., Alexopoulos, A., Agnanti, N., Batistatou, A. and Harisis, H. 2018. Expression and Clinical Significance of Claudin-7, PDL-1, PTEN, c-Kit, c-Met, c-Myc, ALK, CK5/6, CK17, p53, EGFR, Ki67, p63 in Triple-negative Breast Cancer-A Single Centre Prospective Observational Study. *In Vivo* 32(2), pp. 303-311. doi: 10.21873/invivo.11238

Copty, A., Golosovsky, M., Davidov, D. and Frenkel, A. 2004. Localized heating of biological media using a 1-W microwave near-field probe. *IEEE Transactions on Microwave Theory and*

Techniques 52(8), pp. 1957-1963. doi: 10.1109/TMTT.2004.831986

Cording, J. et al. 2013. In tight junctions, claudins regulate the interactions between occludin, tricellulin and marvelD3, which, inversely, modulate claudin oligomerization. *Journal of Cell Science* 126(2), pp. 554-564. doi: 10.1242/jcs.114306

Correa-Gallego, C. et al. 2014. A Retrospective Comparison of Microwave Ablation vs. Radiofrequency Ablation for Colorectal Cancer Hepatic Metastases. *Annals of Surgical Oncology* 21(13), pp. 4278-4283. doi: 10.1245/s10434-014-3817-0

Croft, R. J., Hamblin, D. L., Spong, J., Wood, A. W., McKenzie, R. J. and Stough, C. 2008. The effect of mobile phone electromagnetic fields on the alpha rhythm of human electroencephalogram. *Bioelectromagnetics* 29(1), pp. 1-10. doi: 10.1002/bem.20352

Czyz, J. et al. 2004. High frequency electromagnetic fields (GSM signals) affect gene expression levels in tumor suppressor p53-deficient embryonic stem cells. *Bioelectromagnetics* 25(4), pp. 296-307. doi: 10.1002/bem.10199

Davoudi, M., Brössner, C. and Kuber, W. 2002. The influence of electromagnetic waves on sperm motility. *Journal fur Urologie und Urogynakologie* 9, pp. 18-22.

De Iuliis, G. N., Newey, R. J., King, B. V. and Aitken, R. J. 2009. Mobile Phone Radiation Induces Reactive Oxygen Species Production and DNA Damage in Human Spermatozoa In Vitro. *PLoS One* 4(7), p. e6446. doi: 10.1371/journal.pone.0006446
Full text linksCite

De Rosa, M., Pace, U., Rega, D., Costabile, V., Duraturo, F., Izzo, P. and Delrio, P. 2015. Genetics, diagnosis and management of colorectal cancer (Review). *Oncol Rep* 34(3), pp. 1087-1096. doi: 10.3892/or.2015.4108

de Tommaso, M., Rossi, P., Falsaperla, R., Francesco Vde, V., Santoro, R. and Federici, A. 2009. Mobile phones exposure induces changes of contingent negative variation in humans. *Neurosci Lett* 464(2), pp. 79-83. doi: 10.1016/j.neulet.2009.08.045

Desgazer, G., Merck, D., Hagmann, M., Dupuy, D. E. and Prakash, P. 2016. Physical modeling of microwave ablation zone linical margin variance. *Med Phys* 43, pp. 1764-1776. doi: 10.1118/1.4942980

Deshmukh, P., Banerjee, B., Abegaonkar, M., Megha, K., Ahmed, R., Tripathi, A. and Mediratta, P. 2013. Effect of low level microwave radiation exposure on cognitive function and oxidative stress in rats. *Indian journal of biochemistry & biophysics* 50, pp. 114-119. doi: https://doi.org/10.3967/bes2016.115

Desouza, M., Gunning, P. W. and Stehn, J. R. 2012. The actin cytoskeleton as a sensor and mediator of apoptosis. *Bioarchitecture* 2(3), pp. 75-87. doi: 10.4161/bioa.20975

Dhawan, P. et al. 2005. Claudin-1 regulates cellular transformation and metastatic behavior in colon cancer. *J Clin Invest* 115(7), pp. 1765-1776. doi: 10.1172/jci24543

Diego, E. J., McAuliffe, P. F., Soran, A., McGuire, K. P., Johnson, R. R., Bonaventura, M. and

Ahrendt, G. M. 2016. Axillary Staging After Neoadjuvant Chemotherapy for Breast Cancer: A Pilot Study Combining Sentinel Lymph Node Biopsy with Radioactive Seed Localization of Pre-treatment Positive Axillary Lymph Nodes. *Ann Surg Oncol* 23(5), pp. 1549-1553. doi: https://doi.org/10.1245/s10434-015-5052-8

Dooley, W. C., Vargas, H. I., Fenn, A. J., Tomaselli, M. B. and Harness, J. K. 2010. Focused Microwave Thermotherapy for Preoperative Treatment of Invasive Breast Cancer: A Review of Clinical Studies. *Annals of Surgical Oncology* 17(4), pp. 1076-1093.

Dorval, M., Maunsell, E., Deschênes, L. and Brisson, J. 1998. Type of mastectomy and quality of life for long term breast carcinoma survivors. *Cancer* 83(10), pp. 2130-2138. doi: 10.1002/(sici)1097-0142(19981115)83:10<2130::aid-cncr11>3.0.co;2-8

Dou, J., Liang, P. and Yu, J. 2016. Microwave ablation for liver tumors. *Abdominal radiology (New York)* 41(4), pp. 650-658. doi: https://doi.org/10.1007/s00261-016-0662-6

Eberhardt, J. L., Persson, B. R., Brun, A. E., Salford, L. G. and Malmgren, L. O. 2008. Blood-brain barrier permeability and nerve cell damage in rat brain 14 and 28 days after exposure to microwaves from GSM mobile phones. *Electromagn Biol Med* 27(3), pp. 215-229. doi: 10.1080/15368370802344037

Edrich, J. 1979. Microwave Techniques in the Diagnosis and Treatment of Cancer. *1979 9th European Microwave Conference*, pp. 25-33. doi: 10.1109/EUMA.1979.332674

Ehtaiba, M. H. A. 2017. *Use of microwave techniques in medical diagnostics and therapy*. Cardiff University.

Ellis, M. J. et al. 2017. Ki67 Proliferation Index as a Tool for Chemotherapy Decisions During and After Neoadjuvant Aromatase Inhibitor Treatment of Breast Cancer: Results From the American College of Surgeons Oncology Group Z1031 Trial (Alliance). *J Clin Oncol* 35(10), pp. 1061-1069. doi: 10.1200/JCO.2016.69.4406

Eng, O. S. et al. 2015. Outcomes of microwave ablation for colorectal cancer liver metastases: a single center experience. *J Surg Oncol* 111(4), pp. 410-413. doi: 10.1002/jso.23849

Erten, O., Li, P., Gokceimam, M., Akbulut, S. and Berber, E. 2021. Impact of ablation algorithm versus tumor-dependent parameters on local control after microwave ablation of malignant liver tumors. *J Surg Oncol* 123(1), pp. 179-186. doi: 10.1002/jso.26237

Fabregat, A. et al. 2016. The Reactome pathway Knowledgebase. *Nucleic Acids Res* 44(D1), pp. D481-487. doi: 10.1093/nar/gkv1351

Fabregat, A. et al. 2017. Reactome pathway analysis: a high-performance in-memory approach. *BMC Bioinformatics* 18(1), p. 142. doi: 10.1186/s12859-017-1559-2

Fanning, A. S., Jameson, B. J., Jesaitis, L. A. and Anderson, J. M. 1998. The Tight Junction Protein ZO-1 Establishes a Link between the Transmembrane Protein Occludin and the Actin Cytoskeleton*. *Journal of Biological Chemistry* 273(45), pp. 29745-29753. doi: https://doi.org/10.1074/jbc.273.45.29745

Feng, Y. et al. 2018. Breast cancer development and progression: Risk factors, cancer stem cells, signaling pathways, genomics, and molecular pathogenesis. *Genes & Diseases* 5, doi: 10.1016/j.gendis.2018.05.001

Fenn, A. J. 2007. *Breast cancer treatment by focused microwave thermotherapy*.

Ferguson, F. M. and Gray, N. S. 2018. Kinase inhibitors: the road ahead. *Nat Rev Drug Discov* 17(5), pp. 353-377. doi: 10.1038/nrd.2018.21

Fink, S. L. and Cookson, B. T. 2005. Apoptosis, pyroptosis, and necrosis: mechanistic description of dead and dying eukaryotic cells. *Infect Immun* 73(4), pp. 1907-1916. doi: 10.1128/iai.73.4.1907-1916.2005

Fisher, B., Anderson, S., Redmond, C. K., Wolmark, N., Wickerham, D. L. and Cronin, W. M. 1995. Reanalysis and results after 12 years of follow-up in a randomized clinical trial comparing total mastectomy with lumpectomy with or without irradiation in the treatment of breast cancer. *N Engl J Med* 333(22), pp. 1456-1461. doi: 10.1056/NEJM199511303332203

Fletcher, S. W. and Elmore, J. G. 2003. Clinical practice. Mammographic screening for breast cancer. *The New England journal of medicine* 348(17), pp. 1672-1680. doi: 10.1056/NEJMcp021804

Fortner, A., Chera, A., Tanca, A. and Bucur, O. 2022. Apoptosis regulation by the tyrosine-protein kinase CSK. *Frontiers in Cell and Developmental Biology* 10, doi: 10.3389/fcell.2022.1078180

Fragopoulou, A. F. et al. 2012. Brain proteome response following whole body exposure of mice to mobile phone or wireless DECT base radiation. *Electromagn Biol Med* 31(4), pp. 250-274. doi: 10.3109/15368378.2011.631068

Gabriel, C., Gabriel, S. and Corthout, E. 1996. The dielectric properties of biological tissues: I. Literature survey. *Physics in Medicine and Biology* 41, pp. 2231-2249. doi: 10.1088/0031-9155/41/11/001

Gajski, G. and Garaj-Vrhovac, V. 2009. Radioprotective effects of honeybee venom (Apis mellifera) against 915-MHz microwave radiation-induced DNA damage in wistar rat lymphocytes: in vitro study. *Int J Toxicol* 28(2), pp. 88-98. doi: 10.1177/1091581809335051

Gardner, R. A., Vargas, H. I., Block, J. B., Vogel, C. L., Fenn, A. J., Kuehl, G. V. and Doval, M. 2002. Focused microwave phased array thermotherapy for primary breast cancer. *Annals of Surgical Oncology* 9(4), pp. 326-332.

Gersten, O. and Wilmoth, J. R. 2002. The cancer tran sition in Japan since 1951. *Demogr Res* 7, pp. 271-306. doi: 10.4054/DemRes.2002.7.5

Giaever, I. and Keese, C. R. 1991. Micromotion of mammalian cells measured electrically. *Proceedings of the National Academy of Sciences of the United States of America* 88(17), pp. 7896-7900. doi: 10.1073/pnas.88.17.7896

Giaever, I. and Keese, C. R. 2012. Electric Cell-Substrate Impedance Sensing Concept to

Commercialization. In: Jiang, W.G. ed. *Electric Cell-Substrate Impedance Sensing and Cancer Metastasis*. Dordrecht: Springer Netherlands, pp. 1-19. doi: 10.1007/978-94-007-4927-6_1

Gill, S., Thomas, R. R. and Goldberg, R. M. 2003. Colorectal cancer chemotherapy. *Alimentary Pharmacology & Therapeutics* 18(7), pp. 683-692. doi: https://doi.org/10.1046/j.1365-2036.2003.01735.x

González-Mariscal, L., Betanzos, A., Nava, P. and Jaramillo, B. E. 2003. Tight junction proteins. *Prog Biophys Mol Biol* 81(1), pp. 1-44. doi: 10.1016/s0079-6107(02)00037-8

Goodwin, R. A. and Asmis, T. R. 2009. Overview of systemic therapy for colorectal cancer. *Clinics in colon and rectal surgery* 22(4), pp. 251-256. doi: 10.1055/s-0029-1242465

Gramont, A. d. et al. 2007. Oxaliplatin/5FU/LV in adjuvant colon cancer: Updated efficacy results of the MOSAIC trial, including survival, with a median follow-up of six years. *Journal of Clinical Oncology* 25(18_suppl), pp. 4007-4007. doi: 10.1200/jco.2007.25.18_suppl.4007

Graser, A. et al. 2009. Comparison of CT colonography, colonoscopy, sigmoidoscopy and faecal occult blood tests for the detection of advanced adenoma in an average risk population. *Gut* 58(2), pp. 241-248. doi: 10.1136/gut.2008.156448

Gröne, J. et al. 2007. Differential expression of genes encoding tight junction proteins in colorectal cancer: frequent dysregulation of claudin-1,-8 and-12. *International journal of colorectal disease* 22(6), pp. 651-659. doi: https://doi.org/10.1007/s00384-006-0197-3

Güler, G., Tomruk, A., Ozgur, E., Sahin, D., Sepici, A., Altan, N. and Seyhan, N. 2012. The effect of radiofrequency radiation on DNA and lipid damage in female and male infant rabbits. *International Journal of Radiation Biology* 88(4), pp. 367-373. doi: 10.3109/09553002.2012.646349

Guler, G., Tomruk, A., Ozgur, E. and Seyhan, N. 2010. The effect of radiofrequency radiation on DNA and lipid damage in non-pregnant and pregnant rabbits and their newborns. *General Physiology and Biophysics* 29, pp. 59-66. doi: 10.4149/gpb_2010_01_59

Günzel, D. and Yu, A. S. 2013. Claudins and the modulation of tight junction permeability. *Physiol Rev* 93(2), pp. 525-569. doi: 10.1152/physrev.00019.2012

Gupta, P. B. and Kuperwasser, C. 2006. Contributions of estrogen to ER-negative breast tumor growth. *The Journal of Steroid Biochemistry and Molecular Biology* 102(1), pp. 71-78. doi: 10.1016/j.jsbmb.2006.09.025

Hadden, J. W. 1999. The immunology and immunotherapy of breast cancer: an update. *Int J Immunopharmacol* 21(2), pp. 79-101. doi: 10.1016/s0192-0561(98)00077-0

Häfner, M. F. and Debus, J. 2016. Radiotherapy for Colorectal Cancer: Current Standards and Future Perspectives. *Visceral medicine* 32(3), pp. 172-177. doi: 10.1159/000446486

Hall, E. J. and Brenner, D. J. 2008. Cancer risks from diagnostic radiology. *Br J Radiol* 81(965), pp. 362-378. doi: 10.1259/bjr/01948454

Han, K. Q. et al. 2015. Targeted silencing of CXCL1 by siRNA inhibits tumor growth and apoptosis in hepatocellular carcinoma. *Int J Oncol* 47(6), pp. 2131-2140. doi: 10.3892/ijo.2015.3203

Han, Y., Yan, X., Zhi, W., Liu, Y., Xu, F. and Yan, D. 2022. Long-term outcome following microwave ablation of lung metastases from colorectal cancer. *Front Oncol* 12, p. 943715. doi: 10.3389/fonc.2022.943715

Hao, D. et al. 2012. Effects of long-term electromagnetic field exposure on spatial learning and memory in rats. *Neurological sciences : official journal of the Italian Neurological Society and of the Italian Society of Clinical Neurophysiology* 34, doi: https://doi.org/10.1007/s10072-012-0970-8

Harrington, S. E. and Smith, T. J. 2008. The role of chemotherapy at the end of life: "when is enough, enough?". *JAMA* 299(22), pp. 2667-2678. doi: 10.1001/jama.299.22.2667

Heiken, J. P., Peterson, C. M. and Menias, C. O. 2005. Virtual colonoscopy for colorectal cancer screening: current status. *Cancer imaging : the official publication of the International Cancer Imaging Society* 5 Spec No A(Spec No A), pp. S133-S139. doi: 10.1102/1470-7330.2005.0108

Hellquist, B. N., Czene, K., Hjälm, A., Nyström, L. and Jonsson, H. 2015. Effectiveness of population-based service screening with mammography for women ages 40 to 49 years with a high or low risk of breast cancer: socioeconomic status, parity, and age at birth of first child. *Cancer* 121(2), pp. 251-258. doi: https://doi.org/10.1002/cncr.29011

Heriot, A. G., Hicks, R. J., Drummond, E. G., Keck, J., Mackay, J., Chen, F. and Kalff, V. 2004. Does positron emission tomography change management in primary rectal cancer? A prospective assessment. *Dis Colon Rectum* 47(4), pp. 451-458. doi: 10.1007/s10350-003-0089-3

Herrero, M. A., Kremsner, J. M. and Kappe, C. O. 2008. Nonthermal Microwave Effects Revisited: On the Importance of Internal Temperature Monitoring and Agitation in Microwave Chemistry. *The Journal of Organic Chemistry* 73(1), pp. 36-47. doi: 10.1021/jo7022697

Hester, R. H., Hortobagyi, G. N. and Lim, B. 2021. Inflammatory breast cancer: early recognition and diagnosis is critical. *American Journal of Obstetrics and Gynecology* 225(4), pp. 392-396. doi: https://doi.org/10.1016/j.ajog.2021.04.217

Hoevel, T., Macek, R., Mundigl, O., Swisshelm, K. and Kubbies, M. 2002. Expression and targeting of the tight junction protein CLDN1 in CLDN1-negative human breast tumor cells. *Journal of Cellular Physiology* 191(1), pp. 60-68. doi: 10.1002/jcp.10076

Hong, J., Kandasamy, K., Marimuthu, M., Choi, C. S. and Kim, S. 2011. Electrical cell-substrate impedance sensing as a non-invasive tool for cancer cell study. *Analyst* 136(2), pp. 237-245. doi: 10.1039/c0an00560f

Hooley, R. J., Scoutt, L. M. and Philpotts, L. E. 2013. Breast ultrasonography: state of the art. *Radiology* 268(3), pp. 642-659. doi: https://doi.org/10.1148/radiol.13121606

Houssami, N., Turner, R. M. and Morrow, M. 2017. Meta-analysis of pre-operative magnetic resonance imaging (MRI) and surgical treatment for breast cancer. *Breast Cancer Research and Treatment* 165(2), pp. 273-283. doi: 10.1007/s10549-017-4324-3

Huang, K., Meng, Y., Lu, J., Xu, L., Wang, S., Wang, H. and Xu, Z. 2022. High expression of MARVELD3 as a potential prognostic biomarker for oral squamous cell carcinoma. *Front Genet* 13, p. 1050402. doi: 10.3389/fgene.2022.1050402

Humphrey, L. 2002. Breast Cancer Screening: A Summary of the Evidence for the U.S. Preventive Services Task Force. *Annals of Internal Medicine* 137, p. 347. doi: 10.7326/0003-4819-137-5_part_1-200209030-00012

Hung, C. S., Anderson, C., Horne, J. A. and McEvoy, P. 2007. Mobile phone 'talk-mode' signal delays EEG-determined sleep onset. *Neurosci Lett* 421(1), pp. 82-86. doi: 10.1016/j.neulet.2007.05.027

Hyland, G. 2000. Physics and biology of mobile telephony. *Lancet* 356, pp. 1833-1836. doi: https://doi.org/10.1016/S0140-6736(00)03243-8

Hynes, R. O. 2002. Integrins: bidirectional, allosteric signaling machines. *Cell* 110(6), pp. 673-687. doi: 10.1016/s0092-8674(02)00971-6

Ibitoye, Z. A., Nwoye, E. O., Aweda, M. A., Oremosu, A. A., Annunobi, C. C. and Akanmu, O. N. 2015. Optimization of dual slot antenna using floating metallic sleeve for microwave ablation. *Medical Engineering & Physics* 37(4), pp. 384-391. doi: https://doi.org/10.1016/j.medengphy.2015.01.015

Ikenouchi , J., Furuse , M., Furuse , K., Sasaki , H., Tsukita , S. and Tsukita , S. 2005. Tricellulin constitutes a novel barrier at tricellular contacts of epithelial cells. *Journal of Cell Biology* 171(6), pp. 939-945. doi: 10.1083/jcb.200510043

Itabe, H., Yamaguchi, T., Nimura, S. and Sasabe, N. 2017. Perilipins: a diversity of intracellular lipid droplet proteins. *Lipids in Health and Disease* 16(1), p. 83. doi: 10.1186/s12944-017-0473-y

J. Louis, H., Meghan, G. L., Timothy, J. Z. and Christopher, L. B. 2014. Percutaneous Tumor Ablation Tools: Microwave, Radiofrequency, or Cryoablation—What Should You Use and Why? *RadioGraphics* 34(5), pp. 1344-1362. doi: https://doi.org/10.1148/rg.345140054
More

Jacques, V. and Luc, V. 2008. Gene and Protein Expression following Exposure to Radiofrequency Fields from Mobile Phones. *Environmental health perspectives* 116(9), pp. 1131-1135. doi: https://doi.org/10.1289/ehp.11279

Jain, A. et al. 2017. Stereotactic core needle breast biopsy marker migration: An analysis of factors contributing to immediate marker migration. *Eur Radiol* 27(11), pp. 4797-4803. doi: 10.1007/s00330-017-4851-7

Jarupat, S., Kawabata, A., Tokura, H. and Borkiewicz, A. 2003. Effects of the 1900 MHz Electromagnetic Field Emitted from Cellular Phone on Nocturnal Melatonin Secretion. *Journal*

of PHYSIOLOGICAL ANTHROPOLOGY and Applied Human Science 22(1), pp. 61-63. doi: 10.2114/jpa.22.61

Jeiwon, C. et al. 2006. In-vivo measurements of the dielectric properties of breast carcinoma xenografted on nude mice. *Int. J. Cancer* 119(3), pp. 593-598. doi: 10.1002/ijc.21896

Jemal, A., Bray, F., Forman, D., O'Brien, M., Ferlay, J., Center, M. and Parkin, D. M. 2012. Cancer burden in Africa and opportunities for prevention. *Cancer* 118(18), pp. 4372-4384. doi: 10.1002/cncr.27410

JI, W., Jiang, W. G. and Martin, T. A. 2023. Abstract P2-26-20: Marvel D3 and its associated junctional proteins in breast cancer. *Cancer Research* 83(5_Supplement), pp. P2-26-20-P22-26-20. doi: 10.1158/1538-7445.Sabcs22-p2-26-20

Jiang, D. P. et al. 2016. Long-term electromagnetic pulse exposure induces Abeta deposition and cognitive dysfunction through oxidative stress and overexpression of APP and BACE1. *Brain Res* 1642, pp. 10-19. doi: 10.1016/j.brainres.2016.02.053

Jiang, W. G., Puntis, M. C. and Hallett, M. B. 1994. Molecular and cellular basis of cancer invasion and metastasis: implications for treatment. *Br J Surg* 81(11), pp. 1576-1590. doi: 10.1002/bjs.1800811107

Jiang, W. G., Watkins, G., Douglas-Jones, A., Holmgren, L. and Mansel, R. E. 2006. Angiomotin and angiomotin like proteins, their expression and correlation with angiogenesis and clinical outcome in human breast cancer. *BMC Cancer* 6(1), p. 16. doi: 10.1186/1471-2407-6-16

Jiang, W. G., Ye, L., Patel, G. and Harding, K. G. 2010. Expression of WAVEs, the WASP (Wiskott-Aldrich syndrome protein) family of verprolin homologous proteins in human wound tissues and the biological influence on human keratinocytes. *Wound Repair Regen* 18(6), pp. 594-604. doi: 10.1111/j.1524-475X.2010.00630.x

Jones, R. P. et al. 2012. Microwave ablation of ex vivo human liver and colorectal liver metastases with a novel 14.5 GHz generator. *International Journal of Hyperthermia* 28(1), pp. 43-54. doi: 10.3109/02656736.2011.610428

Jonker, D. J., Spithoff, K. and Maroun, J. 2011. Adjuvant systemic chemotherapy for Stage II and III colon cancer after complete resection: an updated practice guideline. *Clin Oncol (R Coll Radiol)* 23(5), pp. 314-322. doi: 10.1016/j.clon.2011.02.010

Joubert, V., Bourthoumieu, S., Leveque, P. and Yardin, C. 2008. Apoptosis is induced by radiofrequency fields through the caspase-independent mitochondrial pathway in cortical neurons. *Radiat Res* 169(1), pp. 38-45. doi: 10.1667/rr1077.1

Jr, G. W. S. 2005. What Is Targeted Therapy? *Journal of Clinical Oncology* 23(8), pp. 1614-1615. doi: 10.1200/jco.2005.01.016

Kalyan, A., Kircher, S., Shah, H., Mulcahy, M. and Benson, A. 2018. Updates on immunotherapy for colorectal cancer. *Journal of gastrointestinal oncology* 9(1), pp. 160-169. doi: 10.21037/jgo.2018.01.17

Kappe, C. O. 2004. Controlled microwave heating in modern organic synthesis. *Angew Chem Int Ed Engl* 43(46), pp. 6250-6284. doi: https://doi.org/10.1002/anie.200400655

Karaca, E. et al. 2011. The genotoxic effect of radiofrequency waves on mouse brain. *Journal of neuro-oncology* 106, pp. 53-58. doi: 10.1007/s11060-011-0644-z

Karampatzakis, A., Kühn, S., Tsanidis, G., Neufeld, E., Samaras, T. and Kuster, N. 2013. Heating characteristics of antenna arrays used in microwave ablation: A theoretical parametric study. *Comput Biol Med* 43(10), pp. 1321-1327. doi: https://doi.org/10.1016/j.compbiomed.2013.07.013

Keangin, P. and Rattanadecho, P. 2013. Analysis of heat transport on local thermal non-equilibrium in porous liver during microwave ablation. *International Journal of Heat and Mass transfer* 67, pp. 46-60. doi: https://doi.org/10.1016/j.ijheatmasstransfer.2013.07.064

Kekelidze, M., D'Errico, L., Pansini, M., Tyndall, A. and Hohmann, J. 2013. Colorectal cancer: current imaging methods and future perspectives for the diagnosis, staging and therapeutic response evaluation. *World journal of gastroenterology* 19(46), pp. 8502-8514. doi: 10.3748/wjg.v19.i46.8502

Kerketta, S. R. and Ghosh, D. 2020. Microwave sensing for human bone health evaluation. *AEU - International Journal of Electronics and Communications* 127, doi: https://doi.org/10.1016/j.aeue.2020.153469

Kesari, K., Siddiqui, M., Meena, R., Verma, H. and Kumar, S. 2013. Cell phone radiation exposure on brain and associated biological systems. *Indian journal of experimental biology* 51, pp. 187-200.

Kesari, K. K. and Behari, J. 2010. Microwave exposure affecting reproductive system in male rats. *Appl Biochem Biotechnol* 162(2), pp. 416-428. doi: 10.1007/s12010-009-8722-9

Keskin, G. and Gumus, A. B. 2011. Turkish hysterectomy and mastectomy patients - depression, body image, sexual problems and spouse relationships. *Asian Pac J Cancer Prev* 12(2), pp. 425-432.

Keum, N. and Giovannucci, E. 2019. Global burden of colorectal cancer: emerging trends, risk factors and prevention strategies. *Nat Rev Gastroenterol Hepatol* 16(12), pp. 713-732. doi: 10.1038/s41575-019-0189-8

Kijima, S., Sasaki, T., Nagata, K., Utano, K., Lefor, A. T. and Sugimoto, H. 2014. Preoperative evaluation of colorectal cancer using CT colonography, MRI, and PET/CT. *World journal of gastroenterology* 20(45), pp. 16964-16975. doi: 10.3748/wjg.v20.i45.16964

Kim, J. H., Lee, J. K., Kim, H. G., Kim, K. B. and Kim, H. R. 2019. Possible Effects of Radiofrequency Electromagnetic Field Exposure on Central Nerve System. *Biomol Ther (Seoul)* 27(3), pp. 265-275. doi: 10.4062/biomolther.2018.152

Kim, R. et al. 2023. Outcomes in patients with non-invasive breast carcinoma. *Cancer Rep (Hoboken)* 6(4), p. e1768. doi: 10.1002/cnr2.1768

Kinoshita, T. and Fujita, M. 2016. Thematic Review Series: Glycosylphosphatidylinositol (GPI) Anchors: Biochemistry and Cell Biology Biosynthesis of GPI-anchored proteins: special emphasis on GPI lipid remodeling. *Journal of Lipid Research* 57(1), pp. 6-24. doi: https://doi.org/10.1194/jlr.R063313

Kitao, H. et al. 2018. DNA replication stress and cancer chemotherapy. *Cancer science* 109(2), pp. 264-271. doi: 10.1111/cas.13455

Kleeff, J. et al. 2001. Altered expression and localization of the tight junction protein ZO-1 in primary and metastatic pancreatic cancer. *Pancreas* 23(3), pp. 259-265. doi: 10.1097/00006676-200110000-00006

Kleinlogel, H., Dierks, T., Koenig, T., Lehmann, H., Minder, A. and Berz, R. 2008. Effects of weak mobile phone - electromagnetic fields (GSM, UMTS) on event related potentials and cognitive functions. *Bioelectromagnetics* 29(6), pp. 488-497. doi: 10.1002/bem.20418

Kluetz, P., Meltzer, C., Villemagne, V., Kinahan, P., Chander, S., Martinelli, M. and Townsend, D. 2000. Combined PET/CT Imaging in Oncology: Impact on Patient Management. *Clinical Positron Imaging* 3, pp. 223-230. doi: https://doi.org/10.1016/S1095-0397(01)00055-3

Köhne-Wömpner, C. H., Schmoll, H. J., Harstrick, A. and Rustum, Y. M. 1992. Chemotherapeutic strategies in metastatic colorectal cancer: an overview of current clinical trials. *Seminars in oncology* 19(2 Suppl 3), pp. 105-125. doi: https://doi.org/10.3816/CCC.2001.n.013

Kojima, T. et al. 2011. Downregulation of tight junction-associated MARVEL protein marvelD3 during epithelial–mesenchymal transition in human pancreatic cancer cells. *Experimental Cell Research* 317(16), pp. 2288-2298. doi: https://doi.org/10.1016/j.yexcr.2011.06.020

Krause, G., Winkler, L., Mueller, S. L., Haseloff, R. F., Piontek, J. and Blasig, I. E. 2008. Structure and function of claudins. *Biochimica et Biophysica Acta (BBA) - Biomembranes* 1778(3), pp. 631-645. doi: https://doi.org/10.1016/j.bbamem.2007.10.018

Krewski, D. et al. 2001. Potential health risks of radiofrequency fields from wireless telecommunication devices. *J Toxicol Environ Health B Crit Rev* 4(1), pp. 1-143. doi: 10.1080/109374001459458

Kuipers, E. J. et al. 2015. Colorectal cancer. *Nat Rev Dis Primers* 1, p. 15065. doi: 10.1038/nrdp.2015.65

Kurilova, I. et al. 2018. Microwave Ablation in the Management of Colorectal Cancer Pulmonary Metastases. *CardioVascular and Interventional Radiology* 41(10), pp. 1530-1544. doi: 10.1007/s00270-018-2000-6

Labianca, R., Nordlinger, B., Beretta, G. D., Mosconi, S., Mandalà, M., Cervantes, A. and Arnold, D. 2013. Early colon cancer: ESMO Clinical Practice Guidelines for diagnosis, treatment and follow-up. *Ann Oncol* 24 Suppl 6, pp. vi64-72. doi: 10.1093/annonc/mdt354

Lahat, E., Eshkenazy, R., Zendel, A., Zakai, B. B., Maor, M., Dreznik, Y. and Ariche, A. 2014. Complications after percutaneous ablation of liver tumors: a systematic review. *Hepatobiliary Surg Nutr* 3(5), pp. 317-323. doi: 10.3978/j.issn.2304-3881.2014.09.07

Lambert, A. W., Pattabiraman, D. R. and Weinberg, R. A. 2017. Emerging Biological Principles of Metastasis. *Cell* 168(4), pp. 670-691. doi: 10.1016/j.cell.2016.11.037

Le Borgne, F., Guyot, S., Logerot, M., Beney, L., Gervais, P. and Demarquoy, J. 2012. Exploration of lipid metabolism in relation with plasma membrane properties of Duchenne muscular dystrophy cells: influence of L-carnitine. *PLoS One* 7(11), p. e49346. doi: 10.1371/journal.pone.0049346

Lee, B., Moon, K. M. and Kim, C. Y. 2018. Tight Junction in the Intestinal Epithelium: Its Association with Diseases and Regulation by Phytochemicals. *J Immunol Res* 2018, p. 2645465. doi: 10.1155/2018/2645465

Lee, W. K., Torchalski, B., Kohistani, N. and Thévenod, F. 2011. ABCB1 protects kidney proximal tubule cells against cadmium-induced apoptosis: roles of cadmium and ceramide transport. *Toxicol Sci* 121(2), pp. 343-356. doi: 10.1093/toxsci/kfr071

Li, S., Qi, S., Li, Y., Zhang, C., Sun, L., Liu, C. and Wang, H. 2023. MARVELD3 inhibits the epithelial-mesenchymal transition and cell migration by suppressing the Wnt/β-catenin signaling pathway in non-small cell lung cancer cells. *Thorac Cancer* 14(12), pp. 1045-1058. doi: 10.1111/1759-7714.14844

Li, Y. et al. 2021a. Role of tight junction-associated MARVEL protein marvelD3 in migration and epithelial-mesenchymal transition of hepatocellular carcinoma. *Cell Adh Migr* 15(1), pp. 249-260. doi: 10.1080/19336918.2021.1958441

Li, Y. et al. 2021b. Role of tight junction-associated MARVEL protein marvelD3 in migration and epithelial–mesenchymal transition of hepatocellular carcinoma. *Cell Adhesion & Migration* 15(1), pp. 249-260. doi: 10.1080/19336918.2021.1958441

Liang, P., Wang, Y., Yu, X. and Dong, B. 2009. Malignant liver tumors: treatment with percutaneous microwave ablation: complications
among cohort of 1,136 patients. *Radiology* 251, pp. 933–940. doi: 10.1148/radiol.2513081740

Lin, J., Hirai, S., Chiang, C., Hsu, W., Su, J. and Wang, Y. 2000. Computer simulation and experimental studies of SAR distributions of interstitial arrays of sleeved-slot microwave antennas for hyperthermia treatment of brain tumors. *IEEE Trans Microwave Theory Tech* 48, pp. 2191-2198. doi: 10.1109/22.884214

Liu, C. 2020. *SIPA1 as a modulator of HGF/MET induced tumour metastasis via the regulation of tight junction based cell to cell barrier.* Cardiff University.

Liu, C. et al. 2012a. Exposure to 1800 MHz radiofrequency electromagnetic radiation induces oxidative DNA base damage in a mouse spermatocyte-derived cell line. *Toxicol Lett* 218(1), pp. 2-9. doi: 10.1016/j.toxlet.2013.01.003
Full text linksCite

Liu, C. L. et al. 2012b. Electric Cell-Substrate Impedance Sensing as a Screening Tool for Wound Healing Agents. In: Jiang, W.G. ed. *Electric Cell-Substrate Impedance Sensing and Cancer Metastasis*. Dordrecht: Springer Netherlands, pp. 203-216. doi: 10.1007/978-94-007-4927-6_11

Longo, D., Jameson, J., Kasper, D., Fauci, A., Loscalzo, J. and Hauser, S. 2015. *Harrison's principles of internal medicine*. McGraw-Hill Education / Medical

Lubner, M. G., Brace, C. L., Hinshaw, L. and Lee, F. T. 2010. Microwave tumor ablatin: mechanism of action, clinical results, and devices. *Journal of Vascular and Interventional Radiology* 21(8), pp. 5192-5203. doi: https://doi.org/10.1016/j.jvir.2010.04.007

Luigi, S., Muneeb, A., Luca, C., Tiziana, I., Michela, B. and Nahun, G. S. 2012. Small liver colorectal metastases treated with percutaneous radiofrequency ablation: local response rate and long-term survival with up to 10-year follow-up. *Radiology* 265(3), pp. 958-968. doi: https://doi.org/10.1148/radiol.12111851

Luria, R., Eliyahu, I., Hareuveny, R., Margaliot, M. and Meiran, N. 2009. Cognitive effects of radiation emitted by cellular phones: the influence of exposure side and time. *Bioelectromagnetics* 30(3), pp. 198-204. doi: 10.1002/bem.20458

Lustenberger, C., Murbach, M., Dürr, R., Schmid, M. R., Kuster, N., Achermann, P. and Huber, R. 2013. Stimulation of the brain with radiofrequency electromagnetic field pulses affects sleep-dependent performance improvement. *Brain Stimul* 6(5), pp. 805-811. doi: 10.1016/j.brs.2013.01.017

Luukkonen, J., Hakulinen, P., Mäki-Paakkanen, J., Juutilainen, J. and Naarala, J. 2009. Enhancement of chemically induced reactive oxygen species production and DNA damage in human SH-SY5Y neuroblastoma cells by 872 MHz radiofrequency radiation. *Mutat Res* 662(1-2), pp. 54-58. doi: 10.1016/j.mrfmmm.2008.12.005

Luyen, H., Gao, F. and Hagness, S. C. 2014. Microwave ablation at 10.0 GHz achieves comparable ablation zones to 1.9 GHz in ex vivo bovine liver. *IEEE TRANSACTIONS ON BIOMEDICAL ENGINEERING* 61(6), pp. 1702-1710. doi: 10.1109/TBME.2014.2300692

Ma, S. C. et al. 2017. Claudin-5 regulates blood-brain barrier permeability by modifying brain microvascular endothelial cell proliferation, migration, and adhesion to prevent lung cancer metastasis. *CNS Neurosci Ther* 23(12), pp. 947-960. doi: 10.1111/cns.12764

Ma, X. et al. 2015. Claudin-4 controls the proliferation, apoptosis, migration and in vivo growth of MCF-7 breast cancer cells. *Oncol Rep* 34(2), pp. 681-690. doi: 10.3892/or.2015.4037

Malhotra, G., Zhao, X., Band, H. and Band, V. 2010. Histological, molecular and functional subtypes of breast cancers. *Cancer biology & therapy* 10, pp. 955-960. doi: 10.4161/cbt.10.10.13879

Mandai, K. et al. 1997. Afadin: A novel actin filament-binding protein with one PDZ domain localized at cadherin-based cell-to-cell adherens junction. *J Cell Biol* 139(2), pp. 517-528. doi: 10.1083/jcb.139.2.517

Mariano, C., Sasaki, H., Brites, D. and Brito, M. A. 2011. A look at tricellulin and its role in tight junction formation and maintenance. *European Journal of Cell Biology* 90(10), pp. 787-796. doi: https://doi.org/10.1016/j.ejcb.2011.06.005

Martin, T. and Jiang, W. eds. 2012. *Tight Junctions in Cancer Metastasis and Their Investigation Using ECIS (Electric Cell-Substrate Impedance Sensing)*. doi: https://doi.org/10.1007/978-94-007-4927-6_7

Martin, T., Ye, L., Sanders, A. J., Lane, J. and Jiang, W. G. 2013. Cancer invasion and metastasis: molecular and cellular perspective. In: Jandial, R. ed. Landes Bioscience

Martin, T. et al. 2021. Abstract PS18-21: Pulsed electric field exposure (PEFE) applied in breast cancer: A potential normothermic clinical cancer therapy. *Cancer Research* 81(4 Supplement), pp. PS18-21-PS18-21. doi: 10.1158/1538-7445.Sabcs20-ps18-21

Martin, T. A. 2014. The role of tight junctions in cancer metastasis. *Semin Cell Dev Biol* 36, pp. 224-231. doi: 10.1016/j.semcdb.2014.09.008

Martin, T. A., Das, T., Mansel, R. E. and Jiang, W. G. 2007. Enhanced tight junction function in human breast cancer cells by antioxidant, selenium and polyunsaturated lipid. *Journal of cellular biochemistry* 101(1), pp. 155-166. doi: 10.1002/jcb.21162

Martin, T. A. and Jiang, W. G. 2001. Tight junctions and their role in cancer metastasis. doi: 10.14670/HH-16.1183

Martin, T. A. and Jiang, W. G. 2009. Loss of tight junction barrier function and its role in cancer metastasis. *Biochim Biophys Acta* 1788(4), pp. 872-891. doi: 10.1016/j.bbamem.2008.11.005

Martin, T. A., Mansel, R. E. and Jiang, W. G. 2010. Loss of occludin leads to the progression of human breast cancer. *Int J Mol Med* 26(5), pp. 723-734. doi: 10.3892/ijmm_00000519

Martin, T. A., Mason, M. D. and Jiang, W. G. 2011. Tight junctions in cancer metastasis. *Front Biosci (Landmark Ed)* 16, pp. 898-936. doi: 10.2741/3726

Martin, T. A., Watkins, G., Mansel, R. E. and Jiang, W. G. 2004. Loss of tight junction plaque molecules in breast cancer tissues is associated with a poor prognosis in patients with breast cancer. *European Journal of Cancer* 40(18), pp. 2717-2725. doi: 10.1016/j.ejca.2004.08.008

Masood, S. 2016. Neoadjuvant chemotherapy in breast cancers. *Women's Health* 12(5), pp. 480-491. doi: 10.1177/1745505716677139

Masoud, V. and Pagès, G. 2017. Targeted therapies in breast cancer: New challenges to fight against resistance. *World journal of clinical oncology* 8(2), pp. 120-134. doi: 10.5306/wjco.v8.i2.120

Matzner, H. and Levy, S. 2002. *Basic RF Technic and Laboratory Manual*. Available at: http://www.hit.ac.il/.upload/engineering/experiment_10_-_swpdirectionalcoupler.pdf [Accessed.

McEwan, A. et al. 2014. *Development of electrical impedance tomography of microwave ablation*. SPIE doi: https://doi.org/10.1117/12.2044766

McNamee, J. P. and Chauhan, V. 2009. Radiofrequency Radiation and Gene/Protein Expression: A Review. *Radiation Research* 172(3), pp. 265-287. doi: 10.1667/RR1726.1

Meaney, P. M. et al. 2012. Clinical microwave tomographic imaging of the calcaneus: A first-in-human case study of two subjects. *IEEE TRANSACTIONS ON BIOMEDICAL ENGINEERING* 59(12), pp. 3304-3313. doi: 10.1109/TBME.2012.2209202

Megha, K., Deshmukh, P. S., Banerjee, B. D., Tripathi, A. K., Ahmed, R. and Abegaonkar, M. P. 2015. Low intensity microwave radiation induced oxidative stress, inflammatory response and DNA damage in rat brain. *Neurotoxicology* 51, pp. 158-165. doi: 10.1016/j.neuro.2015.10.009

Mehta, P., Chand, K., Narayanswamy, D., Beetner, D. G., Zoughi, R. and Stoecker, W. V. 2006. Microwave reflectometry as a novel diagnostic tool for detection of skin cancers. *IEEE Transactions on Instrumentation and Measurement* 55(4), pp. 1309-1316. doi: 10.1109/TIM.2006.876566

Merritt, J. H., Chamness, A. F. and Allen, S. J. 1978. Studies on blood-brain barrier permeability after microwave-radiation. *Radiat Environ Biophys* 15(4), pp. 367-377. doi: 10.1007/bf01323461

Migowski, A. 2015. Early detection of breast cancer and the interpretation of results of survival studies. *Cien Saude Colet* 20(4), p. 1309. doi: 10.1590/1413-81232015204.17772014

Miller, A. B., Sears, M. E., Morgan, L. L., Davis, D. L., Hardell, L., Oremus, M. and Soskolne, C. L. 2019. Risks to Health and Well-Being From Radio-Frequency Radiation Emitted by Cell Phones and Other Wireless Devices. *Frontiers in public health* 7, pp. 223-223. doi: 10.3389/fpubh.2019.00223

Miwa, N., Furuse, M., Tsukita, S., Niikawa, N., Nakamura, Y. and Furukawa, Y. 2001. Involvement of claudin-1 in the β-catenin/Tcf signaling pathway and its frequent upregulation in human colorectal cancers. *Oncology Research Featuring Preclinical and Clinical Cancer Therapeutics* 12(11-12), pp. 469-476. doi: 10.3727/096504001108747477

Mohamed, A., Krajewski, K., Cakar, B. and Ma, C. X. 2013. Targeted Therapy for Breast Cancer. *The American Journal of Pathology* 183(4), pp. 1096-1112. doi: https://doi.org/10.1016/j.ajpath.2013.07.005

Murakami, T., Felinski, E. A. and Antonetti, D. A. 2009. Occludin Phosphorylation and Ubiquitination Regulate Tight Junction Trafficking and Vascular Endothelial Growth Factor-induced Permeability*. *Journal of Biological Chemistry* 284(31), pp. 21036-21046. doi: https://doi.org/10.1074/jbc.M109.016766

Nagata, K., Ota, Y., Okawa, T., Endo, S. and Kudo, S. E. 2008. PET/CT colonography for the preoperative evaluation of the colon proximal to the obstructive colorectal cancer. *Dis Colon Rectum* 51(6), pp. 882-890. doi: 10.1007/s10350-008-9236-1

Naik, M. U., Naik, T. U., Suckow, A. T., Duncan, M. K. and Naik, U. P. 2008. Attenuation of junctional adhesion molecule-A is a contributing factor for breast cancer cell invasion. *Cancer Res* 68(7), pp. 2194-2203. doi: 10.1158/0008-5472.Can-07-3057

Narayanan, S. N., Kumar, R. S., Potu, B. K., Nayak, S., Bhat, P. G. and Mailankot, M. 2010. Effect of radio-frequency electromagnetic radiations (RF-EMR) on passive avoidance behaviour and hippocampal morphology in Wistar rats. *Ups J Med Sci* 115(2), pp. 91-96. doi: 10.3109/03009730903552661
Full text linksCite

Narod, S. A., Iqbal, J. and Miller, A. B. 2015. Why have breast cancer mortality rates declined? *Journal of Cancer Policy* 5, pp. 8-17. doi: https://doi.org/10.1016/j.jcpo.2015.03.002

Neal, R. D., Allgar, V. L., Ali, N., Leese, B., Heywood, P., Proctor, G. and Evans, J. 2007. Stage, survival and delays in lung, colorectal, prostate and ovarian cancer: comparison between diagnostic routes. *British Journal of General Practice* 57(536), pp. 212-219.

Nelson, H. D., Tyne, K., Naik, A., Bougatsos, C., Chan, B. K. and Humphrey, L. 2009. Screening for breast cancer: an update for the U.S. Preventive Services Task Force. *Ann Intern Med* 151(10), pp. 727-737. doi: 10.7326/0003-4819-151-10-200911170-00009

Ni, S., Yu, Y., Zhang, Y., Wu, W., Lai, K. and Yao, K. 2013. Study of oxidative stress in human lens epithelial cells exposed to 1.8 GHz radiofrequency fields. *PLoS One* 8(8), p. e72370. doi: https://doi.org/10.1371/journal.pone.0072370

NiationalInstruments. *Vector Signal Analyzer NI PXIe-5663, NI PXIe-5663E*. Available at: https://s1.dtsheet.com/store/data/000681681.pdf?key=3f069169823020eebe4186fa6b5f9582&r=1 [Accessed.

Nikfarjam, M., Muralidharan, V. and Christophi, C. 2005. Mechanisms of Focal Heat Destruction of Liver Tumors. *The Journal of surgical research* 127(2), pp. 208-223. doi: 10.1016/j.jss.2005.02.009

Nittby, H., Brun, A., Eberhardt, J., Malmgren, L., Persson, B. R. and Salford, L. G. 2009. Increased blood-brain barrier permeability in mammalian brain 7 days after exposure to the radiation from a GSM-900 mobile phone. *Pathophysiology* 16(2-3), pp. 103-112. doi: 10.1016/j.pathophys.2009.01.001

Odaci, E., Bas, O. and Kaplan, S. 2008. Effects of prenatal exposure to a 900 MHz electromagnetic field on the dentate gyrus of rats: A stereological and histopathological study. *Brain research* 1238, pp. 224-229. doi: 10.1016/j.brainres.2008.08.013

Oh, D. Y. and Bang, Y. J. 2020. HER2-targeted therapies - a role beyond breast cancer. *Nat Rev Clin Oncol* 17(1), pp. 33-48. doi: 10.1038/s41571-019-0268-3

Omran, A. R. 1971. The epidemiologic transi tion. A theory of the epidemiology of pop ulation change. *Milbank Mem Fund Q* 49, pp. 509-538. doi: 10.1111/j.1468-0009.2005.00398.x

Onitilo, A. A., Engel, J. M., Greenlee, R. T. and Mukesh, B. N. 2009. Breast cancer subtypes based on ER/PR and Her2 expression: comparison of clinicopathologic features and survival.

Clinical medicine & research 7(1-2), pp. 4-13. doi: 10.3121/cmr.2009.825

Otitoloju, A. A., Obe, I. A., Adewale, O. A., Otubanjo, O. A. and Osunkalu, V. O. 2010. Preliminary study on the induction of sperm head abnormalities in mice, Mus musculus, exposed to radiofrequency radiations from global system for mobile communication base stations. *Bull Environ Contam Toxicol* 84(1), pp. 51-54. doi: 10.1007/s00128-009-9894-2

Ozmen, N., Dapp, R., Zapf, M., Gemmeke, H., Ruiter, N. V. and van Dongen, K. W. 2015. Comparing different ultrasound imaging methods for breast cancer detection. *IEEE Trans Ultrason Ferroelectr Freq Control* 62(4), pp. 637-646. doi: 10.1109/TUFFC.2014.006707
Full text linksCite

Phillips, J. L., Singh, N. P. and Lai, H. 2009. Electromagnetic fields and DNA damage. *Pathophysiology* 16(2-3), pp. 79-88. doi: 10.1016/j.pathophys.2008.11.005
Free article

Pickard, M. R., Mourtada-Maarabouni, M. and Williams, G. T. 2011. Candidate tumour suppressor Fau regulates apoptosis in human cells: An essential role for Bcl-G. *Biochimica et Biophysica Acta (BBA) - Molecular Basis of Disease* 1812(9), pp. 1146-1153. doi: https://doi.org/10.1016/j.bbadis.2011.04.009

Pisano, E. D. et al. 2005. Diagnostic performance of digital versus film mammography for breast-cancer screening. *N Engl J Med* 353(17), pp. 1773-1783. doi: 10.1056/NEJMoa052911

Prat, A. et al. 2010. Phenotypic and molecular characterization of the claudin-low intrinsic subtype of breast cancer. *Breast cancer research* 12(5), pp. 1-18. doi: 10.1186/bcr2635

Qin, S. et al. 2019. The local efficacy and influencing factors of ultrasound-guided percutaneous microwave ablation in colorectal liver metastases: a review of a 4-year experience at a single center. *Int J Hyperthermia* 36(1), pp. 36-43. doi: 10.1080/02656736.2018.1528511

Rahman, A. R. A., Lo, C. and Bhansali, S. 2009. A Detailed Model for High-Frequency Impedance Characterization of Ovarian Cancer Epithelial Cell Layer Using ECIS Electrodes. *IEEE Transactions on Biomedical Engineering* 56(2), pp. 485-492. doi: 10.1109/TBME.2008.2008488

Raleigh, D. R. et al. 2010a. Tight junction-associated MARVEL proteins marveld3, tricellulin, and occludin have distinct but overlapping functions. *Mol Biol Cell* 21(7), pp. 1200-1213. doi: 10.1091/mbc.e09-08-0734

Raleigh, D. R. et al. 2010b. Tight Junction–associated MARVEL Proteins MarvelD3, Tricellulin, and Occludin Have Distinct but Overlapping Functions. *Molecular Biology of the Cell* 21(7), pp. 1200-1213. doi: 10.1091/mbc.e09-08-0734

Rao, R. 2009. Occludin phosphorylation in regulation of epithelial tight junctions. *Ann N Y Acad Sci* 1165, pp. 62-68. doi: 10.1111/j.1749-6632.2009.04054.x

Raya-Sandino, A. et al. 2021. Regulation of intestinal epithelial intercellular adhesion and barrier function by desmosomal cadherin desmocollin-2. *Mol Biol Cell* 32(8), pp. 753-768. doi: 10.1091/mbc.E20-12-0775

Regel, S. J. et al. 2007. Pulsed radio frequency radiation affects cognitive performance and the waking electroencephalogram. *NeuroReport* 18(8), doi: 10.1097/WNR.0b013e3280d9435e

Reiter, R. J. 1993. The melatonin rhythm: both a clock and a calendar. *Experientia* 49(8), pp. 654-664. doi: 10.1007/BF01923947

Resnick, M. B., Konkin, T., Routhier, J., Sabo, E. and Pricolo, V. E. 2005. Claudin-1 is a strong prognostic indicator in stage II colonic cancer: a tissue microarray study. *Modern Pathology* 18(4), pp. 511-518. doi: 10.1038/modpathol.3800301

Rezk, A., Abdulqawi, K., Mustafa, R., El-Azm, T. and Al-Inany, H. 2008. Fetal and neonatal responses following maternal exposure to mobile phones. *Saudi medical journal* 29, pp. 218-223.

Riazuddin, S. et al. 2006. Tricellulin is a tight-junction protein necessary for hearing. *Am J Hum Genet* 79(6), pp. 1040-1051. doi: 10.1086/510022

Robilliard, L. D., Kho, D. T., Johnson, R. H., Anchan, A., O'Carroll, S. J. and Graham, E. S. 2018. The Importance of Multifrequency Impedance Sensing of Endothelial Barrier Formation Using ECIS Technology for the Generation of a Strong and Durable Paracellular Barrier. *Biosensors (Basel)* 8(3), doi: 10.3390/bios8030064

Rojavin, M. A. and Ziskin, M. C. 1998. Medical application of millimeter waves. *QJM* 91(1), pp. 57-66. doi: 10.1093/qjmed/91.1.57

Rosen, A., Stuchly, M. A. and Vorst, A. V. 2002. Applications of RF/microwaves in medicine. *IEEE Transactions on Microwave Theory and Techniques* 50, pp. 963-974. doi: 10.1109/22.989979

Rosenberg, J., Chia, Y. and Plevritis, S. 2005. The effect of age, race, tumor size, tumor grade, and disease stage on invasive ductal breast cancer survival in the U.S. SEER database. *Breast Cancer Research and Treatment* 89(1), pp. 47-54. doi: 10.1007/s10549-004-1470-1

Ross, K. F. A. and Gordon, R. E. 1982. Water in malignant tissue, measured by cell refractometry and nuclear magnetic resonance. *Journal of Microscopy* 128, pp. 7-21. doi: 10.1111/j.1365-2818.1982.tb00433.x

Rougier, C., Prorot, A., Chazal, P., Leveque, P. and Leprat, P. 2014. Thermal and nonthermal effects of discontinuous microwave exposure (2.45 gigahertz) on the cell membrane of Escherichia coli. *Appl Environ Microbiol* 80(16), pp. 4832-4841. doi: 10.1128/aem.00789-14

Rowland, J. H., Desmond, K. A., Meyerowitz, B. E., Belin, T. R., Wyatt, G. E. and Ganz, P. A. 2000. Role of breast reconstructive surgery in physical and emotional outcomes among breast cancer survivors. *J Natl Cancer Inst* 92(17), pp. 1422-1429. doi: 10.1093/jnci/92.17.1422

Saccomandi, P. et al. 2015. Temperature monitoring during microwave ablation in ex vivo porcine livers. *European Journal of Surgical Oncology (EJSO)* 41(12), pp. 1699-1705. doi: 10.1016/j.ejso.2015.08.171

Sagripanti, J. L., Swicord, M. L. and Davis, C. C. 1987. Microwave effects on plasmid DNA. *Radiat Res* 110(2), pp. 219-231. doi: https://doi.org/10.2307/3576900

Saito, A. C., Endo, C., Fukazawa, Y., Higashi, T. and Chiba, H. 2022. Effects of TAMP family on the tight junction strand network and barrier function in epithelial cells. *Ann N Y Acad Sci* 1517(1), pp. 234-250. doi: 10.1111/nyas.14889

Saklani, A. P., Bae, S. U., Clayton, A. and Kim, N. K. 2014. Magnetic resonance imaging in rectal cancer: a surgeon's perspective. *World journal of gastroenterology* 20(8), pp. 2030-2041. doi: 10.3748/wjg.v20.i8.2030

Salama, N., Kishimoto, T., Kanayama, H. and Kagawa, S. 2009. The mobile phone decreases fructose but not citrate in rabbit semen: a longitudinal study. *Systems biology in reproductive medicine* 55(5-6), pp. 181-187. doi: 10.3109/19396360903013126

Salvador, E., Burek, M. and Förster, C. Y. 2016. Tight Junctions and the Tumor Microenvironment. *Current Pathobiology Reports* 4(3), pp. 135-145. doi: 10.1007/s40139-016-0106-6

Sanders, A. J., Jiang, D. G., Jiang, W. G., Harding, K. G. and Patel, G. K. 2011. Activated leukocyte cell adhesion molecule impacts on clinical wound healing and inhibits HaCaT migration. *Int Wound J* 8(5), pp. 500-507. doi: 10.1111/j.1742-481X.2011.00823.x

Sandoval-Leon, A. C., Drews-Elger, K., Gomez-Fernandez, C. R., Yepes, M. M. and Lippman, M. E. 2013. Paget's disease of the nipple. *Breast Cancer Research and Treatment* 141(1), pp. 1-12. doi: 10.1007/s10549-013-2661-4

Schepps, J. L. and Foster, K. R. 1980. The UHF and microwave dielectric properties of normal and tumour tissues: variation in dielectric properties with tissue water content. *Phys Med Biol* 25(6), pp. 1149-1159. doi: 10.1088/0031-9155/25/6/012

Schneble, E. J. et al. 2014. Future directions for the early detection of recurrent breast cancer. *J Cancer* 5(4), pp. 291-300. doi: 10.7150/jca.8017

Sha, L., Ward, E. R. and Stroy, B. 2002. A review of dielectric properties of normal and malignant breast tissue. IEEE doi: 10.1109/SECON.2002.995639

Shi, J., Barakat, M., Chen, D. and Chen, L. 2018. Bicellular Tight Junctions and Wound Healing. *Int J Mol Sci* 19(12), doi: 10.3390/ijms19123862

Shi, Y. et al. 2021. Long-term results of percutaneous microwave ablation for colorectal liver metastases. *HPB* 23(1), pp. 37-45. doi: https://doi.org/10.1016/j.hpb.2020.04.007

Shiou, S.-R., Singh, A. B., Moorthy, K., Datta, P. K., Washington, M. K., Beauchamp, R. D. and Dhawan, P. 2007. Smad4 Regulates Claudin-1 Expression in a Transforming Growth Factor-β–Independent Manner in Colon Cancer Cells. *Cancer Research* 67(4), pp. 1571-1579. doi: 10.1158/0008-5472.Can-06-1680

Siegel, R. L., Miller, K. D. and Jemal, A. 2018. Cancer statistics, 2018. *CA Cancer J Clin* 68,

pp. 7-30. doi: 10.3322/caac.21442

Simonov, N. and Son, S. 2019. Focused microwave thermotherapy technique based on microwave tomographic imaging. *Electronics Letters* 55(11), pp. 633-634. doi: https://doi.org/10.1049/el.2019.1004

Singh, R., Letai, A. and Sarosiek, K. 2019. Regulation of apoptosis in health and disease: the balancing act of BCL-2 family proteins. *Nat Rev Mol Cell Biol* 20(3), pp. 175-193. doi: 10.1038/s41580-018-0089-8

Snipstad, K., Fenton, C. G., Kjaeve, J., Cui, G., Anderssen, E. and Paulssen, R. H. 2010. New specific molecular targets for radio-chemotherapy of rectal cancer. *Mol Oncol* 4(1), pp. 52-64. doi: 10.1016/j.molonc.2009.11.002

Sokolovic, D. et al. 2012. The effect of melatonin on body mass and behaviour of rats during an exposure to microwave radiation from mobile phone. *Bratislavske lekarske listy* 113(5), pp. 265-269. doi: 10.4149/bll_2012_062

Soler, A. P., Miller, R. D., Laughlin, K. V., Carp, N. Z., Klurfeld, D. M. and Mullin, J. M. 1999. Increased tight junctional permeability is associated with the development of colon cancer. *Carcinogenesis* 20(8), pp. 1425-1431. doi: 10.1093/carcin/20.8.1425

Song, X. L., Wang, C. H., Hu, H. Y., Yu, C. and Bai, C. 2011. Microwave induces apoptosis in A549 human lung carcinoma cell line. *Chin Med J (Engl)* 124(8), pp. 1193-1198.

Splatt, A. M. and Steinke, K. 2015. Major complications of high-energy microwave ablation for percutaneous CT-guided treatment of lung malignancies: single-centre experience after 4 years. *J Med Imaging Radiat Oncol* 59(5), pp. 609-616. doi: 10.1111/1754-9485.12345

Steed, E. 2011. *Functional analysis of MarvelD3, a novel transmembrane protein of the tight junction.* University College London.

Steed, E. et al. 2014. MarvelD3 couples tight junctions to the MEKK1–JNK pathway to regulate cell behavior and survival. *Journal of Cell Biology* 204(5), pp. 821-838. doi: 10.1083/jcb.201304115

Steed, E., Rodrigues, N. T. L., Balda, M. S. and Matter, K. 2009. Identification of MarvelD3 as a tight junction-associated transmembrane protein of the occludin family. *BMC Cell Biology* 10(1), p. 95. doi: 10.1186/1471-2121-10-95

Stenmark, H. 2009. Rab GTPases as coordinators of vesicle traffic. *Nature Reviews Molecular Cell Biology* 10(8), pp. 513-525. doi: 10.1038/nrm2728

Sun, S. et al. 2023. The Bacillus cereus toxin alveolysin disrupts the intestinal epithelial barrier by inducing microtubule disorganization through CFAP100. *Sci Signal* 16(785), p. eade8111. doi: 10.1126/scisignal.ade8111

Sun, X. et al. 2020. The modification of ferroptosis and abnormal lipometabolism through overexpression and knockdown of potential prognostic biomarker perilipin2 in gastric carcinoma. *Gastric Cancer* 23(2), pp. 241-259. doi: 10.1007/s10120-019-01004-z

Sun, Y., Cheng, Z., Dong, L., Zhang, G., Wang, Y. and Liang, P. 2012. Comparison of temperature curve and ablation zone between 915- and 2450-MHz cooled-shaft microwave antenna: Results in ex vivo porcine livers. *European Journal of Radiology* 81(3), pp. 553-557. doi: https://doi.org/10.2214/AJR.07.3828

Sun, Y., Wang, Y., Ni, X., Gao, Y., Shao, Q., Liu, L. and Liang, P. 2009. Comparison of Ablation Zone Between 915- and 2,450-MHz Cooled-Shaft Microwave Antenna: Results in In Vivo Porcine Livers. *American Journal of Roentgenology* 192(2), pp. 511-514. doi: Comparison of Ablation Zone Between 915- and 2,450-MHz Cooled-Shaft Microwave Antenna: Results in In Vivo Porcine Livers

Sung, H., Ferlay, J., Siegel, R. L., Laversanne, M., Soerjomataram, I., Jemal, A. and Bray, F. 2021. Global Cancer Statistics 2020: GLOBOCAN Estimates of Incidence and Mortality Worldwide for 36 Cancers in 185 Countries. *CA: A Cancer Journal for Clinicians* 71(3), pp. 209-249. doi: https://doi.org/10.3322/caac.21660

Swartling, T., Kälebo, P., Derwinger, K., Gustavsson, B. and Kurlberg, G. 2013. Stage and size using magnetic resonance imaging and endosonography in neoadjuvantly-treated rectal cancer. *World J Gastroenterol* 19(21), pp. 3263-3271. doi: 10.3748/wjg.v19.i21.3263

Syn, N. L., Teng, M. W. L., Mok, T. S. K. and Soo, R. A. 2017. De-novo and acquired resistance to immune checkpoint targeting. *Lancet Oncol* 18(12), pp. 731-741. doi: https://doi.org/10.1016/S1470-2045(17)30607-1

Sypniewska, R. K., Millenbaugh, N. J., Kiel, J. L., Blystone, R. V., Ringham, H. N., Mason, P. A. and Witzmann, F. A. 2010. Protein changes in macrophages induced by plasma from rats exposed to 35 GHz millimeter waves. *Bioelectromagnetics* 31(8), pp. 656-663. doi: 10.1002/bem.20598

Szasz, O. 2013. Essentials of Oncothermia. doi: https://doi.org/10.1155/2013/159570

Szulcek, R., Bogaard, H. J. and van Nieuw Amerongen, G. P. 2014. Electric cell-substrate impedance sensing for the quantification of endothelial proliferation, barrier function, and motility. *Journal of visualized experiments : JoVE* (85), p. 51300. doi: 10.3791/51300

Tammam, E., Said, A. M., Ibrahim, A. A. and Galal, A. I. 2020. About the Interstitial Microwave Cancer Ablation: Principles, Advantages and Challenges. *IEEE access* 8, pp. 1-1. doi: 10.1109/ACCESS.2020.2978210

Tamura, A. et al. 2008. Megaintestine in claudin-15-deficient mice. *Gastroenterology* 134(2), pp. 523-534. doi: 10.1053/j.gastro.2007.11.040

Tang, Y., Zhou, Y., Fan, S. and Wen, Q. 2022. The multiple roles and therapeutic potential of HSP60 in cancer. *Biochemical Pharmacology* 201, p. 115096. doi: https://doi.org/10.1016/j.bcp.2022.115096

Töpfer, F. and Oberhammer, J. 2017. Chapter 3 - Microwave cancer diagnosis. In: LI, C., TOFIGHI, M.-R., SCHREURS, D. and HORNG, T.-S.J. eds. *Principles and Applications of RF/Microwave in Healthcare and Biosensing, Academic Press*. pp. 103-149.

Tran, T. B., Cho, S. and Min, J. 2013. Hydrogel-based diffusion chip with Electric Cell-substrate Impedance Sensing (ECIS) integration for cell viability assay and drug toxicity screening. *Biosensors and Bioelectronics* 50, pp. 453-459. doi: https://doi.org/10.1016/j.bios.2013.07.019

Trivino Pardo, J. C., Grimaldi, S., Taranta, M., Naldi, I. and Cinti, C. 2012. Microwave electromagnetic field regulates gene expression in T-lymphoblastoid leukemia CCRF-CEM cell line exposed to 900 MHz. *Electromagn Biol Med* 31(1), pp. 1-18. doi: 10.3109/15368378.2011.596251

Tsuji, S. et al. 2012. Potential responders to FOLFOX therapy for colorectal cancer by Random Forests analysis. *Br J Cancer* 106(1), pp. 126-132. doi: 10.1038/bjc.2011.505

Tutt, A. N. J., Plunkett, T. A., Barrington, S. F. and Leslie, M. D. 2004. The role of positron emission tomography in the management of colorectal cancer. *Colorectal Disease* 6(1), pp. 2-9. doi: https://doi.org/10.1111/j.1463-1318.2004.00592.x

Usami, Y. et al. 2006. Reduced expression of claudin-7 correlates with invasion and metastasis in squamous cell carcinoma of the esophagus. *Hum Pathol* 37(5), pp. 569-577. doi: 10.1016/j.humpath.2005.12.018

Vaidya, Y., Vaidya, P. and Vaidya, T. 2015. Ductal Carcinoma In Situ of the Breast. *Indian J Surg* 77(2), pp. 141-146. doi: 10.1007/s12262-013-0987-0

Van Cutsem, E., Cervantes, A., Nordlinger, B. and Arnold, D. 2014. Metastatic colorectal cancer: ESMO Clinical Practice Guidelines for diagnosis, treatment and follow-up. *Ann Oncol* 25 Suppl 3, pp. iii1-9. doi: 10.1093/annonc/mdu260

van de Velde, C. J. et al. 2014. EURECCA colorectal: multidisciplinary management: European consensus conference colon & rectum. *Eur J Cancer* 50(1), pp. 1.e1-1.e34. doi: 10.1016/j.ejca.2013.06.048

Vansteenkiste, J. F. et al. 1998. FDG-PET scan in potentially operable non-small cell lung cancer: do anatometabolic PET-CT fusion images improve the localisation of regional lymph node metastases? The Leuven Lung Cancer Group. *Eur J Nucl Med* 25(11), pp. 1495-1501. doi: 10.1007/s002590050327

Vargas, H. I., Dooley, W. C., Gardner, R. A., Gonzalez, K. D., Venegas, R., Heywang-Kobrunner, S. H. and Fenn, A. J. 2004. Focused microwave phased array thermotherapy for ablation of early-stage breast cancer: results of thermal dose escalation. *Ann Surg Oncol* 11(2), pp. 139-146. doi: 10.1245/aso.2004.03.059

Vecchio, F., Babiloni, C., Ferreri, F., Curcio, G., Fini, R., Percio, C. and Rossini, P. M. 2007. Mobile phone emission modulates interhemispheric functional coupling of EEG alpha rhythms. *The European journal of neuroscience* 25, pp. 1908-1913. doi: 10.1111/j.1460-9568.2007.05405.x

Vecsei, Z., Csatho, A., Thuroczy, G. and Hernadi, I. 2013. Effect of a single 30 min UMTS mobile phone-like exposure on the thermal pain threshold of young healthy volunteers.

Bioelectromagnetics 34(7), pp. 530-541. doi: 10.1002/bem.21801

Vekic, B. et al. 2020. A Correlation Study of the Colorectal Cancer Statistics and Economic Indicators in Selected Balkan Countries. *Frontiers in public health* 8, pp. 29-29. doi: 10.3389/fpubh.2020.00029

Vermette, D., Hu, P., Canarie, M. F., Funaro, M., Glover, J. and Pierce, R. W. 2018. Tight junction structure, function, and assessment in the critically ill: a systematic review. *Intensive Care Med Exp* 6(1), p. 37. doi: 10.1186/s40635-018-0203-4

Verschaeve, L. 2009. Genetic damage in subjects exposed to radiofrequency radiation. *Mutat Res* 681(2-3), pp. 259-270. doi: Genetic damage in subjects exposed to radiofrequency radiation

Vogl, T. J. et al. 2022. Long-term outcomes following percutaneous microwave ablation for colorectal cancer liver metastases. *Int J Hyperthermia* 39(1), pp. 788-795. doi: 10.1080/02656736.2022.2077991

Volkow, N. D. et al. 2011. Effects of cell phone radiofrequency signal exposure on brain glucose metabolism. *JAMA* 305(8), pp. 808-813. doi: 10.1001/jama.2011.186

Voogd, A. C. et al. 2001. Differences in risk factors for local and distant recurrence after breast-conserving therapy or mastectomy for stage I and II breast cancer: pooled results of two large European randomized trials. *J Clin Oncol* 19(6), pp. 1688-1697. doi: 10.1200/JCO.2001.19.6.1688

Vrba, J. and Oppl, L. 2008. Prospective Applications of Microwaves in Medicine. *2008 14th Conference on Microwave Techniques*, pp. 1-4. doi: 10.1109/COMITE.2008.4569911

Vrba, J., Vrba, D., Fiser, O., Oppl, L. and Merunka, I. 2019. Applications of Microwaves in Medicine and Biology. *2019 European Microwave Conference in Central Europe (EuMCE)*, pp. 496-499. doi: 10.5772/intechopen.105492

Vu, T. and Datta, P. K. 2017. Regulation of EMT in Colorectal Cancer: A Culprit in Metastasis. *Cancers (Basel)* 9(12), doi: 10.3390/cancers9120171

Wang, L. 2017. Early Diagnosis of Breast Cancer. *Sensors* 17(7), p. 2017. doi: https://doi.org/10.3390/s17071572

Wang, M., He, X., Chang, Y., Sun, G. and Thabane, L. 2017. A sensitivity and specificity comparison of fine needle aspiration cytology and core needle biopsy in evaluation of suspicious breast lesions: A systematic review and meta-analysis. *Breast* 31, pp. 157-166. doi: 10.1016/j.breast.2016.11.009

Wang, T., Zhao, G. and Qiu, B. 2015. Theoretical evaluation of the treatment effectiveness of a novel coaxial multi-slot antenna for conformal microwave ablation of tumors. *International Journal of Heat and Mass transfer* 90, pp. 81-91. doi: https://doi.org/10.1016/j.ijheatmasstransfer.2015.06.030

Wei, N., Fu, T., Lv, Z. and Wang, P. 2018. *Latest Progress of Percutaneous Thernel Ablation*

Treatment for Secondary Hyperparathyroidism (a Literature Review). doi: 10.1109/ITME.2018.00058

Weigelt, B., Geyer, F. C. and Reis-Filho, J. S. 2010. Histological types of breast cancer: how special are they? *Mol Oncol* 4(3), pp. 192-208. doi: 10.1016/j.molonc.2010.04.004

Wensheng, L. et al. 2019. MBD1 promotes the malignant behavior of gallbladder cancer cells and induces chemotherapeutic resistance to gemcitabine. *Cancer Cell International* 19(1), p. 232. doi: 10.1186/s12935-019-0948-1

Whitaker, K. 2020. Earlier diagnosis: the importance of cancer symptoms. *The Lancet Oncology* 21(1), pp. 6-8. doi: https://doi.org/10.1016/S1470-2045(19)30658-8

Wu, X., Lin, B. and Xu, B. 2016. Theoretical evaluation of high frequency microwave ablation applied in cancer therapy. *Applied Thermal Engineering* 107, pp. 501-507. doi: https://doi.org/10.1016/j.applthermaleng.2016.07.010

Xie, Y.-H., Chen, Y.-X. and Fang, J.-Y. 2020. Comprehensive review of targeted therapy for colorectal cancer. *Signal Transduction and Targeted Therapy* 5(1), p. 22. doi: 10.1038/s41392-020-0116-z

Xu, J. et al. 2018. Microwave ablation of benign breast tumors: a prospective study with minimum 12 months follow-up. *International Journal of Hyperthermia* 35(1), pp. 253-261. doi: 10.1080/02656736.2018.1494340

Yamamoto, M. et al. 2008. Phosphorylation of claudin-5 and occludin by rho kinase in brain endothelial cells. *Am J Pathol* 172(2), pp. 521-533. doi: 10.2353/ajpath.2008.070076

Yan, X., Yan, L., Liu, S., Shan, Z., Tian, Y. and Jin, Z. 2015. N-cadherin, a novel prognostic biomarker, drives malignant progression of colorectal cancer. *Mol Med Rep* 12(2), pp. 2999-3006. doi: 10.3892/mmr.2015.3687

Yang, D., Converse, M. C., Mahvi, D. M. and Webster, J. G. 2007. Measurement and analysis of tissue temperature during microwave liver ablation. *IEEE TRANSACTIONS ON BIOMEDICAL ENGINEERING* 54(1), pp. 150-155. doi: 10.1109/TBME.2006.884647

Yang, J. et al. 2016. Catenin delta-1 (CTNND1) phosphorylation controls the mesenchymal to epithelial transition in astrocytic tumors. *Human Molecular Genetics* 25(19), pp. 4201-4210. doi: 10.1093/hmg/ddw253

Yang, J. et al. 2004. Twist, a master regulator of morphogenesis, plays an essential role in tumor metastasis. *Cell* 117(7), pp. 927-939. doi: 10.1016/j.cell.2004.06.006

Yang, Q. et al. 2020. Ultrasound-guided percutaneous microwave ablation for 755 benign breast lesions: a prospective multicenter study. *European radiology* 30(9), pp. 5029-5038. doi: 10.1007/s00330-020-06868-9

Yang, T. J. and Ho, A. Y. 2013. Radiation Therapy in the Management of Breast Cancer. *Surgical Clinics of North America* 93(2), pp. 455-471. doi: 10.1016/j.suc.2013.01.002

Yao, K. et al. 2008. Electromagnetic noise inhibits radiofrequency radiation-induced DNA damage and reactive oxygen species increase in human lens epithelial cells. *Molecular vision* 14, pp. 964-969.

Yarnold, J. et al. 2005. Fractionation sensitivity and dose response of late adverse effects in the breast after radiotherapy for early breast cancer: long-term results of a randomised trial. *Radiother Oncol* 75(1), pp. 9-17. doi: 10.1016/j.radonc.2005.01.005

Yee, J., Weinstein, S., Morgan, T., Alore, P. and Aslam, R. 2013. Advances in CT Colonography for Colorectal Cancer Screening and Diagnosis. *J Cancer* 4(3), pp. 200-209. doi: 10.7150/jca.5858

Yoon, J., Cho, J., Kim, N., Kim, D., Lee, E., Cheon, C. and Kwon, Y. 2011. High-frequency microwave ablation method for enhanced cancer treatment with minimized collateral damage. *International Journal of Cancer* 129(8), pp. 1970-1978. doi: https://doi.org/10.1002/ijc.25845

Yu, J. et al. 2017a. Ultrasound guided percutaneous microwave ablation of benign breast lesions. *Oncotarget* 8(45), pp. 79376-79386. doi: 10.18632/oncotarget.18123

Yu, J. et al. 2017b. Ultrasound guided percutaneous microwave ablation of benign breast lesions. *Oncotarget* 8(45), pp. 79376–79386. doi: 10.18632/oncotarget.18123

Yu, J. et al. 2020. Microwave Ablation Versus Nipple Sparing Mastectomy for Breast Cancer ≤5 cm: A Pilot Cohort Study. *Frontiers in oncology* 10, doi: 10.3389/fonc.2020.546883

Yu, J., Liang, P., Yu, X. L., Cheng, Z. G., Han, Z. Y. and Mu, M. J. 2012. US-guided percutaneous microwave ablation of renal cell carcinoma: intermediate-term results. *Radiology* 263, pp. 900-908. doi: 10.1148/radiol.12111209

Yue, J. and López, J. M. 2020. Understanding MAPK Signaling Pathways in Apoptosis. *Int J Mol Sci* 21(7), doi: 10.3390/ijms21072346

Zhang, K. et al. 2016a. Impact of timing and cycles of systemic chemotherapy on survival outcome of colorectal liver metastases patients treated by percutaneous microwave ablation. *Int J Hyperthermia* 32(5), pp. 531-538. doi: 10.3109/02656736.2016.1156169

Zhang, W. et al. 2019. Clinical application of ultrasound-guided percutaneous microwave ablation for benign breast lesions: a prospective study. *BMC Cancer* 19(1), pp. 345-355. doi: 10.1186/s12885-019-5523-6

Zhang, X., Huang, W. J. and Chen, W. W. 2016b. Microwaves and Alzheimer's disease. *Exp Ther Med* 12(4), pp. 1969-1972. doi: 10.3892/etm.2016.3567

Zhao, M., Mishra, L. and Deng, C. X. 2018. The role of TGF-β/SMAD4 signaling in cancer. *Int J Biol Sci* 14(2), pp. 111-123. doi: 10.7150/ijbs.23230

Zhao, R., Zhang, S., Xu, Z., Ju, L., Lu, D. and Yao, G. 2007a. Studying gene expression profile of rat neuron exposed to 1800MHz radiofrequency electromagnetic fields with cDNA microassay. *Toxicology* 235(3), pp. 167-175. doi: https://doi.org/10.1016/j.tox.2007.03.015

Zhao, T., Zou, S. and Knapp, P. E. 2007b. Exposure to cell phone radiation up-regulates apoptosis genes in primary cultures of neurons and astrocytes. *Neuroscience letters* 412(1), pp. 34-38. doi: 10.1016/j.neulet.2006.09.092

Zhao, X., Dong, G. and Wang, C. 2021. The non-thermal biological effects and mechanisms of microwave exposure. *International Journal of Radiation Research* 19(3), pp. 483-494. doi: 10.18869/acadpub.ijrr.19.3.483

Zhao, Z. 2020. *Pulsed Electromagnetic Field Exposure: A Novel Microwave Technique in Potential Breast Cancer Treatment.* Cardiff University.

Zhou, W. et al. 2014. Image and pathological changes after microwave ablation of breast cancer: A pilot study. *European Journal of Radiology* 83(10), pp. 1771-1777. doi: 10.1016/j.ejrad.2014.06.015

Zhou, W. et al. 2013. Comparison of ablation zones among different tissues using 2450-MHz cooled-shaft microwave antenna: results in ex vivo porcine models. *PLoS One* 8(8), p. e71873. doi: https://doi.org/10.1371/journal.pone.0071873

Zhou, W. et al. 2017. Ultrasound-guided microwave ablation: a promising tool in management of benign breast tumours. *International Journal of Hyperthermia* 33(3), pp. 263-270. doi: 10.1080/02656736.2016.1253876

Zhou, W. et al. 2012. US-guided percutaneous microwave coagulation of small breast cancers: a clinical study. *Radiology* 263(2), pp. 364-373. doi: https://doi.org/10.1148/radiol.12111901

Zhu, W. et al. 2013. Inhibitory effect of microwave radiation on proliferation of human pancreatic cancer JF305 cells and its mechanism. *Wei Sheng Yan Jiu* 42(6), pp. 1008-1011.

Zhu, W., Zhang, W., Wang, H., Xu, J., Li, Y. and Lv, S. 2014. Apoptosis induced by microwave radiation in pancreatic cancer JF305 cells. *Can J Physiol Pharmacol* 92(4), pp. 324-329. doi: 10.1139/cjpp-2013-0220

Zielinska, M., Ropelewska, E., Xiao, H., Mujumdar, A. S. and Law, C. L. 2020. Review of recent applications and research progress in hybrid and combined microwave-assisted drying of food products: Quality properties. *Critical Reviews in Food Science and Nutrition* 60(13), pp. 2212-2264. doi: 10.1080/10408398.2019.1632788

Supplement materials

Supplement-1 Human Colon Cancer TMA

CO2161b : Colon cancer with colon tissue array, including pathology grade, TNM and clinical stage, 216 cases/216 cores, replacing CO2161a

Microarray Panel	Colon carcinoma with colon tissue microarray, containing 204 cases of adenocarcinoma, 4 signet-ring cell carcinoma, 8 colon tissue, single core per case
Cores	216
Cases	216
Row number	12
Column number	18
Core Diameter (mm)	1
Thickness (μm)	5
Quality Control	H&E and IHC confirmed
Tissue Array Type	FFPE
Species	Human
Applications	Routine histology procedures including Immunohistochemistry (IHC) and In Situ Hybridization (ISH), protocols which can be found at our support page.
Notes	1. TMA slides were sectioned and stored at 4°C and may not be fresh cut, but still suitable for IHC. Please request fresh cut if experiment involves phospho-specific antibodies, RNA studies, FISH or ISH, etc. A minimum of 3 slides per TMA must be purchased to cover the cost of trimming for fresh sectioning. 2. Most TMA slides were not coated with an extra layer of paraffin (tissue cores can be easily seen on the glass). **To prevent tissue detachment during antigen retrieval, unbaked slides must be baked for at least 30 to 120 minutes at 60°C**. before putting into xylene for de-paraffinization. Baked slides were sent out baked for 2 hours. In the following specsheet,"*" means invalid core; "-" means no applicable or negative in IHC markers.

CO2161b H&E

Mouseover and click individual cores to view high resolution images.

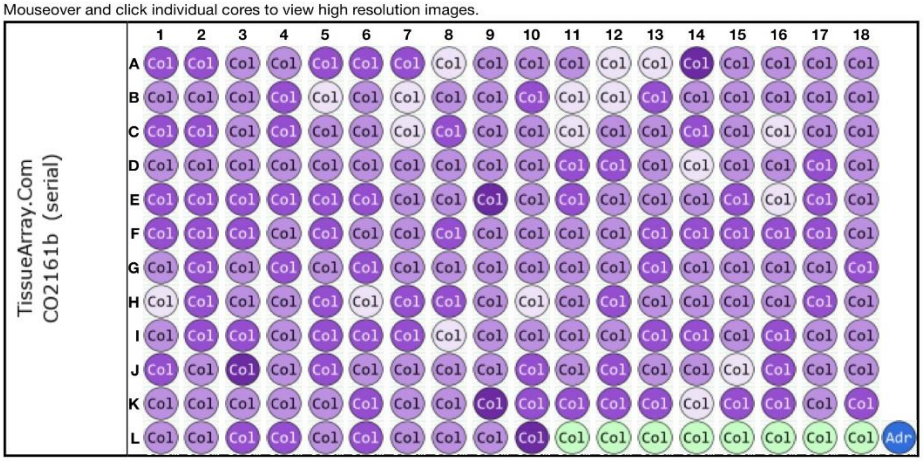

Legend:Col - Colon

- Malignant tumor, - Malignant tumor (stage I), - Malignant tumor (stage IIA), - Malignant tumor (stage IIB), - Malignant tumor (stage IIIA), - Malignant tumor (stage IIIB), - Malignant tumor (stage IIIC), - Malignant tumor (stage IV), - Normal tissue

, tissue IDs are available in exported Excel files.

Pos.	No.	Age	Sex	Organ/Anatomic Site	Pathology diagnosis	TNM	Grade	Stage	Type	Image
A1	1	55	F	Colon	Adenocarcinoma	T3N1M0	2	IIIB	Malignant	
A2	2	46	M	Colon	Mucinous adenocarcinoma	T4N1M0	1	IIIB	Malignant	
A3	3	44	F	Colon	Mucinous adenocarcinoma	T3N0M0	1	IIA	Malignant	
A4	4	40	F	Colon	Mucinous adenocarcinoma	T3N0M0	1	IIA	Malignant	
A5	5	56	M	Colon	Mucinous adenocarcinoma	T3N2M0	1	IIIB	Malignant	
A6	6	51	M	Colon	Mucinous adenocarcinoma	T2N1M0	1	IIIA	Malignant	
A7	7	68	F	Colon	Mucinous adenocarcinoma	T3N1M0	1	IIIB	Malignant	
A8	8	68	M	Colon	Adenocarcinoma	T2N0M0	1	I	Malignant	
A9	9	32	M	Colon	Adenocarcinoma	T4N0M0	1	IIB	Malignant	
A10	10	74	F	Colon	Mucinous adenocarcinoma with necrosis (sparse)	T3N0M0	-	IIA	Malignant	

A11	11	53	F	Colon	Adenocarcinoma	T3N0M0	1	IIA	Malignant
A12	12	49	F	Colon	Adenocarcinoma	T2N0M0	3	I	Malignant
A13	13	-	-	Colon	Adenocarcinoma	T2N0M0	2	I	Malignant
A14	14	48	F	Colon	Adenocarcinoma	T4N0M1	2	IV	Malignant
A15	15	64	M	Colon	Adenocarcinoma	T4N0M0	1	IIB	Malignant
A16	16	41	M	Colon	Adenocarcinoma	T4N0M0	2	IIB	Malignant
A17	17	34	M	Colon	Adenocarcinoma	T4N0M0	2	IIB	Malignant
A18	18	64	M	Colon	Adenocarcinoma	T4N0M0	2	IIB	Malignant
B1	19	31	M	Colon	Adenocarcinoma	T4N0M0	2	IIB	Malignant
B2	20	50	F	Colon	Adenocarcinoma	T3N0M0	2	IIA	Malignant
B3	21	62	F	Colon	Adenocarcinoma	T4N0M0	2	IIB	Malignant
B4	22	46	M	Colon	Adenocarcinoma	T3N2M0	2	IIIB	Malignant
B5	23	24	F	Colon	Adenocarcinoma	T2N0M0	2	I	Malignant
B6	24	56	M	Colon	Adenocarcinoma	T3N0M0	2	IIA	Malignant
B7	25	45	M	Colon	Adenocarcinoma	T2N0M0	2	I	Malignant
B8	26	70	F	Colon	Adenocarcinoma	T4N0M0	2	IIB	Malignant
B9	27	41	F	Colon	Adenocarcinoma	T3N0M0	2	IIA	Malignant
B10	28	71	M	Colon	Adenocarcinoma	T4N2M0	2	IIIC	Malignant
B11	29	63	F	Colon	Adenocarcinoma	T2N0M0	2	I	Malignant
B12	30	49	M	Colon	Adenocarcinoma	T2N0M0	2	I	Malignant
B13	31	56	F	Colon	Adenocarcinoma	T2N1M0	2	IIIA	Malignant
B14	32	40	F	Colon	Adenocarcinoma	T4N0M0	2	IIB	Malignant
B15	33	75	M	Colon	Adenocarcinoma	T3N0M0	2	IIA	Malignant
B16	34	48	F	Colon	Adenocarcinoma	T3N0M0	2	IIA	Malignant
B17	35	61	M	Colon	Adenocarcinoma	T4N0M0	2	IIB	Malignant
B18	36	45	M	Colon	Adenocarcinoma	T3N0M0	2	IIA	Malignant
C1	37	49	F	Colon	Adenocarcinoma	T3N1M0	2	IIIB	Malignant
C2	38	50	M	Colon	Adenocarcinoma	T4N1M0	2	IIIB	Malignant
C3	39	69	F	Colon	Adenocarcinoma	T3N0M0	2	IIA	Malignant
C4	40	51	M	Colon	Adenocarcinoma	T4N2M0	2	IIIC	Malignant
C5	41	45	F	Colon	Adenocarcinoma	T3N0M0	2	IIA	Malignant
C6	42	59	M	Colon	Adenocarcinoma	T4N0M0	2	IIB	Malignant
C7	43	72	M	Colon	Adenocarcinoma	T2N0M0	2	I	Malignant
C8	44	68	F	Colon	Adenocarcinoma	T4N2M0	2	IIIC	Malignant
C9	45	50	M	Colon	Adenocarcinoma	T3N0M0	2	IIA	Malignant
C10	46	43	M	Colon	Adenocarcinoma	T4N0M0	2	IIB	Malignant
C11	47	51	M	Colon	Adenocarcinoma	T2N0M0	2	I	Malignant
C12	48	50	M	Colon	Adenocarcinoma	T3N0M0	2	IIA	Malignant
C13	49	38	F	Colon	Adenocarcinoma	T3N0M0	2	IIA	Malignant
C14	50	38	M	Colon	Adenocarcinoma	T4N1M0	2	IIIB	Malignant
C15	51	64	M	Colon	Adenocarcinoma	T4N0M0	2	IIB	Malignant
C16	52	43	F	Colon	Adenocarcinoma	T1N0M0	2	I	Malignant
C17	53	67	F	Colon	Adenocarcinoma	T3N0M0	2	IIA	Malignant
C18	54	40	M	Colon	Adenocarcinoma	T3N0M0	2	IIA	Malignant
D1	55	59	M	Colon	Adenocarcinoma	T4N0M0	*	IIB	Malignant
D2	56	53	M	Colon	Adenocarcinoma	T4N0M0	2	IIB	Malignant
D3	57	66	M	Colon	Adenocarcinoma	T4N0M0	2	IIB	Malignant
D4	58	39	M	Colon	Adenocarcinoma	T3N0M0	*	IIA	Malignant
D5	59	64	F	Colon	Adenocarcinoma	T3N0M0	2	IIA	Malignant
D6	60	70	F	Colon	Adenocarcinoma	T3N0M0	2	IIA	Malignant
D7	61	50	M	Colon	Adenocarcinoma	T3N0M0	2	IIA	Malignant
D8	62	54	M	Colon	Adenocarcinoma	T3N0M0	2	IIA	Malignant
D9	63	73	M	Colon	Adenocarcinoma	T3N0M0	2	IIA	Malignant
D10	64	66	M	Colon	Adenocarcinoma	T4N0M0	2	IIB	Malignant
D11	65	52	F	Colon	Adenocarcinoma	T3N1M0	2	IIIB	Malignant
D12	66	50	M	Colon	Adenocarcinoma	T4N1M0	*	IIIB	Malignant
D13	67	41	M	Colon	Adenocarcinoma	T4N0M0	2	IIB	Malignant
D14	68	72	M	Colon	Adenocarcinoma	T2N0M0	2	I	Malignant
D15	69	32	M	Colon	Mucinous adenocarcinoma	T3N0M0	1--2	IIA	Malignant
D16	70	70	F	Colon	Mucinous adenocarcinoma	T3N0M0	1--2	IIA	Malignant
D17	71	45	F	Colon	Mucinous adenocarcinoma	T4N2M0	1--2	IIIC	Malignant
D18	72	69	M	Colon	Adenocarcinoma	T4N0M0	2	IIB	Malignant
E1	73	71	M	Colon	Adenocarcinoma	T4N2M0	2	IIIC	Malignant
E2	74	38	F	Colon	Adenocarcinoma	T3N1M0	2	IIIB	Malignant
E3	75	51	M	Colon	Adenocarcinoma	T3N1M0	*	IIIB	Malignant
E4	76	64	F	Colon	Adenocarcinoma	T3N1M0	2	IIIB	Malignant

E5	77	68	M	Colon	Adenocarcinoma	T4N2M0	*	IIIC	Malignant
E6	78	42	M	Colon	Adenocarcinoma	T3N1M0	2	IIIB	Malignant
E7	79	40	M	Colon	Adenocarcinoma	T4N0M0	2	IIB	Malignant
E8	80	63	F	Colon	Adenocarcinoma	T3N0M0	2	IIA	Malignant
E9	81	51	F	Colon	Adenocarcinoma	T4N0M1	2	IV	Malignant
E10	82	76	M	Colon	Adenocarcinoma	T3N0M0	2	IIA	Malignant
E11	83	74	M	Colon	Adenocarcinoma	T4N2M0	2	IIIC	Malignant
E12	84	51	F	Colon	Adenocarcinoma	T4N0M0	2	IIB	Malignant
E13	85	56	F	Colon	Adenocarcinoma	T3N0M0	2	IIA	Malignant
E14	86	73	F	Colon	Adenocarcinoma	T4N0M0	2	IIB	Malignant
E15	87	70	M	Colon	Adenocarcinoma	T3N2M0	2	IIIB	Malignant
E16	88	69	M	Colon	Adenocarcinoma	T2N0M0	2	I	Malignant
E17	89	69	M	Colon	Adenocarcinoma	T4N2M0	2	IIIC	Malignant
E18	90	46	M	Colon	Adenocarcinoma	T3N0M0	2	IIA	Malignant
F1	91	80	M	Colon	Adenocarcinoma	T4N1M0	2	IIIB	Malignant
F2	92	72	M	Colon	Adenocarcinoma	T4N2M0	2	IIIC	Malignant
F3	93	69	F	Colon	Adenocarcinoma	T3N1M0	2	IIIB	Malignant
F4	94	58	F	Colon	Adenocarcinoma	T4N0M0	2	IIB	Malignant
F5	95	48	F	Colon	Adenocarcinoma	T4N1M0	2	IIIB	Malignant
F6	96	62	M	Colon	Adenocarcinoma	T3N0M0	2	IIA	Malignant
F7	97	62	M	Colon	Adenocarcinoma	T3N0M0	*	IIA	Malignant
F8	98	64	M	Colon	Adenocarcinoma	T3N1M0	2--3	IIIB	Malignant
F9	99	66	F	Colon	Adenocarcinoma	T4N0M0	2	IIB	Malignant
F10	100	65	M	Colon	Adenocarcinoma	T3N0M0	2	IIA	Malignant
F11	101	82	M	Colon	Adenocarcinoma	T4N0M0	*	IIB	Malignant
F12	102	71	M	Colon	Adenocarcinoma	T3N0M0	2	IIA	Malignant
F13	103	45	M	Colon	Adenocarcinoma	T4N1M0	2	IIIB	Malignant
F14	104	62	F	Colon	Adenocarcinoma	T4N1M0	2	IIIB	Malignant
F15	105	52	F	Colon	Adenocarcinoma	T3N1M0	2	IIIB	Malignant
F16	106	40	M	Colon	Adenocarcinoma (sparse)	T4N1M0	2	IIIB	Malignant
F17	107	61	M	Colon	Adenocarcinoma	T3N2M0	2	IIIB	Malignant
F18	108	34	M	Colon	Adenocarcinoma	T3N0M0	2	IIA	Malignant
G1	109	70	M	Colon	Adenocarcinoma	T3N0M0	2	IIA	Malignant
G2	110	67	F	Colon	Adenocarcinoma	T3N1M0	2	IIIB	Malignant
G3	111	69	M	Colon	Adenocarcinoma	T3N0M0	2	IIA	Malignant
G4	112	58	F	Colon	Adenocarcinoma	T3N1M0	2	IIIB	Malignant
G5	113	70	M	Colon	Adenocarcinoma	T4N0M0	2	IIB	Malignant
G6	114	61	M	Colon	Adenocarcinoma	T3N1M0	2	IIIB	Malignant
G7	115	70	F	Colon	Adenocarcinoma	T3N0M0	2	IIA	Malignant
G8	116	71	M	Colon	Adenocarcinoma	T4N0M0	*	IIB	Malignant
G9	117	49	F	Colon	Adenocarcinoma	T3N0M0	*	IIA	Malignant
G10	118	45	M	Colon	Adenocarcinoma	T3N0M0	2	IIA	Malignant
G11	119	62	M	Colon	Adenocarcinoma	T4N0M0	2	IIB	Malignant
G12	120	-	-	Colon	Adenocarcinoma	T3N0M0	2	IIA	Malignant
G13	121	38	F	Colon	Adenocarcinoma	T4N1M0	2	IIIB	Malignant
G14	122	58	F	Colon	Adenocarcinoma	T3N0M0	2	IIA	Malignant
G15	123	53	M	Colon	Adenocarcinoma	T3N0M0	2	IIA	Malignant
G16	124	34	M	Colon	Adenocarcinoma	T3N0M0	2	IIA	Malignant
G17	125	53	M	Colon	Adenocarcinoma	T3N0M0	2	IIA	Malignant
G18	126	67	M	Colon	Adenocarcinoma	T4N2M0	2	IIIC	Malignant
H1	127	53	F	Colon	Adenocarcinoma	T2N0M0	2	I	Malignant
H2	128	54	F	Colon	Adenocarcinoma	T4N1M0	2	IIIB	Malignant
H3	129	64	M	Colon	Adenocarcinoma	T3N0M0	*	IIA	Malignant
H4	130	65	M	Colon	Adenocarcinoma with necrosis	T3N0M0	2	IIA	Malignant
H5	131	59	M	Colon	Adenocarcinoma	T3N1M0	2	IIIB	Malignant
H6	132	52	M	Colon	Adenocarcinoma	T2N0M0	2	I	Malignant
H7	133	64	M	Colon	Adenocarcinoma	T2N2M0	3	IIIB	Malignant
H8	134	74	M	Colon	Mucinous adenocarcinoma	T3N1M0	2	IIIB	Malignant
H9	135	56	M	Colon	Adenocarcinoma	T3N0M0	2	IIA	Malignant
H10	136	70	M	Colon	Adenocarcinoma	T2N0M0	2	I	Malignant
H11	137	79	F	Colon	Adenocarcinoma	T4N0M0	2	IIB	Malignant
H12	138	77	M	Colon	Adenocarcinoma	T3N1M0	2	IIIB	Malignant
H13	139	49	M	Colon	Adenocarcinoma	T4N0M0	2	IIB	Malignant
H14	140	38	M	Colon	Mucinous adenocarcinoma (sparse)	T3N0M0	2	IIA	Malignant
H15	141	68	M	Colon	Mucinous adenocarcinoma (sparse)	T3N0M0	2	IIA	Malignant
H16	142	44	F	Colon	Mucinous adenocarcinoma	T3N0M0	2	IIA	Malignant

H17	143	34	M	Colon	Mucinous adenocarcinoma	T3N1M0	2	IIIB	Malignant
H18	144	62	M	Colon	Mucinous adenocarcinoma	T3N0M0	2	IIA	Malignant
I1	145	34	F	Colon	Adenocarcinoma	T4N0M0	3	IIB	Malignant
I2	146	65	M	Colon	Adenocarcinoma	T3N1M0	3	IIIB	Malignant
I3	147	41	F	Colon	Adenocarcinoma	T3N1M0	3	IIIB	Malignant
I4	148	-	-	Colon	Adenocarcinoma	T3N0M0	2	IIA	Malignant
I5	149	55	M	Colon	Adenocarcinoma	T3N1M0	2--3	IIIB	Malignant
I6	150	56	F	Colon	Adenocarcinoma	T3N1M0	2--3	IIIB	Malignant
I7	151	72	F	Colon	Adenocarcinoma	T3N1M0	2	IIIB	Malignant
I8	152	67	F	Colon	Adenocarcinoma	T2N0M0	3	I	Malignant
I9	153	74	M	Colon	Adenocarcinoma	T3N0M0	2	IIA	Malignant
I10	154	56	M	Colon	Adenocarcinoma	T3N0M0	3	IIA	Malignant
I11	155	47	F	Colon	Adenocarcinoma	T3N0M0	3	IIA	Malignant
I12	156	42	F	Colon	Adenocarcinoma	T3N0M0	2--3	IIA	Malignant
I13	157	80	F	Colon	Adenocarcinoma	T3N1M0	3	IIIB	Malignant
I14	158	57	M	Colon	Mucinous adenocarcinoma	T3N1M0	2--3	IIIB	Malignant
I15	159	50	M	Colon	Adenocarcinoma	T3N0M0	*	IIA	Malignant
I16	160	47	M	Colon	Adenocarcinoma	T4N2M0	3	IIIC	Malignant
I17	161	54	F	Colon	Adenocarcinoma	T4N0M0	3	IIB	Malignant
I18	162	73	F	Colon	Adenocarcinoma	T3N0M0	3	IIA	Malignant
J1	163	62	F	Colon	Adenocarcinoma	T3N1M0	3	IIIB	Malignant
J2	164	64	M	Colon	Adenocarcinoma	T3N0M0	3	IIA	Malignant
J3	165	48	F	Colon	Adenocarcinoma	T4N1M1	3	IV	Malignant
J4	166	72	M	Colon	Adenocarcinoma	T3N0M0	3	IIA	Malignant
J5	167	40	M	Colon	Adenocarcinoma	T4N2M0	3	IIIC	Malignant
J6	168	42	F	Colon	Adenocarcinoma	T3N0M0	3	IIA	Malignant
J7	169	47	F	Colon	Adenocarcinoma	T3N0M0	3	IIA	Malignant
J8	170	49	M	Colon	Adenocarcinoma	T3N0M0	2	IIA	Malignant
J9	171	78	M	Colon	Adenocarcinoma	T3N0M0	3	IIA	Malignant
J10	172	22	F	Colon	Adenocarcinoma	T4N2M0	3	IIIC	Malignant
J11	173	48	F	Colon	Adenocarcinoma	T3N0M0	3	IIA	Malignant
J12	174	73	F	Colon	Adenocarcinoma	T4N1M0	3	IIIB	Malignant
J13	175	38	M	Colon	Adenocarcinoma	T4N0M0	3	IIB	Malignant
J14	176	75	M	Colon	Adenocarcinoma	T4N0M0	3	IIB	Malignant
J15	177	50	M	Colon	Adenocarcinoma	T2N0M0	3	I	Malignant
J16	178	49	F	Colon	Adenocarcinoma with necrosis	T4N2M0	3	IIIC	Malignant
J17	179	72	F	Colon	Adenocarcinoma	T3N0M0	3	IIA	Malignant
J18	180	30	M	Colon	Adenocarcinoma	T3N0M0	3	IIA	Malignant
K1	181	76	F	Colon	Adenocarcinoma	T3N0M0	3	IIA	Malignant
K2	182	39	M	Colon	Adenocarcinoma	T3N0M0	3	IIA	Malignant
K3	183	51	M	Colon	Adenocarcinoma	T3N0M0	3	IIA	Malignant
K4	184	35	M	Colon	Adenocarcinoma	T4N0M0	3	IIB	Malignant
K5	185	50	M	Colon	Adenocarcinoma	T4N0M0	3	IIB	Malignant
K6	186	78	F	Colon	Adenocarcinoma	T3N1M0	3	IIIB	Malignant
K7	187	72	M	Colon	Adenocarcinoma	T4N0M0	3	IIB	Malignant
K8	188	41	M	Colon	Adenocarcinoma	T4N0M0	3	IIB	Malignant
K9	189	53	M	Colon	Adenocarcinoma	T3N2M1	*	IV	Malignant
K10	190	48	F	Colon	Adenocarcinoma	T4N2M0	3	IIIC	Malignant
K11	191	43	F	Colon	Adenocarcinoma	T3N1M0	*	IIIB	Malignant
K12	192	48	M	Colon	Adenocarcinoma	T4N2M0	3	IIIC	Malignant
K13	193	69	M	Colon	Adenocarcinoma	T3N1M0	3	IIIB	Malignant
K14	194	71	M	Colon	Adenocarcinoma	T2N0M0	3	I	Malignant
K15	195	56	M	Colon	Mucinous adenocarcinoma	T4N2M0	3	IIIC	Malignant
K16	196	70	F	Colon	Adenocarcinoma	T3N1M0	3	IIIB	Malignant
K17	197	24	M	Colon	Mucinous adenocarcinoma	T3N0M0	3	IIA	Malignant
K18	198	68	F	Colon	Mucinous adenocarcinoma	T3N1M0	3	IIIB	Malignant
L1	199	58	F	Colon	Mucinous adenocarcinoma	T3N0M0	3	IIA	Malignant
L2	200	46	M	Colon	Mucinous adenocarcinoma	T3N0M0	3	IIA	Malignant
L3	201	81	F	Colon	Mucinous adenocarcinoma	T4N2M0	3	IIIC	Malignant
L4	202	28	F	Colon	Mucinous adenocarcinoma	T4N1M0	3	IIIB	Malignant
L5	203	42	M	Colon	Mucinous adenocarcinoma	T3N0M0	3	IIA	Malignant
L6	204	34	M	Colon	Mucinous adenocarcinoma	T3N1M0	3	IIIB	Malignant
L7	205	71	M	Colon	Signet ring cell carcinoma	T4N0M0	-	IIB	Malignant
L8	206	37	F	Colon	Signet ring cell carcinoma	T3N0M0	-	IIA	Malignant
L9	207	75	F	Colon	Signet ring cell carcinoma	T3N0M0	-	IIA	Malignant
L10	208	48	F	Colon	Signet ring cell carcinoma	T4N0M1	-	IV	Malignant

L11	209	35	M	Colon	Colon tissue	-	-	-	Normal
L12	210	40	M	Colon	Colon tissue	-	-	-	Normal
L13	211	21	F	Colon	Colon tissue	-	-	-	Normal
L14	212	45	M	Colon	Colon tissue	-	-	-	Normal
L15	213	38	M	Colon	Colon tissue	-	*	-	Normal
L16	214	30	M	Colon	Colon tissue	-	-	-	Normal
L17	215	45	M	Colon	Colon tissue	-	-	-	Normal
L18	216	22	M	Colon	Colon tissue	-	-	-	Normal
-	0	42	M	Adrenal gland	Pheochromocytoma (tissue marker)		-		Malignant

Supplement-2 Human Breast Cancer TMA

BR1503f : Breast cancer tissue array, including TNM and pathology grade, with IHC results of Her-2\ER\PR\Ki67, 75 cases/ 150 cores, replaced by BR1503h

Microarray Panel	Breast invasive ductal carcinoma tissue microarray, containing 3 each cases of adjacent normal breast tissue and breast fibroadenoma, 2 breast cystosarcoma phyllodes, 7 breast i invasive ductal carcinoma, duplicate cores per case
Cores	150
Cases	75
Row number	10
Column number	15
Core Diameter (mm)	1
Thickness (μm)	5
Tissue Array Type	FFPE
Species	Human
Applications	Routine histology procedures including Immunohistochemistry (IHC) and In Situ Hybridization (ISH), protocols which can be found at our support page.
Notes	1. TMA slides were sectioned and stored at 4°C and may not be fresh cut, but still suitable for IHC. Please request fresh cut if experiment involves phospho-specific antibodies, RN of 3 slides per TMA must be purchased to cover the cost of trimming for fresh sectioning. 2. Most TMA slides were not coated with an extra layer of paraffin (tissue cores can be ea **tissue detachment during antigen retrieval, unbaked slides must be baked for at least 30 to 120 minutes at 60°C**. before putting into xylene for de-paraffinization. Baked slid In the following specsheet,"*" means invalid core; "-" means no applicable or negative in IHC markers.

BR1503f H&E

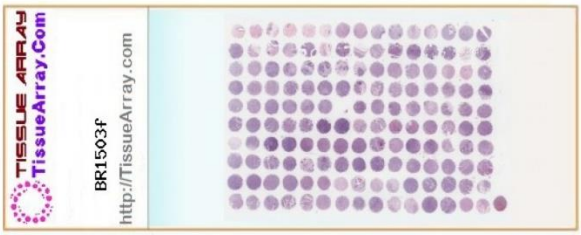

Mouseover and click individual cores to view high resolution images.

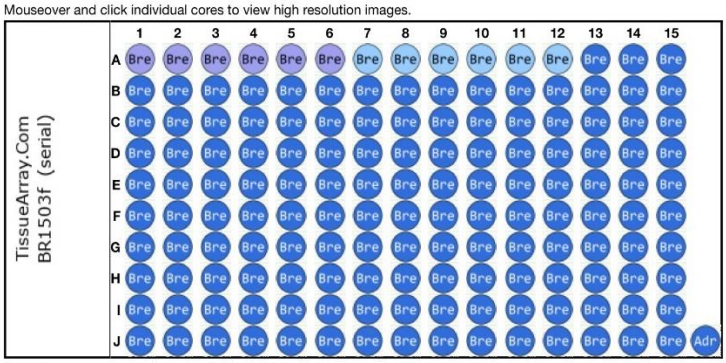

Legend: **Bre** - Breast
- Benign tumor, - Malignant tumor, - NAT

, tissue IDs are available in exported Excel files.

Pos.	No.	Age	Sex	Organ/Anatomic Site	Pathology diagnosis	TNM	Grade	Stage	Type	ER	PR
A1	1	46	F	Breast	Adjacent normal breast duct tissue	-	-		NAT	+	+
A2	2	46	F	Breast	Adjacent normal breast tissue	-	-		NAT	+	+
A3	3	42	F	Breast	Adjacent normal breast tissue	-	-		NAT	-	++
A4	4	42	F	Breast	Adjacent normal breast tissue(fibrous tissue)	-	-		NAT	*	*
A5	5	43	F	Breast	Adjacent normal breast tissue (fibrous tissue)	-	-		NAT	*	*
A6	6	43	F	Breast	Adjacent normal breast tissue	-	-		NAT	+	+
A7	7	48	F	Breast	Fibroadenoma	-	-		Benign	++	+
A8	8	48	F	Breast	Fibroadenoma	-	-		Benign	++	+
A9	9	19	F	Breast	Fibroadenoma	-	-		Benign	+++	+++
A10	10	19	F	Breast	Fibroadenoma	-	-		Benign	+++	+++
A11	11	54	F	Breast	Fibroadenoma	-	-		Benign	-	-
A12	12	54	F	Breast	Fibroadenoma	-	-		Benign	-	-
A13	13	49	F	Breast	Lowly malignant cystosarcoma phyllodes	-	-		Malignant	+	+++
A14	14	49	F	Breast	Lowly malignant cystosarcoma phyllodes	-	-		Malignant	+	+++
A15	15	69	F	Breast	Lowly malignant cystosarcoma phyllodes	-	-		Malignant	++	+++
B1	16	69	F	Breast	Lowly malignant cystosarcoma phyllodes	-	-		Malignant	-	-
B2	17	49	F	Breast	Intraductal carcinoma(breast tissue)	TisN0M0	-		Malignant	+	+
B3	18	49	F	Breast	Intraductal carcinoma(breast tissue)	TisN0M0	-		Malignant	+	+
B4	19	50	F	Breast	Intraductal carcinoma(sparse)	TisN0M0	-		Malignant	-	-
B5	20	50	F	Breast	Intraductal carcinoma	TisN0M0	-		Malignant	-	-
B6	21	36	F	Breast	Intraductal carcinoma(blank)	TisN0M0	-		Malignant	*	*
B7	22	36	F	Breast	Intraductal carcinoma	TisN0M0	-		Malignant	+++	+++
B8	23	67	F	Breast	Intraductal carcinoma(sparse)	TisN0M0	-		Malignant	-	-
B9	24	67	F	Breast	Intraductal carcinoma with early infiltrate(sparse)	TisN0M0	-		Malignant	-	-
B10	25	43	F	Breast	Intraductal carcinoma with early infiltrate	TisN0M0	-		Malignant	+++	++
B11	26	43	F	Breast	Intraductal carcinoma	TisN0M0	-		Malignant	+++	++
B12	27	54	F	Breast	Intraductal carcinoma	TisN0M0	-		Malignant	+++	+++
B13	28	54	F	Breast	Intraductal carcinoma	TisN0M0	-		Malignant	+++	+++
B14	29	45	F	Breast	Intraductal carcinoma(adipose tissue)	TisN0M0	-		Malignant	*	*
B15	30	45	F	Breast	Intraductal carcinoma	TisN0M0	-		Malignant	+++	+++
C1	31	54	F	Breast	Invasive ductal carcinoma	T3N1M0	1		Malignant	-	-

C2	32	54	F	Breast	Invasive ductal carcinoma	T3N1M0	1		Malignant	-	-
C3	33	60	F	Breast	Invasive ductal carcinoma	T2N0M0	1		Malignant	-	-
C4	34	60	F	Breast	Invasive ductal carcinoma	T2N0M0	1		Malignant	-	-
C5	35	38	F	Breast	Invasive ductal carcinoma	T3N0M0	1--2		Malignant	+++	+++
C6	36	38	F	Breast	Invasive ductal carcinoma	T3N0M0	1--2		Malignant	+++	+++
C7	37	41	F	Breast	Invasive ductal carcinoma	T2N0M0	1--2		Malignant	+	+
C8	38	41	F	Breast	Invasive ductal carcinoma	T2N0M0	1--2		Malignant	++	++
C9	39	71	F	Breast	Invasive ductal carcinoma	T4N2M0	2		Malignant	++	+++
C10	40	71	F	Breast	Invasive ductal carcinoma	T4N2M0	2		Malignant	++	+++
C11	41	70	F	Breast	Invasive ductal carcinoma	T2N0M0	2		Malignant	-	-
C12	42	70	F	Breast	Invasive ductal carcinoma	T2N0M0	2		Malignant	-	-
C13	43	64	F	Breast	Invasive ductal carcinoma	T2N0M0	2		Malignant	-	++
C14	44	64	F	Breast	Invasive ductal carcinoma(blank)	T2N0M0	2		Malignant	*	*
C15	45	47	F	Breast	Invasive ductal carcinoma	T3N0M0	2		Malignant	+++	++
D1	46	47	F	Breast	Invasive ductal carcinoma	T3N0M0	2		Malignant	+++	++
D2	47	69	F	Breast	Invasive ductal carcinoma	T4N0M0	2		Malignant	-	++
D3	48	69	F	Breast	Invasive ductal carcinoma	T4N0M0	2		Malignant	-	++
D4	49	51	F	Breast	Invasive ductal carcinoma	T2N2M0	2		Malignant	-	-
D5	50	51	F	Breast	Invasive ductal carcinoma	T2N2M0	2		Malignant	-	-
D6	51	58	F	Breast	Invasive ductal carcinoma	T2N0M0	2		Malignant	-	-
D7	52	58	F	Breast	Invasive ductal carcinoma	T2N0M0	2		Malignant	-	-
D8	53	31	F	Breast	Invasive ductal carcinoma	T2N0M0	2		Malignant	++	+++
D9	54	31	F	Breast	Invasive ductal carcinoma	T2N0M0	2		Malignant	++	+++
D10	55	64	F	Breast	Invasive ductal carcinoma	T2N0M0	2		Malignant	-	-
D11	56	64	F	Breast	Invasive ductal carcinoma	T2N0M0	2		Malignant	-	-
D12	57	55	F	Breast	Invasive ductal carcinoma	T3N2M0	2		Malignant	+++	+++
D13	58	55	F	Breast	Invasive ductal carcinoma	T3N2M0	2		Malignant	+++	+++
D14	59	52	F	Breast	Invasive ductal carcinoma	T2N2M0	2		Malignant	+	+++
D15	60	52	F	Breast	Invasive ductal carcinoma	T2N2M0	2		Malignant	+	+++
E1	61	42	F	Breast	Invasive ductal carcinoma	T2N2M0	2		Malignant	+++	+++
E2	62	42	F	Breast	Invasive ductal carcinoma	T2N2M0	2		Malignant	+++	+++
E3	63	47	F	Breast	Invasive ductal carcinoma	T4N1M0	2		Malignant	++	+++
E4	64	47	F	Breast	Invasive ductal carcinoma	T4N1M0	2		Malignant	++	+++
E5	65	50	F	Breast	Invasive ductal carcinoma	T2N1M0	2		Malignant	+	+++
E6	66	50	F	Breast	Invasive ductal carcinoma	T2N1M0	2		Malignant	++	+++
E7	67	74	F	Breast	Invasive ductal carcinoma(blank)	T2N1M0	-		Malignant	*	*
E8	68	74	F	Breast	Invasive ductal carcinoma	T2N1M0	2		Malignant	+++	+++
E9	69	41	F	Breast	Invasive ductal carcinoma	T2N2M0	2		Malignant	+++	+++
E10	70	41	F	Breast	Invasive ductal carcinoma	T2N2M0	2		Malignant	+++	+++
E11	71	34	F	Breast	Invasive ductal carcinoma	T3N0M0	2		Malignant	-	+++
E12	72	34	F	Breast	Invasive ductal carcinoma	T3N0M0	2		Malignant	-	+++
E13	73	60	F	Breast	Invasive ductal carcinoma	T2N2M0	2		Malignant	-	-
E14	74	60	F	Breast	Invasive ductal carcinoma	T2N2M0	2		Malignant	-	-
E15	75	50	F	Breast	Invasive ductal carcinoma	T4N0M0	2		Malignant	-	-
F1	76	50	F	Breast	Invasive ductal carcinoma	T4N0M0	2		Malignant	-	-
F2	77	55	F	Breast	Invasive ductal carcinoma	T2N0M0	2		Malignant	+	+++
F3	78	55	F	Breast	Invasive ductal carcinoma	T2N0M0	2		Malignant	+	+++
F4	79	65	F	Breast	Invasive ductal carcinoma	T2N1M0	2		Malignant	-	-
F5	80	65	F	Breast	Invasive ductal carcinoma	T2N1M0	2		Malignant	-	-
F6	81	48	F	Breast	Invasive ductal carcinoma	T2N2M0	2		Malignant	+++	+++
F7	82	48	F	Breast	Invasive ductal carcinoma	T2N2M0	2		Malignant	+++	+++
F8	83	38	F	Breast	Invasive ductal carcinoma	T2N1M0	2		Malignant	-	-
F9	84	38	F	Breast	Invasive ductal carcinoma	T2N1M0	2		Malignant	-	-
F10	85	45	F	Breast	Invasive ductal carcinoma	T4N2M0	2		Malignant	+++	+++
F11	86	45	F	Breast	Invasive ductal carcinoma	T4N2M0	2		Malignant	+++	+++
F12	87	43	F	Breast	Invasive ductal carcinoma	T2N0M0	2		Malignant	+++	++
F13	88	43	F	Breast	Invasive ductal carcinoma(adipose tissue)	T2N0M0	2		Malignant	*	*
F14	89	48	F	Breast	Invasive ductal carcinoma	T2N0M0	2		Malignant	+	+++
F15	90	48	F	Breast	Invasive ductal carcinoma	T2N0M0	2		Malignant	++	+++
G1	91	52	F	Breast	Invasive ductal carcinoma(fibrous tissue)	T2N0M0	-		Malignant	*	*
G2	92	52	F	Breast	Invasive ductal carcinoma	T2N0M0	2		Malignant	++	+++
G3	93	51	F	Breast	Invasive ductal carcinoma	T3N1M0	2		Malignant	-	-
G4	94	51	F	Breast	Invasive ductal carcinoma	T3N1M0	2		Malignant	-	-
G5	95	52	F	Breast	Invasive ductal carcinoma	T3N0M0	2		Malignant	-	++
G6	96	52	F	Breast	Invasive ductal carcinoma	T3N0M0	2		Malignant	-	+++
G7	97	45	F	Breast	Invasive ductal carcinoma	T1N0M0	2		Malignant	-	-
G8	98	45	F	Breast	Invasive ductal carcinoma	T1N0M0	2		Malignant	-	-
G9	99	40	F	Breast	Invasive ductal carcinoma	T2N0M0	2		Malignant	++	++
G10	100	40	F	Breast	Invasive ductal carcinoma	T2N0M0	2		Malignant	++	++
G11	101	30	F	Breast	Invasive ductal carcinoma	T4N0M0	2--3		Malignant	+++	+++
G12	102	30	F	Breast	Invasive ductal carcinoma	T4N0M0	2--3		Malignant	+++	+++
G13	103	33	F	Breast	Invasive ductal carcinoma	T1N0M0	2--3		Malignant	+	+
G14	104	33	F	Breast	Invasive ductal carcinoma	T1N0M0	2--3		Malignant	+	+
G15	105	35	F	Breast	Invasive ductal carcinoma	T2N0M0	2--3		Malignant	-	-
H1	106	35	F	Breast	Invasive ductal carcinoma	T2N0M0	2--3		Malignant	-	-
H2	107	44	F	Breast	Invasive ductal carcinoma	T2N0M0	2--3		Malignant	-	++
H3	108	44	F	Breast	Invasive ductal carcinoma	T2N0M0	2--3		Malignant	-	++
H4	109	43	F	Breast	Invasive ductal carcinoma	T2N1M0	2--3		Malignant	+	+++

H5	110	43	F	Breast	Invasive ductal carcinoma	T2N1M0	2--3		Malignant	+	+++
H6	111	41	F	Breast	Invasive ductal carcinoma	T3N1M0	2--3		Malignant	-	-
H7	112	41	F	Breast	Invasive ductal carcinoma	T3N1M0	2--3		Malignant	-	-
H8	113	59	F	Breast	Invasive ductal carcinoma	T2N0M0	2--3		Malignant	++	+++
H9	114	59	F	Breast	Invasive ductal carcinoma	T2N0M0	2--3		Malignant	++	+++
H10	115	34	F	Breast	Invasive ductal carcinoma	T4N0M0	2--3		Malignant	+	+++
H11	116	34	F	Breast	Invasive ductal carcinoma	T4N0M0	2--3		Malignant	+	+++
H12	117	47	F	Breast	Invasive ductal carcinoma	T2N0M0	2--3		Malignant	++	+
H13	118	47	F	Breast	Invasive ductal carcinoma	T2N0M0	2--3		Malignant	++	+
H14	119	45	F	Breast	Invasive ductal carcinoma	T3N0M0	3		Malignant	-	-
H15	120	45	F	Breast	Invasive ductal carcinoma with necrosis	T3N0M0	3		Malignant	-	-
I1	121	34	F	Breast	Invasive ductal carcinoma	T2N0M0	3		Malignant	-	-
I2	122	34	F	Breast	Invasive ductal carcinoma	T2N0M0	3		Malignant	-	-
I3	123	56	F	Breast	Invasive ductal carcinoma	T3N0M0	3		Malignant	+	+++
I4	124	56	F	Breast	Invasive ductal carcinoma	T3N0M0	3		Malignant	+	+++
I5	125	44	F	Breast	Invasive ductal carcinoma	T2N2M0	3		Malignant	-	-
I6	126	44	F	Breast	Invasive ductal carcinoma	T2N2M0	3		Malignant	-	-
I7	127	62	F	Breast	Invasive ductal carcinoma(fibrous tissue)	T2N1M0	-		Malignant	*	*
I8	128	62	F	Breast	Invasive ductal carcinoma	T2N1M0	3		Malignant	-	-
I9	129	49	F	Breast	Invasive ductal carcinoma	T3N1M0	3		Malignant	-	-
I10	130	49	F	Breast	Invasive ductal carcinoma	T3N1M0	3		Malignant	-	-
I11	131	50	F	Breast	Invasive ductal carcinoma	T2N0M0	3		Malignant	+++	+++
I12	132	50	F	Breast	Invasive ductal carcinoma	T2N0M0	3		Malignant	++	+++
I13	133	50	F	Breast	Invasive ductal carcinoma	T2N2M0	3		Malignant	-	-
I14	134	50	F	Breast	Invasive ductal carcinoma	T2N2M0	3		Malignant	-	-
I15	135	62	F	Breast	Invasive ductal carcinoma	T1N0M0	3		Malignant	-	-
J1	136	62	F	Breast	Invasive ductal carcinoma	T1N0M0	3		Malignant	-	-
J2	137	58	F	Breast	Invasive ductal carcinoma	T2N0M0	3		Malignant	-	-
J3	138	58	F	Breast	Invasive ductal carcinoma	T2N0M0	3		Malignant	-	-
J4	139	57	F	Breast	Invasive ductal carcinoma	T3N0M0	3		Malignant	-	-
J5	140	57	F	Breast	Invasive ductal carcinoma	T3N0M0	3		Malignant	-	-
J6	141	56	F	Breast	Invasive ductal carcinoma	T2N0M0	3		Malignant	+	++
J7	142	56	F	Breast	Invasive ductal carcinoma	T2N0M0	3		Malignant	++	++
J8	143	50	F	Breast	Invasive ductal carcinoma	T2N2M0	3		Malignant	++	+++
J9	144	50	F	Breast	Invasive ductal carcinoma	T2N2M0	3		Malignant	++	+++
J10	145	53	F	Breast	Invasive ductal carcinoma	T4N2M0	3		Malignant	-	+++
J11	146	53	F	Breast	Invasive ductal carcinoma	T4N2M0	3		Malignant	-	+++
J12	147	43	F	Breast	Invasive ductal carcinoma	T2N0M0	3		Malignant	-	-
J13	148	43	F	Breast	Invasive ductal carcinoma	T2N0M0	3		Malignant	-	-
J14	149	81	F	Breast	Invasive ductal carcinoma	T3N0M0	3		Malignant	-	-
J15	150	81	F	Breast	Invasive ductal carcinoma (sparse)	T3N0M0	-		Malignant	-	-
-	0	42	M	Adrenal gland	Pheochromocytoma (tissue marker)		-		Malignant		